ONR-R-96

ANDERSON/SPRINGER/WARDER

Physico-Chemical Diagnostics of Plasmas

N65 14264
(ACCESSION NUMBER)
442
(PAGES)
CR 60781
(NASA CR OR TMX OR AD NUMBER)
(THRU)
(CODE)
23
(CATEGORY)
FACILITY FORM 602

PROCEEDINGS OF THE FIFTH BIENNIAL GAS DYNAMICS SYMPOSIUM

Edited by

Thomas P. Anderson,

Robert W. Springer,

Richard C. Warder, Jr.

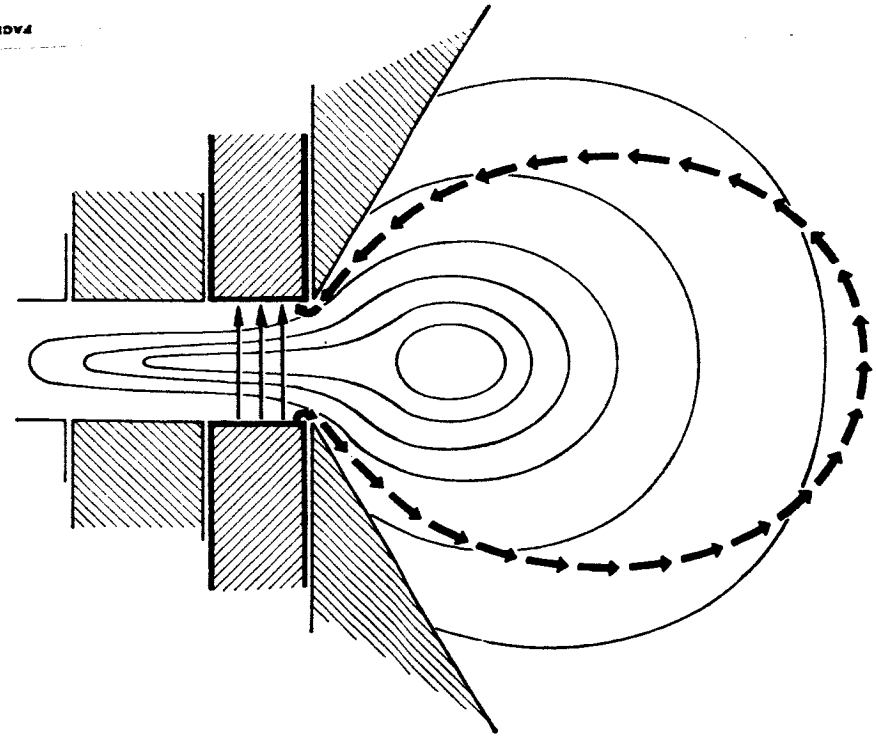

estern
rsity
ss

Physico-Chemical Diagnostics of Plasmas

The American Institute
of Aeronautics and Astronautics
AND
The Gas Dynamics Laboratory
Northwestern University

Physico-Chemical Diagnostics of Plasmas

Proceedings of the Fifth Biennial Gas Dynamics Symposium

EDITORS
Thomas P. Anderson
Robert W. Springer
Richard C. Warder, Jr.

NORTHWESTERN UNIVERSITY PRESS
Evanston

LIBRARY OF CONGRESS CATALOG CARD NUMBER: 64–14421

Printed in Great Britain

PREFACE

In 1955 The American Institute of Aeronautics and Astronautics (then The American Rocket Society) and Northwestern University initiated a series of biennial symposia on gas dynamics to deal with recent and specialized fundamental aspects of jet propulsion. Since then these meetings have widened in scope to stay abreast of advances in science and technology. Thus previous symposia have treated Aerothermochemistry (1955), Transport Properties in Gases (1957), Dynamics of Conducting Gases (1959), and Magnetohydrodynamics (1960).

The present volume constitutes the Proceedings of the Fifth Biennial Gas Dynamics Symposium which was held in Evanston on August 14, 15, and 16, 1963. Continuing along the lines established by the earlier meetings—that of treating interdisciplinary topics of current interest to the scientist-engineer—the theme of this symposium was the physico-chemical diagnostics of plasmas. Nearly all aspects of experimental plasma diagnostics were discussed in the twenty-one papers presented. The topics include both research papers and reviews of the current state-of-the-art.

The contributions to this volume have been edited as little as possible and no attempt has been made to change the style and nomenclature of the various authors. The editors hope that this volume will prove to be a useful reference for the fields considered.

THOMAS P. ANDERSON
ROBERT W. SPRINGER
RICHARD C. WARDER, JR.

Evanston, Illinois
November, 1963

ACKNOWLEDGMENTS

Acknowledgment of each of the great number of people who contributed to the success of this symposium is not possible beyond this general thank you. However, the editors would like to note the contributions of some who deserve special mention.

First of all we thank Professor Ali Bulent Cambel, who initiated the Gas Dynamics Symposium and has continued to serve as Co-Chairman of the Symposium Committee, for his cooperation and advice in the organization of this meeting and the publication of this volume.

The speakers were of course essential and deserve particular thanks for the time and effort spent in the preparation and presentation of the various studies. Also deserving of special note are the session chairmen, Daniel Bershader, Eino Latvala, Martin Lessen, and Henri Hodara, for their able guidance of the sessions' business. Robert B. Banks gave a very interesting banquet speech and his effort in this regard, along with that of Martin Lessen who served as Toastmaster, was appreciated.

Thanks are extended to the staff of the American Institute of Aeronautics and Astronautics, in particular to James J. Harford and Miss Bobbie Chifos; to J. Roscoe Miller, President of Northwestern University, who gave the opening remarks; and to Mrs. Ethel Majerus and the rest of the secretarial staff of the Gas Dynamics Laboratory. The following students gave valuable assistance: Daniel P. Aeschliman, James M. Berry, Charles A. Boitnott, David L. Hector, William F. Hug, and Said E. Matar.

Finally, the financial aspects of such a meeting are no small matter, and we would like to acknowledge the generosity of the following government and industrial sponsors for their support, without which the symposium would not have been possible.

Government Sponsors:

Advanced Research Projects Agency
National Aeronautics and Space Administration
United States Air Force, Office of Scientific Research
United States Army Research Office (Durham)
United States Navy, Office of Naval Research

Industrial Sponsors:

Aerojet-General Corporation
Aerospace Corporation
The Bendix Corporation
The Boeing Company
Ford Motor Company
The Garrett Corporation
General Motors Corporation
International Harvester Company
Ling-Temco-Vought, Incorporated
Litton Systems, Incorporated
North American Aviation, Incorporated
Northrop Corporation
Phillips Petroleum Company
The Pure Oil Company
Radio Corporation of America
Republic Aviation Corporation
Texaco, Incorporated
Thiokol Chemical Corporation

THE EDITORS

CONTENTS

PREFACE v

ACKNOWLEDGMENTS vii

CHARLES B. WHARTON: *Plasma Diagnostic Techniques* . . . 3

JOHN A. THORNTON: *Electric and Electromagnetic Shock Tubes* . . 27

H. N. OLSEN: *The Measurement of Argon Transition Probabilities and Computation of Thermodynamic Properties of the Argon Plasma* 47

J. H. DE LEEUW: *Electrostatic Plasma Probes* 65

PAUL C. WILBER: *Experimental Investigation of the Characteristics of a Langmuir Probe in Ionized Low-Density Flows* . . . 97

ROBERT BETCHOV and EUGENE B. TURNER: *Measurements of MHD Turbulence with Magnetic Probes* 113

R. M. MONTGOMERY and R. A. HOLMES: *Some Experiments in Radio-Frequency Diagnostics of Partially-Ionized Plasmas* . . . 131

W. K. MCGREGOR: *Spectroscopic Measurements in Plasmas* . . . 143

KENNETH M. FOREMAN and MAURICE E. LEVY: *Comparative Spectroscopic Studies of Electromagnetically-Driven Hypersonic Waves in Elemental Gases and Detonable Mixtures* . . . 167

ROBERT B. SPIERS, JR, and CHARLES HUSSON: *Development of a Rocket-borne Spectroradiometer to Measure the Radiation Environment of a Reentry Vehicle* 187

M. R. DENISON and R. W. ZIEMER: *Investigation of the Phenomena in Crossed-Field Plasma Accelerators* 201

ALAN F. KLEIN: *A Survey of Optical Interferometry as Applied to Plasma Studies* 233

KOICHI OSHIMA: *Microwave Diagnostics of a Partly-Ionized Flow in the Presence of a Magnetic Field* 247

CHARLES E. SHEPARD and VELVIN R. WATSON: *Performance of a Constricted-Arc Discharge in a Supersonic Nozzle* . . . 261

PHILIP BROCKMAN, ROBERT V. HESS, and RICHARD E. WEINSTEIN: *Measurements and Theoretical Interpretation of Hall Currents for Steady Axial Discharges in Radial Magnetic Fields* . . 273

STERGE T. DEMETRIADES: *Momentum Transfer to Plasmas by Lorentz Forces* 297

L. J. KRZYCKI, H. M. LARSEN, and W. M. BYRNE, JR.: *Magnetohydrodynamic Power Generation from a Supersonic Rocket Exhaust* 329

A. I. CARSWELL, M. P. BACHYNSKI, and G. G. CLOUTIER: *Microwave Measurements of Electromagnetic Properties of Plasma Flow-Fields* 355

ALLEN E. FUHS: *Flight Instrumentation for the Reentry Plasma Sheath* 383

BORIS RAGENT: *X-Ray Densitometer for Use in Plasma Streams* . 403

T. HERBERT DIMMOCK and WILLIAM R. KINEYKO: *Ionization Profiles in Low-Pressure Exhausts* 423

Physico-Chemical Diagnostics of Plasmas

1. Charles B. Wharton: *Plasma Diagnostic Techniques*

The study of plasma diagnostics is concerned with making significant, nonperturbing measurements of plasma. The term "diagnostics" implies that compatible conclusions are drawn simultaneously from several observed symptoms. Ideally, the diagnostic measurements from any one plasma event should be self-sufficient, without relying on the repetition of successive events. This qualification may require the data-producing instrument to have large bandwidth and dynamic range (and perhaps multiple-channel capabilities) so that it can respond to rapid fluctuations.

A number of techniques have been widely developed, while others, although they may have intrinsic merit, for some reason or other have not had as wide an application. Some external measurements, notably microwave diagnostics, optical spectroscopy, and interferometry and radiometry, essentially do not perturb the plasma. Others involve internal probing, such as Langmuir probes, magnetic probes, RF probes, and particle beams, leading to various degrees of perturbation.

This paper presents a catalog of a number of useful techniques, grouped according to the quantities measured. Certain of the methods that have been extensively developed or have considerable potential are then expanded upon in detail. A number of illustrative examples are given and comparisons of techniques are made where possible. Photographs and sketches of some of the instruments are shown.

A number of interesting plasma diagnostic techniques have evolved over the last few years. Some have found wide application while others are lacking in some respect. Some measurements involve internal probing, such as Langmuir and magnetic probes, with the possibility of severely perturbing the plasma. Others are external measurements, such as microwave or optical probing and optical spectroscopy. In the latter methods the technology of the method itself is as complicated as the applications to plasma diagnostics. Other techniques are useful only in dense plasmas or in hot plasmas or in plasmas confined by an intense magnetic field. To sort out the measurements useful for a given kind of determination a brief survey of several techniques, grouped according to the quantities measured, is given in sections 1 through 9. Certain of the methods that have been extensively developed or have considerable potential are then expanded upon in the rest of the paper.

ED. NOTE: Dr. Wharton is at the General Atomic Division, General Dynamics Corporation, San Diego, California.

1. Electron Density and Distribution

a) Microwave interferometer; $10^{10} < n_e < 10^{14}/\text{cm}^3$
b) Microwave cavity perturbation; $10^{8} < n_e < 10^{12}/\text{cm}^3$
c) RF conductivity probes; $10^{8} < n_e < 10^{15}/\text{cm}^3$; for high collision rates
d) Microwave scattering; $10^{12} < n_e < 10^{14}/\text{cm}^3$; sensitive to instabilities
e) Optical interferometer; $10^{14} < n_e < 10^{19}/\text{cm}^3$
f) Optical Faraday rotation; $n_e > 10^{16}/\text{cm}^3$ for 10,000 gauss
g) Optical spectroscopic intensities; $n_e > 10^{13}$; equilibrium plasmas
h) Optical scattering; $10^{14} < n_e < 10^{19}/\text{cm}^3$
i) Optical Balmer series limit; $10^{13} < n_e < 10^{15}/\text{cm}^3$
j) Particle collectors; $10^{-6} < J_e < 1$ amp/cm^2; yields product qn_ev
k) Electron or ion beam scattering; sensitive to potential fluctuations

2. Electron Temperature

a) Microwave radiation intensities; $Te \gtrsim 0.1$ eV; stable plasmas
b) Doppler broadening of cyclotron radiation line; $Te \gtrsim 50$ eV.
c) Infrared and optical intensities; $Te \gtrsim 10$ eV; equilibrium plasmas
d) X-ray intensities; $Te \gtrsim 6$ keV; wall problems
e) Relative intensities of spectral lines; $1 < Te < 50$ eV.
f) Relative intensities of bremsstrahlung and recombination radiation
g) Doppler broadening of optical (Thomson) scattering; $Te \gtrsim 5$ eV.
h) Langmuir probes; $0.1 < Te < 1000$ eV; moderate densities

3. Ion Density and Distribution

a) Stark broadening of spectral lines; $n_i \gtrsim 10^{15}/\text{cm}^3$
b) Langmuir probes, single and double
c) Electron, ion, neutral atom, or neutron beam probes; $n_i \gtrsim 10^{14}/\text{cm}^3$
d) Diamagnetic effect (requires knowledge of temperature)
e) Alfvén and sound wave propagation; dense plasmas
f) Calorimetry (requires knowledge of temperature)
g) Radioactive gas tracers and collimated detectors
h) Charge-exchange neutral detectors

4. Ion Temperature and Energy

a) Calorimetry; total energy and momentum
b) Doppler broadening of spectral lines; $T_i > 5$ eV
c) External energy-momentum analyzer; samples escaping ions
d) Time-of-flight; gives particle or shock-front velocity
e) Diamagnetic effect; use magnetic probes inside and outside plasma

5. Neutral Density, Distribution, and Identity

a) Shielded ionization gauge
b) Ion or neutral atom beam scattering
c) Rayleigh scattering and resonance absorption of infrared and light photons by bound electrons
d) Schlieren and Mach–Zehnder photography
e) Charge-exchange detectors; fast neutrals
f) Molecular resonance spectroscopy; RF and infrared
g) Re-ionization by delayed ionizing pulses

6. Drift Velocity, Shock Velocity, Rotation, and Thrust

a) Doppler frequency of reflected microwaves
b) Doppler shift of synchrotron radiation
c) Doppler shift of spectral lines
d) Ballistics and calorimetry
e) Time-flight; probes, light, and microwave sampling
f) Nonreciprocity of phase shift for space charge and EM wave propagation

7. Instabilities and Turbulence

a) Electron and ion energy-momentum analysis; external measurement
b) Microwave radiation (nonthermal effects)
c) Microwave scattering from turbulence
d) Electron and ion beam scattering
e) Fast photography; time-resolved spectroscopy and total light; high densities
f) Magnetic probes and Rogowski loops
g) RF and Langmuir probes
h) External voltage–current measurements
i) X-rays (if high-energy electrons are generated)
j) Neutron energy analysis (if high-energy ions are present)

8. Sheath Regions

a) Langmuir probes
b) RF probes (sheath oscillations and space charge waves)
c) Electron and ion beam probes
d) Microwave scattering from sheath oscillations

9. Constituent Identity (Purity)

a) Optical and atomic-resonance spectroscopy
b) Ion cyclotron resonance absorption; e/m ratio
c) Magnetic analyzer; escaping ions
d) Mass spectrometer; neutral gas

10. Microwave Diagnostics

The standard techniques of interferometry and radiometry are useful in many plasma experiments (**1, 2**). Equipment in the spectrum of 1 cm to 4 mm wavelength is found to be convenient for a variety of plasma experiments.

Small-diameter, high-density plasmas require the highest frequencies available to have $\omega > \omega_p$, to avoid scattering and to have as many wavelengths as possible inside the plasma. Horn or other antennas must be kept small to provide narrow probing areas. The surrounding walls will then have to be coated with nonreflecting surfaces (commercially available) to inhibit stray reflection of the noncaptured part of the wave beam. Larger, lower density plasma experiments require lower frequencies.

The quantities measurable are the electron density, its spatial distribution, the cross section and collision frequency for momentum transfer, the electron temperature, the presence of certain plasma oscillation modes and instabilities, the drift velocities of electron streams, the velocity and position in time of wriggling columns, shock fronts, etc., and the local magnetic field strength—all as functions

of time. A composite microwave interferometer and radiometer system is shown in Figure 1. Not all of the components are necessary for some measurements. Some additional components will be needed for the measurement of Faraday rotation and shock-front velocity. Two or more systems, at different frequencies,

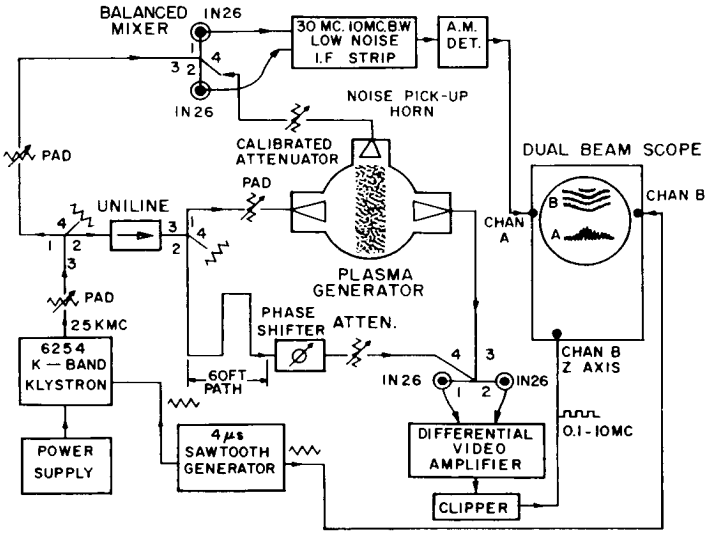

FIGURE 1. Composite microwave interferometer and radiometer for plasma diagnostics. The zebra stripe data presentation is generated.

running simultaneously are always preferred. Often the same radiators and circuits can be used for both frequencies by sorting out the waves at the detectors with filters.

This method of diagnostics does not perturb the plasma and has very short resolving times. The components are all available and the techniques well established.

10a. Microwave Transmission

A review of the relationships on which the techniques are based will be useful here to show how they are applied. Many of the relationships are exceedingly complicated, and the reader is referred to the references for their derivations. The plasma frequency, the natural oscillation frequency, is

$$\omega_p = \left(\frac{ne^2}{m\varepsilon_0}\right)^{1/2} \tag{1}$$

When a magnetic field is present in the plasma, the microwave conductivity is anisotropic. The index of refraction then must be described by tensors. Certain wave-polarizations, however, remain unchanged as they propagate and the index of refraction can then be written algebraically. These waves are called characteristic waves. A plane, transverse-electromagnetic (TEM) wave, incident at an angle θ (in respect to the magnetic field) on a plasma will generate a pair of these characteristic waves, each one having completely different properties. In optics the wave

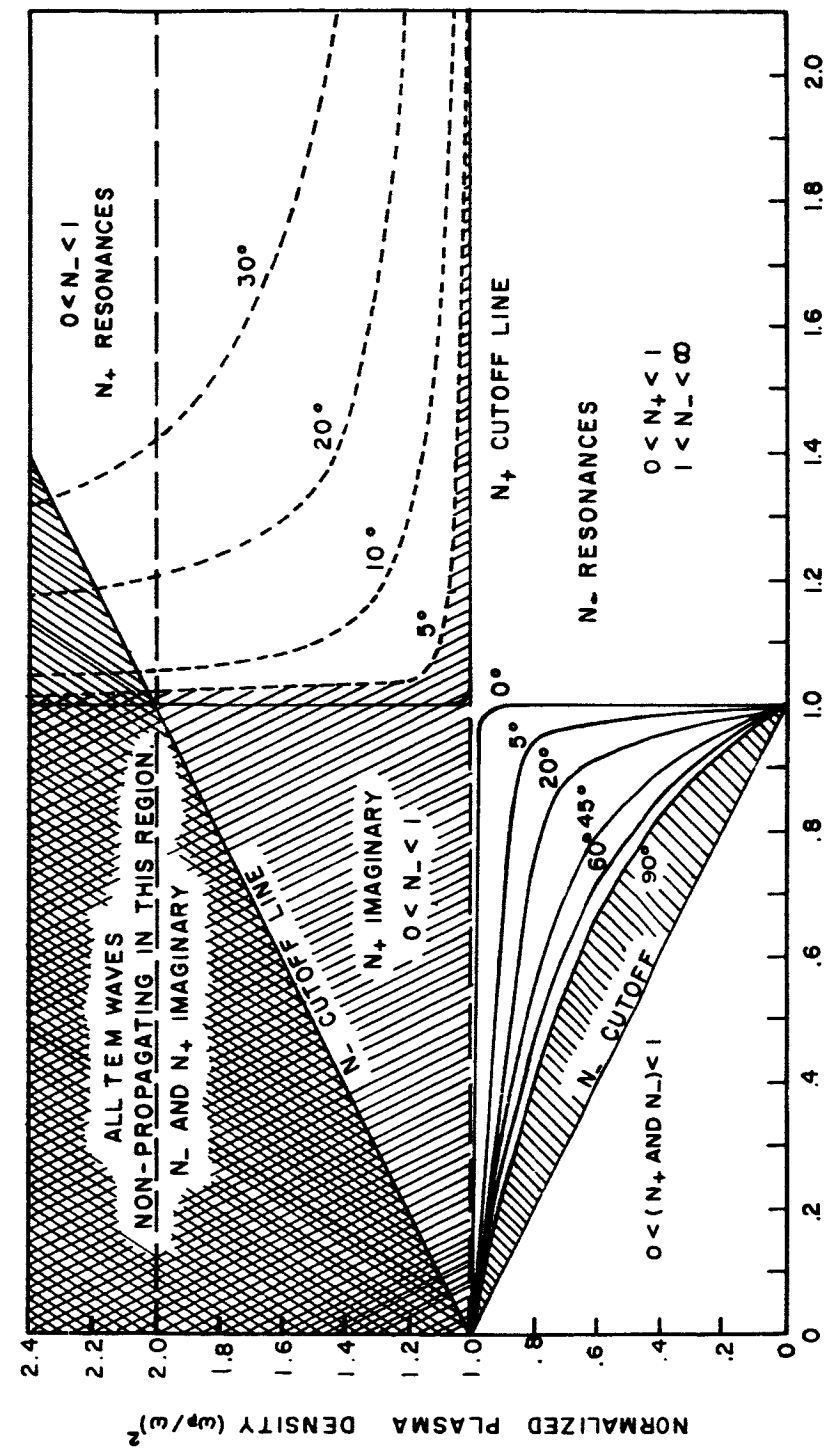

FIGURE 2. Cutoff intercepts of ordinary and extraordinary waves in the $\omega_b - \omega_p^2$ plane.

which is most nearly like that in the absence of the magnetic field is called the "ordinary wave". The other wave is the "extraordinary wave".

The cyclotron frequency, the angular frequency at which electrons spiral in a magnetic field, is

$$\omega_b = 2\pi f_b = \frac{e}{m} B \tag{2}$$

Expressed in megacycles and gauss

$$f_b = 2.8B \tag{3}$$

Figure 2 shows the intersection loci of the index of refraction, N, with the cutoff plane, ($N=0$), for some characteristic waves. The plus sign (taken from a $\pm$ in the equation for refractive index) corresponds to the ordinary wave; the minus sign to the extraordinary. The angles indicated are for θ, 0° being along B. The ranges of index are indicated in the various zones. The resonances are difficult to observe in practice. The electron density always falls to a low value at the walls of an experiment, so that a wave must go through a cutoff region to reach a resonance region, unless the magnetic field is increasing outwardly in a certain way. Synchrotron radiation emanating from a plasma thus is found to lie within a narrow cone about the field lines. "Whistler mode" propagation also is explained by this effect. Internal mode conversion and evanescent coupling through thin cutoff regions do allow resonances to be seen for waves propagating across field lines, especially at high plasma temperatures.

Figure 3a shows the real index, N, or Φ' for waves propagating in a plasma as a function of plasma density, for plasmas having various spatial distributions.

For propagation along magnetic field lines ($\theta=0°$) the characteristic waves are circularly polarized, contrarotating. They propagate at different velocities, so that when they re-emerge from the plasma the reconstituted plane wave has had its

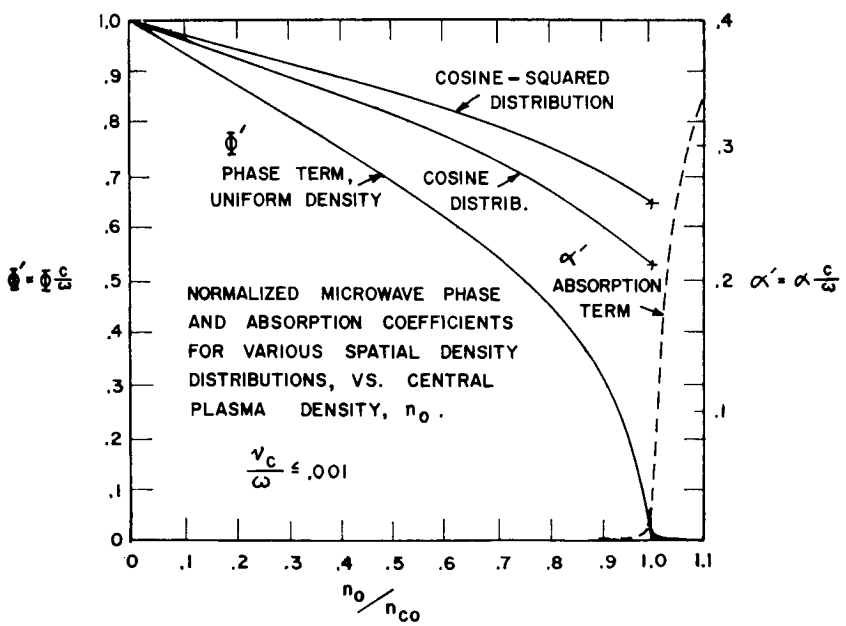

FIGURE 3a. Wave phaseshift in a plasma of various spatial distributions as a function of density.

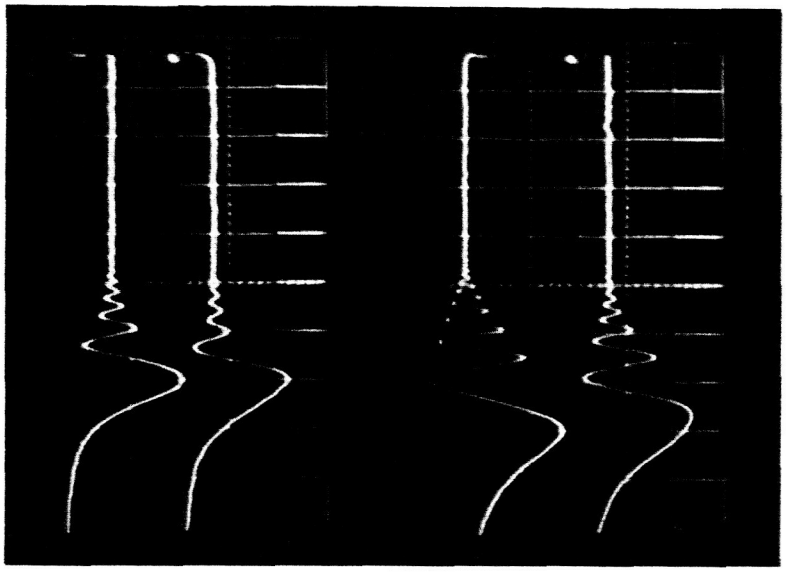

FIGURE 3b. Phaseshift data presented as interferometer fringes at frequencies of 70 Gc and 90 Gc. At the top the plasma was in helium at 80 microns pressure. The bottom fringes were obtained after 200 microns of argon had been added, showing the effect of collisions.

plane of polarization rotated. This phenomenon is known as the Faraday effect. The angle of rotation for a non-uniform path, L, is

$$\psi = \frac{1}{2}\frac{\omega}{c}\int_0^L [N_+(Z) - N_-(Z)]\,dZ \text{ radians} \tag{4}$$

where N_+ and N_- are the indexes of refraction of the two characteristic waves (functions of position). If the path has uniform density

$$\psi = \frac{\omega}{2c}[N_+ - N_-]L = 180^\circ[N_+ - N_-]\frac{L}{\lambda} \text{ degrees} \tag{5}$$

Equations (4) and (5) are strictly valid only if the wave damping is small. If the damping of one wave is larger than that of the other the emerging wave is not plane, but elliptically, polarized. Properly interpreted measurements thus are able to determine the density and its spatial distribution along the field lines, and the collision rates. If one wave is completely cut off, the emerging wave is circularly polarized. In Figure 2 the shaded triangle defined by $\omega_b/\omega > 1.0$, $\omega_p^2/\omega^2 > 2.0$, and the N cutoff line, for $\theta = 0^\circ$, represents such a medium. The index, N, is quite large, so that the plasma wavelength is short and waves cling closely to field lines. This wave type has been called variously "Whistler mode", "ducted-wave mode", and "high-density-window mode". Experimentally it can be seen only if the electron collision rate is low, since the damping is relatively large.

If the electrons are drifting, say to the right along a plasma column, the cyclotron frequency as measured from right to left will be higher than that from left to right, due to Doppler shift. The indexes and the Faraday rotation also will be nonreciprocal. The drift velocity is thus measurable.

When the density in a moving plasma front, such as a shock front or a wriggling arc column, is above cutoff, the reflected wave will be Doppler shifted and a Doppler radar system gives the instantaneous velocity. Occasionally velocities

measured in this way do not agree with those obtained optically or with probes. Supposedly, the velocities of charged particles (microwave) and excited particles (light emission) are not the same as the front expands.

10b. Microwave Radiation

Radiation emanating from the plasma bears a relationship to the density and temperature.

Blackbody Radiation: A dense plasma whose electrons have a thermal distribution (thermalization times short compared to characteristic plasma transients)

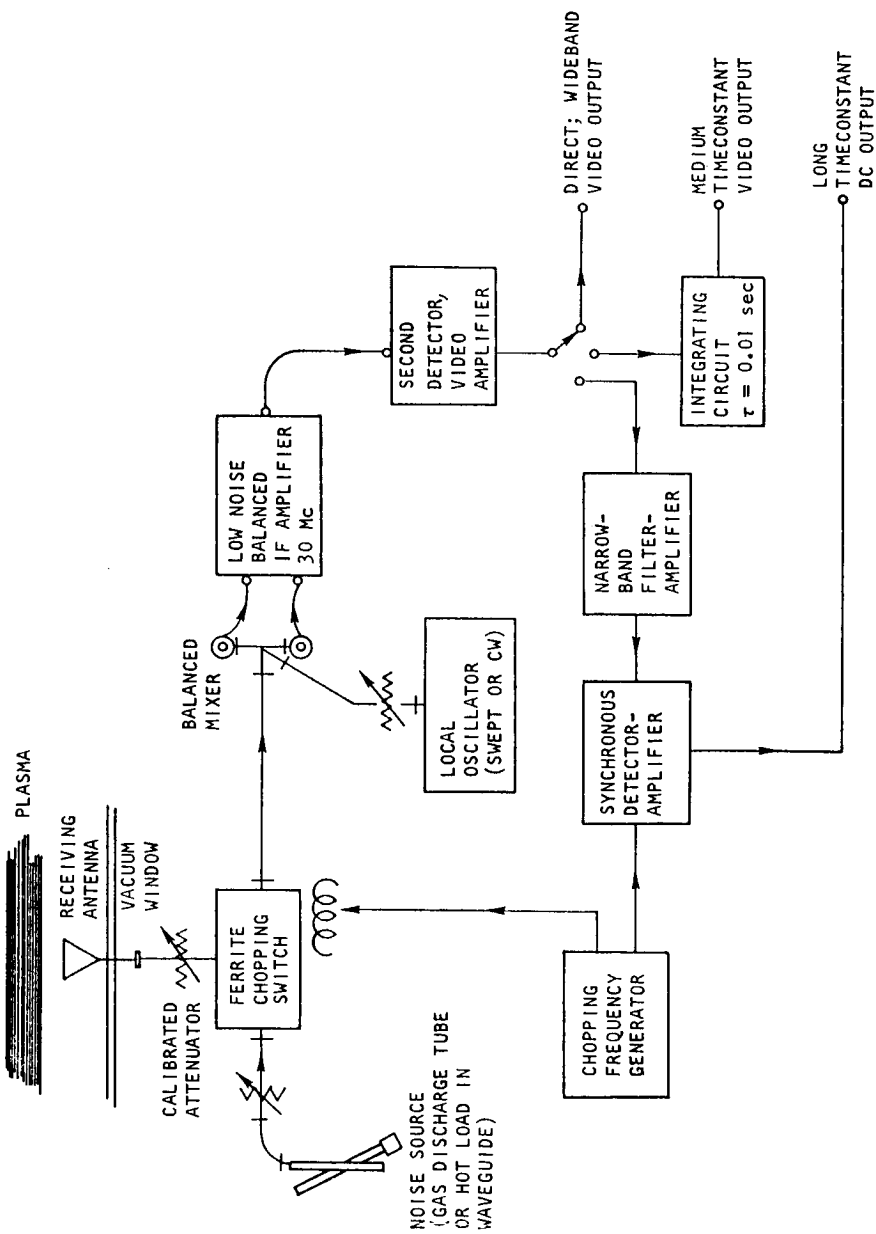

FIGURE 4. Microwave radiometer for plasma radiation studies. The receiver may be operated either with or without coherent detection.

will radiate much as a blackbody in the microwave spectrum. If the collision rate is high or the radiation is viewed at a frequency near a resonance, the plasma appears opaque. The radiated power density per frequency interval Δf is then

$$\Delta P = 8\pi k T_e (f^2/c^2)\,\Delta f \text{ watts/m}^2 \tag{6}$$

where T_e is the electron kinetic temperature in degrees Kelvin.

$k = 1.38 \times 10^{-23}$ joule/°K, Boltzmann's constant

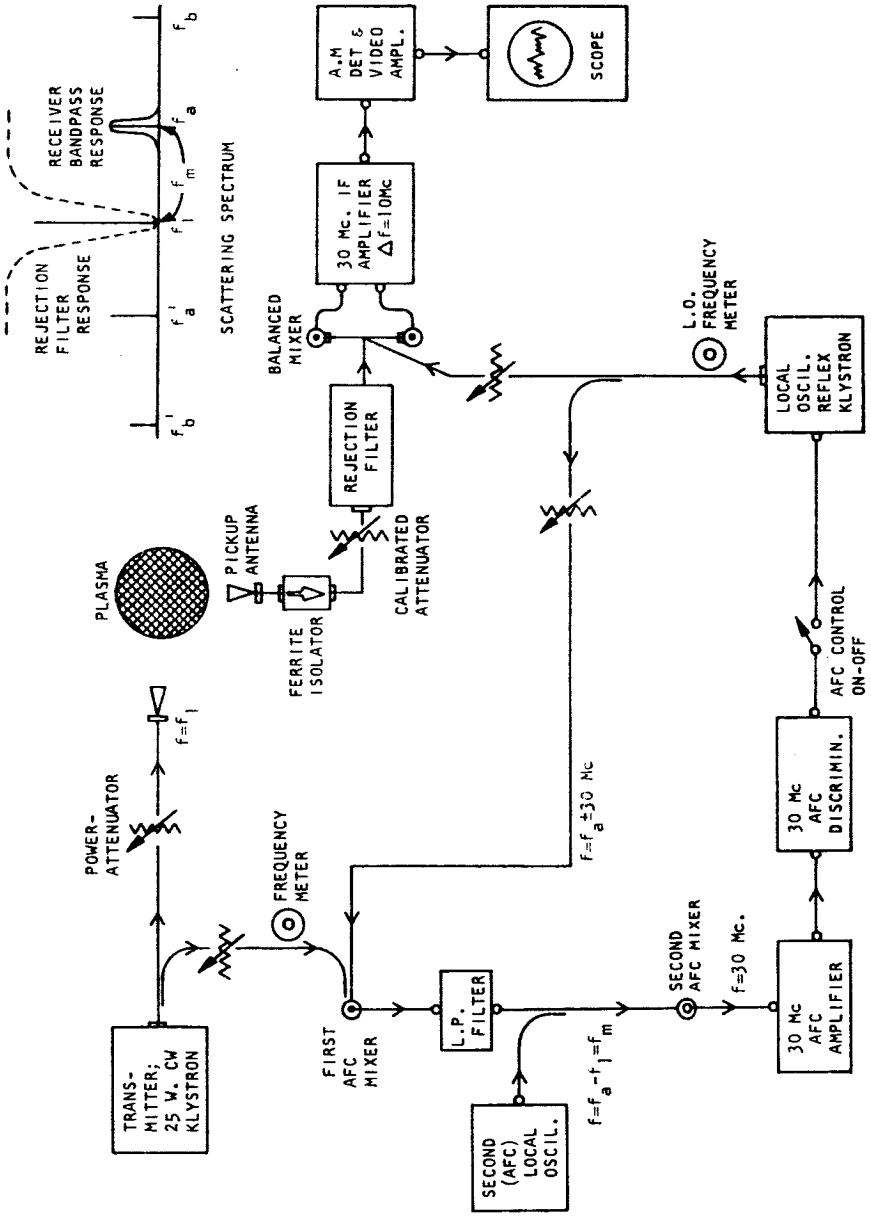

FIGURE 5. Transmitter-receiver system used to study the scattering from an oscillating plasma. The receiver is tuned to one of the sidebands and locked there by an AFC (automatic frequency control), the difference frequency being determined by the second local oscillator.

If the radiating surface is viewed by a directive antenna, which sees only the surface, the directivity just cancels the frequency dependence of equation (6) and the blackbody power received is

$$P_{bb} = kT_e \Delta f \text{ watts} \tag{7}$$

A region which is not totally opaque loses some of its power "out the back door". The received power is then

$$\frac{P}{P_{bb}} = \int_0^L \exp(-2\alpha z)\, d(-2\alpha z) \tag{8}$$

where α is the absorption coefficient, a function of n and ν. (See Figure 3.) A microwave radiometer is sketched in Figure 4.

Other Radiations: Electrons orbiting in a magnetic field emit synchrotron radiation, which is peaked at the electron gyrofrequency, ω_b, and its harmonics. If the electron density is high and no cooperative effects operate, the self-absorption limits the radiation intensity to the blackbody level shown earlier.

If the cooperative effects, due to violent oscillations and instabilities, are present, the radiation intensity scales as n_c^2 where n_c is the number of in-phase radiators. Incoherent radiation scales as n. The radiation intensity from cooperative effects thus has little to do with the electron temperature. Fortunately, the radiations from cooperative oscillations are trapped within the plasma region and seldom are coupled to external radiation fields, so that radiometry still yields valid electron temperatures in most cases.

10c. Microwave Scattering

The scattering from individual electrons, that is, Thomson scattering, has a very small cross section

$$q_T = \frac{8\pi}{3} r_0^2 \tag{9}$$

where $r_0 = 2.8 \times 10^{-15}$ meter, the electron radius. When plasma waves or other density fluctuations are present, however, the cross section may be enhanced by as much as 10^6 or so and the scattered signal emerges in only a narrow cone about the Bragg scattering angle (**3, 4**). The spectrum of scattered waves will contain sidebands similar to a phase modulation spectrum, where the modulation frequency is that of the plasma waves. Figure 5 shows the block diagram of a microwave scattering system, with a typical spectrum shown in the inset.

11. Optical and Infrared Probing

Probing by means of light beams is in principle very similar to microwave probing and the bulk of the theory applies. The techniques differ somewhat, but numerous parallels can be drawn.

Optical interferometers that are direct analogs of the microwave interferometer are useful for dense plasma measurements. The Mach–Zehnder interferometer sketched in Figure 6 is an example (**5**). A monochromatic light source is required; the smaller the wavelength spread, the sharper the interferences. Optical masers, or lasers, intrinsically are excellent monochromatic sources, but for transient events it is difficult to achieve accurate timing without elaborate pumping and triggering arrangements. A number of pulsed and C.W. lasers are now available commercially (**6**) covering wavelength ranges from 6900 Å to 72,000 Å (7.2 μ). Spark and arc-light sources, followed by a filter or monochromator are also useful

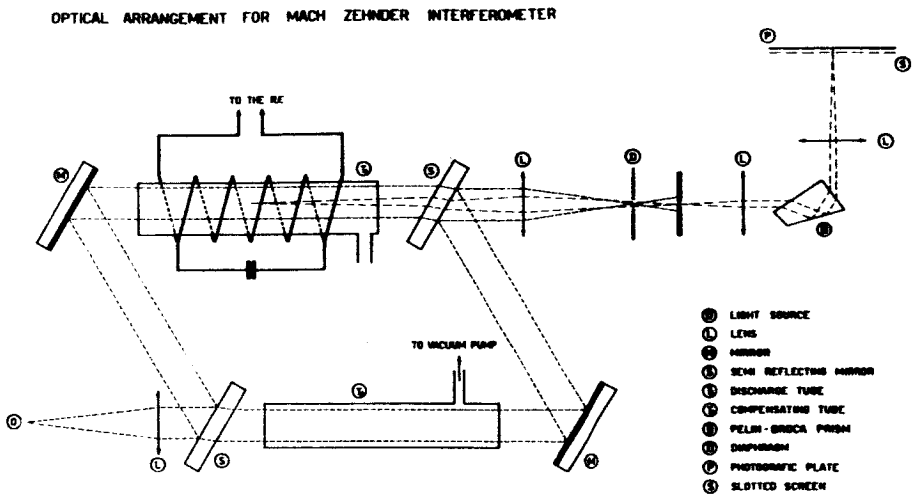

FIGURE 6. Mach–Zehnder interferometer used for studies of plasma refractive index. (After Ascoli-Bartoli, Frascati, Rome, Italy.)

for interferometers of medium resolution. Magnesium electrode spark sources can produce microsecond pulses of intense light, having jitter times of only a few nanoseconds. A wratten filter accepts the 3838 Å line, rejecting the others, as well as plasma-generated light. The light from the source must be much more intense than that from the plasma, of course, at the wavelength of interest.

A tabulation of some useful intense monochromatic light sources is given in Table I, together with wavelengths of peak outputs. Also shown are the oscillation frequencies, the corresponding plasma cutoff densities, and the electron densities required to give 90° of phaseshift in a 10-cm path.

TABLE I. SEVERAL INTENSE LIGHT SOURCES FOR OPTICAL PROBING, GIVING WAVELENGTHS FREQUENCIES, CORRESPONDING PLASMA CUTOFF DENSITIES n_c, AND ELECTRON DENSITIES GIVING 90° OF PHASESHIFT IN A 10-cm PATH LENGTH.

Light Source	*Wavelength* (microns)	*Wave Frequency* (cps)	*Plasma Cutoff Density* (no./cm^3)	*Plasma Density for* $\Delta\Phi = 90°$ *in* $L = 10$ cm (no./cm^3)
Microwave	10,000	3.3×10^{10}	1.35×10^{13}	1.5×10^{11}
	1,000	3.3×10^{11}	1.35×10^{15}	1.5×10^{12}
Mg spark	0.3838	7.83×10^{14}	7.73×10^{21}	1.48×10^{16}
Hg^{198} arc	0.4358	6.89×10^{14}	5.89×10^{21}	
Ruby/cr^3 laser	0.6943	4.33×10^{14}	2.32×10^{21}	8.05×10^{15}
Rb^{85} flash lamp	0.7800	3.85×10^{14}	1.835×10^{21}	7.16×10^{15}
	0.7948	3.78×10^{14}	1.77×10^{21}	7.04×10^{15}
Xenon flash lamp	0.8200	3.66×10^{14}	1.66×10^{21}	6.8×10^{15}
GaAs junction	0.90	3.34×10^{14}	1.38×10^{21}	6.2×10^{15}
$CaWo_4/Nd^3$ laser	1.06	2.83×10^{14}	9.9×10^{20}	5.25×10^{15}
He–Ne gas laser	1.153	2.60×10^{14}	8.40×10^{20}	4.85×10^{15}
	1.207	2.48×10^{14}	7.61×10^{20}	4.6×10^{15}
CaF_2/U^3 laser	2.6	1.15×10^{14}	1.64×10^{20}	2.13×10^{15}
Cs vapor laser	3.20	9.37×10^{13}	1.09×10^{20}	1.74×10^{15}
	7.18	4.18×10^{13}	2.17×10^{19}	7.78×10^{14}

A 1-microsecond recording of the interferences obtained by an interferometer from a dense plasma jet expanding into a low-pressure chamber is shown in Figure 7. The shock waves and turbulence are plainly visible.

A similar optical arrangement is used for Schlieren photography, except that changes in refractive index are recorded as modulations of light intensity, rather than interference fringes. An experimental arrangement for studying shock waves can be made up rather simply with lenses and a knife edge (**7**). The light source is a spark between tungsten electrodes in nitrogen. The accurate timing necessary to follow the fast front is obtained by a Kerr cell light shutter. A typical photograph is shown in Figure 8, showing the sharp electron density gradient in the "snow plow" front.

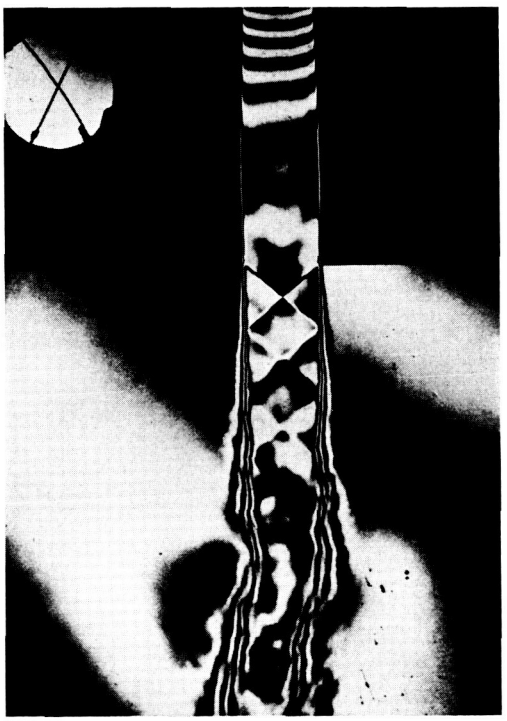

FIGURE 7. Interference fringes obtained by a Mach–Zehnder interferometer viewing a plasma jet expanding into a low-pressure chamber. (Courtesy Prof. D. Bershader, Stanford University.)

Optical Faraday rotation can be used to study dense plasmas in strong magnetic fields (**8**). The total rotation is given by Equation (5), where the collisionless linear approximation is easily justified for these frequencies. Equation (5) then reduces to

$$\psi = 180^\circ \frac{L}{\lambda} \frac{n}{n_c} \frac{B/B_R}{1 - B^2/B_R^2} \tag{10}$$

where B is the magnetic field and B_R is the magnetic field necessary to give gyro resonance, $B_R = \omega_b m/e$. As an example, the plasma density in a 10-cm path with 20 kilogauss applied, necessary to give 90° of rotation at $\lambda = 2.6$ microns, is $4.36 \times 10^{18}/\text{cm}^3$. The sensitivity increases in direct proportion to the density, the

path length, and the magnetic field applied. Crossed polarization plates, sensitive to rotation as small as 5°, are experimentally feasible.

12. Conductivity Probes

Plasmas having high collision rates have appreciable real components of conductivity. A small RF coil immersed in such a plasma will induce currents in the plasma. The current is complex, the real part extracting power and the imaginary part changing the coil's effective inductance by diamagnetic effects. In Figure 9

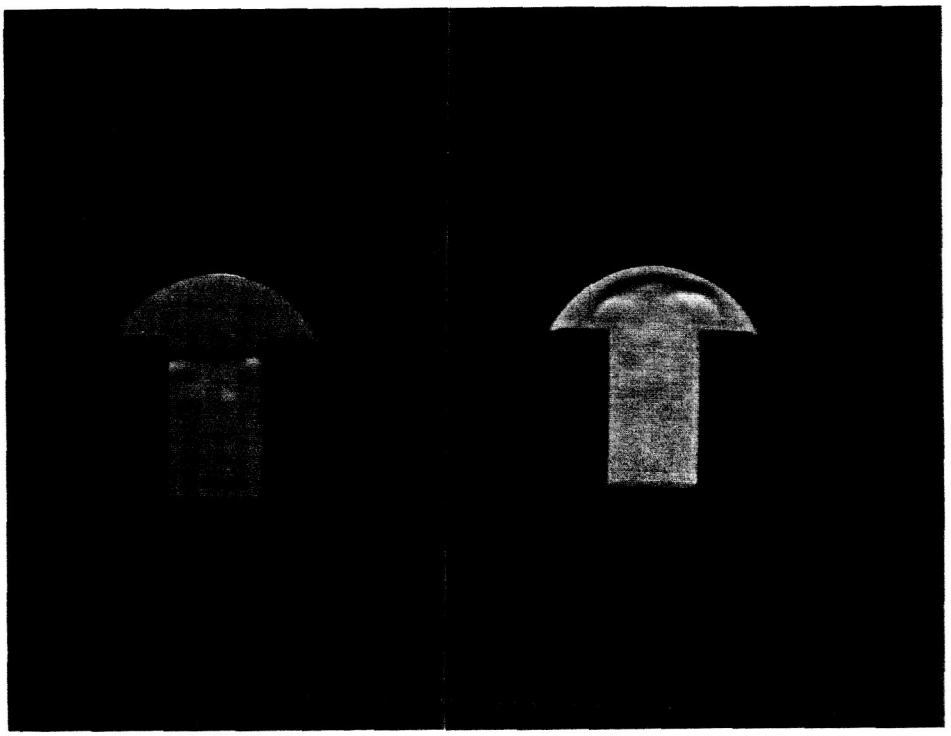

FIGURE 8. Schlieren photographs of a current sheet, traveling at 7 cm/μsec between parallel plates in a plasma accelerator. (Courtesy R. Lovberg, General Atomic, San Diego, California.)

the unloaded coil is resonated at the drive frequency f_0. The plasma current then both detunes and de-Q's the circuit much as in the case of resonant cavities. When $\nu \gg \omega$ and $\omega_p \gg \omega$, the major effect of the plasma on the coil is in lowering its Q. If the coil is immersed in the plasma so that the plasma conductivity σ is uniform in space, the change in Q is approximately

$$\frac{1}{Q_1(t)} - \frac{1}{Q_0} = \frac{\sigma_r(t)}{\varepsilon_0 \omega} \tag{11}$$

In most experiments, however, σ is not uniform, since the coil is mounted on a form or otherwise obstructs the plasma. Calibration is then conveniently carried out with ionic solutions (**9**), whose conductivities can be measured directly with a platinum electrode conductivity cell. For example, the data of Figure 9 was

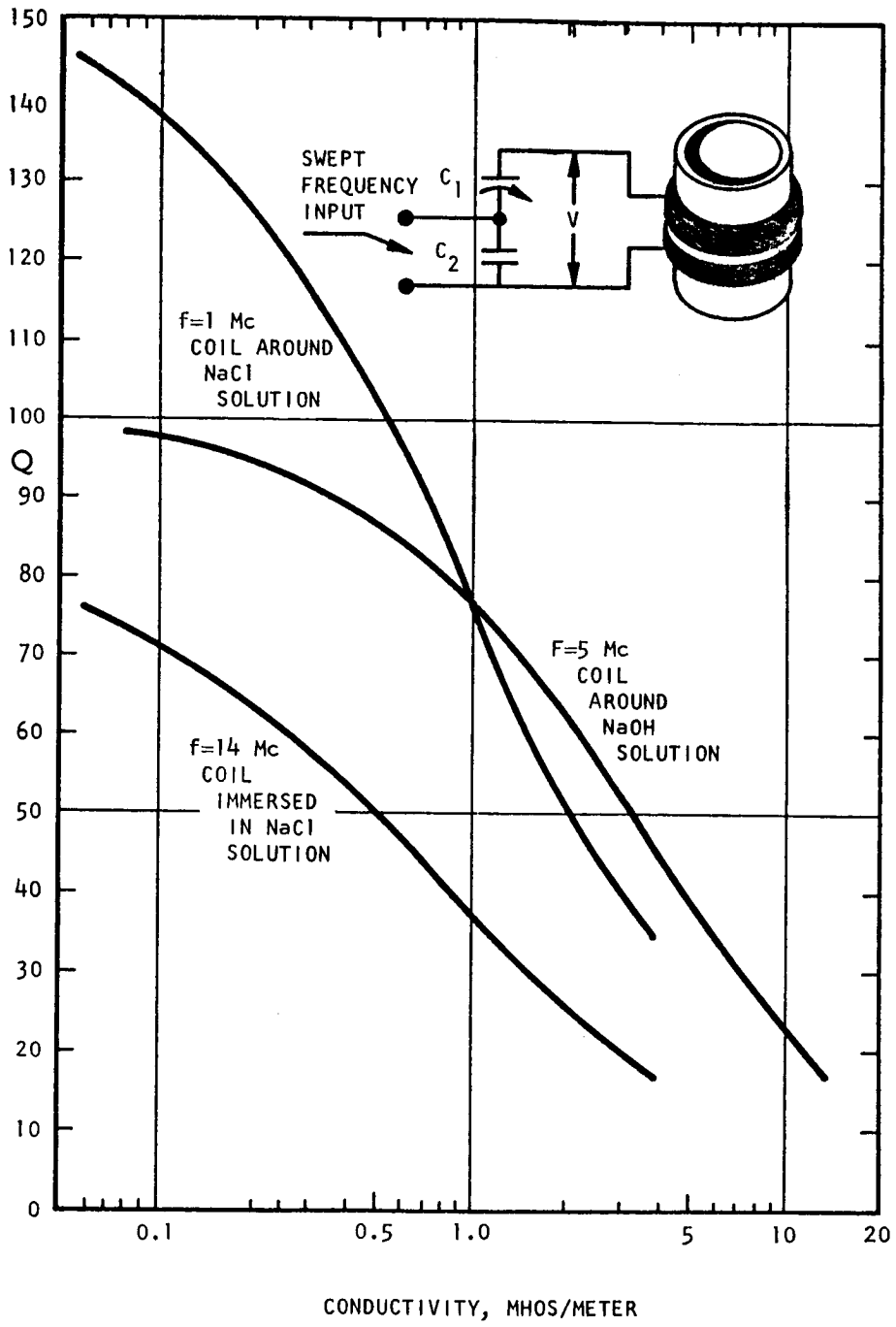

FIGURE 9. RF conductivity probe calibration data. The changes in Q of resonant circuits due to the conductivity of enclosed ionic solutions are shown for frequencies of 1, 5, and 14 Mc. (After Wharton, Hawke, and Katz 1962.)

obtained in an experiment at Livermore (**10**) from a coil wrapped around a section of pyrex plasma chamber which had been removed and filled with a conducting solution. The Q was measured by observing the width ξf at half-height of the frequency response, where

$$Q = \frac{f}{\xi f} \tag{12}$$

The center frequency f_0 was held constant by trimming C_1 slightly as the conductivity was varied. Q_0 was 105 for the 5-Mc coil and 85 for the 14-Mc coil, with distilled water in the chamber. A Faraday screen inside the coil helped reduce electrostatic effects between the coil and the solution, and later when the assembly was used to study high density plasmas.

13. Langmuir Probes

A conducting probe immersed in a plasma will emit or collect current, depending upon the voltage impressed (**11**). The technique has been extensively used and in many cases the quantities measured compare very well with those obtained by other means (**12**).

13a. Single Langmuir Probes

Typical characteristics for a single probe, whose dimensions are small compared to electron and ion mean-free paths, are shown for a plasma in the absence of magnetic field, in Figure 10.

The probe potential is measured in respect to some convenient, fixed-potential point, such as the anode or walls of a discharge tube or a floating "wall probe" which has an area at least 50 times as large as the probe itself.

When the probe potential V is made very negative all electrons are repelled and only ions collected. The random ion current passing through an area A in the plasma is related to the ion density and the velocity

$$J_+ = \frac{I_+}{A_p} = \frac{n_+ v_{th}}{4} = \frac{n_+}{4}\sqrt{\frac{2kT}{m_+}} \tag{13}$$

where I_+ is the random ion current, amp,
J_+ is the random ion current density, amp/m^2,
A_p is the area of the probe, m^2,
m_+ is the ion mass, 1.67×10^{-27} kgm for protons,
n_+ is the ion density, no./m^3,
$v_{th} = (2kT/m_+)^{1/2}$ = mean kinetic ion velocity, m/sec.

Equation (13) would be valid also for ion current collected by a probe if the presence of the probe caused no perturbation in the surrounding random plasma currents. The probe *does* perturb the plasma, however. The volume which the probe occupies provides an energy sink for all particles which strike it and the fringing fields extend for a considerable distance into the surroundings (**13**). As a result, the collected ion current density seems to be more a function of the electron temperature than of the ion temperature. This effect is due to the formation of a positive sheath around the probe. The extent of the sheath's influence is determined by the electron temperature. For $T_i < T_e$ the ion current density is nearly independent of the ion temperature, and equation (13) can be modified to (**14**)

$$J_+ \simeq 0.4 n_+ \sqrt{\frac{2kT_e}{m_+}} \text{ amp/m}^2 \tag{14}$$

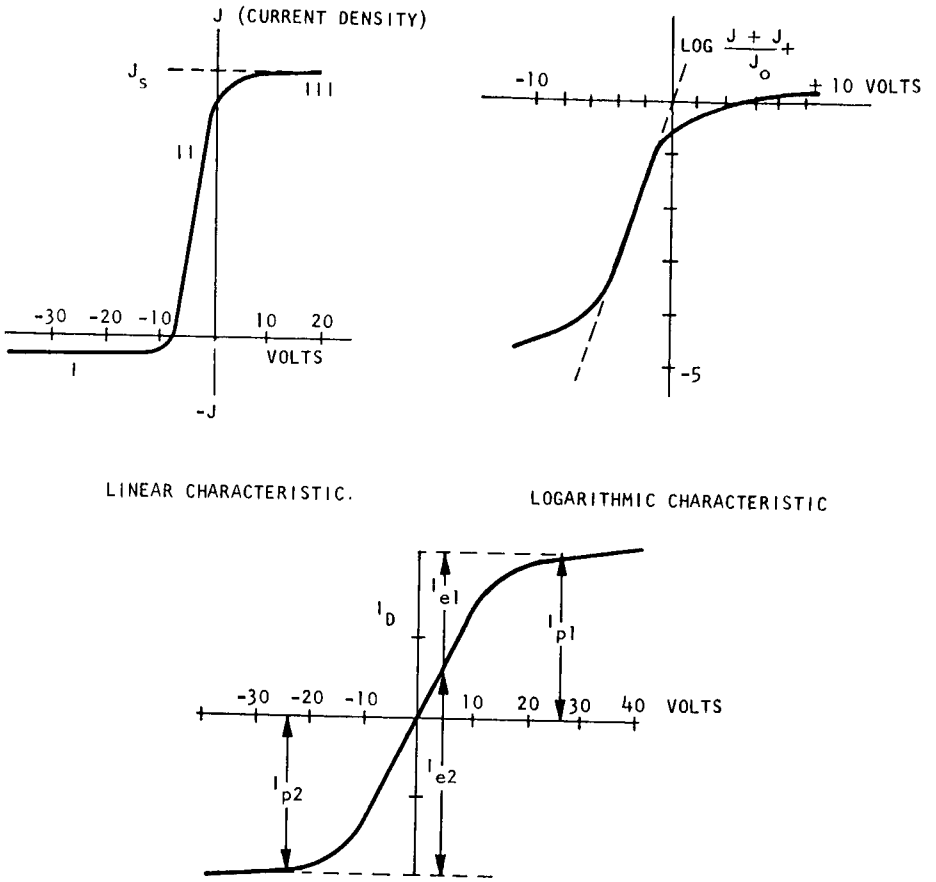

FIGURE 10. Langmuir probe characteristics plotted on linear and logarithmic scales.

If secondary electrons are emitted by the collected ions they also give a positive current indistinguishable from the ion current.

When V is made less negative, a few of the high-energy electrons are collected, partially cancelling the positive ion current. As the potential is changed further in the positive direction, the random ion and electron currents collected just cancel. This probe-plasma potential, V_F in Figure 10, is the "floating potential". For a thermalized plasma this voltage is approximately $\frac{1}{2}kT_e$ (expressed in electron volts).

Increasing V beyond V_F results in a steep rise in electron current, in region II. This current eventually saturates at the "space potential" value, V_s, due to space-charge limitation in current collection. According to the sketch in Figure 10, we have $V_s = 0$. In region II the probe electron current follows a logarithmic dependence

$$\ln I_e = +\left(\frac{e}{kT_e}\right) V + \ln A_s J_0 \tag{15}$$

where A_s is the area of the probe sheath $\approx A_p$,

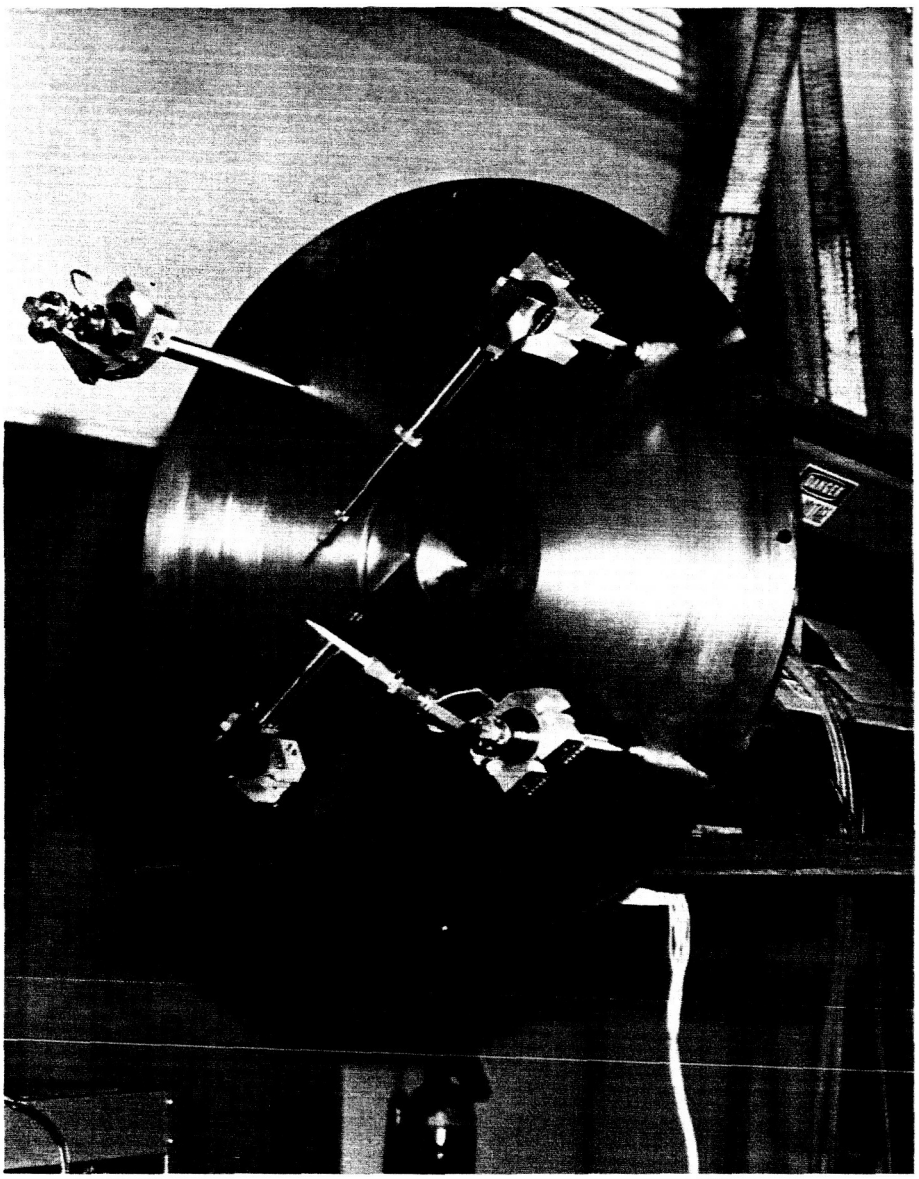

FIGURE 11. Probe and waveguide assemblies mounted in tubing introduced through a vacuum wall with Wilson seals. (Courtesy General Atomic, San Diego, California.)

J_0 is the random electron current density, amp/m^2; $J_0 = J_s + |J_-|$.
e is the electron charge, 1.6×10^{-19} coulomb.
kT_e is expressed in electron volts.

The total probe current is the difference between the electron current and ion current. Since it is the total probe current, I, that is measured, to find I_e in equation (15) we write

$$I_e = I + |I_-| \quad \text{and} \quad J_e = J + |J_-| \tag{16}$$

Equation (16) implies that the probe sheath is thin compared to probe dimensions, so that $A_s \approx A_p$ and is constant in size. In many experiments the sheath thickness $X < 0.1$ mm and we are justified in using equation (16).

When we plot the logarithm of J_e versus probe voltage V or display the current on an oscilloscope having a logarithmic amplifier, as in Figure 10, the slope yields the electron temperature

$$T_e = \frac{dV}{d[\ln (J + |J_+|)]} \approx \frac{\Delta V}{\Delta[\ln (J + |J_+|)]} \text{ eV} \tag{17}$$

The slope of Figure 10 corresponds to ~ 1.5 eV.

Increasing the probe voltage beyond V_s does not cause J to rise much higher than J_s, due to spacecharge. The spacecharge saturation current is

$$I_s = J_s A_s \approx J_0 A_s = \frac{n_e A_s}{4} \frac{2kT_e}{m_e} \tag{18}$$

Comparing equation (18) with equation (14) we note that

$$\frac{J_s}{J_+} \approx \sqrt{\frac{m_+}{2m_e}} \tag{19}$$

13b. Single Probe with a Magnetic Field

When a magnetic field is present, conditions alter. Since the effective mean-free-paths may now compare to prove dimensions, the electron spacecharge saturation current is reduced. It is only the mobility transverse to the field which is impaired, however, and electrons may flow along the lines essentially unimpeded, so that the probe may actually be sampling the conditions in the plasma some distance away. There may also be a "short-circuiting" effect if magnetic lines connect the probe with conducting surfaces, so that current can flow in the conductor across the field lines.

Since the ion gyro radius is much bigger than that of electrons, the ion saturation current, J_+, is not affected much until the field strength is fairly large.

By ordering the axis of the probe either along or across the field lines, the collection of electrons across and along field lines, respectively, may be observed. The I–V slopes at low current values are essentially the same and at moderate field strengths the log-plot still yields valid electron temperatures (**14**).

Figure 11 shows two Langmuir probes and two microwave horns mounted in movable vacuum seals that permit positioning the probes anywhere inside a chamber within 0.05 inch.

13c. Double Floating Probes

To avoid drawing the large electron currents of region III in Figure 10 the double floating probe technique is useful (**15**). Two probes, ordinarily of equal area, are inserted into the plasma and the difference in current due to an applied voltage difference is measured.

13d. Double Probes, No Magnetic Field

In the absence of a magnetic field the characteristics look similar to the bottom graph of Figure 10. For equal probe areas the top and bottom parts are symmetrical and represent only the magnitude of the saturated ion current. This is so since the difference of the probe currents must be zero and when the negative probe reaches

ion saturation the current of the positive probe must also saturate. The saturation value is again given by equation (14) if the electron temperature is known. Since a plasma is grossly neutral we may presume that $n_e = n_+$.

To find the electron temperature we may use equation (15) again. It will be convenient to rewrite it in the notation used in the bottom graph of Figure 10. We shall be very general and presume that the probe areas are not equal and therefore $I_{p1} \neq I_{p2}$.

Since the net current to the system must be zero,

$$I_{p1}+I_{p2} = \sum I_p = I_{e1}+I_{e2} = A_1 J_0 \exp(\phi V_1)+A_2 J_0 \exp(\phi V_2) \qquad (20)$$

where $A_{1,2}$ is the area of the respective probes,
J_0 is the random electron space current density,
$V_{1,2}$ is the plasma-to-probe potential,
$V_D = V_2 - V_1$,
$I_D = I_{p1} - I_{e1} = I_{e2} - I_{p2}$,
$$\phi = \frac{e}{kT_e} = \frac{1}{T_e\,(\text{eV})} = \frac{11{,}600}{T_e\,(^\circ\text{K})}.$$

The logarithm of equation (20) is

$$\ln\left[\frac{\sum I_p}{I_{e2}} - 1\right] = -\phi V_D + \ln\frac{A_1}{A_2} \qquad (21)$$

The slope of equation (21) plotted against V_D yields the electron temperature, just as in section 13a.

13e. Double Probes in a Magnetic Field

Double probes are not influenced as much by magnetic fields as are single probes. The collected current is governed by ion mobility and it is not until the magnetic field strength is very large (several thousand gauss) that the ion gyro radius is as small as the probe size.

When the field is large so that the collected ion current is limited by the orbital motion, the Mott-Smith (**16**) theory applies. For large negative potentials (large sheath thickness) the slope of ion current squared versus voltage gives the ion density

$$\frac{d(J_i^2)}{dV} = -\frac{2e^3}{\pi^2 m_i} n_i^2 \qquad (22)$$

14. Plasma Wave and Resonant Probes

When plasma waves or oscillations are present they may be detected with probes. Spacecharge waves may also be launched with probes, but this method of launching tends to excite all modes. Langmuir-type probes having coaxial shields brought up near the collecting surface are adequate for many measurements up to frequencies of 1000 Mc (**17**). A pair of small disc probes has been used successfully to measure ω_p in dilute plasma (**18**) and, in fact, wire and disc probes were used in experiments that probably were the first microwave diagnostic measurements (**9**).

Probes fed by resonant transmission lines (**19**) permit measurement of the plasma impedance, wave damping, and wavelength. Probes loosely coupled to a tunable filter, such as a motor-driven coaxial resonator (**20**), permit rapid analysis of the frequency spectrum of oscillations picked up in the plasma, or as a means to filter received signals. The movable probes shown in Figure 11 were used for these purposes, as well as for Langmuir probes.

15. Magnetic Probes

Small inductive probes immersed in the plasma will have voltages induced in them by changes in the local magnetic field, dB/dt (**21, 22**). Field sensitive elements, such as Hall current probes, measure the instantaneous magnitude of the magnetic field, B_0. Magnetic probes may be made as small as 1 mm in diameter and grouped in x–y–z arrays to measure three-dimensional field configurations (**23**). Current density contours and the presence of hydromagnetic instabilities in dense plasmas are measured by a linear array across current channels. The data can be displayed by rapid sampling. The output voltage of the coil-type probe may be integrated to yield the magnitude of field. The resulting signals are very small (depending on the integration time) and care must be used to avoid stray pickup. Hall probes have outputs of a volt or so, response times up into the megacycle range, and are easily calibrated with a standard magnet. They are somewhat temperature-sensitive.

Another kind of coil assembly that measures rates of change in enclosed current channels is the Rogowsky loop or girdle (**24**). The assembly consists of two sets of coils, one around the entire experimental region and the other around only the current channel or a part of it. The difference in induced voltage represents the currents not enclosed, such as wall currents. The coils may be segmented, with leads brought out separately, to indicate current profiles.

Low inductance coils can also be used to pick up high-frequency fluctuations, such as those associated with ion wave instabilities or ion cyclotron frequency instabilities. These frequencies are typically from 10 kc to 10 Mc.

16. Optical Spectroscopy

Spectroscopic observations have been extensively used for plasma studies, especially for equilibrium plasmas, where the Saha conditions apply (**25**). A great deal of work has been done in applying the "standard techniques" of Doppler broadening, Stark broadening, Zeeman splitting, and line identification to the understanding of intense discharges. For atoms that exhibit first-order Stark effect, some idea of the ion density can be derived through application of microfield theories from measurements on the extent of the profile wings. The use of a Fabry–Perot interferometer increases the resolution (**26**).

The thermal Doppler broadening of such lines as the ionized He II 4686 Å provides direct measure of the mean kinetic energy of the ions, when no mass motions are present. Presuming equilibrium, the Doppler width is (**27**)

$$\frac{\Delta\lambda_D}{\lambda} = \frac{v_{th}}{c} = \frac{1}{c}\sqrt{\frac{2kT_i}{m_i}} \tag{23}$$

The line half width then becomes

$$2\Delta'\lambda = 1.67\Delta\lambda_D = 7.1\times10^{-7}\sqrt{\frac{T_i}{A}}$$

where A is the ion mass relative to hydrogen. This is typically a fraction of an Ångstrom at temperatures of 10^6 °K.

Stark broadening becomes measurable only at ion densities above $10^{16}/\text{cm}^3$. Below this density (and even above, if the ion temperature is high) the Doppler broadening dominates.

Electron density in hydrogenic plasmas can be measured by observing the Balmer series of lines. The last resolvable line is somewhat below the theoretical

limit because of the smearing of emission wavelengths due to the microfields. The last resolvable line is given by Inglis and Teller (**28**)

$$3.7\,\frac{\frac{3}{2}a_0}{z}\,N_m^2 n_e^{2/3} e^2 = \frac{\frac{1}{2}e^2 z^2}{a_0 N_m^3} \tag{24}$$

or when expressed in terms of density

$$n_e \approx \frac{10^{23}}{N_m^{15/2}} \tag{25}$$

where a_0 is the atomic Bohr radius,
Z is the atomic number,
N_m is the total quantum number of the last distinguishable line,
e is the electron charge,
n_e is the electron density.

For hydrogen when H_{20} can just be resolved, the density is $n_e \approx 3 \times 10^{13}/\text{cm}^3$. The Balmer limit is at $\lambda \approx 3650$ Å.

At high temperatures the plasma is almost totally ionized and very little visible light is emitted. Most of the faint emission then appears in the ultraviolet and special techniques must then be used (**29**). In some experiments there are impurities such as O or C whose radiation can be viewed, or impurities such as He or A may be added.

17. Fast Photography

Discharges which emit intense light, such as pinches and shocks, may be studied with time-resolved photography. The diameter of the luminous column may be recorded as a function of time by sweeping the image of a viewing slit with a rotating mirror. Framed pictures may also be taken with Kerr cells, image-converter tubes, and rotating-mirror framing cameras. The lines of a spectrometer may be scanned by the use of rotating slits or mirrors, to give time-resolved spectra. Such measurements of the luminous features of discharges must be backed up by other measurements. For example, in shock tubes "precursors" and other fast ionization and excitation fronts often precede the main shock front. The details of constriction often follow the dips of current in fast pinches and the development of instabilities is easily discernible.

REFERENCES

1. Wharton, C. B., "Microwave Diagnostics for Controlled Fusion Research", Univ. of California Radiation Lab. Report UCRL–4836 (Rev.) (September 1957).
2. Heald, M. A., and Wharton, C. B., *Plasma Diagnostics with Microwaves* (to be published by John Wiley and Sons, 1964).
3. Drummond, W. E., "Microwave Scattering from Unstable Plasma Waves", *Phys. Fluids*, **5**, 9, 1133 (1962).
4. Boley, F. J., "Scattering of Microwave Radiation by a Plasma Column", *Nature*, **182**, 790 (1958).
5. Ascoli-Bartoli *et al.*, "Interferometric Study of a RF Discharge", paper presented at VI Inter. Conf. on Ionization Phen. in Gases, Paris, 1963.
6. Serchuck, A., "Commercially Available Optical Masers", *Microwave*, **1**, 54–57 (1962).

7. Lovberg, R., "Acceleration of a Plasma by Displacement Currents Resulting from Ionization", paper presented at VI Inter. Conf. on Ionization Phen. in Gases, Paris, 1963.
8. Dougal, A. A., "Optical Maser Probing Theory for Magnetoplasma Diagnostics", paper presented at 4th Symposium on Engineering Aspects of Magnetohydrodynamics, Univ. of California, Berkeley, 1963.
9. van der Pol, B., "The Influence of an Ionized Gas on the Propagation of Electromagnetic Waves" (Thesis, Utrecht University, The Netherlands, April, 1920).
10. Wharton, C. B., and Hawke, R., "Calibration of RF Conductivity Probes by Immersion in Ionic Solutions", Univ. of California, Lawrence Radiation Lab. Electronics Engineering Report (July, 1962).
11. Tonks, L., and Langmuir, I., "Theory of the Arc Plasma", *Phys. Rev.*, **34**, 876 (1929).
12. Schulz, G. J., and Brown, S. C., "Microwave Study of Positive Ion Collection by Probes", *Phys. Rev.*, **98**, 6, 1642–49 (June, 1955).
13. Generalov, N. P., "The Theory of Probes", *J. Nuclear Energy*, **9**, 148 (1959), translated from *Atomnaya Energiya*, **4**, 183 (1958).
14. Bohm, D., Burhop, E. H. S., and Massey, H. S. W., "Use of Probes for Plasma Exploration", in A. Guthrie and R. K. Wakerling, eds., *The Characteristics of Electrical Discharges in Magnetic Fields* (New York: McGraw-Hill, 1949), Chapters 2 and 9.
15. Johnson, E. O., and Malter, L., "A Floating Double Probe Method for Measurements in Gas Discharges", *Phys. Rev.*, **80**, 58 (1950).
16. Langmuir, I., and Mott-Smith, H., "Studies of Electric Discharges in Gases at Low Pressures", *Gen. Elect. Rev.*, **27**, 449, 538, 616, 762, 810 (1924).
17. Bailey, R. A., and Emeleus, K. G., "Plasma Electron Oscillations", *Proc. Roy. Irish Acad.*, **57A**, 53 (May, 1955).
18. Yeung, T. H. Y., and Sayers, J., "An RF Probe Technique for the Measurement of Plasma Electron Concentrations in the Presence of Negative Ions", *Proc. Phys. Soc. (England)* N451B, **70**, 663 (1957).
19. Levitskii, I., and Shashurin, S., "Resonant Microwave Probe for Measuring Charge Density in a Plasma", *Zh. Tekh. Fiz. (USSR)*, **31**, 4, 436 (1961).
20. Malmberg, J. *et al.*, "A Collisionless Plasma for Wave Propagation Studies", paper presented at VI Inter. Conf. on Ionization Phen. in Gases, Paris, 1963.
21. Lovberg, R., "The Use of Magnetic Probes in Plasma", *Ann. Phys. (New York)*, **8**, 3, 311 (November, 1959).
22. Colgate, S. A., "A Summary of the Berkeley and Livermore Pinch Programs", Proc. 2nd U.N. Conf. on Peaceful Uses of Atomic Energy (Geneva) P/1064 and P/369, **32**, 123–139 (1958).
23. Pollock, H., Goldman, L., and Westendorp, W., "Multiple Magnetic Probe Measurements in Compressed Deuterium Plasma", *Bull. Amer. Phys. Soc.*, **5**, 337–383 (1960).
24. Golovin, I. N. *et al.*, "Stable Plasma Column in a Longitudinal Magnetic Field", Proc. 2nd U.N. Conf. on Peaceful Uses of Atomic Energy (Geneva) P/2226, **32**, 72–81 (1958).
25. Griem, H., and Kolb, A., "Advances in the Theory of Broadening of Spectral Lines", paper presented at IV Inter. Conf. on Ioniz. Phen. in Gases, Uppsala, Sweden, 1959.
26. Gardner, A. *et al.*, "Diagnostic Measurements on the P–4 Steady State Plasma", Univ. of California Radiation Lab. Report UCRL–6562 (October, 1961).

27. Wulff, H., "Plasma Diagnostics by Spectroscopical Means", *Nuclear Instruments and Methods*, **4**, 352 (1959).
28. Inglis, D. R., and Teller, E., "Ionic Depression of Series Limits in One-electron Spectra", *Astrophys. J.*, **90**, 439 (1939).
29. Kelly, R. L., "A Grazing Incidence Vacuum Spectrograph of Simple Design", Stanford Research Institute Report SD-3006-2 TR1 (December, 1959).

2. John A. Thornton: *Electric and Electromagnetic Shock Tubes*

The classical diaphragm shock tube presents serious limitations in the production of very high temperatures and velocities. Accordingly, electric and electromagnetic shock tubes have received considerable attention as devices capable of generating shock waves both of extremely high Mach numbers, up to several hundred, and of extremely high temperatures, over one hundred thousand degrees Kelvin. Recent investigations have indicated several characteristics, such as electron-driven shocks, precursor effects, and driver-driven gas mixing, which affect the applicability of these shock tubes as research tools. These investigations are surveyed and consideration is given to the potentialities, limitations, and design trends which they suggest for electric and EM shock tubes as laboratory devices. Finally, important diagnostic techniques are surveyed.

INTRODUCTION AND GENERAL DISCUSSION

An electric shock tube is defined as a shock tube in which the driving energy is imparted to the gas by electric means, and an electromagnetic or EM shock tube as a device in which the driving energy is imparted to the gas by both electric and magnetic means. The emphasis in this paper is directed at the electric and EM shock tubes as laboratory devices for experimental studies in plasma physics although it is to be noted that the driving processes in many of the pulsed-plasma accelerator concepts being investigated for propulsion applications are very similar to those in EM shock tubes.

The conventional gas-driven diaphragm shock tube has become a very important research tool in experimental gas dynamics because the thermodynamic state of the shocked gas is completely defined, in principle, at least, by three easy-to-measure parameters: the pressure and temperature in the expansion chamber and the shock velocity (**1–4**). Nevertheless, such shock tubes are severely limited in producing high-velocity, highly-ionized plasmas. To understand these limitations and the potentialities of electric and EM shock tubes, it is profitable to consider briefly the classical shock tube formalism. Figure 1 is a sketch of the theoretical pressure distribution in a classical shock tube shortly after the diaphragm has been broken. The regions defined in this figure have become incorporated into standard shock tube nomenclature as subscripts and will be used throughout this paper.

According to a linearized perfect gas analysis, the shock Mach number M_s is a function of the initial pressure ratio p_4/p_1 and the species of the gases in the driver

ED. NOTE: Dr. Thornton is with the Space Sciences Laboratory, Litton Systems, Inc., Beverly Hills, California. This work was performed under the sponsorship of the Air Force Office of Scientific Research under grant No. AFOSR 62-307.

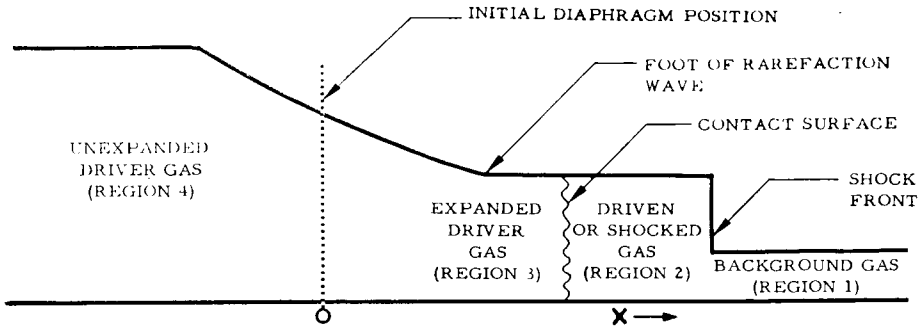

FIGURE 1. Pressure distribution in a diaphragm shock tube (theoretical).

section (region 4) and the expansion section (region 2); it is given implicitly by the following equation:

$$\frac{p_4}{p_1} = \frac{2\gamma_1 M_s^2 - (\gamma_1 - 1)}{\gamma_1 + 1} \left[\frac{1}{1 - \frac{(\gamma_4 - 1)}{(\gamma_1 + 1)} \frac{a_1}{a_4} \left(M_s - \frac{1}{M_s} \right)} \right]^{2\gamma_4/(\gamma_4 - 1)} \tag{1}$$

where a is the sonic velocity and γ is the ratio of specific heats. Equation (1) can be thought of as defining the regime of performance of the classical shock tube concept (see Figure 2). This regime is bounded by two extremes in the shock tube driving potential; at one extreme the pressure ratio p_4/p_1 is due to a density-generated pressure in the driver (p_4) and at the other extreme to a thermal-generated pressure in the driver gas. The low performance curve on the left in Figure 2 represents a density-driven shock tube with identical gas species at identical temperatures on both sides of the diaphragm and is defined by setting $N_4 > N_1$, $\gamma_1 = \gamma_4$, and $T_4 = T_1 = T$, and noting that $a = \sqrt{\gamma RT}$ in equation (1) (N = particle number density). The high performance curve corresponds to a thermal-driven shock tube with identical gas species at identical densities on both sides of the diaphragm and is defined by setting $T_4 > T_1$, $\gamma_1 = \gamma_4$, and $N_4 = N_1$.

It is easily shown that in the limit of an infinite pressure ratio the maximum obtainable shock Mach number is independent of the pressure ratio and depends primarily on the sonic velocities in the driver and driven gases (**1**). Accordingly, diaphragm shock tube performance is improved by using light gases such as hydrogen or helium in the driver; in addition, the driver gas is often heated by combustion or by an electric discharge technique (**4**). Theoretical performance curves for several driver configurations are shown in Figure 2, where it can be seen that they simply tend to make the shock tube performance curve approach that of the thermal shock tube. Equation (1) has been solved for a thermal shock tube with a γ of 5/3, yielding (**5**)

$$V_s = 0.775 \left(\frac{kT_4}{m_i} \right)^{1/2} \tag{2}$$

where m_i is the ion mass. Equation (2) can be written as

$$M_s = \frac{V_s}{a_1} = 0.60 \left(\frac{a_4}{a_1} \right) = 0.60 \left(\frac{p_4}{p_1} \right)^{1/2} \tag{3}$$

Indeed, the thermal shock tube, in which the driving pressure is generated entirely by the temperature and which has, therefore, the highest possible driver-section

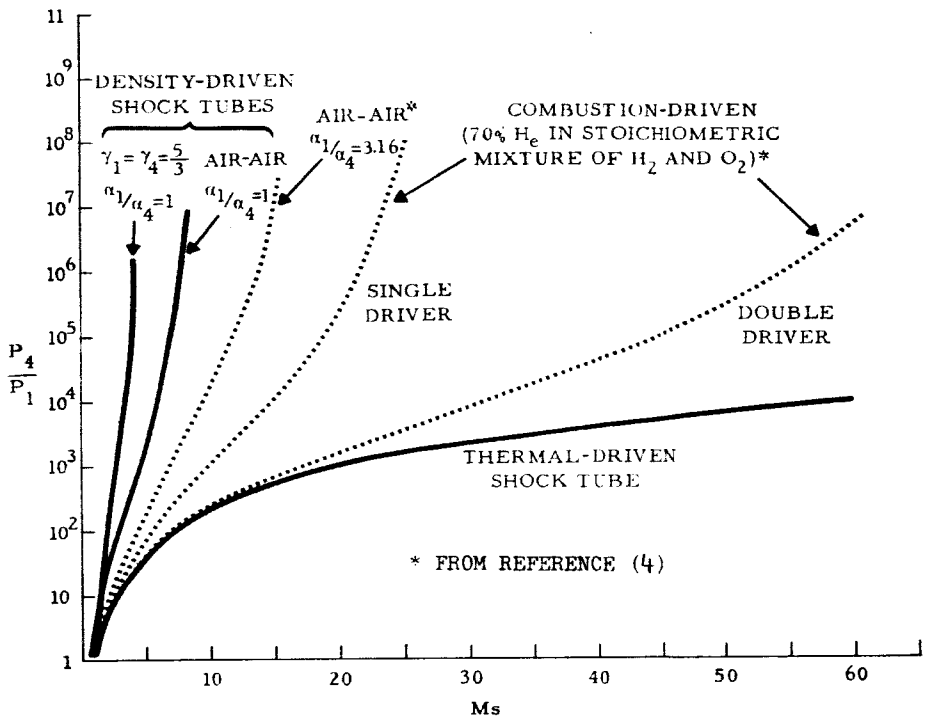

FIGURE 2. Diaphragm shock tube performance (theoretical).

sonic velocity for a given gas species and pressure, constitutes the performance limit for the classical shock tube concept and accordingly might be called the idealized shock tube.

The simple electric shock tube such as the T-tube shown in Figure 3 is an example of a thermal shock tube. The potential energy is stored in power storage capacitors and enters the gas in a very short time via an electric discharge, thereby generating a high temperature plasma in the electrode region. This discharge

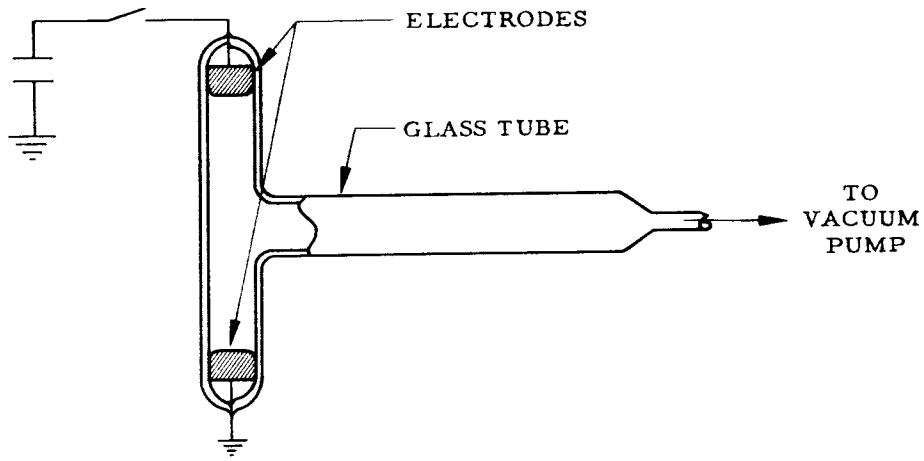

FIGURE 3. Fowler's T-tube apparatus.

plasma then constitutes the driver gas of the electric shock tube. In the EM shock tube the discharge plasma is in effect given an additional acceleration by the interaction of a magnetic field with the discharge current. Although the electric discharge produces a thermal driver and makes the electric and EM shock tubes capable of extremely high Mach numbers, it also introduces several serious complications which affect their applicability as research tools. These characteristics, outlined as follows, are discussed in more detail in subsequent sections:

(1) Even though much research has been done on the electric discharge, it remains one of the least understood of nature's phenomena. Thus it is not possible to predict the conditions in the discharge plasma from the initial conditions of capacitor energy and ambient pressure, and reproducibility is often poor.

(2) A high driver-section sonic velocity is desirable for high shock velocities; however, coupled with the short lengths of the driver plasma and the short periods of coupling between the magnetic field and the discharge plasma in most EM configurations, this results in severe shock velocity attenuation.

(3) Measurements in electric shock tubes are usually made at points much closer to the electrode region than to the diaphragm in classical shock tubes in corresponding measurements. This results in a short region of shocked gas. Also, the ambient pressures employed in electric shock tubes are generally less by orders of magnitude than the pressures employed in diaphragm shock tubes. Accordingly, under some conditions the discharge plasma may be out of equilibrium during the acceleration and expansion processes. Also, the contact surface breaks down, and at low pressures a complete mixing of the driver and driven gases occurs. Not only are the shocked gases perturbed from behind by the breakdown of the contact surface, but also the cold gas ahead of the shock front is perturbed by the absorption of ultraviolet and X-ray radiation from the discharge. Therefore the Rankine–Hugoniot equations generally cannot be used with a simple measurement of the shock velocity and ambient pressure to compute the thermodynamic state of the gas behind the shock front.

DEVELOPMENT OF ELECTRIC AND ELECTROMAGNETIC SHOCK TUBES

While the diaphragm shock tube seems to have been a rather logical invention extending from the definition of a shock wave, the electric shock tube was discovered in 1951 by R. G. Fowler and his students (**6–7**), who were using the T-tube arrangement shown in Figure 3 to investigate the luminosity which invaded branch paths after low pressure gaseous discharges. They observed this luminosity in the side arm of the T-tube, attributed it to a violent expansion of the ion cloud created in the discharge, and concluded that the expansion frequently generates luminosity-producing shock waves with Mach numbers as high as 30. Recognizing the possibilities of an electric shock tube for aerodynamic investigations, Fowler's group continued their work (**8–10**).

Elsewhere, however, diaphragm shock tubes were considered adequate for generating the thermodynamic states of interest at that time (Mach 20 and less) and they continued to dominate the scene for the next five years. By 1955 the increased interest in controlled thermonuclear fusion, space propulsion, and hypersonic aerodynamics (particularly reentry problems) made it desirable to produce in the laboratory high temperature plasmas, often with extremely high

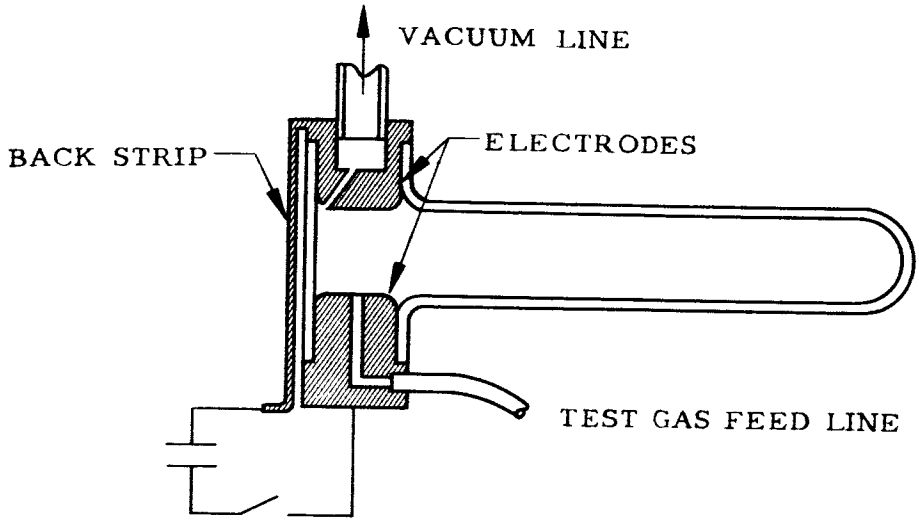

FIGURE 4. Electromagnetic T-tube.

velocities. In 1956 Kolb added an external magnetic field to Fowler's T-tube (**11–12**), thus forming the first EM shock tube. The field was provided by coupling a backstrap or coil to the primary discharge or by a separate but synchronized current source. The primary circuit backstrap type of the EM T-tube is shown in Figure 4.

Soon many additional EM shock tube geometries were developed. Blackman discharged a low-inductance condenser through a single-turn copper coil wrapped

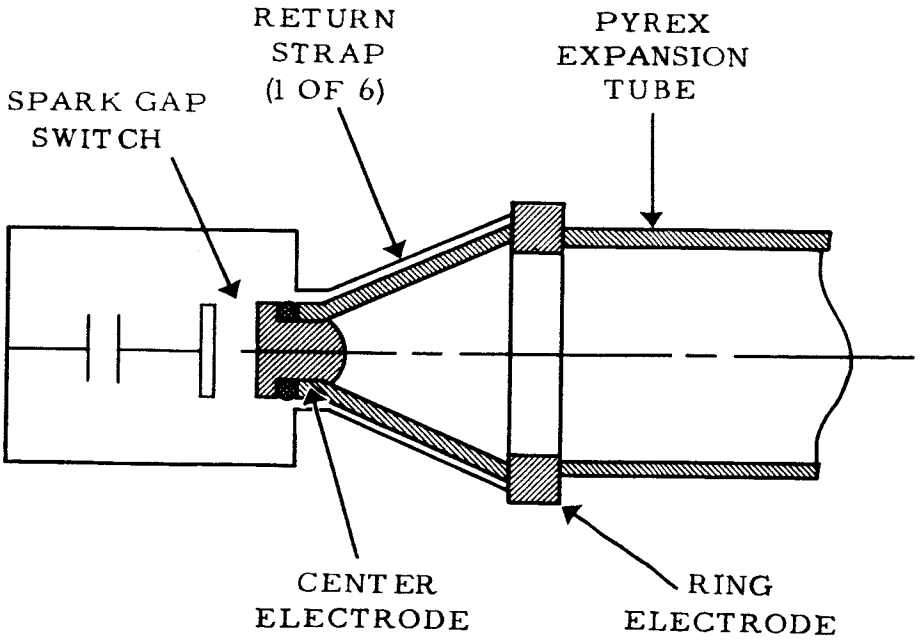

FIGURE 5. Conical electromagnetic shock tube.

around a straight glass tube and generated reasonably plane shock waves (**13**). The group at AVCO developed an annular electromagnetic shock tube (MAST) which has produced strong one-dimensional shock waves of over 200 (**14–15**). The MAST has been used in a continuing research program to study the structure of strong shock waves propagating into a transverse magnetic field (**16–18**). Josephson developed the conical configuration shown in Figure 5 in attempting to obtain less contamination of the gas (**19**). A group at Lockheed conducted experiments using EM T-tubes, conical tubes, and the cylindrical configuration shown in Figure 6 (**20–22**).

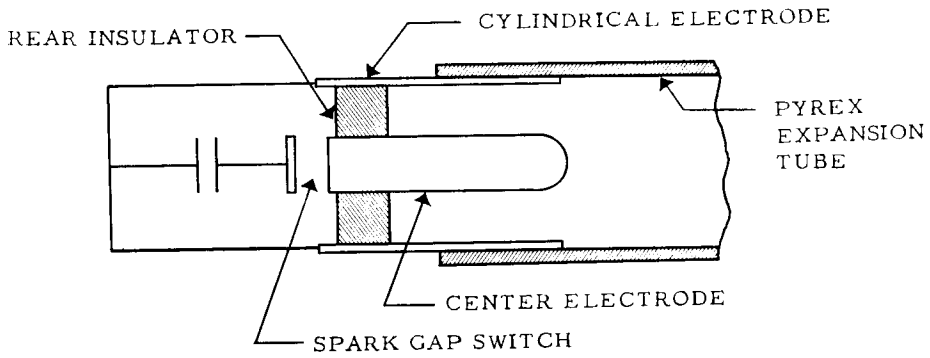

FIGURE 6. Cylindrical electrode electromagnetic shock tube.

In subsequent years many investigations have been conducted, not only in the laboratories where these original geometries were developed but also in other industrial and university laboratories in this country and abroad, as summarized in Table I. In a number of the early investigations it was enthusiastically assumed that many of the desirable characteristics of the classical shock tubes would also be applicable to the electric and EM shock tubes. Later investigations discovered the limitations listed in the introduction.

Recent reports describe new configurations attempting to minimize the limitations and to make electric and EM shock tubes more useful laboratory tools.

Smy (**23**) reports a new EM shock tube designed with a Mylar diaphragm separating the electrode region from the expansion tube. A dense gas such as nitrogen is used as the driver to impede the attenuation process. It was noted in the preceding section that the result of a very high sonic velocity in the driver is a high initial shock velocity and a high rate of shock velocity attenuation. Thus Smy's intention was to reduce the velocity attenuation at the expense of the initial shock velocity. Also his diaphragm shields the cold gas from precursor radiation originating in the electric discharge.

It might be said that Smy's modifications are moving in the direction of a compromise between the EM shock tube and classical gas-driven shock tube. Indeed this is the case in a new configuration developed by Camm and Rose (**24**). Energy densities of up to 400 J/cc are discharged into a helium filled driver section $10\frac{1}{2}$ inches long. The helium, which is initially at a pressure of a few hundred psi, is raised to 10,000 to 20,000 psi and a temperature of 10,000 to 20,000°K. The high pressure bursts a scribed diaphragm and drives a shock wave with velocities as high as 43,000 ft/sec down a 20-ft expansion tube filled with air. Electrical heating of the driver in a classical shock tube is not new (**4**), but the Camm–Rose tube is believed to be the first of this type in which the major component of the driving pressure is thermal-generated, and accordingly we classify it as an electric shock tube. Initial

TABLE I. SUMMARY OF DIAGNOSTIC TECHNIQUES USED IN EXPERIMENTAL ELECTRIC AND ELECTROMAGNETIC SHOCK TUBE RESEARCH

KEY

Shock tube type

- T Electric T-tube
- EM-T Electromagnetic T-tube
- C Conical electromagnetic (*-electrodeless)
- Cyl Cylindrical electromagnetic
- Coil Electrodeless coil
- MAST Magnetic annular shock tube

Instrumentation

- A Smear camera velocity measurement
- B Photocell or photomultiplier velocity measurement
- C Magnetic microphone velocity measurement
- D Kerr cell or rotating mirror record of shock shape
- E Crystal probe pressure measurement
- F Microwaves
- G Time-integrated spectroscopy
- H Time-resolved spectroscopy (film)
- J Time-resolved spectroscopy (photomultipliers)
- K Magnetic probes
- L Image converter camera
- M Ballistic pendulum
- N Lin, Resler, Kantrowitz—conductivity coils
- P X-ray probe
- Q Electrical probes
- R Optical interferometer
- S Infrared or ultraviolet heat transfer gauge

Author and Publication	*Tube type (typical Mach no.)*	*Test gas*	*Instrumentation*	*Objective*
Fowler *et al.* (**7–10**)	T (30)	H_2, H_e, N_e, N_2,A	A, B, C, D, E, G, H	Source of luminosity in T-tube
Kolb (**11–12**)	EM-T (100)	H_2, D_2, H_e	A, D, G, H	Development of EM T-tube
Blackman *et al.* (**13**)	Coil (10–30)	H_2, A, Air	A	Relaxation time and effect of B-field
Kash *et al.* (**20–21**)	EM-T, C (< 50)	Air	B, F, G	Shock velocity and temperature estimate
Patrick *et al.* (**14, 16**)	MAST (200)	H_2	B, J, K, S	Collisionless shocks
Josephson (**19, 53**)	C (100)	D_2	A, B, Q	Development of conical tube
Josephson and Hales, *Phys. Fluids*, **4**, 373 (1961)	C (100)	D_2, Air	A, B	
Eastmond *et al.*, STL no. GM–TR–0127–00497 (1959)	C (100)	D_2, H_2	A, L	Effect of electrode geometry in conical tube
Hart (**22**)	C (100)	Air	A	
Turner *et al.*, STL no. GM–TR–0165–00514 (1958)	C (60)	H_2, D_2	N	Electrical conductivity
Scott *et al.*, *Phys. Fluids*, **6**, 609 (1959)	C (100)	D_2	B, K	Magnetic disturbance behind shock front
Vali *et al.*, *Phys. Fluids*, **3**, 1029 (1960)	C (140)	Air	A, K	

Author and Publication	*Tube type (typical Mach no.)*	*Test gas*	*Instrumentation*	*Objective*
Ziemer (**71–73**)	C	Air	A, L, S	Magnetoaerodynamics and instrumentation development
Ziemer, *Dyn. Cond. Gas.*, ed. Cambel and Fenn (Evanston: Northwestern University Press, 1960), 139	C (40)	Air	A, L	Duration of steady flow behind shock
Scott *et al.*, in *Plasma in Mag. Field*, ed. Landshoff (Stanford: Stanford University Press, 1958), 110	C (100)	D_2	A, D, K, J	Interaction of high velocity plasma with magnetic field
Scott *et al.* (**74–75**)	C (100)	D_2	B, K, J	
Atkinson *et al.*, *J. Appl. Phys.*, **30**, 801 (1959)	T	H_2	A	
Fowler *et al.* (**84**)	Cyl (60)	D_2	A, D, K	Magnetically insulated shock tube
Pax, MS thesis, Northwestern University, 1959	C (30)	Air	B	Shock velocity
Thornton *et al.* (**37**)	C (40)	Air	B	Effect of radiation on velocity attenuation
Rockman, *Bull. APS*, **7**, 378 (1962)	EM electrodeless	Noble gases	A	Relaxation times
Lauer, *Bull. APS*, **4**, 138 (1959)	EM-T	N_2	Mass spec.	Chemical reactions
Hess *et al.*, *Ann der Phys.*, **8**, 189 (1961)	T	A	A	Performance of T-tube
McLean *et al.* (**58**)	EM-T (30)	H_e	A, D, F, G, H, J	Experimental determination of thermodynamic state
Wiese *et al.* (**82**)	EM-T (30)	H_e, H	B, H, J	
Thornton (**27**)	C (20)	A	B, F, G, J	
Fuchs *et al.* (**59**)	C* (50)	H_e	A, D, J	
Barnard *et al.* (**83**)	EM-T (50)	H_e, A	B, H, J	
Head (**89**)	C	H_2, Air	G	
McLean *et al.* (**48**)	EM-T	H_e	J	Precursor effects
Voorhies *et al.* (**49**)	C (55)	H_e	J	
Pugh (**55**)	Cyl		A, B, D	
Gerardo *et al.* (**51**)	C	N_e, A	P	
Mahaffey *et al.* (**85**)	T	N_e, A, H_e	B, F	
Hopson *et al.*, Microwave Physics Lab., General Telephone and Elec. Labs., Inc., Rep. no. RADC TDR–62–186 (1962)	C* (10)	H_e	B, F	Electron diffusion ahead of shock
Lee *et al.*, *Bull. APS*, **7**, 568 (1962)	EM-T (60)	A	A, B	Luminosity rise times behind shock front
Wiese *et al.*, *Phys. Fluids*, **4**, 250 (1961)	EM-T (25)	H_e	B, J	

Author and Publication	*Tube type (typical Mach no.)*	*Test gas*	*Instrumentation*	*Objective*
Berg *et al.* (**69**)	EM-T	H, H_e	B, G, J	Spectral line structure
Cunningham *et al.* (**80**)	C	H_e, D_2	J	
Andrew *et al.*, *Phys. Fluids*, **4**, 160 (1961)	C (50)	A	B, M	Impulse of accelerated plasma
Cloupeau (**51, 60–63**)	EM-T (20)	H_2, H_e, A, N_2, Air	A, J	Investigate contact surface breakdown
Edwards (**65**)	EM-T (20)	H_2, A	A, J	
Yamanaka *et al.*, *Tech. Rep. Osaka Univ.*, **10**, 303 (1960) and **10**, 553 (1960)	Coil	A	A, G, H, Q	Shocks in preionized gas
Takeda, *J. Phys. Soc. Japan*, **16**, 1395 (1961)	(5)	A	F	
Chang (**60**)	Cyl (65)	H_2	A, E	Luminous and pressure fronts
Smy (**23**)	EM-T	H_e, N_2, Air	A	Reduction of shock attenuation
Safronov *et al.*, *Soviet Phys. Tech. Phys.*, **6**, 777 (1962)	EM-T, C	H_2, A, Air	B	Effect of impurities on successive shock waves
Kholev *et al.* (**39**)	Cyl (200)	Air	A	Performance of shock tube
Borzunov *et al.*, *Soviet Phys. JETP*, **9**, 502 (1959)	C (100)	D_2	A, E	Investigate discharge
Griem *et al.* (**70**)	EM-T	H_2, H_e	J	Ultraviolet spectroscopy
Ramsden *et al.* (**78**)	EM-T	H_2	R	Use of optical interferometer
Klein (**77**)	C (35)	H_2	A, R	
Takeda (**81**)		A	F	Measure electron density

tests indicate that the average shock velocity attenuation is low and that test time intervals between the shock front and contact surface approach theoretical values. However, despite the fact that their shock tube is a recent innovation, Camm and Rose conclude that the device is operating near the limits of test time and velocity which can be expected from a shock tube operating in this manner, since radiation effects appear to make it difficult to maintain the driver temperature above 20,000°K regardless of the initial conditions.

Recently Fowler has tested an electric shock tube with a segmented many-electrode driver section 1 m long (**25**). Early experiments indicate that shock Mach numbers of several hundred can be obtained. The long driver section maintains a high electron temperature (estimated $\sim 10^{6}$°K), and preliminary tests indicate that shock velocity attenuation is small.

THE ELECTRIC DISCHARGE AND THE SHOCK EXPANSION

During the low pressure gaseous discharge in an electric or EM shock tube, the electric field imparts the capacitor energy preferentially to the electrons. This is due to the inertial effect which prevents the ions from being accelerated between collisions to the same velocity as the electrons. Thus, at the conclusion of the discharge, if the pressure is low, the electron temperature may be several orders of magnitude greater than the neutral or ion temperature. The characteristic time for thermal equilibration between electrons and ions in a fully-ionized gas is a function of $1/N_e$ and $T_e^{3/2}$ and a weak function of T_i for $T_e > T_i$ (**26**). For example, in an argon plasma with an electron temperature of 20,000°K, an ion temperature of about 1000°K, and an electron density of 10^{17} electrons/cc, the thermal equilibration times have been estimated to be of the order of 0.1 μsec; but when $N_e = 10^{15}$, the equilibration times can be of the order of 10 μsec (**27**). Under such conditions the electron partial pressure in the driver plasma is indeed the primary source of shock motion for sustained lengths of time. The instantaneous total pressure in the driver plasma is the sum of the partial pressures of the electrons and the heavy particles. Therefore, because of the competing processes of energy injection and thermal equilibration, it is possible under certain conditions of tube size and voltage for the total pressure to exhibit two maximums, the first giving rise to the electron-driven shock wave and the second resulting from equilibration and providing the source for a second shock wave which we shall arbitrarily call the "hydrodynamically-driven shock wave" because the driver plasma is now in or near thermal equilibrium.

The existence of electron-driven shock waves was first recognized by Fowler (**28**), who observed that in small-diameter electric shock tubes (~ 1 mm) and at low pressures (~ 1 mm Hg) electron-driven shock waves would propagate from the electrode region at times which were nearly an order of magnitude too brief for thermal equilibration. In larger diameter tubes at low pressures, two shock fronts were observed: an electron-driven front followed by a hydrodynamic shock front. In these large diameter tubes at higher pressures only the hydrodynamic fronts were observed.

Fowler concluded experimentally (**28**) that the velocity of the electron-driven shock fronts can be approximated by

$$V_s \propto \left(\frac{kT_e}{m_i}\right)^{1/2} \tag{4}$$

where $a_4 = (kT_e/m_i)^{1/2}$ is the effective sonic velocity of the non-equilibrium driver. The similarity between equation (4) and equation (2) for the thermal shock tube will be noted.

The energy exchange process in the EM shock tube is complicated by the coupling provided by interaction between the discharge current and the magnetic field and is therefore very sensitive to the electrode geometry. While various attempts have been made to uncouple the magnetic and thermal driving processes for the purpose of analysis (**29–34**), the emphasis here will be on the qualitative features of the problem. In effect a "glob" of driver plasma is created by the electric discharge and is driven from the electrode region by the magnetic field. In most configurations the magnetic acceleration is of limited duration. After that the moving plasma undergoes an expansion which approaches that of a one-dimensional blast wave because of the short length of the glob of accelerated plasma (**21, 35–37**).

In the conical configuration the driver plasma is compressed as it is driven from the electrode region. This increase in the density of the driver plasma thereby increases the rate of thermal equilibration and decreases the threshold pressure below which electron-driven shock waves are expected. Though electron driven shock waves have been reported in conical tubes (**28**), evidence of thermal equilibration has been found at a point 8 inches from the ring electrode in a 3-inch diameter tube operating with argon at an ambient pressure of 50 μ-Hg (**27**).

Fowler (**38**) has noted that although the driving effect of the magnetic field in the EM T-tube can be thought of as forcing the discharge current loop into the side arm, where its driving effect is replaced by a rail-type drive produced by the efforts of the hairpin current to straighten itself, the major effect of the magnetic field may be to force hot electrons of the main discharge into the side arm where their electron pressure supplies a drive which is not weakened by expansion as in the classical shock tube. The blast wave nature of the ensuing shock motion would then be explained by noting that $T_e \propto E \propto V/x$ where E is the electric field strength at the shock front, V is the voltage on the capacitors, and x is the position of the shock. The electron-driven shock front would then exhibit the same velocity attenuation characteristics as the blast wave, i.e., $V_s \propto x^{-1/2}$ [equation (4)].

In general the highest velocities are obtained when the electrode geometry is designed for an effective transmission-line or rail-type drive in which the magnetic forces are more fully utilized (**39**). The MAST is such a device. The discharge begins as a radial current in the annulus between concentric electrode cylinders. The current sheet is then driven outward by the interaction between these radial currents and the azimuthal fields which are present in the region between the electrodes, and into an annular expansion tube with non-conducting walls. Thus, as the drive progresses, two concentric axial sheet-current arcs form to connect the electrodes with the propagating radial arc.

During the initial phases of the electric discharge, the electron temperature can become very high resulting in large radiation losses and the removal of large amounts of contaminants from the tube walls. Cases have been reported (**40**) in which impurities have been vaporized from the driver section in sufficient amounts to counteract the rarefaction waves and significantly reduce shock velocity attenuation. Experiments show high levels of silicon wall impurities even in the conical EM shock tubes which were designed to minimize this effect (**27**). These contaminants increase radiation losses from the driver. Estimates made from data obtained in electric (**41**) and conical-type EM (**27**) shock tubes indicate that only 1% or 2% of the stored capacitor energy can be accounted for in thermal and kinetic energy of the expanding plasma. It is interesting to note that the rate of shock velocity attenuation is not affected by radiation losses under most shock tube operating conditions (**37**).

PRECURSOR EFFECTS

We shall define a precursor effect as any effect which results in a perturbation of the state of the background gas ahead of a shock front. It is difficult to generalize on precursor observations reported in the literature, because many of the papers do not itemize information such as electrode material or the existence of ground loops in the shock tube circuit—information which can be important in determining what precursor process dominates in a given situation. However, precursor phenomena can be attributed to three general processes—electron diffusion, radiation, or breakdown waves—and have been observed in conventional, electric, and electromagnetic shock tubes. Electron diffusion appears to be the dominant mechanism in diaphragm shock tubes (**42–44**), although radiation effects have been reported (**45–47**). Radiation and breakdown waves are the principal causes of precursor effects in electric and EM shock tubes.

Radiation from the high temperature gaseous discharge results in photoelectric emission from metallic surfaces within the shock tube and pre-excitation of the background gas due to absorption. Radiation investigations generally consist of three parts: (1) postulation of a type of radiation which would result in the observed perturbation of the cold gas; (2) an experiment to show that the observed phenomenon was not caused by fast electrons escaping from the highly ionized plasma; and (3) an experiment to identify the source of the radiation. Although photoelectric emission was observed in the first electric shock tube (**8**), recent investigations have verified the existence of unbroadened precursor line emission from the cold gas ahead of the shock front in both the T- (**48**) and conical (**49**) EM shock tubes. The primary source of this precursor effect has been traced to radiation emitted from the discharge region (**50**); and since the cold low pressure gas ahead of the shock front is optically thin to radiation in the visible region, the source must be attributed to radiation in the vacuum ultraviolet ($\lambda < 2000$ Å) or the X-ray regions ($\lambda < 50$ Å). Although kinetic models have been suggested (**48–49**) for the absorption of ultraviolet radiation and the ultimate emission of the observed line radiation, X-rays have been found prominent in forming an ionizing precursor disturbance which travels through the background gas during the electric discharge (**51**). This X-ray effect was observed in a conical EM shock tube, where the background gas faces the positive center electrode, when the discharge voltage was above the threshold value needed to produce K_α radiation from the positive electrode. Radiation precursor effects have been found to be strongly dependent on the impurity level in the background gas (**85**).

When electric or EM shock tubes are operated at low pressures, stray currents have been observed to propagate downstream to grounded points along the expansion tube such as vacuum system junctions (**27, 52–53**). Such currents, and other propagating disturbances which cannot be attributed to radiation processes, will be classified as breakdown waves. For example, an electrostatic disturbance with associated faint luminous front has been reported (**54**) moving ahead of the shock at approximately 3×10^7 cm/sec in a conical tube, and Kerr cell studies (**55**) have shown what appeared to be the formation of a precursor boundary layer on the surface of a probe placed in a cylindrical type tube. Luminosity producing precursor waves have been observed (**56**) leaving the electrode region of the segmented electrode electric shock tube immediately after the discharge and moving more than a meter into the field-free region at velocities of 10^8 cm/sec. The waves are attributed (**57**) to the very high electron pressure which develops in such a device.

It is very difficult to make accurate quantitative judgments of how much these precursor processes perturb the cold gas. Although microwave experiments can be used to obtain information on the electron density [10^{10}–10^{13} cm^{-3} (**85–86**)], it is difficult to estimate the degree of excitation of the bound states since the background gas is not in equilibrium. The internal excitation of the bound states can have a pronounced effect on the thermodynamic state which develops behind the shock front (**58–59**). It should be noted, however, that under some low pressure operating conditions contact surface breakdown would make it impossible to use the Rankine–Hugoniot equations even if the state ahead of the shock front were accurately known.

CONTACT SURFACE BREAKDOWN

The concept of a contact surface originates from the diaphragm shock tube formalism and is defined as the diffusion interface which separates the gas which was originally in the electrode region from that originally in the expansion tube. The low pressures at which electric and EM shock tubes are often operated result in a breakdown of the contact surface. The importance of this effect has been illustrated by the experimental observations of Fowler (**8**), using electric shock tubes, and of Chang (**60**), Cloupeau (**52, 61–64**), and this author (**27**), using EM shock tubes. Fowler, Chang, and Cloupeau investigated the behavior of the shock and contact surfaces as they were reflected from an obstacle or another shock front. Chang identified the shock front by mounting a piezoelectric pressure probe in the end plate of the shock tube. Fowler (**8**) and Cloupeau (**52**) identified the source of the radiation by placing different gas species in the electrode and expansion tube regions and making time-resolved spectroscopic observations. This investigator, using time resolved spectroscopy, found evidence of impurities from the discharge region throughout the slug of accelerated plasma in a conical EM shock tube. The results of these observations can be summarized as follows:

(1) The dynamics of the driver and driven gases and the existence of a luminous well-defined shock-heated region are very dependent on the ambient pressure, test gas species, and firing voltage.

(2) At high pressures no luminosity is observed from the shocked gas even after the shock is reflected, although the driver plasma is clearly luminous. Spectroscopic investigations at these conditions in EM shock tubes show that, although the contact surface has not broken down, some of the driven gas is passing through the contact surface rather than being compressed in front of it.

(3) As the pressure is lowered while the test gas and firing voltage are kept identical with (2), above, the reflected shock becomes visible; and finally, after continuing to lower the pressure one reaches a point where luminosity can be observed from behind the shock front as it separates and moves ahead of the contact surface. (The distance which the driver plasma propagates downstream and the point of onset of the luminosity from behind the shock front are very dependent on the test gas species and firing voltage.) Spectroscopic studies in EM shock tubes show that at these conditions there exists a region of pure shocked gas followed by the driver plasma, mixed with some of the driven gas. As the pressure is further reduced the primary shock front becomes progressively more luminous and the contact surface becomes indistinguishable. Under these conditions spectroscopic investigations in an EM T-tube show that the contact surface has completely broken down and that the driver plasma species can be found at the shock front (**65**).

The cause of the complete mixing is not clear at this point. It has been observed at pressures which, in terms of equilibration times, are marginal for the existence of electron driven shock waves. However, it has been noted in the preceding section that a high electron pressure may be maintained at the leading edge of the plasma as long as the discharge current continues to flow. Streak photographs indicate that the current was still flowing when the mixing was observed. Cloupeau has suggested that the discharge plasma may move into the tube as a projectile (or a group of projectiles), creating a shock wave whose front stays scarcely detached from the projectile. This model is very similar to Fowler's proposed theory for electron driven shock waves (**66**) in which it is assumed that a hot electron gas expands down the tube pulling a cold positive ion wind by the action of Coulomb forces. All electron-neutral collisions are neglected except for ionizing ones, so that an incident neutral atom passes through the front and continues at a constant velocity until it is ionized.

Several other mechanisms might be suggested to explain the contact surface breakdown. The deflection of the discharge current by the magnetic field may cause a turbulent mixing of the driver and driven gases. This process may be important in the conical tube where mixing has been observed in plasmas which appear to be in thermal equilibrium. Other possibilities might be a boundary layer allowing driven gas to escape past the contact surface (**67**) or a diffusion process, since under some conditions the density of the driven gas at the contact surface will be higher than that of the higher temperature driver plasma. The diffusion process is of particular interest since, when two fluids are accelerated in a direction perpendicular to their interface and in a direction from the less dense to the more dense, small irregularities in the interfacial boundary grow exponentially and turbulence develops (Taylor instability) (**68**). Kerr cell photographs show that the shape of the luminous front often is not reproducible and appears turbulent in form (**55, 87**).

CONCLUSIONS

Electric and EM shock tubes are capable of generating gas samples with higher temperatures and velocities than can be obtained in conventional gas-driven diaphragm shock tubes. However, the simple electric and EM shock tubes of the T-, cylindrical, and conical types are not suited for quantitative aerodynamic studies because of the brevity of available test times and the blast wave nature of the expansion, resulting in severe gradients in the thermodynamic state; nor are they suited for chemical kinetic studies involving the reactions in the shock front, because of precursor effects and contact surface mixing. Nevertheless, simple electric and EM shock tubes are very useful when a high-temperature, high-velocity gas sample is required. For example, EM T-tubes have been used for measuring Stark profiles of helium and hydrogen lines in the visible spectrum (**69**), and for ultraviolet line profile and oscillator strength measurements (**70, 88**). Conical EM tubes have been used for semiquantitative magnetoaerodynamic studies (**71**), for studying a small wire-resistance heat transfer gauge (**72**) and an infrared heat transfer gauge (**73**), and to inject plasma samples into both cusp and perpendicular magnetic fields (**74–75**). The simplicity and low cost of these shock tubes make them particularly suitable for educational laboratories (**76**).

Although the Rankine–Hugoniot equations cannot be used to determine accurately the thermodynamic state of the plasma sample (**77**), this information can be obtained experimentally. Optical interferometers have been successfully

used to make time-resolved electron density measurements (**77–78**). Time-integrated spectroscopy is useful in determining the impurities which are present, and time-resolved line emission spectroscopy can be used to obtain the electron temperature and density and the atom and ion densities throughout the accelerated plasma if the electron density is high enough to insure a Boltzmann distribution over the bound states (**79**). Time resolved spectroscopic measurements can be made either by placing a rotating mirror or drum camera in series with the spectrograph, or by mounting one or more photomultipliers behind slits in the focal plane of the spectrograph and feeding their outputs to oscilloscopes. Since a spectrograph with a small aperture ratio is required to expose the photographic film, the photomultiplier method is recommended when spatial resolution is important. Both smear camera (**58**) and photomultiplier techniques have been used to make time-resolved line profile measurements (**80**). Microwave techniques such as interferometry, attenuation, and phase shift have been used to measure plasma velocities (**20**) and to investigate electron densities (**81**). The microwave techniques are limited by rather poor spatial resolution but are particularly well suited for precursor measurements where spatial resolution is not important and where electron densities are too low for quantitative spectroscopic studies. Several other diagnostic tools such as piezoelectric crystals, magnetic probes, and magnetic microphones have been used in electric and EM shock tube studies. These are summarized in Table I. Although there have been a limited number of experimental investigations of the thermodynamic states which are generated in electric and EM shock tubes, these studies show that collision-dominated equilibrium plasmas can be generated, and that in general the temperatures are higher than the values predicted by the Rankine–Hugoniot equations. Typical data obtained with EM shock tubes using the time resolved spectroscopic technique are summarized in Table II.

TABLE II

					Densities (cm^{-3})	
Ref.	*Tube type*†	*Test gas*	*Electron temp.* (*ev*)	*Electron density*	*Atom density*	*First ion density*
(**82**)	A	Hydrogen	2.4	2.5×10^{17}		
(**58**)	A	Helium	3.98	1.2×10^{17}	6.7×10^{13}	8.2×10^{16}
(**27**)	B	Argon	1.27	9.3×10^{16}	6.5×10^{16}	9.3×10^{16}
(**59**)	C	Helium	~4	$\sim 10^{17}$		
(**83**)	A	Helium	4.3	5×10^{17}		

† A = EM T-tube; B = conical tube; C = conical electrodeless.

The purpose of this paper has been to try to summarize the recent developments in electric and EM shock tube research. These developments have had the effect of providing a better understanding of the limitations of the original conical and T-tube geometries and to suggest modifications which make more effective use of the phenomena which are occurring. Accordingly, it is of interest to speculate on what future trends might be expected. It is believed that work may develop in two directions. One direction may be toward a compromise with the diaphragm shock tube in order to develop a shock tube with a clean shock front for high-temperature studies in chemical kinetics. The new AVCO tube is a device of this nature (**24**). The other direction may be on the development of plasma accelerators

for the generation and acceleration of sufficiently long plasma samples for flow studies. In such devices the emphasis would be on the preparation of a plasma specimen followed by magnetic acceleration rather than depending on the action of a shock front. Another line of development may follow Fowler's new segmented-electrode electric shock tube, which takes advantage of the concept of an electron-driven shock front. Axial magnetic fields along the expansion tube may be used to reduce heat transfer to the walls (**84**).

ACKNOWLEDGMENTS

Much of the material presented in this paper was gathered while the author was associated with the Northwestern University Gas Dynamics Laboratory, and he wishes to express his appreciation to Dr. Ali Bulent Cambel, Laboratory Director, for his interest and helpful suggestions.

REFERENCES

1. Resler, E. L., Lin, S. C., and Kantrowitz, A., "The Production of High Temperature Gases in Shock Tubes", *J. Appl. Phys.*, **23**, 12, 1390 (1952).
2. Glass, I. I., "Shock Tubes, Part I, Theory and Performance of Simple Shock Tubes", *UTIA Review*, No. 12, Part I, Institute of Aerophysics, University of Toronto (1958).
3. Hall, J. G., "Shock Tubes, Part II, Production of Strong Waves, Shock Tube Applications, Design and Instrumentation", *UTIA Review*, No. 12, Part II, Institute of Aerophysics, University of Toronto (1958).
4. Ferri, A., ed., *Fundamental Data Obtained From Shock-Tube Experiments* ["AGARDograph No. 41" (New York: Pergamon Press, 1961)].
5. Weymann, H. D., "Comments on the Theory of Electron Driven Shock Waves", *Phys. Fluids*, **4**, 12, 1573 (1961).
6. Lee, R. J., and Fowler, R. G., "Rayleigh Afterglow in Hydrogen Discharges", *Phys. Rev.*, **81**, 3, 457 (1951).
7. Fowler, R. G., Goldstein, J. S. and Clotfelter, B. E., "Luminous Fronts in Pulsed Gas Discharges", *Phys. Rev.*, **82**, 6, 879 (1951).
8. Fowler, R. G., Atkinson, W. R., Clotfelter, B. E., and Lee, R. J., "Final Report—Research on Radiation Transients in Gas Discharges", Project 52, University of Oklahoma Research Institute, *ASTIA* No. 196378 (1952).
9. Fowler, R. G., Atkinson, W. R., and Marks, L. W., "Ion Concentrations and Recombination in Expanding Low Pressure Sparks", *Phys. Rev.*, **87**, 6, 966 (1952).
10. Fowler, R. G., Atkinson, W. R., Compton, W. D., and Lee, R. J., "Shock Waves in Low Pressure Spark Discharges", *Phys. Rev.*, **88**, 1, 137 (1952).
11. Kolb, A. C., "Production of High-Energy Plasmas by Magnetically Driven Shock Waves", *Phys. Rev.*, **107**, 2, 345 (1957).
12. Kolb, A. C., "Experiments at the U.S. Naval Research Laboratory", in *Magnetohydrodynamics*, ed. R. Landshoff (Stanford: Stanford University Press, 1957), 76–91.
13. Blackman, V. H., and Niblett, B., "Experiments Using a Hydromagnetic Shock Tube", in *The Plasma in a Magnetic Field*, ed. R. Landshoff (Stanford: Stanford University Press, 1958), 87–98.
14. Patrick, R. M., "High-Speed Shock Waves in a Magnetic Annular Shock Tube", *Phys. Fluids*, **2**, 6, 589 (1959).
15. Kemp, N. H., and Petschek, H. E., "Theory of the Flow in the Magnetic Annular Shock Tube", *Phys. Fluids*, **2**, 6, 599 (1959).

16. Patrick, R. M., and Camac, M., "Shock Waves in Collision-Free Plasmas", in *Plasma Hydromagnetics*, ed. D. Bershader (Stanford: Stanford University Press, 1962), 97–123.
17. Gerry, E. T., Kantrowitz, A. R., and Petschek, H. E., "Alternate Explanation of MAST Shock Thickness Measurements", *Bull. Am. Phys. Soc.*, **8**, 158 (1963).
18. Petschek, H. E., and Gerry, E. T., "Structure of an Ionizing Shock in a Magnetic Field", *Bull. Am. Phys. Soc.*, **8**, 158 (1963).
19. Josephson, V., "Production of High Velocity Shocks", *J. Appl. Phys.*, **29**, 1, 30 (1958).
20. Kash, S., "Experiments at Lockheed Missile Systems Division", in *Magneto-hydrodynamics*, ed. R. Landshoff (Stanford: Stanford University Press, 1957), 92–98.
21. Kash, S., Gauger, J., Starr, W., and Vali, V., "Velocity Measurements in Magnetically Driven Shock Tubes", in *The Plasma in a Magnetic Field*, ed. R. Landshoff (Stanford: Stanford University Press, 1958), 99–109.
22. Hart, P. J., "Effect of Gas Pressure and Cone Angle on the Velocity of Electrically Excited Shock Waves", *J. Appl. Phys.*, **31**, 2, 436 (1960).
23. Smy, P. R., "Electromagnetic Shock Tube Capable of Producing a Well-Formed Shock Wave of Low Attenuation", *Nature*, **193**, 4819, 969 (1962).
24. Camm, J. C., and Rose, P. H., "Electric Arc-Driven Shock Tube", *Phys. Fluids*, **6**, 663 (1963).
25. Fowler, R. G., "Experiments with the Electric Shock Tube", Lecture presented at the Gas Dynamics Colloquium, Northwestern University, Evanston, Illinois, November 27, 1962.
26. Spitzer, L., Jr., *Physics of Fully Ionized Gases* (New York: Interscience, 1956).
27. Thornton, J. A., "A Spectroscopic Study of the Argon Plasmas Generated in a Conical Electromagnetic Shock Tube", Gas Dynamics Laboratory Report No. B–2–63, Northwestern University (1963) (to be published in *J. Quant. Spec. Radiat. Transfer*).
28. Fowler, E. G., Paxton, G. W., and Hughes, H. G., "Electrons as a Shock Driver Gas", *Phys. Fluids*, **4**, 2, 234 (1961).
29. Mitchner, M., "Magnetohydrodynamic Flow in a Shock Tube", *Phys. Fluids*, **2**, 62 (1959).
30. Wright, J. K., and Black, M. C., "A Theory of Electromagnetically Driven Shock Waves", *J. Fluid Mech.*, **6**, 2, 289 (1959).
31. Banister, J. R., "Separation of Magnetic Driving and Ohmic Heating", *Phys. Fluids*, **3**, 4, 648 (1960).
32. Gartenhaus, S., and Tannenwald, L. M., "Propulsion from Pinch Collapse", in *Plasma Acceleration*, ed. S. Kash (Stanford: Stanford University Press, 1960), 73–78.
33. Hart, P. J., "Plasma Acceleration with Coaxial Electrodes", *Phys. Fluids*, **5**, 1, 38 (1962).
34. Cameron, I. G., "Hydromagnetic Shock Fronts in Low Pressure Gases," *Quart. J. Mech. and Appl. Math.*, **15**, 153 (1962).
35. Harris, E. G., "Exact and Approximate Treatments of the One-Dimensional Blast Wave", U.S. Naval Research Laboratory Report No. 5858 (1956).
36. Morgenroth, H., Hess, H., Kischel, K., Rademacher, R., and Seliger, K., "On the Theory of Shock Wave Propagation and Channel Formation in Spark Discharges", *Annalen Der Physik*, **8**, 3–4, 175 (1961).
37. Thornton, J. A., and Cambel, A. B., "The Effect of Radiative Losses on the Attenuation of Electromagnetically Driven Shock Waves", *J. Quant. Spec. Radiat. Transfer*, **2**, 3, 249 (1962).

38. Fowler, R. G., "Origin of the Driving Force in Electromagnetic Shock Tubes", *Phys. Fluids*, **6**, 548 (1963).
39. Kholev, S. R., and Poltavchenko, D. S., "Acceleration of the Plasma of a Discharge and Production of Strong Shock Waves in a Shock Tube With Coaxial Electrodes", *Soviet Phys. Doklady*, **5**, 2, 356 (1960).
40. Bershader, D., "Some Remarks on Electric-Discharge Shock-Tube Diagnostics", *Rev. Mod. Phys.*, **32**, 4, 780 (1960).
41. Fowler, R. G., and Turner, E. B., "Magnetically Insulated Shock Tube", *Phys. Fluids*, **4**, 5, 544 (1961).
42. Weymann, H. D., "Electron Diffusion Ahead of Shock Waves in Argon", *Phys. Fluids*, **3**, 4, 545 (1960).
43. Groenig, H., "Measurement of the Diffusion of Electrons out of Strong Shock Waves", *ASTIA* Report AD 232 219 (1959).
44. Wetzel, L., "Precursor Effects and Electron Diffusion from a Shock Front", *Phys. Fluids*, **5**, 7, 824 (1962).
45. Hollyer, R. N., "Preliminary Studies in the APL High Temperature Shock Tube", Applied Physics Laboratory, Report No. CM-903, Johns Hopkins University (1957).
46. Gloersen, P., "Some Unexpected Results of Shock-Heating Xenon", *Phys. Fluids*, **3**, 6, 857 (1960).
47. Hammerling, P., "Ionization Effects of Precursor Radiation from Shocks in Air", AVCO Everett Research Laboratory, Report No. 98 (1960).
48. McLean, E. A., Kolb, A. C., and Griem, H. R., "Visible Precursor Radiation in an Electromagnetic Shock Tube", *Phys. Fluids*, **4**, 8, 1055 (1961).
49. Voorhies, H. G., and Scott, F. R., "Anomalous Precursor Signals in Helium Shocks", *Phys. Fluids*, **2**, 5, 576 (1959).
50. Analytical work by Biberman and Veklenko, *Soviet Phys. JETP*, and recent microwave observations at Boeing (**85**) indicate that radiation from behind the shock may contribute significantly to the perturbation of the gas directly in front of the shock.
51. Gerardo, J. B., and Goldstein, L., "Precursor Effects in Electrically Driven Shocktubes", *Bull. Am. Phys. Soc.*, **8**, 2, 167 (1963).
52. Cloupeau, M., "Interpretation of Luminous Phenomena Observed in Electromagnetic Shock Tubes", *Phys. Fluids*, **6**, 679 (1963).
53. Byron, S., private communication.
54. Hales, R. W., and Josephson, V., "Electromagnetic Structure in a Shock Front", *Bull. Am. Phys. Soc.*, **5**, 1, 42 (1960).
55. Pugh, E. R., "Studies of the Phenomena Occurring in an Electromagnetic Shock Tube" (Ph.D. thesis, Graduate School of Aeronautical Engineering, Cornell University, 1962).
56. Fowler, R. C., and Hood, J. D., Jr., "Very Fast Dynamical Wave Phenomenon", *Phys. Rev.*, **128**, 991 (1962).
57. Paxton, G. W., and Fowler, R. G., "Theory of Breakdown-Wave Propagation", *Phys. Rev.*, **128**, 993 (1962).
58. McLean, E. A., Faneuff, C. E., Kolb, A. C., and Griem, H. R., "Spectroscopic Study of Helium Plasmas Produced by Magnetically Driven Shock Waves", *Phys. Fluids*, **3**, 6, 843 (1960).
59. Fuchs, Von W., Bohn, W. L., Heinrich, G., and Platz, P., "Elektronendichten und Elektronentemperaturen bei Verdichtungsstossen", *Z. Phys.*, **170**, 409 (1962).
60. Chang, C. T., "Shock Wave Phenomena in Coaxial Plasma Guns", *Phys. Fluids*, **4**, 9, 1085 (1961).

61. Cloupeau, M., "On the True Nature of Luminous Phenomena Observed in Magnetically Driven Shock Tubes", *Compt. Rend.*, **251**, 7, 918 (1960).
62. Cloupeau, M., "Properties of Shock Waves Produced by Condensed Discharges in a Low Pressure Gas", *J. Phys. Radium*, **21**, 3, 189 (1960).
63. Cloupeau, M., "The Origin of the Ionization in Electromagnetically Driven Shock Tubes", *Compt. Rend.*, **253**, 10, 1160 (1961).
64. Cloupeau, M., "Photoelectric Studies in a Two-Gas Magnetically Driven Shock Tube", *Compt. Rend.*, **254**, 2, 213 (1962).
65. Time resolved spectroscopy by B. D. Edwards, *Nature*, **196**, 833 (1962), in which all permutations of hydrogen and argon at 1 mm Hg placed on each side of a diaphragm 17 cm from the electrodes in an EM T-tube showed no indication of driver plasma downstream of diaphragm. It is difficult to ascertain the role which the diaphragm played in inhibiting the motion of the driver gas. Cloupeau (**51**) used a diffusion interface to initially separate the gases in the electrode region and expansion tube.
66. Fowler, R. G., and Fried, B. D., "Theory of Electron Driven Shock Waves", *Phys. Fluids*, **4**, 6, 767 (1961).
67. Roshko, A., "On Flow Duration in Low-Pressure Shock Tubes", *Phys. Fluids*, **3**, 6, 835 (1960).
68. Aranow, R. H., and Witten, L., "Effect of Diffusion on Interfacial Taylor Instability", *Phys. Fluids*, **6**, 535 (1963).
69. Berg, H. F., Ali, A. W., Lincke, R., and Griem, H. R., "Measurement of Stark Profiles of Neutral and Ionized Helium and Hydrogen Lines from Shock-Heated Plasmas in Electromagnetic T-Tubes", *Phys. Rev.*, **125**, 1, 199 (1962).
70. Griem, H. R., and Kolb, A. C., "Radiation from High Temperature Collision Dominated Plasmas", *J. Quant. Spect. Radiat. Transfer*, **2**, 4, 503 (1962).
71. Ziemer, R. W., "Experimental Investigations in Magneto-aerodynamics", *Am. Rocket Soc. J.*, **29**, 9, 642 (1959).
72. Ziemer, R. W., "Heat Transfer Gage for Use in Highly Ionized Gases", *Am. Rocket Soc. J.*, **31**, 1, 78 (1961).
73. Ziemer, R. W., "Instrumentation for Magneto-aerodynamic Heat Transfer", Physical Research Laboratory Report No. STL/TR-60-0000-09290, Space Technology Laboratories (1960).
74. Scott, F. R., and Wenzel, R. F., "Experimental Plasma Flow into a Vacuum Magnetic Cusp Field," *Phys. Rev.*, **119**, 4, 1187 (1960).
75. Tuckfield, R. G., Jr., Scott, F. R., and Krall, N. A., "Injection of a Plasma into a Perpendicular Magnetic Field", *Bull. Am. Phys. Soc.*, **8**, 162 (1963).
76. Seemann, G. R., Thornton, J. A., and Cambel, A. B., "Laboratory Observations in Conical Electromagnetic Shock Tubes", *J. Eng. Ed.*, **53**, 5, 322 (1963).
77. There are preliminary indications of density ratio agreement with the Rankine-Hugoniot equations at large distances from the electrode region and $P_1 =$ 2 mm Hg. Klein, A. F., *Phys. Fluids*, **6**, 310 (1963).
78. Ramsden, S. A., and McLean, E. A., "Optical Refractivity of Free Electrons", *Nature*, **194**, 4830, 761 (1962).
79. Wilson, R., "The Spectroscopy of Non-Thermal Plasmas", *J. Quant. Spec. Radiat. Transfer*, **2**, 4, 477 (1962).
80. Cunningham, S. P., Scott, F. R., and Wenzel, R. F., "Time Behavior of Spectral Line Shapes Behind Strong Shocks", *Bull. Am. Phys. Soc.*, **5**, 1, 124 (1960).
81. Takeda, S., "Microwave Study of Plasmas Produced by Electromagnetically Driven Shock Waves", *Bull. Am. Phys. Soc.*, **8**, 130 (1963).

82. Wiese, W., Berg, H. F., and Griem, H. R., "Measurements of Temperatures and Densities in Shock Heated Hydrogen and Helium Plasmas", *Phys. Rev.*, **120**, 4, 1079 (1960).
83. Barnard, A. J., Cormack, G. D., and Simkinson, W. V., "Spectroscopic Studies of Helium and Argon Plasmas Produced by Electromagnetically Driven Shock Waves", *Canadian J. Phys.*, **40**, 531 (1962).
84. Fowler, R. G., and Turner, E. B., "Magnetically Insulated Shock Tube", *Phys. Fluids*, **4**, 5, 544 (1961).
85. Mahaffey, W., Sanga, L., and Schoen, R. I., "Precursor Effects in an Electrically Driven Shock Tube," paper presented at 5th Annual Meeting, Div. of Plasma Physics of the Amer. Phys. Soc., San Diego, California, November 6-9, 1964.
86. Quinn, J. M. P., and Bodin, H. A. B., "A Microwave Study of the Precursor Effect", paper presented at VIth Inter. Conf. on Ionization Phen. in Gases, July 8–13, 1963.
87. Barnard, A. J., and Cormack, G. D., "Luminosity Structures of Plasmas in Electromagnetic Shock Tubes", paper presented at VIth Inter. Conf. on Ionization Phen. in Gases, July 8–13, 1963.
88. McLean, E. A., "Measurement of Neon Transition Probabilities using an Electromagnetic Shock Tube", paper presented at VIth Inter. Conf. on Ionization Phen. in Gases, July 8–13, 1963.
89. Head, R. M., "A Spectrographic Analysis of Hydrogen and Air Plasmas", paper presented at VIth Inter. Conf. on Ionization Phen. in Gases, July 8–13, 1963.
90. Brederlow, G., "The Structure of the Plasma Cloud in the Electromagnetically Operated Shock Tube", paper presented at VIth Inter. Conf. on Ionization Phen. in Gases, July 8–13, 1963.

3. H. N. Olsen: *The Measurement of Argon Transition Probabilities and Computation of Thermodynamic Properties of the Argon Plasma*

After considerable discussion by a number of authors it is now generally agreed that for plasmas having electron densities below a critical value of $\sim 10^{19}$ cm^{-3} *the correction for the lowering of the ionization potential should be determined from the Debye–Hückel limiting law corrections to the internal energy. The mathematical form of the correction is obtained automatically when the Saha equation is derived by extremizing the free energy.*

Numerous attempts at a direct measurement of the lowering of the ionization potential have been made with widely differing results. A common error is the failure to recognize the fundamental difference between the value determined from radiation measurements and that which appears in the Saha equation. It has been pointed out earlier by the author that an experimental check of the theoretical value to be used in the Saha equation is difficult and can probably be made only by comparing it with the value required to bring computed densities into agreement with experimental values measured by some method which is independent of the computed composition.

In this paper the agreement between a measured and computed ionic transition probability is used as a crude criterion for selecting the Debye–Hückel polarization theory as the best basis for treating the plasma corrections. Results of the work are (1) *a computed composition of the atmospheric pressure argon plasma,* (2) *corrected partition functions,* (3) *absolute values of transition probabilities, and* (4) *corrected thermodynamic properties of the plasma.*

INTRODUCTION

In order to determine the best possible values for spontaneous transition probabilities from measured absolute spectral line intensities emitted from a thermal arc plasma it was essential that the highest possible accuracy be attained in the theoretical calculation of the plasma composition. Several studies have treated the corrections which must be considered in computing the composition of

ED. NOTE: Dr. Olsen is at the Northrop Space Laboratories, Northrop Corporation, Hawthorne, California.

a laboratory plasma: lowering of the ionization potential, cutoff of the partition function, and the Debye polarization contribution to the total pressure.

After considerable discussion by several people studying the problem, it is now generally accepted that for plasmas having electron densities below a critical value of about 10^{19} cm^{-3}, the correction for the lowering of the ionization potential should be determined from the Debye–Hückel limiting law corrections to the internal energy. This correction leads automatically to a lowering of the ionization potential when the Saha equation is derived by extremizing the free energy.

In evaluating the internal partition functions it is conventional (**1, 2**) to sum over the unperturbed energy levels up to the effective ionization limit defined by the lowered ionization potential. Griem (**2**) has estimated the errors resulting from such a cutoff in the case of hydrogen and points out that it will rarely exceed one-tenth of one per cent in normal laboratory plasmas. He states, therefore, that it hardly seems justified to replace the straightforward cutoff by more involved methods.

Whereas corrections for the ionization-potential lowering and partition-function cutoff have generally been considered, the pressure corrections in the equations of state are seldom considered in the computation of plasma compositions. Duclos and Cambel (**3**) have reviewed this problem in great detail and have shown that in most laboratory plasmas the Debye–Hückel limiting laws are generally applicable. As pointed out by Griem (**2**), and found also to be the case in the work reported here, this correction will never amount to more than a few per cent. Thus errors due to uncertainties in the correction can generally be neglected.

Numerous attempts at a direct measure of the lowering of the ionization potential have been made with widely differing results. A common error is the failure to recognize the difference between the ΔV_R which is determined from radiation measurements and the ΔV_s which appears in the Saha equation. This distinction was first pointed out by Ecker and Wiezel (**4**), and later by Olsen (**1**). In the latter paper it was also pointed out that an experimental check of the theoretical value for ΔV_s is difficult and can probably be made only by comparing it with the value required to bring computed densities into agreement with experimental values measured by some method which is independent of the computed composition. In the present paper the agreement between a measured and computed ionic line transition probability is used as a crude criterion for selecting the best method for treating the plasma corrections. Results of this work are: (1) a computed composition of the atmospheric-pressure argon plasma; (2) corrected partition functions; (3) absolute values for transition probabilities; and (4) corrected thermodynamic properties of the plasma.

PLASMA COMPOSITION

Detailed calculations of the plasma composition involve reversible ionization reactions of the form

$$[A_i] \rightleftarrows [A_{i+1}] + [e] - e(V_i - \Delta V_i) \tag{1}$$

where $[A_i]$ represents the initial particle, $[A_{i+1}]$ the next fold ionized particle, and $[e]$ the electron liberated by the process which consumes a quantity of energy, $e(V_i - \Delta V_i)$, where V_i is the free particle ionization potential and ΔV_i is the lowering caused by the interaction of the neighboring plasma particles. There are z such reactions, where i is an integer ranging from 1 to z, and z is the highest fold of ionization existing in the plasma.

Under the assumption of LTE, quasineutrality, and the applicability of Dalton's law, the system of equations to be solved may be written as follows:

$$\frac{P_{i+1}P_e}{P_i} = F_i(T) = \frac{u_{i+1}}{u_i} A(T) \exp\left[-e(V_i - \Delta V_i)/kT\right] \tag{2}$$

where $A(T) = 2[2\pi m/h^2]^{3/2}(kT)^{5/2} = 6.5180 \times 10^{-7} T^{5/2}$, the u_i are the internal electron partition functions, and all pressures are in atmospheres. The z Saha equations are combined with the quasineutrality condition (conservation of charge)

$$P_e = \sum_{i=1}^{z} (i-1)P_i \tag{3}$$

and Dalton's Law (conservation of particles)

$$P = P_I + P_D$$

where

$$P_I = \sum_{i=1}^{z} iP_i$$

and the added pressure term P_D is due to the Debye–Hückel polarization.

It is now generally accepted that the Debye–Hückel limiting law corrections to the internal energy, free energy, and pressure may be determined as follows (**1, 2, 3, 4**):

$$E_D = \frac{-kT}{8\pi D^3}, \qquad F_D = \frac{-kTV}{12\pi D^3}, \qquad P_D = \frac{-kT}{24\pi D^3} \tag{5}$$

where V is the volume and D the Debye radius given by

$$D = \left[\frac{kT}{4\pi e^2 \sum_i n_i z_i^2}\right]^{1/2}$$

and the sum is over all particles of charge Z_i including the electrons. In the process of deriving the Saha equation by extremizing the free energy with respect to the ionization process given by equation (1), a correction in the direction of lowering the ionization potential enters in the amount of

$$\Delta V_i = i\frac{e}{D}, \quad i = 1, 2, \ldots z \tag{6}$$

This leads to a value that is, by about a factor of 4, smaller than the value given by the Unsöld (**5**) relation which considers only the microfield of the nearest ion—much in the same manner as an electric field lowers the work function at a surface. Ecker and Weizel (**4**) proceeded to add the Debye polarization term equation (6) to the Unsöld relation giving what is now recognized as too large a correction for any laboratory plasma.

Ecker and Kröll (**6**) have recently treated this problem in theoretical detail confirming the conclusion of Duclos and Cambel that there is a critical electron density below which only the polarization term is to be retained. The Unsöld relation has been erroneously used almost consistently in the earlier published works on plasma spectroscopy.

The partition functions appearing in equation (2) are given by

$$u_i = \sum_{l}^{l_c} g_{i,l} \exp\left(-E_{i,l}/kT\right) \tag{7}$$

where $g_{i,l}$ are the statistical weights and $E_{i,l}$ are the unperturbed excitation energies of the levels l of species i. Because of the nonconvergence of this sum at temperatures above about 15,000°K in argon, it must be cut off at some upper energy level E_{i,l_c} which fulfills the condition $E_{i,l_c} \leqq e(V_i - \Delta V_i)$.

Griem (**2**) has considered in detail all of the above internally consistent corrections for the Saha equation, the equations of state, and the partition functions, and has shown that errors due to remaining uncertainties in the corrections are usually below one per cent. With the above corrections given, the final set of equations to be solved is given below:

$$P = P_e\left[\left(1+\sum_{j=1}^{z}(j+1)C_j\right)\Big/\sum_{j=1}^{z} jC_j\right] - \frac{e^3\pi^{1/2}}{3(kT)^2}\left[P_e\sum_{j=1}^{z}(j+1)jC_j\Big/\sum_{j=1}^{z} jC_j\right]^{3/2} \tag{8}$$

where $C_j = \prod_{i=1}^{i}(F_i/P_e)$, the F_i are given by equation (2), and

$$\Delta V_i = i\left[\frac{4\pi}{kT}\right]^{1/2} e^2\left[P_e\sum_{j=1}^{z}(j+1)jC_j\Big/\sum_{j=1}^{z} jC_j\right]^{1/2} \tag{9}$$

Equation (8) must first be iteratively solved for P_e from which all of the species' partial pressures can subsequently be determined according to

$$P_1 = P_e\Big/\sum_{j=1}^{z} jC_j; \qquad P_{i+1} = P_1C_i \quad \text{for} \quad i = 1, 2, \ldots, z-1 \tag{10}$$

where the subscript 1 is associated with the neutral atoms to be consistent with standard spectroscopic notation. An iterative computation of these equations has been programmed for the IBM 7090 to give particle number densities, partition functions, lowering of ionization potentials, and the effective charge of the ions. The numerical results are tabulated in Tables I and II.

TRANSITION PROBABILITIES

Detailed methods for obtaining transition probabilities from measured line intensities using the 400-amp argon arc plasma at a total pressure of 1.1 atmospheres have been thoroughly described in a recent paper (**7**). In that work a novel method for determining transition probabilities from measured emission coefficients of a prominent pair of lines defined as reference lines (λ6965 ArI and λ4806 ArII) was presented. This method has been advantageously employed here to confirm the theoretical conclusions regarding methods to be applied in correcting the computed plasma compositions.

The emission coefficient of a spectral line emitted in watt/(cm^3 − steradian) by a particle of number density n_i from a volume unit at temperature T°K is defined as

$$S_i = A_i\left[K_i\frac{n_i}{u_i}\exp\left(-E_{im}/kT\right)\right] \tag{11}$$

where $K_i = 1.582\times10^{-24}(g_m/\lambda)$ Å, g_m is the statistical weight of the upper energy level E_{im} and λ is the wavelength in cm. The portion of equation (11) in brackets is defined as the normalized emission coefficient (S_i^*) which can be calculated directly from the plasma composition.

Figure 1 is a plot of the measured emission coefficients of the above reference lines emitted by the 1.1-atmosphere argon plasma. This plot can be represented by the following parametric equations:

$$\begin{aligned} x &= \log S_1 = \log A_1 + \log S_1^* \\ y &= \log S_2 = \log A_2 + \log S_2^* \end{aligned} \tag{12}$$

TABLE I. PARTICLE NUMBER DENSITIES (CM^{-3}) FOR ARGON AT 1 ATMOSPHERE PRESSURE

T (°K)	N_1	N_2	N_3	N_4	N_5	N_6	N_E	N_I	N_T
4.000E 03	1.8350E 18	1.2724E 10	0.	0.	0.	0.	1.2724E 10	1.2724E 10	1.8350E 18
4.500E 03	1.6311E 18	1.6733E 11	0.	0.	0.	0.	1.6733E 11	1.6733E 11	1.6311E 18
5.000E 03	1.4680E 18	1.3186E 12	0.	0.	0.	0.	1.3186E 12	1.3186E 12	1.4680E 18
5.500E 03	1.3346E 18	7.1588E 12	0.	0.	0.	0.	7.1588E 12	7.1588E 12	1.3346E 18
6.000E 03	1.2233E 18	2.9386E 13	0.	0.	0.	0.	2.9386E 13	2.9386E 13	1.2234E 18
6.500E 03	1.1291E 18	9.7277E 13	0.	0.	0.	0.	9.7277E 13	9.7277E 13	1.1293E 18
7.000E 03	1.0480E 18	2.7191E 14	0.	0.	0.	0.	2.7191E 14	2.7191E 14	1.0486E 18
7.500E 03	9.7736E 17	6.6371E 14	0.	0.	0.	0.	6.6371E 14	6.6371E 14	9.7869E 17
8.000E 03	9.1462E 17	1.4507E 15	0.	0.	0.	0.	1.4507E 15	1.4507E 15	9.1752E 17
8.500E 03	8.5778E 17	2.8939E 15	2.5862E 05	0.	0.	0.	2.8939E 15	2.8939E 15	8.6357E 17
9.000E 03	8.0493E 17	5.3449E 15	2.3362E 06	0.	0.	0.	5.3449E 15	5.3449E 15	8.1562E 17
9.500E 03	7.5427E 17	9.2421E 15	1.6861E 07	0.	0.	0.	9.2421E 15	9.2421E 15	7.7275E 17
1.000E 04	7.0405E 17	1.5087E 16	1.0052E 08	0.	0.	0.	1.5087E 16	1.5087E 16	7.3422E 17
1.050E 04	6.5265E 17	2.3396E 16	5.0844E 08	0.	0.	0.	2.3396E 16	2.3396E 16	6.9944E 17
1.100E 04	5.9867E 17	3.4624E 16	2.2303E 09	0.	0.	0.	3.4624E 16	3.4624E 16	6.6792E 17
1.150E 04	5.4117E 17	4.9054E 16	8.6380E 09	0.	0.	0.	4.9054E 16	4.9054E 16	6.3928E 17
1.200E 04	4.7986E 17	6.6658E 16	2.9982E 10	0.	0.	0.	6.6658E 16	6.6658E 16	6.1317E 17
1.250E 04	4.1538E 17	8.6960E 16	9.4426E 10	0.	0.	0.	8.6960E 16	8.6960E 16	5.8930E 17
1.300E 04	3.4933E 17	1.0903E 17	2.7268E 11	3.3671E-01	0.	0.	1.0903E 17	1.0903E 17	5.6740E 17
1.350E 04	2.8443E 17	1.3137E 17	7.2848E 11	1.5259E 01	0.	0.	1.3138E 17	1.3137E 17	5.4718E 17
1.400E 04	2.2353E 17	1.5243E 17	1.8146E 12	1.2355E 02	0.	0.	1.5243E 17	1.5243E 17	5.2840E 17
1.450E 04	1.6992E 17	1.7044E 17	4.2429E 12	8.8852E 02	0.	0.	1.7045E 17	1.7045E 17	5.1082E 17
1.500E 04	1.2538E 17	1.8443E 17	9.3714E 12	5.7396E 03	0.	0.	1.8445E 17	1.8444E 17	4.9426E 17
1.550E 04	9.0468E 16	1.9404E 17	1.9663E 13	3.3605E 04	0.	0.	1.9408E 17	1.9406E 17	4.7861E 17
1.600E 04	6.4414E 16	1.9963E 17	3.9389E 13	1.7958E 05	0.	0.	1.9971E 17	1.9967E 17	4.6379E 17
1.650E 04	4.5683E 16	2.0192E 17	7.5674E 13	8.8074E 05	0.	0.	2.0207E 17	2.0200E 17	4.4975E 17
1.700E 04	3.2534E 16	2.0175E 17	1.3997E 14	3.9838E 06	0.	0.	2.0203E 17	2.0189E 17	4.3645E 17
1.750E 04	2.3416E 16	1.9985E 17	2.5008E 14	1.6694E 07	0.	0.	2.0035E 17	2.0010E 17	4.2387E 17
1.800E 04	1.7105E 16	1.9677E 17	4.3274E 14	6.5085E 07	0.	0.	1.9764E 17	1.9721E 17	4.1195E 17
1.850E 04	1.3276E 16	1.9260E 17	7.2677E 14	2.3731E 08	1.5440E-05	0.	1.9406E 17	1.9333E 17	4.0066E 17
1.900E 04	1.0153E 16	1.8813E 17	1.1869E 15	8.1005E 08	2.3628E-03	0.	1.9051E 17	1.8932E 17	3.8998E 17

TABLE I (CONT.)

T (°K)	N_1	N_2	N_3	N_4	N_5	N_6	N_E	N_I	N_T
1.950E 04	7.9119E 15	1.8314E 17	1.8855E 15	2.5982E 09	1.1726E–01	0.	1.8691E 17	1.8503E 17	3.7986E 17
2.000E 04	6.2789E 15	1.7761E 17	2.9181E 15	7.8564E 09	8.9612E–01	0.	1.8345E 17	1.8053E 17	3.7025E 17
2.050E 04	5.0626E 15	1.7144E 17	4.3979E 15	2.2423E 10	6.1838E 00	0.	1.8024E 17	1.7584E 17	3.6114E 17
2.100E 04	4.1363E 15	1.6450E 17	6.4509E 15	6.0464E 10	3.8665E 01	0.	1.7740E 17	1.7095E 17	3.5249E 17
2.150E 04	3.4139E 15	1.5662E 17	9.1999E 15	1.5409E 11	2.1963E 02	0.	1.7503E 17	1.6582E 17	3.4426E 17
2.200E 04	2.8365E 15	1.4769E 17	1.2740E 16	3.7116E 11	1.1358E 03	0.	1.7318E 17	1.6043E 17	3.3645E 17
2.250E 04	2.3639E 15	1.3765E 17	1.7111E 16	8.4503E 11	5.3593E 03	0.	1.7188E 17	1.5476E 17	3.2901E 17
2.300E 04	1.9691E 15	1.2657E 17	2.2266E 16	1.8194E 12	2.3132E 04	0.	1.7111E 17	1.4884E 17	3.2192E 17
2.350E 04	1.6339E 15	1.1465E 17	2.8067E 16	3.7096E 12	9.1653E 04	0.	1.7080E 17	1.4272E 17	3.1516E 17
2.400E 04	1.3466E 15	1.0223E 17	3.4286E 16	7.1786E 12	3.3489E 05	0.	1.7082E 17	1.3652E 17	3.0869E 17
2.450E 04	1.0999E 15	8.9708E 16	4.0642E 16	1.3226E 13	1.1346E 06	6.2957E–09	1.7103E 17	1.3036E 17	3.0250E 17
2.500E 04	8.8918E 14	7.7520E 16	4.6842E 16	2.3291E 13	3.5863E 06	1.4354E–06	1.7127E 17	1.2439E 17	2.9655E 17
2.550E 04	7.1104E 14	6.6044E 16	5.2622E 16	3.9363E 13	1.0641E 07	1.1770E–03	1.7141E 17	1.1871E 17	2.9082E 17
2.600E 04	5.6258E 14	5.5572E 16	5.7780E 16	6.4117E 13	2.9820E 07	6.5083E–03	1.7132E 17	1.1342E 17	2.8530E 17
2.650E 04	4.4084E 14	4.6279E 16	6.2189E 16	1.0107E 14	7.9372E 07	3.3374E–02	1.7096E 17	1.0857E 17	2.7997E 17
2.700E 04	3.4263E 14	3.8232E 16	6.5797E 16	1.5476E 14	2.0168E 08	1.5977E–01	1.7029E 17	1.0418E 17	2.7482E 17
2.750E 04	2.6458E 14	3.1404E 16	6.8612E 16	2.3098E 14	4.9137E 08	7.1819E–01	1.6932E 17	1.0025E 17	2.6983E 17
2.800E 04	2.0336E 14	2.5705E 16	7.0682E 16	3.3697E 14	1.1523E 09	3.0460E 00	1.6808E 17	9.6724E 16	2.6501E 17
2.850E 04	1.5584E 14	2.1007E 16	7.2081E 16	4.8172E 14	2.6089E 09	1.2240E 01	1.6661E 17	9.3570E 16	2.6034E 17
2.900E 04	1.1997E 14	1.7170E 16	7.2886E 16	6.7617E 14	5.7183E 09	4.6765E 01	1.6497E 17	9.0732E 16	2.5582E 17
2.950E 04	9.1519E 13	1.4266E 16	7.3033E 16	9.3195E 14	1.2146E 10	1.7024E 02	1.6313E 17	8.8230E 16	2.5145E 17
3.000E 04	7.0060E 13	1.1739E 16	7.2868E 16	1.2668E 15	2.5102E 10	5.9284E 02	1.6128E 17	8.5874E 16	2.4722E 17
3.050E 04	5.3700E 13	9.6926E 15	7.2300E 16	1.6971E 15	5.0489E 10	1.9775E 03	1.5938E 17	8.3690E 16	2.4313E 17
3.100E 04	4.1225E 13	8.0325E 15	7.1365E 16	2.2421E 15	9.8936E 10	6.3284E 03	1.5749E 17	8.1639E 16	2.3917E 17
3.150E 04	3.8191E 13	6.6813E 15	7.0082E 16	2.9221E 15	1.8903E 11	1.9458E 04	1.5561E 17	7.9686E 16	2.3534E 17
3.200E 04	2.9432E 13	5.5761E 15	6.8473E 16	3.7566E 15	3.5221E 11	5.7523E 04	1.5379E 17	7.7806E 16	2.3163E 17
3.250E 04	2.2711E 13	4.6693E 15	6.6537E 16	4.7657E 15	6.4058E 11	1.6373E 05	1.5204E 17	7.5973E 16	2.2804E 17
3.300E 04	1.7535E 13	3.9199E 15	6.4282E 16	5.9640E 15	1.1372E 12	4.4895E 05	1.5038E 17	7.4166E 16	2.2456E 17
3.350E 04	1.3539E 13	3.2966E 15	6.1713E 16	7.3604E 15	1.9707E 12	1.1865E 06	1.4881E 17	7.2372E 16	2.2120E 17
3.400E 04	1.0446E 13	2.7751E 15	5.8845E 16	8.9557E 15	3.3340E 12	3.0245E 06	1.4735E 17	7.0579E 16	2.1793E 17
3.450E 04	8.0488E 12	2.3364E 15	5.5701E 16	1.0740E 16	5.5074E 12	7.4394E 06	1.4598E 17	6.8783E 16	2.1477E 17

TABLE I (CONT.)

T (°K)	N_1	N_2	N_3	N_4	N_5	N_6	N_E	N_I	N_T
3.500E 04	6.1885E 12	1.9655E 15	5.2317E 16	1.2693E 16	8.8841E 12	1.7670E 07	1.4471E 17	6.6985E 16	2.1171E 17
3.550E 04	4.7451E 12	1.6509E 15	4.8742E 16	1.4781E 16	1.4000E 13	4.0561E 07	1.4354E 17	6.5189E 16	2.0873E 17
3.600E 04	3.6261E 12	1.3836E 15	4.5036E 16	1.6963E 16	2.1562E 13	9.0068E 07	1.4243E 17	6.3404E 16	2.0584E 17
3.650E 04	2.7606E 12	1.1563E 15	4.1265E 16	1.9189E 16	1.2477E 13	1.9369E 08	1.4138E 17	6.1643E 16	2.0303E 17
3.700E 04	2.0904E 12	1.0422E 15	3.7467E 16	2.1392E 16	4.7860E 13	4.0381E 08	1.4034E 17	5.9949E 16	2.0029E 17
3.750E 04	1.5787E 12	8.6877E 14	3.3785E 16	2.3548E 16	6.9139E 13	8.1782E 08	1.3936E 17	5.8271E 16	1.9763E 17
3.800E 04	1.1873E 12	7.2167E 14	3.0239E 16	2.5597E 16	9.7966E 13	1.6109E 09	1.3838E 17	5.6656E 16	1.9504E 17
3.850E 04	8.8957E 11	5.9743E 14	2.6881E 16	2.7498E 16	1.3632E 14	3.0913E 09	1.3740E 17	5.5113E 16	1.9251E 17
3.900E 04	6.6415E 11	4.9301E 14	2.3748E 16	2.9221E 16	1.8649E 14	5.7876E 09	1.3640E 17	5.3649E 16	1.9005E 17
3.950E 04	4.9437E 11	4.0570E 14	2.0868E 16	3.0743E 16	2.5115E 14	1.0589E 10	1.3538E 17	5.2268E 16	1.8764E 17
4.000E 04	3.6708E 11	3.3305E 14	1.8250E 16	3.2052E 16	3.3331E 14	1.8959E 10	1.3432E 17	5.0969E 16	1.8529E 17
4.050E 04	2.7205E 11	2.7287E 14	1.5899E 16	3.3144E 16	4.3643E 14	3.3265E 10	1.3325E 17	4.9752E 16	1.8300E 17
4.100E 04	2.0135E 11	2.2321E 14	1.3805E 16	3.4019E 16	5.6431E 14	5.7265E 10	1.3215E 17	4.8612E 16	1.8076E 17
4.150E 04	1.4890E 11	1.8238E 14	1.1955E 16	3.4684E 16	7.2120E 14	9.6827E 10	1.3103E 17	4.7543E 16	1.7857E 17
4.200E 04	1.1008E 11	1.4890E 14	1.0331E 16	3.5146E 16	9.1169E 14	1.6096E 11	1.2990E 17	4.6538E 16	1.7643E 17
4.250E 04	8.1385E 10	1.2149E 14	8.9129E 15	3.5414E 16	1.1407E 15	2.6328E 11	1.2875E 17	4.5590E 16	1.7434E 17
4.300E 04	6.0191E 10	9.9094E 13	7.6792E 15	3.5500E 16	1.4134E 15	4.2404E 11	1.2761E 17	4.4692E 16	1.7230E 17
4.350E 04	4.4543E 10	8.0805E 13	6.6092E 15	3.5410E 16	1.7349E 15	6.7284E 11	1.2647E 17	4.3836E 16	1.7031E 17
4.400E 04	3.2987E 10	6.5877E 13	5.6831E 15	3.5155E 16	2.1104E 15	1.0523E 12	1.2534E 17	4.3015E 16	1.6836E 17
4.450E 04	2.4447E 10	5.3694E 13	4.8827E 15	3.4741E 16	2.5447E 15	1.6227E 12	1.2423E 17	4.2224E 16	1.6645E 17
4.500E 04	1.8128E 10	4.3739E 13	4.1906E 15	3.4178E 16	3.0410E 15	2.4675E 12	1.2314E 17	4.1456E 16	1.6459E 17
4.550E 04	1.6191E 10	3.5618E 13	3.5940E 15	3.3469E 16	3.6037E 15	3.7021E 12	1.2207E 17	4.0706E 16	1.6277E 17
4.600E 04	1.2023E 10	2.8984E 13	3.0792E 15	3.2623E 16	4.2339E 15	5.4801E 12	1.2102E 17	3.9971E 16	1.6099E 17
4.650E 04	8.9301E 09	2.6622E 13	2.6349E 15	3.1647E 16	4.9315E 15	8.0044E 12	1.2000E 17	3.9248E 16	1.5925E 17
4.700E 04	6.6338E 09	2.1639E 13	2.2518E 15	3.0552E 16	5.6948E 15	1.1538E 13	1.1902E 17	3.8532E 16	1.5755E 17
4.750E 04	4.9269E 09	1.7562E 13	1.9213E 15	2.9348E 16	6.5193E 15	1.6414E 13	1.1806E 17	3.7822E 16	1.5588E 17
4.800E 04	3.6575E 09	1.4227E 13	1.6365E 15	2.8047E 16	7.3984E 15	2.3047E 13	1.1714E 17	3.7119E 16	1.5426E 17
4.850E 04	2.7132E 09	1.1501E 13	1.3912E 15	2.6664E 16	8.3232E 15	3.1945E 13	1.1624E 17	3.6422E 16	1.5266E 17
4.900E 04	2.0109E 09	9.2772E 12	1.1802E 15	2.5216E 16	9.2827E 15	4.3718E 13	1.1537E 17	3.5732E 16	1.5110E 17
4.950E 04	1.4886E 09	7.4650E 12	9.9902E 14	2.3721E 16	1.0264E 16	5.9082E 13	1.1452E 17	3.5051E 16	1.4957E 17
5.000E 04	1.1006E 09	5.9916E 12	8.4373E 14	2.2198E 16	1.1254E 16	7.8869E 13	1.1369E 17	3.4380E 16	1.4807E 17

TABLE II. PARTITION FUNCTIONS FOR ARGON AT 1 ATMOSPHERE PRESSURE

T (°K)	U_1	U_2	U_3	U_4	U_5	U_6	ΔV_1 (cm^{-1})	Z_{eff}
4.000E 03	1.0000E 00	5.1949E 00	0.	0.	0.	0.	4.2480E 01	1.0000E 00
4.500E 03	1.0000E 00	5.2653E 00	0.	0.	0.	0.	1.4524E 00	1.0000E 00
5.000E 03	1.0000E 00	5.3245E 00	0.	0.	0.	0.	3.8679E 00	1.0000E 00
5.500E 03	1.0000E 00	5.3751E 00	0.	0.	0.	0.	8.5929E 00	1.0000E 00
6.000E 03	1.0000E 00	5.4187E 00	0.	0.	0.	0.	1.6668E 01	1.0000E 00
6.500E 03	1.0000E 00	5.4567E 00	0.	0.	0.	0.	2.9137E 01	1.0000E 00
7.000E 03	1.0000E 00	5.4900E 00	0.	0.	0.	0.	4.6942E 01	1.0000E 00
7.500E 03	1.0000E 00	5.5196E 00	0.	0.	0.	0.	7.0853E 01	1.0000E 00
8.000E 03	1.0000E 00	5.5459E 00	0.	0.	0.	0.	1.0143E 02	1.0000E 00
8.500E 03	1.0000E 00	5.5695E 00	8.7222E 00	0.	0.	0.	1.3897E 02	1.0000E 00
9.000E 03	1.0001E 00	5.5908E 00	8.8267E 00	0.	0.	0.	1.8355E 02	1.0000E 00
9.500E 03	1.0001E 00	5.6100E 00	8.9289E 00	0.	0.	0.	2.3492E 02	1.0000E 00
1.000E 04	1.0003E 00	5.6276E 00	9.0286E 00	0.	0.	0.	2.9255E 02	1.0000E 00
1.050E 04	1.0005E 00	5.6436E 00	9.1261E 00	0.	0.	0.	3.5553E 02	1.0000E 00
1.100E 04	1.0010E 00	5.6584E 00	9.2212E 00	0.	0.	0.	4.2256E 02	1.0000E 00
1.150E 04	1.0014E 00	5.6719E 00	9.3140E 00	0.	0.	0.	4.9191E 02	1.0000E 00
1.200E 04	1.0024E 00	5.6845E 00	9.4045E 00	0.	0.	0.	5.6135E 02	1.0000E 00
1.250E 04	1.0042E 00	5.6961E 00	9.4928E 00	0.	0.	0.	6.2821E 02	1.0000E 00
1.300E 04	1.0061E 00	5.7069E 00	9.5789E 00	0.	0.	0.	6.8978E 02	1.0000E 00
1.350E 04	1.0101E 00	5.7170E 00	9.6628E 00	5.1920E 00	0.	0.	7.4300E 02	1.0000E 00
1.400E 04	1.0135E 00	5.7264E 00	9.7446E 00	5.3005E 00	0.	0.	7.8591E 02	1.0000E 00
1.450E 04	1.0209E 00	5.7352E 00	9.8244E 00	5.4108E 00	0.	0.	8.1662E 02	1.0000E 00
1.500E 04	1.0313E 00	5.7436E 00	9.9022E 00	5.5225E 00	0.	0.	8.3522E 02	1.0001E 00
1.550E 04	1.0457E 00	5.7514E 00	9.9780E 00	5.6353E 00	0.	0.	8.4285E 02	1.0001E 00
1.600E 04	1.0652E 00	5.7589E 00	1.0052E 01	5.7491E 00	0.	0.	8.4155E 02	1.0002E 00
1.650E 04	1.0910E 00	5.7660E 00	1.0124E 01	5.8636E 00	0.	0.	8.3366E 02	1.0004E 00
1.700E 04	1.1248E 00	5.7728E 00	1.0194E 01	5.9785E 00	0.	0.	8.2136E 02	1.0007E 00
1.750E 04	1.1680E 00	5.7794E 00	1.0263E 01	6.0937E 00	0.	0.	8.0639E 02	1.0012E 00
1.800E 04	1.2225E 00	5.7858E 00	1.0330E 01	6.2090E 00	0.	0.	7.9009E 02	1.0022E 00
1.850E 04	1.3510E 00	5.7920E 00	1.0395E 01	6.3242E 00	0.	0.	7.7284E 02	1.0038E 00
1.900E 04	1.4523E 00	5.7982E 00	1.0459E 01	6.4393E 00	0.	0.	7.5653E 02	1.0063E 00

TABLE II (CONT.)

T (°K)	U_1	U_2	U_3	U_4	U_5	U_6	ΔV_1 (cm^{-1})	Z_{eff}
1.950E 04	1.5752E 00	5.8076E 00	1.0521E 01	6.5540E 00	9.7093E 00	0.	7.4111E 02	1.0102E 00
2.000E 04	1.7230E 00	5.8154E 00	1.0582E 01	6.6684E 00	9.7813E 00	0.	7.2705E 02	1.0162E 00
2.050E 04	1.8986E 00	5.8240E 00	1.0642E 01	6.7822E 00	9.8518E 00	0.	7.1479E 02	1.0250E 00
2.100E 04	2.1056E 00	5.8336E 00	1.0700E 01	6.8955E 00	9.9208E 00	0.	7.0473E 02	1.0377E 00
2.150E 04	2.3472E 00	5.8445E 00	1.0758E 01	7.0082E 00	9.9885E 00	0.	6.9720E 02	1.0555E 00
2.200E 04	2.6271E 00	5.8572E 00	1.0814E 01	7.1201E 00	1.0055E 01	0.	6.9238E 02	1.0794E 00
2.250E 04	2.9489E 00	5.8721E 00	1.0869E 01	7.2314E 00	1.0120E 01	0.	6.9028E 02	1.1106E 00
2.300E 04	3.3162E 00	5.8897E 00	1.0923E 01	7.3418E 00	1.0184E 01	0.	6.9063E 02	1.1496E 00
2.350E 04	3.7326E 00	5.9106E 00	1.0976E 01	7.4514E 00	1.0247E 01	0.	6.9288E 02	1.1967E 00
2.400E 04	4.2020E 00	5.9356E 00	1.1028E 01	7.5602E 00	1.0309E 01	0.	6.9632E 02	1.2512E 00
2.450E 04	4.7278E 00	5.9654E 00	1.1080E 01	7.6682E 00	1.0370E 01	0.	7.0015E 02	1.3120E 00
2.500E 04	5.3139E 00	6.0009E 00	1.1131E 01	7.7752E 00	1.0431E 01	0.	7.0363E 02	1.3770E 00
2.550E 04	5.9638E 00	6.0433E 00	1.1181E 01	7.8814E 00	1.0490E 01	5.5765E 00	7.0615E 02	1.4440E 00
2.600E 04	6.6809E 00	6.0934E 00	1.1231E 01	7.9867E 00	1.0549E 01	5.5905E 00	7.0731E 02	1.5106E 00
2.650E 04	7.4688E 00	6.1528E 00	1.1280E 01	8.0911E 00	1.0608E 01	5.6047E 00	7.0693E 02	1.5747E 00
2.700E 04	8.3309E 00	6.2226E 00	1.1329E 01	8.1947E 00	1.0665E 01	5.6190E 00	7.0498E 02	1.6345E 00
2.750E 04	9.2702E 00	6.3044E 00	1.1378E 01	8.2973E 00	1.0722E 01	5.6335E 00	7.0160E 02	1.6890E 00
2.800E 04	1.0290E 01	6.3999E 00	1.1426E 01	8.3992E 00	1.0779E 01	5.6482E 00	6.9698E 02	1.7377E 00
2.850E 04	1.1393E 01	6.5108E 00	1.1474E 01	8.5001E 00	1.0835E 01	5.6632E 00	6.9137E 02	1.7806E 00
2.900E 04	1.2658E 01	6.6390E 00	1.1523E 01	8.6002E 00	1.0891E 01	5.6784E 00	6.8502E 02	1.8182E 00
2.950E 04	1.3945E 01	6.9054E 00	1.1572E 01	8.6995E 00	1.0947E 01	5.6940E 00	6.7787E 02	1.8489E 00
3.000E 04	1.5324E 01	7.0979E 00	1.1620E 01	8.7979E 00	1.1003E 01	5.7098E 00	6.7077E 02	1.8781E 00
3.050E 04	1.6798E 01	7.3180E 00	1.1670E 01	8.8956E 00	1.1058E 01	5.7259E 00	6.6362E 02	1.9045E 00
3.100E 04	1.8369E 01	7.5684E 00	1.1719E 01	8.9925E 00	1.1113E 01	5.7424E 00	6.5658E 02	1.9291E 00
3.150E 04	2.4144E 01	7.8521E 00	1.1770E 01	9.0887E 00	1.1168E 01	5.7592E 00	6.4980E 02	1.9528E 00
3.200E 04	2.6302E 01	8.1722E 00	1.1824E 01	9.1841E 00	1.1223E 01	5.7764E 00	6.4343E 02	1.9766E 00
3.250E 04	2.8586E 01	8.5322E 00	1.1878E 01	9.2788E 00	1.1278E 01	5.7940E 00	6.3757E 02	2.0013E 00
3.300E 04	3.0997E 01	8.9353E 00	1.1932E 01	9.3728E 00	1.1333E 01	5.8120E 00	6.3228E 02	2.0276E 00
3.350E 04	3.3539E 01	9.3853E 00	1.1988E 01	9.4662E 00	1.1388E 01	5.8304E 00	6.2762E 02	2.0562E 00
3.400E 04	3.6211E 01	9.8857E 00	1.2046E 01	9.5590E 00	1.1443E 01	5.8492E 00	6.2360E 02	2.0877E 00
3.450E 04	3.9016E 01	1.0440E 01	1.2106E 01	9.6511E 00	1.1498E 01	5.8684E 00	6.2021E 02	2.1223E 00

TABLE II (CONT.)

T (°K)	U_1	U_2	U_3	U_4	U_5	U_6	ΔV_1 (cm^{-1})	Z_{eff}
3.500E 04	4.1954E 01	1.1053E 01	1.2169E 01	9.7427E 00	1.1554E 01	5.8881E 00	6.1738E 02	2.1604E 00
3.550E 04	4.5028E 01	1.1728E 01	1.2234E 01	9.8337E 00	1.1609E 01	5.9082E 00	6.1502E 02	2.2019E 00
3.600E 04	4.8238E 01	1.2470E 01	1.2302E 01	9.9243E 00	1.1665E 01	5.9287E 00	6.1303E 02	2.2464E 00
3.650E 04	5.1584E 01	1.3282E 01	1.2374E 01	1.0014E 01	1.1721E 01	5.9497E 00	6.1126E 02	2.2936E 00
3.700E 04	5.5067E 01	1.5345E 01	1.2450E 01	1.0104E 01	1.1778E 01	5.9711E 00	6.0947E 02	2.3410E 00
3.750E 04	5.8688E 01	1.6454E 01	1.2530E 01	1.0193E 01	1.1835E 01	5.9930E 00	6.0780E 02	2.3916E 00
3.800E 04	6.2446E 01	1.7660E 01	1.2614E 01	1.0282E 01	1.1892E 01	6.0154E 00	6.0601E 02	2.4425E 00
3.850E 04	6.6343E 01	1.8968E 01	1.2704E 01	1.0371E 01	1.1949E 01	6.0382E 00	6.0400E 02	2.4931E 00
3.900E 04	7.0377E 01	2.0383E 01	1.2799E 01	1.0459E 01	1.2007E 01	6.0616E 00	6.0174E 02	2.5424E 00
3.950E 04	7.4549E 01	2.1911E 01	1.2901E 01	1.0547E 01	1.2065E 01	6.0854E 00	5.9917E 02	2.5900E 00
4.000E 04	7.8858E 01	2.3556E 01	1.3010E 01	1.0635E 01	1.2124E 01	6.1096E 00	5.9631E 02	2.6354E 00
4.050E 04	8.3304E 01	2.5325E 01	1.3125E 01	1.0723E 01	1.2183E 01	6.1344E 00	5.9317E 02	2.6782E 00
4.100E 04	8.7887E 01	2.7222E 01	1.3249E 01	1.0811E 01	1.2243E 01	6.1596E 00	5.8978E 02	2.7184E 00
4.150E 04	9.2605E 01	2.9253E 01	1.3382E 01	1.0899E 01	1.2303E 01	6.1853E 00	5.8617E 02	2.7560E 00
4.200E 04	9.7458E 01	3.1424E 01	1.3524E 01	1.0987E 01	1.2364E 01	6.2115E 00	5.8241E 02	2.7912E 00
4.250E 04	1.0244E 02	3.3739E 01	1.3676E 01	1.1075E 01	1.2425E 01	6.2381E 00	5.7854E 02	2.8242E 00
4.300E 04	1.0757E 02	3.6204E 01	1.3839E 01	1.1163E 01	1.2487E 01	6.2653E 00	5.7461E 02	2.8554E 00
4.350E 04	1.1282E 02	3.8824E 01	1.4014E 01	1.1252E 01	1.2549E 01	6.2929E 00	5.7067E 02	2.8851E 00
4.400E 04	1.1820E 02	4.1604E 01	1.4201E 01	1.1341E 01	1.2612E 01	6.3210E 00	5.6678E 02	2.9139E 00
4.450E 04	1.2371E 02	4.4551E 01	1.4402E 01	1.1431E 01	1.2675E 01	6.3496E 00	5.6297E 02	2.9422E 00
4.500E 04	1.2935E 02	4.7668E 01	1.4617E 01	1.1525E 01	1.2740E 01	6.3787E 00	5.5929E 02	2.9703E 00
4.550E 04	1.6261E 02	5.0961E 01	1.4847E 01	1.1616E 01	1.2805E 01	6.4082E 00	5.5575E 02	2.9987E 00
4.600E 04	1.6973E 02	5.4435E 01	1.5094E 01	1.1709E 01	1.2870E 01	6.4382E 00	5.5239E 02	3.0277E 00
4.650E 04	1.7699E 02	6.5642E 01	1.5358E 01	1.1803E 01	1.2936E 01	6.4687E 00	5.4921E 02	3.0576E 00
4.700E 04	1.8441E 02	7.0063E 01	1.5640E 01	1.1898E 01	1.3003E 01	6.4997E 00	5.4624E 02	3.0888E 00
4.750E 04	1.9197E 02	7.4710E 01	1.5942E 01	1.1995E 01	1.3071E 01	6.5311E 00	5.4346E 02	3.1215E 00
4.800E 04	1.9968E 02	7.9588E 01	1.6264E 01	1.2093E 01	1.3139E 01	6.5630E 00	5.4087E 02	3.1557E 00
4.850E 04	2.0752E 02	8.4701E 01	1.6607E 01	1.2194E 01	1.3208E 01	6.5954E 00	5.3846E 02	3.1914E 00
4.900E 04	2.1551E 02	9.0056E 01	1.6974E 01	1.2296E 01	1.3278E 01	6.6282E 00	5.3619E 02	3.2287E 00
4.950E 04	2.2364E 02	9.5656E 01	1.7364E 01	1.2401E 01	1.3349E 01	6.6615E 00	5.3404E 02	3.2673E 00
5.000E 04	2.3190E 02	1.0151E 02	1.7779E 01	1.2508E 01	1.3420E 01	6.6952E 00	5.3198E 02	3.3070E 00

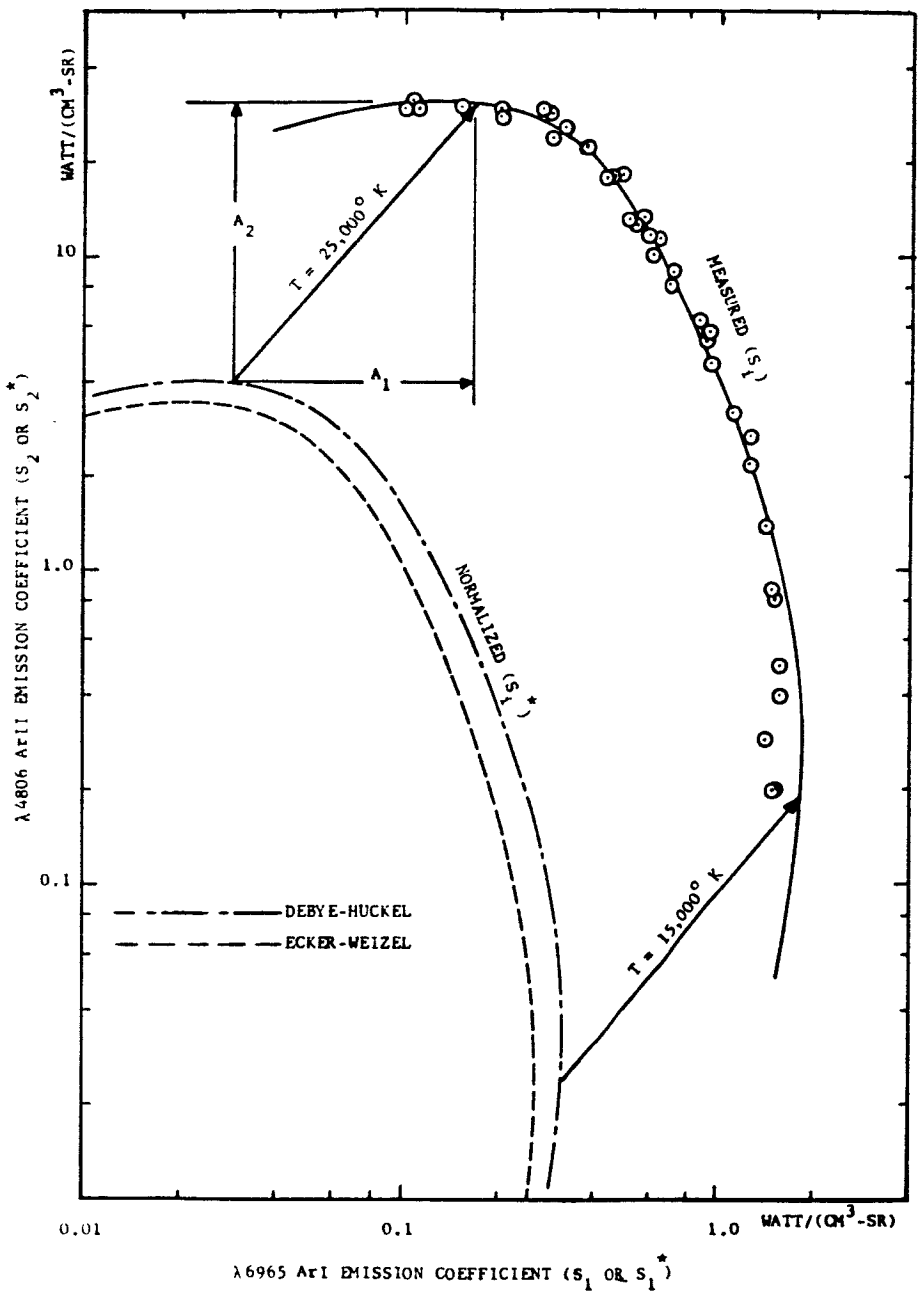

FIGURE 1. Log–log plot of measured absolute emission coefficients (S_i) and theoretical normalized emission coefficients (S_i^*) for atomic (I) and ionic (II) spectral lines emitted from a 1.1-atmosphere argon plasma. The arrows demonstrate the method used to determine absolute transition probabilities (A_i).

If the transition probabilities are normalized to unity, a similar plot of the normalized emission coefficients is obtained as shown in Figure 1 where the results of two different methods for correcting the composition are indicated. There are two principal advantages in this type of plot. First of all, since the parameter on the experimental curve is temperature (or plasma radius) the results of measurements of both lines at common points throughout the entire plasma as well as measurements made in different arcs at the same total pressure can be readily compared. Secondly, as can be seen by the equations (12) and as indicated in Figure 1, the numerical factors required to shift the theoretical curve to best fit the experimental points are precisely the transition probabilities sought.

The experimental points plotted in Figure 1 represent averages of at least six independent measurements. By independent, it is meant that intensities of the two lines were measured at the same position in a given arc, but that each set of measurements was made in a different arc in the sense that it had been re-struck with replaced electrodes at the same current and pressure. Measurements in the same arc were also made at three different positions along the arc axis; the points at the top of the curve were measured near the cathode and those at the bottom midway between the electrodes. The deviation of experimental points toward lower values for the λ6965 ArI line at the lower temperature has been explained (**7**) by absorption of the cooler layers of gas through which one must look to observe the core of the plasma.

The solid curve through the experimental points represents the best fit of the normalized emission coefficients which correspond with the plasma composition corrected according to the now accepted Debye–Hückel theory for the lowering of the ionization potential. Because of the similarity in shapes of the theoretical curves, both can be fitted—with practically the same degree of precision—to the experimental points resulting in the following A-values in units of $\sec^{-1}$.

	A_1	A_2
Ecker–Weizel	0.67×10^7	9.20×10^7
Debye–Hückel	0.57×10^7	7.86×10^7

A theoretical value of 7.88×10^7 $\sec^{-1}$ has been computed from intermediate coupling line strengths calculated by Garstang (**8**). The excellent agreement between this value and the experimental value obtained from the plasma composition based on the theoretically accepted Debye–Hückel polarization correction represents the first experimental evidence in support of the theory. In all fairness, these results should be looked upon only as indications at this time since the accuracy of the theoretical A-value is not considered by Garstang to be better than 50 per cent, and we are trying to separate an effect which differs by 15 per cent. The results do show, however, that the experimental precision is sufficient to observe the difference between the two corrections provided a more precise theoretical A-value can be obtained. The observed agreement between measured and computed A-values, coupled with the state of the theory on plasma corrections, was at the very least a guide in selecting the correct theory applied in determining the composition of the plasma and its thermodynamic properties.

THERMODYNAMIC PROPERTIES

Using the computed particle densities, partition functions, and ΔV the following have been computed: heat content, Gibbs free energy, entropy, and constant pressure specific heat. The computations include the contributions from translation, ionization, internal excitation, mixing (in the case of the entropy and free energy) and Debye–Hückel polarization. The equations used in all computations

are given below where M is the molecular weight in grams/mole, R is the gas constant expressed in ergs/mole, k is Boltzmann's constant, and h is Planck's constant. It should be noted that the partition functions and their derivatives with respect to temperature were determined first on a per-particle basis and then multiplied by the number of particles per gram to give the corresponding totals. Since the derivatives should be evaluated at constant volume rather than constant pressure this can introduce some error. However, as is shown in Figure 2, the

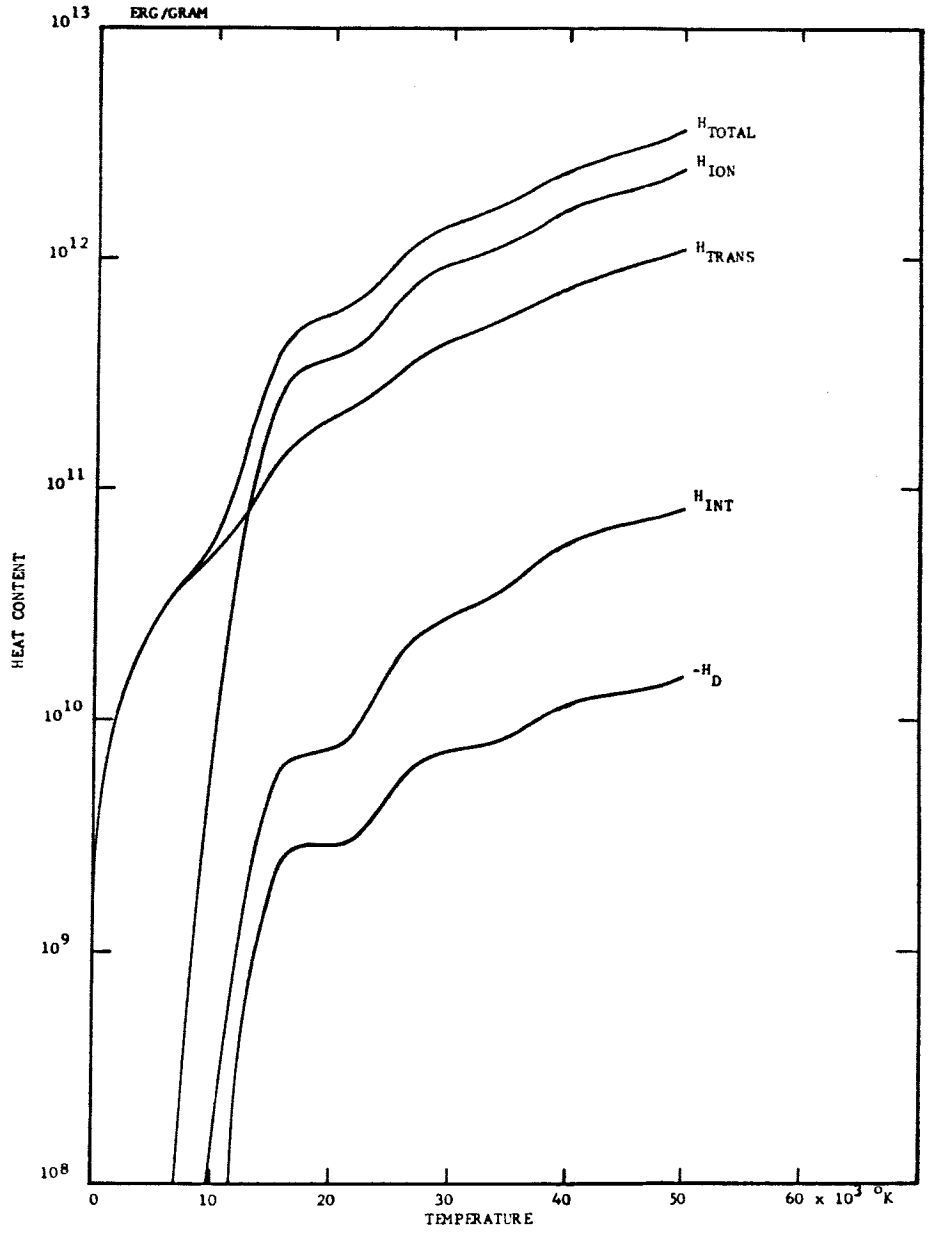

FIGURE 2. Temperature dependence of relative contributions to total computed heat content of a 1-atmosphere argon plasma.

contributions of internal excitations to the total heat content under the conditions covered here are practically negligible. The error introduced by the incorrect differentiation may, therefore, certainly be neglected.

Heat content

$$H_{\text{trans}} = \frac{5}{2}\frac{RT}{M}; \qquad H_{\text{int}} = \frac{RT^2}{MP_I}\sum_{i=1}^{z} P_i \frac{d}{dT}\ln u_i$$

$$H_{\text{ion}} = \frac{R}{MkP_I}\sum_{j=2}^{z} P_j \sum_{i=1}^{j} e(V_i - i\Delta V); \qquad H_D = \frac{4RT}{M}\left(\frac{P_D}{P_I}\right)$$

Gibbs free energy

$$G_{\text{trans}} = \frac{RT}{M}\left[\ln P_I - \frac{5}{2}\ln T + (K_e - K_a)\frac{P_e}{P_I} + K_a\right]$$

where $K_e = -\frac{3}{2}\ln(2\pi m_e k^{5/3}/h^2)$ and $K_a = -\frac{3}{2}\ln(2\pi m_a k^{5/3}/h^2)$

$$G_{\text{int}} = -\frac{RT}{MP_I}\left[\sum_{i=1}^{z} P_i \ln u_i + P_e \ln u_e\right]; \qquad G_{\text{ion}} = H_{\text{ion}}$$

$$G_{\text{mix}} = -\frac{RT}{MP_I}\left[\sum_{i=1}^{z} P_i \ln (P_i/P_I) + P_e \ln (P_e/P_I)\right]; \qquad G_D = \tfrac{3}{4}H_D$$

Entropy

$$S_{\text{trans}} = \frac{5}{2}\frac{R}{M} - \frac{G_{\text{trans}}}{T}$$

$$S_{\text{int}} = \frac{R}{MP_I}\left[\sum_{i=1}^{z} P_i\left(\ln u_i + T\frac{d}{dT}\ln u_i\right) + P_e \ln u_e\right]$$

$$S_{\text{mix}} = -\frac{G_{\text{mix}}}{T}; \qquad S_D = -\frac{H_D}{4T}$$

Specific heat at constant pressure

$$C_{\text{trans}} = \frac{5}{2}\frac{R}{M}; \qquad C_{\text{int}} = \frac{RT}{MP_I}\left\{\sum_{i=1}^{z} P_i\left[2\frac{d}{dT}\ln u_i + T\frac{d^2}{dT^2}\ln u_i\right]\right\}$$

$$C_{\text{ion}} = \frac{dH_{\text{ion}}}{dT}; \qquad C_D = \frac{dH_D}{dT}$$

The totals of each of the thermodynamic properties computed for the atmospheric pressure argon plasma are given in Table III, along with the mass density ρ in grams/cm^3, molar volume V in cm^3, the molecular weight M in grams/mole, and the ideal gas pressure P_I and Debye–Hückel pressure corrections P_D in atmospheres for temperatures in the range of 4000 to 50,000°K. All energies are referred to as zero at the absolute temperature zero.

ACKNOWLEDGMENTS

I wish to acknowledge the support of the Lockheed California Company of Burbank, California, in programming and performing the machine computations of the plasma compositions prior to my joining the Northrop Space Laboratories. The measured absolute line intensities were taken from work reported previously as completed at the Linde Company Speedway Laboratories, Indianapolis, Indiana.

TABLE III. THERMODYNAMIC FUNCTIONS FOR ARGON AT 1 ATMOSPHERE PRESSURE

T (°K)	H (erg/gm)	S (erg/gm-°K)	G (erg/gm)	C_p (erg/gm-°K)	ρ (gm/cm^3)	V (cm^3/mole)	M (gm/mole)	P_I (atm)	P'_D (atm)
4.000E 03	2.0821E 10	5.2663E 07	−1.8823E 11	5.2054E 06	1.2166E-04	3.2832E 05	3.9944E 01	1.0000E 00	3.5287E-13
4.500E 03	2.3423E 10	5.2874E 07	−2.1451E 11	5.2058E 06	1.0814E-04	3.6936E 05	3.9944E 01	1.0000E 00	1.5866E-11
5.000E 03	2.6026E 10	5.3423E 07	−2.4109E 11	5.2088E 06	9.7330E-05	4.1040E 05	3.9944E 01	1.0000E 00	3.3297E-10
5.500E 03	2.8631E 10	5.3920E 07	−2.6793E 11	5.2206E 06	8.8482E-05	4.5144E 05	3.9944E 01	1.0000E 00	4.0159E-09
6.000E 03	3.1241E 10	5.4385E 07	−2.9502E 11	5.2568E 06	8.1107E-05	4.9248E 05	3.9943E 01	1.0000E 00	3.1978E-08
6.500E 03	3.3869E 10	5.4791E 07	−3.2228E 11	5.3504E 06	7.4863E-05	5.3351E 05	3.9941E 01	1.0000E 00	1.8504E-07
7.000E 03	3.6545E 10	5.5185E 07	−3.4975E 11	5.5598E 06	6.9504E-05	5.7455E 05	3.9934E 01	1.0000E 00	8.3327E-07
7.500E 03	3.9325E 10	5.5562E 07	−3.7739E 11	5.9762E 06	6.4843E-05	6.1559E 05	3.9917E 01	1.0000E 00	3.0700E-06
8.000E 03	4.2313E 10	5.5933E 07	−4.0515E 11	6.7418E 06	6.0736E-05	6.5663E 05	3.9881E 01	1.0000E 00	9.6060E-06
8.500E 03	4.5684E 10	5.6369E 07	−4.3345E 11	8.0078E 06	5.7063E-05	6.9767E 05	3.9811E 01	1.0000E 00	2.6255E-05
9.000E 03	4.9687E 10	5.6823E 07	−4.6172E 11	1.0010E 07	5.3722E-05	7.3871E 05	3.9685E 01	1.0001E 00	6.4047E-05
9.500E 03	5.4692E 10	5.7360E 07	−4.9023E 11	1.3004E 07	5.0621E-05	7.7975E 05	3.9472E 01	1.0001E 00	1.4174E-04
1.000E 04	6.1194E 10	5.8020E 07	−5.1901E 11	1.7240E 07	4.7679E-05	8.2079E 05	3.9135E 01	1.0003E 00	2.8814E-04
1.050E 04	6.9814E 10	5.8944E 07	−5.4910E 11	2.3074E 07	4.4822E-05	8.6183E 05	3.8629E 01	1.0005E 00	5.4305E-04
1.100E 04	8.1351E 10	5.9904E 07	−5.7759E 11	3.0502E 07	4.1988E-05	9.0287E 05	3.7910E 01	1.0010E 00	9.5514E-04
1.150E 04	9.6602E 10	6.1231E 07	−6.0755E 11	4.0036E 07	3.9132E-05	9.4391E 05	3.6937E 01	1.0016E 00	1.5753E-03
1.200E 04	1.1662E 11	6.2894E 07	−6.3811E 11	5.1572E 07	3.6234E-05	9.8495E 05	3.5689E 01	1.0024E 00	2.4428E-03
1.250E 04	1.4241E 11	6.4950E 07	−6.6946E 11	6.3694E 07	3.3306E-05	1.0260E 06	3.4171E 01	1.0036E 00	3.5664E-03
1.300E 04	1.7426E 11	6.7389E 07	−7.0180E 11	7.6664E 07	3.0390E-05	1.0670E 06	3.2427E 01	1.0049E 00	4.9100E-03
1.350E 04	2.1259E 11	7.0219E 07	−7.3536E 11	8.6540E 07	2.7568E-05	1.1081E 06	3.0547E 01	1.0064E 00	6.3726E-03
1.400E 04	2.5585E 11	7.3308E 07	−7.7046E 11	9.3420E 07	2.4926E-05	1.1491E 06	2.8643E 01	1.0078E 00	7.8210E-03
1.450E 04	3.0256E 11	7.6533E 07	−8.0717E 11	9.3536E 07	2.2566E-05	1.1901E 06	2.6857E 01	1.0091E 00	9.0875E-03
1.500E 04	3.4933E 11	7.9671E 07	−8.4573E 11	8.7342E 07	2.0541E-05	1.2312E 06	2.5290E 01	1.0101E 00	1.0058E-02
1.550E 04	3.9300E 11	8.2519E 07	−8.8604E 11	7.6602E 07	1.8864E-05	1.2722E 06	2.4000E 01	1.0107E 00	1.0680E-02
1.600E 04	4.3130E 11	8.4948E 07	−9.2786E 11	6.4052E 07	1.7509E-05	1.3133E 06	2.2994E 01	1.0110E 00	1.0974E-02
1.650E 04	4.6333E 11	8.6924E 07	−9.7092E 11	5.2092E 07	1.6421E-05	1.3543E 06	2.2239E 01	1.0110E 00	1.1002E-02
1.700E 04	4.8937E 11	8.8498E 07	−1.0151E 12	4.2112E 07	1.5542E-05	1.3953E 06	2.1687E 01	1.0108E 00	1.0841E-02
1.750E 04	5.1043E 11	8.9745E 07	−1.0601E 12	3.4577E 07	1.4819E-05	1.4364E 06	2.1286E 01	1.0106E 00	1.0561E-02
1.800E 04	5.2772E 11	9.0734E 07	−1.1055E 12	2.9108E 07	1.4209E-05	1.4774E 06	2.0993E 01	1.0102E 00	1.0217E-02
1.850E 04	5.4227E 11	9.1566E 07	−1.1517E 12	2.4637E 07	1.3698E-05	1.5185E 06	2.0800E 01	1.0098E 00	9.8277E-03
1.900E 04	5.5546E 11	9.2293E 07	−1.1981E 12	2.5354E 07	1.3225E 05	1.5595E 06	2.0625E 01	1.0095E 00	9.4677E-03

TABLE III (CONT.)

T (°K)	H (erg/gm)	S (erg/gm-°K)	G (erg/gm)	C_p (erg/gm-°K)	ρ (gm/cm^3)	V (cm^3/mole)	M (gm/mole)	P_I (atm)	P_D (atm)
1.950E 04	5.6848E 11	9.2989E 07	−1.2448E 12	2.6544E 07	1.2792E−05	1.6005E 06	2.0474E 01	1.0091E 00	9.1347E−03
2.000E 04	5.8175E 11	9.3678E 07	−1.2918E 12	2.9445E 07	1.2385E−05	1.6416E 06	2.0332E 01	1.0088E 00	8.8458E−03
2.050E 04	5.9648E 11	9.4423E 07	−1.3392E 12	3.4405E 07	1.1994E−05	1.6826E 06	2.0181E 01	1.0086E 00	8.6160E−03
2.100E 04	6.1368E 11	9.5261E 07	−1.3868E 12	4.1522E 07	1.1608E−05	1.7237E 06	2.0009E 01	1.0085E 00	8.4586E−03
2.150E 04	6.3444E 11	9.6248E 07	−1.4349E 12	5.0773E 07	1.1221E−05	1.7647E 06	1.9801E 01	1.0084E 00	8.3852E−03
2.200E 04	6.5983E 11	9.7420E 07	−1.4834E 12	6.1897E 07	1.0825E−05	1.8057E 06	1.9547E 01	1.0084E 00	8.4038E−03
2.250E 04	6.9078E 11	9.8808E 07	−1.5324E 12	7.4323E 07	1.0418E−05	1.8468E 06	1.9239E 01	1.0085E 00	8.5168E−03
2.300E 04	7.2794E 11	1.0044E 08	−1.5821E 12	8.7161E 07	9.9987E−06	1.8878E 06	1.8876E 01	1.0087E 00	8.7190E−03
2.350E 04	7.7152E 11	1.0230E 08	−1.6326E 12	9.9300E 07	9.5709E−06	1.9289E 06	1.8461E 01	1.0090E 00	8.9960E−03
2.400E 04	8.2117E 11	1.0438E 08	−1.6840E 12	1.0957E 08	9.1407E−06	1.9699E 06	1.8006E 01	1.0093E 00	9.3249E−03
2.450E 04	8.7595E 11	1.0663E 08	−1.7364E 12	1.1697E 08	8.7161E−06	2.0109E 06	1.7528E 01	1.0097E 00	9.6772E−03
2.500E 04	9.3444E 11	1.0899E 08	−1.7902E 12	1.2081E 08	8.3057E−06	2.0520E 06	1.7043E 01	1.0100E 00	1.0023E−02
2.550E 04	9.9484E 11	1.1136E 08	−1.8449E 12	1.2091E 08	7.9173E−06	2.0930E 06	1.6571E 01	1.0103E 00	1.0333E−02
2.600E 04	1.0553E 12	1.1371E 08	−1.9011E 12	1.1756E 08	7.5568E−06	2.1341E 06	1.6127E 01	1.0106E 00	1.0588E−02
2.650E 04	1.1141E 12	1.1594E 08	−1.9584E 12	1.1148E 08	7.2274E−06	2.1751E 06	1.5720E 01	1.0108E 00	1.0774E−02
2.700E 04	1.1698E 12	1.1803E 08	−2.0170E 12	1.0359E 08	6.9301E−06	2.2161E 06	1.5358E 01	1.0109E 00	1.0887E−02
2.750E 04	1.2216E 12	1.1993E 08	−2.0766E 12	9.4887E 07	6.6639E−06	2.2572E 06	1.5042E 01	1.0109E 00	1.0930E−02
2.800E 04	1.2691E 12	1.2166E 08	−2.1373E 12	8.6251E 07	6.4263E−06	2.2982E 06	1.4769E 01	1.0109E 00	1.0910E−02
2.850E 04	1.3122E 12	1.2319E 08	−2.1988E 12	7.8355E 07	6.2140E−06	2.3393E 06	1.4536E 01	1.0108E 00	1.0839E−02
2.900E 04	1.3514E 12	1.2458E 08	−2.2613E 12	7.1629E 07	6.0235E−06	2.3803E 06	1.4338E 01	1.0107E 00	1.0728E−02
2.950E 04	1.3872E 12	1.2582E 08	−2.3244E 12	6.6469E 07	5.8558E−06	2.4213E 06	1.4179E 01	1.0106E 00	1.0575E−02
3.000E 04	1.4204E 12	1.2695E 08	−2.3880E 12	6.3073E 07	5.6981E−06	2.4624E 06	1.4031E 01	1.0104E 00	1.0420E−02
3.050E 04	1.4519E 12	1.2800E 08	−2.4522E 12	6.1442E 07	5.5522E−06	2.5034E 06	1.3900E 01	1.0103E 00	1.0258E−02
3.100E 04	1.4827E 12	1.2902E 08	−2.5169E 12	6.1439E 07	5.4154E−06	2.5445E 06	1.3779E 01	1.0101E 00	1.0098E−02
3.150E 04	1.5134E 12	1.3002E 08	−2.5822E 12	6.4005E 07	5.2857E−06	2.5855E 06	1.3666E 01	1.0099E 00	9.9464E−03
3.200E 04	1.5454E 12	1.3103E 08	−2.6479E 12	6.7191E 07	5.1605E−06	2.6265E 06	1.3554E 01	1.0098E 00	9.8100E−03
3.250E 04	1.5790E 12	1.3210E 08	−2.7141E 12	7.2344E 07	5.0385E−06	2.6676E 06	1.3441E 01	1.0097E 00	9.6933E−03
3.300E 04	1.6152E 12	1.3321E 08	−2.7807E 12	7.8872E 07	4.9184E−06	2.7086E 06	1.3322E 01	1.0096E 00	9.5996E−03
3.350E 04	1.6546E 12	1.3439E 08	−2.8479E 12	8.6536E 07	4.7992E−06	2.7497E 06	1.3196E 01	1.0095E 00	9.5312E−03
3.400E 04	1.6979E 12	1.3569E 08	−2.9158E 12	9.4992E 07	4.6801E−06	2.7907E 06	1.3061E 01	1.0095E 00	9.4889E−03
3.450E 04	1.7454E 12	1.3709E 08	−2.9842E 12	1.0382E 08	4.5609E−06	2.8317E 06	1.2915E 01	1.0095E 00	9.4721E−03

TABLE III (CONT.)

T (°K)	H (erg/gm)	S (erg/gm-°K)	G (erg/gm)	C_p(erg/gm-°K)	ρ (gm/cm^3)	V (cm^3/mole)	M (gm/mole)	P_I (atm)	P_D (atm)
3.500E 04	1.7973E 12	1.3859E 08	−3.0533E 12	1.1255E 08	4.4415E−06	2.8728E 06	1.2759E 01	1.0095E 00	9.4783E−03
3.550E 04	1.8535E 12	1.4019E 08	−3.1231E 12	1.2067E 08	4.3223E−06	2.9138E 06	1.2594E 01	1.0095E 00	9.5041E−03
3.600E 04	1.9139E 12	1.4187E 08	−3.1938E 12	1.2769E 08	4.2039E−06	2.9549E 06	1.2422E 01	1.0095E 00	9.5444E−03
3.650E 04	1.9777E 12	1.4364E 08	−3.2653E 12	1.3169E 08	4.0871E−06	2.9959E 06	1.2245E 01	1.0096E 00	9.5938E−03
3.700E 04	2.0436E 12	1.4544E 08	−3.3378E 12	1.3698E 08	3.9748E−06	3.0369E 06	1.2071E 01	1.0096E 00	9.6397E−03
3.750E 04	2.1121E 12	1.4729E 08	−3.4111E 12	1.3881E 08	3.8635E−06	3.0780E 06	1.1892E 01	1.0097E 00	9.6900E−03
3.800E 04	2.1815E 12	1.4914E 08	−3.4859E 12	1.3873E 08	3.7564E−06	3.1190E 06	1.1716E 01	1.0097E 00	9.7325E−03
3.850E 04	2.2508E 12	1.5095E 08	−3.5606E 12	1.3696E 08	3.6541E−06	3.1600E 06	1.1547E 01	1.0098E 00	9.7631E−03
3.900E 04	2.3193E 12	1.5273E 08	−3.6370E 12	1.3366E 08	3.5570E−06	3.2011E 06	1.1386E 01	1.0098E 00	9.7789E−03
3.950E 04	2.3861E 12	1.5443E 08	−3.7137E 12	1.2933E 08	3.4654E−06	3.2421E 06	1.1235E 01	1.0098E 00	9.7783E−03
4.000E 04	2.4508E 12	1.5606E 08	−3.7917E 12	1.2436E 08	3.3793E−06	3.2832E 06	1.1095E 01	1.0098E 00	9.7610E−03
4.050E 04	2.5130E 12	1.5762E 08	−3.8706E 12	1.1914E 08	3.2986E−06	3.3242E 06	1.0965E 01	1.0097E 00	9.7276E−03
4.100E 04	2.5725E 12	1.5909E 08	−3.9500E 12	1.1405E 08	3.2230E−06	3.3652E 06	1.0846E 01	1.0097E 00	9.6796E−03
4.150E 04	2.6296E 12	1.6048E 08	−4.0304E 12	1.0945E 08	3.1521E−06	3.4063E 06	1.0737E 01	1.0096E 00	9.6192E−03
4.200E 04	2.6843E 12	1.6180E 08	−4.1114E 12	1.0556E 08	3.0855E−06	3.4473E 06	1.0637E 01	1.0095E 00	9.5488E−03
4.250E 04	2.7371E 12	1.6306E 08	−4.1930E 12	1.0263E 08	3.0226E−06	3.4884E 06	1.0544E 01	1.0095E 00	9.4710E−03
4.300E 04	2.7884E 12	1.6427E 08	−4.2754E 12	1.0077E 08	2.9631E−06	3.5294E 06	1.0458E 01	1.0094E 00	9.3885E−03
4.350E 04	2.8388E 12	1.6545E 08	−4.3583E 12	1.0007E 08	2.9063E−06	3.5704E 06	1.0377E 01	1.0093E 00	9.3039E−03
4.400E 04	2.8888E 12	1.6660E 08	−4.4418E 12	1.0058E 08	2.8519E−06	3.6115E 06	1.0300E 01	1.0092E 00	9.2196E−03
4.450E 04	2.9391E 12	1.6775E 08	−4.5258E 12	1.0287E 08	2.7995E−06	3.6525E 06	1.0225E 01	1.0091E 00	9.1376E−03
4.500E 04	2.9905E 12	1.6891E 08	−4.6104E 12	1.0519E 08	2.7485E−06	3.6936E 06	1.0152E 01	1.0091E 00	9.0599E−03
4.550E 04	3.0431E 12	1.7008E 08	−4.6957E 12	1.0906E 08	2.6988E−06	3.7346E 06	1.0079E 01	1.0090E 00	8.9879E−03
4.600E 04	3.0977E 12	1.7128E 08	−4.7814E 12	1.1358E 08	2.6501E−06	3.7756E 06	1.0006E 01	1.0089E 00	8.9228E−03
4.650E 04	3.1545E 12	1.7252E 08	−4.8677E 12	1.1936E 08	2.6022E−06	3.8167E 06	9.9316E 00	1.0089E 00	8.8651E−03
4.700E 04	3.2141E 12	1.7381E 08	−4.9548E 12	1.2536E 08	2.5547E−06	3.8577E 06	9.8552E 00	1.0088E 00	8.8157E−03
4.750E 04	3.2768E 12	1.7514E 08	−5.0422E 12	1.3164E 08	2.5076E−06	3.8988E 06	9.7766E 00	1.0088E 00	8.7744E−03
4.800E 04	3.3426E 12	1.7652E 08	−5.1302E 12	1.3794E 08	2.4610E−06	3.9398E 06	9.6959E 00	1.0087E 00	8.7406E−03
4.850E 04	3.4116E 12	1.7795E 08	−5.2189E 12	1.4400E 08	2.4148E−06	3.9808E 06	9.6129E 00	1.0087E 00	8.7138E−03
4.900E 04	3.4836E 12	1.7943E 08	−5.3083E 12	1.4962E 08	2.3691E−06	4.0219E 06	9.5281E 00	1.0087E 00	8.6927E−03
4.950E 04	3.5584E 12	1.8094E 08	−5.3983E 12	1.5448E 08	2.3239E−06	4.0629E 06	9.4417E 00	1.0087E 00	8.6763E−03
5.000E 04	3.6357E 12	1.8249E 08	−5.4890E 12	1.5848E 08	2.2794E−06	4.1040E 06	9.3545E 00	1.0087E 00	8.6631E−03

REFERENCES

1. Olsen, H. N., "Partition Function Cutoff and Lowering of the Ionization Potential in an Argon Plasma", *Phys. Rev.*, **124**, 1703 (1961).
2. Griem, H. R., "High-Density Corrections in Plasma Spectroscopy", *Phys. Rev.*, **128**, 997 (1962).
3. Duclos, D. P., and Cambel, A. B., "The Equation of State of an Ionized Gas", *Z. Naturforsch.*, **16a**, 711 (1961).
4. Ecker, G., and Weizel, W., "Partition Functions and Ionization Potentials of Atoms in the Interior of a Plasma", *Ann. Physik*, **17**, 126 (1956).
5. Unsold, A., "On the Calculation of Partition Functions for Atoms and Ions in a Partially Ionized Gas", *Z. Astrophys.*, **24**, 355 (1948).
6. Ecker, G., and Kroll, W., "Lowering of the Ionization Energy for a Plasma in Thermodynamic Equilibrium", *Phys. Fluids*, **6**, 62 (1963).
7. Olsen, H. N., "Measurement of Argon Transition Probabilities using the Thermal Arc Plasma as a Radiation Source", *J. Quant. Spectrosc. Radiat. Transfer*, **3**, 596 (1963).
8. Garstang, R. H., "Intermediate Coupling Line Strengths", *Mon. Not. R. Astr. Soc.*, **114**, 118 (1954).

4. J. H. de Leeuw: *Electrostatic Plasma Probes*

A brief review is given of the use of electrostatic probes for the measurement of plasma properties. A central problem is the theoretical interpretation of the measured probe characteristic. The available treatments for a variety of plasma conditions are discussed. In addition, the sources of error and the practical form and arrangement of probes are considered.

1. INTRODUCTION

The use of electrostatic probes constitutes possibly one of the earliest techniques for the study of plasmas. Essentially, the method is based on the interpretation of the current collected by a small probe in the plasma as a function of the voltage applied to the probe. Basically, then, the use of such probes is attractive because it requires only relatively simple equipment. On the other hand, there are problems in their use. Many secondary phenomena often introduce errors in the measurements and problems also arise as a result of the absence of available theory for probe operation—theory valid to cover all conditions that may be encountered in practice.

Although electrostatic probes were already used late in the last century, there did not exist any adequate theory until the classical work by Langmuir (**1**), who laid the basis for the theory of probe operation for electropositive stationary plasmas when the collection of charged particles takes place under essentially collision-free conditions. In low-pressure gas discharges probes can be made small enough to satisfy these conditions and the "Langmuir" probe was used extensively in the investigation of such discharges with a considerable measure of success. Loeb (**2**) has given a comprehensive review of all aspects of probe use in 1955. However, the problem of the interpretation of probe readings is still the subject of investigation and it is not completely solved for the entire range of plasma conditions at the present time. This is hardly surprising in view of the fact that the behavior of the probe depends on a considerable number of parameters.

(a) In the first place, when the probe is at a potential different from that of the local plasma, when it is negative with respect to it, for instance, electrons will be repelled and positive ions will be attracted to it. This creates a region near the probe, a sheath, in which there exists a net charge density in contrast to the body of the plasma in which neutrality prevails.

ED. NOTE: Professor de Leeuw is with the Institute of Aerophysics, University of Toronto, Toronto, Canada. This work was supported in part by the U.S. Air Force Office of Scientific Research, under Grant AF–AFOSR 366–63.

The thickness of the sheath depends on the Debye length which for the electrons is given by

$$\lambda_D = 70\sqrt{\frac{T_e}{n_e}} \quad \text{(m)} \tag{1.1}$$

where T_e = electron temperature
n_e = electron number density

This sheath has the effect of shielding the plasma from the disturbing probe potential; it is therefore to be expected that the ratio of Debye length to the probe radius, r_p, will be of significance.

(b) Secondly, the motion of the charged particles in the field near the probe will be modified by collisions. The probe's current-voltage curve will therefore depend on the electron and ion mean free paths relative to the probe size.

(c) A third parameter will be the ratio of electron and ion temperatures. Since the energy exchange between the light electrons and much heavier ions is relatively poor, it often happens that these two species can have appreciably different temperatures. In low-pressure gas discharges, where the energy is primarily fed to the electrons, it is, for instance, usual to find electron energy orders of magnitude larger than those of the ions. Conversely, it is possible to have larger ion energies when the energy loss is primarily from the electrons as in extremely high temperature plasmas.

(d) A fourth parameter, of special interest at our laboratory where plasma flows are studied, is the effect of plasma mass motion relative to the probe as it can be indicated by a Mach number or the speed ratio of directed velocity relative to a mean random speed of the ions.

(e) Further complications arise when electronegative ions are present in considerable number. This occurs in discharges when electron-attaching species are present. Such ions are also present in the ionosphere.

(f) Finally, the presence of magnetic fields will influence the motion and hence the collection of charged particles. The electrons are especially sensitive because at relatively weak magnetic fields these will have gyromagnetic radii comparable to the probe and sheath sizes.

In this paper the characteristics of probes in stationary plasmas will be discussed. The cylindrical probe is of special interest, since it is reasonable to expect that under collision-free conditions, when the probe axis is parallel to the flow direction, such a probe will measure the plasma properties even in a moving plasma. In addition, some aspects of the influence of flow velocity on probe behavior for other shapes or orientations will be discussed.

2. INTERPRETATION OF SINGLE-PROBE CHARACTERISTIC

The single probe is used with a circuit as indicated in Figure 1. The voltage on the probe is varied with respect to one of the electrodes of the arc or discharge and the current to the probe is measured. The probe itself can be plane, cylindrical, or spherical in shape. A typical probe characteristic is shown in Figure 2a. The potential at which the current is zero is called the floating potential, V_F. At this potential most of the electrons are repelled by the probe to provide a balance of electron and ion currents, and at more negative potentials practically all electrons are prevented from reaching the probe and only positive ions are collected. The probe is surrounded by an ion sheath and the dependence of current on voltage is a

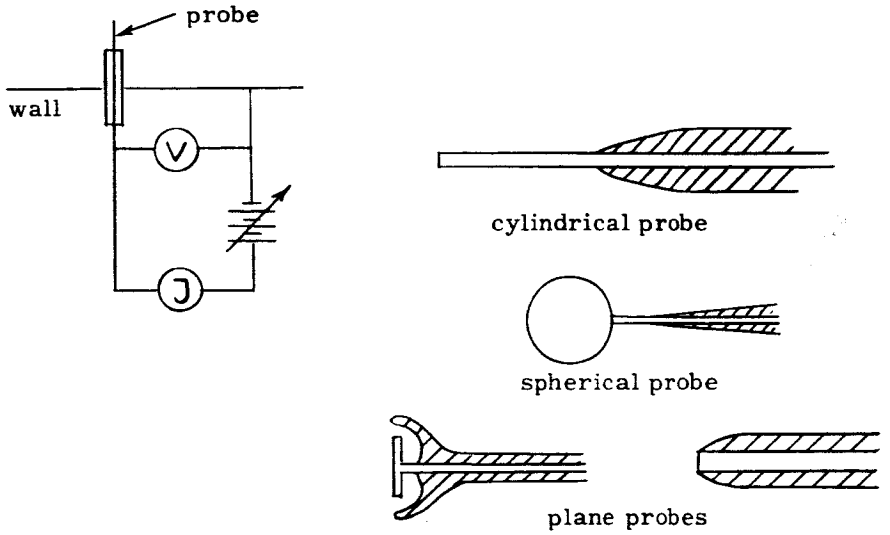

FIGURE 1. Probes and basic circuit.

rather weak one. For increasing potentials more and more of the electrons will reach the probe, resulting in a rapidly increasing electron current. When the probe is at the plasma potential, V_∞, the probe collects both ions and electrons from the plasma without the aid of electric fields. This means that as a result of the greater random speed of the electrons, the probe is drawing a negative current, much larger than the magnitude of the ion current at negative potentials. For potentials positive with respect to V_∞, the ions are repelled and an electron sheath controls the magnitude of the "saturation" electron current.

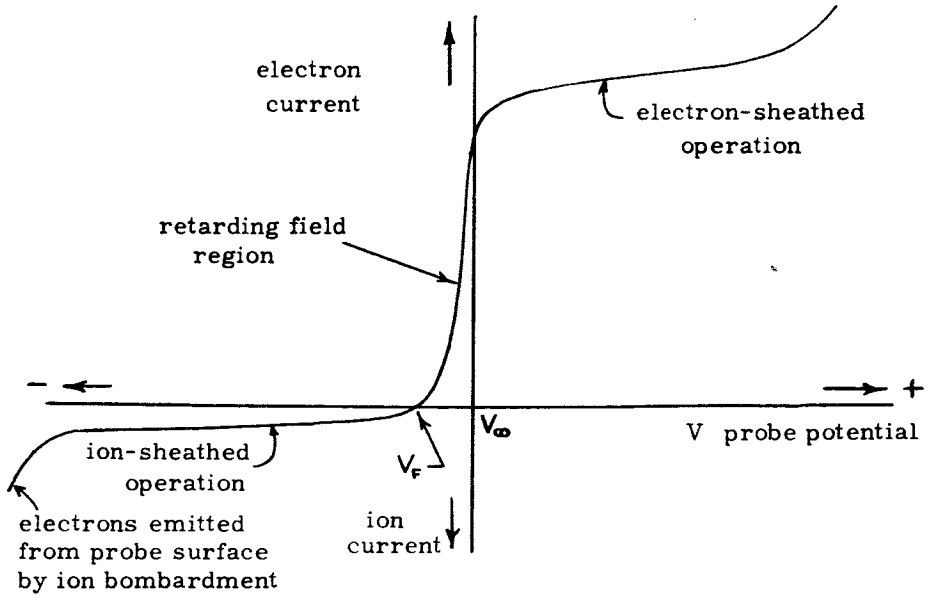

FIGURE 2a. Probe characteristics.

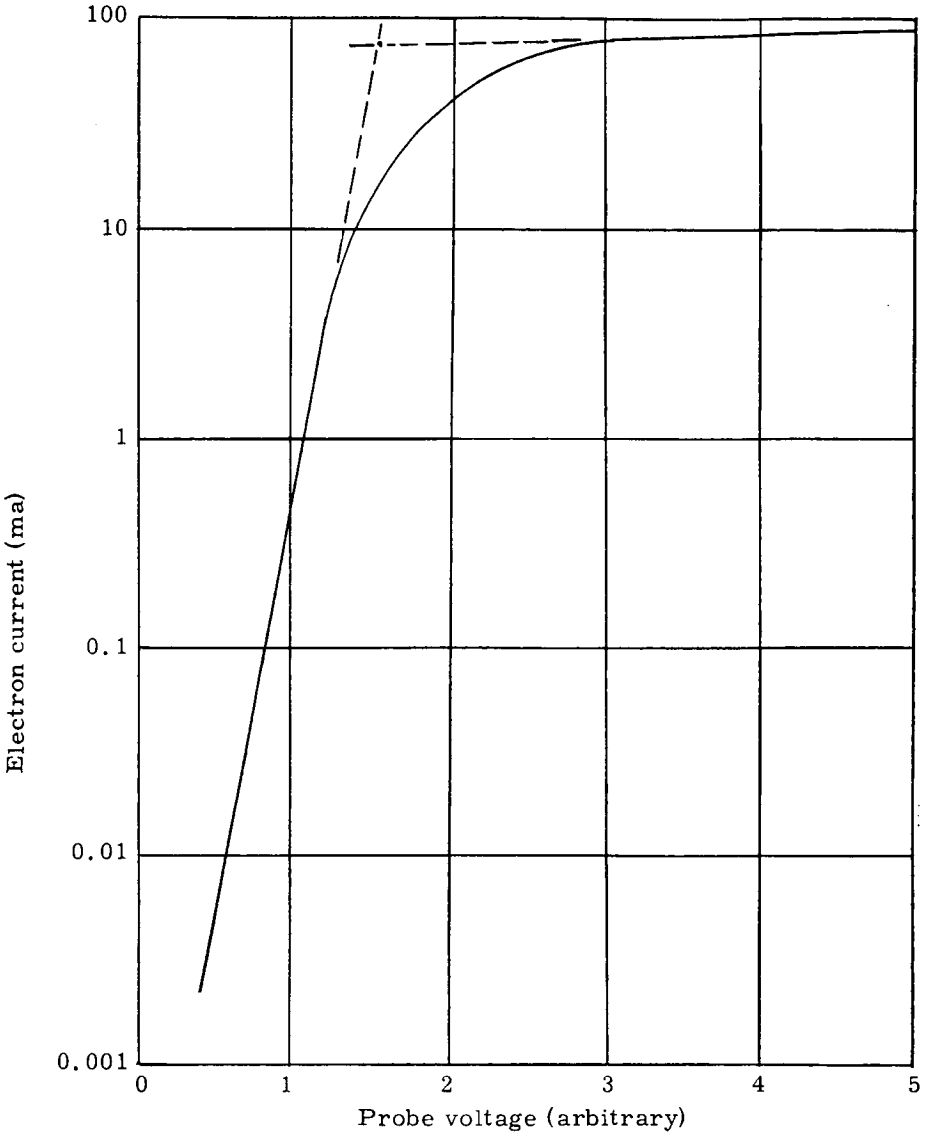

FIGURE 2b. Single probe characteristics.

The interpretation of the probe characteristic will be discussed first. We will assume that collision-free conditions exist, so that the ion and electron mean free paths are to be larger than the probe and sheath size, and that secondary phenomena are absent.

2.1. ELECTRON COLLECTION AT RETARDING POTENTIALS

When the probe is slightly negative with respect to the plasma potential some, but not all, electrons will be prevented from reaching the probe, because those electrons having sufficient energy in the direction towards the probe, i.e.,

$$\tfrac{1}{2}m_e c_{e_1}^2 > e|V_p - V_\infty| \qquad (2.1.1)$$

will be able to reach the probe if the potential distribution is assumed to be monotonic. The total electron current will therefore be an integral over the distribution function,

$$I_e = \frac{\mathcal{I}_e}{A} = en_\infty \int_{c_1}^{\infty} \int_{-\infty}^{\infty} \int_{-\infty}^{\infty} c_n f \, dc \tag{2.1.2}$$

where I_e = electron current density,
$\mathcal{I}_e$ = total electron current,
A = probe area,
n_∞ = undisturbed electron number density,
f = distribution function

If the electron collision frequency is high it may be expected that the electron distribution function is Maxwellian and equation (2.1.2) may be written

$$|I_e| = en_\infty \sqrt{\frac{kT_e}{2\pi m_e}} \exp\left[-\frac{e(V_p - V_\infty)}{kT_e}\right] \tag{2.1.3}$$

which is true independent of probe shape, as shown by Langmuir and Mott-Smith (**3**).

Taking the logarithm of equation (2.1.3) this becomes

$$\ln |I_e| = \frac{-e}{kT_e}(V_p - V_\infty) + \ln\left(en_\infty \sqrt{\frac{kT_e}{2\pi m_e}}\right) \tag{2.1.4}$$

Assuming that V_∞ is a constant and differentiating with respect to V_p leads to

$$\frac{d \ln |I_e|}{dV_p} = -\frac{e}{kT_e} = \frac{11{,}700}{T_e} \tag{2.1.5}$$

so that a linear dependence of $\ln |I_e|$ on voltage indicates a Maxwellian distribution and the slope of this straight line yields the electron temperature.

The electron current is obtained from the probe current by noting that

$$|\mathcal{I}_e| = |\mathcal{I}| + \mathcal{I}_+ \tag{2.1.6}$$

In order to obtain $\mathcal{I}_e$ the ion current has to be known. The ion current depends in general on voltage and some extrapolation from the measured ion current at large negative potentials is therefore in order. However, when λ_D/r_p is small this variation is not too severe and furthermore in the characteristic of a single probe the electron current becomes much larger than the ion current as the plasma potential is approached, so that the extrapolation error in $\mathcal{I}_+$ will not be important.

A completely analogous situation exists for the ion collection at slightly positive potentials. Unfortunately, in the normal use of a probe, the ion contribution to the probe current near plasma potential is masked by that of the electrons. However, when the Debye lengths in the plasma are relatively large, it is possible to separate the two current components by the use of fine grids. Boyd (**4**) made attempts, which were partly successful, to do this in the laboratory. More recently this technique has been applied for the investigation of the ionosphere where the Debye length is of the order of a few centimeters. The use of such multi-electrode probes will be discussed in section 5.

When the distribution function is not Maxwellian, but still isotropic, the probe characteristic in the retarding field region can be used to find the shape of the distribution function. A method to do this is given in reference (**3**) by relating

the second derivative of the probe current with respect to voltage to the distribution function in the form

$$\frac{d^2|\mathscr{I}_e|}{dV_p^2} = \frac{Aen_\infty}{2}\sqrt{\frac{e}{2m_e(V_p - V_\infty)}}\, f(V_p - V_\infty) \tag{2.1.7}$$

Sloane and McGregor (**5**) following a suggestion by Emeleus indicated an experimental method, later improved by Boyd and Twiddy (**6**), to obtain the second derivative directly. They measure the d-c collected current without and with a small superimposed sinusoidal a-c signal of amplitude ΔV at various values of the d-c voltage. They showed that the difference in d-c collected current is given by the expression

$$\Delta I_{\text{d-c}} = \frac{(\Delta V)^2}{4}\frac{d^2 I_e}{dV_p^2} \tag{2.1.8}$$

where $(V_p - V_\infty)$ is the voltage equivalent of the electron kinetic energy. This method was also suggested as a means of finding the value of V_∞, the plasma potential, in reference (**5**), by taking as the value of V_∞, that value of V_p for which the amplitude of the a-c variation in the current disappears.

It should be pointed out that the theoretical basis for the use of superimposed voltage fluctuations rests on the assumption of quasi-stationary conditions, so that when the frequency of the fluctuations becomes comparable to the electron plasma frequency the method loses its validity.

As a matter of fact, the resonance that occurs at plasma frequency is a useful indicator of electron density as Takayama, Ikegami, and Miazaki (**7**) have pointed out and as shown in careful experiments by Cairns (**8**). However, as long as the applied frequency is much lower than the plasma frequency the above method is indeed valid and independent of frequency.

2.2 SPACE POTENTIAL AND OPERATION AT POSITIVE POTENTIALS

When the probe potential is at the local plasma potential, there are no electric fields around the probe and it will accept the random fluxes of electrons and ions normally incident on it, i.e., per unit area $n_\infty\sqrt{kT_e/2\pi m_e}$ electrons and $n_\infty\sqrt{kT_+/2\pi m_+}$ ions will be collected. It is clear that the electron current will far outweigh the ion current because their ratio is $\sqrt{m_+T_e/m_eT_+}$. Consequently, unless $T_+ \gg T_e$ the current collected at space potential is in good approximation entirely due to the electrons, so that the current at plasma potential gives information about the charged particle density since

$$\frac{\mathscr{I}_{e_0}}{A} = 0.4n_\infty e\sqrt{\frac{kT_e}{m_e}} \tag{2.2.1}$$

and the value of T_e can be determined from the retarding field region.

As soon as V_p becomes larger than V_∞, ions are repelled and an electron sheath forms which will control the collection of electrons. It is normally assumed that when $T_+/T_e < 1$ the electrons reach the sheath edge at their normal random current density so that

$$\mathscr{I}_e = eA_s n_\infty\sqrt{\frac{kT_e}{2\pi m_e}} = 0.4n_\infty eA_s\sqrt{\frac{kT_e}{m_e}} \tag{2.2.2}$$

where A_s is the effective collection area at the sheath edge. Since the sheath thickness will grow with increasing voltage, for instance, for a thin sheath which may be approximated by a plane sheath, the thickness is given by

$$d_e = \left[\frac{(V_p - V_\infty)^{3/2}}{9\pi\sqrt{\frac{m_e}{2e}}\, I_e}\right]^{1/2} \tag{2.2.3}$$

the electron current will depend on voltage through the dependence of A_s on the sheath thickness. This dependence is a much weaker one, though, than the exponential dependence in the retarding field region. This simple picture of electron collection is not quite correct, as will be discussed in section 2.4. However, the procedure for finding the electron current at space potential described in the following rests on an extrapolation from the electron current curve to the value at plasma potential and the description here is adequate for the purpose.

The change in dependence of I_e on V_p shows on the logarithmic plot of current versus voltage as a change from a steep straight line to a much less steep curve at $V_p > V_\infty$. For thin sheaths under ideal conditions this change is abrupt and there is little difficulty in fixing the value of V_∞. In reality the curve often changes rather more smoothly as a result of secondary effects to be discussed in section 4 and it is customary to locate plasma potential at the intersection of the straight line in the retarding field region and a reasonable straight line through the data for $V_p > V_\infty$.

When the sheath is not very thin with respect to the probe, say for Debye lengths $\lambda_D \approx \frac{1}{10} r_p$, the curve shows a pronounced rounding even under ideal conditions and the plasma potential should be taken at the point where the measured curve starts to deviate from the straight line representing the exponential increase of the electron current. However, since secondary effects may be present there is an inherent uncertainty in the value of V_∞, with a corresponding uncertainty in the electron density determination when equation (2.2.1) is used. It is partly for this reason that the accuracy of the probe method is limited in many cases.

2.3. ION COLLECTION AT LARGE NEGATIVE POTENTIALS

When the probe is strongly negative with respect to the plasma potential virtually all electrons will be repelled. This will be the case when $e|V_p - V_\infty| \gg kT_e$ and as a result the electrons will take on an equilibrium Boltzmann distribution when the distribution function far from the probe is Maxwellian, i.e.,

$$n_e = n_\infty \exp\left[-\frac{e|V_p - V_\infty|}{kT_e}\right] \tag{2.3.1}$$

For the case of very low charged particle density, such that the Debye length is very much larger than the probe radius, the collection of ions will be controlled by the essentially unshielded Coulomb potential of the probe. In reference (**3**) the ion collection for a spherical probe under these conditions is given by the relation

$$\mathscr{I}_+ = An_\infty\sqrt{\frac{kT_+}{2\pi m_+}}\left(1 - \frac{V_p - V_\infty}{V_0}\right) \tag{2.3.2}$$

in which $V_0 = kT_+/e$ the voltage equivalent of the ion energy when the ions are Maxwellian and A = probe area. Similarly, a cylindrical probe would collect

$$\mathscr{I}_+ = An_\infty\sqrt{\frac{kT_+}{2\pi m_+}}\sqrt{\frac{4}{\pi}}\left(1 - \frac{V_p - V_\infty}{V_0}\right)^{1/2} \tag{2.3.3}$$

It must be noted that the collection depends only on the probe voltage and not on the ratio λ_D/r_p. These equations are valid only when the Debye length is so large that everywhere in the field around the probe the following inequality is satisfied

$$\frac{V(r)-V_\infty}{V_p-V_\infty} > \left(\frac{r_p}{r}\right)^2 \tag{2.3.4}$$

A test could be made by using different sized probes to experimentally show the independence of the results on

$$\frac{\lambda_D}{r_p}$$

When the inequality, equation (2.3.4), is not fulfilled the analysis of the problem of ion collection is very complicated and only approximate solutions are available. Bohm, Burhop, and Massey (**9**) treated the problem of a spherical probe by using equation (2.3.1) for the electron density and assuming that the field around the probe could be represented by an extremely thin sheath surrounded by quasi-neutral plasma. In addition, the assumption was made that the ions at infinity had random motion but were all mono-energetic. Their results showed that the electric field in the quasi-neutral plasma region attained an infinite slope as a function of position and they located the sheath edge at the position where this occurred. For zero energy ions this procedure resulted in a potential at the sheath edge of $|V_e-V_\infty|=\frac{1}{2}\,kT_e/e$ which showed that the plasma region cannot support more than this potential difference. Bohm (**10**) derived a criterion for the formation of a sheath indicating that the potential should be larger or equal to this value. So for the zero energy case these two criteria lead to the conclusion that at the sheath edge this value of the potential must exist, meaning that the plasma beyond the sheath is significantly disturbed. In the first place the charged particle density will be smaller than at infinity as a result of the Boltzmannian distribution of electrons and secondly the ions will have been accelerated towards the probe so that they enter the sheath with a finite energy corresponding to $\frac{1}{2}kT_e$.

The calculations for two different ion energies gave the following results:

ion energy $0.01kT_e$ $$\mathscr{T}_+ = 0.57n_\infty e\left(\frac{kT_e}{m_+}\right)^{1/2} A \tag{2.3.5}$$

ion energy $0.5kT_e$ $$\mathscr{T}_+ = 0.54n_\infty e\left(\frac{kT_e}{m_+}\right)^{1/2} A \tag{2.3.6}$$

The implication of these calculations is that for the case of thin sheaths the ion current is controlled by the electron temperature alone as long as $T_+/T_e<1$.

Allen, Boyd, and Reynolds (**11**) refined the analysis for zero energy ions by removing the assumption of a quasi-neutral plasma region. Their results, reproduced in Figure 3, show that at values for $\mathscr{T}_+/\mathscr{T}_D$ of about 10^4, where $\mathscr{T}_D$ represents essentially the random ion current passing through a Debye sphere, the plasma solution of reference (**10**) is indeed a good one. For smaller values of this ratio, i.e., larger ratios of λ_D/r_p, the approximation becomes increasingly less valid and their full analysis has to be used. Their solution for the thin sheath case for zero energy ions is given by

$$\mathscr{T}_+ = 0.61n_\infty e\sqrt{\frac{kT_e}{m_+}}\,A \tag{2.3.7}$$

and is in good agreement with equation (2.3.5) and applicable for $\mathscr{T}_+/\mathscr{T}_D \geq 10^4$ or $\lambda_D/r_p \leq 0.01$.

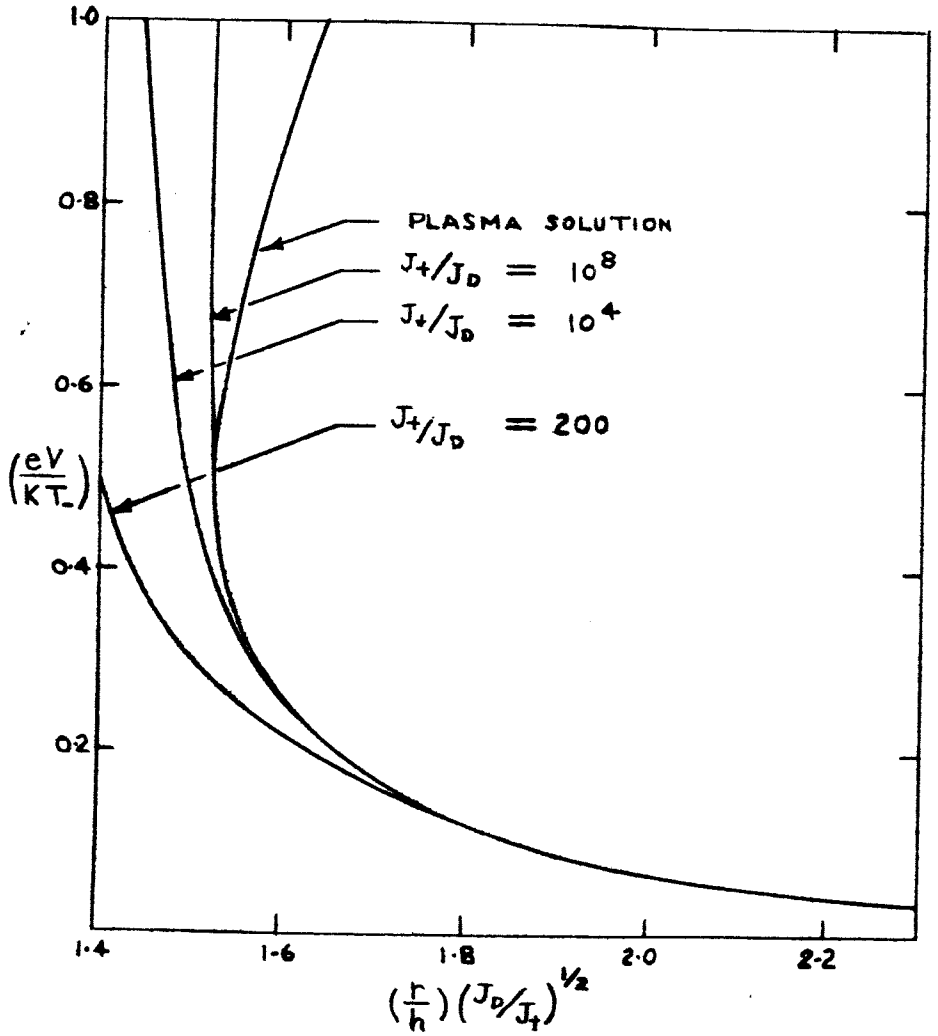

FIGURE 3. The electrostatic field near a spherical Langmuir probe.

For ratios of λ_D/r_p between $\frac{1}{4}$ to $\frac{1}{8}$ they present ion collection curves for zero energy ions, which are reproduced in Figure 4.

More recently, Bernstein and Rabinowitz (**12**) have treated the cases of spherical and cylindrical probes, solving the self-consistent field problem for mono-energetic ions. Their results were obtained for a range of values of λ_D/r_p down to about $\frac{1}{10}$. The results of their calculations for a spherical probe are reproduced in Figure 5 in which non-dimensional current is plotted versus $e|V_p - V_\infty|/kT_e$ for the case of $\lambda_D = 0.1 r_p$. The graph indicates that an increase in ion energy decreases the current by a small amount, which is however larger than the extremely small differences found by Bohm *et al.* in reference (**10**). For instance, an increase of T_+/T_e from 0.01 to 0.1 causes a 10% decrease in ion current. From the trend of the curves in reference (**12**) it is further apparent that for smaller Debye lengths this difference decreases in accordance with the findings of Bohm *et al.* which are true in the limiting case of an extremely small Debye length.

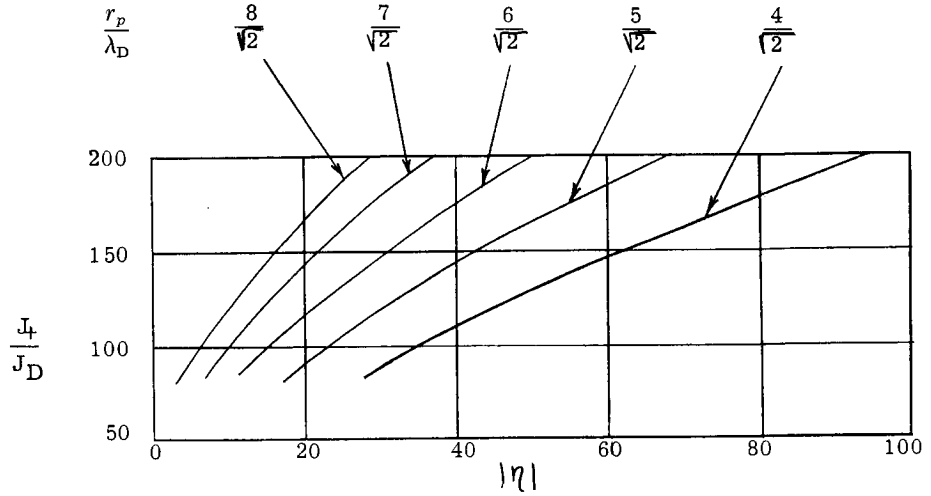

FIGURE 4. Ion collection curves.

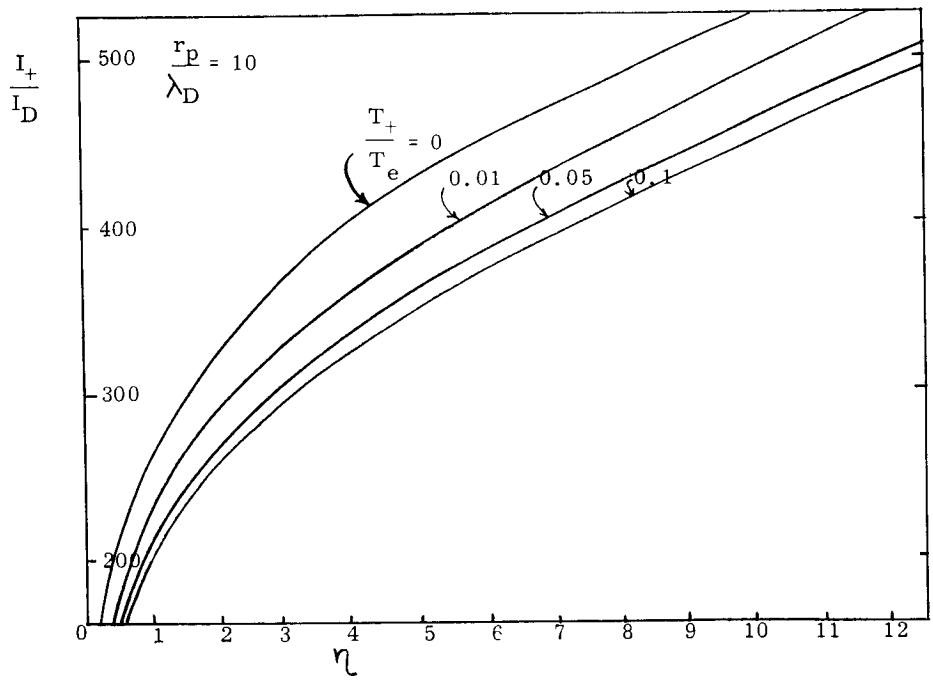

FIGURE 5. Ion collection curves.

Since the ion collection is found to depend on T_+/T_e over an important range of λ_D/r_p, it may be expected that the assumption of mono-energetic ions is not quite adequate to describe the ion collection because their energy distribution is Maxwellian in practice. Hall (**13**) has indicated a computational scheme to treat such cases and Laframboise (**14**) of our own laboratory has independently calculated entire probe characteristics based on Maxwellian distributions for both electrons

and ions at different temperatures. Some of his results will be discussed in section 2.4.

The importance of the ion collection part of the probe characteristic lies in the facts that relatively little current is drawn from the plasma in contradistinction to the situation near plasma potential and that in the presence of moderate magnetic fields the ion collection will be little influenced. The practical implications of the foregoing discussion may be summarized as follows:

(a) For very large values of λ_D/r_p, equations (2.3.2) and (2.3.3) can be used to give the quantity $n_\infty\sqrt{T_+/m_+}$, which when the ion temperature is known yields n_∞. The results are independent of λ_D/r_p but a test may have to be made for this by using two different probe sizes.

(b) When $\lambda_D/r_p \ll 1$, as indicated for instance by an ion current practically independent of probe potential, equation (2.3.7) can be used, which means that the charged particle density can be found when T_e is measured according to the method described in section 2.1.

(c) When the Debye length is in the range from $\frac{1}{2}$ to $\frac{1}{10}$ of the probe radius the ion collection depends both on T_+/T_e and λ_D/r_p. Awaiting the availability of calculations for the case of Maxwellian ion distribution functions, the curves of Bernstein and Rabinowitz should be used. However, it will be necessary to have additional information. For instance, if the electron temperature and number density can be determined from other parts of the probe characteristic or from independent measuring techniques, then the Debye length is known and the ion collection may give an indication of ion temperature.

An alternative approach is to ignore the small differences in ion collection as a function of T_+/T_e and consider the curves for zero ion energy of Allen *et al.* in reference (**11**) as a first approximation. Their curves are given in terms of $\mathscr{T}_+/\mathscr{T}_D$, where

$$\mathscr{T}_D = \frac{\varepsilon_0}{e}\frac{(kT_e)^{3/2}}{\sqrt{2m_+}} \tag{2.3.8}$$

which only depends on T_e. The electron temperature can be obtained from the probe characteristic and a curve of $\mathscr{T}_+/\mathscr{T}_D$ versus $\eta = e(V_p - V_\infty)/kT_e$ can be plotted. Such an experimental curve should coincide with a calculated curve for some value of λ_D/r_p so that λ_D can be determined and consequently the charged particle density can be found.

This procedure will undoubtedly introduce some error, but the method of determining the electron density at plasma potential suffers also from some uncertainty. Furthermore, the measured probe current at negative potentials can include the effects of secondary electron emission due to the incidence of photons and metastable atoms so that the actual ion current can possess a certain uncertainty.

At space potential the ratio of electron and ion currents is given by

$$\left(\frac{m_+ T_e}{m_e T_+}\right)^{1/2}$$

However, the ratio of electron current at space potential to the ion saturation current for cases where the latter is well defined, i.e., when $r_p \gg \lambda_D$, is considerably smaller,

$$\frac{\mathscr{T}_{e0}}{\mathscr{T}_+} = \frac{0.4}{0.61}\sqrt{\frac{m_+}{m_e}} = 0.66\sqrt{\frac{m_+}{m_e}}$$

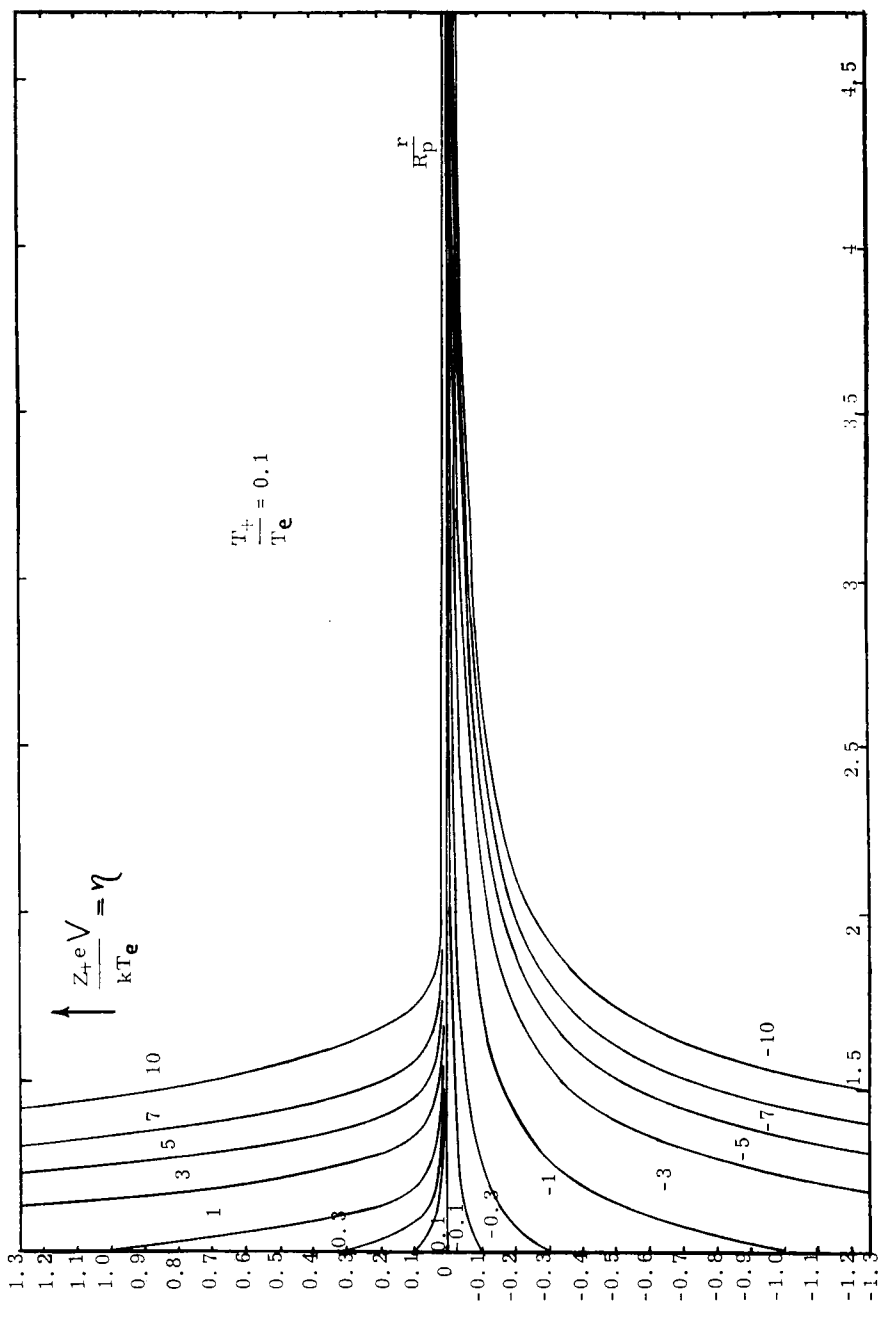

FIGURE 6. Spherical probe potential as a function of radius for various values of probe potential. (Probe radius = 10 Debye lengths.)

For argon with $\sqrt{m_+/m_e}=271$, this ratio becomes $\mathscr{T}_{e0}/\mathscr{T}_+=178$, which is considerably smaller than the ratio at space potential, especially if $T_e \gg T_+$. Since under the condition $r_p \gg \lambda_D$ the ion current does not change much with T_+/T_e, at least up to $T_+/T_e=0.5$ according to equations (2.3.5) and (2.3.6), the value of $\mathscr{T}_{e0}/\mathscr{T}_+$ should also be independent of T_+/T_e over this range. In experiments

with single probes, this ratio should be checked as an indication of the self-consistency of the measured probe characteristic.

2.4. EFFECTS OF LARGE ION TEMPERATURES

It was indicated in the previous section that the ion current depends only slightly on T_+/T_e as long as this ratio is smaller than 0.5. French (**15**) pointed out that, since the trajectories of electrons at positive potentials are kinematically similar to those of ions at negative potentials when the temperature ratio is reversed, the collection of electrons at positive potentials will become controlled by the ion temperature when $T_+/T_e > 2$, leading by analogy to the expressions

$$I_e = \frac{\mathscr{T}_e}{A} = 0.61 e n_\infty \sqrt{\frac{kT_+}{m_e}} \tag{2.4.1}$$

and

$$I_+ = \frac{\mathscr{T}_+}{A_s} = 0.4 e n_\infty \sqrt{\frac{kT_+}{m_+}} \tag{2.4.2}$$

for the case of small sheath thicknesses. Laframboise (**14**) has undertaken calculations to shed some light on the details of the transitions that occur when T_+/T_e becomes larger than unity. For this purpose he has calculated the entire probe characteristic for a spherical probe for Maxwellian ions and electrons at arbitrary temperatures but he assumed that the plasma is bounded by a spherical surface at a finite distance. Some preliminary results of his as yet unpublished work are shown in Figures 6, 7, and 8.

The potential distributions near the probe are shown in Figure 6 as a function of non-dimensional distance from the probe for different values of the probe potential $\eta = eV/kT_e$. The case was for an electron Debye length of $\frac{1}{10}$ probe radius and a value of $T_+/T_e = 0.1$. The difference in electron sheath and ion sheath formation is marked. The ion sheath only partly shields the probe and the penetration of the field beyond the sheath which is responsible for the increased ion collection is very pronounced. On the other hand the electron sheath shields the probe almost entirely because only a small remnant of the field is seen to penetrate to a considerable distance from the probe. This is explicated in Figure 7, which shows the electron and ion density distributions for the positive probe. It is seen there that at the sheath edge where electron and ion densities depart, the electron density is noticeably lower than that far away. This implies that also in the case of a positive probe the plasma supports a potential difference, but this is basically of the order of the energy of the repelled particles and therefore small compared to the electron energy. One may visualize this as arising from the local decrease in electron density as a result of the removal of electrons by the probe.

The non-dimensional electron and ion currents are shown separately in Figure 8 for values of $T_+/T_e = 1.0$ and $T_+/T_e = 0.1$. The electron current is non-dimensionalized by its value at plasma potential but the ion current for both temperatures is normalized in terms of the value at plasma potential for the case $T_+/T_e = 1.0$. It may be noted that the differences in ion current as a result of the different ion temperatures are only pronounced near plasma potential. Since the probe current there is almost equal to the electron current these differences in ion collection will be effectively masked in a probe characteristic.

However, when $T_+/T_e > 1$ similar large changes will occur in the electron current at potentials a little above V_∞ and these will show up in the probe characteristic to give some indication of the value of T_+/T_e. Situations with $T_+/T_e > 1$ can occur in

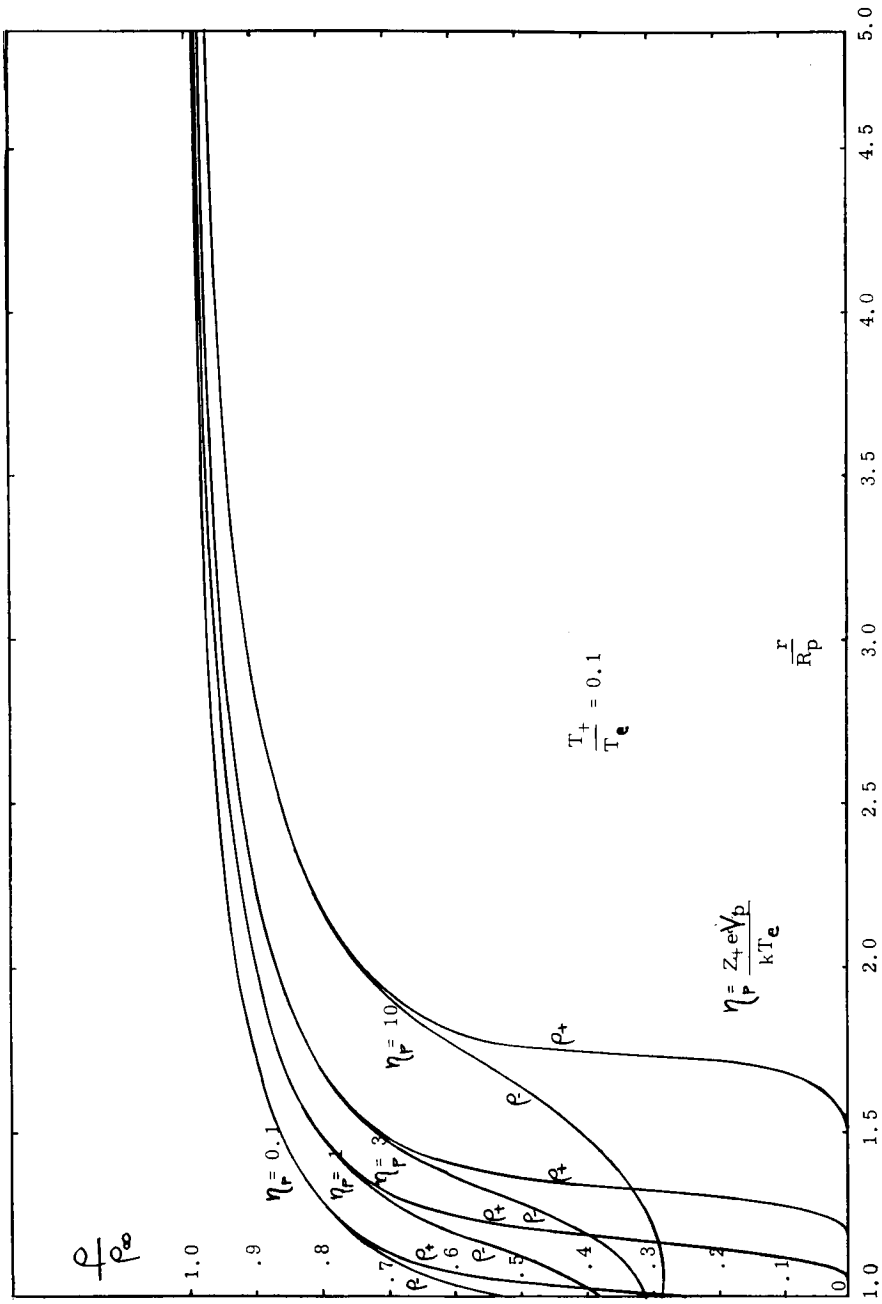

FIGURE 7. Positive and negative charge densities versus radius for positive values of probe potential. (Probe radius = 10 Debye lengths.)

decaying discharges, when the electrons experience a larger cooling effect than the ions as a result of the preferential loss of high-energy electrons in the antipolar diffusion process as noted by Biondi (**16**). Similar situations will occur in extremely hot plasmas when the electrons are mainly responsible for the radiation cooling. In such plasmas, however, magnetic fields will be present and these will modify the electron collection so that the above analysis will not be valid.

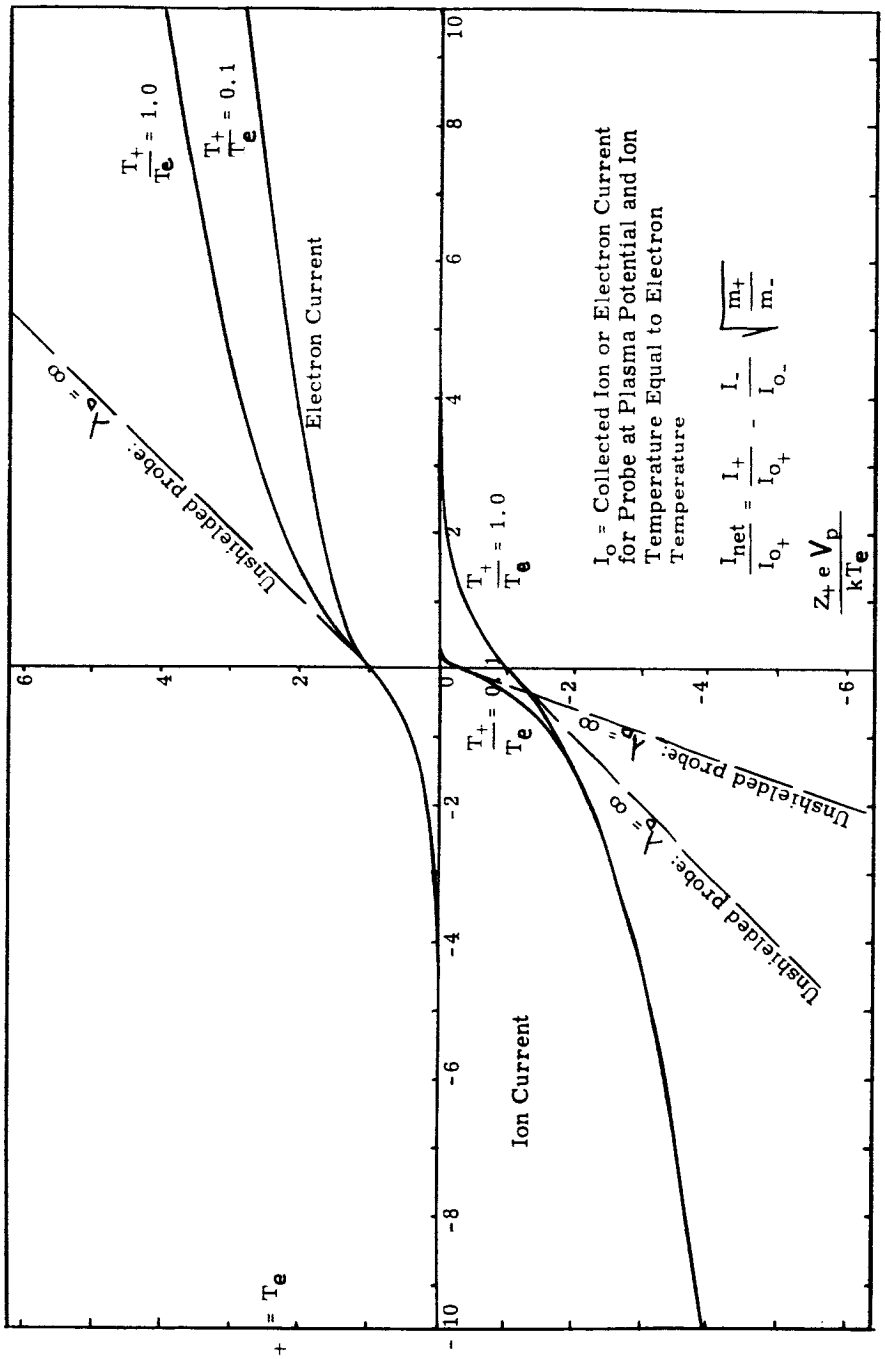

FIGURE 8. Influence of ion temperature on current collection spherical probe: non-dimensional ion and electron current versus non-dimensional probe potential. (Probe radius = 10 Debye lengths.)

Another observation that may be made is that when $T_+/T_e < 1$ the electron current stems basically from the incidence of the normal kinetic flux,

$$\frac{n_\infty}{4}\sqrt{\frac{8kT_e}{\pi m_e}},$$

on the effective sheath boundary. Conversely, when $T_+/T_e > 1$ it is to be expected that the ion current will be determined by the analogous process.

2.5. PRESENCE OF ELECTRONEGATIVE IONS

Boyd and Thompson (**17**) have considered the theory of ion collection when electronegative ions are present. They assumed that the positive ions were at rest at infinity and that the sheath was so thin that the field could be split in a quasi-neutral plasma and a sheath similar to the analysis by Bohm *et al.* (**9**). They found that for ratios of electron-to-negative ion temperature $T_e/T_- > 30$ and concentration ratios $(n_-/n_e)_\infty < 2$, the positive ion current in terms of the electron current at plasma potential is unaffected by the presence of electronegative ions, i.e.,

$$\frac{\mathscr{T}_{e0}}{\mathscr{T}_+} = 0.66\sqrt{\frac{m_+}{m_e}} \tag{2.5.1}$$

so that the electron concentration can be found from this relation when the electron temperature is known, whereas no information about the negative ions is obtained.

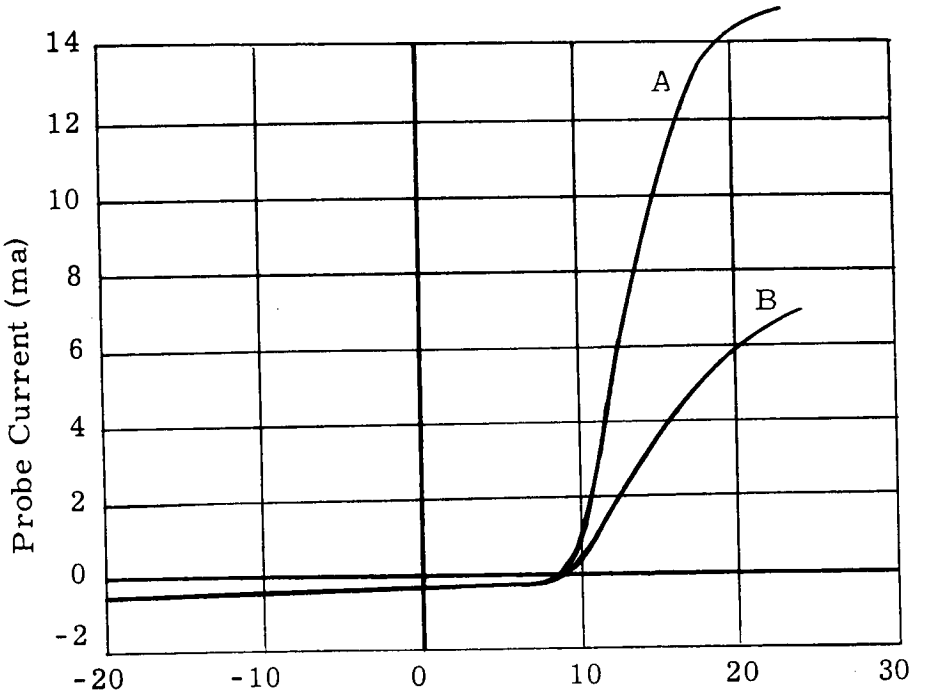

Curve A - Probe Perpendicular to B
Curve B - Probe Parallel to B

FIGURE 9. Effect of magnetic field orientation.

For a strongly electronegative gas, i.e., $n_-/n_e \gg 1$, for which $T_+ = T_-$, it is found that the potential at the sheath edge is very close to the plasma potential in terms of the electron energy. This fact is used in the analysis to consider that the positive ions will arrive at the sheath edge by their random kinetic motion based on the ion temperature T_+. The problem therefore reduces to a proper choice of the effective sheath radius and a semi-graphical process for this choice is described in reference (**17**). Essentially, the quantity $n_+\sqrt{T_+}$, and therefore $n_-\sqrt{T_-}$, can be determined from this procedure so that additional information about the ion temperature is required before n_+ can be determined.

2.6. INFLUENCE OF MAGNETIC FIELDS

The presence of a magnetic field modifies the motion of the charged particles in the electric field of the probe. Since the trajectories of the electrons are disturbed at weaker magnetic fields than the ions are, the effects of magnetic fields will first be noticed in the electron current to the probe. An experimental curve in Figure 9, reproduced from reference (**9**), shows the effect of the orientation of a plane probe with respect to the direction of a magnetic field of 1.5 weber/m^2 in a nitrogen plasma. It is seen that the ion collection is uninfluenced and also that the shapes of the curves at potentials somewhat below plasma potential are similar, so that this region most likely will yield reasonable electron temperatures. It is also clear that for both probe orientations the electron-to-ion current ratio is much lower than that for the case of $B=0$. It is also pointed out in reference (**9**) that as long as the gyromagnetic radius of the ions is larger than the probe and sheath size, the ion collection is but slightly influenced so that for this part of the characteristic the considerations of section 2.3 apply.

For very strong magnetic fields the entire probe characteristic is influenced and reference must be made to an appropriate theory. Very recently Bertotti (**18**) has presented such an analysis. The theory is quite complicated and the reader has to be referred to the paper itself for any application.

2.7. PROBE OPERATION AT HIGH DENSITY

All the foregoing discussion of single probe operation was valid for probes at low density, such that the ion and electron mean free paths are larger than the probe and sheath size. At higher densities these conditions will no longer be satisfied and the current to the probe will be modified as a result, because the motion of the charged particles in the electric field will be disturbed by collisions.

When the ratio of charged to neutral particles in a partially-ionized gas is very small these collisions will primarily involve neutral particles and in the case of ion-neutral encounters momentum exchange as well as charge exchange events will have to be taken into account. The cross sections for these encounters are not accurately known at low ion energies for many gases and there is therefore some uncertainty in determining the mean free paths. In highly-ionized gases the collisions will primarily occur between ions and electrons.

Theories for probe operation at densities where collisions are important are given, among others, by Zakharova, Kagan, Mustafin and Perel (**19**), who present a theory for the behavior of spherical and cylindrical probes when the density is so high that the supply of charged particles is mobility- and diffusion-controlled.

For the ion collection at large negative potentials they assumed that the field can be split in a quasi-neutral plasma region and a well-defined sheath. In addition they assumed that at such potentials the effect of concentration gradients is

unimportant and that the ion drift velocity is proportional to the electric field. Only collisions with neutral particles were considered.

The ion currents are presented as follows:

spherical probe
$$I_+ = \frac{\mathscr{I}_+}{A} = \frac{x_0 n_\infty T_e}{2} \frac{L_+}{r_p} \frac{10^{-11}}{\sqrt{M_+ T_+}} \left(\frac{\text{amp}}{m^2}\right) \tag{2.7.1}$$

cylindrical probe
$$I_+ = \frac{\mathscr{I}_+}{A} = \frac{n_\infty T_e L_+}{2 r_p \ln (l/x_0 r_p)} \frac{10^{-11}}{\sqrt{M_+ T_+}} \tag{2.7.2}$$

M_+ is the ion atomic weight, L_+ is the ion mean free path, and x_0 is the value of r/r_p where the quasi-neutral plasma solution indicates an infinite slope for the electric field. The values of x_0 are found from the following:

spherical probe
$$\frac{1}{x_0} = b \equiv 0.85 \frac{L_+}{r_p} \frac{T_e}{T_+} \frac{n_\infty e \sqrt{\dfrac{kT_+}{2\pi m_+}}}{I_+} \tag{2.7.3}$$

cylindrical probe
$$\ln \left(\frac{l}{r_p x_0}\right) = b \tag{2.7.4}$$

where l = length of the cylindrical probe.

The equations essentially constitute implicit expressions for I_+ when n_∞, T_e, T_+, and L_+ are known. However, when the Debye length is very much smaller than r_p, so that the sheath is thin, then x_0 may be taken as unity and only equations (2.7.3) and (2.7.4) need be used. It is, however, clear that estimates of L_+ and T_e are required for the determination of n_∞.

At plasma potential the motion of the charged particles is controlled by diffusion as a result of concentration gradients. The electron currents are found to be

spherical probe
$$(I_e)_0 = \frac{n_\infty e \sqrt{\dfrac{kT_e}{2\pi m_e}}}{1 + \dfrac{3}{4} \dfrac{r_p}{L_e}} \tag{2.7.5}$$

cylindrical probe
$$(I_e)_0 = \frac{n_\infty e \sqrt{\dfrac{kT_e}{2\pi m_e}}}{1 + \dfrac{3}{4} \dfrac{r_p}{L_e} \ln \left(\dfrac{l}{r_p}\right)} \tag{2.7.6}$$

The electron current in the retarding field region is given in approximation by

$$I_e = n_\infty e \sqrt{\frac{kT_e}{2\pi m_e}} \left[\frac{\exp \eta_p}{1 + \dfrac{3}{4} \dfrac{r_p}{L_e} \displaystyle\int_1^{x_\infty} \frac{1}{x^\gamma} \exp \{-\eta_p + \eta(x)\}\, dx} \right] \tag{2.7.7}$$

where $\eta_p = e(V_p - V_\infty)/kT_e$
$x = r/r_p$
$\gamma = 1$ for cylindrical geometry
$= 2$ for spherical geometry
$x_\infty = \infty$ for spherical probe
$= l/r_p$ for cylindrical probe

In the derivation of this expression both mobility and diffusion were considered and free motion was assumed over the last mean free path near the probe. Equation (2.7.7) shows clearly that the simple exponential nature of the electron current

versus voltage curve is disturbed. Also it can be shown that the deviations become appreciable at lower values of η_p as the mean free path for electrons becomes smaller. The usual analysis of the retarding field region therefore has to be confined to values of η_p where equation (2.7.7) is dominated by the exponential term. This may still be the case for potentials slightly larger than V_F so that the electron temperature can still be evaluated as long as the mean free path is not too small.

A more refined analysis of the problem which avoids the artifice of splitting the field into a plasma region and a sheath region has more recently been presented by Su and Lam (**20**). Their work is valid for small values of L/r_p. Probe characteristics at large negative potentials are presented in their work.

Both these analyses are based on a continuum treatment. For cases where the mean free paths are of the same order of magnitude as the probe and sheath size the conditions for a continuum description are not fulfilled. The work of Schulz and Brown (**21**) is of special interest in this area, since their experimental comparison of ion current drawn by probes with microwave data covers the region where collision-free conditions prevail as well as that in which collisions just start to become of importance. In addition, they present simplified analyses to explain their experimental results.

2.8. EFFECTS OF PLASMA MASS MOTION

2.8.1. Collision-free Conditions

First the case will be considered in which the mean free paths are large and the Debye length is small compared with the probe. In most flow situations, even when the directed velocity is much larger than the random speed of the ions, the electron random speed will still be much larger than the flow velocity. Situations like this occur in the flight of a satellite through the upper ionosphere and they can also be realized in the laboratory, for instance in plasma tunnels.

As far as the probing of such flows is concerned, French (**15**) has pointed out that a cylindrical probe aligned with the flow direction and long enough so that end effects can be ignored will behave as if it were in a stationary plasma. Hence, the static plasma properties can be measured with such a probe using the methods outlined in previous sections. Taylor, Rothman, and Morita (**22**) recently reported experiments in an electromagnetic shock tube at velocities up to 8000 m/sec. Measurements of the electron density made with cylindrical probes were compared with microwave interferometer data and a reasonably good correspondence independent of flow velocity was obtained.

For other probe orientations and geometries, the probe characteristic will be influenced by the flow velocity. However, since the ratio of directed to random speed of the electrons is much smaller than unity (in argon, for instance, when the directed velocity to random ion speed ratio is as high as 20 this ratio for electrons is only 0.07) it is to be expected that the electron temperature can still be obtained from the retarding field region in the manner described in section 2.1. This was experimentally verified by French (**15**) at an ion speed ratio of about 2 by comparing the results from a cylindrical probe parallel to the flow with those from the same probe at a perpendicular orientation.

Theoretical calculations for the ion collection of a spherical body have been made by Davis and Harris (**23**). They showed that the ion current corresponds essentially to the flux of ions that cross the frontal area of the body as a result of the flow velocity. A small increase in the effective area over the geometric area accounts for the influence of the electric field around the body. Meckel (**24**) and

Clayden (**25**) have basically used this result in their investigation of high speed plasma flows in the laboratory. The ion current measurements yield the product, $n_\infty U$, of number density and flow velocity.

More recently, Clayden (**26**) and Smetana (**27**) reported calculations based on simplified models for the behavior of spherical probes in plasma flows. Medicus (**28**) also treated this case for a drifting Maxwellian distribution function ignoring the non-spherical nature of the sheath that results from the non-isotropy of the undisturbed distribution function. Without further experimental evidence it is difficult to assess the validity of the assumptions made by these authors. It is very important to have reliable theories for spherical probes because in the probing of complicated flow fields it may be impractical to use aligned cylindrical probes since the flow direction will not be known in advance.

At a relatively low speed ratio of about 1.5 French (**15**) found that the ratio of ion current for cylindrical probes perpendicular and parallel to the flow equalled the ratio of ions striking the probe, calculated on the basis of kinetic theory ignoring the influence of electric fields entirely. This result is explained by French by noting that the electron temperature in his experiment appeared to be lower than the ion temperature, so that ion collection would be controlled by the ion kinetic flux. Since the Debye length in his experiment was very small compared to the probe size this can account for the fact that the electric fields had no influence.

2.8.2. Effect of Electron-Ion Collisions

Plasma conditions can also occur in which the charged particle density is so high that the ion-electron and ion-ion mean free paths are small compared to the probe size, whereas the electron-neutral and ion-neutral mean free paths are still large in terms of the probe size. When this is the case the electron collection by the probe can be significantly altered by the flow even though the speed ratio of the electrons is negligible. The results of an experiment under these conditions are described by French (**15**). Plane probes were placed perpendicular and parallel to the flow. The experimental arrangement is given in Figure 10, which shows the plasma source and the nozzle to provide the supersonic plasma flow. The results for the apparent electron number density for the two probe orientations is shown in Figure 11, which indicates that the ratio is largest at the center of the plasma jet where the velocity is highest.

The proposed explanation for this phenomenon is as follows. When the probe is perpendicular to the flow and at positive potential, ions are reflected back into the flow. These reflected ions collide with oncoming ions and form an ion shock wave which increases the ion density just in front of the probe. Since at the conditions of the experiment, $n_e \sim 10^{19}/\mathrm{m}^3$, the sheath thickness is very small compared to the probe and the electron density will follow the ion density increase in order to maintain neutrality of the plasma. Consequently, the probe is drawing more electrons than it does in the parallel orientation where this mechanism will be absent. The current ratio is found to be less than the density ratio across a normal shock wave based on a measured flow Mach number. This may possibly be explained by the fact that the propagation speed for small disturbances in a plasma without neutral particles is larger than that in a neutral gas at the same temperature as the ion gas. This means that the effective Mach number should have been taken somewhat lower than the Mach number inferred from impact probe pressures, which are essentially associated with the properties of the neutral gas. Again, much more systematic experimentation is required to verify the proposed explanation definitively.

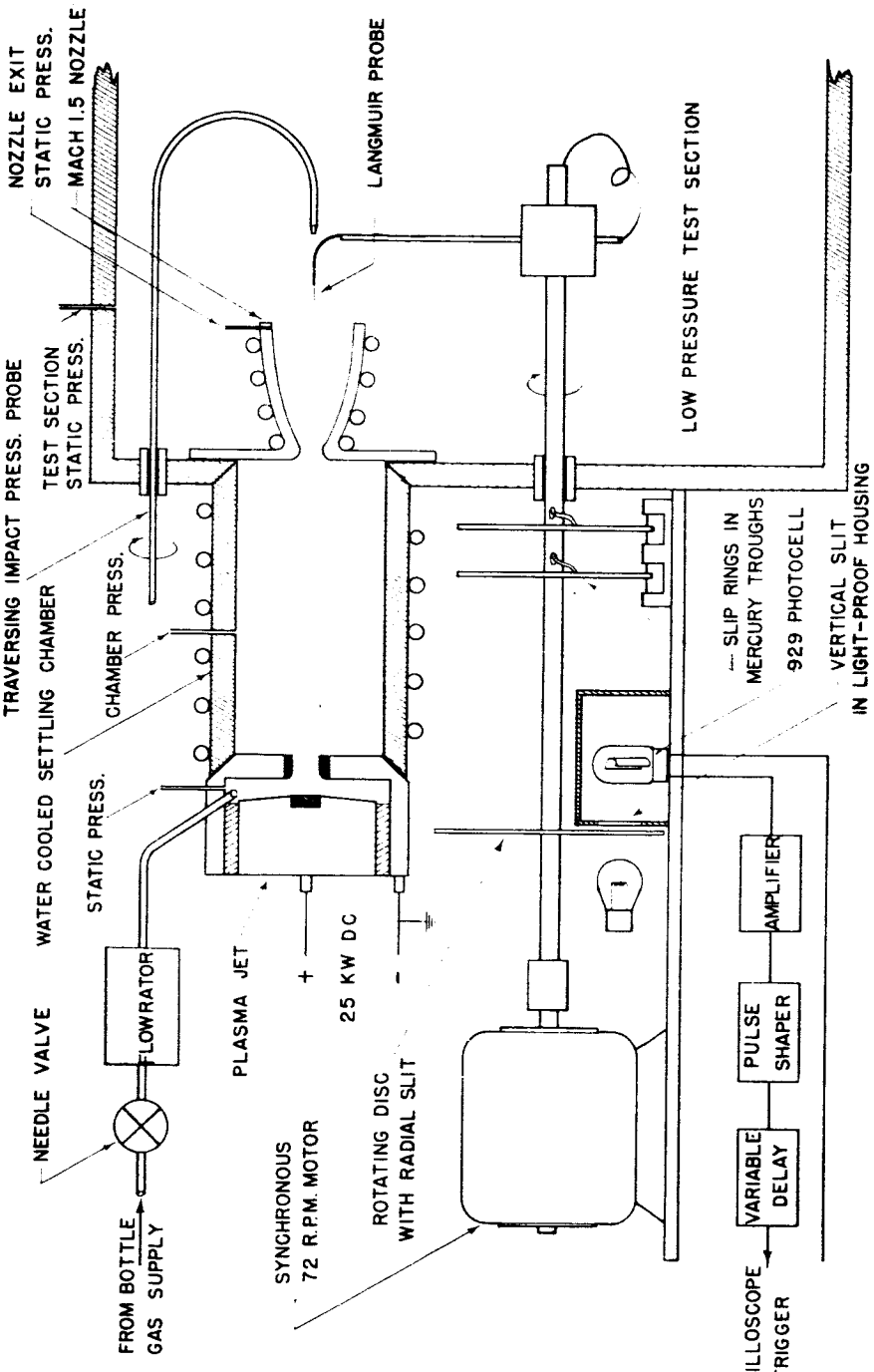

FIGURE 10. Schematic diagram of experiment.

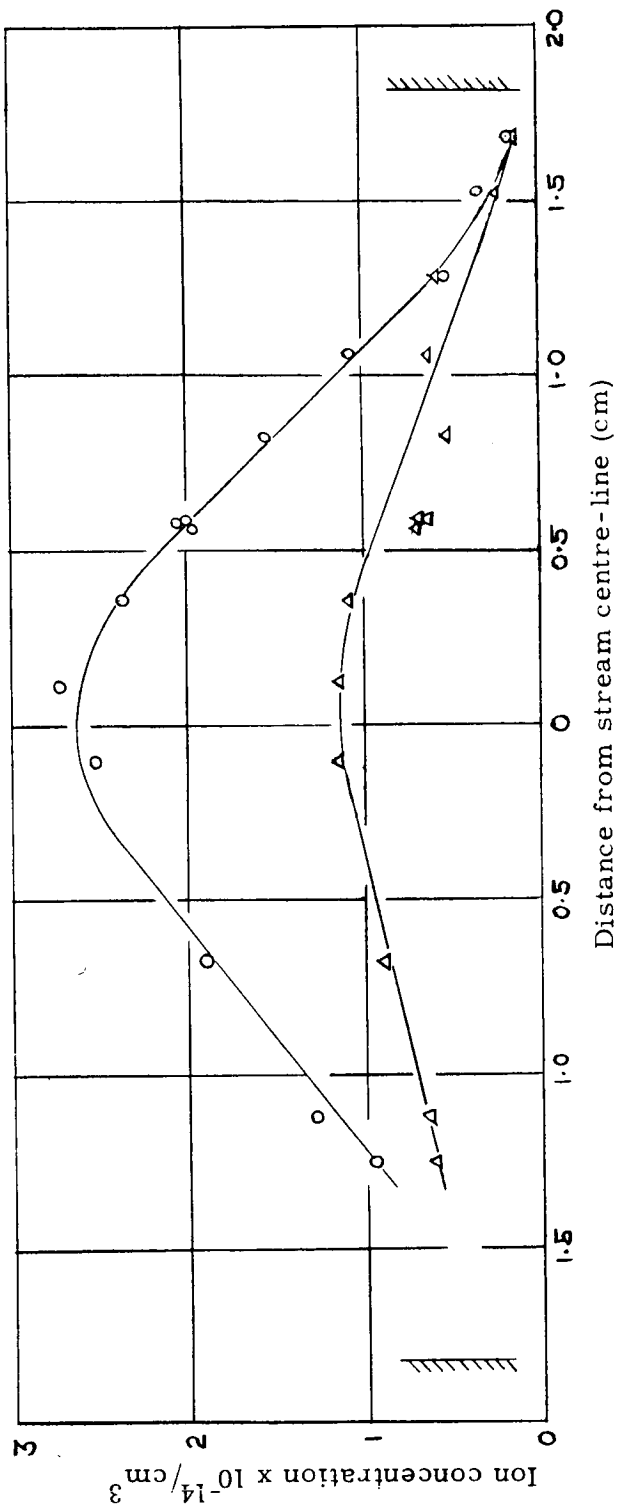

FIGURE 11. Stream traverse: comparison of apparent ion concentrations as determined by plane Langmuir probes transverse and parallel to the stream direction.

2.8.3. Continuum Description

At high gas densities when all mean free paths are smaller than the probe dimension, the supply of charged particles to a probe will be collision dominated and a continuum description of the problem is in order. Some work has been done on this problem under the assumption that the densities are still low enough to ensure that recombination in the cooler gas near a probe does not occur. Talbot (**29**) has analyzed the properties of the gas in the vicinity of the stagnation point of a blunt body that is at floating potential. He suggested that a small probe buried at the stagnation point can be used to sample the local electron density under zero velocity conditions. Since the theory relates the electron density near the stagnation point to that of the free stream, the latter can be determined. The use of such probes was investigated by Brundin, Talbot, and Katz (**30**) in a plasma tunnel by comparing the probe data with microwave interferometric electron density measurements. The results were reasonably encouraging. Pollin (**37**) has studied similar probes in a shock tube and in his theoretical work he took into account the fact that net current must exist. Lam at Princeton has recently reported that work is in progress on the behavior of arbitrarily-shaped probes. This research promises to give a comprehensive theory for the entire probe characteristic.

3. THEORY OF THE DOUBLE PROBE

The use of the single probe is predicated on the availability of a convenient reference electrode. In some applications these are not available (for example, in the case of electrodeless discharges). For such situations the use of double probes is indicated. The basic circuit for the use of such probes is pictured in Figure 12a.

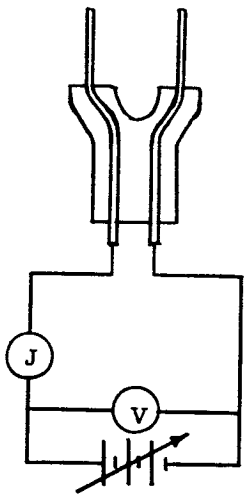

FIGURE 12a. Double probe circuit.

Two probes are placed in the plasma at such a separation that there is no mutual interference, and the current is measured as a function of the potential difference applied between the two probes. A typical current-voltage curve is shown in Figure 12b. Johnson and Malter (**31**) have given a detailed account of the use of this type of probe arrangement. The characteristic curve can be understood in

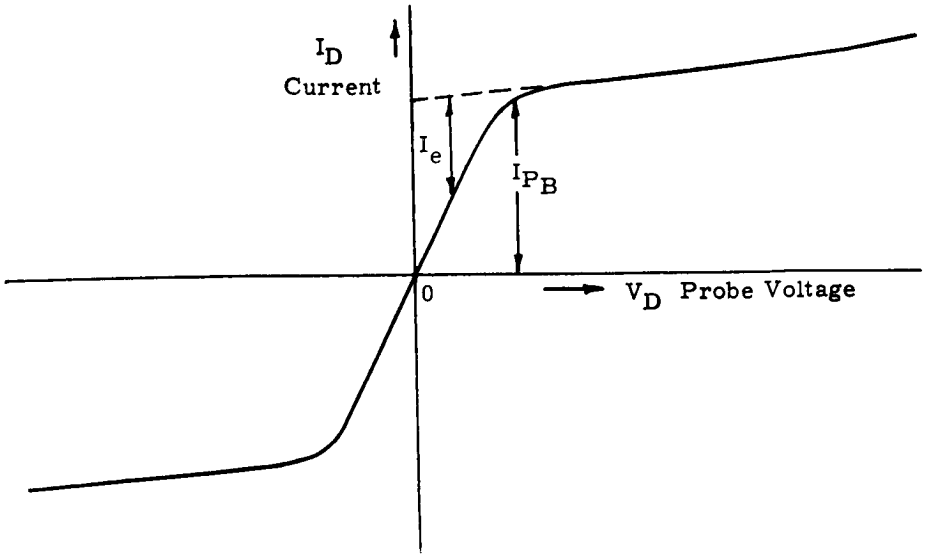

FIGURE 12b. Double probe characteristics for equal probe sizes.

terms of the single probe characteristic. As a result of current continuity the positive current to one probe must be equal in magnitude to the electron current to the other. When, as is usual, the two probes are of the same size and therefore would have the same single probe characteristic, it is clear that the maximum electron current is no larger than the ion saturation current. Especially when the ion collection curve is flat, this means that as the voltage difference is increased the potential of the electron collecting probe remains fixed while the other becomes more and more negative. In this case the current depends little on voltage. On the other hand, for small voltage differences both probes will approach the floating potential of the single probes and the net current will tend to zero. The variation of current with voltage is primarily due to the changing electron current to the probe that is above floating potential.

A simple analysis valid for collision free operation allows the electron temperature to be determined from the probe characteristic. Using the notation of Figure 12b, it is shown in reference (**31**) that for equal probe sizes and the same local plasma conditions

$$\ln\left[\frac{2I_{p_B}}{I_e}-1\right] = -\frac{e}{kT_e}V_D \tag{3.1}$$

where I_{p_B} is defined, as in Figure 12b, to be the value of the probe current at the "break point" in the characteristic and $I_e = I_D - I_p$ and I_D = current in the circuit.

It is pointed out that any uncertainty in the determination of I_{p_B} is not too serious since I_p occurs in the expression for I_e and a certain compensation of errors takes place. I_p is the ion current to probe 2 at the value of V_D and it will have to be estimated from the ion saturation current at large values of V_D. Johnson and Malter describe a suitable extrapolation procedure for this purpose.

A simple formula for the calculation of T_e from the probe characteristic when the two probes are equal is based on the so-called equivalent resistance method. It takes the form

$$T_e = \tfrac{1}{2}R_0 I_p \tag{3.2}$$

where $R_0 = dV_D/dI_D$ at $V_D = 0$, and again I_p is the value of the current at the "break point" of the characteristic.

Since the value of I_p is important in this simple evaluation, the electron temperature is expected to be accurate only when the break point is well defined, i.e., when the sheath thickness is small.

It is to be noted that only a small fraction of the electrons (those in the high-energy tail of the distribution) contribute to the measured current with the above methods since only electron current at potentials close to V_P can be accepted, so that the "temperature" that is measured is associated with the high-energy electrons. If this is objectionable, when there is suspicion that the distribution is non-Maxwellian, for instance, it is possible to obtain information over a larger range of electron energies by making one of the two probes considerably larger than its partner. Equation (3.1) will then only have to be slightly modified.

For the determination of ion densities, the ion saturation parts of the curves can be used. Since at large voltage differences these are similar to the single probe curves all considerations about the ion collection of the single probe apply here as well.

A hybrid double probe circuit is described by Garscadden and Palmer (**32**) who use two probes in parallel and apply to each an almost equal potential with respect to a reference electrode. However, the difference in current as a result of the small difference in voltage is measured. It is shown that this method allows the deduction of the shape of the distribution function similar to the methods in section 2.1, but with greatly improved stability of the results in the presence of fluctuations in the plasma properties.

4. PROBE ERRORS

There are many secondary phenomena that can become sources of error. Loeb (**2**) has given an extensive account of these and only a brief summary will be presented here.

4.1. PRESENCE OF THE PROBE

The insertion of the probe in the plasma may alter the plasma properties to be measured. To minimize this source of error small probes are preferred. Nevertheless, even small probes can draw electron currents that are appreciable in comparison with the currents that maintain the plasma, as in low pressure discharges, for instance. When this takes place it is necessary to keep the voltage below an upper limit that is just above the floating potential. It is one of the virtues of the double probe that such limiting action occurs automatically. It is also possible in a very hot plasma that the probe erodes and so produces contamination products that seriously disturb the plasma.

On the other hand there are many situations where this first type of error is not troublesome as can be ascertained by showing that one probe is not affected by the presence of a second probe in its vicinity.

4.2. REFLECTION AND SECONDARY EMISSION

The interpretation of the probe characteristic rests on the assumption made in the theories that all particles that reach the probe are collected and that no additional charged particles are produced either at the probe wall or in the gas. Reflection, instead of collection of a charged particle when it arrives at the wall, is

a possibility. If the probe field is such as to attract the particle, a reflected particle will eventually be recaptured because its energy after reflection will be less than that originally. So there will be no direct effect on the current. However, the presence of reflected particles in the vicinity of the probe will alter the field distribution in the sheath and so exert a secondary influence. If the field is such as to repel a particle that nevertheless reaches the probe, then reflection will mean decreased current. Langmuir and Mott-Smith (**3**) showed that the shape of the electron current in the retarding field region is unchanged when the reflection coefficient depends only on energy and the distribution is Maxwellian. The only effect is an overall shift of the curve and a discontinuity at plasma potential, since at positive potentials reflected particles will be recaptured. Such discontinuities are not noticed in probe characteristics so it is unlikely that reflection is a serious problem.

The presence of secondary emission of electrons at large negative potential, however, is serious since it leads to a spurious increase in the apparent ion current. Such emission may be due to the incidence of photons and metastable atoms on the probe surface and also due to the bombardment of the ions themselves. The use of multi-grid probes makes it possible to suppress the secondary emission, but in the case of normal probes estimates of the mentioned effects on the apparent ion current have to be made. Careful outgassing of the probe can sometimes reduce the magnitude of the effects.

4.3. THERMAL ELECTRON EMISSION

Thermal electron emission from hot probes can completely alter the character of the probe characteristic. Hence in cases where the probe will become too hot when left in the plasma, the probe will have to be cooled or moved quickly so that it does not reach an objectionable temperature. This makes it necessary to produce an entire characteristic in a short time so that the probe has not moved too much.

Hot probes are sometimes used purposely to define the plasma potential, since the current changes abruptly when the voltage of the probe swings through the plasma potential.

4.4. EFFECTS OF CONTACT POTENTIALS

The measured value of the probe voltage will differ from the effective surface potential by the contact potential. As long as the contact potential is uniform over the probe surface and remains fixed in time the shape of the probe characteristic is unchanged except for a shift along the voltage axis. This does not affect any of the measurements except for an uncertainty in the value of the plasma potential. However, Wehner and Medicus (**33**) have shown that changes in contact potential can occur while the probe voltage is changed as a result of contamination of the probe surface. Furthermore, these changes can occur reproducibly so that a real distortion of the probe characteristic can result. Wehner and Medicus also showed that careful cleaning of the probe, by electron or ion bombardment, to red heat under vacuum can remove contamination from the probe and that changes in contact potential during the production of a probe curve can be minimized by doing it quickly.

Medicus (**34**) has also suggested that a variation of contact potential over the probe surface will produce distortions in the probe curve essentially by an averaging process for the current over a voltage range. This will tend to round off abrupt

changes in the characteristic such as the "break" in the electron current near plasma potential.

A somewhat different difficulty is associated with the deposition of conductive coatings on the insulators near the active probe surface. As a result, the effective probe area may be significantly increased.

4.5. PRESENCE OF FLUCTUATIONS AND OSCILLATIONS

It is to be noted that when probe measurements are made by using a number of steady voltages at which d-c currents are measured, quite important changes occur in the probe characteristic in the presence of oscillations in the plasma. When measurements are made where oscillations are expected, tests should be made to find whether they are present or not. When fluctuations of relatively low frequency are present it should be possible to study the fluctuation of the plasma properties by using techniques to produce the probe characteristic within a time short compared to a typical fluctuation period. In the case of real plasma oscillations the frequency is likely to be too high for such a method to be applicable.

5. EXPERIMENTAL ARRANGEMENTS

A variety of probe shapes and circuits have been used. Only a few examples will be given.

Single and double probes can be made in plane, cylindrical, or spherical forms as indicated in Figure 1. Cylindrical probes have been made as small as 0.02 mm in diameter. Tungsten and molybdenum are favorite materials. Plane probes can be almost as small. Spherical probes are normally somewhat bigger since the support should be small compared to the sphere radius.

A circuit for obtaining a probe characteristic in about one millisecond is shown in Figure 13. Higher speeds are possible; curves have been obtained in less than 10 microseconds. At such high rates of voltage change it is, however, extremely important to keep the capacitance of the probe to a very small value because otherwise spurious capacitive currents will be measured.

A plane multigrid probe for use in a satellite is described by Bourdean, Donley, and Whipple (**35**). The basic structure is shown in Figure 14. Grid A is flush with the satellite skin and electrically connected to it. Grid B is the control grid and C represents the collector. The current to C is measured by a high sensitivity electrometer. When grid B is biased positively with respect to grid A all ions can be repelled, so that only electrons can penetrate beyond B. By making the collector slightly negative with respect to A, the electrons can reach C only when they have enough kinetic energy at their arrival at A to overcome the potential difference between A and C. By varying the bias on C the electron current will yield the electron temperature in the same manner as described in section 2.1. It is also possible to locate the plasma potential relative to the satellite potential by choosing the value of collector bias where the electron current curve deviates from its exponential form.

By biasing grid B negatively all electrons can be repelled and secondary emission electrons from the collector can be suppressed. In this way the ion current can be measured and it is possible by varying the collector potential to measure the energy of the ions. Since the velocity of the satellite is accurately known this makes it possible to determine the mass of the ions. Similar gridded spherical probes are also used, as described by Boyd (**36**).

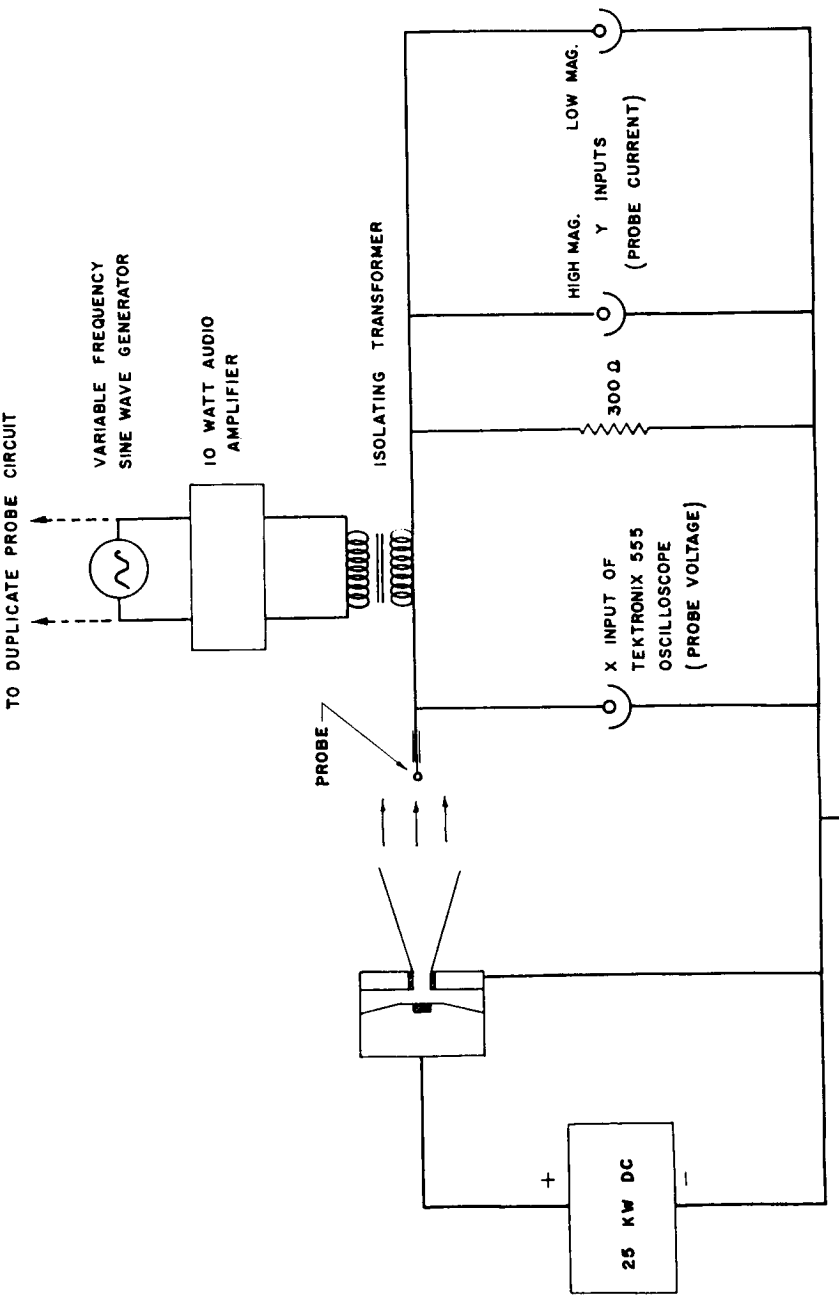

FIGURE 13. Circuit diagram for Langmuir probe.

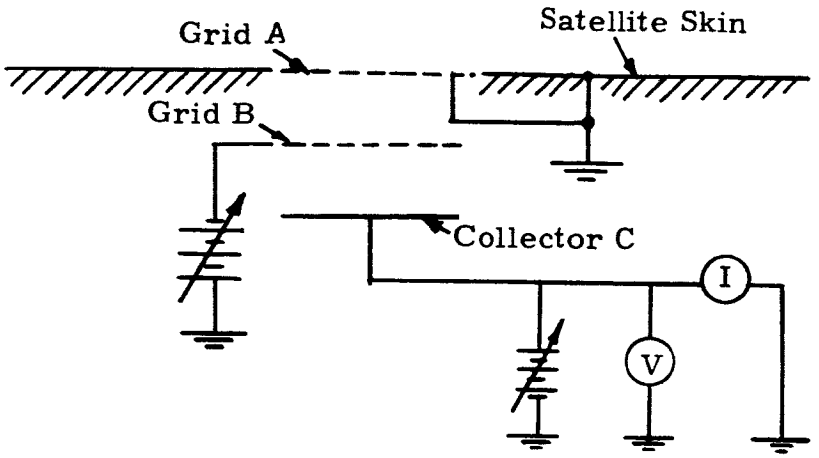

FIGURE 14. Multi-electrode plane probe.

6. CONCLUDING REMARKS

The electrostatic probe is a very useful device in plasma diagnostics in spite of the difficulties in interpretation and the many possible sources of error. Probes can be used over an enormous dynamic range. In satellites probes have measured electron densities as low as $10^{10}/m^3$ and in the laboratory densities of $10^{20}/m^3$ have been determined. In addition, they are capable of making local measurements so that even under unfavorable conditions they can indicate at least the shape of spatial distributions. These advantages are strong incentives for the further development of theories and for verifying experimental work applicable to those conditions for which the probe response is at present not quantitatively known.

NOMENCLATURE

A	Probe area
b	Quantity defined in equation (2.7.3)
B	Magnetic flux density
c	Molecular velocity
d	Sheath thickness
e	Electron charge
f	Velocity distribution function
I	Current density
$\mathcal{I}$	Total current
k	Boltzmann constant
l	Length of cylindrical probe
L	Mean free path
m	Mass of Particle
M	Atomic weight
n	Number density of one kind of charged particle
r	Radius
R_0	Equivalent resistance
T	Temperature

V	Potential
x_0	Quantity defined in equation (2.7.3)
γ	$=1$ cylindrical geometry $=2$ spherical geometry
ε_0	Permittivity of free space
η	Non-dimensional potential
λ_D	Debye length

Subscripts

e	Electrons
F	Floating
p	Probe
s	At sheath edge
$+$	Positive ion
$-$	Negative ion
0	Condition at plasma potential
∞	Undisturbed conditions far away from probe

REFERENCES

1. Langmuir, I., and Compton, K. T., "Electric Discharges in Gases", *Rev. Mod. Phys.*, **3**, 191 (1931).
2. Loeb, L. B., *Basic Processes of Gaseous Electronics* (Berkeley: University of California Press, 1955).
3. Langmuir, I., and Mott-Smith, H., "Theory of Collectors in Gaseous Discharges", *Phys. Rev.*, **28**, 727 (1926).
4. Boyd, R. L. F., "The Collection of Positive Ions by a Probe in an Electric Discharge", *Proc. Roy. Soc. A.*, **201**, 329 (1950).
5. Sloane, R. H., and MacGregor, E. I. R., "An Alternating Current Method for Collector Analysis of Discharge-tubes", *Phil. Mag.* (Series 7), **18**, 193 (1934).
6. Boyd, R. L. F., and Twiddy, N. D., "Electron Energy Distributions in Plasmas I.", *Proc. Roy. Soc. A.*, **250**, 53 (1959).
7. Takayami, K., Ikegami, H., and Miyazaki, I., "Plasma Resonance in a Radio-Frequency Probe", *Phys. Rev. Letters*, **5**, 238 (1960).
8. Cairns, R. B., *Report I. M. 58*, Radio Research Station, Slough, Bucks.
9. Bohm, D., Burhop, E. H. S., and Massey, H. S. W., "The Use of Probes for Plasma Exploration in Strong Magnetic Fields", in *Characteristics of Electrical Discharges in Magnetic Fields* (New York: McGraw-Hill, 1949).
10. Bohm, D., "Minimum Ionic Kinetic Energy for a Stable Sheath", in *Characteristics of Electrical Discharges in Magnetic Fields.*
11. Allen, J. E., Boyd, R. L. F., and Reynolds, P., "The Collection of Positive Ions by a Probe Immersed in a Plasma", *Proc. Phys. Soc. B.*, **70**, 297 (1957).
12. Bernstein, I. B., and Rabinowitz, I. N., "Theory of Electrostatic Probes in a Low Density Plasma", *Phys. Fluids*, **2**, 112 (1959).
13. Hall, L. S., "Probes and Magnetic Pumping in Plasma", *UCRL-6535*, University of California (1961).
14. Laframboise, J., "Theory of Electrostatic Probes in a Collisionless Plasma" (thesis, University of Toronto, to be published).
15. French, J. B., "Langmuir Probes in a Flowing Low Density Plasma", *UTIA Rep. No. 79*, Institute of Aerophysics, University of Toronto (1961).

16. Biondi, M. A., "Diffusion Cooling of Electrons in Ionized Gases", *Phys. Rev.*, **93**, 1136 (1954).
17. Boyd, R. L. F., and Thompson, J. B., "The Operation of Langmuir Probes in Electronegative Plasmas", *Proc. Roy. Soc. A.*, **253**, 102 (1959).
18. Bertotti, B., "Theory of an Electrostatic Probe in a Magnetic Field", *Phys. Fluids*, **5**, 1010 (1962).
19. Zakharova, V. M., Kagan, Y. M., Mustafin, K. S., and Perel, V. I., "Probe Measurements at Medium Pressures", *Zh. Tekh. Fiz.*, **30**, 442 (1960).
20. Su, C. H., and Lam, S. H., "The Continuum Theory of Spherical Electrostatic Probes", *Dept. of Aero. Eng. Report 605*, Princeton University (1962).
21. Schulz, G. J., and Brown, S. C., "Microwave Study of Positive Ion Collection by Probes", *Phys. Rev.*, **98**, 1642 (1955).
22. Taylor, W. C., Rothman, H. S., and Morita, T., "Shocktube and Flame Diagnostics by Ion Probes", *Bull. Am. Phys. Soc.* (Series 11), **8**, 437 (1963).
23. Davis, A. H., and Harris, I., "Interaction of a Charged Satellite with the Atmosphere", in *Rarefied Gas Dynamics* (New York: Academic Press, 1961).
24. Meckel, B. B., "Experimental Study of the Interaction of a Moving Body with a Plasma", in *Rarefied Gas Dynamics.*
25. Clayden, W. A., "Recent Research in the ARDE Low Density Wind Tunnel with a Plasma Jet Heater", in *Rarefied Gas Dynamics.*
26. Clayden, W. A., "Langmuir Probe Studies in the RARDE Plasma Jet", Third International Symposium on Rarefied Gas Dynamics, 1962.
27. Smetana, W. O., "On the Current Collected by a Charged Circular Cylinder Immersed in Two-Dimensional Rarefied Plasma Stream", Third International Symposium on Rarefied Gas Dynamics, 1962.
28. Medicus, G., "Spherical Langmuir Probe in Drifting and Accelerated Maxwellian Distribution", *J. Appl. Phys.*, **33**, 3094 (1962).
29. Talbot, L., "Theory of the Stagnation Point Langmuir Probe", *Phys. Fluids*, **3**, 2 (1960).
30. Brundin, C. L., Talbot, L., and Katz, J. E., "A Comparison Between Langmuir Probes and Microwave Electron Density Measurements in an Arc Heated Low Density Supersonic Wind Tunnel", University of California *Tech. Rep. HE-150-186* (1961).
31. Johnson, E. O., and Malter, L., "A Floating Double Probe Method for Measurements in Gas Discharges", *Phys. Rev.*, **80**, 58 (1950).
32. Garscadden, A., and Palmer, R. S., "Langmuir Probe Derivatives Using a Double Probe Method", *ARL-63-50*, Aero. Res. Lab., U.S. Air Force, 1963.
33. Wehner, G., and Medicus, G., "Reliability of Probe Measurements in Hot Cathode Gas Diodes", *J. Appl. Phys.*, **23**, 1035 (1952).
34. Medicus, G., "Theory of Probes with Non-Uniform Work Function", *Vth Inter. Conf. on Ionization Phen. in Gases* (Amsterdam: North-Holland, 1962), 1397.
35. Bourdeau, R. E., Donley, J. L., and Whipple, E. C., "The Ionosphere Direct Measurements Satellite", *NASA TN D-414* (1962).
36. Boyd, R. L. F., "Plasma Probes on Space Vehicles", *Vth Inter. Conf. on Ionization Phen. in Gases* (Amsterdam: North-Holland, 1962), 1387.
37. Pollin, I., private communication.

5. Paul C. Wilber: *Experimental Investigation of the Characteristics of a Langmuir Probe in Ionized Low-Density Flows*

An experimental study of the performance of a charged circular cylinder immersed in an essentially-uniform rarefied plasma stream is described. Data are presented for wide ranges of speed ratio, electron and neutral particle number densities, and electron temperature with the collector axis oriented both parallel and transverse to the flow. Results are discussed with respect to a theory recently developed at the University of Southern California Engineering Center which relates the probe measurements to local charged particle density and temperature in the flowing plasma.

INTRODUCTION

Approximately two years ago a program was begun at the University of Southern California Engineering Center to investigate the possibility of making local measurements of charged-particle number density in rarefied plasma streams. A theoretical study was carried out by Dr. F. O. Smetana (1) in which he was able to calculate the flux of charged particles to a cylindrical collector immersed in the stream as a function of its potential, relative to the plasma, for wide ranges of the flow parameters. His results provide a means of interpreting the measured characteristic quantitatively in terms of the charge number density if the other parameters are known. Since the theoretical analysis was based on several assumptions which may or may not hold in general, an experimental study was initiated to assess the validity of the theory. This paper discusses what has been accomplished experimentally to date.

REVIEW OF THEORY

Since the experimental work to be discussed has the checking of a theory as one of its principal objectives, a brief outline of that theory and its results will be presented first. Smetana's analysis is an extension of the work of Mott-Smith and

ED. NOTE: Mr. Wilber is with the Celestial Research Corporation, South Pasadena, California. The research reported in this paper was conducted at the University of Southern California Engineering Center and was sponsored by the Aeronautical Systems Division, Wright-Patterson Air Force Base, under Contract AF-33(657)-7760.

Langmuir on probes in rarefied stationary plasmas (**2, 3**) to the case of mass mean motion. The basis of the method is the calculation of particle flux to the probe by summing the distribution function over all particle velocities such that the free-space trajectory intersects the collecting surface. A Maxwell-Boltzmann distribution is assumed.

For the analysis of the case of a moving plasma the following assumptions were made:

1. The plasma is composed of three species: singly-ionized positive ions, electrons, and neutral molecules.
2. Each species is in local thermodynamic equilibrium and the ions and neutrals have the same temperature (which may, however, differ from that of the electrons).
3. The number densities of ions and electrons are equal; the number densities are small compared with those of the neutrals.
4. Collisions between charged particles are neglected in comparison with collisions between charged particles and neutrals.
5. The stream is moving with a uniform velocity, U_0, perpendicular to the axis of a right circular cylindrical collector.
6. The cylinder diameter is small compared with both the electron-neutral and ion-neutral mean free path lengths.
7. The field of the cylinder does not perturb the plasma significantly beyond one electron-neutral or ion-neutral path length. Thus the region of effective charge collection is collisionless.
8. The nature of the field about the collector is not altered by the motion of the stream (i.e., it remains a central force field as in the case of a stationary plasma).

Application of these assumptions resulted in the expression shown for the flux of one of the charged species to the cylinder:

$$N = n_0\left(\frac{2\pi kT}{m}\right)^{-3/2}\frac{r_e}{r_c}\int_{-\infty}^{\infty}\int_{-c_{2\max}}^{c_{2\max}}\int_{-U_0\sin\theta}^{\infty}(c_1+U_0\sin\theta) \times \varepsilon^{-(m/2kt)(c_1^2+c_2^2+c_3^2)}\,dc_1\,dc_2\,dc_3 \tag{1}$$

where n_0 = free stream number density of the species collected
r_c = cylinder radius
r_e = radius at which the potential on the cylinder no longer effects collection of charge
c_1, c_2, c_3 = components of the random thermal motion in the r, θ, and z-directions respectively
$c_{2\max}$ = the maximum value of c_2 for the given value of c_1 for which the particle will be collected

If we define

$$\beta = \sqrt{\frac{m}{2kT}} \tag{2}$$

$$s = U_0\beta \tag{3}$$

$$\eta = \frac{eV_0}{kT} \tag{4}$$

$$V_0 = \text{probe potential} \tag{5}$$

then substituting these, and substituting for $c_{2\max}$ in terms of c_1 and S, and integrating equation (1) twice yields

$$N = n_0\sqrt{\frac{m}{8\pi kT}}\frac{r_e}{r_c}\int_{-U_0\sin\theta}^{\infty}(c_1+U_0\sin\theta)\varepsilon^{-\beta^2c_1^2}\left[\operatorname{erf}\left(S\cos\theta+\frac{r_c}{r_e}Z\right)-\operatorname{erf}\left(S\cos\theta-\frac{r_c}{r_e}Z\right)\right]dc_1 \tag{6}$$

where

$$Z^2 = \frac{r_e^2}{r_e^2-r_c^2}[(\beta c_1+S\sin\theta)^2+\eta_0]$$

Equation (6) cannot be integrated directly except for certain special cases. For the case of $S=0$ it yields the well-known results of Langmuir. For the general case numerical methods are necessary; they yield the desired results provided r_e is finite. The result can be conveniently expressed as

$$J_1 = 2\pi r_c n_0\sqrt{\frac{kT}{2\pi m}}\,F\left(\eta_0, S, \frac{r_e}{r_c}\right) \tag{7}$$

Since J_1 is the flux of a single charged species to the cylinder; the net current to the probe will have the form:

$$I = (J_1-J_2)Le \tag{8}$$

where J_2 = flux of the oppositely charged species
L = length of collector
e = electronic charge

If one puts

$$\alpha = \left(\frac{m_eT_i}{m_iT_e}\right)^{1/2} \tag{9}$$

$$\gamma = \frac{T_e}{T_i} \tag{10}$$

$$S_0 = U_0\left(\frac{m_i}{2kT_i}\right)^{1/2} = \text{Speed ratio of the neutral species} \tag{11}$$

$$\bar{\eta}_0 = \frac{eV_0}{kT_e} \tag{12}$$

equation (8) can be rewritten

$$I = Kn_0r_c\sqrt{T_e}\,\tilde{I}\left(\bar{\eta}_0, \alpha S_0, \frac{r_e}{r_c}\right) \tag{13}$$

For fixed values of γ, S_0, and r_e/r_c, $\tilde{I}$ is a fixed function of $\bar{\eta}_0$. If, in addition, we are given a fixed probe geometry and a constant ion temperature, the probe characteristic equation, equation (13), has only the charge number density as parameter and thus becomes a convenient measure of charge density.

This analysis hinges on two basic assumptions: (1) that the probe possesses a central force field and (2) that there is a finite radius, r_e, for which the field of the probe, in effect, terminates. The problem becomes how to insure the validity of these assumptions. The first assumption can probably best be verified by experiment, but a reasonable estimate of limits on the second can be obtained by solving a suitable

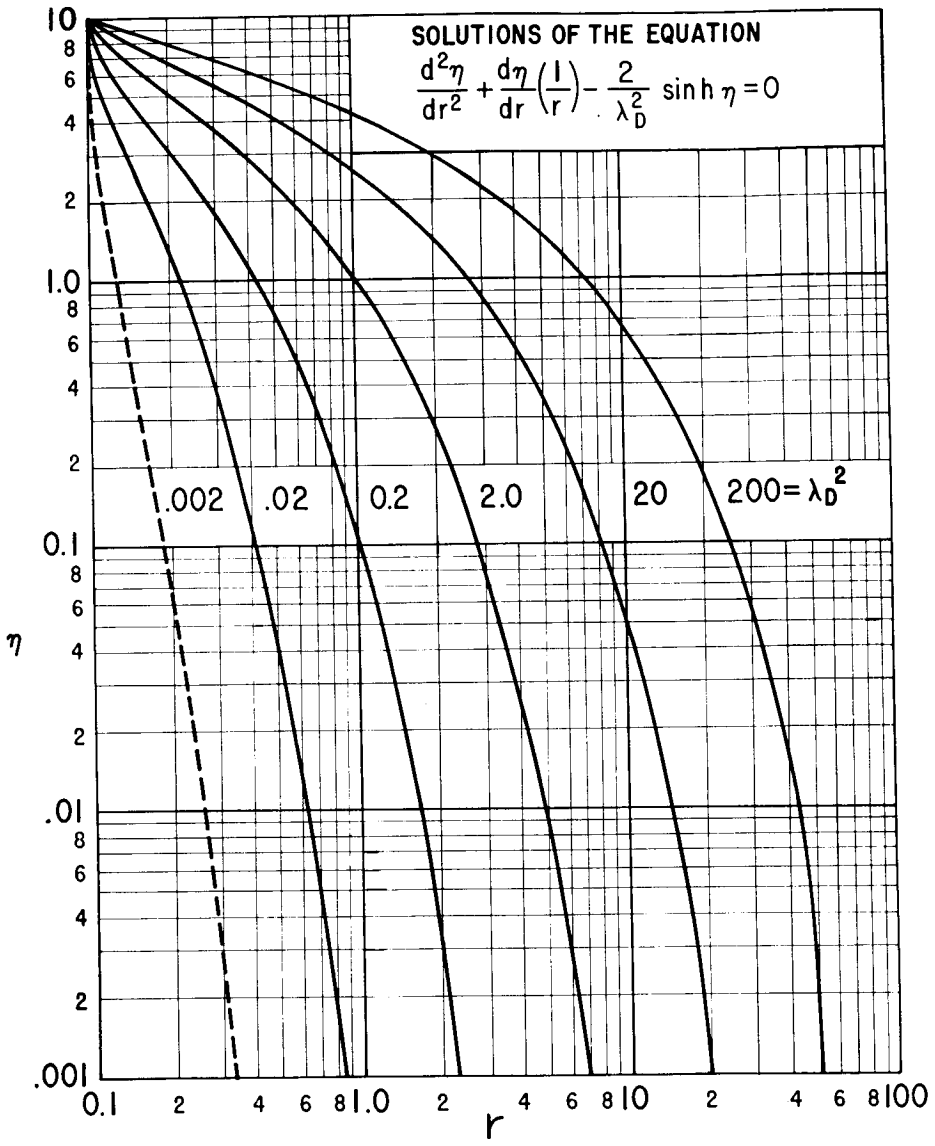

FIGURE 1. Solutions of the one-dimensional Poisson equation for the cylinder with $S=0$ and $I=0$.

form of the Poisson equation. This has been done for the one-dimensional case with $S=0$ and no current drawn by the cylinder. The result is shown in Figure 1.

While the conditions assumed in obtaining a solvable form of the Poisson equation are not very realistic, it is evident from Figure 1 that considerable changes can occur in the charge distribution near the cylinder without altering r_e appreciably. Thus when $r_e/r_c > 10$, the error induced in the flux calculation by the use of the results in Figure 1 would seem to be negligible.

With the above in mind, theoretical probe characteristics have been prepared for proposed probe geometries and conditions anticipated in the Engineering Center's experimental facilities. The plasma was assumed to consist of electrons, nitrogen

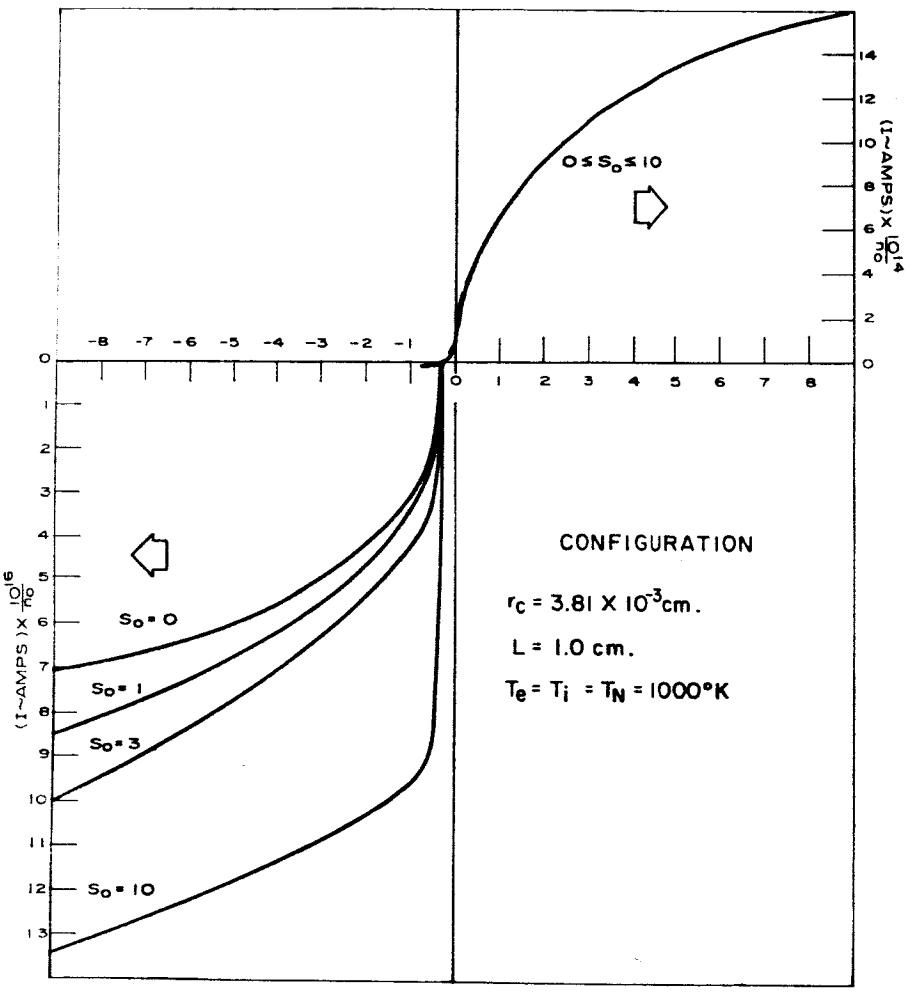

FIGURE 2. Theoretical Langmuir probe characteristic for a typical case of thermal equilibrium.

molecules, and N_2 ions. Since the Center's facilities can generate only relatively low enthalpy plasmas and then only such that $T_e > T_i, T_n$, discussion will be limited to such cases.

The theoretical characteristics were based on the nominal diameters of tungsten wires which could be fabricated into satisfactory probes. Limits on the range of charged-particle number density for which the theory could be expected to hold were found by imposing the conditions: (1) that the region of charge collection be collisionless with respect to electron-neutral or ion-neutral collisions, and (2) that the value of the probe's field at the maximum allowable value for r_e must always be 1/100th its value at r_c. Based on Figure 1 and the desire to make the theory applicable to values of charge density as low as possible, the maximum value for r_e was taken to be $100r_c$.

Figure 2 shows a theoretical probe characteristic for a typical case of thermal equilibrium. This illustrates the effect of speed ratio on ion current even at very low probe potentials when the electron temperature is low.

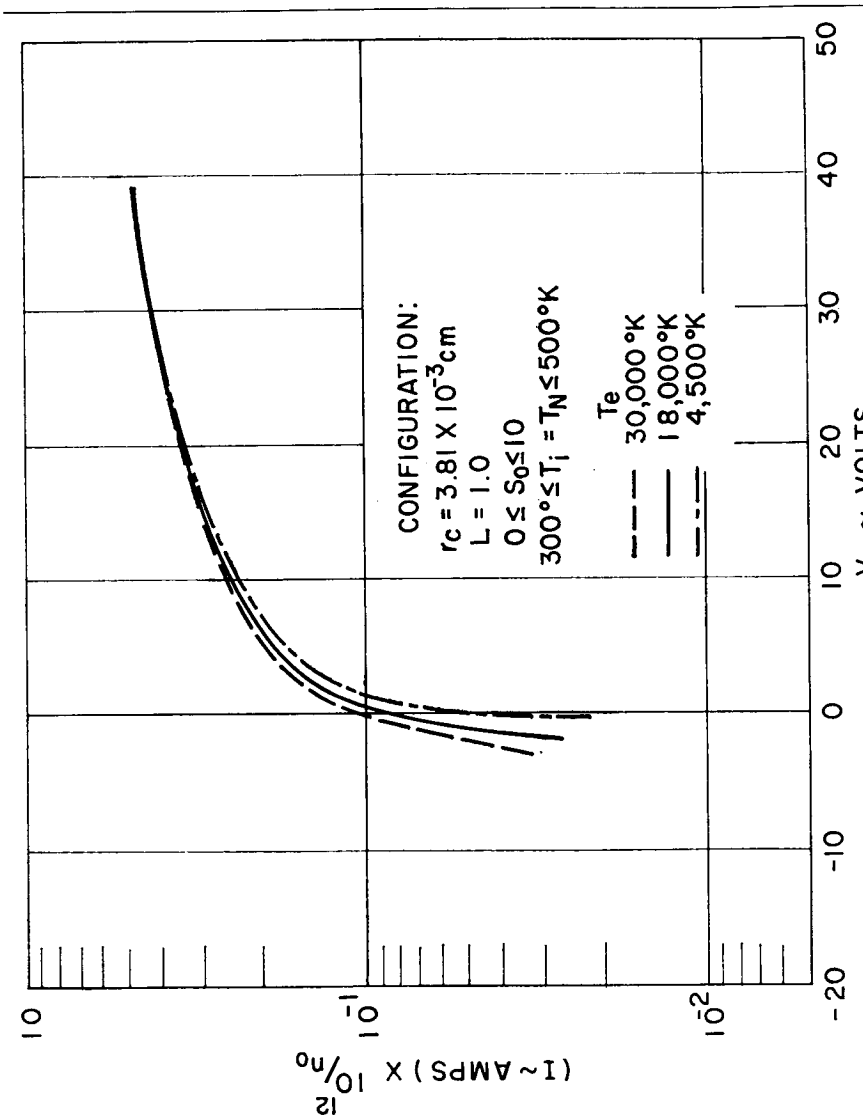

FIGURE 3. Theoretical probe characteristics illustrating the independence of the electron-sheathed region from both speed-ratio and electron temperature within the usual experimental ranges.

Unfortunately the RF discharge produces plasmas which are far from being in a state of thermal equilibrium. This means that the following temperatures were expected in the experiments: $T_i = T_N \approx 300°\text{K}$, $4500°\text{K} \lesssim T_e \lesssim 30{,}000°\text{K}$. Thus γ might vary between 15 and 100 and, hence, for a given experimental configuration, the probe characteristic would have both n_0 and T_e as parameters. If the probe characteristic exhibits a strong dependence on T_e throughout the ranges of S_0 and V_0 available experimentally then unique determination of charge density would depend on knowing the electron temperature. To determine if such were the case theoretical probe characteristics were prepared for the above conditions. Figure 3 shows the results. The electron-sheathed region is seen to be relatively independent of electron temperature and thus provides a unique measure of charge density. If T_e and S_0 are known the ion sheathed region also determines n_0 uniquely.

EXPERIMENTAL SETUP

In an attempt to verify the above theory, an experimental program is being carried out in the Engineering Center's low-density, Mach-6, axisymmetric test facility sketched in Figure 4. Commercial grade liquid nitrogen provides the working gas. The stream, upon leaving the nozzle, passes through a boron nitride constant-area heating section approximately 10 inches long. From this it exits into a $6\frac{1}{2}$-inch I.D. teflon test section having various openings for observation of the flow. The facility is instrumented to provide plenum chamber pressure, test station static and pitot pressures, and the approximate stagnation temperature. It can be driven by either a large mechanical vacuum pump, a cryopump, or both.

The discharge can be produced anywhere along the boron nitride section by suitable positioning of the external ring electrodes. Power is supplied either by a 2-kw, 10-Mc/sec generator or a 12-kw, 12.8-Mc/sec generator. Overall heating efficiency is estimated to be not more than 20%.

The probe instrumentation is shown in Figure 5. Because of the non-equilibrium nature of the RF plasma the entire system must be floated with respect to ground to minimize disturbance of the plasma and to get satisfactory measurements. Probe currents are measured with a Kay Lab model 203R microammeter. Probe potential is measured with respect to a floating reference probe kept at a fixed position in the stream. To insure isolation of the reference probe voltages are measured with a Sensitive Research Electrostatic Voltmeter having an insulation resistance $\geq 10^{15}\Omega$. To obtain maximum resolution in the voltage measurements, the meter is biased to the upper end of its scale by a suitable potentiometer. A reversing switch allows measurement of probe voltages both positive and negative with respect to the reference electrode.

The probe potential is varied with respect to the plasma by applying a voltage between the probe and a cylindrical copper return-electrode lining the inside of the teflon test section. Although there is considerable speculation as to how much this technique disturbs the plasma, visual observations indicate little effect and the distance between the probe and the reference electrode is kept as small as possible to minimize the effects of whatever changes do occur. Surveys of various plasma streams at the test station indicated very small gradients in the core of the flow for the case where the probe draws no current.

Because the RF discharge in this experimental configuration appears to act like a battery, producing voltages up to 400 volts between interior points and points on the boundary of the plasma, a relatively high voltage potentiometer is needed to bias the probe with respect to the plasma. The potentiometer used consists of two variable voltage sources in series. The coarse pot has a range of 0 to 1000 volts while the fine pot can be varied from 0 to 24 volts, in steps of approximately 0.2 volts. This system is connected to the probe-return-electrode combination by a reversing switch to again provide choice of sign.

The probe itself consists of a tungsten collector welded to a No. 30 copper lead with the combination supported in a pyrex tube of approximately 0.055-inch O.D. and 0.035-inch I.D. The tube is bent so that the axis of the collector is perpendicular to the axis of the support tube and centered on it. The pyrex tube is necked down and ground off until the tungsten just passes through it. Microscopic examination indicates maximum clearance between the collector and the pyrex to be about 0.0003 inches. The diameter of the collector is nominally either 0.003 inches or 0.0012 inches. Lengths of the cantilevered collector section equivalent to a length-to-diameter ratio of 600 have been produced without significant droop.

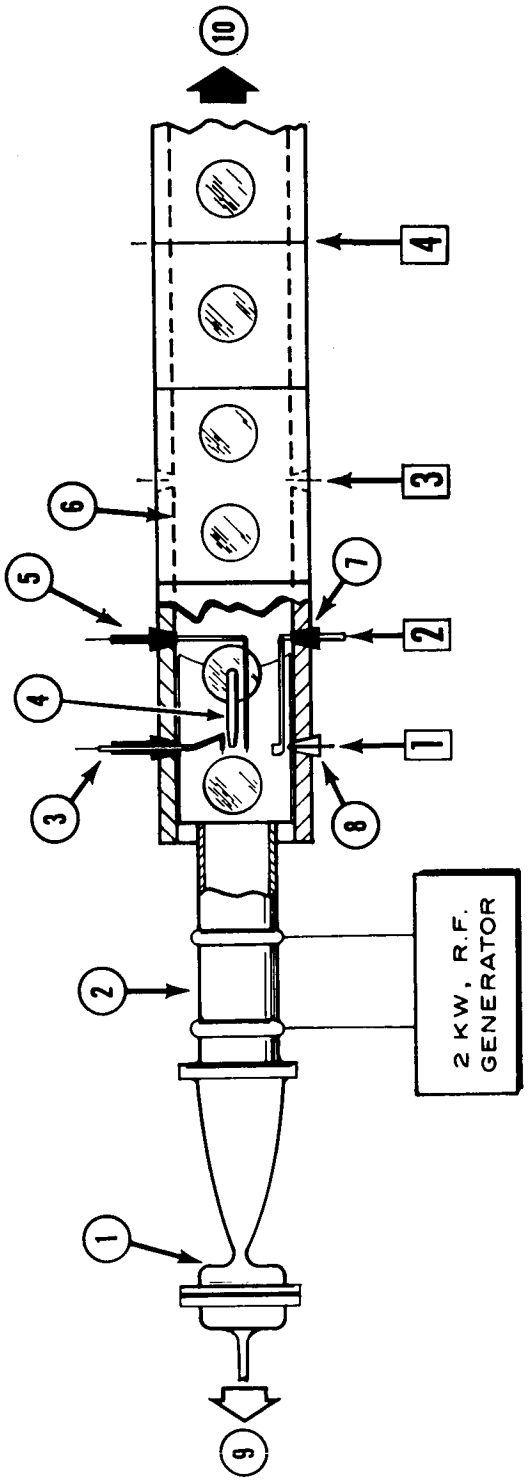

1	M=6 NOZZLE	7	STATIC PRESSURE PICKUP
2	BORON NITRIDE DISCHARGE SECTION	8	RETURN ELECTRODE AND LEAD
3	LANGMUIR PROBE	9	TO GAS SUPPLY AND METERING SYSTEM
4	PITOT PROBE	10	THRU HEAT EXCHANGER – TO MECHANICAL PUMP AND/OR CRYOPUMP
5	FLOATING REFERENCE PROBE		
6	6½"– I.D. TEFLON TEST SECTION		

FIGURE 4. Sketch of test section.

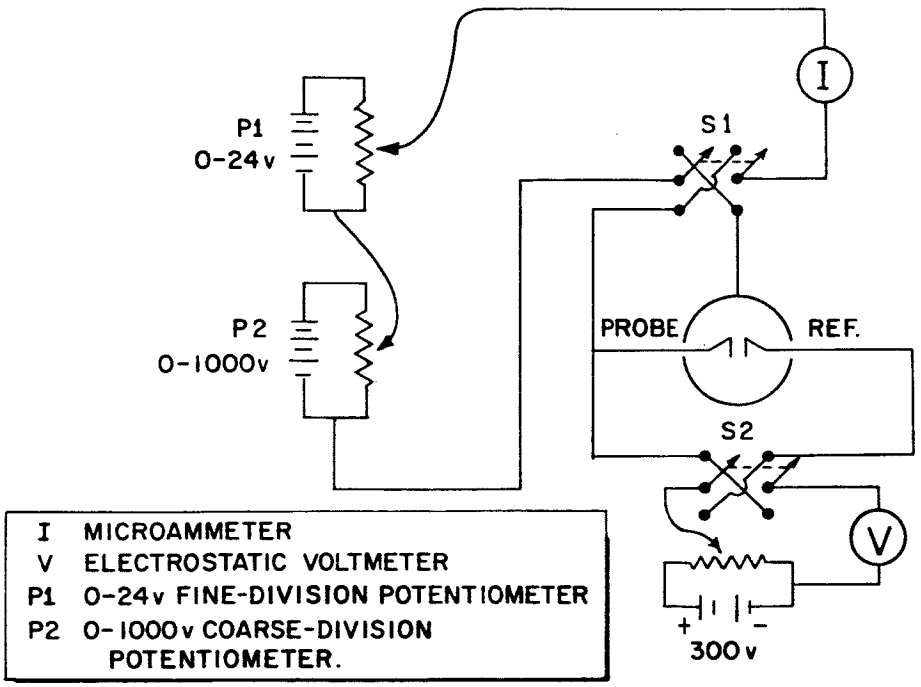

FIGURE 5. Probe instrumentation schematic.

The probe support system allows the probe to traverse the plasma in a vertical direction and to have its axis oriented at any angle with respect to the direction of flow. Since the collector is centered on the axis of the support tube, displacement of the probe in the plasma during a rotation is minimized.

Using this experimental system a number of measurements of probe characteristics have been made for several combinations of the parameters involved. Although the ranges of variation are not as great as were originally anticipated, they do seem to provide some significant effects with which to study the theory. The principal problem encountered in the work to date has been that of isolating the probe instrumentation from the RF fields and noise associated with the generator and discharge. Failure to properly solve this problem has limited the measurements to a much lower upper limit on charge number density than was originally anticipated. As a result it has not been possible to make simultaneous independent measurements of charge density by microwave methods.

RESULTS AND DISCUSSION

A number of runs using three different probes in various flow conditions have been made. Significant portions of probe characteristics were obtained in fourteen cases which are described by Table I. Since an infinitely long probe oriented with its axis parallel to the direction of flow is obviously a very good approximation to the stationary case, most data was taken with the collector in this orientation in order to allow interpretation by Langmuir's well established theory. In addition, experiments showed that when placed transverse to the flow the collectors were bent off axis by varying amounts depending upon probe geometry, flow conditions,

TABLE I. EXPERIMENTAL CONDITIONS

Run No.	*Probe location*	*Probe axis orientation*	r_c (cm × 10^3)	L $2r_c$	*Neutral particle number density,* n_N (cm^{-3})	T_N, T_i (°K)	*Speed ratio* (S_0)	*Discharge power* (*Watts*)
1	Centerline	Parallel	3.68	119.5	3.7×10^{15}	~300	~5	~250
2			2.52	10.7	3.5×10^{15}	~290	~5	~200
3					2×10^{16}	~330	~0.5	
4					6.8×10^{15}	~330	~0.5	
5					2.6×10^{15}	~330	~0.1	
6			2.52	10.7	1.9×10^{15}	~340	~5	
7			1.52	605	8.1×10^{15}	~325	~0.05	~200
8					1.8×10^{15}	~330	~5	~100
9					3.2×10^{15}	~290		~200
10	Centerline				4.7×10^{15}	~280		
11	0.55 inch below Centerline	Parallel			4.7×10^{15}	~280		
12	0.55 inch below Centerline	Transverse			4.7×10^{15}	~280		
13	Centerline	Parallel			8.0×10^{15}	~275		~200
14	Centerline	Parallel			8.0×10^{15}	~280		~400

voltage, and length of operation. The present theory was therefore checked by taking a series of pairs of comparison points except for the curve obtained in run No. 12 during which the collector's tip suffered a permanent set of 18° off axis. Table II lists the pairs of points obtained.

TABLE II. COMPARISON POINTS INDICATIVE OF EFFECT OF ORIENTATION ON PROBE CHARACTERISTIC AT VARIOUS CONDITIONS.

Pair number	*Run number*	*Probe location (below centerline)*	*Parallel* V_p (volts)	*Parallel* I_p (amps)	*Transverse* V_p (volts)	*Transverse* I_p (amps)
1	7	0.14″	−175	-9.56×10^{-6}	−174	9.64×10^{-6}
2	7		50.2	0.907×10^{-3}	50.0	0.963×10^{-3}
3	8		−175	-3.45×10^{-5}	−175	-3.40×10^{-5}
4	8		63.8	3.20×10^{-3}	60.3	3.20×10^{-3}
5	9		−195	-2.48×10^{-4}	−195	-2.60×10^{-4}
6	9		45.2	4.96×10^{-3}	42.3	4.96×10^{-3}
7	10		−201	-4.07×10^{-5}	−201	-4.84×10^{-5}
8	10		35.8	3.63×10^{-3}	32.6	3.60×10^{-3}
9	13		−113	-3.01×10^{-5}	−114	-3.36×10^{-5}
10	13		22.1	4.84×10^{-4}	22.2	6.61×10^{-4}
11	14		−195	-6.25×10^{-5}	−195	-8.56×10^{-5}
12	14		49.8	2.89×10^{-3}	46.6	2.83×10^{-3}

To aid in interpreting the results, theoretical probe characteristics corresponding to the nominal geometries of the experimental probes and covering the range of experimental conditions studied are presented in Figure 6. The values of I_p shown are per centimeter of collector length. Since the RF plasma was expected to be out of equilibrium between species with temperatures as shown on page 102, most of the experimental data was taken in the electron-collection regions of characteristics such that the data could be compared with theory directly without first determining T_e.

All the theoretical curves are based on the value $n_0 = 10^9$ cm^{-3}. The value of n_0 observed experimentally is obtained by multiplying 10^9 by the factor corresponding

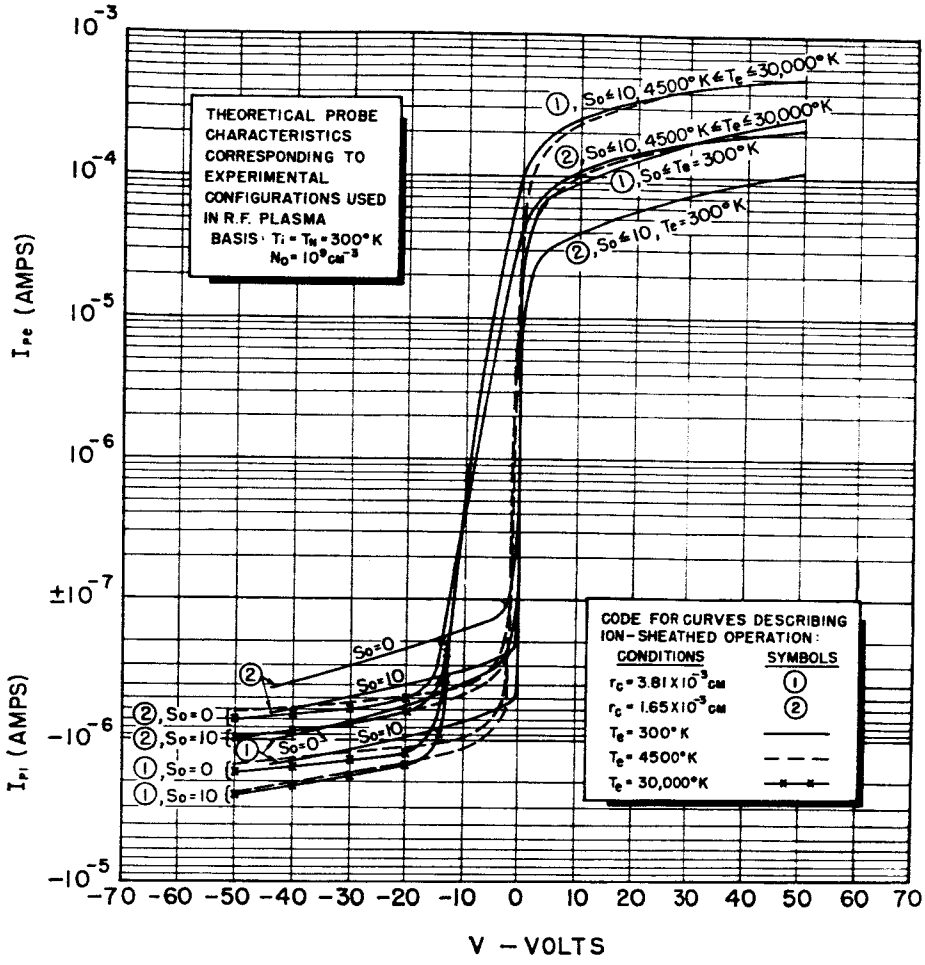

FIGURE 6. Theoretical probe characteristics corresponding to experimental configurations ($T_i = T_N = 300°K$).

to the number of decades up or down that the appropriate section of the theoretical curve has to be shifted to make it match the observed curve. Since the probe voltage is measured with respect to that of a floating reference electrode located at a different position in the plasma, there is a horizontal displacement of each experimental curve, relative to its corresponding theoretical characteristic, which can be ignored. Since plasma conditions vary from run to run, the shifts in the observed results cannot be expected to be constant.

Figures 7, 8, and 9 show the fourteen measured characteristics. The current has been "normalized" to correspond to that of a collector whose length is 1 cm and whose radius is either 3.81×10^{-3} cm (for runs 1 through 6) or 1.65×10^{-3} cm (for runs 7 through 14). The scatter in the observed data is apparently due to several factors: (1) random fluctuations in the plasma conditions, (2) insufficient resolution of the voltmeter readings, and (3) interaction of the ammeter with the RF field which caused shifts in the characteristics of certain input shunting resistors during some of the runs. Lack of sufficient data to accurately define the retarding

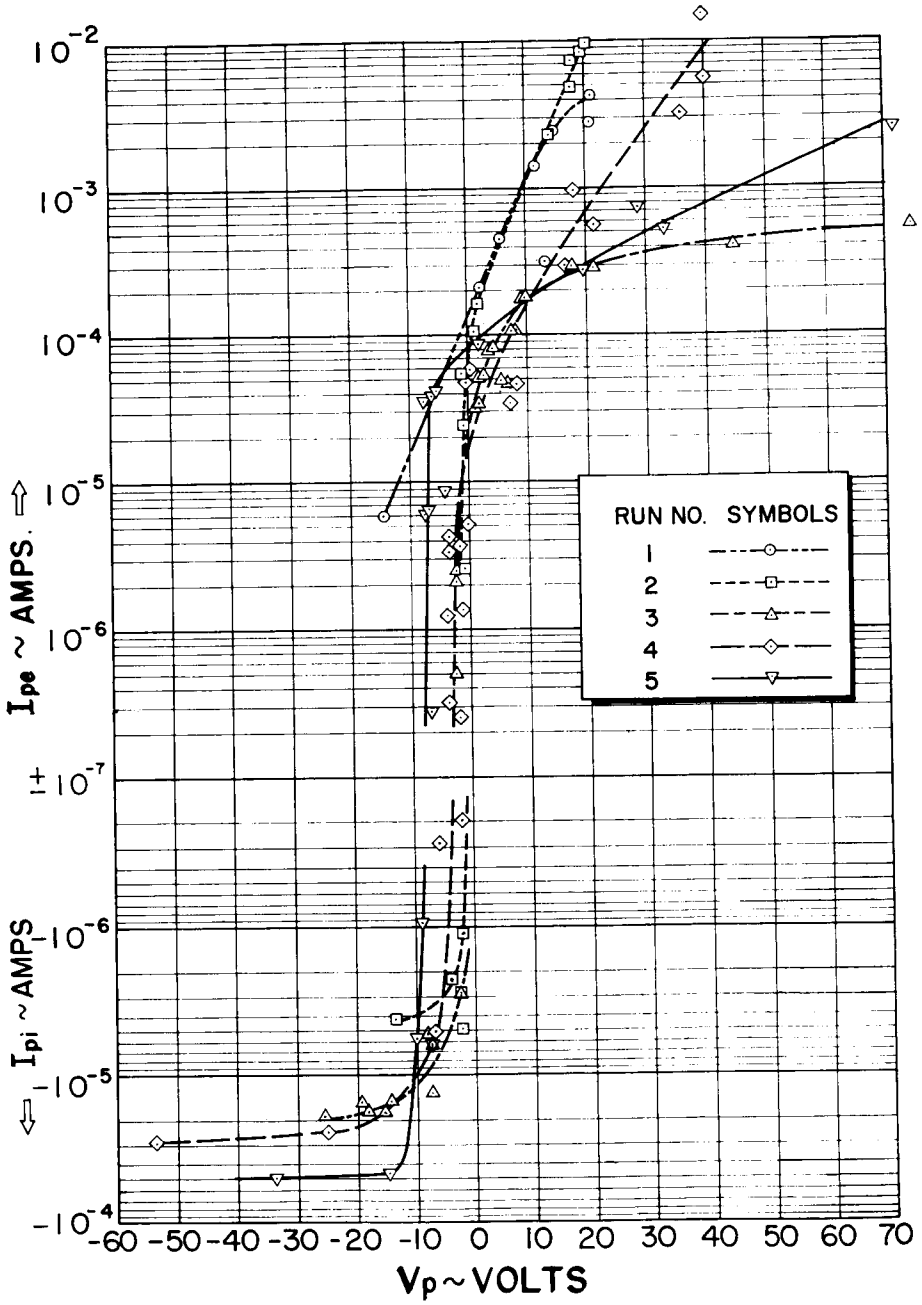

FIGURE 7. Experimental probe characteristics for runs 1 through 5.

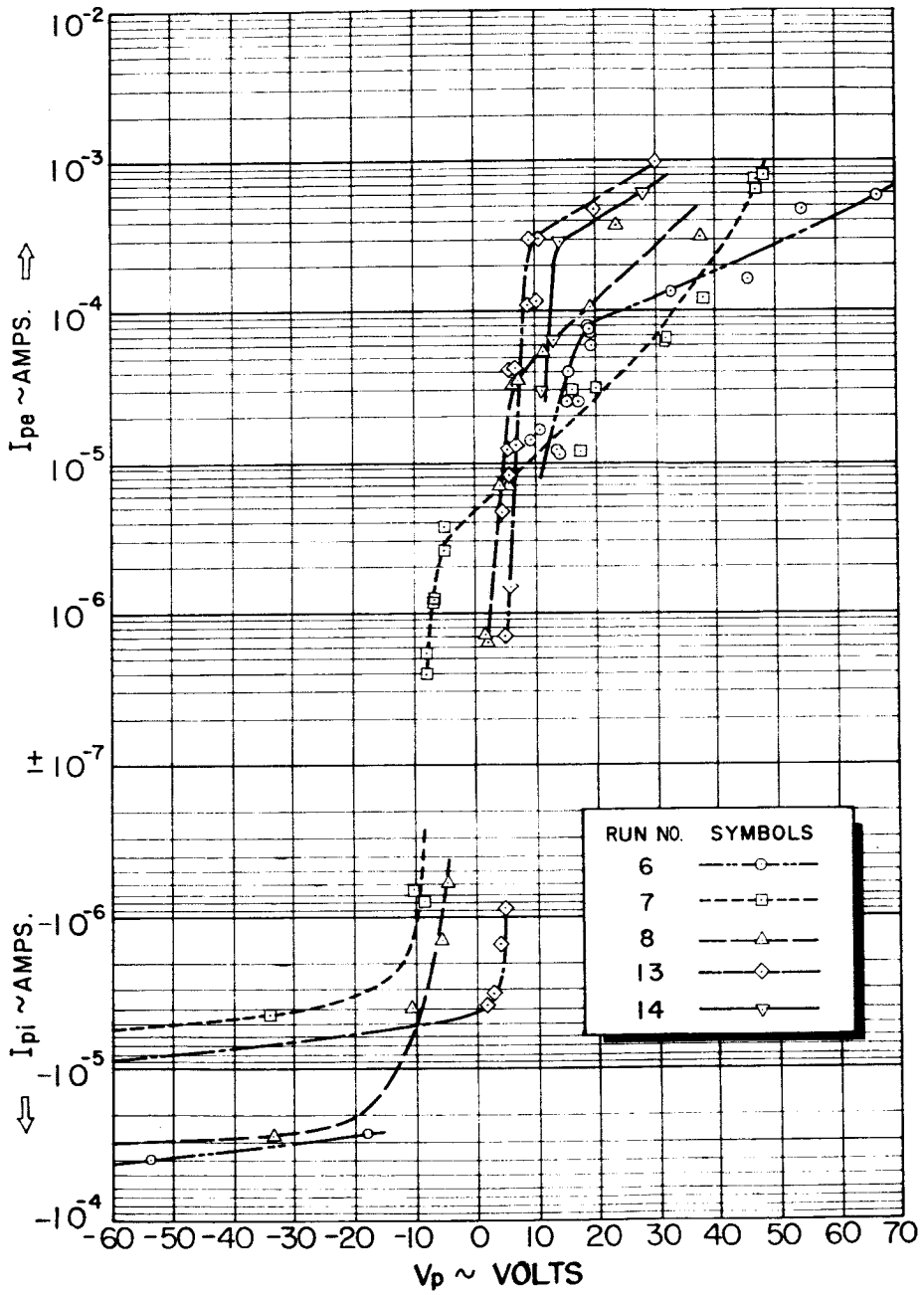

FIGURE 8. Experimental probe characteristics for runs 6, 7, 8, 13, and 14.

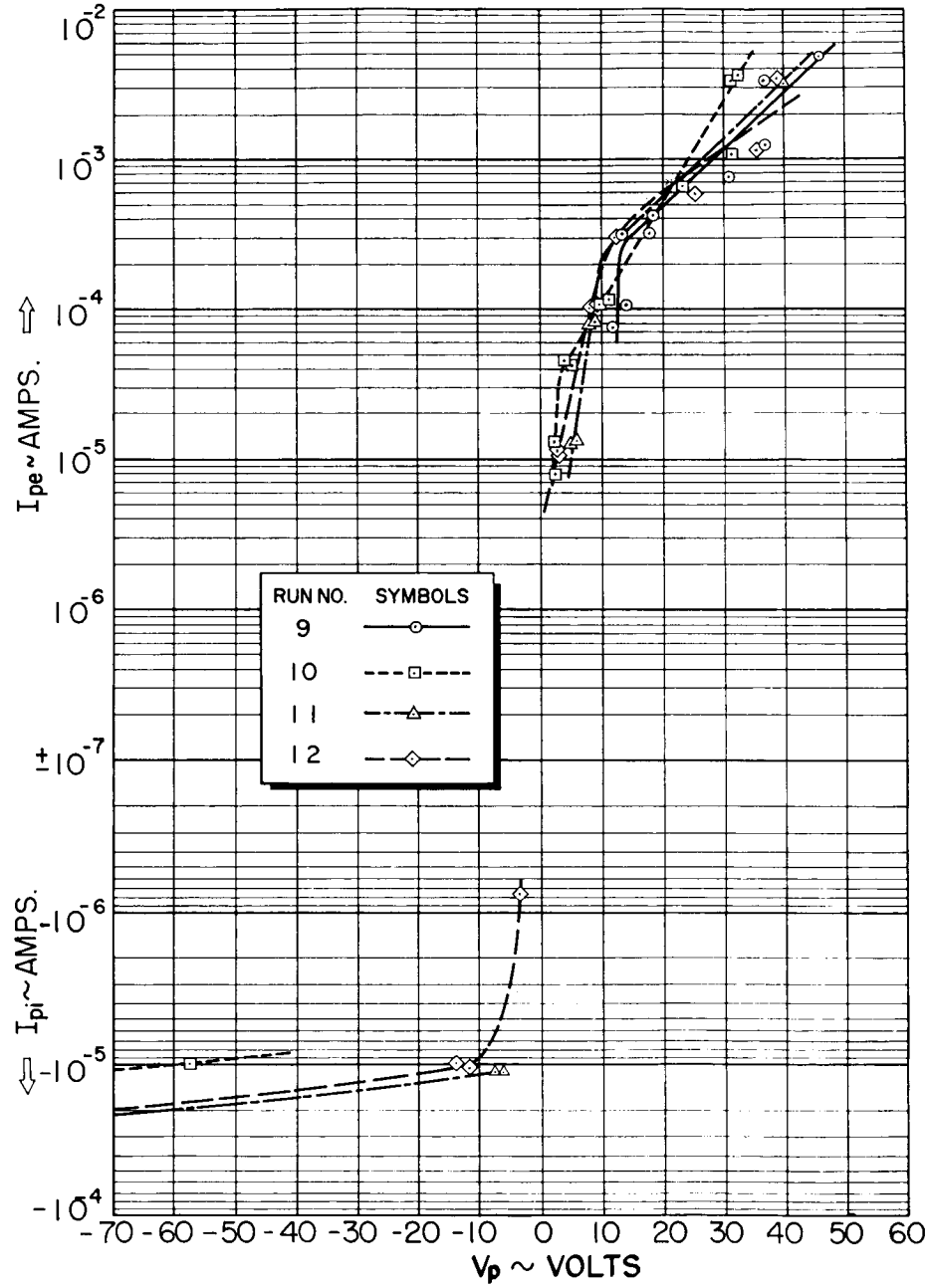

FIGURE 9. Experimental probe characteristics for runs 9 through 12.

field region in a number of the runs was primarily due to two factors: (1) random plasma fluctuations of such period and magnitude as to make reading the current on the more sensitive scales impossible, and (2) absorption of sufficient RF power by the ammeter to cause failure of the resistors shunting the 10 μa, and/or 100 μa scales.

Comparison of the experimental with the theoretical curves immediately suggests that in the region of electron collection electron production processes are sufficiently active over the entire electron-sheathed region so as to alter that section of the observed characteristic to such an extent that alignment with the theoretical curve is impossible. The retarding field region is always so steep that its alignment is too inaccurate in all cases. However, all measured slopes correspond to electron temperatures between 300°K and 75,000°K which was anticipated. Unfortunately in all except three cases the measured temperatures lie between 11,000°K and 75,000°K and therefore alignment should be made with the missing ion-collection sections of the non-equilibrium curves in order to determine electron number density with best accuracy, but for the experimental results this region is defined very inaccurately because of erratic ammeter performance in the corresponding current range.

In the absence of the preferred method, it appears that the next best thing to do is align the transition regions from the retarding field to the electron-sheathed condition. If this is done comparison with the theoretical curves yields number densities ranging from 5×10^7 (for run 7 where high pressure and low speed would produce a maximum amount of recombination before reaching the probe) to 4.4×10^9 (for run 14 where high speed and increased discharge power would be indicative of an increased degree of ionization at the probe).

Additional correlations between the experimental conditions and the electron densities measured by aligning the "knees" of the curves can be made. For example, it was noted in runs 1 and 2 that light emission from the plasma stream reached a peak in intensity in an annular region extending from about 0.35 inches to 0.7 inches from the centerline. To see if this was indicative of increased charge density, runs 10 and 11 were made. The probe measurements made in these two cases indicate that the charge density increases by a factor of about 2 in going from the centerline out to a point 0.55 inches away.

Good temperature correlation is also observed. In those cases where the neutral-particle number density is high and the speed is low, the electron temperature is lower by a factor of one-half to one-fifth compared to that in runs where the opposite conditions hold. For example, compare run 7 with run 12.

With respect to the pairs of comparison points verification of theory for the stationary plasma case is provided by pairs 1 and 2. Pairs 3 through 12 apparently all correspond to the $T_e \gg T_i$ case and should show little difference between the currents collected in the parallel and transverse orientations. This is what is observed in pairs 3 through 8 where the neutral-particle number density is apparently low enough for the probe to appear free-molecular with respect to electron-neutral and ion-neutral collisions. Points 9 through 12, however, show significant differences between the parallel and transverse values of the ion-sheathed current. This may be because the neutral particle number density is high enough to keep the probe from experimentally satisfying the theoretical free-molecular condition stated above. However, for these runs a wake was observed to extend downstream of the probe as much as 800 diameters. This may be indicative of a highly non-central force field which might or might not have a significant effect on current collection. The numerical values of T_e and n_0 obtained in the experiments are summarized in Table III.

TABLE III. EXPERIMENTAL RESULTS

Run number	T_e (°K)	n_0† (*ion-sheathed section*) (cm^{-3})	n_0 (*transition section*) (cm^{-3})
1	53,000	—	1.9×10^{10}
2	6,300	4.5×10^{9}	1.6×10^{9}
3	44,000	1.5×10^{10}	9.2×10^{8}
4	35,000	1.9×10^{10}	2.0×10^{8}
5	14,500	4.4×10^{10}	7.1×10^{8}
6	75,000	2.1×10^{10}	4.4×10^{9}
7	58,000	8.0×10^{9}	5.0×10^{7}
8	72,500	3.7×10^{10}	5.4×10^{8}
9	10,000	8.0×10^{10}	5.3×10^{9}
10	11,000	1.3×10^{10}	6.0×10^{8}
11	24,500	2.7×10^{10}	3.4×10^{9}
12	56,000	1.7×10^{10}	4.3×10^{9}
13	10,000	1.2×10^{10}	4.5×10^{9}
14	11,000	1.1×10^{10}	4.4×10^{9}

† The value of n_0 in this column is generally considered to be the less accurate of the pair.

CONCLUSION

The principal results of the experimental program can be summarized as follows:

1. Although the probe instrumentation system lacked sufficient sophistication to definitely establish the proposed theory and its limits of applicability, it did display all the qualitative behavior the theory predicts and was in good enough quantitative agreement to lead one to suspect the instrumentation rather than the theory.

2. The electrons, although in a noisy plasma with significant RF fields, high-concentration gradients, and complete lack of thermal equilibrium between species, still satisfy the Maxwell energy distribution.

3. At probe potentials more than just a few volts above (+) the floating potential the theory deviates significantly from reality due to secondary emission from the collector's surface.

4. The single probe is definitely a useful experimental tool for obtaining significant local values of the electron temperature and charge density in a flowing low-density plasma stream.

The experimental work to date has been very encouraging. However, additional studies of the cases when the plasma is in equilibrium and where $T_i > T_e$ must be made to complete the verification. Also the free-molecular condition should be better satisfied experimentally than it has been to date in order to avoid any ambiguity. This means operation at lower pressures and a more limited range of application or else a smaller collector and much more difficult fabrication problems. In any case further study appears justified.

REFERENCES

1. Smetana, F. O., "On the Current Collected by a Charged Circular Cylinder Immersed in a Two-Dimensional Rarefied, Plasma Stream", Third International Symposium on Rarefied Gas Dynamics, Paris, France, June, 1962.
2. Mott-Smith, H. M., and Langmuir, I., "The Theory of Collectors in Gaseous Discharges", *Phys. Rev.*, **28**, 727 (1926).
3. Langmuir, I., and Compton, K. T., "Electrical Discharges in Gases. Part II. Fundamental Phenomena in Electrical Discharges", *Revs. Mod. Phys.*, **3**, 191 (1931).

6. Robert Betchov and Eugene B. Turner: *Measurements of MHD Turbulence with Magnetic Probes*

Small magnetic probes have been used in this laboratory to make a systematic study of MHD turbulence in a linear pinch stabilized with an initial longitudinal magnetic field. The presence of MHD turbulence in such a device was first reported by Burkhardt and Lovberg (**1**) *of Los Alamos. The pinch is produced in a 5-inch I.D., 24-inch-long tube filled with deuterium gas by the discharge of an* 85-μf *capacitor bank charged to* 15 kv. *The stabilizing field is* 2000 *gauss and the gas pressure is typically* 80 μHg. *The small magnetic probes, with a frequency response up to* 50 Mc, *are inserted into the plasma through a slot in the cathode and are moved radially by traversing screws. The probe signals, which are proportional to* $\dot{B}$, *are integrated to give* B, *the magnetic field strength. Differentiating once gives* $\ddot{B}$ *which is a very sensitive measure of the onset and duration of the turbulence. A complete mapping of the pinch was done using the* $\ddot{B}$ *signal to find the onset of turbulence as a function of radius and time. The correlation between two probe signals has been obtained as a function of the probe separation using a technique employing an x-y oscilloscope. One probe signal is put into the horizontal amplifier and the other into the vertical amplifier. Many shots are required to obtain a relatively smooth pattern which has an elliptical shape with the major axis lying at* 45° *to the horizontal. The correlation is a function of the ratio of minor to major axis of an elliptical brightness contour.*

INTRODUCTION

The main impetus for this program was provided by the experimental work of Burkhardt and Lovberg (**1**) at Los Alamos. A report of their work was delivered at the Second United Nations Conference on the Peaceful Uses of Atomic Energy held in Geneva in September, 1958. They made extensive measurements with small magnetic probes on the magnetic fields in a linear pinch device, designated Columbus S-4. From these data, they were able to deduce the magnetic fields, currents, and plasma pressure distributions throughout the cylindrical tube as a function of time. The probe signals at a given point were reproducible up to a time

ED. NOTE: Mr. Betchov and Mr. Turner are at the Aerospace Corporation, El Segundo, California.

of 2.5 μsec after the start of the discharge current, but for later times the signals exhibited random fluctuations. Also, the conductivity of the plasma, calculated from the magnetic probe data, was found to drop sharply at 2.5 μsec. Using the published data of Burkhardt and Lovberg, Kovásznay (**2**) developed an elementary theory of magnetohydrodynamic turbulence applicable for this case and was able to explain the apparent decrease in the electrical conductivity of the plasma. What happens, essentially, is that energy is fed into plasma turbulence by the large electrical currents in the plasma, and this energy, in turn, is dissipated in the plasma by joule heating. With the additional energy dissipation, the plasma appears to have a higher electrical resistivity.

The work of Burkhardt and Lovberg was performed primarily with single probes, although some qualitative correlation was done by mounting four magnetic probes 15 mm apart in a quartz tube. Similarity was noted in the signals of adjacent probes, indicating a degree of correlation.

It was recognized in this laboratory that the experimental study of magnetohydrodynamic turbulence would be very important to plasma physics and magnetohydrodynamics. Except for the work of Burkhardt and Lovberg, there had been no experimental work in this field. It was therefore decided to build a linear pinch apparatus, similar to Columbus S-4, and to make quantitative studies of plasma turbulence in a systematic manner. The experimental work described in this paper was carried out during the period of January, 1961, to March, 1963.

DESCRIPTION OF THE APPARATUS

A schematic diagram of the linear pinch device is shown in Figure 1. The discharge tube is a Pyrex glass or Mullite† tube with an internal diameter of 5 inches. At the two ends are flat-faced electrodes of stainless steel which fill the entire cross section. The discharge path is 24 inches long. The current enters the tube at the bottom electrode, the anode, flows through the gas to the top electrode, the cathode, and returns to the capacitor bank through a copper screen which fits tightly around the discharge tube. This provides a coaxial return conductor of minimum inductance.

Surrounding the discharge tube is a solenoid which is used to produce a longitudinal magnetic field of up to 4000 gauss. A field strength of 2000 gauss was used for most of the experiments. This longitudinal magnetic field produces a so-called "stabilized pinch". The current through the solenoid is supplied by a 400-μf, 4-kv capacitor bank. After triggering an ignitron switch the current rises sinusoidally to a maximum value in about 400 μsec at which time the main discharge is fired. In this relatively long time of 400 μsec the magnetic field penetrates the copper screen and fills the discharge tube. For the short time duration (about 12 μsec) of the main discharge, however, the thickness of the copper screen is greater than the skin depth, and the fields are trapped inside.

The main capacitor bank consists of six low-inductance capacitors rated at 14.1 μf each and 20 kv. Each capacitor is connected to an ignitron tube which, in turn, is connected to a bus leading to the anode. The capacitor bank is discharged through the pinch tube by triggering the six ignitrons simultaneously. By using coaxial mounts for the ignitrons and parallel-plate transmission lines for the other connections, the total parasitic inductance of the discharge circuit, including ignitron switches, was only 0.033 μh. The General Electric type 7171 ignitrons which were used are rated at 10 kv, but can be operated very reliably at 15 kv by heating the anode region of the tubes with infrared lamps.

† Mullite is a high temperature porcelain ceramic.

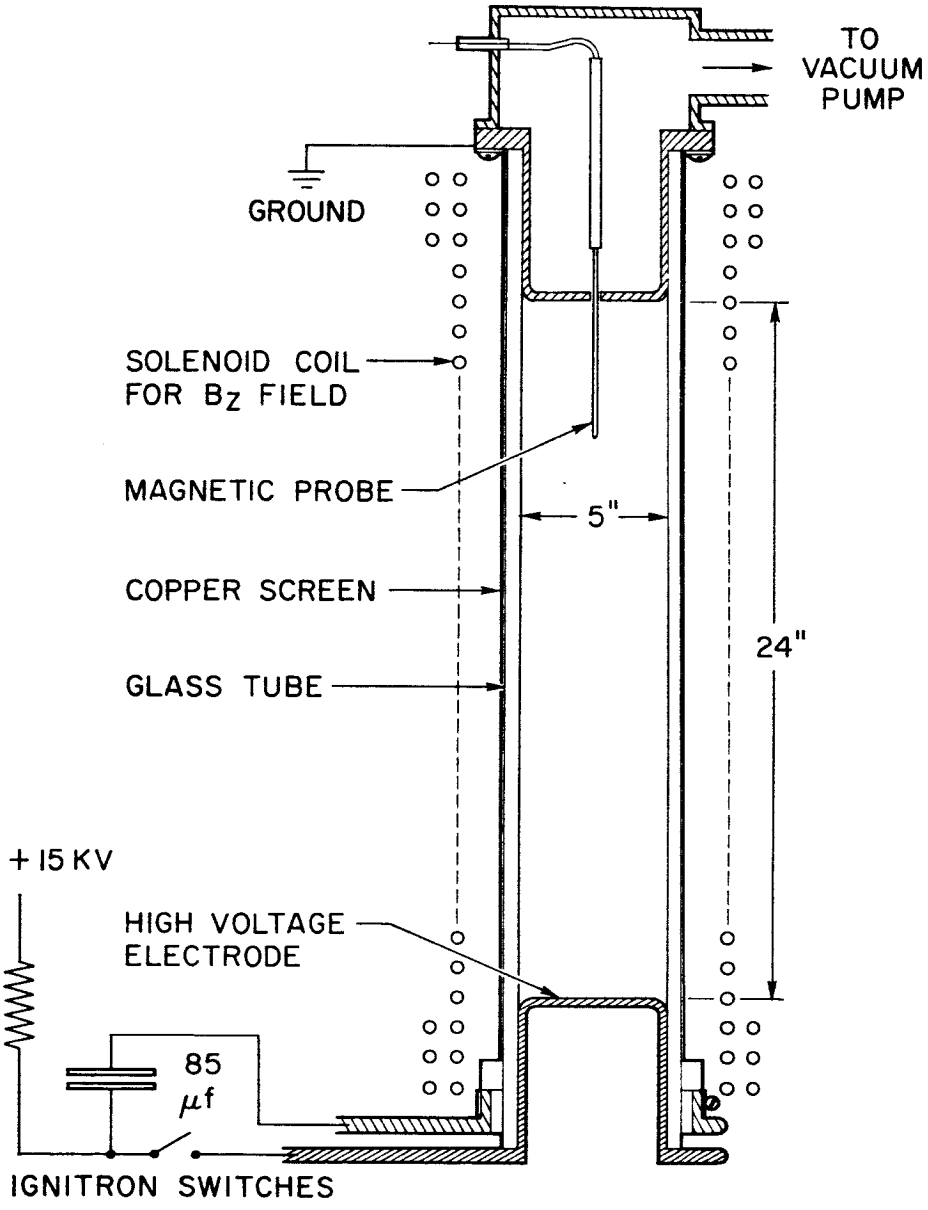

FIGURE 1. Schematic diagram of the linear pinch device.

The magnetic probes, described in the next section, protrude into the plasma through a diametrical slot in the upper electrode which is at ground potential. Two traversing screws are used to move the probes in a radial direction. One of the probes can also be moved up and down or rotated through 360° by a gear train located above the cathode. The discharge tube is evacuated with an MCF–60, 2-inch diffusion pump which gives an ultimate vacuum of 2×10^{-6} mm Hg. Deuterium gas can be continuously fed into the discharge at the bottom through a

hot palladium thimble which passes only hydrogen or deuterium gas. At the same time the tube is pumped out at the top through a small valve which can be adjusted to give the desired pressure in the tube. The gas pressure is measured continuously with a Pirani type vacuum gauge calibrated for deuterium.

The apparatus is equipped with a pneumatically-operated vacuum valve and relay meters on the power supplies which automatically shut off when the proper voltage is reached. Remote reading meters and controls are installed in the screen room. These make it possible to fire the device every 2 minutes. Such speed is important since it is often necessary to fire a series of 24 shots or more to obtain sufficient data for a statistical analysis of the turbulence.

MAGNETIC PROBES

The use of small magnetic probes for the measurement of transient magnetic fields inside a plasma discharge was first reported by Russian physicists studying the pinch effect (**3**). Magnetic probes provide much valuable data about the plasma discharge. From a knowledge of the magnetic fields inside the plasma as a function of position and time, it is possible to determine the electrical current distribution and the gas pressure in the plasma. A description of the magnetic probes used at the Los Alamos Scientific Laboratories, together with some of the early results, was reported by Karr (**4**). The design of our first magnetic probes was copied from the description given by Karr.

The first magnetic probes consisted of small coils with 24 turns of no. 40 formvar covered wire wound in three layers of 8 turns each on a 0.030-inch diameter core. The leads from the coil were twisted and soldered to a miniature coaxial cable connector at the other end of the probe. The probe coil and twisted leads were enclosed in a non-magnetic stainless steel tube which was thinned to a 4-mil wall near the coil and slotted at 90° intervals. The probes were designed to extend 4 inches into the plasma, so the last 6 inches of the probe were enclosed in a 2-mm I.D., 3-mm O.D. fused quartz tube for electrical insulation. The total length of the probe was 12 inches. Probes were made with the coil axis both longitudinal and transverse so that all three components of the magnetic field could be measured.

Although this first type of probe appeared to give satisfactory results, we endeavored to develop a technique to measure the probe sensitivity as a function of frequency. After much difficulty a method was finally devised which gave accurate values of the probe sensitivity over the frequency range of 1–50 Mc using conventional electronic equipment. A Tektronix 190A signal generator, which has a sine wave output of 10 volts peak to peak into a 50 ohm load, was used to feed current into a small Helmholtz coil. The two individual coils had a radius of 2 cm and a spacing of 2 cm. The Helmholtz coil produces at the center a very homogeneous magnetic field which can be accurately calculated. A series of four coils with 10 turns, 4 turns, 2 turns, and 1 turn were required to adequately cover the frequency range. The maximum frequency at which a particular Helmholtz coil can be used should be less than approximately $\frac{1}{4}$ the resonant frequency of the coil so that the current in the coil is close to the measured current. The minimum frequency is determined by the point at which the coil begins to load the oscillator. The current input to the Helmholtz coil was measured with a Tektronix current probe and oscilloscope which had been calibrated at frequencies of up to 50 Mc.

The magnetic probe was properly positioned in the center of the Helmholtz coil, and the output was measured with a Boonton RF voltmeter. It was necessary to put the RF voltmeter in a screen room with the oscillator outside to reduce pickup. The output voltages from the probes were only a few millivolts. With the

probe outside the Helmholtz coil, no signal was observed. An example of probe sensitivity as a function of frequency determined by this technique is shown in Figure 2.

These measurements showed that the sensitivity of the first magnetic probes fell off badly above 10–15 Mc. For this study of MHD turbulence, however, it was desirable to have a frequency response that was fairly flat out to 40 Mc or more. Therefore, in order to design better probes, it became necessary to investigate the factors affecting the frequency response. At approximately this point in our research, a paper by Segre and Allen (5) was brought to our attention. This paper discusses the factors affecting the frequency response of magnetic probes. The

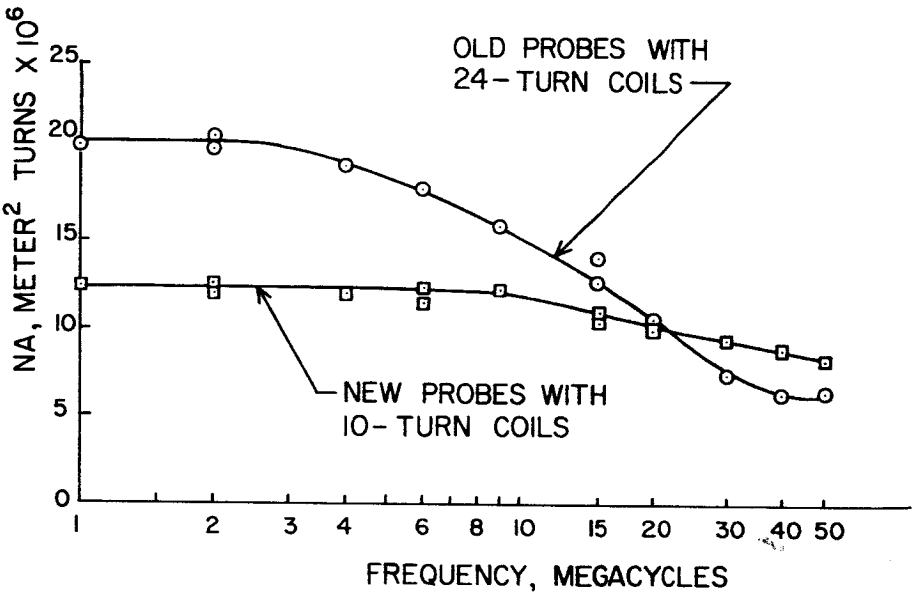

FIGURE 2. Probe sensitivity curves.

major factor causing the falloff of sensitivity at high frequencies in the first probes was the relatively high inductance of the probe coils. When ωL becomes comparable with the characteristic impedance of the coax line (50 ohms in our case), the probe signal is partially integrated; this produces a phase shift and a reduction in signal. The inductance was calculated to be 0.4 μh so $\omega L = 50$ ohms at 20 Mc. It was also found that the fairly thick stainless steel wall (4 mil) surrounding the coil for electrostatic shielding, attenuated the signal at higher frequencies—especially for the probes with transverse coil orientations.

New magnetic probes were designed to provide, among other improvements, good frequency response up to 50 Mc. The number of turns in the coil was reduced to 10—2 layers of 5 turns each on a 0.042-mil diameter core. The calculated coil inductance was thereby reduced to 0.12 μh. The coil leads were connected directly to a small coaxial cable instead of twisted leads. By placing the probe coil at the end of the coaxial cable, it was possible to push the coil into quartz tubing bent into various shapes as shown in Figure 3. The L and hook probe shapes were designed for some of the correlation studies. The coils were electrostatically shielded with 1 mil strips of nichrome, but we doubt that any shielding at all is required as the probes have a quite low impedance. Frequency calibrations of the new probes, such as shown in Figure 2, confirmed that the frequency response was satisfactory up to 50 Mc.

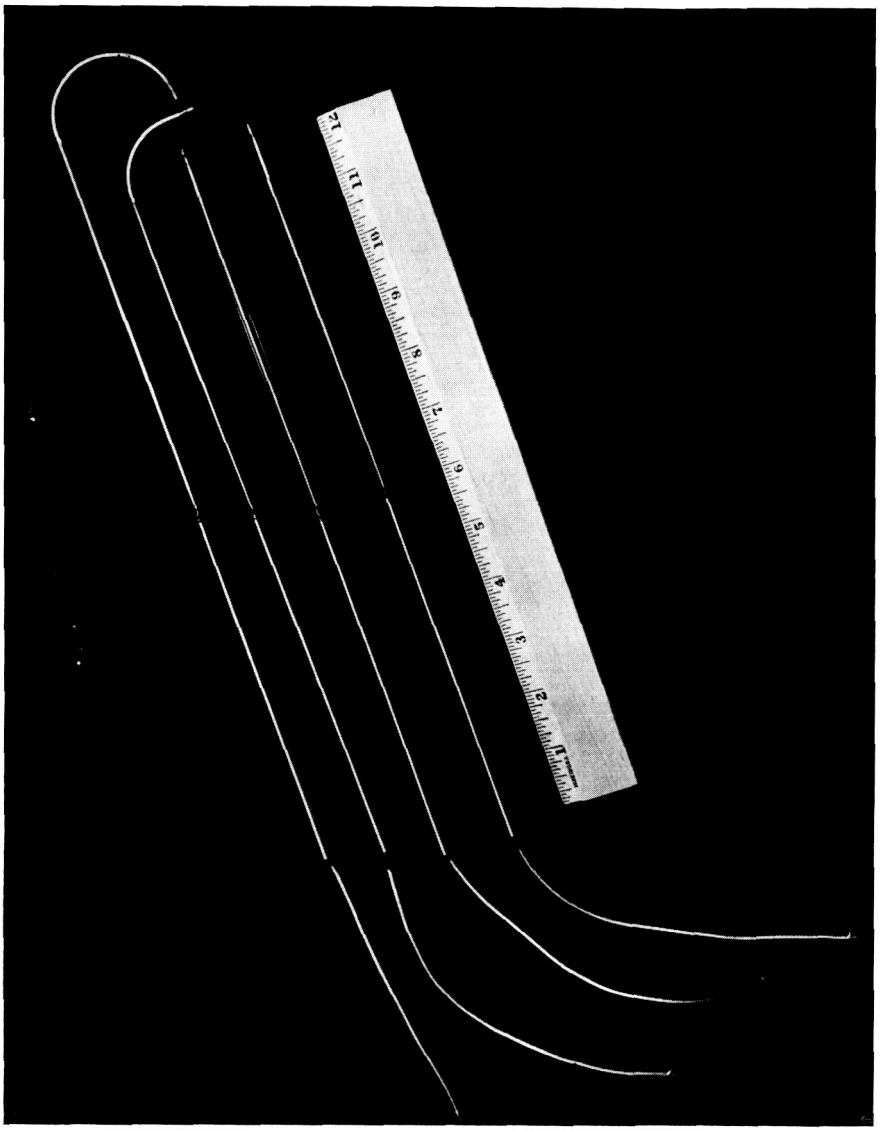

FIGURE 3. Photograph of new magnetic probes.

The magnetic probe signal is $V = NA\dot{B}$ where $\dot{B} = dB/dt$, N is the number of turns in the coil and A is effective coil area. For the new probes, the value of NA was about 1.2×10^{-5} square meter turns. The maximum signal strengths from these probes was often greater than 100 volts. The so-called "ground potential" was found to vary during a shot by 50 volts from the upper manifold, which is bolted to the cathode, to the ground side of the capacitor bank. To avoid spurious signals on the probes, it was necessary to connect a wide sheet-aluminum ground strap from the screen room to the upper manifold where the probes were located. The coaxial cables carrying the probe signals were then laid on the ground sheet.

To obtain signals proportional to the magnetic field, R-C passive integrators

were used. Initially, a 500-ohm resistor and five 0.02-μf ceramic capacitors connected in parallel were used to give an R-C time constant of 50 μsec. The capacitors were found to have an L-C resonance at 22 Mc, so they were replaced with five 0.001-μf capacitors with a 10K resistor. The latter were found to be satisfactory up to 50 Mc. The passive integrating circuit and the terminating resistor were mounted together in a brass cylinder. The terminating resistance consisted of five resistors in parallel soldered radially from the central conductor to the shell. The 10K-resistor was then mounted on axis followed by the five capacitors soldered radially to the shell. This arrangement minimized parasitic inductance and thus increased the frequency response of the circuit.

PLASMA CHARACTERISTICS

The theory of the linear pinch is given in several books on thermonuclear research (**6, 7**) and will not be described here. We would like to give only a qualitative description of the operation of this device, together with some experimental observations, in order to better understand the signals produced by the magnetic probes. When the ignitrons are triggered, the capacitor bank discharges through the gas in the tube. Under the usual conditions of 15-kv potential on the capacitor bank and a 2000-gauss initial longitudinal magnetic field, the duration of the first half-cycle is about 12 μsec and the peak value of the current is about 250,000 amperes. A typical pair of voltage and current traces is shown in Figure 4.

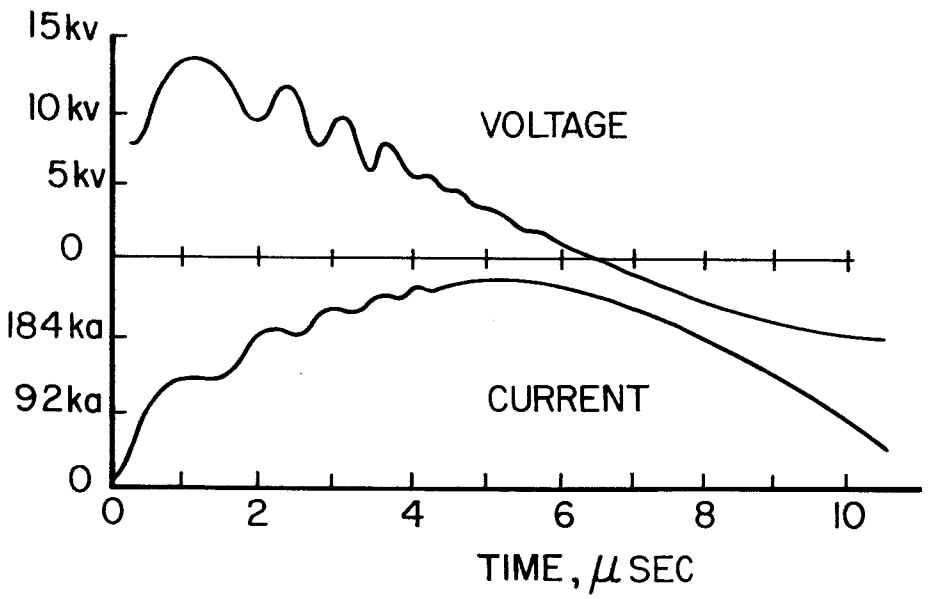

FIGURE 4. Current and voltage in the pinch device. Initial conditions: 15 kv, 2000 gauss B_z and 80 μHg of deuterium.

Initially, the current begins to flow in the gas closely following the walls of the tube. Soon, however, the magnetic pressure associated with the current in the gas pulls the plasma off the wall, and the plasma column begins to rapidly implode toward the center. The longitudinal magnetic field is trapped inside and compressed as the column contracts since the plasma is highly conducting. The change in the diameter of the plasma column with time is shown in Figure 5. This was

calculated from probe measurements of the longitudinal magnetic field. A similar sort of time variation of the radius was also observed with a rotating-mirror streak camera. One sees that the radius of the plasma column oscillates with a frequency increasing from 1 to 2 Mc until about 4 μsec. This oscillation also shows up in the voltage and current traces (see Figure 4). The increase of inductance associated with a decrease in radius causes a decrease in current and an increase in the voltage across the discharge tube. The oscillation of the plasma column also shows up in the magnetic probe signals.

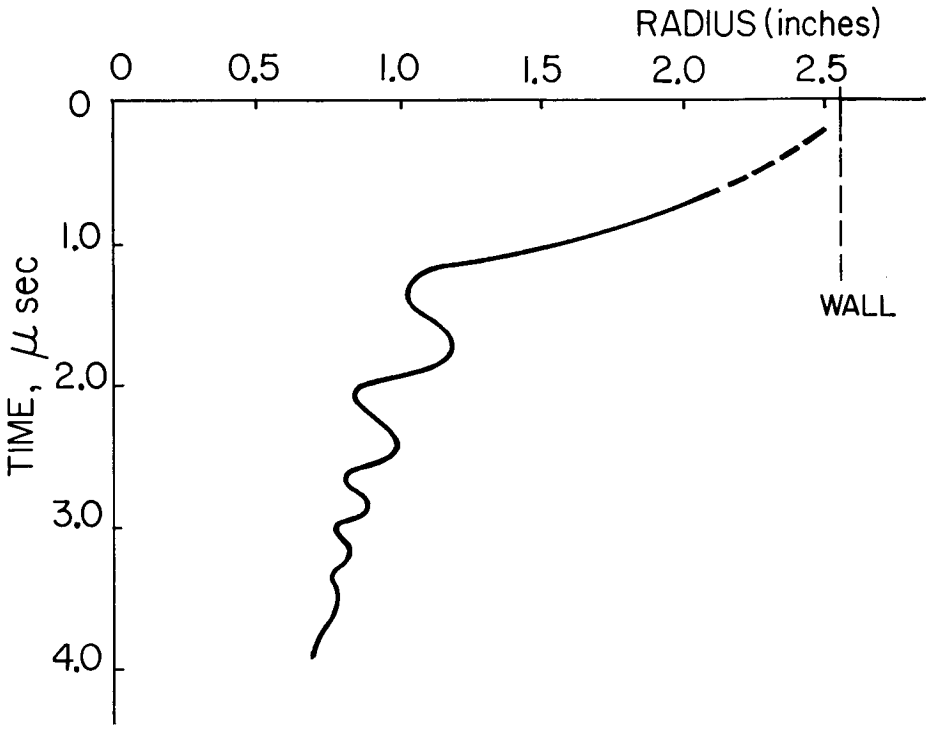

FIGURE 5. Radius of plasma column.

Under the assumption that the current flows in an infinitely thin layer along the surface of a perfectly-conducting plasma, the longitudinal magnetic field can theoretically completely stabilize the plasma column. Due to the finite conductivity of the plasma, however, the magnetic fields can diffuse through the plasma. We surmise that the MHD turbulence observed in the plasma column accelerates this diffusion process. The longitudinal magnetic field trapped inside the plasma column diffuses outwardly, and the azimuthal magnetic field outside the plasma column, which is due to the current through the gas, diffuses inwardly. The mixing of the two fields results in a net helical field which, in turn, results in a helical instability of the plasma column. The behavior of the plasma column with time is shown by the series of Kerr-cell camera photographs in Figure 6. The column appears to be fairly stable until 5 μsec when the helical distortion begins to appear. This helix expands rapidly and the plasma hits the walls after 7 μsec or so. Any magnetic probe measurements which we wish to make on the "stable" plasma column are meaningless after 5 μsec. An "unstabilized" pinch column, produced without the

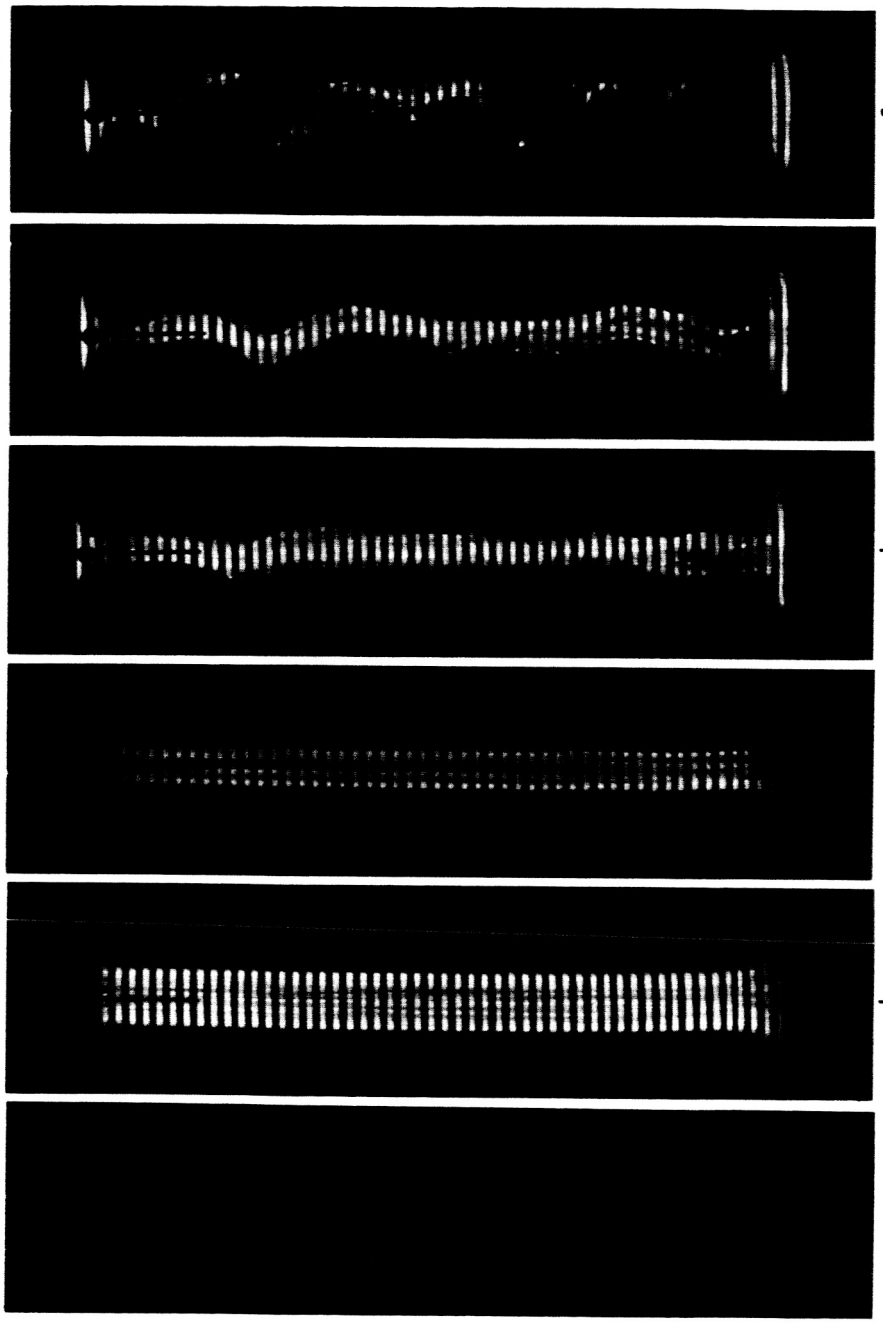

FIGURE 6. Series of Kerr-Cell photographs of a B_z-stabilized pinch. Initial conditions: 15 kv, 2000 gauss B_z, 500 μHg of deuterium. Delay times: (a) 1.5 μsec, (b) 2.0 μsec, (c) 2.5 μsec, (d) 5.0 μsec, (e) 6.0 μsec, (f) 7.0 μsec.

initial longitudinal magnetic field, reaches a smaller minimum diameter and breaks up somewhat sooner due to other instabilities which are inhibited by the trapped longitudinal field in the "stabilized" case.

MAGNETIC PROBE MEASUREMENTS

Two magnetic probes were mounted in the upper manifold and extended into the plasma a distance of about 4 inches through a diametrical slot in the cathode. The probes could be moved radially by means of traversing screws. In addition, one probe could be moved up and down or rotated with an external gear train. Surveys were made with single probes aligned to measure B_z, B_r, and B_θ. Also, pairs of probes were used to measure correlation as a function of probe spacing.

Figure 7 shows oscilloscope traces obtained with B_z and B_θ probes inside the plasma column. The upper trace is the direct probe signal proportional to $\dot{B}$, while the lower trace is the integrated probe signal, proportional to B. Four oscilloscope

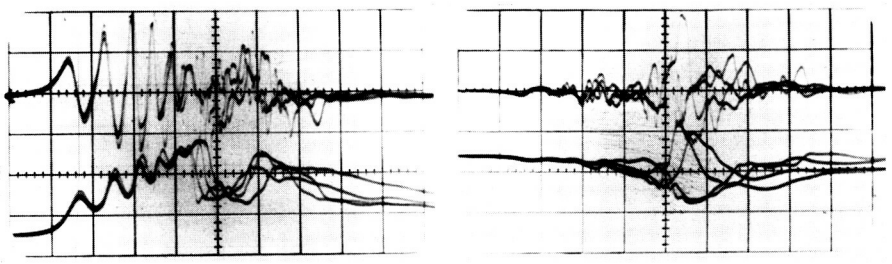

FIGURE 7. Four superimposed oscilloscope traces of magnetic probe signals in the plasma column. Upper traces are B and lower traces are $\dot{B}$. B_z-signals are on the left and B_θ traces are on the right. Sweep speed is 1 μsec per division.

pictures have been superimposed to show the fluctuations in the magnetic field from one shot to the next. The fluctuations, which start at about 2.5 μsec, show up much better in the direct probe signals than in the integrated signals since integration suppresses the higher frequencies. These fluctuations have been interpreted as evidence of MHD turbulence. The B_z signal shows the compression and oscillation of the B_z field trapped inside the plasma column. The fluctuations in B_z are somewhat smaller than the periodic changes in B_z due to these oscillations. The B_θ signal should, of course, be zero as long as all the current is flowing on the outside of the plasma column. The small fluctuations in B_θ are evidence of local currents inside the column. After 5 μsec or so, the plasma column becomes unstable, and the probe traces show large excursions.

The best indication of the onset of plasma turbulence is the second time derivative of the magnetic field. This is easily obtained by differentiating the direct probe signal. The type of signal obtained is shown in Figure 8. Using the second derivative, we have mapped the onset and duration of MHD turbulence as a function of radius and time. It was found that the turbulence apparently starts on the surface of the plasma column and spreads rapidly both inwardly and outwardly as shown in the diagram of Figure 9. Although the region outside the plasma column is not luminous, there is apparently a tenuous plasma left behind which supports the turbulence. It has been found by other investigators that there are

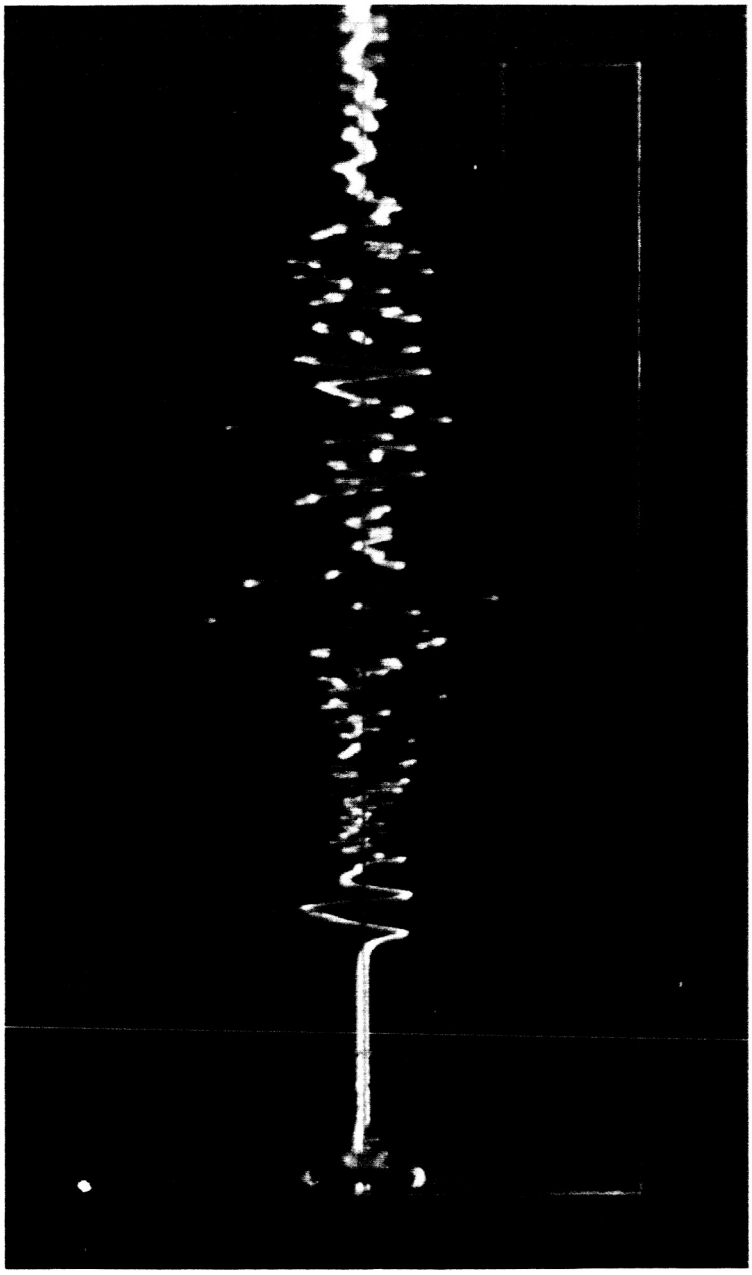

FIGURE 8. Differentiated probe signal, proportional to $\dot{B}$. Sweep speed is 1 μsec per division.

currents in the region between the main plasma column and the wall (**4**), and substantial currents near the wall have been found to move in a direction opposite to the main current. Kovásznay (**2**) has shown that MHD turbulence results in an increase of the effective resistivity of the plasma. This, in turn, results in more rapid diffusion of the magnetic field through the plasma and is probably responsible for the relatively fast breakup of the so-called "stabilized" plasma.

One of the most powerful techniques used in the experimental study of turbulence is the measurement of the correlation between signals from two measuring probes as a function of the distance between the probes. For the short time duration and rather high frequency of the turbulence, the best method of correlation determination appeared to be the use of an x-y oscilloscope. This method is described by Barber (**8**) and has been used by several investigators, for example, A. Favre *et al.* (**9**), for studies of turbulence. The signal from one probe is put on the horizontal

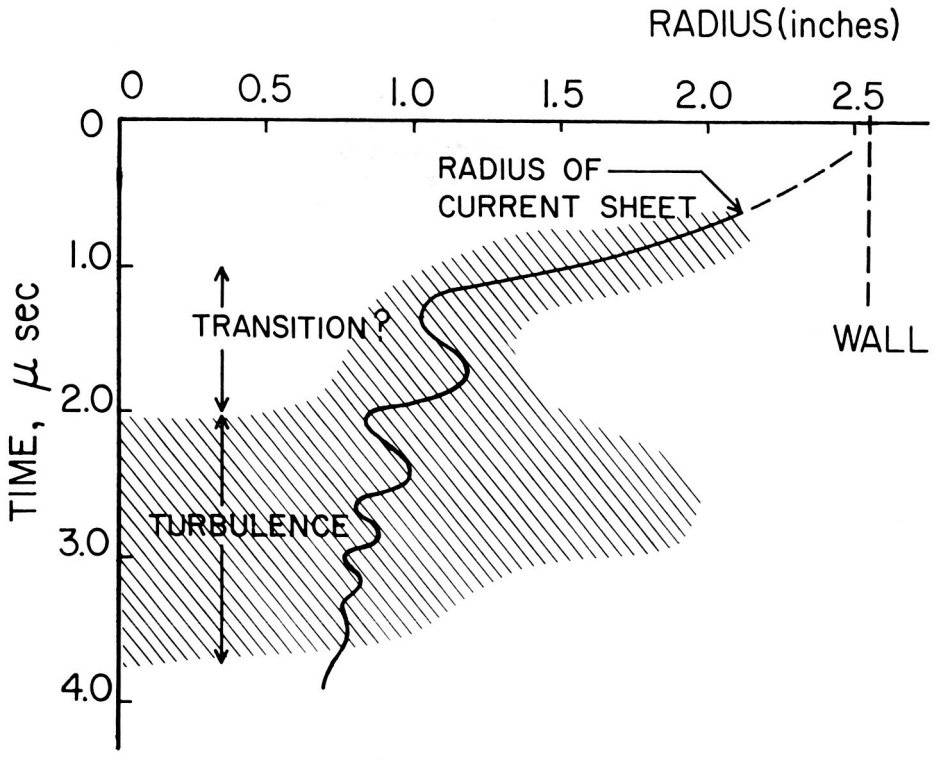

FIGURE 9. Space-time diagram showing spread of turbulence.

amplifier, and the signal from the other probe is put on the vertical amplifier. For normal distributions, the brightness contours are generally elliptical with the major axis of the elliptical contours lying at 45° to the horizontal if the rms values of the two signals are equal. The degree of correlation can be determined from the shape of the ellipses. For zero correlation the contours are circular, and for a correlation close to unity the ellipses are very thin.

Calibration patterns can be obtained by the use of two noise generators with mixing circuits. Let the signal from one noise generator be $f(t)$ and the signal from the other be $g(t)$. The rms outputs are adjusted to be equal so

$$\overline{f^2(t)} = \overline{g^2(t)}$$

Since the two signals are independent

$$\overline{f(t)g(t)} = 0$$

Now with mixing circuits form two new signals, $F(t)$ and $G(t)$ such that

$$F(t) = f(t) + ag(t)$$

and

$$G(t) = f(t) - ag(t)$$

The factor a can vary between zero and unity, and represents the fractional output of a variable attenuator on the second noise generator. The correlation, R, between the two new signals is

$$R = \frac{\overline{F(t)G(t)}}{\sqrt{\overline{F^2(t)}\,\overline{G^2(t)}}}$$

Substituting for $F(t)$ and $G(t)$ one finds

$$R = \frac{1-a^2}{1+a^2}$$

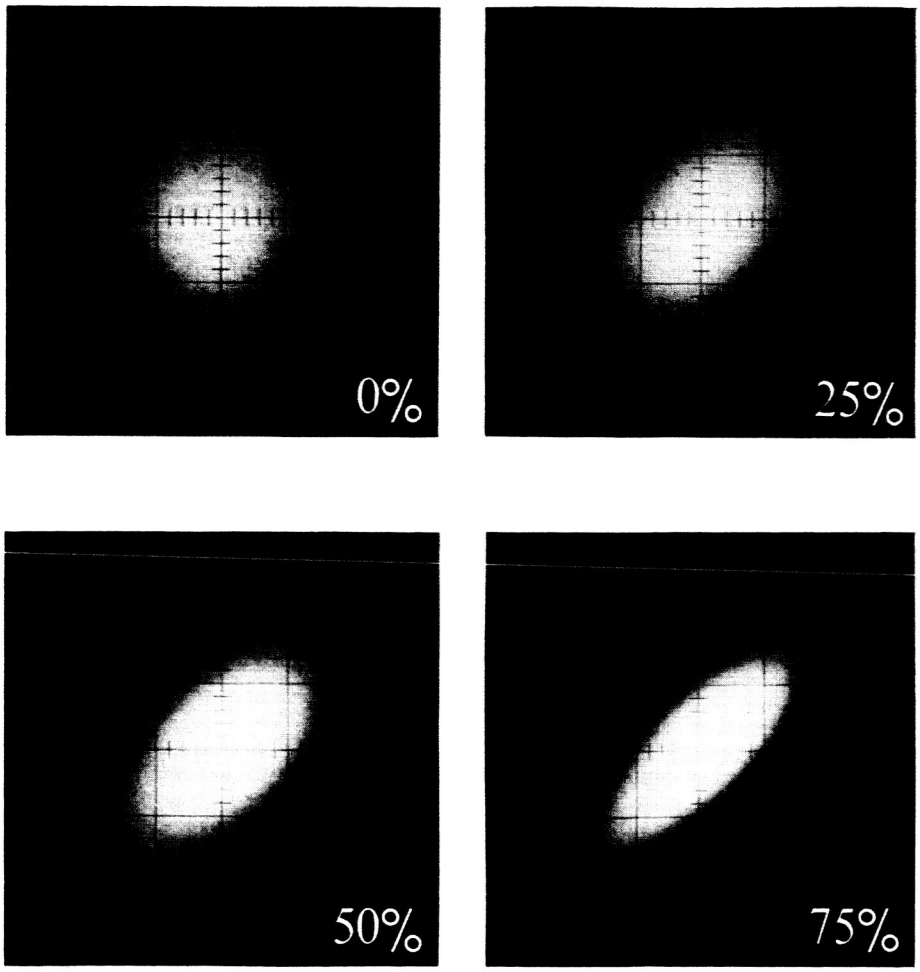

FIGURE 10. Four x-y oscilloscope calibration patterns obtained using noise generators; degrees of correlation noted in lower right-hand corner.

Thus, any value of R from zero to unity can be obtained by varying the factor a between unity and zero. A series of x-y oscilloscope patterns obtained in this manner are shown in Figure 10. To obtain reasonably smooth x-y correlation patterns of magnetic probe signals, traces from a large number of shots (usually 24) must be superimposed. A 65-volt positive gate signal is applied to the unblanking terminal of the x-y oscilloscope during the period of time that the plasma exhibits MHD turbulence. This starts at about 2.5 μsec and stops at 5.5 μsec when the plasma column begins breaking up because of helical instability. Thus the x-y trace is recorded only during the period of MHD turbulence. High-pass filters are used to eliminate any effect due to the gross motions of the plasma column (particularly the "breathing" mode which has a frequency of 1–2 Mc). So far, x-y correlation patterns have been obtained from two B_z probes with varying diametrical and longitudinal separations. A series of four such x-y oscilloscope pictures using B_z probes with a diametrical separation are shown in Figure 11. The probes were placed equal distances from the tube axis and on opposite sides

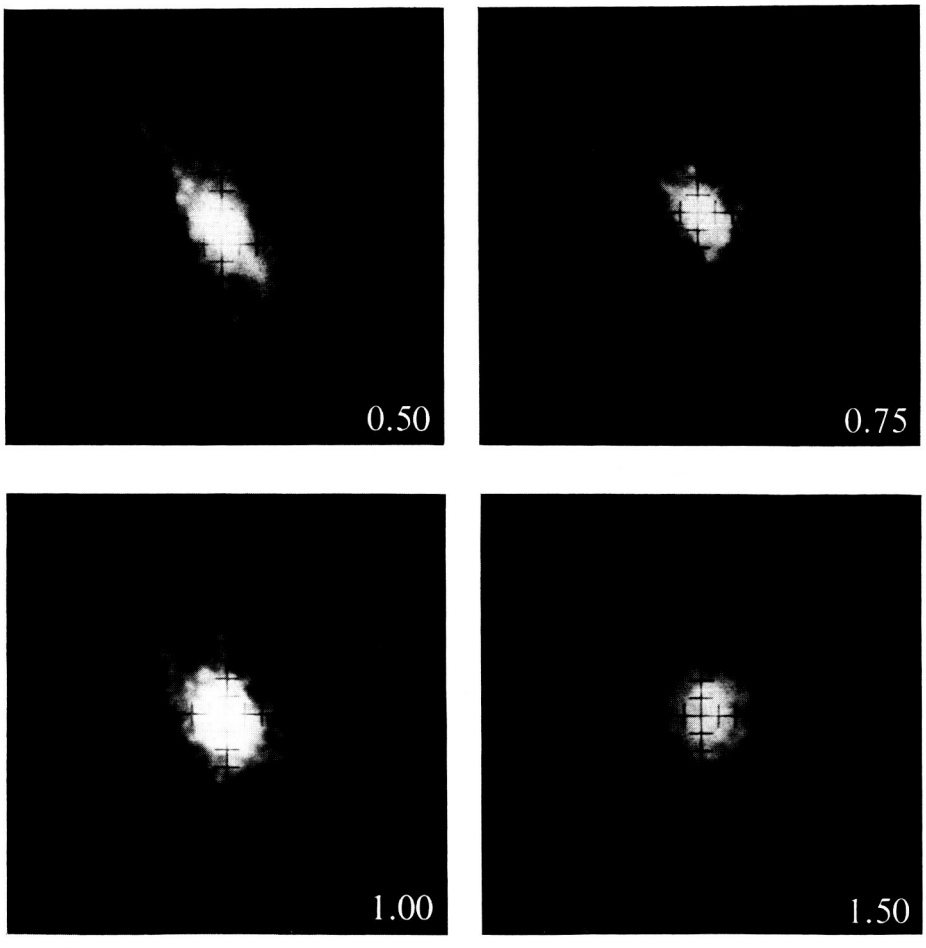

FIGURE 11. Four x-y oscilloscope patterns of B_z turbulence; diametrical probe separations, noted in lower right-hand corner, are in inches.

of it. At a spacing of 0.5 inches, the correlation is very high (estimated at about 0.9); at 0.75 inches, the correlation falls to about 0.7; and at 1.00 inches, it is less than 0.5. Almost no correlation exists at a spacing of 1.5 inches.

In principle, it is possible to obtain the energy spectrum $E(k)$ of the turbulence as a function of a wave number, k, by taking a Fourier transform of the correlation function. To get a reasonably good curve for $E(k)$, however, many more points should be obtained for correlation versus separation, and the correlation must be obtained by a more accurate method than visual estimation.

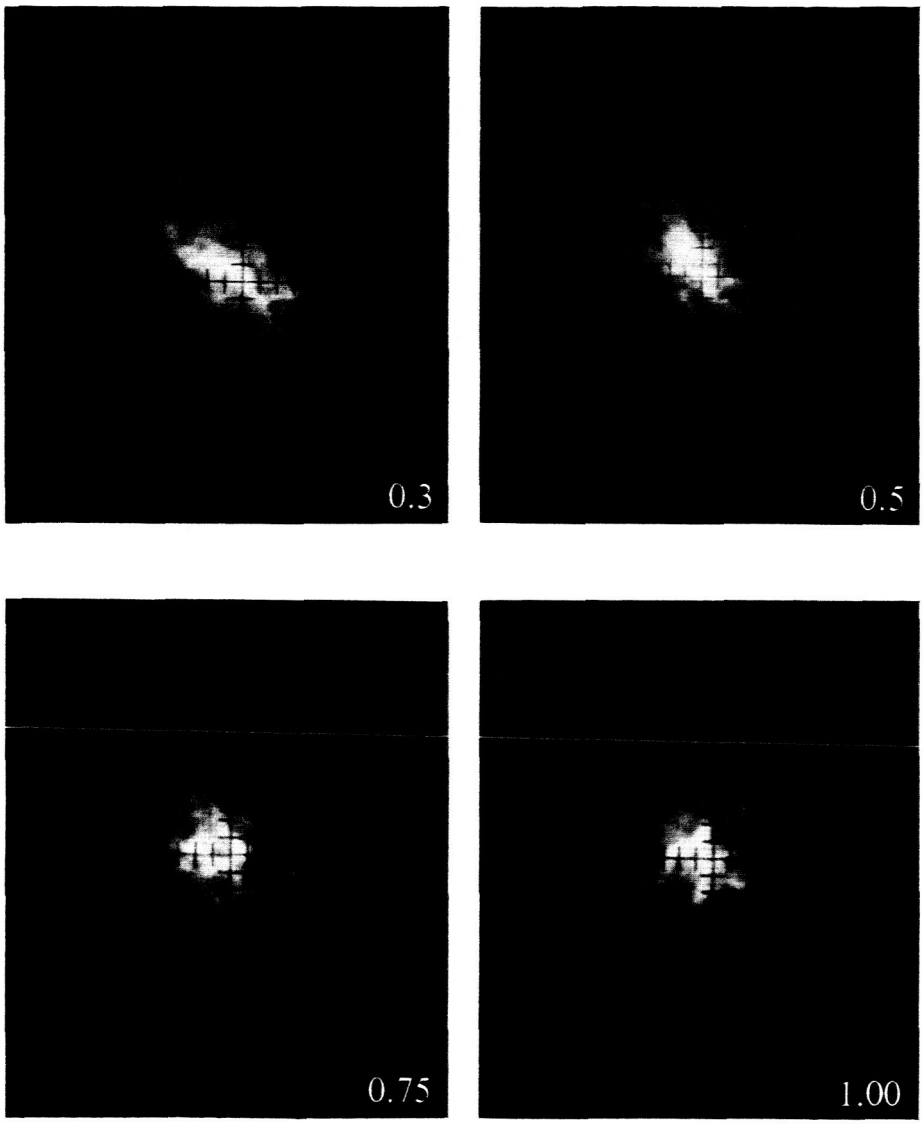

FIGURE 12. Four x-y oscilloscope patterns of B_z turbulence; longitudinal probe separations, noted in lower right-hand corner, are in inches.

Correlation patterns obtained with a z-separation† of B_z probes were especially interesting. A hook probe and a straight probe were used with the straight probe being raised and lowered with a rack and pinion gear. The x-y oscilloscope patterns were unusually elliptical in shape as seen in Figure 12. Oscilloscope patterns obtained for single shots, which were a little too light for good photographic reproduction, showed elliptical paths which appeared to be sections of Lissajous figures. This suggested that the turbulent magnetic field fluctuations were being propagated in the z direction with a definite velocity. An obvious explanation is that Alfvén waves are being propagated along the B_z magnetic field lines which are trapped inside the plasma column. The velocity of an Alfvén wave is

$$v_A = \frac{B}{\sqrt{\mu_0 \rho}}$$

in mks units. The Alfvén wave velocity was calculated from the measured value of B and the value of ρ there would be assuming all the gas is swept into the central plasma column. This velocity calculated using this assumption was only one-half the velocity determined from the Lissajous patterns, however. One must therefore consider the possibility that much of the gas is left behind as the current sheath pinches inwardly.

It was found that the presence of one probe reduces the signal picked up by a second probe. The region of influence is elongated in the direction of the B_z magnetic field lines. The range of influence in the direction perpendicular to the magnetic field lines was smaller than 0.5 cm, but in the direction of the field lines the range of influence was found to be several centimeters. This is undoubtedly due to the propagation of Alfvén waves along the field lines. In view of this, the probes should have been inserted deeper into the plasma since the cathode must influence the turbulence for a considerable distance. Also, much care must be taken so that one probe does not lie directly above another, i.e., on the same B_z field lines. Therefore it may have been better to have inserted the probes radially through the tube walls rather than through the cathode as we have done.

Estimates were made of the rms values of B, $\dot{B}$, and $\ddot{B}$ by comparing these signals with oscilloscope pictures of noise-generator signals whose rms values were measured with a meter. The magnitude of the fluctuations in the three perpendicular directions were equal within a factor of two. The estimated magnitudes were:

$$(\Delta B)_{\text{rms}} = 200 \text{ gauss}$$
$$(\Delta \dot{B})_{\text{rms}} = 5 \times 10^9 \text{ gauss/sec}$$
$$(\Delta \ddot{B})_{\text{rms}} = 1.5 \times 10^{17} \text{ gauss/sec}^2$$

These values are probably accurate only to $\pm 50\%$ since they are visual comparisons. For reference, the value of B_z when the plasma column is constricted is about 16,000 gauss.

It is useful to form the following nondimensional quantity:

$$\frac{(\Delta B)(\Delta \ddot{B})}{(\Delta \dot{B})^2}$$

This quantity cannot be less than unity. For a pure sine wave it is unity, and for random noise with a gaussian distribution it is $\sqrt{3}$. For the values given above, this quantity is slightly greater than unity.

† The z-direction is parallel to the tube axis.

A study was made to find the highest frequencies present in the MHD turbulence, i.e., the high frequency cutoff of the energy spectrum. The low frequencies were reduced to a small value by using an R-C differentiating circuit. The resulting $\ddot{B}$ signals were displayed on a Tektronix 517 oscilloscope, which has a frequency response of greater than 50 Mc. Frequencies of up to 20 Mc were observed. The ion cyclotron frequency is about 12 Mc, so the high frequency cutoff is almost twice the ion cyclotron frequency. The ion cyclotron frequency therefore appears to have no effect on the maximum frequency of MHD turbulence.

When the survey work was being done using $\ddot{B}$ signals to trace the space-time growth of the turbulence, it became evident that there was an inherent 180° asymmetry in the amplitude of the turbulence. Rotating the cathode and external solenoid had no effect, so it was suspected that feeding the current at the bottom of the tube from one side might be the cause. Furthermore, it was felt that since the pinch discharge was very transient in nature, it would not be worthwhile to use this device for further, more quantitative, work. For these reasons, the work has not been continued.

ACKNOWLEDGMENTS

The authors would like to acknowledge the invaluable assistance of Professor Leslie S. G. Kovásznay, a consultant to this laboratory. He gave us many valuable suggestions on experimental techniques that could be applied to this problem, and he provided much theoretical insight into the processes involved. An explanation which he gave on the manner in which the turbulence spread through the tube was fairly well borne out by the survey using $\ddot{B}$ signals. Most of the experimental work on this project, including much of the electronics construction, was carried out by Mr. Ronald C. Phillips while still a student at Long Beach State College. His excellent workmanship and dedicated efforts are gratefully acknowledged.

REFERENCES

1. Burkhardt, L. C., and Lovberg, R. H., *Proc. Second U.N. Conf. on the Peaceful Uses of Atomic Energy*, **32**, 29 (1958).
2. Kovásznay, Leslie S. G., *Rev. Mod. Phys.*, **32**, 815 (1960).
3. Kurchatov, I. V., *Atomnaya Energiya*, **1**, 65 (1956); Artsimovich, L. A. *et al.*, *Atomnaya Energiya*, **1**, 76 (1956). These two papers were reprinted in *J. Nuclear Energy*, II, **4** (1957), and in *Nucleonics*, **14** (1956).
4. Karr, Hugh J., in *The Plasma in a Magnetic Field*, ed. R. K. M. Landshoff (Stanford: Stanford University Press, 1958), 40–59.
5. Segre, S. E., and Allen, J. E., "Magnetic Probes of High Frequency Response", *J. Sci. Inst.*, **37**, 369 (1960).
6. Glasstone, S., and Lovberg, R. H., *Controlled Thermonuclear Reactions* (New York: Van Nostrand, 1960).
7. Simon, Albert, *An Introduction to Thermonuclear Research* (New York: Pergamon Press, 1959).
8. Barber, N. F., *Experimental Correlograms and Fourier Transforms* (New York: Pergamon Press, 1961), Chapter 8.
9. Favre, A. *et al.*, *Actes du Colloque International de Mécanique, Portiers*, III (1950); also *Publ. Sc. et Tech. du Ministére de l'Air*, No. 251 (1950).

7. R. M. Montgomery and R. A. Holmes: *Some Experiments in Radio-Frequency Diagnostics of Partially-Ionized Plasmas*

In this work the sheath theory developed by Bohm is applied to solve for the potential near a negatively-biased electrode in a neutral plasma. Approximate expressions are derived for the sheath thickness as a function of the electrode potential. The time-independent solution is then used with a perturbation technique to solve for the high-frequency electric field in the sheath and plasma. This field is then used to calculate the impedance between coaxial plasma-filled electrodes. Various portions of the impedance versus bias voltage curve and impedance versus frequency curve are related to the plasma density and temperature. The actual measured impedance between coaxial cylinders is compared to that calculated and these quantities are found to be in good agreement.

INTRODUCTION

Radio-frequency (RF) impedance measurements on a large-area probe in a plasma can be interpreted to find the plasma electron density and electron temperature. Two common plasma diagnostic techniques, the Langmuir probe technique and the microwave cavity method, are accomplished either at essentially static (d-c) conditions in the first method or at frequencies well above the plasma frequency in the second method. The RF measurements to be described, however, are carried out at, or not too far below, the plasma frequency—the very frequency range in which the plasma might be expected to exhibit its most interesting behavior. Furthermore, in some plasma devices of current interest, measurements of bulk plasma properties could be made by this technique using electrodes already present for other purposes, eliminating the need for auxiliary probes.

The specific experiments to be analyzed and described were done with a negatively-biased cylindrical probe electrode in a cylindrical low-pressure mercury-arc discharge; the other electrode in the impedance measurement was a coaxial cylinder wrapped around the discharge tube wall. This geometry is shown in Figure 1. The net impedance from the inner cylinder to the outer one will be composed of four parts: (1) the plasma sheath impedance (capacitive) at the inner electrode; (2) the impedance of the spatially-varying bulk plasma (inductive, resistive, capacitive); (3) the glass tube wall sheath impedance (capacitive and

ED. NOTE: Mr. Montgomery and Mr. Holmes are in the Department of Electrical Engineering at Purdue University.

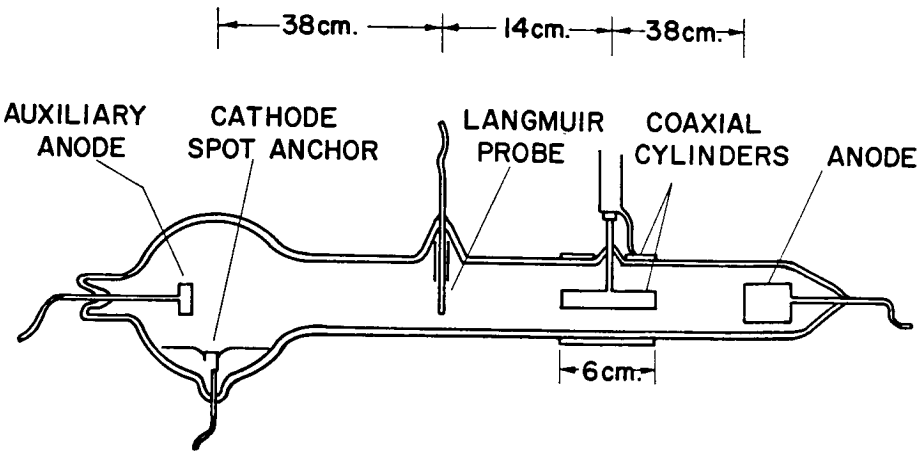

FIGURE 1. The experimental discharge tube.

practically negligible); and (4) the impedance of the glass wall (capacitive). The organization of the results of this work logically follows this layout of the parts of the overall impedance. First, the static behavior of the sheath at the inner electrode is reviewed to lay the foundation for the behavior of sheath capacitance. Next, an RF perturbation analysis is developed to find the electric fields in the sheath and bulk plasma. Following this, the material is applied to impedance measurements at low radio frequencies where most of the impedance is in the sheath capacitance (the bulk plasma being a good conductor), then applied at radio frequencies in the neighborhood of ω_p for the bulk plasma.

THE D-C SHEATH

Before discussing time-dependent sheath phenomena, it is convenient to briefly review the well known static sheath theory. The plasma boundary or wall under consideration is assumed to be negatively biased to the point that the electron current to it is a negligible fraction of the random electron current in the plasma. (The average velocity of the electrons, **u**, is assumed to be zero.) The electrons are also assumed to be near thermal equilibrium at a temperature T which is much larger than the positive ion temperature, and the sheath thickness is taken to be small so that no collisions occur in the sheath region.

Under these conditions the sheath theory of Bohm (**1**) is applicable and the model for the sheath will be that shown in Figure 2. In this model the ions are accelerated in the pre-sheath region and arrive at the sheath edge with a kinetic energy equal to $\frac{1}{2}kT$. The derivative of the potential at the sheath edge is small compared to its value inside the sheath.

The basic equations describing the sheath include the electron momentum equation

$$0 = -neE - kT\frac{dn}{dx} \tag{1}$$

the continuity and momentum equations for positive ions

$$\frac{d}{dx}(NU) = 0 \tag{2}$$

$$NM\frac{dU}{dx} = NeE \tag{3}$$

and Poisson's equation

$$\frac{d^2V}{dx^2} = -\frac{e}{\varepsilon_0}(N-n) \tag{4}$$

where e is the charge on an electron and n is the electron density. N, M, and U are the positive ion density, mass, and average velocity, respectively; V is the potential and E the electric field strength; ε_0 is the permittivity of free space and k is Boltzmann's constant.

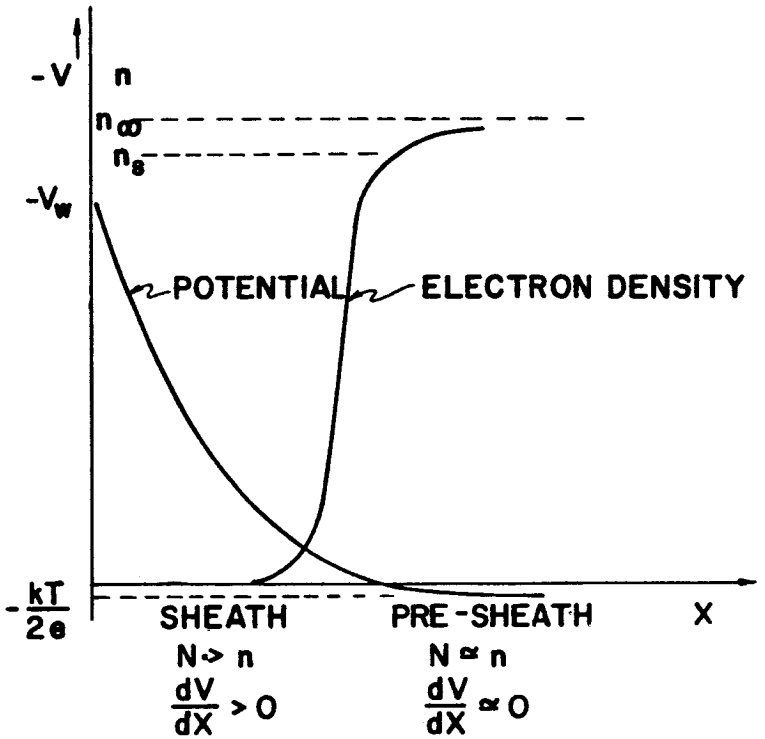

FIGURE 2. The assumed form of the potential and the electron density.

Equations (1) through (4) can be reduced to the single equation

$$\frac{d^2\eta}{d\xi^2} = \left(\frac{\frac{1}{2}}{\eta+\frac{1}{2}}\right)^{1/2} - e^{-\eta} \tag{5}$$

where the normalized variables

$$\eta = -\frac{eV}{kT} \quad \text{and} \quad \xi = \frac{X}{(\varepsilon_0 kT/ne^2)^{1/2}} = \frac{X}{\lambda_D}$$

have been substituted.

For large values of η (approximately $\eta > 4$) this equation can be solved to obtain

$$\left(\frac{\eta}{2}\right)^{1/2}\left[\left(\frac{\eta}{2}\right)^{1/2}+2\right]^{1/2} = -\tfrac{3}{4}\xi + \left(\frac{\eta_w}{2}\right)^{1/2}\left[\left(\frac{\eta_w}{2}\right)^{1/2}+2\right]^{1/2} \tag{6}$$

where η_w is the normalized potential at the wall.

For small values of η (approximately $\eta < 5$) a solution to equation (6) is obtained by expanding $\eta(\xi)$ in a power series about the point where $\eta = 5$. Calling this point ξ_1, the power series for η becomes

$$\eta(\xi) = 5 - 1.63(\xi - \xi_1) + 0.147(\xi - \xi_1)^2 - 0.00345(\xi - \xi_1)^3 + 0.000033(\xi - \xi_1)^4 + 0.0000275(\xi - \xi_1)^5 \quad (7)$$

The graph of η versus ξ which is obtained from equations (6) and (7) is shown in Figure 3 for $\eta_w = 50$. Equation (6) has been compared to and found to be in good agreement with the experimental data obtained by Von Gierke (**2**).

RF ELECTRIC FIELDS IN THE PLASMA AND SHEATH

From Figure 3 it can be seen that a reasonable approximation to the electron density at the plasma edge is a step function occurring at the point where $n/n_s = \frac{1}{2}$.

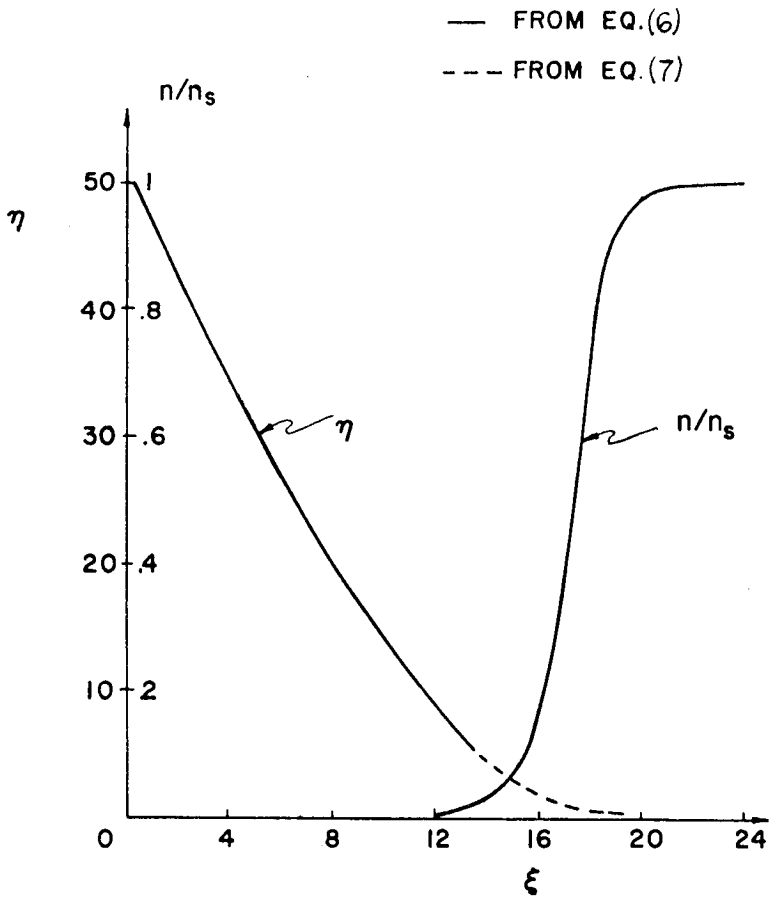

FIGURE 3. Variations of η and n for $\eta_w = 50$.

This closely corresponds to the point where $\eta = 0$ in the approximation of equation (6). This result will be used to define the sheath thickness in calculating the capacitance across the sheath.

If one now assumes that the wall potential, V_w, has a small sinusoidal perturbation imposed upon it and that the electron density, n, and average velocity, u,

are similarly perturbed, then the continuity and momentum equations for electrons become

$$\frac{d}{dx}(n_0 u_1) = -j\omega n_1$$

$$j\omega n_0 u_1 = n_0 e \frac{dV_1}{dX} + e n_1 \frac{dV_0}{dX} - kT \frac{dn_1}{dX}$$

and Poisson's equation reduces to

$$\frac{d^2 V_1}{dX^2} = \frac{e n_1}{\varepsilon_0}$$

Here the variables with the subscript 1 refer to small perturbations about the equilibrium values which have the subscript 0. Second order perturbation terms have been neglected and, for simplicity, the electron temperature has been assumed constant in time and space.

It is possible to eliminate n_1 and u_1 from these equations to obtain

$$\left[\frac{n_0 e^2}{\varepsilon_0 m} - \omega^2\right] E_1 + \omega^2 E_s = -\frac{e}{m}\frac{dE_1}{dX}\frac{dV_0}{dX} + \frac{kT}{m}\frac{d^2 E_1}{dX^2} \tag{8}$$

where E_s is the perturbation electric-field strength at the wall. In the sheath region $n_0 \simeq 0$ and $n_1 \simeq 0$, implying that

$$\frac{dE_1}{dX} = 0 \quad \text{and} \quad \frac{d^2 E_1}{dX_2} = 0$$

and equation (8) reduces to $E_1 = E_s$. On the other hand, in the pre-sheath and plasma regions

$$\frac{dV_0}{dX} \simeq 0$$

and equation (8) becomes

$$\left[\frac{n_0 e^2}{\varepsilon_0 m} - \omega^2\right] E_1 + \omega^2 E_s = \frac{kT}{m}\frac{d^2 E_1}{dX^2}$$

For the moment, n_0 will be assumed independent of x outside the sheath and the following substitutions will be made:

$$\omega_p^2 = \frac{n_0 e^2}{\varepsilon_0 m} \qquad \lambda_d^2 = \frac{kT}{\omega_p^2 m}$$

The resulting equation

$$\frac{1}{\lambda_D^2}\left[1 - \frac{\omega^2}{\omega_p^2}\right] E_1 + \frac{\omega^2 m}{kT} E_s = \frac{d^2 E_1}{dX^2} \tag{9}$$

has the solution

$$E_1 = \frac{E_s}{1 - \omega_p^2/\omega^2} + A \exp\left[-\frac{x}{\lambda_0}\left(1 - \frac{\omega^2}{\omega_p^2}\right)^{1/2}\right] \tag{10}$$

This solution is strictly correct only for the case when n_0, hence ω_p, is independent of x; however, the "relaxation length",

$$\frac{\lambda_D}{[1 - (\omega^2/\omega_p^2)]^{1/2}}$$

is found to be somewhat greater than the Debye length for $\omega < \omega_p$. Thus, in a region where n_0 does not vary appreciably over a Debye length, the second term in equation (10) is negligible and E_1 becomes

$$E_1 = \frac{E_s}{1-(\omega_p^2(X)/\omega^2)}$$

Returning to equation (10) it will be noted that the second term may be written as

$$A \exp\left[-j\frac{X}{\lambda_D}\left(\frac{\omega^2}{\omega_p^2}-1\right)^{1/2}\right]$$

and for $\omega > \omega_p$ it represents the usual "plasma wave" propagating with a wave length

$$\lambda = \frac{2\pi\lambda_D}{[(\omega^2/\omega_p^2)-1]^{1/2}}$$

EXPERIMENTAL MEASUREMENT OF SHEATH THICKNESS

In the preceding development it was shown that for ω considerably less than ω_p the RF electric field in a plasma is given by

$$E_1 = \frac{E_s}{1-(\omega_p^2/\omega^2)}$$

This indicates that for $\omega \ll \omega_p$, the field in the plasma becomes much smaller than the field in the sheath and opposite in sign. This also means that for sufficiently high plasma density, the RF potential difference between two electrodes in a plasma will appear almost entirely across the plasma sheaths surrounding these electrodes. Thus the impedance between these electrodes will be only the sheath impedance, and hence a method for measuring sheath thickness is obtained. Of course, the sheath edge must be reasonably well defined if this measurement is to have any meaning. The d-c sheath theory presented previously indicates that the sheath edge is reasonably well defined and that it is located at that value of ξ for which $\eta = 0$ in equation (6) or

$$d = \frac{4}{3}\lambda_D\left(\frac{\eta_w}{2}\right)^{1/2}\left[\left(\frac{\eta_w}{2}\right)^{1/2}+2\right]^{1/2} \tag{11}$$

where d is the sheath thickness.

The impedance presented by the sheath is then

$$Z_s = \frac{d}{j\omega\varepsilon_0 A} = \frac{4}{3}\frac{\lambda_D}{j\omega\varepsilon_0 A}\left(\frac{\eta_w}{2}\right)^{1/2}\left[\left(\frac{\eta_w}{2}\right)^{1/2}+2\right]^{1/2} \tag{12}$$

where A is the area of the sheath.

Equation (12) involves two unknown parameters—the electron density, and the electron temperature; all other quantities are either known or measurable. Thus, the measurement of the impedance, Z_s, for two different values of d-c potential, V_w, makes it possible to determine n and T from equation (12).

The validity of equation (12) was checked in the experimental discharge tube shown in Figure 1. The impedance between the coaxial cylinders was measured with various values of d-c bias on the inner cylinder. These measured impedances were then corrected for the impedance of the glass tube wall and compared to

those calculated with equation (12). The radius of the inner electrode was made large compared to the sheath thickness to insure the applicability of planar sheath theory; all calculated values of Z_s were based on Langmuir probe measurements of n and T. The results of this investigation appear in Figure 4.

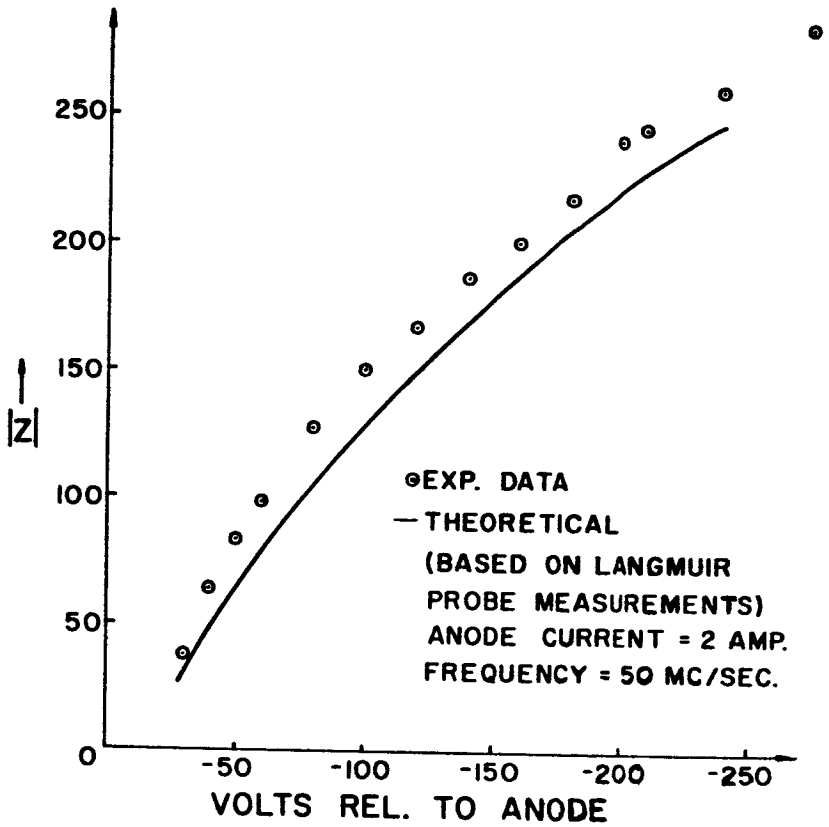

FIGURE 4. The variation of RF impedance with d-c bias.

RF BEHAVIOR NEAR THE PLASMA FREQUENCY

At frequencies which are near the plasma frequency the electric field in the plasma is no longer negligible. The impedance between the concentric cylinders of Figure 1 will now be studied for frequencies in this region. In order to simplify the discussion the diameter of the inner cylinder and the spacing between cylinders will be taken to be much greater than the Debye length. Furthermore, the effect of the plasma wave represented by the second term in equation (10) will be considered negligible. That is, the plasma may be characterized by the usual dielectric constant

$$\varepsilon = \varepsilon_0\left(1-\frac{\omega_p^2}{\omega^2-j\omega\nu_c}\right)$$

for purposes of calculating impedance. The $j\omega\nu_c$ term in this expression arises because of the effect of collisions on the particle motions. This effect was neglected in writing the equations of the preceding sections of this paper, but it could be

accounted for by introducing a viscous-like term in the electron momentum equation. The effects of collisions in the plasmas referred to in this paper are usually small; however, they become very important near certain resonant frequencies.

If one considers an arrangement similar to Figure 1 with electrode length l, inner cylinder radius a, sheath radius b, and plasma column radius c, then the RF electric field in the plasma is

$$E_1 = \frac{aE_s}{\{1-[\omega_p^2/(\omega^2-j\omega\nu_c)]\}r}$$

where E_s is the field at the surface of the inner cylinder. If the electron density is then approximated by the expression

$$n(r) = \frac{(\alpha-1)n_0}{C-b}\,r + n_0\,\frac{\alpha b - C}{b-C} \tag{13}$$

then the impedance between the cylinders becomes

$$Z_t = \frac{1}{2\pi j\omega\varepsilon_0 l}\,\frac{\dfrac{\omega^2}{\omega_0^2}-j\,\dfrac{\omega\nu_c}{\omega_0^2}}{\dfrac{\omega^2}{\omega_0^2}-j\,\dfrac{\omega\nu_c}{\omega_0^2}-\dfrac{C-\alpha b}{C-b}}\ln\left[\frac{C\left\{\dfrac{\omega^2}{\omega_0^2}-1-j\,\dfrac{\omega\nu_c}{\omega_0^2}\right\}}{b\left\{\dfrac{\omega^2}{\omega_0^2}-\alpha-j\,\dfrac{\omega\nu_c}{\omega_0^2}\right\}}\right] \tag{14}$$

$$+\frac{1}{2\pi j\omega\varepsilon_0 l}\ln\frac{b}{a}+Z_g$$

where ω_0 is defined by the relation

$$\omega_0^2 = \frac{n_0 e^2}{\varepsilon_0 m}$$

and Z_g is the impedance presented by the glass tube envelope.

The experimental conditions used to investigate equation (14) were such that the planar d-c sheath theory is not applicable; however, the sheath thickness can still be determined from the value of the impedance at low frequencies ($\omega \ll \omega_p$).

The following parameters are those of the discharge tube used in the experiments described here.

$$\begin{aligned} Z_g &= -j2\pi\times 10^9/\omega \\ a &= 2.31\times 10^{-3}\ \text{meters} \\ C &= 1.85\times 10^{-2}\ \text{meters} \\ l &= 6\times 10^{-2}\ \text{meters} \end{aligned}$$

The sheath radius was determined from the low-frequency behavior of the impedance:

$$b = 3.44\times 10^{-3}\ \text{meters}$$

The collision frequency, ν_c, was determined by measurement of the high-frequency impedance of solenoid surrounding the plasma, a technique which has been developed by Persson (**3**).

Calculations were made for two values of $\alpha\cdot\alpha = \frac{1}{2}$ which, according to the results of Parker (**4**), makes equation (13) into a reasonable approximation for the electron density in a cylindrical discharge and $\alpha = 1$ (uniform electron density).

With the preceding numerical values inserted, equation (14) becomes

$$Z_t = -j55\left(\frac{f_0}{f}\right) - j124\left(\frac{f_0}{f}\right)\left[\frac{(f/f_0)^2 - j0.0261(f/f_0)}{(f/f_0)^2 - 1.11 - j0.0261(f/f_0)}\right] \ln 5.4\left[\frac{(f/f_0)^2 - 1 - j0.0261(f/f_0)}{(f/f_0)^2 - \frac{1}{2} - j0.0261(f/f_0)}\right] \quad (15)$$

for $\alpha = \frac{1}{2}$ and

$$Z_t = -j26.1\left(\frac{f_0}{f}\right)\left\{2.1 + 8\left[\frac{(f/f_0)^2 - j0.0261(f/f_0)}{(f/f_0)^2 - 1 - j0.0261(f/f_0)}\right]\right\} \quad (16)$$

for $\alpha = 1$.

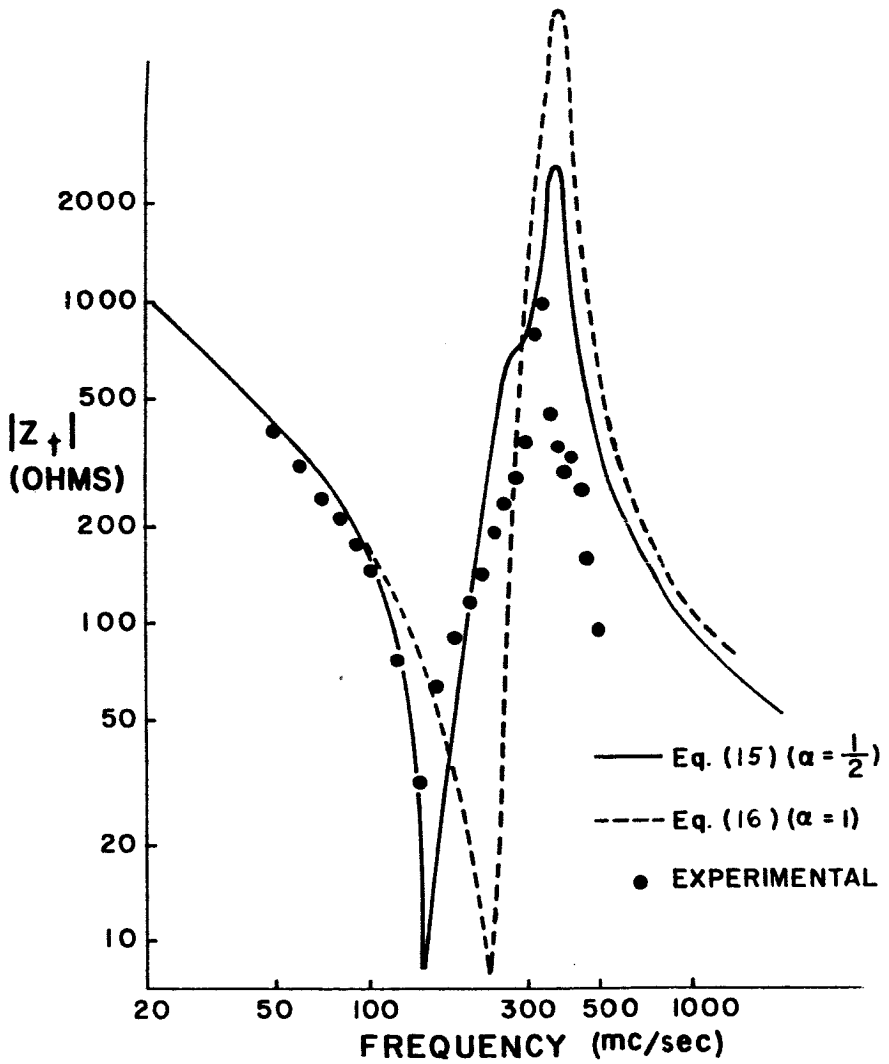

FIGURE 5. Magnitude of the experimental and theoretical impedance between coaxial cylinders.

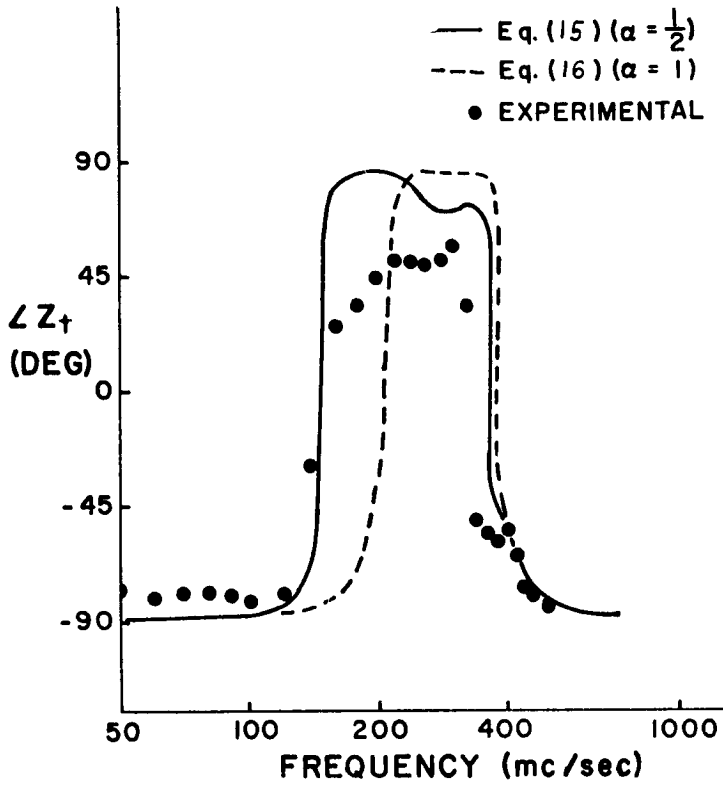

FIGURE 6. Theoretical and experimental variation of impedance phase angle with frequency.

These two equations are plotted in Figures 5 and 6 and the experimentally measured impedance values appear as the dots on these figures.

The general appearance of these curves is briefly explained as follows: At low frequencies the impedance asymptotically approaches the impedance of the sheath alone as previously explained. Thus the low frequency asymptote on a log–log plot is a straight line with a slope of minus one. At a somewhat higher frequency the sheath capacitance and the inductance presented by the bulk of the plasma form a series resonant circuit and there is an impedance minimum. At a still higher frequency (the plasma frequency for the case of uniform electron density) the inductive currents produced by the electron motion in the plasma cancel with the displacement currents in the plasma and an impedance maximum occurs. The magnitudes of the maximum and minimum impedance are determined by the collision frequency. As can be seen in Figure 5, the calculated impedance minimum is about four times smaller than the measured value and the calculated maximum is about twice the measured value. This indicates either that the solenoidal measurement of collision frequency yielded too low a value, or that there are some losses associated with the coaxial cylinder impedance measurements which were not present in the solenoid measurements.

The frequencies at which the impedance maxima and minima occur are in good agreement with the calculated frequencies which are based on Langmuir probe measurements of electron density.

CONCLUSIONS

The results of the experiments performed show that high-frequency methods can be applied to measure plasma sheath thickness directly. They also show that the high-frequency impedance between electrodes in a plasma can be accurately predicted and that the plasma electron density, temperature, and collision frequency can be determined from this impedance.

REFERENCES

1. Bohm, D., "Minimum Ionic Kinetic Energy for a Stable Sheath", in *Characteristics of Electrical Discharges in Magnetic Fields*, ed. A. Guthrie and R. K. Wakerling (New York: McGraw-Hill, 1949), 77.
2. Von Gierke, G., Ott, W., and Schwirzke, F., "Untersuchung von Plasma Grenzschichten mit einer Electronenstrahl-Sonde", in *Ionization Phenomena in Gases*, ed. H. Maecker (Amsterdam: North-Holland, 1962), 1412.
3. Persson, K. B., "A Method for Measuring the Conductivity in a High Electron Density Plasma", *J. appl. Phys.*, **32**, 2631 (1961).
4. Parker, Jerald V., Technical Report No. 19, California Institute of Technology, Nonr 220(13) (December, 1962).

8. W. K. McGregor: *Spectroscopic Measurements in Plasmas*

The possible uses of spectroscopy in the diagnostics of plasmas are described. Brief descriptions of the methods used in measurement of temperature are given and an attempt is made to identify the governing energy distribution in each case. Identification with the translational velocity distribution makes the method valid; identification with some other distribution makes closer study necessary. Some actual data from arc plasma jets are used to illustrate the arguments. The classical criteria for equilibrium are re-examined briefly and some additional limitations imposed. The influence of metastable atoms on the interpretation of the spectra from low density streams is discussed and some application to temperature measurement given.

INTRODUCTION

This paper deals with a narrow slice of a very broad subject. The title is much too broad for the material that is to be covered. In the first place, the word "plasma", meaning any gas that is ionized to some extent, must be narrowed in the treatment to include only those plasmas applicable to gas dynamics studies and to exclude gas discharge tubes, stellar atmospheres, or the high-energy plasmas associated with fusion research. The gas dynamics realm of plasmas includes the plasmas generated by gases flowing through electrical discharges and gases heated in shock tubes. However, it is preferred to omit even the latter from the discussion because the mechanism of excitation is much different, and, too, the author is more familiar with the processes going on in plasma generators.

The concept of spectroscopy must also be narrowed for the purpose of this paper in order to deal only with those methods and concepts which do not push the state of the spectroscopic art. For this reason, little note will be made of the more fundamental problems—which are, even now, not completely treated—such as the cross sections for various excitation mechanisms and the validity of transition probabilities.

It is also not intended that this be a review paper because (1) many review papers exist on gas discharge phenomena and the author would not attempt to improve upon them (**1**); (2) the methods of spectroscopic diagnostics have been adequately treated in many places (**2**), and it is desired only to summarize them briefly here; and (3) the applications of gas discharge phenomena and spectroscopic measurements in flowing systems are not yet adequately reported so that an accumulation of material for a critical evaluation of methods and results is premature. Rather, it is hoped that this paper will serve to illuminate some of the

ED. NOTE: Mr. McGregor is with ARO Incorporated, Tullahoma, Tennessee. The research reported in this paper was sponsored by the U.S. Air Force under contract AF 40(600)-1000.

essential mechanisms giving rise to radiation in gas-dynamic-type plasmas and to stir some interest in solving some of the remaining problems. The theme of the paper will be better understood if it is defined as a review of the essential mechanisms giving rise to the radiation and an interpretation of some of the reported measurements.

That spectroscopy is a very powerful diagnostic tool goes without question. As an example of the power of a single measurement, the writer recently witnessed an experiment in which a narrow portion of the spectrum from an enclosed helium discharge was used as the single diagnostic tool. Only three spectral lines were employed, the 5015 and 5047 Å neutral atom lines and the 5411 Å ionized line. From a single photograph, the experimenter was determining the temperature in three different ways, and the electron density or degree of ionization in two ways, and from these measurements calculating the pressure of the gas within the discharge chamber. One might question the validity of the interpretations being made, or perhaps the constants being used, but certainly not the methods and principles employed. The task remaining for the researcher on diagnostics is that of perfecting the understanding of the measurements, and to that end this paper is dedicated.

MODEL

In order to get at the points to be emphasized, a model of a flowing plasma generator and the supersonic plasma stream which results will be considered. The model will possess most of the characteristics to be discussed. The device to be considered is normally called a "plasma jet" (**3**), which exhausts into a low pressure

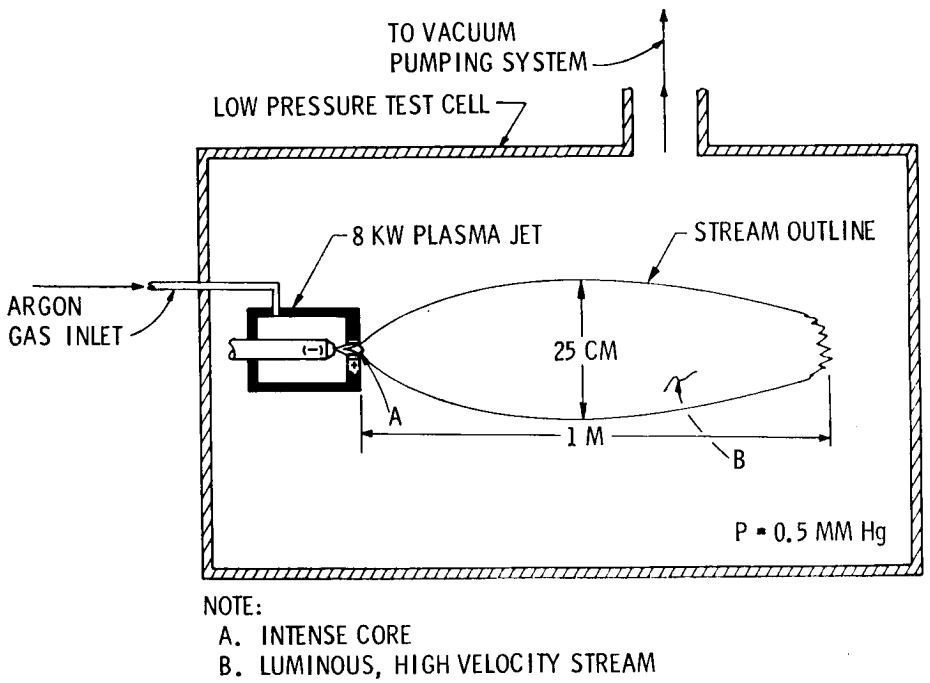

FIGURE 1. Apparatus schematic and plasma stream characteristics.

test cell; the essential features of this device are shown in Figure 1. A gas is forced through an electrical discharge between two electrodes, and energy is added to the gas in various forms. By far the greatest amount of energy is in the form of kinetic energy; however, some of the energy added goes into excitation with subsequent photon emission at prescribed wavelengths, and this is the energy to be used as a spectral diagnostic tool. Still another portion of the energy goes into dissociating the molecules of the gas, and another goes into ionization of some of the atoms and produces the property which allows the gas stream that emerges from the discharge to be called a "plasma".

In this apparatus, the electrode configuration has been illustrated as the "Gerdien" type (**4**), and this configuration is used for these discussions. However, the basic premises of the discussion will be applicable also to the more complicated magnetically-driven spinning arcs (**5**) and also to the stationary arcs with their associated gas pumping action (**6**). The essentials of all such apparatus is that there is a region of electrical discharge with a gas flowing through it which receives kinetic and excitation energy.

The region of most interest to the gas dynamicist is the gas stream after it leaves the discharge. At high pressure exit conditions, the definition of just where this separation between discharge and the field free gas stream takes place has caused some serious study and conjecture and is still a controversial subject (**7, 8**). However, when the gas is expanded to a low pressure, a highly supersonic plume is formed which can, most times, be seen by the light emitted from it. A typical low pressure stream from a plasma jet is shown in Figure 2. The stream appears to behave as an ordinary supersonic stream, with expected shock structure well defined and boundaries clearly visible.

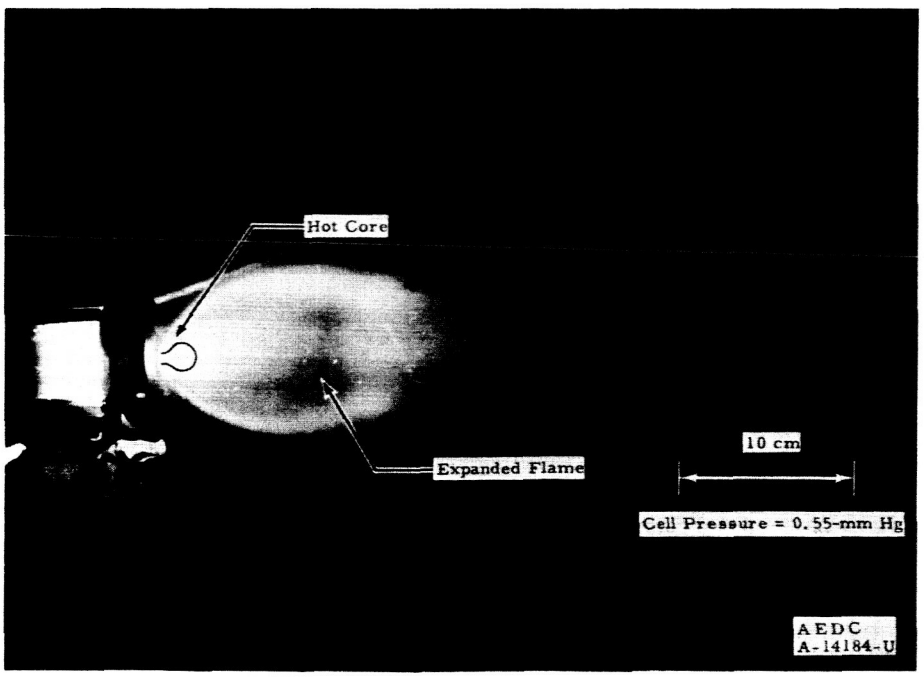

FIGURE 2. Argon plasma jet expanding to a low pressure.

SPECTRAL MEASUREMENTS

The measurements which can be made on the plasma source with the spectroscope shall now be considered. The emission spectrum from any point in the stream provides a measurement of:

(1) the wavelengths of the spectral lines emitted;
(2) the intensity of the spectral lines emitted;
(3) the line intensity profile of the spectral lines emitted; and
(4) the intensity of any continuum radiation that might be present.

If a light source is now provided, the amount of radiation absorbed by the gas stream as a function of the wavelength can be measured.

Typical spectrograms of the discharge region and the supersonic plume region of an argon plasma are shown in Figure 3. The wavelength range is from about 3500 to 7000 Å units. This spectrum was photographed with a grating instrument. A small portion of the spectrum is shown in Figure 4, which was obtained using a direct recording prism instrument with a photo-multiplier detector. These spectra will be considered later.

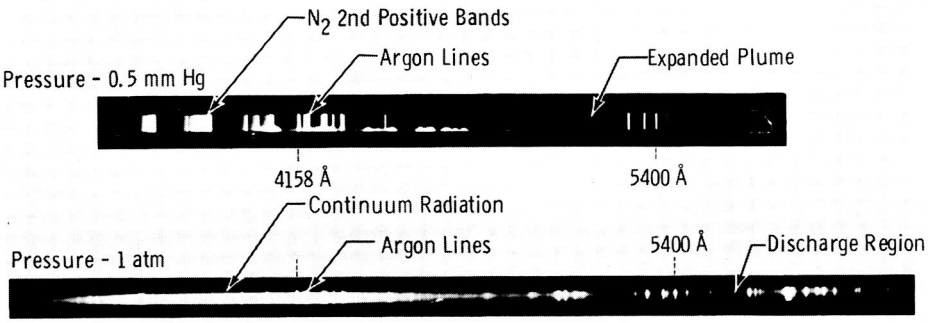

FIGURE 3. Spectra of argon plasma jet. (Note: The spectra were taken with spherical gratings of different focal length.)

The application of these measurements to diagnostics of conditions within the plasma stream involves the use of a great deal of physics. The measurements may be put into three classes of uses: (1) identification of species; (2) thermal properties; and (3) phenomenological measurements. Application of these to the model suggested will be made in order to demonstrate what is believed to be the proper diagnostic attitude.

IDENTIFICATION OF SPECIES

The oldest use of spectroscopy is undoubtedly the identification of substances by the wavelengths of the spectral lines they emit. This was, indeed, the first use to which the spectrograph was put in the plasma diagnostics at AEDC (**9**). There was considerable concern about contamination of the gas stream with electrode material, as had been reported by other investigators using very high-energy arcs. Such contamination would have ill effects on the experiments which were to be of a very basic nature. The resulting spectra taken from the emission just at the orifice exit when the plasma jet was exhausting to atmospheric pressure, or into a low

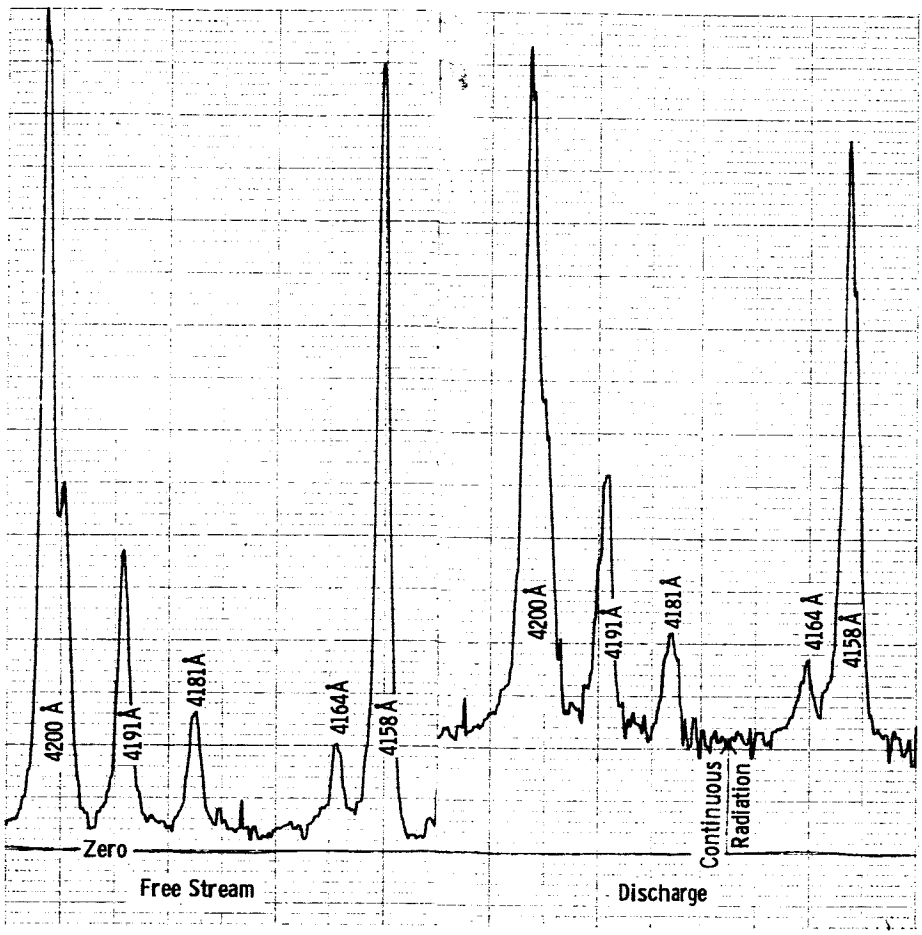

FIGURE 4. Illustrative spectral data from an argon plasma.

pressure cell, showed that, for devices of the 10 to 60 kw range, no appreciable contamination could be detected from the spectra. In fact, in argon, helium, and nitrogen, no spectral lines other than those of the gases being used could be identified. Other investigators reported like results for similar small plasma jets, and, thus, assurance was given that the gases heated by this method could be considered as adequate plasma sources for many laboratory gas dynamics experiments.

Many other qualitative conclusions can be gained by merely examining the wavelengths of the lines emitted. Thus, the appearance of both the nitrogen molecular bands and the atomic lines in a nitrogen plasma is an indication of the dissociation of the molecule (**10**). This type of interpretation has been used to locate inner zones in a nitrogen plasma where dissociation is detectably present, and thus to establish an isotherm if the dissociation is known as a function of the temperature. Another useful fact that can be obtained from the spectra is whether ionization is present in any appreciable amount by the appearance of ionized lines. Spectra taken of the discharge region in helium and argon exhibit many lines attributable to the ionized species.

THERMAL PROPERTIES

The measurement of temperature is perhaps the most important task laid upon the spectroscopist since the advent of the laboratory plasma. The relation of the energy radiated by a gas to its temperature is a very old subject and one that has been thoroughly explored in fields such as astrophysics. Only a brief summary of the principles involved is presented because many writers have attempted to assemble the details of these methods.

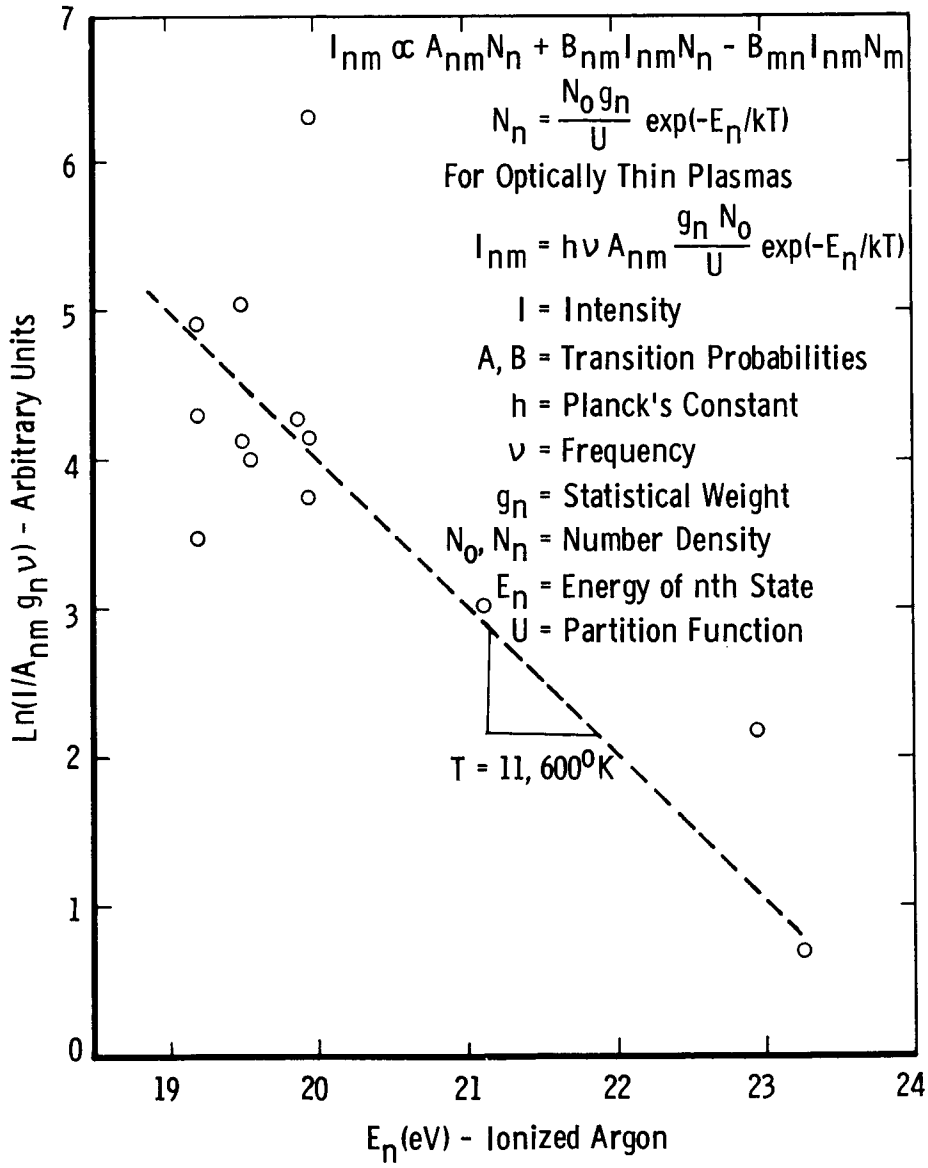

FIGURE 5. Illustration of spectral line intensity distribution methods of temperature measurement. Example data taken from reference (12) for an argon plasma jet.

METHODS OF TEMPERATURE MEASUREMENT

Spectral Line Intensity

The relation of the intensity of an atomic spectral line to the temperature is given in Figure 5. Generally, methods using the intensity relation are employed only for spectroscopically-thin sources—that is, where there is no appreciable selfabsorption or induced emission and the equation reduces to the more simple expression shown. At least four temperature-measuring techniques utilize this equation. First, the absolute intensity of the line is measured by calibrating the spectrograph with a source such as a tungsten ribbon filament lamp or a Kiel arc, and since the constants are known, the temperature is calculated. The difficulty here is the absolute intensity calibration. The problem is relieved somewhat by

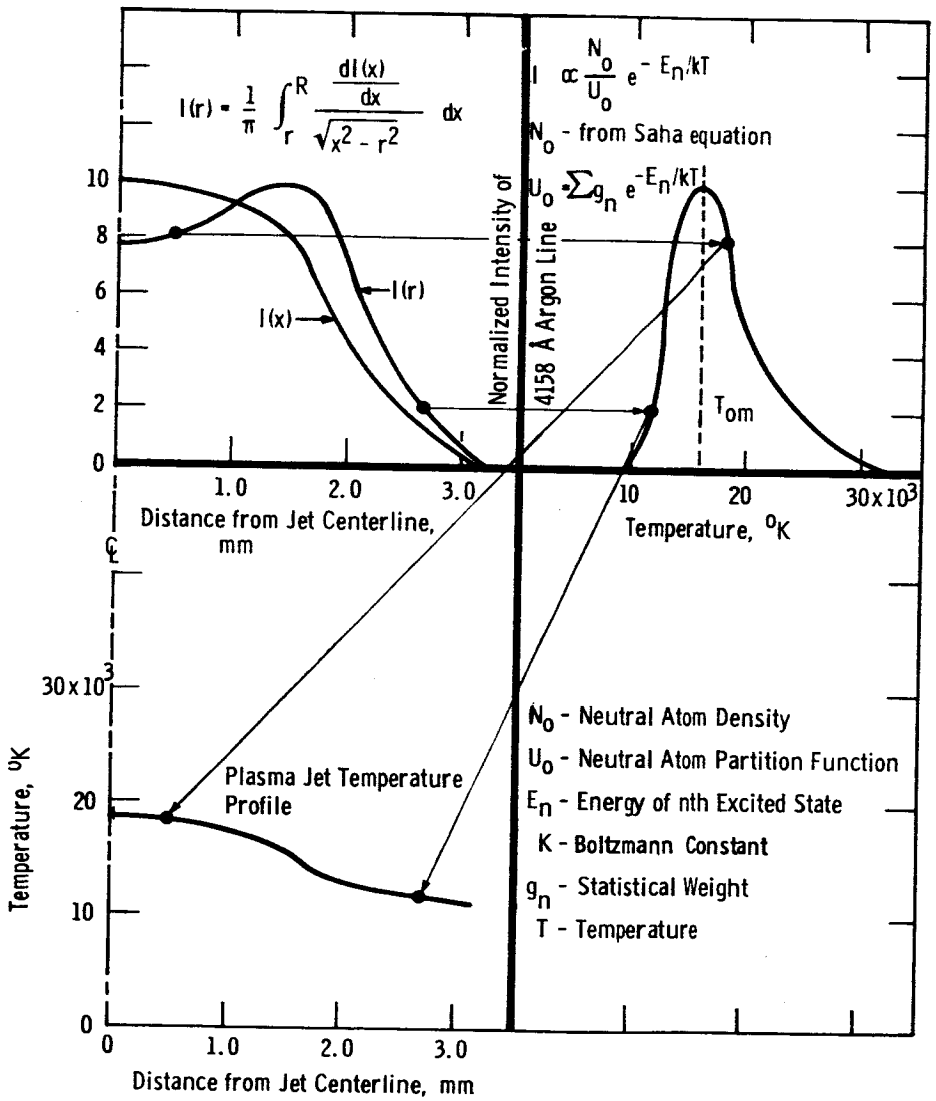

FIGURE 6. Illustration of peaking function method for measuring temperature; data shown for an argon plasma jet using the 4158 Å line.

taking the ratio of the intensities of two lines so that only a relative intensity calibration at the two wavelengths is required (**11**). Further confidence is lent to the latter method by using several lines and plotting log $IU/\nu A_{nm}$ versus E_n; the slope of the resulting straight line will be $1/kT$ as indicated in Figure 5. The data points shown are typical of an argon discharge (**12**). The difficulty with this method is that the transition probabilities, A_{nm}, must be accurately known when actually very few transition probabilities are known with precision. Still another method that is applicable in some cases and avoids the necessity for calibration as well as knowledge of the transition probability is the "peaking function" method (**13, 14, 15**), which is based on the fact that the intensity of any spectral line must reach a maximum at some temperature, T_m, which can be calculated. The method is illustrated in Figure 6 for a particular argon spectral line, and has been used by

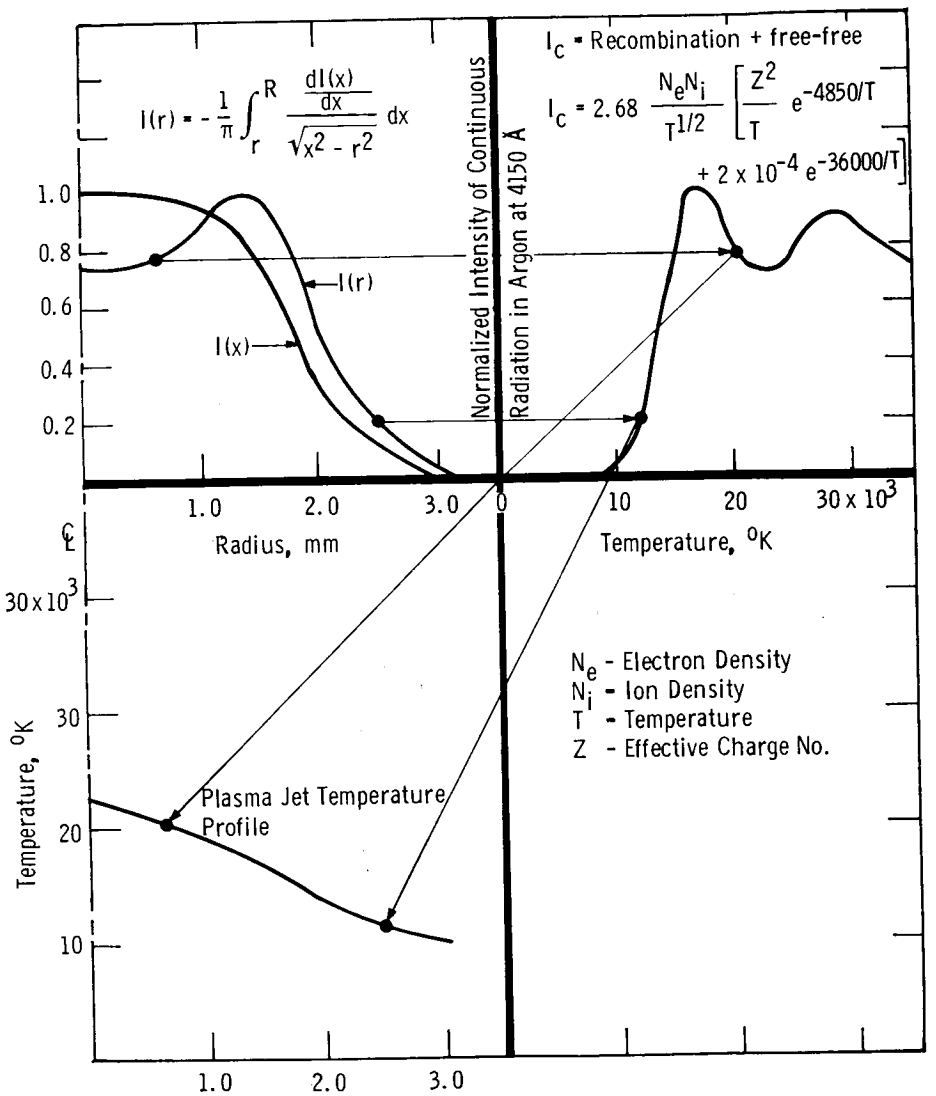

FIGURE 7. Illustration of peaking function method of temperature measurement using continuum intensity; data shown for an argon plasma jet at 4150 Å.

many investigators on both plasma generators and stationary arcs. (The data shown were taken by the author and associates from the region just downstream of the orifice of an argon plasma jet (**16**) using the 4158 Å line.)

Continuous Emission

Radiation that is continuous with frequency is emitted in plasmas by the interaction of free electrons with nuclei and also by recombination. The formulas governing the intensity of such radiation as functions of temperature are shown in Figure 7 (**16**). Here, again, measurement of the absolute intensity at a single wavelength provides a measurement of the temperature. However, uncertainties in the constants and in the calibration make this method somewhat doubtful. Also, it is not clear just how much of the radiation is due to free-bound and how much to free-free transitions. The peaking-function method may be used here, too, and this method seems more reliable where temperatures are large enough so that it can be applied. The peaking function is illustrated for argon in Figure 7, where the data were taken from the continuous emission adjacent to the 4158 Å line of argon used for the data shown in Figure 6.

Molecular Band Distributions

The same basic formulas as given in Figure 5 are applicable to the vibrational and rotational transitions which produce molecular band structure (**17**). Use of such bands has been successful for a few molecules such as NO, CN, and the C_2 Swan bands, but the transition probabilities of only a few molecules are well enough known. The advantage of using such a band is that no relative calibration is usually required because of the small range of the spectrum covered. Disadvantages are that bands are generally very complicated and high resolution instruments are required.

Planck-Kirchhoff Law

A method which has been used quite successfully for determining flame temperatures in combustion has also been applied to plasmas. This method must be used in a region of the spectrum where there is a large amount of absorption, but it has been found useful only for wavelengths longer than about 8000 Å. The method is illustrated in Figure 8 (**18**). Measurement is made of the absolute intensity emitted by a given section of plasma; then the percentage of absorption by the same stream volume is measured and set equal to the emissivity via Kirchhoff's law for radiators in equilibrium; temperature is then determined from the relation $J_b(T)=J/\varepsilon$ where J_b is the blackbody radiation at a temperature T as determined from Planck's formula. Some typical data are shown in Figure 8, also. The difficulties with this method are that selfabsorption and temperature gradients are difficult to take into account, and both these phenomena exist in plasma-jets.

Spectral Line Profile

The use of spectral line profiles, half-widths, wing structure, and peak shifts cannot be adequately considered here. We can only attempt to separate the mechanisms giving rise to the phenomena in order to determine whether the method gives a measure of the electron or gas temperature. Three different phenomena give rise to line broadening of sufficient width for measurement purposes: Doppler broadening, collisional broadening, and Stark broadening. The first, Doppler broadening, is related to temperature in a quite normal way through the velocity

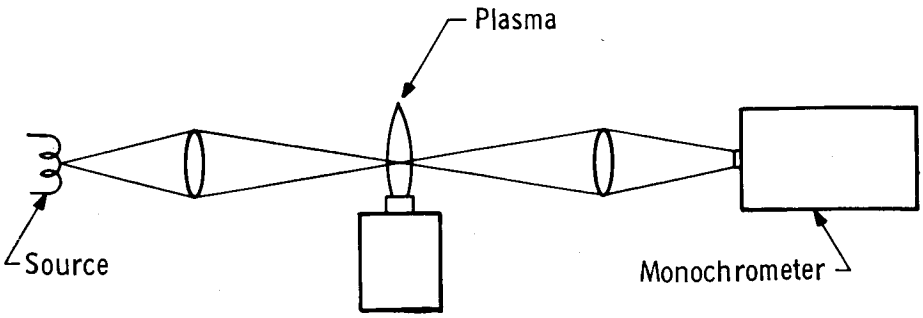

$$J(\text{plasma}) = \frac{J(\text{source}) - J(\text{plasma})}{J(\text{source})} \; J(\text{black-body})$$

$$J(\text{black-body}) = \frac{C_1}{\lambda^5 \left(e^{C_2/\lambda T} - 1 \right)}$$

C_1, C_2 = Constants
J = Radiancy
λ = Wave Length
T = Temperature

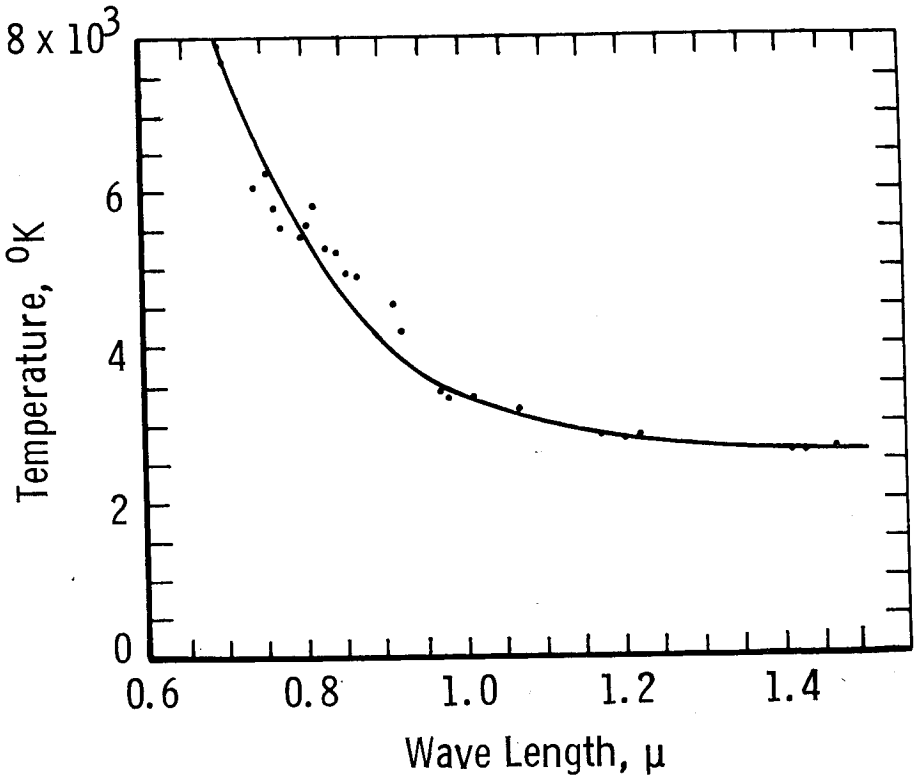

FIGURE 8. Illustration of radiation emission-absorption method of temperature measurement using Planck's and Kirchhoff's laws.

distribution of the radiating atoms and, thus, provides direct measurement of the gas temperature through the relation shown in Figure 9. Unfortunately, the amount of Doppler broadening is quite small (less than 0.1 Å for most plasma applications) and is usually overshadowed in ionized gases by other mechanisms. Collisional broadening is also very small at the densities currently encountered so that it is not an important mechanism. The broadening caused by perturbing fields due to the presence of electrons or ions near the radiating atom seems to be the chief concern in plasmas. This is the Stark broadening which may take a variety of forms that have been treated by many investigators. Curve fitting techniques, line half-widths, and the wavelength shift of the peak intensity are the three methods that are used most for the measurements. Some formulas are given in Figure 9. The

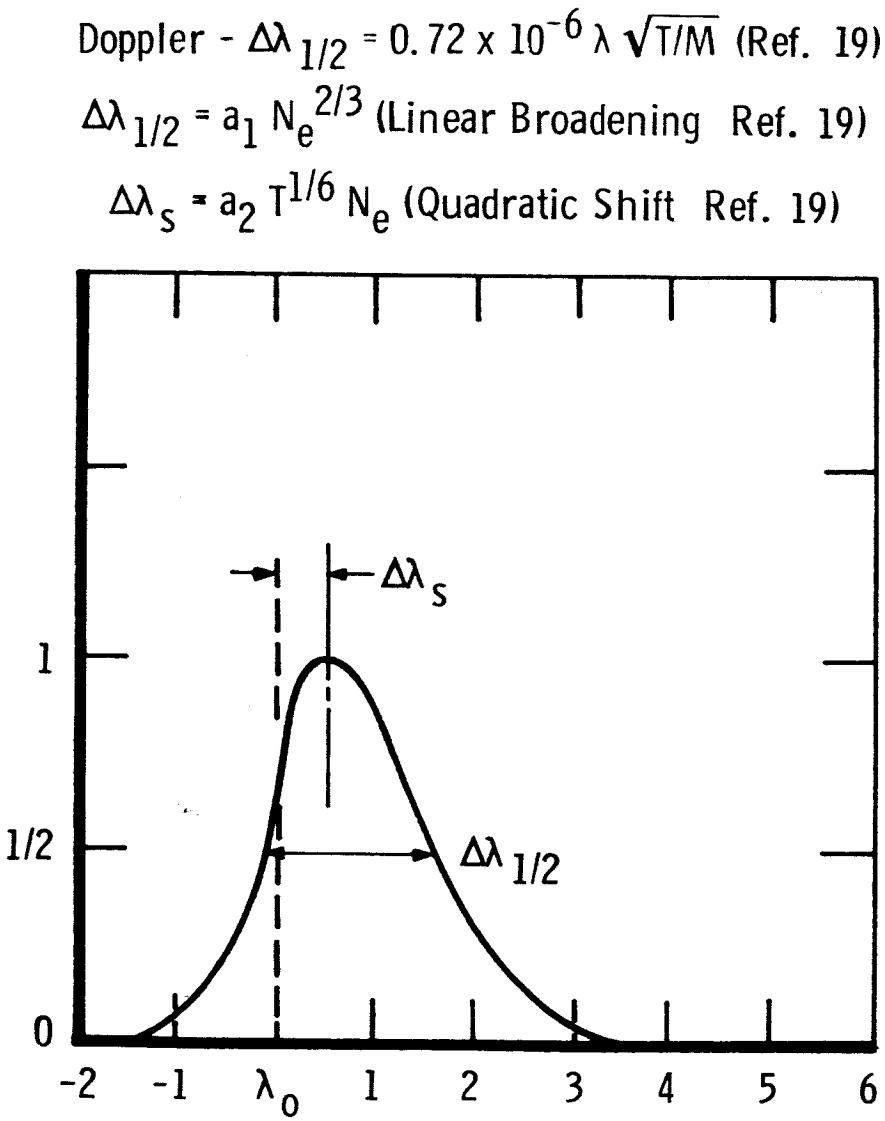

FIGURE 9. Illustration of line profile and line shift methods of temperature measurement.

measurements are fairly insensitive to temperature but serve very well as a measure of the electron density. Thus, to obtain a temperature, the electron density is put into the Saha equations and temperature obtained in this way. [Many recent articles exist on this subject, but for a good starting point, the reader is referred to the work of H. Margenau (**19**).]

COMMON FACTOR IN ALL METHODS

It is not surprising, that in all the methods considered, a common denominator can be found. This is the fact that the concept of a Maxwell–Boltzmann distribution of some energy parameter has entered into each formula. It is only through such most-probable distributions that a temperature is defined. For the spectral line intensity formulas, the distribution was of the excited electronic states of the atom; this distribution in turn was dependent upon the kinetic energy distribution of the governing excitation collisions. For application of the peaking function method, the additional requirement of chemical equilibrium was applied, which again was dependent upon the energy distribution of the particle collision governing the ionization of the atom. The governing collision can be identified fairly well for a high density discharge. The frequency of electron–atom encounters is so much greater than that of atom–atom collisions that it is clear that the electrons govern the excitation and ionization in a discharge.

In the case of the continuous emission, the governing distribution is clearly the free electron velocity distribution. For the molecular band intensity method, the distribution of vibrational or rotational states is the prime factor relating to temperature; but these in turn are maintained by collisional activity which again brings us to a particle velocity distribution. The Planck–Kirchhoff method, however, departs from this pattern in that the underlying distribution function is of the energy in harmonic oscillators. At first glance, this method would seem to depend upon radiative equilibrium rather than any kinetic velocity distribution. However, the equivalence of the method to the spectral line intensity distribution is demonstrated in reference (**18b**).

The line profile method using the Doppler broadening is quite clearly related to temperature through the velocity distribution of the emitting species. The Stark effects, of course, are only slightly dependent upon the temperature, but the relation to a Maxwell–Boltzmann energy distribution is obtained by going from the electron density to temperature via the Saha equation, which, in turn, is governed by an M–B distribution of the kinetic velocities of the colliding particles which produce the ionizing reaction.

All this leads to the point of considering just what has been measured by the various spectrographic methods. In each case the governing factor has been traced to a kinetic velocity distribution. This is good because this is precisely what is required: to measure the parameter T in the velocity distribution of the gas particles, $v^2 \exp(-mv^2/2kT)$. Two difficulties appear now which must be reckoned with if the measurements are to be understood. First, is it true that the velocity distribution of the particles governing the excitation and radiation processes is Maxwellian? Second, even though the distribution is Maxwellian, does it have the same parameter T as the gas particle velocity distribution whose parameter T is being sought?

To the first question, it is highly unlikely that any of the kinetic energy distributions would not be Maxwellian (**1**). Observation of electron velocity distributions are almost always reported to be Maxwellian, even in fields where the strength is several hundred volts per centimeter, except at very low pressures. Relaxation

times for heavy particles may be somewhat longer but certainly no longer than a micro-second. It is expected that the velocity distributions would be Maxwellian, and this would also suggest that excited electronic, vibrational, and rotational states should be distributed accordingly. It is also expected that chemical reactions would behave in an equilibrium manner and at a temperature ascribed to the velocity distribution of the particle governing the collision.

There is not so much confidence in the answer to the question of whether all distributions can be described by the same temperature parameter. In order to arrive at a meaningful answer, some actual data will be considered.

EXAMPLE OF MEASUREMENTS ON ARC PLASMA JET

Consider the plasma jet, being used as the model, exhausting into atmospheric pressure. Certainly it is expected that all particle velocities, mean free paths, and other particle kinetic properties will be distributed in a Maxwell–Boltzmann manner at these high densities. The second question, that of the equality of the electron and gas temperatures, has been answered by some investigators by the following argument:

> The value of E/p (field strength in volts/cm divided by the pressure in mm of Hg) is much less than one—about 0.01, in fact. Therefore, elastic collisions are dominant. At these pressures and field strengths, terminal velocity of the electrons is reached in a very short space. Therefore, the energy gained by the electrons between collisions is all given up as kinetic energy in the next collision. Thus the equation
>
> $$\frac{T_e - T_g}{T_e} = \frac{M}{8m} \frac{eE\lambda_0^2}{\frac{3}{2}kT_e}$$
>
> holds. If values of the constants for argon are substituted, it is found that $T_e - T_g \leq 0.02 T_e$, and thus it has been concluded that the gas temperature is sufficiently close to the electron temperature so that a measure of T_e is sufficient to define T_g. Now a measure of temperature by any of the spectroscopic methods on line intensities or the continuum radiation is clearly dependent on the distribution of velocities in the tail of the distribution function so that the measurement is considered a valid measure of T_e or T_g.

Many investigators have made measurements of temperature spectroscopically at positions just downstream of the orifice in plasma jets. Most of the results gave temperatures of 15,000 to 20,000°K at the center of the jet, tapered to 8000 to 10,000°K at the edges, and then dropped sharply to ambient. Although most investigators who made simultaneous energy-balance measurements found this temperature to be smaller by a factor of 5 or so, the usual explanation was that gradients in the boundary layer were so steep that if an average over all the mass were taken, the average spectroscopic temperature would be equal to the energy balance temperature. It is proposed that this may not be an adequate interpretation.

In the measurement program in our laboratory, measurements of temperature using the Fowler–Milne method were made, and results similar to those reported in Figure 6 for an argon plasma using both the 4158 Å line and the adjacent continuum radiation were obtained (**16**). Similar results were obtained for a nitrogen plasma (**20**). An attempt to locate the stream boundary showed it to be almost identical with the radiation boundary. Then, when an enthalpy calculation across the stream was performed by using corrected values of enthalpy as a function of temperature, it was found that the enthalpy differed by a large factor from the known energy input. The inescapable conclusion was then that $T_e \neq T_g$.

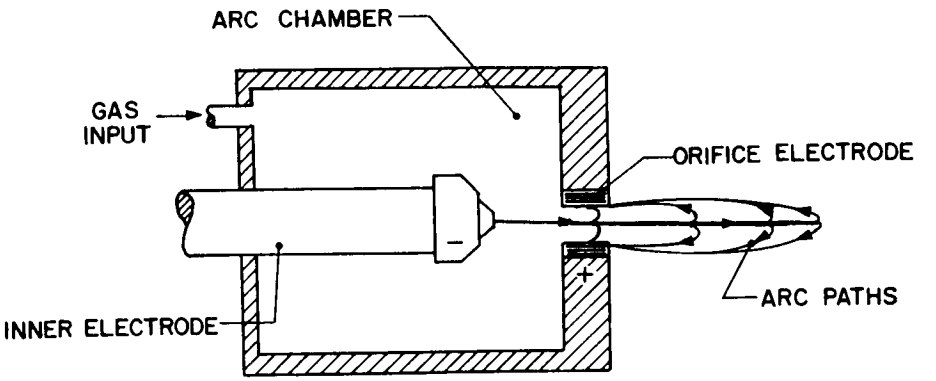

FIGURE 10. Illustration of the blown-arc mechanism in plasma jets having the Gerdien electrode configuration.

The above decision was somewhat altered by later work with probes which showed that the arc was in reality a filament of discharge moving about over the envelope at high frequency. See Figure 10 (7). This allowed two possible interpretations. First, the discharge region could have consisted of an electron gas at a much higher temperature than the heavy particles. Second, local thermodynamic equilibrium could have existed but only over a very small volume at any one time, so that $T_e \simeq T_g$ locally but the average T_g was much lower than measured spectroscopically. Which interpretation to use will not be discussed here, but it must be noted that this is a case where the spectroscopic methods gave correct results but the wrong answers.

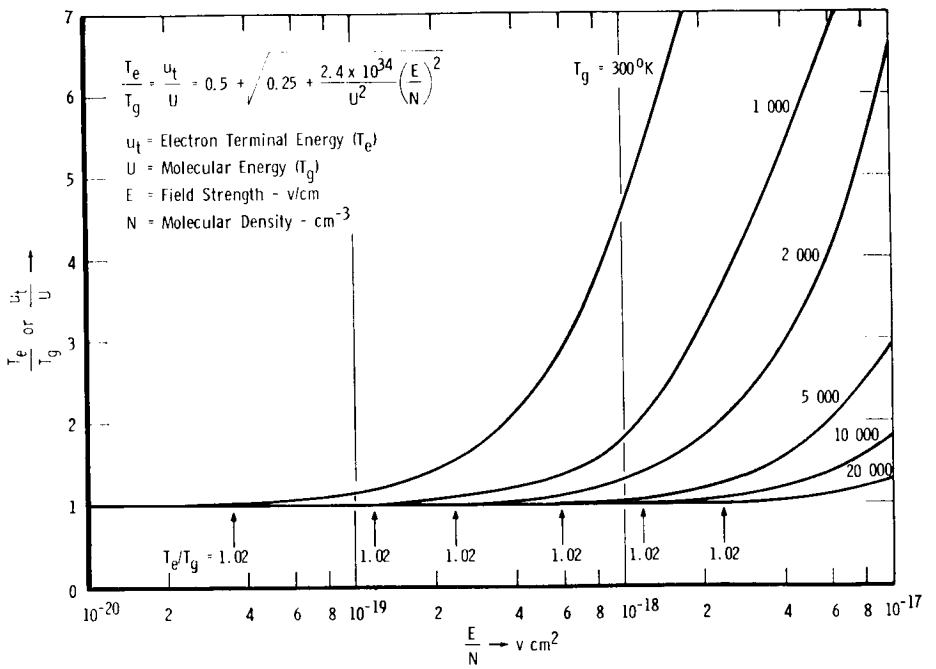

FIGURE 11. u_t/U versus E/N for various gas energies; condition for electron terminal energy to be reached. (Argon used for calculation.)

LIMITATION OF E/p CRITERIA

This seems a good place also to discuss the reasoning leading to the above conclusion that $T_e = T_g$ merely from the E/p criteria and the equation. A re-examination of that criteria (**20**) reveals that the original treatment did not consider the flow of gas through the tube but dealt only with closed discharge tubes. Also, the mechanism of energy loss to the apparatus was not considered since the principle concern at that time was with measurements on electron behavior. Two results of such a re-examination are shown in Figures 11 and 12, where argon gas has been taken as the test gas. In the first, it is shown that the approach of T_e to T_g is a function not only of E/N, where N is the particle density per cm^3, but also of T_g itself which is governed either by energy transfer to the walls of a container or by flow of the gas through the discharge. Thus, at a normal field strength of 20 volts/cm and a density of 10^{19} per cm^3, $T_e/T_g \simeq 2$. The other facet of this re-examination introduces the dwell time of the heavy particles in the discharge for gases that flow through the discharge freely or are forced through. Shown in Figure 12 is a plot of the approach of T_g to T_e as the gas flows through the discharge and also a plot of the time necessary for $T_g = 0.98T_e$ as a function of the pressure. For example, at a pressure of one atmosphere, the time required is about 11 μsec. A gas flowing at

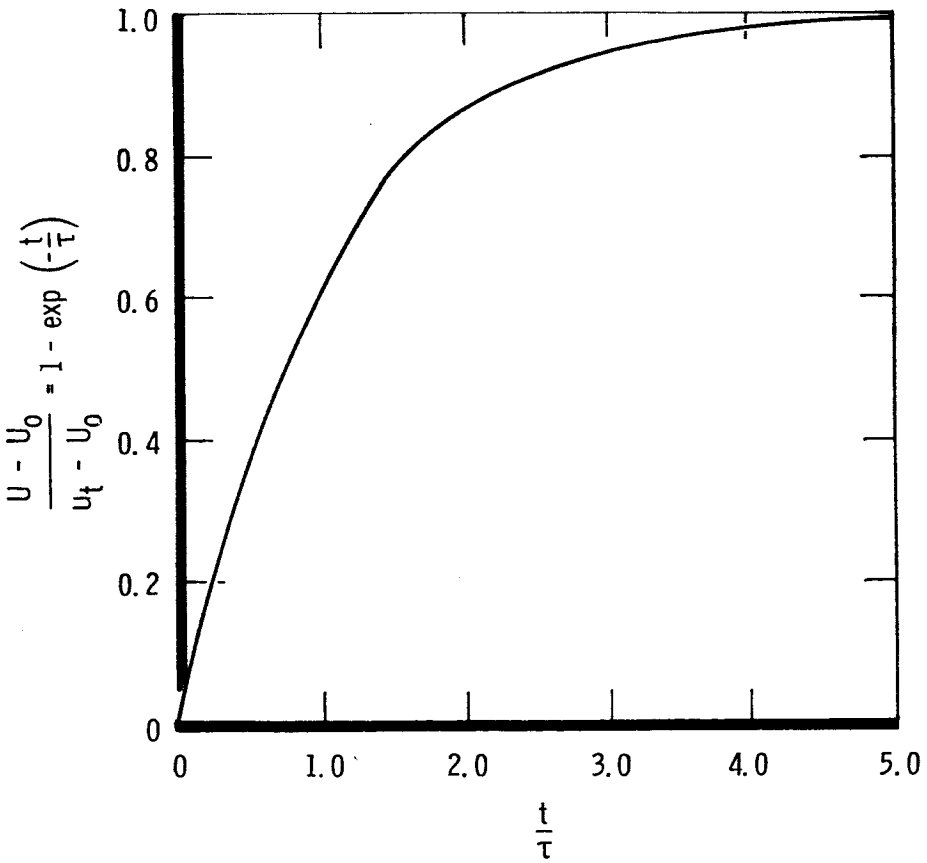

FIGURE 12a. $(U-U_0)/(U_t-U_0)$ **versus** t/τ, **showing the approach of the molecular energy toward the electron energy when the molecule either enters the discharge by convection or is forced through by a pressure field.**

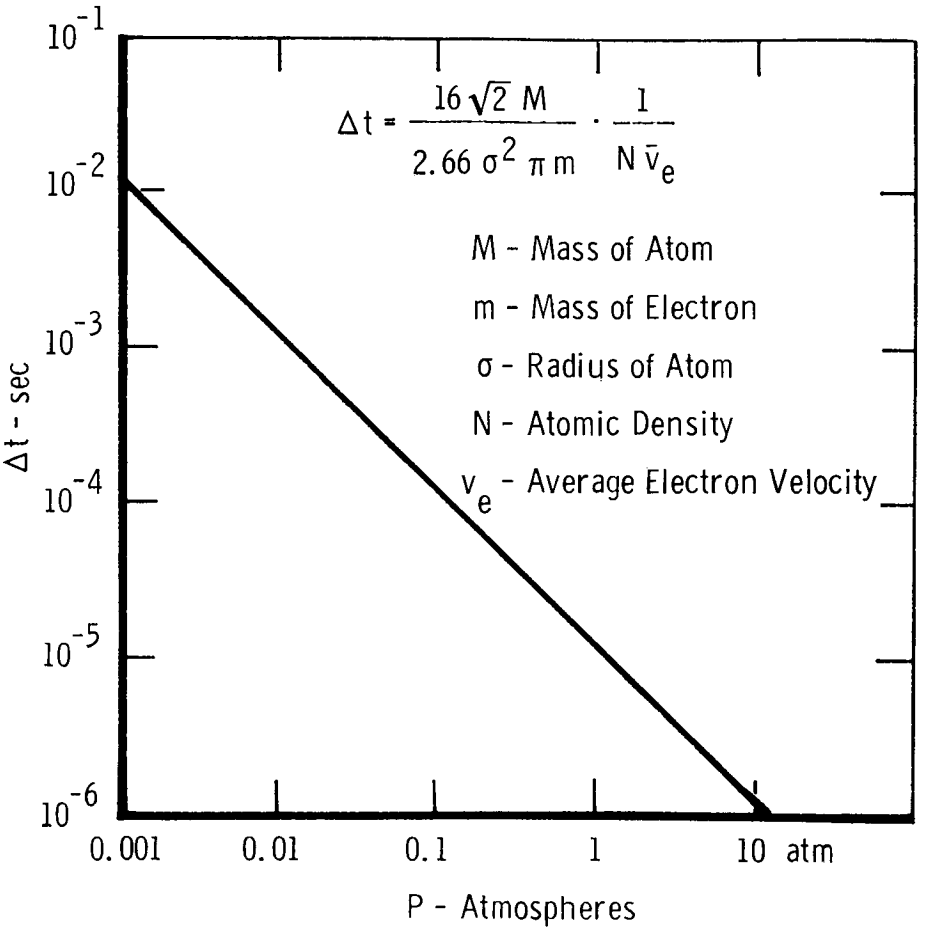

FIGURE 12b. Time required for temperature of heavy particles to approach temperature of electrons as a function of pressure; curve shown is for argon at a temperature of 5000°K.

Mach 0.9 through a 1-inch-long orifice would remain in the discharge for about 20 μsec, and almost complete heating would be expected. However, the Gerdien arc, with its blown, high-frequency arc channels, does not comply with the idealized 1-inch-long discharge considered in reference (**20**). The point is this: that most of the arc discharges being used are on the borderline insofar as the theoretical prediction of $T_e = T_g$ is concerned and that some of the more exotic forms of electrode configuration simply do not provide enough dwell time of the heavy particle in the discharge. Therefore, on such devices one would expect the spectroscopic temperature to be the electron temperature, and a closer look would be required in order to say how T_e differed from the gas temperature.

VALID MEASUREMENTS

The results and interpretations given above for the blown arc configuration are not, of course, always encountered. In many cases reported, references (**11**) and (**18**), for example, the spectroscopic measurements of the temperature of atmospheric jets seemed quite reasonable and agreed with expected temperatures from

energy-balance considerations. Closer examination showed that these measurements were made under low flow operating conditions where the arc was not blown outside the nozzle. This mode of operation is sometimes referred to as the "laminar mode". Thus, it appears that the prime consideration of the experimenter should be to know something of the plasma region being measured except that it radiates light. If the region contains a part of the discharge, then caution is in order; if it is the field-free region, then (barring a case to be presented in the next section) good measurements can be obtained.

PHENOMENOLOGICAL MEASUREMENTS

The spectrograph has always been employed to study occurrences in nature by a sort of detective pattern, particularly by the chemist. A rare opportunity has recently come to light in working with low-pressure plasma plumes. Perhaps first the dilemma of the visibly-radiating, low-pressure plume should be explained. Considering the plume shown in Figure 2, suppose the temperature at the exit is of the order of 5000°K, then the static temperature in the expanded plume will range from some 300° to 500°K upstream of the normal shock to some 1200° to 1500°K downstream of the shock. Both of these temperature ranges are much too low to produce thermal radiation from the argon gas. Furthermore, the lifetimes of the excited states are of the order of 10^{-8} to 10^{-7} seconds so that any excitation in the arc region would radiate within about a millimeter. If recombination were the exciting mechanism, some continuum radiation would be expected. This does not occur, as shown in Figures 3 and 4. Also, recombination rates are such that any recombination in argon would be expected to occur well downstream. Electron excitation is ruled out because of the low electron temperature measured with Langmuir probes. Therefore, the source of the radiation was at first a mystery.

MECHANISM OF RADIATION

Dr. John Dicks suggested that the radiation might be the result of metastable atoms that are excited in the arc region, proceed downstream, and then are further excited by collisions and radiate to the ground state (**21**). Spectrographic studies to determine if this hypothesis was indeed true led L. E. Brewer of ARO, Incorporated, into some quite interesting phenomenological evidence (**22, 23**). It was discovered that the metastables were responsible for the radiation by noting the behavior of the stream under a series of quenching experiments. It was found, for example, that the addition of a small amount of hydrogen to the cell would effectively quench the radiating stream, whereas helium had little effect upon it. The key experiment was perhaps the selective excitation of the nitrogen molecule which was mixed with the stream from the ambient gases. It was found that the second positive N_2 band always appeared in the spectrum, while bands originating from levels higher than about 11.75 volts just did not appear. Figure 13 illustrates that this phenomenon is almost perfectly explicable in the light of excitation by collisions with the metastable argon. Many other interesting excitation processes, such as production of the CO^+ comet tail system when CO_2 was added, were observed.

The importance of this carrier of metastable atoms into a field-free region where reactions with various molecules can be observed is just now being realized. Other experimenters working at the University of Texas (**24**) have recently reported on similar phenomena, using apparatus which is excited initially by RF energy. Previous investigations of this kind have been confined to short-lived afterglow apparatus in which the measurements had to be made in about 0.1 μsec. Here the

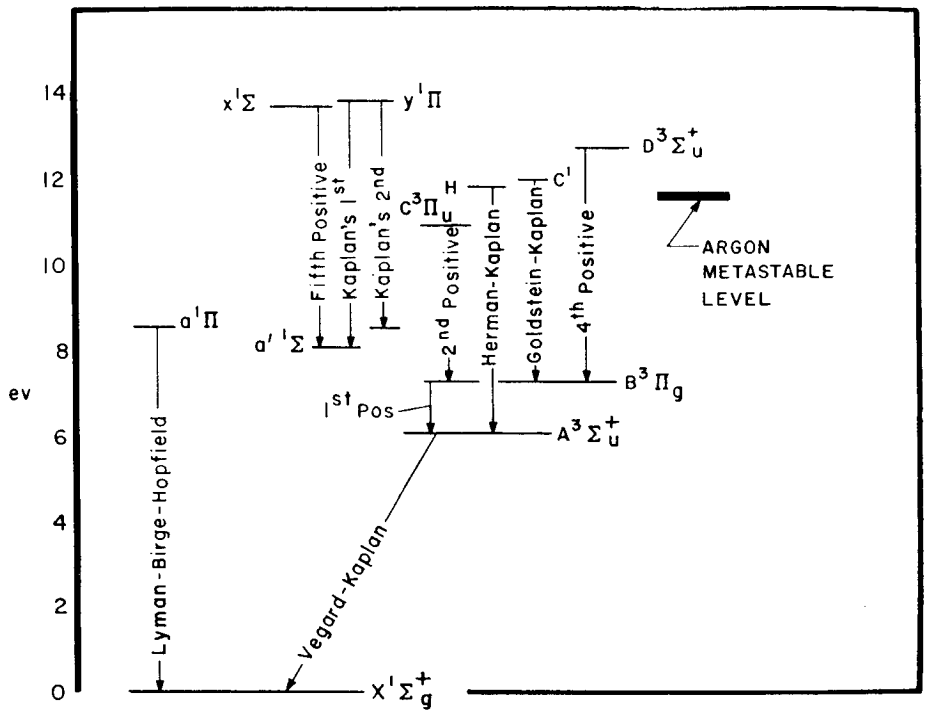

FIGURE 13. Partial energy level diagram of N_2 illustrating the selective excitation of the second positive system by collisions with argon metastables.

plasma stream might be termed a "continuous afterglow", spread out in time by the flow process. Some worthwhile fundamental work using this apparatus is anticipated.

MECHANISM OF EXCITATION

The next question that arose was the mechanism of the excitation of the metastable argon, since radiation from levels as much as 3.5 eV above the metastable level was detected. Three possible sources were suggested: electrons, photons, or thermal collisions. The first was ruled out because of the low density. The second was considered unlikely but possible. The third was intuitively discarded at first because of the very low temperatures. In investigating the latter mechanism, a new way of writing the distribution function for excited states was tried (**25**). Two distributions were written, one with ground level at zero and the other with ground level at the metastable energy. These were then summed to give a new distribution function. The results were quite surprising. For example, if the density of metastables is taken as the value that would be excited at the 15,000°K electron temperature measured in the discharge, and if the gas temperature is assumed to be 5000°K, the population of excited states is altered by several orders of magnitude. In this case, the number of metastables would be only 0.0009% of the total particle density. This is shown by the two distributions in Figure 14. Although this calculation seems a bit fictitious upon first glance it does indicate the tremendous effect that a few metastables can have. The effect is also seen by the illustrative energy distribution shown in Figure 15. Here the kinetic energy of the colliding particles is shown, and the excitation energies of the argon levels are drawn in.

$$\frac{N_n}{N_0} = \left[\frac{1}{U_0} - \frac{N_m}{N_0 U_0} + \frac{N_m}{N_0 U_m}\exp(E_m/kT)\right] g_n \exp(-E_n/kT)$$

N_0, N_m, N_n = Number Density of gnd. State, Metastable and Excited Atoms

U_0, U_m = Partition Function of gnd. State and Metastable Atoms

E_m, E_n = Energy of Metastable and Excited Levels

g_n = Statistical Weight

k = Boltzmann Constant

T = Temperature

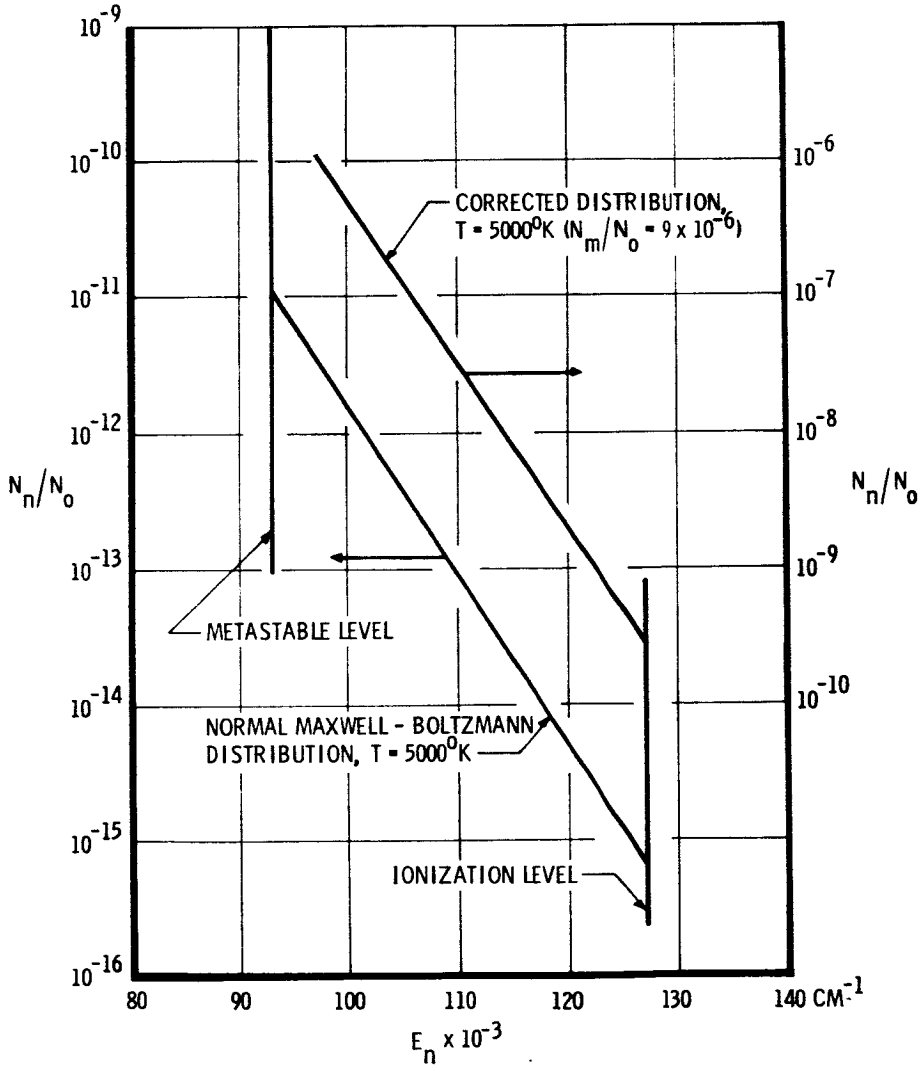

FIGURE 14. Energy state distributions for argon showing influence of metastable states.

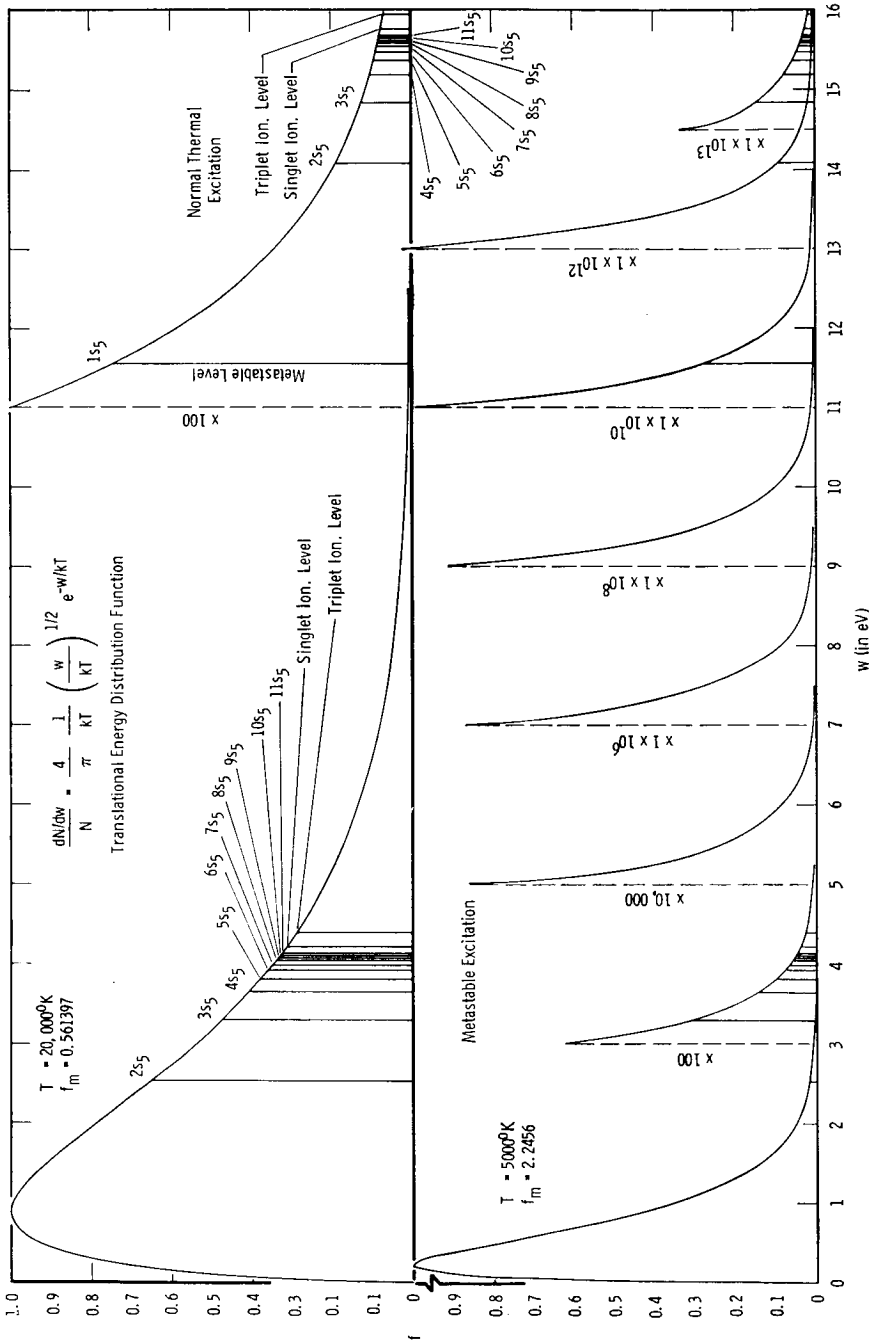

FIGURE 15. Illustration of collisional excitation mechanisms and the influence of metastable states on the number of possible excitation collisions.

At the far right, the normal excitation by collisions is illustrated. At the left, the energy required to excite a metastable level to a higher level is shown, and the tremendous difference in the number of such possible collisions is graphically portrayed.

TEMPERATURE MEASUREMENT

Another unexpected result of this analysis was that the character of the exponential distribution was retained (see the equation in Figure 14). This suggested a closer examination of the spectrum of the expanded plume to see if the distribution was actually retained. Successful verification would not only provide confidence in the principle used but would also provide a temperature measurement. Preliminary results from such measurements do indeed verify that an exponential distribution of excited states exists and, in addition, the temperatures so measured agree favorably with calculated values from energy balance and aerodynamic calculations. It remains for more data to be obtained so as to verify unquestionably these preliminary measurements.

CONCLUDING REMARKS

To summarize briefly the remarks on temperature measurement by spectroscopy, the methods which use the spectral line intensity or the continuum intensity formulas may be used to obtain a measurement of the excitation temperature of plasmas which are employed for gas dynamic purposes. However, in order to relate the excitation temperature to gas temperature it is necessary to know the mechanism of excitation. In arc discharge regions, excitation is almost always a result of electron-atom collisions, and thus the measured temperature is the electron temperature. Then other methods or analyses are required in order to ascertain if the gas temperature and electron temperature are the same. In low pressure, field-free regions where metastable atoms are the chief contributors to the radiation, absolute intensity measurements mean little unless the formulas are modified in the manner discussed. However, it has been shown that a relative line intensity method is valid for the higher excited levels.

For gases containing molecules which have a band structure that is relatively simple, the individual lines within the band are excited for the most part by molecule–molecule collisions so that they provide quite a good thermometer. Unfortunately, most of the molecules which can be used are impurities, such as CN or C_2, or are formed under mysterious circumstances, such as NO, so that they are not of as much use as would be thought.

The practice of using impurity metallic lines is considered by this author to be somewhat open to question because of the proper mixing and vaporization. Insertion of slight impurities of a vaporable metal is better but still frowned upon. After all, one purpose of the gas dynamics facility is to provide a non-contaminated gas stream. Then, too, it just does not seem quite right to use radiation other than from one of the molecules present in the test gas.

The methods employing Planck's energy distribution and Kirchhoff's laws seem to give adequate results, but the dependence upon wavelength does not seem to be fully explained. Another concern is with the gradient across the stream and the complicated way in which this affects the absorption. The restriction to infrared wavelengths is not necessarily a problem but one which needs more study.

The methods which employ Stark broadening and shift of spectral lines are very good tools for high-temperature plasmas. The wealth of literature on this subject attests to its value. However, at lower temperatures—3000° to 15,000°K—the

methods are not generally applicable because of the instrument resolution problem and the overlapping of several broadening processes. Doppler broadening, which seems a very good technique conceptually, also suffers from the overlapping problem, particularly by pressure broadening as the pressures of plasma jets are continually pushed upward. Unfortunately, pressure broadening is not well enough defined that measurement techniques can be based upon it at present. These methods then would seem to require more study before they can be put to work for arc-heated plasmas.

The material presented in this paper has not been aimed primarily at introducing new methods or data for the diagnostics of plasmas. Rather, the theme has been that of stressing the importance of proper interpretation of the results of spectral measurements. Two concepts have been presented that are of most significance. First, seemingly good temperature measurements using spectroscopic data, even by two or three methods, should not be accepted without critical review of the physical situation. Second, metastable states, which occur in all but single electron atoms, play an important role in the radiative emission process. Still, the spectroscopic methods of diagnostics are the most powerful at our disposal for the understanding of plasmas.

ACKNOWLEDGMENT

The author gratefully acknowledges the contributions to this paper by his colleagues, Messrs. M. T. Dooley and L. E. Brewer, who have greatly influenced the interpretations which have been presented on the spectroscopic measurement of plasmas.

REFERENCES

1. Druyvesteyn, M. J., and Penning, F. M., "The Mechanism of Electrical Discharges in Gases at Low Pressure", *Rev. Mod. Phys.*, **12**, No. 2, 87 (April, 1940).
2. Aller, Lawrence, H. *Astrophysics* (New York: Ronald Press, 1953).
3. Browning, J. A., "Techniques for Producing Plasma Jets", in *Dynamics of Conducting Gases* (Evanston: Northwestern University Press, 1960), 126–138.
4. Gerdien, H., and Lotz, A., "On a Light Source of Very High Surface Brightness", in *Wissenshaftliche Veroffantlichungen aus den Siemens-Werken*, **2**, 489 (1922).
5. Reid, J. W., "High Pressure Arc Jets", *ASME Paper No. 61–WA–246*, presented at Winter Annual Meeting, 1961.
6. Schoeck, P. A., and Eckert, R. G., "An Investigation of Anode Heat Transfer in High Intensity Arcs", in *Vth Inter. Conf. on Ionization Phen. in Gases* (Amsterdam: North-Holland, 1961), 1812–1829.
7. Dooley, M. T., McGregor, W. K., and Brewer, L. E., "Characteristics of the Arc in a Gerdien-type Plasma Generator", *ARS Journal*, **32**, 1392–1394 (1962); comments on "Characteristics of the Arc in a Gerdien-type Plasma Generator", *AIAA Journal*, **1**, 3, 723 (1963).
8. Harvey, J. K., Simpkins, P. G., and Adcock, B. D., "Instability of Arc Columns", *AIAA Journal*, **1**, 3, 714–716 (1963).
9. McGregor, W. K., Erlich, J. J., and Bratcher, J. D., "The Visible Plasma Flame Spectra of Argon and Helium", *AEDC–TN–59–134* (December, 1959).
10. Brewer, L. E., McGregor, W. K., and Dooley, M. T., "Spectral-line Intensities from Argon and Nitrogen Plasmas", *J. Am. Opt. Soc.*, **52**, 829 (1962).
11. Winter, E. R. F., and Cremers, C. J., "Temperature Distribution in a Low Mass Flux Argon Plasma Jet", *ARL 62–388*, University of Minnesota (July, 1962).

12. Shipley, K. L., "Preliminary Study of Spectrographic Temperature Measurements of an Argon Plasma Jet", Tech. Memo. of the Sandia Corp. (May, 1961).
13. Fowler, R. H., and Milne, E. A., *Monthly Not. R.A.S.*, **83**, 403 (1923); **84**, 499 (1924).
14. Olsen, H. N., "Thermal and Electrical Properties of an Argon Plasma", *Phys. Fluids*, **2**, 6, 614–623 (1959).
15. Knopp, C. F., Gottschlich, C. F., and Cambel, A. B., "A Spectroscopic Technique for the Measurement of Temperature in Transparent Plasmas", *AF-OSR-1100*, Northwestern University (July, 1961).
16. McGregor, W. K., and Dooley, M. T., "Spectroscopic Diagnostics of a Gerdien-Type Plasma Stream Using Argon", in *Temperature—Its Meas. and Cont. in Sc. and Ind.* (New York: Reinhold, 1962) **3**, Part 2, 467–477.
17. Dickerman, P. J., and Morris, J. C., "Experimental Studies of the Temperature in a Field-Free Plasma", in *Optical Spectrometric Measurements of High Temperatures* (Chicago: University of Chicago Press, 1961), 170–180.
18. (a) Tourin, R. H., *Temperature—Its Meas. and Cont. in Sc. and Ind.* (New York: Reinhold, 1962) **3**, Part 2, 455–466; (b) Ryan, L. R., Babrov, H. J., and Tourin, R. H., *Infrared Spectra and Temperatures of Plasma Jets* (New York: Warner and Swasey Company, 1962).
19. Margenau, H., "The Structure of Spectral Lines from Plasmas", in *IVth Inter. Conf. on Ionization Phen. in Gases*, Vol. II (1959), 791–807.
20. McGregor, W. K., and Brewer, L. E., "Re-examination of the Criteria for Thermal Equilibrium in Electrical Discharges", in *VIth Inter. Conf. on Ionization Phen. in Gases*, Paper No. II-28 (Paris, 1963).
21. Templemeyer, K. E., and Dicks, J. B., "Some Gas Dynamic Characteristics of Argon Plasma—Application to Jet Spreading", *AEDC-TDR-62-88* (July, 1962).
22. Brewer, L. E., and McGregor, W. K., "Excitation of Nitrogen by Metastable Argon Atoms", *Phys. Fluids*, **5**, 1485–1486 (November, 1962).
23. Brewer, L. E., and McGregor, W. K., "The Radiative Decay of Metastable Argon Atoms in a Low-Density Argon Plasma Stream", *AEDC-TDR-63-5* (January, 1963).
24. Collins, C. B., and Robertson, W. W., "Helium—Admixed Gas Reactions in a Flow System", in *VIth Inter. Conf. on Ionization Phen. in Gases* (Paris, 1963).
25. Brewer, L. E., and McGregor, W. K., "The Influence of Metastable Atoms on the Population of Excited States in a Thermal Plasma", in *VIth Inter. Conf. on Ionization Phen. in Gases* (Paris, 1963).

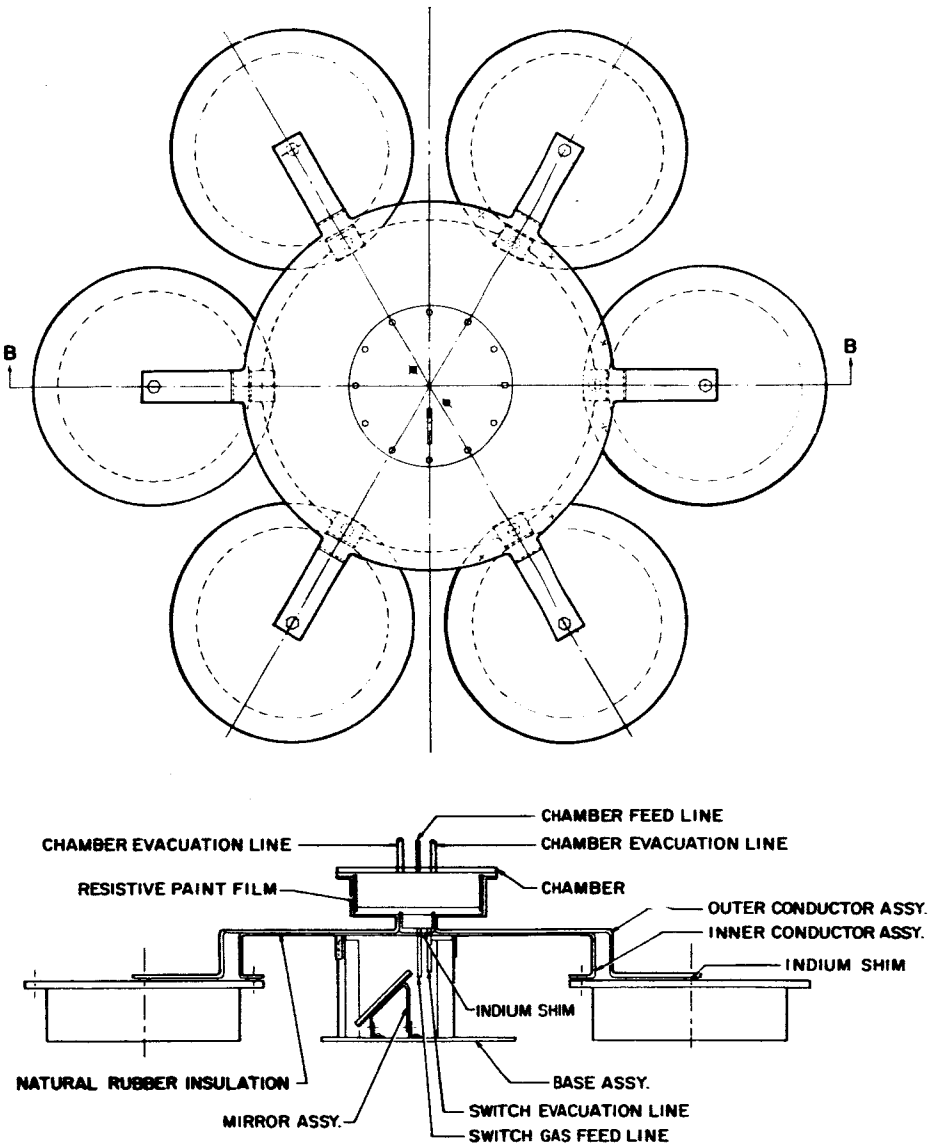

FIGURE 1. Test rig assembly.

One of the promising techniques for investigating plasma processes is the monitoring, on a time-resolved basis, of their radiation by spectroscopic and photographic means. It is the purpose of this paper to describe a preliminary experimental program designed to reveal, principally by submicrosecond-resolved emission spectroscopy, the types of specie excitation and induced chemical reactions created by a hypersonically-driven arc discharge in initially quiescent, low-pressure, elemental gases and detonable mixtures. In this case, the arc discharge is the plasma source.

9. Kenneth M. Foreman and Maurice E. Levy: *Comparative Spectroscopic Studies of Electromagnetically-Driven Hypersonic Waves in Elemental Gases and Detonable Mixtures*

Time-resolved emission spectroscopy has been used to analyze electro-magnetically driven plasmas created by arc discharges in quiescent, low-pressure elemental gases and detonable mixtures. The electrical energy was supplied by an R–L–C circuit in the form of an 8-μ*sec pulse. Stainless steel electrodes with a hyperbolic contour, mounted in parallel within a cylindrical discharge chamber, created a constant-area flow channel in which wave speeds between* 8,000 *and* 25,000 *ft/sec were recorded.*

The relative excitation of hydrogen Balmer lines, the long decay time of the 5876 Å *helium emission line, and the time variation of molecular-oxygen ion emission are typical data presented (and related to the arc-discharge–current waveform). Also presented is the emission spectrum from a stoichiometric hydrogen–oxygen mixture.*

Radiation from the $H_2 + \frac{1}{2}O_2$ *mixture with an initial pressure between* 1 *and* 11 mm Hg (*absolute*) *includes the* 5126 Å *band attributed to* OH. *This data indicates that it is likely that an exothermic chemical reaction proceeds within the order of* 1 μ*sec downstream of the driven hypersonic-wave field. It is believed that the reaction mechanism can be partially attributed to photochemical processes caused by ultraviolet radiative transfer from the intensely luminous plasma in the arc region.*

INTRODUCTION

A current part of the national space program is the effort to develop plasma devices for the primary propulsion of aerospace vehicles or the position and attitude control of artificial satellites. Knowledge of the composition and energy partition of plasmas used by these devices can lead to optimum designs and encourage more widespread application of these devices, including applications within the earth's atmosphere (**1, 2**).

ED. NOTE: Mr. Foreman and Mr. Levy are at the Republic Aviation Corporation, Farmingdale, Long Island, New York.

DESCRIPTION OF EXPERIMENT APPARATUS

TEST STAND

The test stand has provisions for six low-inductance capacitors arranged in parallel around a centrally-located discharge chamber. The capacitors are attached by an equal number of tabs radiating out from two collector plates (see Figure 1). These plates are separated by a 0.036-inch-thick, natural-rubber insulator that can withstand 10,000 volts.

The vacuum chamber and gas-fired switch are centrally located immediately above the collector plates. The electrode holder plates can accommodate 8-inch diameter electrodes and are separated by a dielectric spacer made of Alumina, fused quartz, or Mykroy. The attachment of the dielectric spacer to the perimeter of the metal electrode holders has been successfully achieved with epoxy cement.

The gas-breakdown electrical switch is ignited by a pulse of nitrogen gas into an initially evacuated chamber that stands off an impressed voltage. As the injected gas fills the switch chamber, the pressure increases until electrical breakdown occurs. Several resistive-paint stripes having a total resistance of 250,000 ohms are located along the dielectric spacer and electrically connect the upper and lower electrode holders to make them, initially, of equal potential. This arrangement permits the switch to be fired but limits current flow to milliamperes so that an arc discharge is provided in the reaction-chamber gas. Three-inch-long quartz windows in the electrodes and electrode holders permit monitoring with optical diagnostic devices.

The cylindrical, stainless-steel electrodes mounted in the chamber have a hyperbolic contour over the outer third of their discharge surface to present, essentially, a constant-area flow channel for the first 1.3 inches of radial travel inward from the periphery. Thereafter, the channel area decreases. Figure 2 shows two photographs of the test stand equipment.

With five capacitors rated at a nominal 6 μf each, a transient, damped-current waveform with an initial peak at 1.8 μsec was produced. The other circuit parameters were computed from ringing-test data using Rogowski-coil pickups with $L=4.4\times10^{-8}$ h and $R=5\times10^{-3}$ ohms. The addition of a 0.10-ohm Nichrome resistance strip to each branch of the circuit produced a total circuit resistance of 2.5×10^{-2} ohms and theoretically attenuated the current to less than 0.1 of the maximum amplitude within 1.5 cycles. The initial rate of rise of current was about 3×10^{10} amp/sec, and current amplitude was related to initial capacitor voltage in the ratio of 16,000 amp/kV. Recorded current traces indicated essentially zero current after 8 μsec.

PHOTOMULTIPLIER RECORDING

A Leiss, single-prism monochromator was used in conjunction with a photomultiplier tube for observation of the emission radiation from the plasma and its flow field. Figure 3 is a schematic diagram of the experimental apparatus and their relative positions. The light transmitted through the quartz window covering slit A on top of the cylindrical discharge chamber is reflected by mirror C. The image of slit A is formed perpendicular to the monochromator entrance slit S_E. (This arrangement permits observation of that particular part of the plasma flow field where the slit S_E intersects the slit-A image.) The light received at slit S_E is then dispersed in the monochromator by a quartz prism. The beam that passes through the exit slit S_x falls on the photocathode of a DuMont 6467 photomultiplier tube, the output of which is displayed as a transient trace on a Tectronix 551

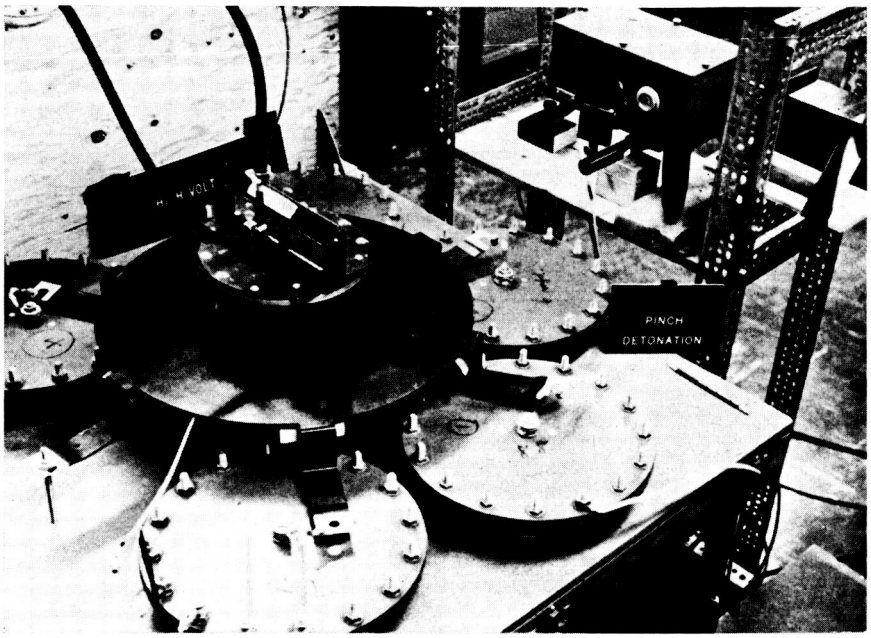

FIGURE 2a. Overall view of research test stand with spectroscopic analysis equipment in place.

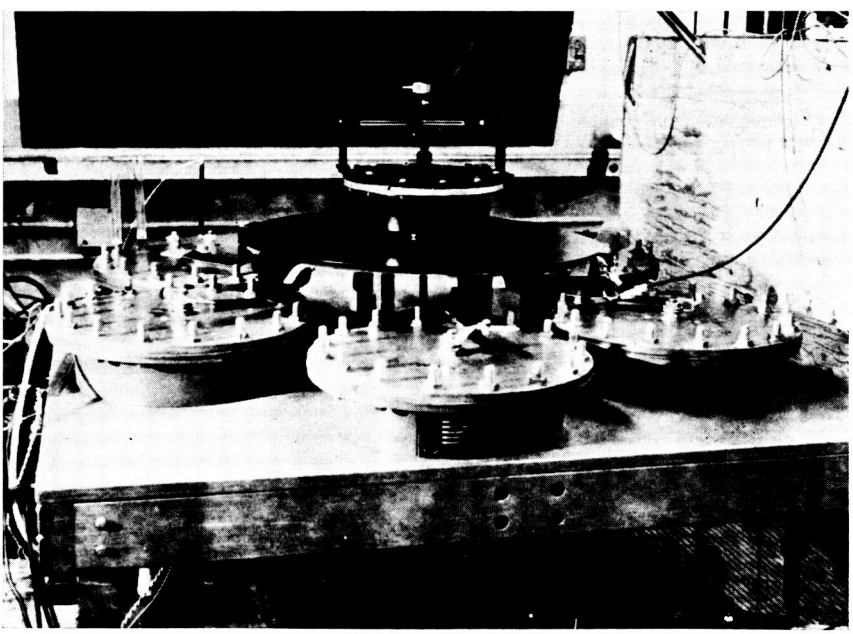

FIGURE 2b. View of research test stand seen from monochromator position.

oscilloscope and is recorded with a Polaroid camera. The photomultiplier tube has an S-11 response, a useful range between 3600 and 6000 Å, and a peak response near 4400 Å. The spectral range of the monochromator is 200 mμ to 20 μ.

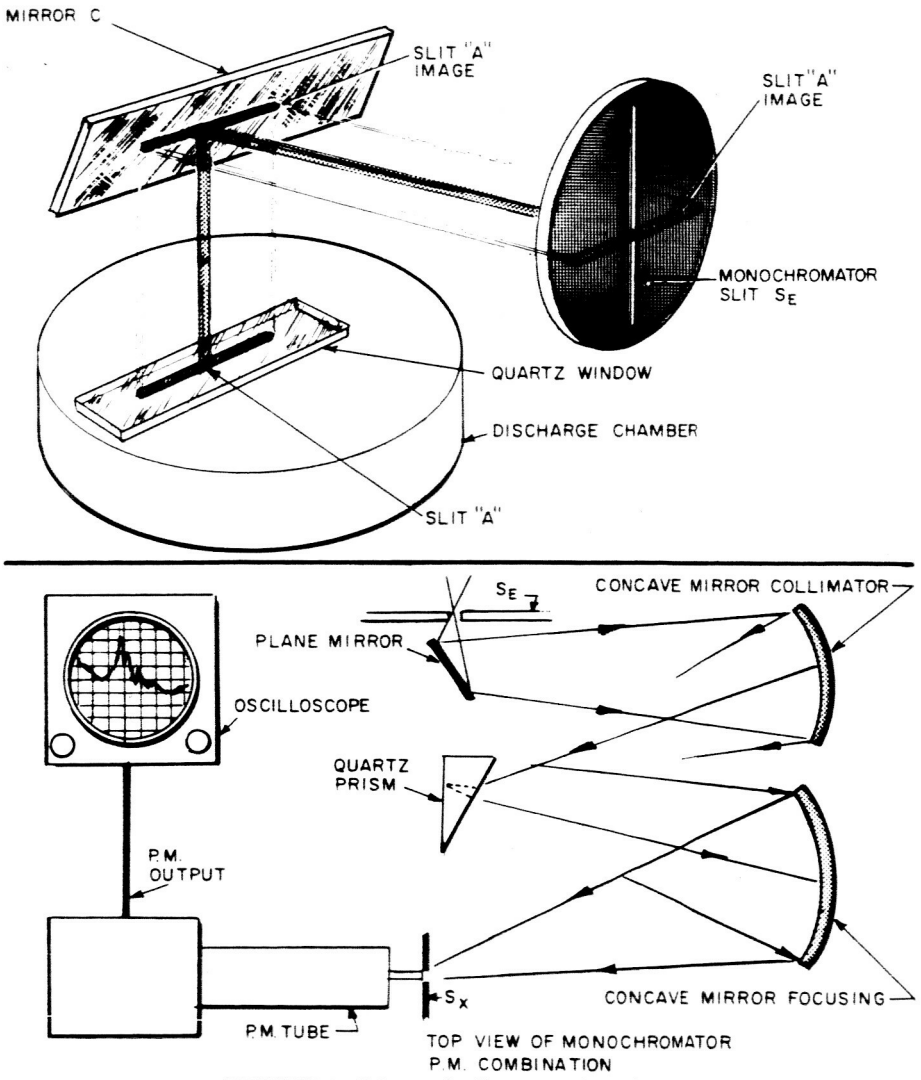

FIGURE 3. Schematic diagram of equipment.

The photomultiplier detector was operated at a supply voltage of 1800 V, and the output voltage was in the linear region of response, thus making it possible to compare relative intensities of emission lines after correcting for the spectral response of the photomultiplier and the transmission of the quartz prism. The photomultiplier circuit contained a 50-ohm output impedance to match the impedance of the unterminated coaxial line. Extraneous electrical noise signals were eliminated for all practical purposes by shielded enclosures around the photomultiplier and its connecting cables and, additionally, by having the photomultiplier about 4 feet from the discharge device.

PHOTOGRAPHIC RECORDING

A Spencer spectrometer (made by American Optical) was used for obtaining time-integrated photographs of a wide field of the discharge spectrum. This

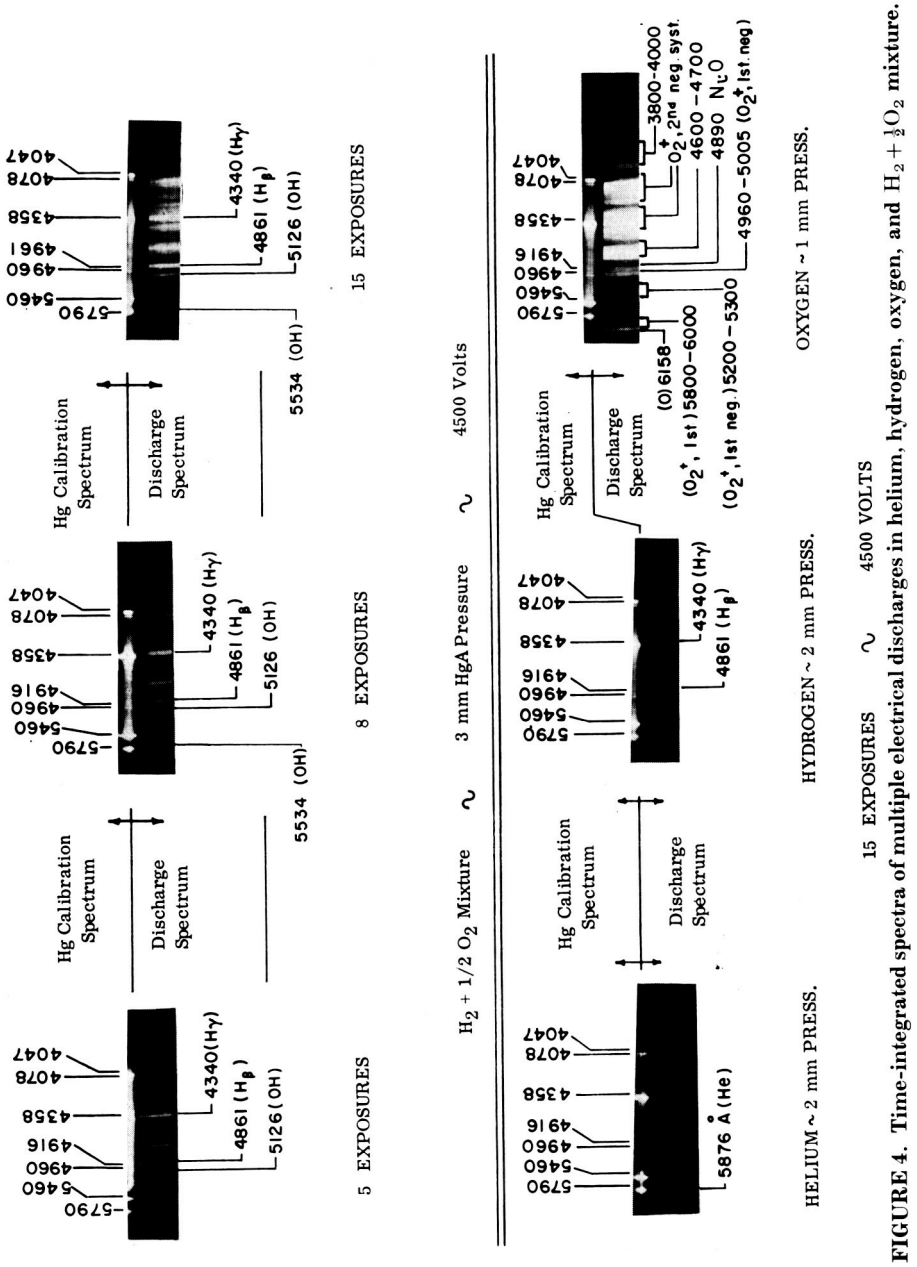

FIGURE 4. Time-integrated spectra of multiple electrical discharges in helium, hydrogen, oxygen, and $H_2 + \frac{1}{2}O_2$ mixture.

instrument has a focal length of 162.5 mm, an aperture of 25.4 mm, and a relative speed of $f/6.4$. The accessory camera supplied with this instrument was modified to accept a Polaroid film holder and was used to record the emission radiation on Polaroid ASA-3000 speed film.

The positioning of the entrance slit of the Spencer spectrometer was identical to the relative positioning of the entrance slit of the Leiss monochromator as shown in Figure 3. The entrance slit of the Spencer spectrometer was not calibrated so

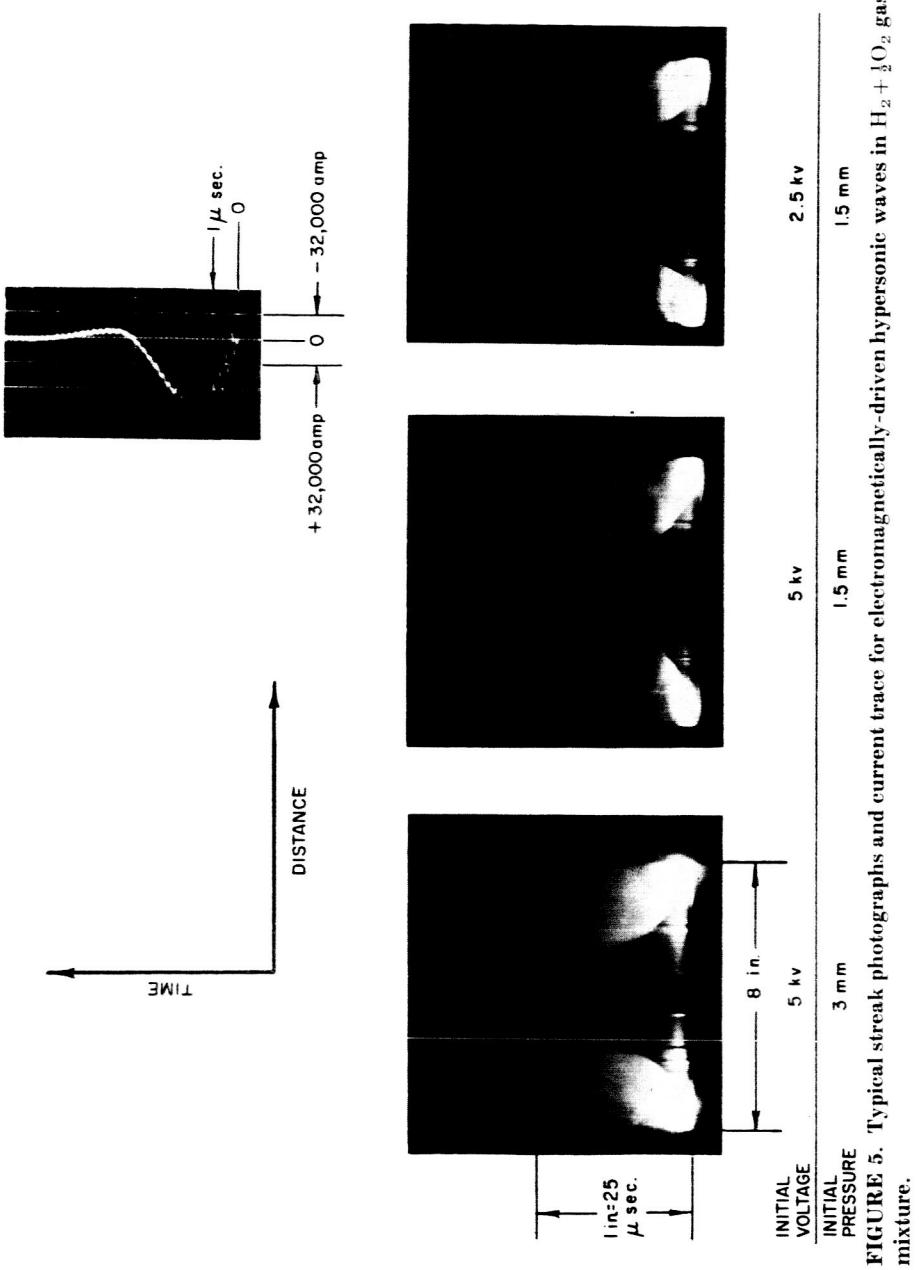

FIGURE 5. Typical streak photographs and current trace for electromagnetically-driven hypersonic waves in $H_2+\frac{1}{2}O_2$ gas mixture.

that it is not known exactly what size openings were used when photographing emission spectra, but it is known that they were of the order of 0.5 mm. It should be noted that despite the wide slit opening used, the $f/6.4$ speed of the instrument, and the ASA-3000 speed of the film, it was necessary to obtain about 15 superimposed discharge images (see Figure 4) to obtain a good photograph for any particular set of conditions. The discharge lasted for a period of about 8 μsec, but some emission lines or bands persisted for a longer period of time.

EXPERIMENTAL PROGRAM

Preliminary to the spectroscopic observations, a high-speed, rotating-mirror camera was used to obtain streak pictures on black and white and color film. These pictures, typified by those of Figure 5, were an aid in guiding the interpretation of the spectroscopic data. The streak pictures, taken through an observation slot in the upper electrode, display the nature of the imploding hypersonic waves driven by the accelerated plasma. The intense white illumination created by the initial arc discharge changes, in the $H_2+\frac{1}{2}O_2$ mixture, to a cherry red leading edge and deep red flow field after the 8-μsec current pulse is extinguished. It is particularly noteworthy that a much less intense region of green and deep blue light can be seen ahead of the flow field, beginning almost at the very onset of the plasma formation and persisting for several microseconds.

The test procedure consisted of obtaining a spectrophotograph of a major portion of the discharge spectrum in the test gas mixture and identifying the emission lines and bands present. Lines or bands of interest subsequently were investigated by means of photomultiplier time-resolved observations. This data then was related to the streak photographs.

The OH emission-band head at 5126 Å (**3, 4**) was investigated with particular care. This band head occurs in a part of the spectrum that is relatively clear of H_2 and O_2 emission and, therefore, can be isolated with comparative ease. In the systematic identification procedure for this particular band, discharges were induced in different nonreacting gases to find other possible contributions of emission near the OH wavelength. Discharges in He revealed a small contribution from metallic elements, such as Fe, Ni, and Cr, which were, presumably, from the stainless-steel electrodes. Discharges in O_2 produced spectra of the metallic oxides, such as FeO, NiO, and CrO, as well as the O_2 bands and lines. Pure H_2 also was used for the discharges, and its Balmer series lines and molecular bands were observed. At times, the nonreacting mixture $He+\frac{1}{2}O_2$ was substituted for $H_2+\frac{1}{2}O_2$ as a further check on the correct identification of the OH spectra.

The dependence of certain spectra on pressure and voltage was studied, along with their time-resolved characteristics. It was found possible to distinguish between two emission spectra occurring at nearly the same wavelength by means of the distinct behavior of their time-resolved characteristics with variation of initial pressure or voltage. Precautions were taken during these experiments to maintain the quality of the data. The discharge chamber was filled with fresh gas before every discharge and was evacuated to about 10 μ after each discharge to prepare it for the next filling. The detonable $(2H_2+O_2)$ mixtures were carefully mixed and were not used for a period of time, usually of the order of weeks, to insure complete diffusion of the component gases into each other.

The reaction chamber was filled with test gas to within ± 5 per cent of the desired pressure. Prior to initiating a discharge, the capacitor voltage was recorded to within ± 2 per cent. Electrical discharge usually was initiated within one minute after the reaction chamber was filled.

Most of the discharge observations were made at about the mid-radius of the 8-inch-diameter reaction chamber. At this position, the imploding hypersonic wave is well developed and starting to enter a converging channel. Some check observations were made near the periphery of the chamber where the plasma is first formed.

All the dual-beam, oscilloscope-trace photographs display, simultaneously, the photomultiplier output signal on the upper beam and the discharge-current signal (integrated Rogowski-coil output) on the lower beam. The current signal triggers the oscilloscope sweep.

EXPERIMENTAL RESULTS

Photomultiplier readout traces of the H_γ, H_δ, and H_ϵ emission lines are included in Figure 6. The relation of this radiation to the transient current waveform governing the discharge in the molecular hydrogen also is shown. These three

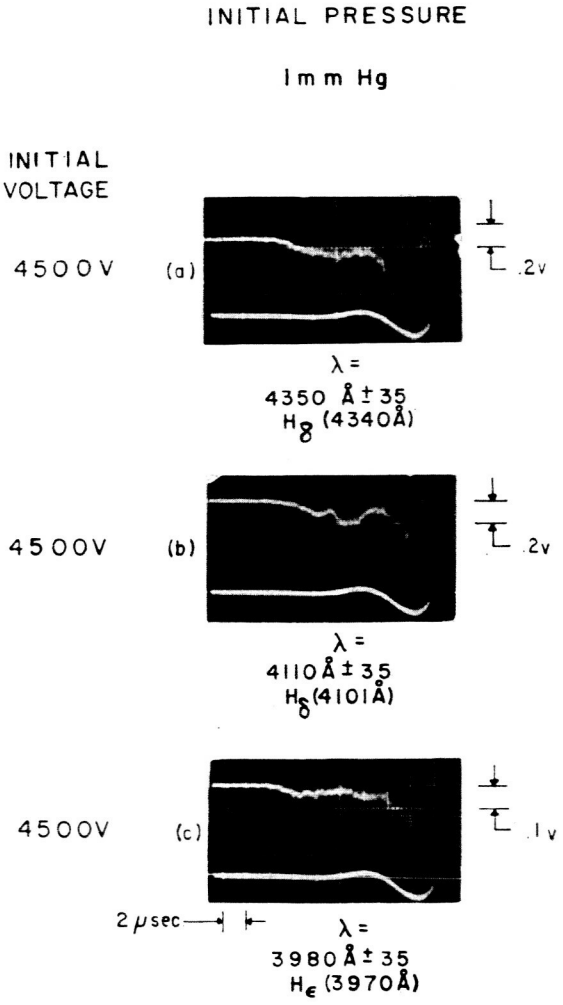

FIGURE 6. Time-resolved spectra of three Balmer series lines for electrical discharges in hydrogen.

Balmer (atomic hydrogen) lines display relative amplitudes similar to those in reference intensity tables (**5**), for example, but in this case the detectable emission persists about 6 μsec after the cessation of current.

Several emission bands identified with molecular-oxygen ions were observed for a similar arc discharge pulse into O_2. A typical set of oscilloscope traces is presented in Figure 7 for various initial-pressure and capacitor-voltage conditions

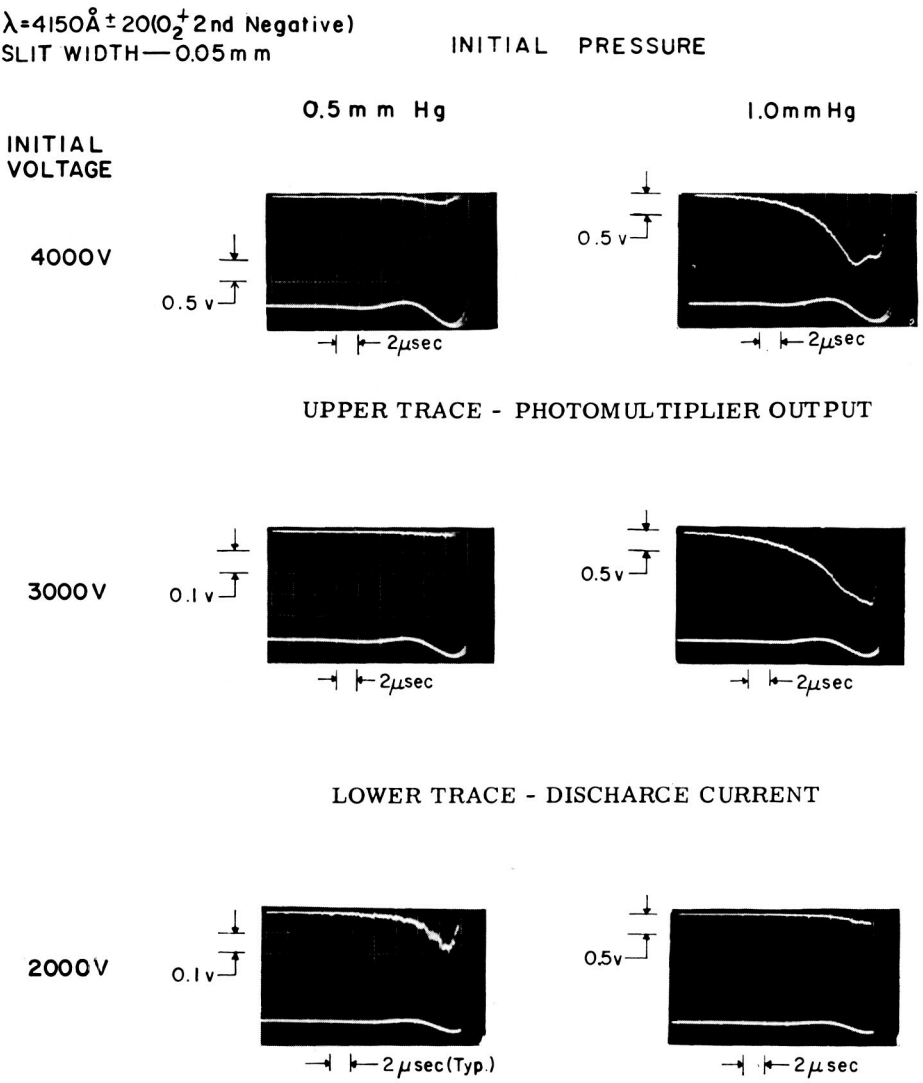

FIGURE 7. Time-resolved spectral characteristics of electrical discharges in oxygen.

at a spectral location associated with the second-negative, oxygen-ion band. The profound effect of these relatively small perturbations in initial test conditions is apparent from the large changes in amplitude.

The discharge in He produces excitation of the 5876 Å line. The spectral profile of this radiation is recorded in Figure 8 as a function of time. This emission persists considerably longer (170 μsec) than the current pulse. The 3889 Å He line was found not to be excited. Other explorations of He discharges in spectral regions where no He lines are expected indicated that, for initial pressures less than 1 mm Hg (absolute) electrode elements (metallic) produced significant background radiation. For pressures greater than about 1 mm Hg (absolute) this radiation appeared to be suppressed.

The observations described were made at a position where the imploding discharge (luminous front) would have had to travel at least to the midradius of the

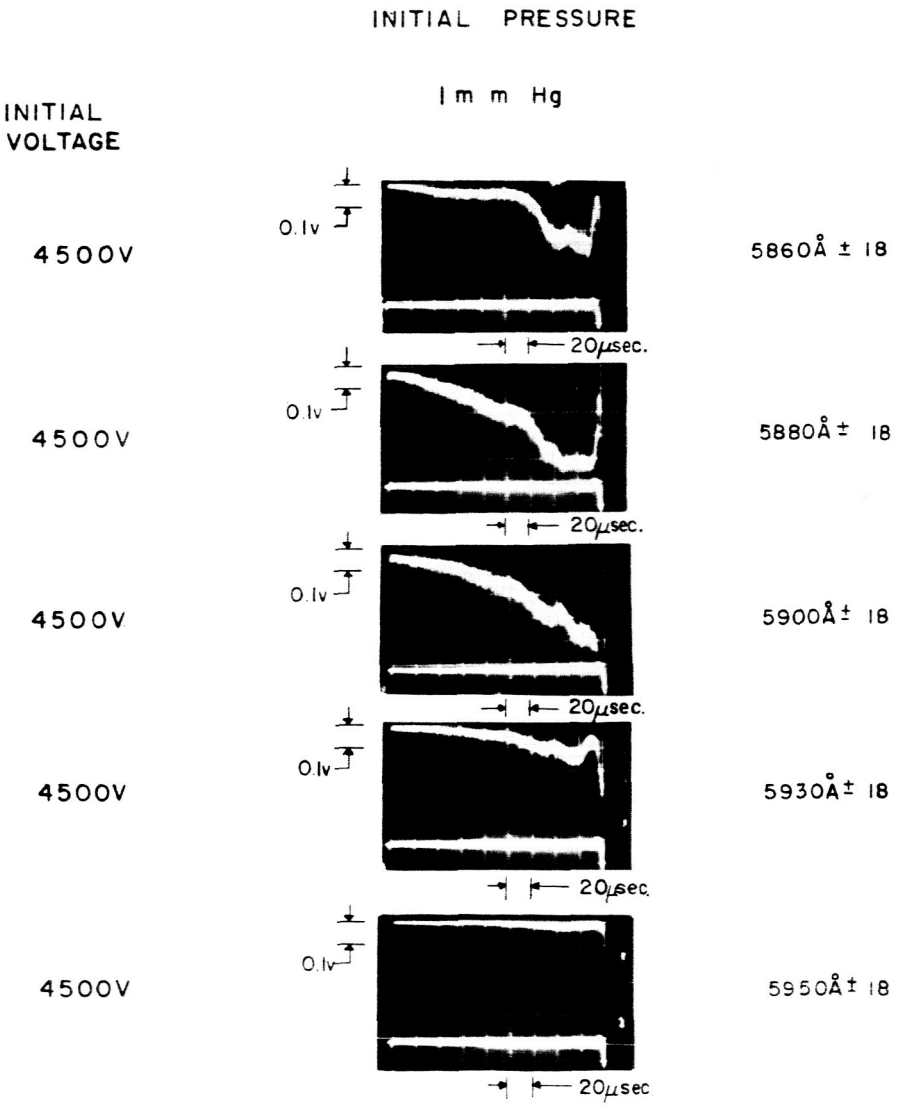

FIGURE 8. Time-resolved spectra circa He 5876 Å line resulting from electrical discharges in helium.

discharge chamber. When H_2 or He was used, the photomultiplier trace of the radiation displayed a dependence on initial capacitor voltage and gas pressure, whereas with O_2 there existed no such well-behaved relationship to discharge voltage or gas pressure. This is an indication reinforced by streak photographs—that the plasma formed in the O_2 probably is irregular and asymmetric. Furthermore, with O_2, the luminous wave front did not always proceed across the point of observation. This resulted in poor overall reproducibility of emission intensity under otherwise identical initial conditions of discharge. When O_2 emission spectra

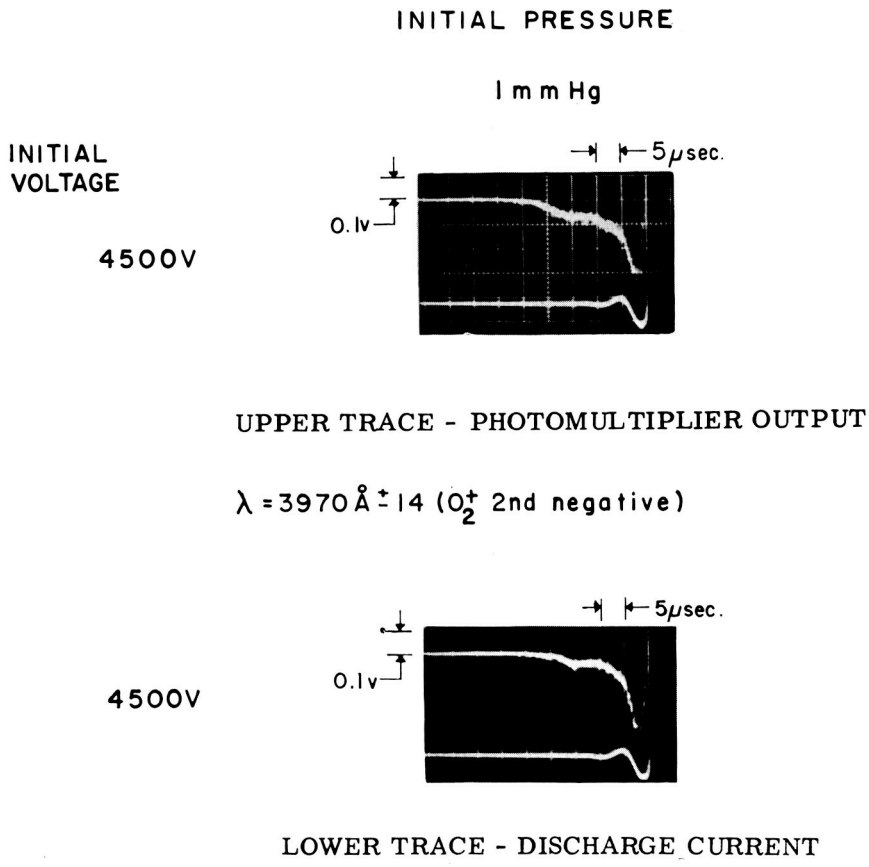

FIGURE 9. Time-resolved spectra of electrical discharges in a stoichiometric hydrogen–oxygen mixture.

were monitored in mixtures containing H_2 or He, a more reproducible condition existed (for example, see Figure 9), presumably as a result of the stabilization of more symmetric plasma cylinders.

A comparison of spectra from discharges in He, $H_2+\frac{1}{2}O_2$, and H_2 under similar test conditions is given by Figure 10. The discharge in He indicates that there is a negligible metallic background emission in the 5100–5200 Å bandwidth, but, in H_2, there is a very small amount of emission by electronic bands. The emission obtained for discharges in $H_2+\frac{1}{2}O_2$, however, is significantly large, which strongly suggests that the radiation is the OH band originating at 5126 Å (**3, 4**).

Further comparisons with data of Figure 11 tend to reinforce this view. Monitoring emission in the 5120–5220 Å range resulting from electrical discharges in three different gas compositions (O_2, $H_2+\frac{1}{2}O_2$, and $He+\frac{1}{2}O_2$) but keeping the partial pressure of O_2 the same, there is significantly greater intensity from the $H_2+\frac{1}{2}O_2$ mixture than from the other two, this, again, can be attributed to the OH emission band. A profile survey of this radiation indicates it to be some 80 to 100 Å wide and degraded toward the red, which is in agreement with the observation of the discoverers (**6**) of this visible spectrum of OH.

Corroboration of the photomultiplier data was obtained by time-integrated,

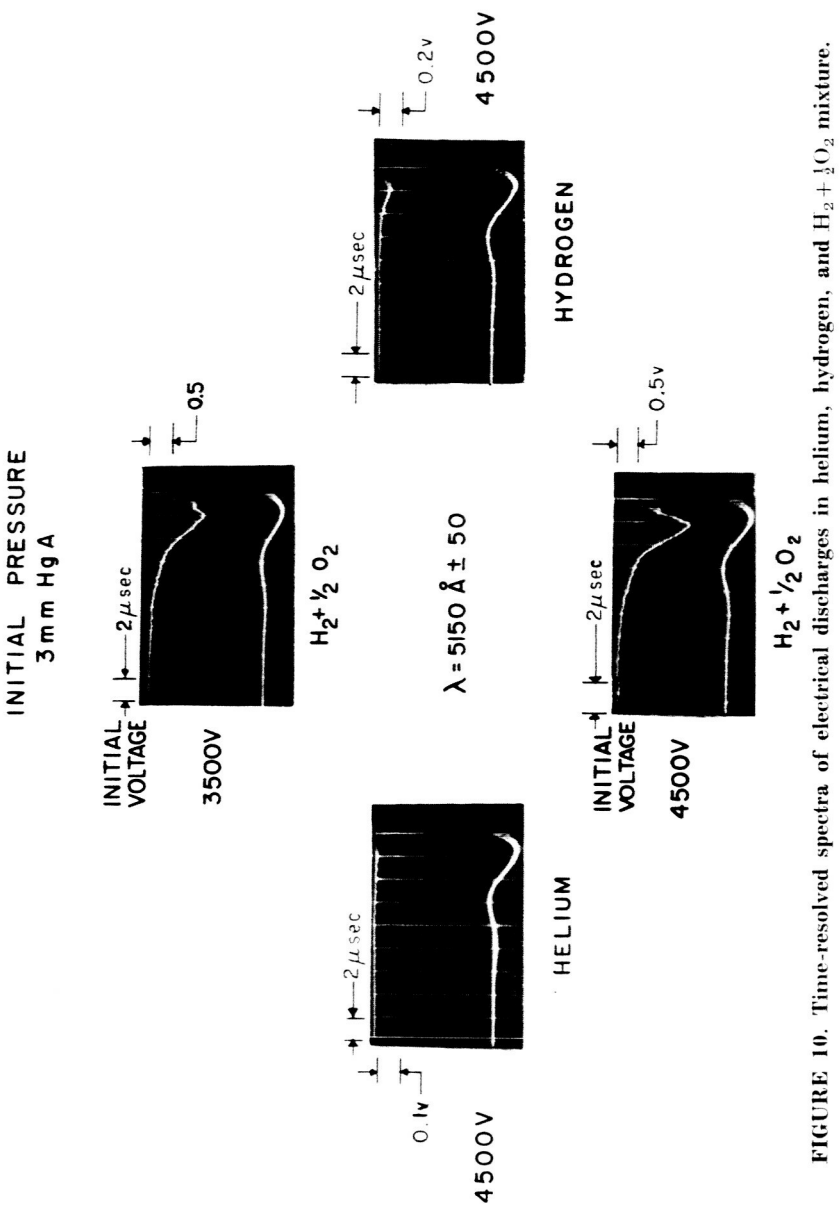

FIGURE 10. Time-resolved spectra of electrical discharges in helium, hydrogen, and $H_2 + \frac{1}{2}O_2$ mixture.

wide-spectra pictures, using the Spencer spectrograph, previously shown by Figure 4. A comparison of spectra for different initial gases shows that two-band systems obtained with the $H_2 + \frac{1}{2}O_2$ mixture cannot otherwise be identified with radiation from hydrogen or oxygen species: one is at (approximately) 5126 Å and the other, of much less intensity, is between the 5460 and 5790 Å mercury lines used for calibration. The former one (5126 Å) we attribute to the OH (0, 7) emission band as a consequence of our more detailed study; the latter is similar to the transition of the OH, either (0, 8) or (1, 9), radical shown by Herman *et al.* (**3**), but we have not investigated it further at this time.

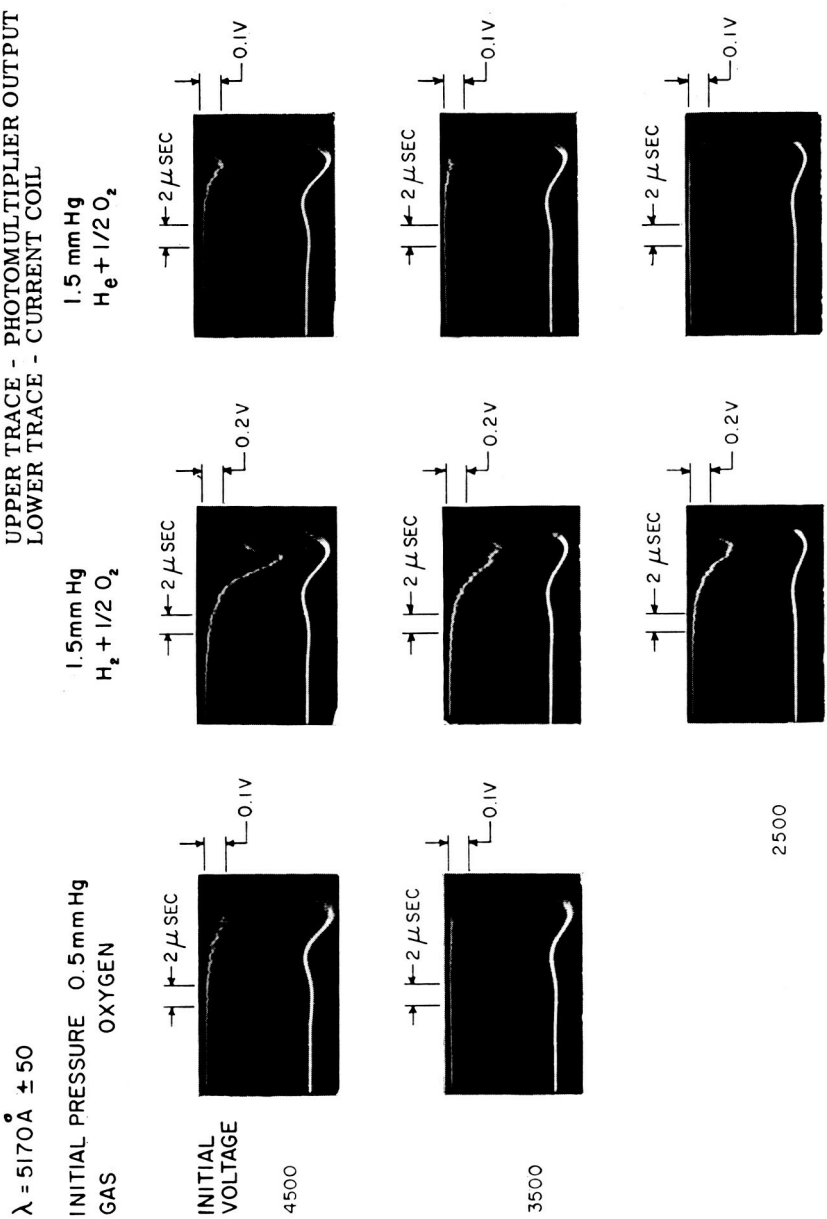

FIGURE 11. Time-resolved spectra of electrical discharges in oxygen, $He+\frac{1}{2}O_2$, and $H_2+\frac{1}{2}O_2$ mixtures.

The data discussed so far were obtained with reactant mixtures at pressures between 1 and 3 mm Hg (absolute). Tests also were conducted, however, with reactant pressures up to 11 mm Hg (absolute) and down to 0.2 mm Hg (absolute). With an initial capacitor potential of 4500 V (corresponding to a peak current of 72,000 amp), it was determined (see Figure 12) that electrical discharges into mixtures at 2–4 mm Hg (absolute) produced the largest peak-amplitude signal for radiation at 5210 Å ± 40. For reactant pressure greater than 6 mm Hg, the peak amplitude was reduced to about 70 per cent of the 2–4 mm Hg pressure-range

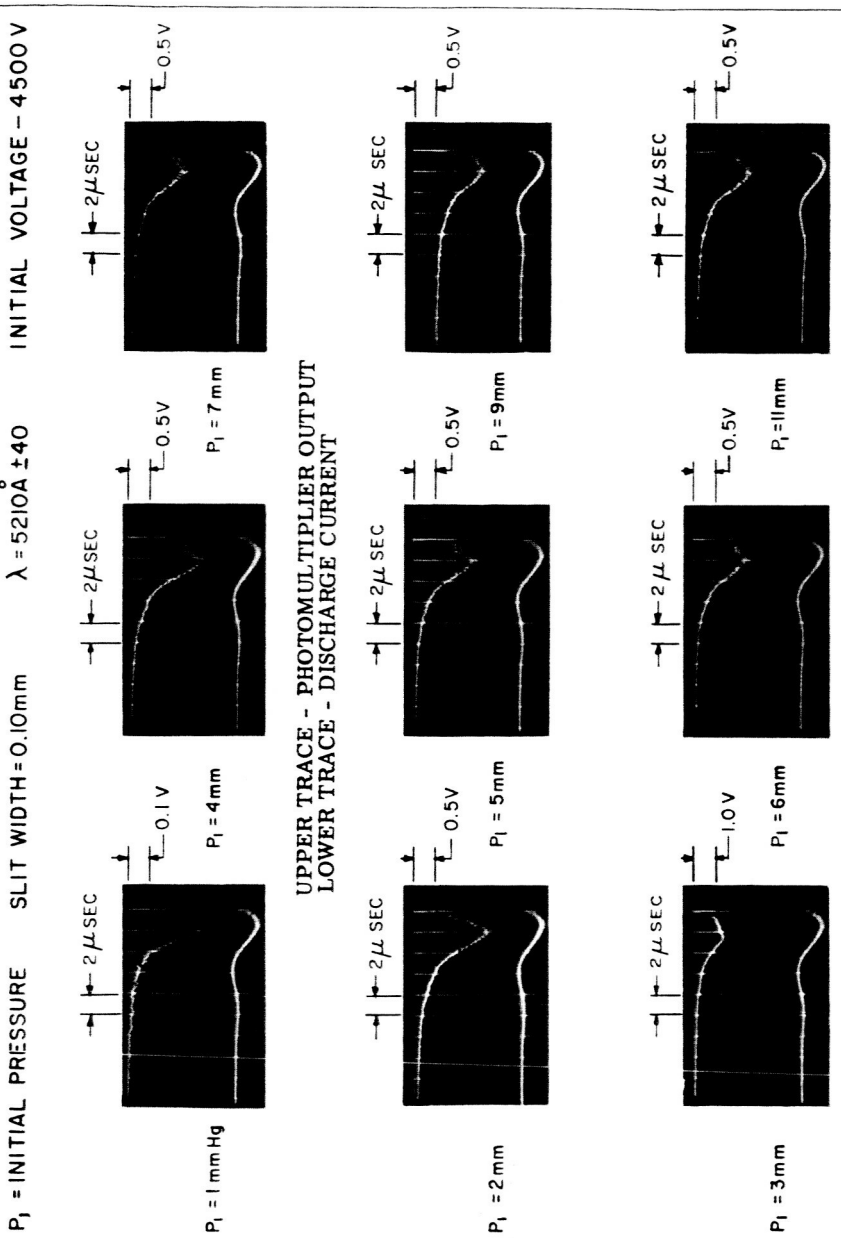

FIGURE 12. Time-resolved spectral characteristics of electrical discharges in $H_2 + \frac{1}{2}O_2$ mixture (variation with reactant pressure).

signal. At all pressures except 3 mm Hg, the peak amplitude occurred at 2 μsec after current initiation; for the exception, it occurred at 2.6 μsec. For these times, the streak pictures indicate the discharge to be about 1 inch away from the position being monitored by the spectrograph. Further, this occurs from 0.2 to 0.8 μsec after the initial peak of the discharge current.

Going to the lower reactant pressure range indicated the apparent existence of an excitation threshold at 1 mm Hg because in no case was a significant radiation signal observed at lower pressures. Furthermore, this threshold appears to be very critical; a reduction of but 0.05 mm Hg initial pressure from this level reduced the

photomultiplier signal trace to about 5 per cent of its higher-pressure peak amplitude.

DISCUSSION

PLASMA PROPERTIES AND PRECURSOR EFFECTS

The work reported here represents an interplay of plasma radiation and low-pressure chemical reactions. Considering the former, although no explicit quantitative data were obtained on the thermodynamic state of the plasma, sufficient accelerator similarities with those of McLean *et al.* (**7**) exist to warrant adoption of their treatment for estimating plasma temperature. This treatment assumes a pre-excitation of the gas downstream of the plasma by a radiation precursor. Thus, assuming that the gas ahead of the driven hypersonic wave lacks internal degrees of freedom (i.e., letting $\frac{1}{2}mv^2 = kT$), the plasma temperature may be estimated from the measured wave velocity by using strong-shock equations (**7**).

In the experiments considered here, the wave velocities, computed from the streak photographs (Figure 5, for example), vary from 0.36 cm/μsec for a capacitor-stored energy of 60 joules to 0.72 cm/μsec for 300 joules. The estimated temperature of the driven plasma, therefore, ranges from 11,000 to 43,000°K. These values are consistent with considerations of the stored energy and species observed.

The acceptance of the pre-excitation theory permits the consideration of a local thermodynamic equilibrium (LTE) condition behind the wave front in shorter times than are associated with the decay of the plasma. That is, the kinetic cross sections of the excited gas atoms are so large that kinetic equilibrium is attained in a negligible time period. Ionization by atom–atom collisions also will be extremely rapid because of the reduced ionization-energy requirements of these already excited atoms. Electrons assume Maxwellian distribution in typical times of 10^{-10} to 10^{-13} seconds and relax with the atom–ion distribution in times of the order of the electron–ion scattering time. The electromagnetically accelerated plasma (produced by the arc discharge) acts, then, as a thermal light source.

The pre-excitation of the "cold" gas ahead of the electromagnetically driven hypersonic wave can be explained as being caused by absorption of vacuum ultraviolet radiation originating in the plasma region. These photons dissociate molecular species and raise atoms to excited states as found for H_2 (**8**) or pre-ionized "cold" gas atoms as was the case for He (**9**) or Argon (**10**).

Under certain conditions, electron diffusion ahead of the shock front can play a role in the pre-excitation process (**11**). A further possible effect in apparatus in which electrodes form the flow channel and high initial voltages are applied is the superposition of a low-current (10^{-3} amp, for example) glow discharge over the entire channel simultaneous with the localized formation of a high current-density arc. The glow electrons, traveling across the electrode gap well downstream of the plasma-driven wave, collide with ground-state or excited species to create conditions similar to the precursor effect.

These precursor effects are not too well understood; each type of experimental setup has to be investigated separately to determine the predominant mechanisms of pre-excitation and ionization of the "cold" gas as well as the state of the plasma. For electromagnetically driven shock waves, precursor "conditioning" of the "cold" gas appears to promote, in some experimental apparatus, rapid kinetic equilibration behind the shock front and results in higher excitation temperature than ordinarily would be predicted by strong-shock theory. Current work indicates that these precursors also promote very fast reactions in chemically reacting mixtures both ahead of and behind the shock-front/plasma complex.

QUALITATIVE ANALYSIS: ELEMENTAL GASES

The relative intensities of the Balmer-series lines of H_2 observed (H_γ, H_δ, H_ε) appear consistent with an equilibrium condition. (See Figure 6.) The time-integrated photograph of the H_2 discharge spectrum (Figure 4), however, although exhibiting the H_β line†, does not show the H_α line that one might expect to be of the greatest intensity. Additionally, photographs of the He discharge spectrum (Figure 4, for example) show the He 5876 Å line but fail to disclose the He 3889 Å line, which should have the same intensity in an equilibrium condition. This evidence supports the conclusion that an equilibrium distribution might not have been established in our apparatus in spite of the apparent precursor conditioning and excitation of the "cold" gas (see Figures 5 and 6) by photolytic or electron-impact processes.

The strong emission identifiable with O_2^+ (see Figure 9) downstream of the discharge may be attributed to collisional processes with glow-discharge electrons. Not excluded, however, is the possibility that strong emission in the vacuum ultraviolet from the oxygen or oxy-hydrogen plasma could cause photoionization of the molecule. Energy absorption of about 12.5 ev is necessary to ionize the molecule, and this could be supplied by photons in the 1000 Å portion of the spectrum. The spectral quality of this radiation is produced by OI and H species (Lyman spectra) in arc discharges (**12**). The exploratory scope of this research program precludes a more quantitative analysis.

QUALITATIVE ANALYSIS: GAS MIXTURES

It long has been recognized (**13, 14, 15**) that irradiation of oxygen-hydrogen mixtures by ultraviolet light affects its explosion limits and provokes rapid reactions at very low pressures. These various investigators (**13, 15**) consider the reaction process to be:

$$O_2 + h\nu \rightarrow 2O \tag{1}$$

$$O + H_2 \rightarrow OH + H \tag{2}$$

$$OH + H_2 \rightarrow H_2O + H \tag{3}$$

It is interesting that previous investigators have used the 3064–3090 Å system of OH almost exclusively for monitoring the reaction kinetics.

Photolysis of water vapor by ultraviolet radiation (**16**) has been examined and shown to yield only small fractions of gaseous molecular-oxygen and hydrogen products. All observations of the hydroxyl-band system at 5126 Å (**3, 4, 6**), on the other hand, have resulted from low-current glow discharges in low-pressure, water-vapor environments. This excited state of the OH radical has been attributed to electronic dissociation of H_2O and the subsequent recombination of atomic hydrogen and excited atomic oxygen; the role of radiation absorption is considered to be secondary (**3**).

It is significant that no other investigators have reported observing the green emission bands of OH from a stoichiometric mixture of the combustible reactants. Furthermore, the advances in photomultiplier detection and recording since 1954 (**15**) have improved the temporal discrimination of this reaction by at least one order of magnitude, so that we now can determine that the reaction proceeds within less than 0.2 μsec after the initiation of the arc discharge.

† The H_γ, H_δ, and H_ε lines were observed with a photomultiplier detector but were not intense enough to be photographed.

The maximum 5126 Å system emission was observed at 3 mm Hg initial pressure. For this condition, the peak emission output is found to be proportional to the peak discharge-current magnitude. Comparison with lower reactant pressure indicates that the emission intensity is slightly less than proportional to initial pressure, and, at the lower initial pressure, is not proportional to the current. With this background data and the apparent reaction threshold at 1 mm Hg the presence of OH is tentatively indicated as resulting from a primary photochemical and a secondary electron-impact process. The former is due to precursor radiation from the plasma and the latter is from the free electrons of the glow discharge. Although it is possible to speculate on various reaction mechanisms and concurrent processes, it is preferable to defer more detailed discussion until additional data from our continuing research program becomes available.

CONCLUSIONS

A preliminary emission spectrographic investigation has been conducted of electromagnetically-driven hypersonic waves into elemental gases and detonable mixtures. The role of precursor radiation from the plasma in affecting gas properties significantly downstream of the plasma/shock-wave field has been observed.

The reported spectroscopic data does not support the conclusion of other researchers that rapid, local kinetic equilibrium is promoted in the wave structure as a result of precursor conditioning of the downstream gas. This evidence, however, is not viewed as being in conflict with other work, but, rather, emphasizes the variation of plasma properties and excitation mechanisms between seemingly similar plasma accelerators and the need for separate evaluation of the characteristics of each device.

The rapid formation of an excited state of the OH radical, not observed in flames, has been detected by emission in the 5126 Å and 5534 Å band systems. This radiation ahead of the plasma commences within 0.2 μsec after initiation of the electric arc discharge (plasma formation) and persists about 6 μsec after extinction of the arc.

A reaction-product threshold has been observed for an initial pressure of 1 mm Hg. Above this pressure level, a reproducible, positive indication is measured up to at least 11 mm Hg, and the maximum radiation signal occurs at 3 mm Hg.

The nature of the present results, reflected against the background of previously reported work, suggests that the OH formation mechanism is associated with plasma precursor radiation excitation of the "cold" gas downstream of the hypersonic wave front. This leads to very fast chemical reactions involving energetic atoms, which produce OH radicals. Secondary electron-impact processes, arising from a glow discharge along the entire flow channel concurrent with the arc, probably combine with the initial photochemical one to excite the unusual OH radiation spectrum reported.

REFERENCES

1. Foreman, K. M., "The Electromagnetic Detonation Concept", PPL–TR–61–10, Republic Aviation Corp., Farmingdale, L. I., N.Y. (Also available as ARS Preprint 1702–61 and AFOSR Document 564.)
2. Foreman, K. M., "Terrestrial Hypersonic Flight Propulsion", AIAA Paper 63110, presented at the AIAA–ASME Hypersonic Ramjet Conference, White Oak, Md., April 23–25, 1963.
3. Herman, L., Felenbok, P., and Herman, R., "Emission Spectra of the OH and OD Radicals", *J. Physique et Radium*, **2**, 83 (1961).

4. Benoist, S., "Contribution to the Study of the Spectra of the OH Molecule", *Ann. Physique*, **10**, 363 (1955).
5. Harrison, G. E., *MIT Wavelength Tables* (New York: Wiley, 1939).
6. Schuler, H., and Woeldike, A., "Uber den Anregungsmechanismus im H_2O—Molekül auf Grund der Befunde an seinem Emissionsspektrum im Sichtbaren", *Physikalische Zeritschrift*, **44**, 355 (1943).
7. McLean, E. A., Faneuff, C. E., Kolb, A. C., and Griem, H. A., "Spectroscopic Study of Helium Plasmas Produced by Magnetically-Driven Shock Waves", *Phys. Fluids*, **3**, 6 (November–December, 1960).
8. Wiese, W., Berg, H. F., and Griem, H. R., "Measurements of Temperatures and Densities in Shock-Heated Hydrogen and Helium Plasmas", *Phys. Rev.*, **120**, 4 (November 15, 1960).
9. McLean, G. A., Kolb, A. C., and Griem, H. R., "Visible Precursor Radiation in an Electromagnetic Shock Tube", *Phys. Fluids*, **4**, 8 (August, 1961).
10. Groenig, H., "Precursor Photoionization and Electrons", *Phys. Fluids*, **6**, 1 (January, 1963).
11. Weyman, H. D., "Electron Diffusion Ahead of Shock Waves in Argon", *Phys. Fluids*, **3**, 545 (1960).
12. *Handbook of Chemistry and Physics* (Cleveland: Chemical Rubber Publishing Co., 1961).
13. Semenov, N. N., *Some Problems in Chemical Kinetics and Reactivity* (Princeton: Princeton University Press, 1959), II.
14. Kaufman, F., "Reactions of Oxygen Atoms", in *Progress in Reaction Kinetics*, ed. G. Porter (New York: Pergamon Press, 1961), I.
15. Norrish, R. G., Porter, G., and Thrush, B. A., "Kinetic Studies of Gaseous Explosions", in *Fifth Symposium on Combustion* (New York: Reinhold Publishing Co., 1955).
16. Chen, M. C., and Taylor, H. A., "Photolysis of Water Vapor", *J. Chem. Phys.*, **27**, 4, 857 (1957).

10. Robert B. Spiers, Jr., and Charles Husson: *Development of a Rocketborne Spectroradiometer to Measure the Radiation Environment of a Reentry Vehicle*

A flight spectroradiometer has been developed for measuring the ultraviolet and visible spectral steradiancy of the hot-gas plasma of a supercircular velocity reentry vehicle. It has a spectral range from 2500 Å *to* 6000 Å *and a dynamic range from* 10^{-7} *to* 10^{-3} watts/cm^2-*steradian-micron. The experimental parameters and vehicle characteristics affecting the spectroradiometer design is presented with a description of the optical window, spectroradiometer design, and calibration procedures. Finally, the flight performance is discussed.*

INTRODUCTION

A flight spectroradiometer has been developed as a reentry payload sensor for the Langley Research Center's Five-Stage Scout Reentry Project. The purpose of the sensor is to measure the spectral and total intensity of the luminescent air in the shock-induced flow field produced by the vehicle reentering the earth's atmosphere at a velocity of approximately 28,000 ft/sec. At this velocity the radiative heat transfer to a vehicle due to the luminescent air is insignificant compared to the convective heat transfer. However, the magnitude of the hot-air radiation should be great enough to detect and measure. Due to the absence of flight data of this type, a radiative heat-transfer experiment was selected as one in a series of reentry experiments to be performed. There are no flight-tested spectroradiometers for use in such experiments, so the development and evaluation of a rocketborne spectroradiometer was taken as an additional objective of the radiative heat-transfer experiment.

The Scout vehicle used to perform these experiments is shown in Figure 1. For the radiative heat-transfer experiment the vehicle is launched from Wallops Island, Virginia, with a trajectory as shown in Figure 2. After launch the vehicle goes through a series of staging events which cause the fifth-stage payload to reenter approximately 275 nautical miles south of Bermuda. A tracking station on Bermuda and one on a ship records the reentry data in real time and delayed time.

ED. NOTE: Mr. Spiers and Mr. Husson are with the NASA Langley Research Center, Langley Station, Hampton, Virginia.

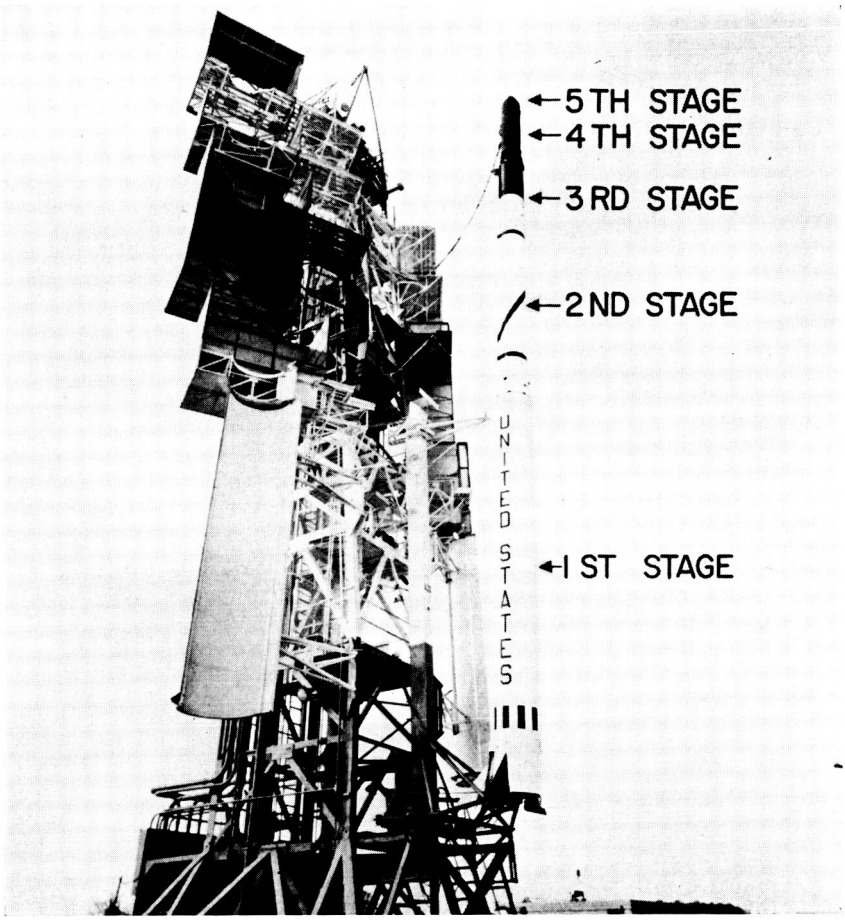

FIGURE 1. Five-stage Scout rocket.

The delayed-time data are provided by an on-board tape recorder in case radio blackout is experienced during the prime data period. A telemeter transmitter in the fifth-stage payload transmits the data to the tracking stations. The payload shown in Figure 3 has a beryllium nose with an optical window on its axis to transfer the radiant energy to the spectroradiometer sensor. There the quantities to be measured are converted into electric signals and fed into the telemetry module for transmission to the tracking stations. The 17-inch-diameter spherical rocket motor boosts the payload to its final reentry velocity. No attempt is made to recover the payload.

The nose window and spectroradiometer part of the fifth stage is discussed in this paper. Their final design and construction resulted from factors peculiar to the radiative heat-transfer experiment and the rocket vehicle used.

DESIGN CONSIDERATIONS

EXPERIMENTAL

As stated before, the experimental quantities to be measured are the spectral and total intensity of the shock-induced, flow-field radiation. An analysis of the

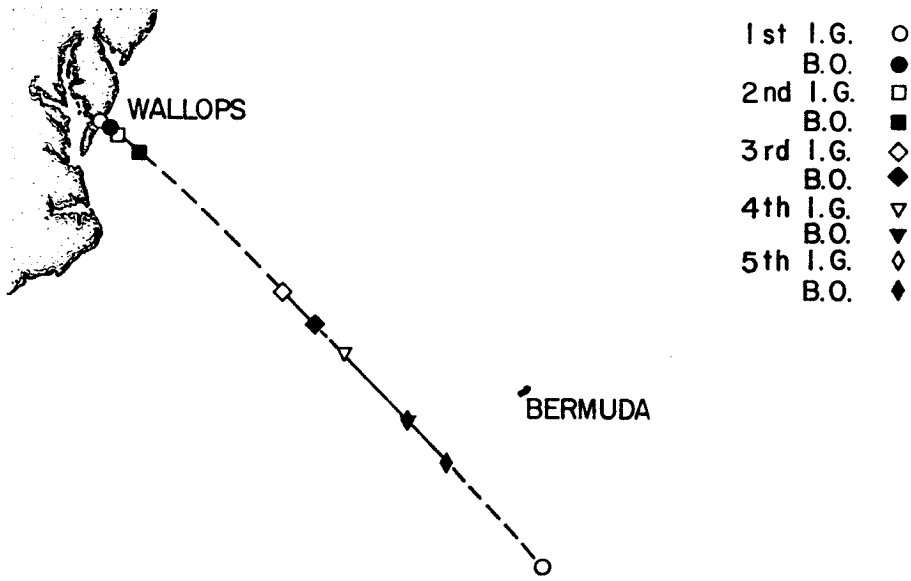

FIGURE 2. Trajectory for the reentry radiative heat-transfer experiment.

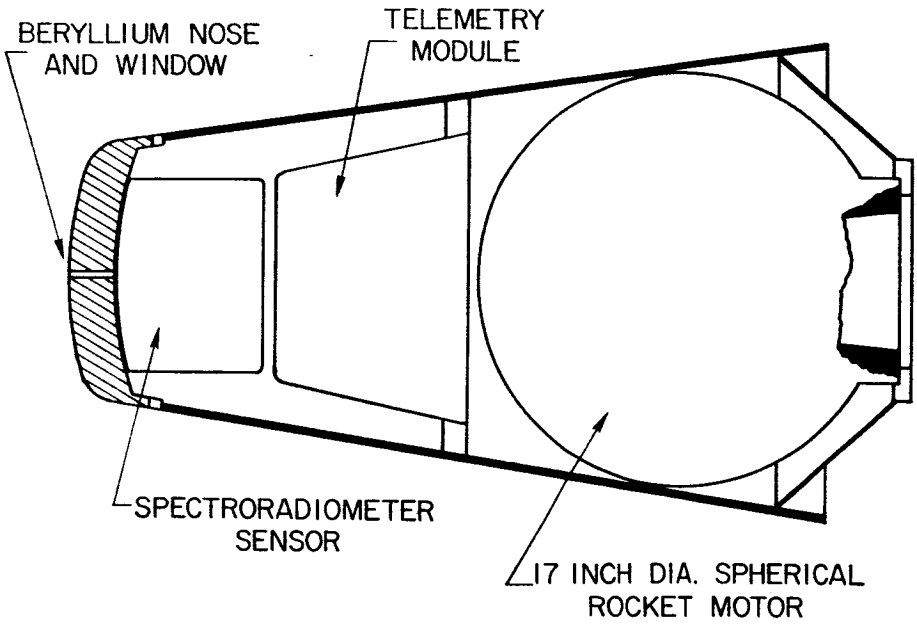

FIGURE 3. Scout fifth-stage payload.

expected hot-air radiation was made in order to determine the required sensor range, sensitivity, frequency response, and resolution. The analysis was made using a theory of hot-air radiation (**1**) which was derived from laboratory measurements. This theory gives sufficient indications of the spectral emission of gases at the temperatures and densities of interest. The expected flow-field gas temperatures and densities were taken from normal shock data (**2**) which applies to the hypervelocity reentry trajectory. An altitude-versus-velocity curve for the experiment is

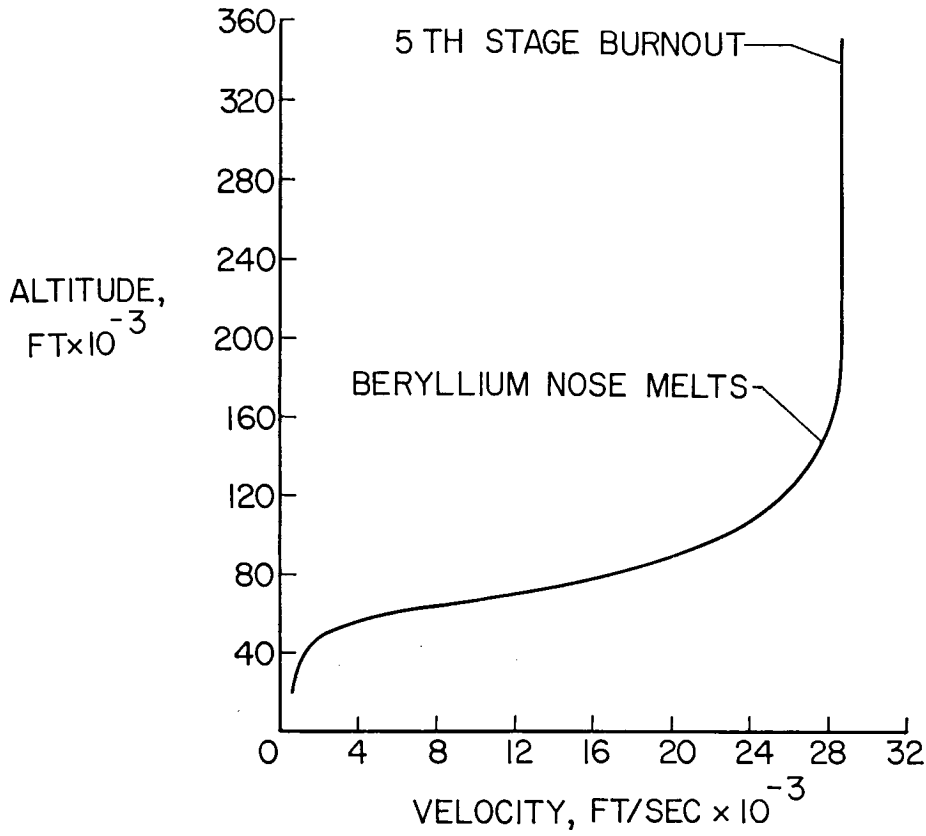

FIGURE 4. Altitude versus velocity.

shown in Figure 4. Radiation from hot air in the altitude range from 350,000 to 150,000 feet was taken as the region of primary interest. Calculations of the spectral radiation from several of the most intense air constituents were made for the various temperatures and densities throughout this altitude range. One set of spectra is shown in Figure 5 for an intermediate altitude. The peaks and inflections in the upper curve indicate the spectral features due to the ionized nitrogen molecule's first negative band system. The lower curves are due to two nitric oxide, NO, band systems. The expected dynamic range of radiant energies is shown in Figure 6. This curve shows the change in specific intensity, or steradiancy, over the reentry period for the 3900 Å radiation of the $N_2^+(1-)$ band system. The steradiancy increases by approximately 7 decades during a 25-sec data period. This analysis of the flow-field radiation suggests the following sensor design characteristics. The sensor should provide a spectrum over the wavelength range from 2000 to 6000 Å and a total radiation measurement over as wide a wavelength range as the window transmits. The spectral part of the sensor should have a resolution of 75 Å to resolve the expected molecular band spectra. It should record the spectrum in approximately $\frac{1}{5}$th of a second if a spectrum is to be obtained which does not change in intensity significantly during the scan. It should be able to detect a minimum steradiancy of 10^{-6} watt/cm^2-steradian-micron and have a dynamic range covering 7 decades of radiant energy. In addition to these characteristics,

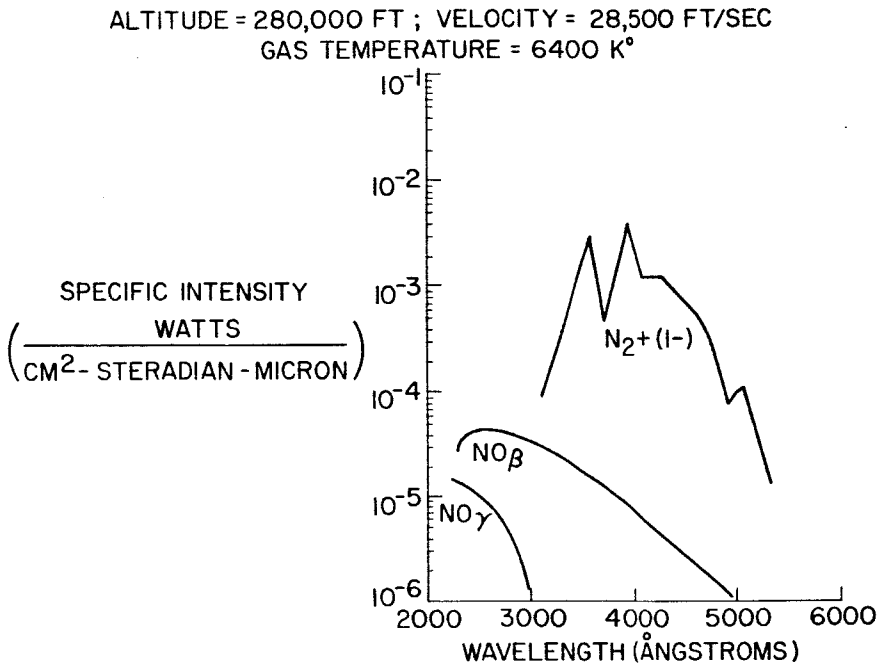

FIGURE 5. Specific intensity versus wavelength.

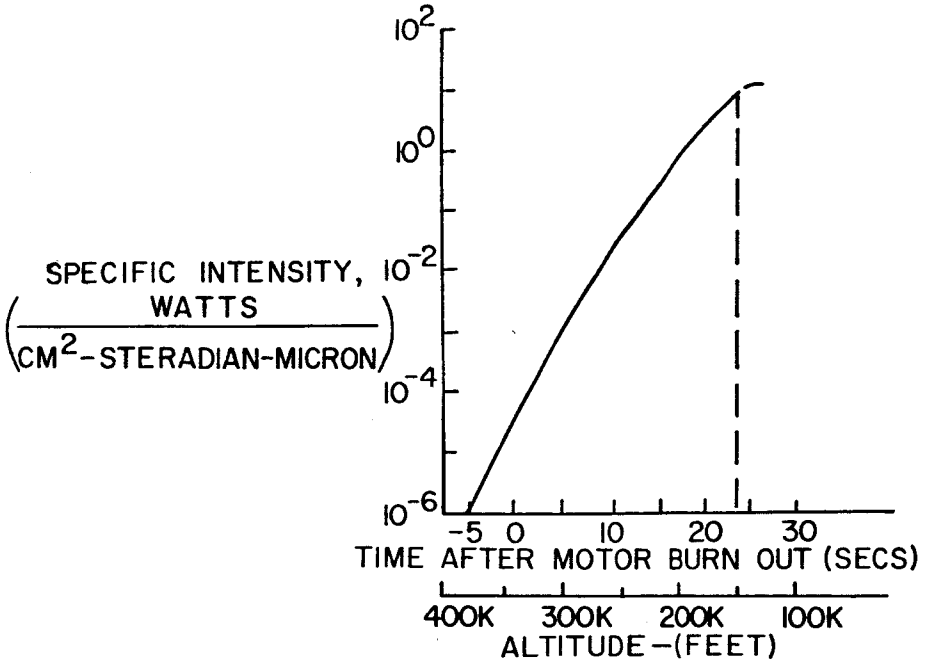

FIGURE 6. Specific intensity versus time and altitude.

the vehicle configuration suggests the sensor be packaged in a cylindrical volume no larger than 10 inches in diameter and 6 inches deep. It should not weigh more than 10 lb.

ENVIRONMENTAL

The environment in which the sensor must operate also affects its design. The maximum vibrations and accelerations are listed in Table I. The temperature will vary from 75° to 130°F and the pressure will vary from 1 atmosphere to the vacuum of space. During the period of reentry the optical window must efficiently transfer the radiation to the spectroradiometer while being subjected to a peak heat pulse of 800 Btu/ft^2-sec.

TABLE I. ENVIRONMENTAL TEST

MAXIMUM LEVELS

TYPE	LEVEL	FREQUENCY	DURATION	DIRECTION
VIBRATION 1. SINUSOIDAL 2. RANDOM	9 G rms 8 1/2 G rms	500-2000 CPS 15-2000 CPS	105 SECS 110 SECS	LONGITUDINAL LONGITUDINAL
ACCELERATION (STEADY STATE)	60 G 6 G		3 MIN 3 MIN	LONGITUDINAL TRANSVERSE
SHOCK	22 G		5-15 MSECS	LONGITUDINAL

DESCRIPTION OF SENSOR

GENERAL

A sketch of the sensor designed to meet the above requirement is shown in Figure 7. It consists of a vehicle nose window, an optical monochromator, a thermistor system, and a photoelectric system. These components are combined into a single unit which forms the nose section of the fifth-stage rocket.

The hot-gas radiation in the stagnation-point region of the nose passes through a fused quartz window, the internal surface of which is used as the entrance slit of a modified Ebert type scanning monochromator (**3**). The radiation passes through the monochromator as shown forming a spectrum at the exit slit. The spectrum is scanned across the exit slit by oscillating the diffraction grating with an electric motor. The narrow spectral band of radiation that passes through the exit slit excites the phototube which provides a voltage output to one channel of the telemetry system. Part of the radiation passing through the nose window illuminates the total radiation thermistor detector. This radiation is chopped by a motor-driven, squirrel-cage chopper. The total range of wavelengths that is transmitted by the window excites the detector which supplies a voltage output to another channel of the telemetry system.

NOSE WINDOW

The nose window is a fused-quartz light pipe 0.020 inch wide, 0.75 inch high, and

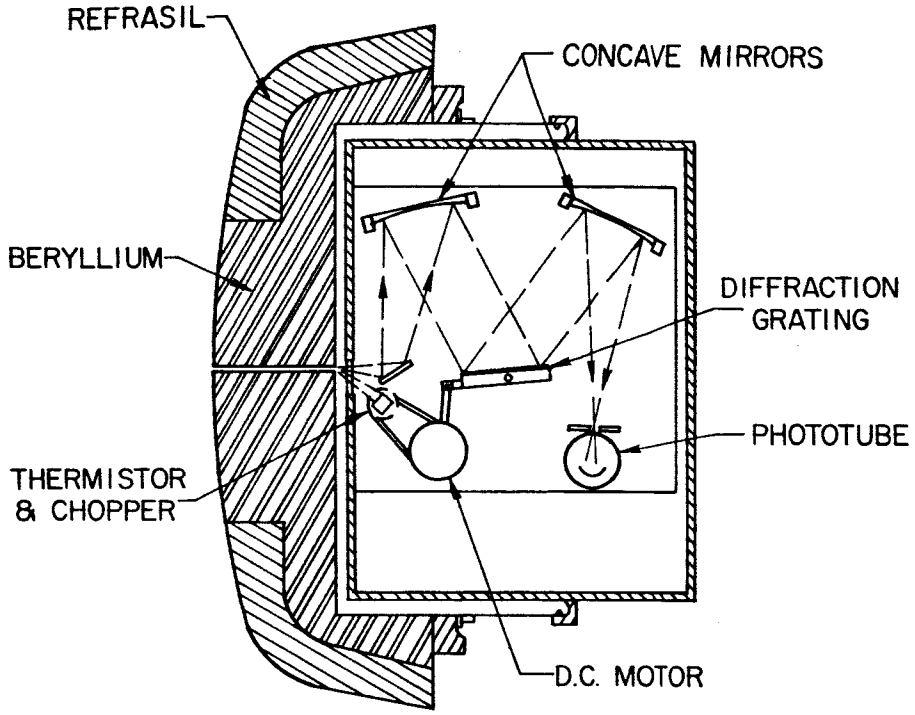

FIGURE 7. Nose-sensor assembly.

2 inches thick. It is heat sink immersed in a beryllium nose. It is so designed to survive the extreme heat generated at the nose and to efficiently transfer radiation to the scanning monochromator and thermistor. It transmits radiation from 2000 to 30,000 Å, has a melting point higher than that of beryllium, and excellent thermal shock characteristics. The 0.020-inch width of the window serves as the entrance slit width of the monochromator.

SCANNING MONOCHROMATOR

The scanning monochromator has an $f/3.3$ spherical concave collimating mirror. The plane reflection diffraction grating has 600 grooves per millimeter and is blazed for the 3000-Å wavelength. The grating is oscillated sinusoidally by a 28-volt d-c electric motor. The grating oscillates at 2.5 cycles/sec, causing the spectrum to scan across the 0.020-inch exit slit five times per second. The halfpeak band width of the radiation that passes through the exit slit to the photodetector is 75 Å wide.

PHOTOMULTIPLIER DETECTION SYSTEM

The photoelectric detector used to record the spectral radiation is a photomultiplier type 1P28. The electronics used are designed to cover approximately 5 decades of radiant energy. This essentially covers the sensitivity range of the 1P28 from a so-called "wide open" gain condition to maximum attenuation. The gain or attenuation of the photomultiplier is achieved by electronic feedback control of the high voltage applied to the photomultiplier. This is a technique employed in conventional devices to achieve a logarithmic energy response with

the photomultiplier. However, all functions are achieved with solid-state devices. A block diagram of the photomultiplier system is shown in Figure 8a. The amplifier fed by the 1P28 controls the amplitude of the high voltage applied to the 1P28. In this manner, optimum operating points for the photomultiplier and amplifier may be chosen. At zero signal condition, 1000 volts are applied to the photomultiplier and the applied voltage is related to the energy level of the radiation input. The output is recorded by monitoring the high voltage through a voltage divider.

THERMISTOR DETECTION SYSTEM

The thermistor detector is essentially a photoresistive bridge device. Adequate compression of the output signal, which covers 5 decades of radiant energy, is achieved by utilizing saturating operational amplifiers. Five operational amplifiers are cascaded and their outputs are divided by 10 to reduce the voltage; they are then summed. Logarithmic compression is achieved by permitting each stage to saturate at an equivalent decade of energy. The last stage saturates at an input of 0.0001 volt and the first stage saturates at an input of 1 volt, indicating all states are saturated. Saturated output for each stage is 10 volts. Dividing by 10 and summing each stage, the maximum output for maximum input is 5 volts. This system was developed as an all-solid-state device. A block diagram of the system is shown in Figure 8b.

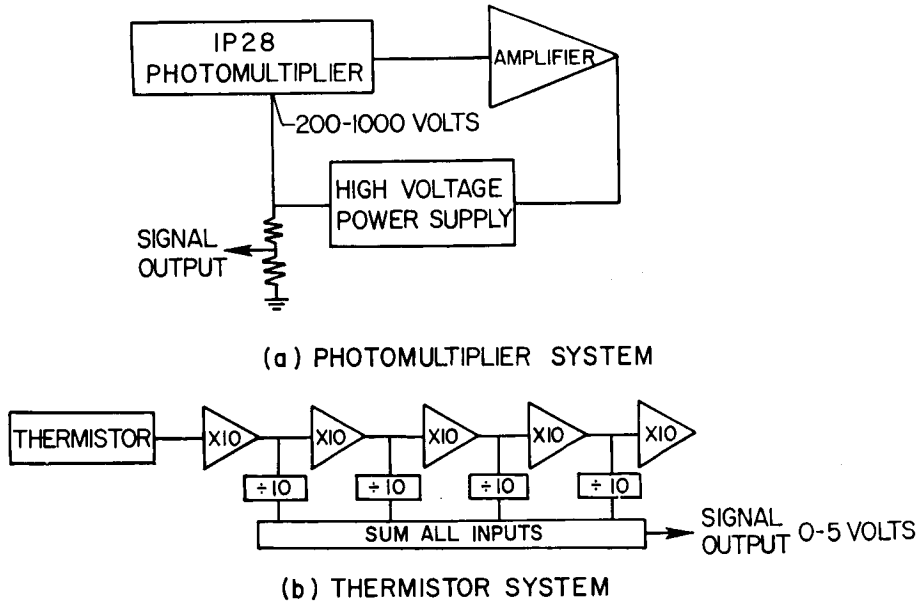

FIGURE 8. Detector electronics.

FINAL CONFIGURATION

The spectroradiometer-nose assembly is shown in an assembled and exploded view in Figure 9. The spectroradiometer is housed in an airtight can which is purged with dry nitrogen to approximately 20 lb/in^2 pressure to eliminate any low-pressure problems that might occur in the vacuum of space. All metal parts

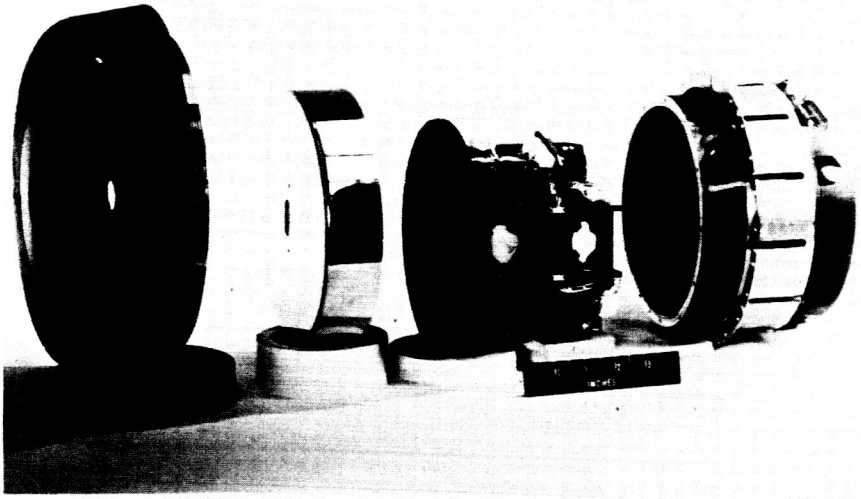

EXPLODED VIEW

ASSEMBLE VIEW

FIGURE 9. Flight spectroradiometer.

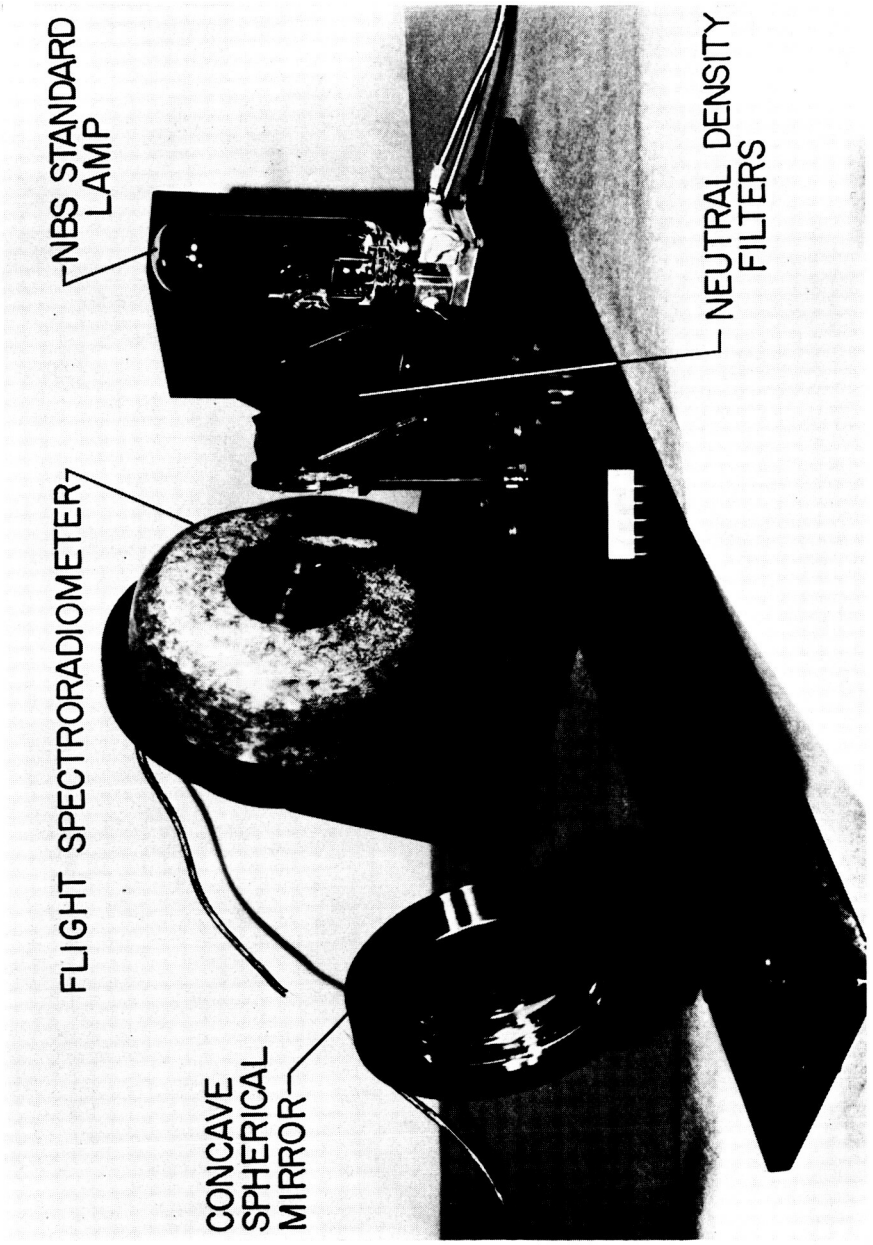

FIGURE 10. Calibration apparatus.

are anodized or painted black to eliminate as much stray light as possible. Lightweight metals such as aluminum and magnesium are used where possible to cut down on the weight of the instrument. The final weight of the spectroradiometer is 10 lb. It is housed in a can 7 inches in diameter and 6 inches deep. The electrical requirements to operate the spectroradiometer are 28 volts, 250 milliamps, d-c.

SENSOR CALIBRATION

CALIBRATION APPARATUS

The spectroradiometer is calibrated with an NBS Standard of Spectral Radiance (4). This is a ribbon filament tungsten lamp which operates at 6 volts and 35 amperes and is calibrated for spectral steradiancy over the wavelength range from 2500 to 26,000 Å. Neutral density filters of the wire screen type and the partially aluminized quartz type are used to attenuate the standard lamp by known amounts. The spectral transmission of these neutral density filters was measured with a spectrophotometer over the wavelength range. The spectral calibration apparatus is shown in Figure 10.

ENERGY

Figure 11 shows the calibration curve for the spectroradiometer. The voltage output versus radiant energy input is shown for three different wavelengths of radiation. There is a change in calibration with wavelength due to nonlinear spectral response of the spectroradiometer. The minimum energy detectable for the

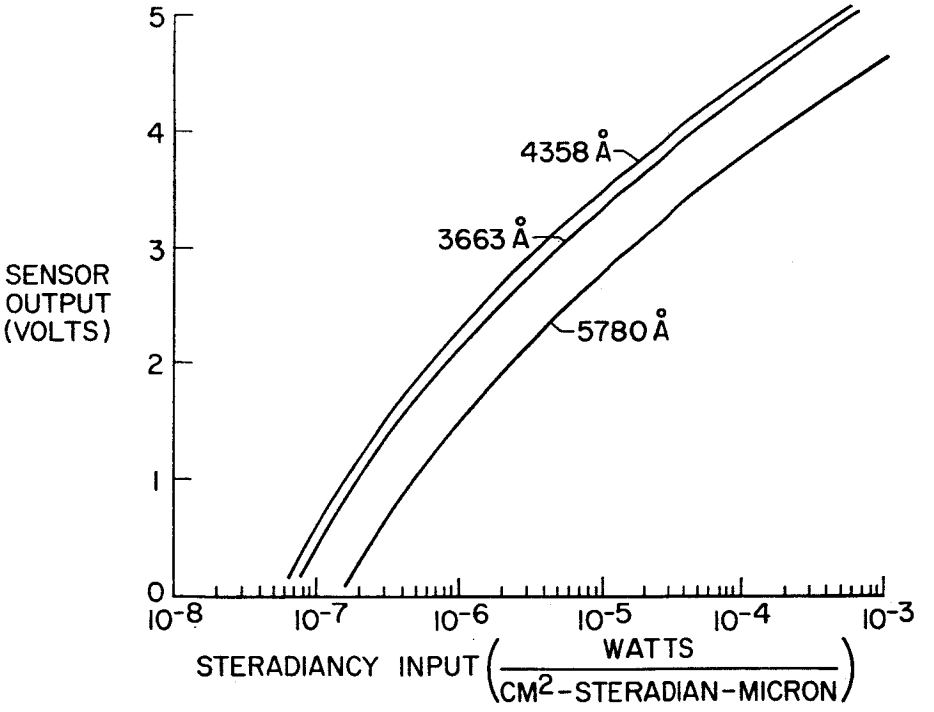

FIGURE 11. Spectroradiometer calibration curve.

spectral detector is approximately 10^{-7} watt/cm^2-steradian-micron. The 0–5 volt output represents approximately 4 decades of radiant energy input. The total radiation thermistor detects a minimum energy of approximately 10^{-3} watt/cm^2-steradian. Due to the less sensitive thermistor which has no radiation-collecting optics, the total radiation detector does not begin to record radiation until the photomultiplier saturates. The thermistor was calibrated using the same NBS standard by integrating the energy under the spectral steradiancy curve from 2500 to 30,000 Å.

WAVELENGTH

The wavelength calibration is made for the spectroradiometer by recording a spectrum of a mercury discharge lamp. A spectrum of the mercury lines is shown in Figure 12 as recorded by the spectroradiometer during a rocket prelaunch system

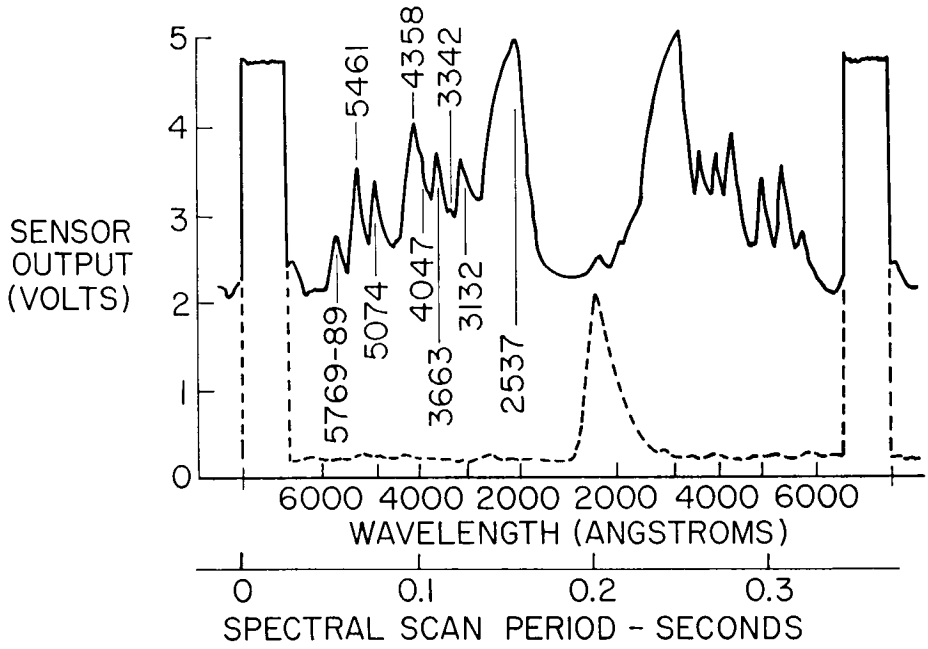

FIGURE 12. Hg spectrum as recorded by the spectroradiometer.

check while on the launching pad. This record shows a forward and reverse scan of the mercury spectrum. The square waves are voltage calibrate pulses at the red end of each spectral scan. The saw-toothed pulse shown by the dotted line is a radiant energy calibrate pulse generated by flashing a small tungsten lamp momentarily at the ultraviolet end of the spectral scan. The voltage and energy calibrate pulses serve to check the integrity of the system during flight. The dotted line shows the zero radiant energy input to the spectroradiometer. The approximately 0.2-volt level is due to instrument noise. The shark-fin appearance of the intense 2537-Å line is due to insufficient frequency response of the system. A radio-frequency filter was added late in the program to eliminate radio-frequency noise in the sensor. This, unfortunately, reduced the sensor frequency response causing the erroneous wave form.

FLIGHT PERFORMANCE

The flight spectroradiometer was launched in the early hours on the morning of August 23, 1962. The vehicle's third stage malfunctioned causing the fifth-stage payload to go into a flat, spinning attitude. Consequently, it reentered the earth's atmosphere at a velocity much lower than predicted. Although the radiative heat-transfer-measurement objectives of the experiment were not obtained, the flight evaluation of the spectroradiometer was quite successful. Telemetry records indicate that the spectroradiometer operated properly throughout the flight. The

velocity of reentry was not determined but an analysis of the flight records showed the velocity could not have been greater than 10,000 ft/sec. Therefore, the probable 2000°–3000°K hot-air radiation could not have been detected with the on-board spectroradiometer. Nevertheless, the ablation of vehicle materials did provide radiation the sensor could detect. One hundred and eighty-one scans of spectral radiation were measured during a 31-sec period. One such recorded spectrum is shown in Figure 13. This spectrum came from a hydrocarbon flame. Most likely it came from charring ablator material (refrasil) used on part of the beryllium nose. An oxy-acetylene flame spectrum is shown with the flight record to show the similarity. The peaks recorded are the carbon, C_2 Swan, band system, and the CH molecular band system. The relative intensities of the two band systems are different for the two records and are due to the different modes of excitation.

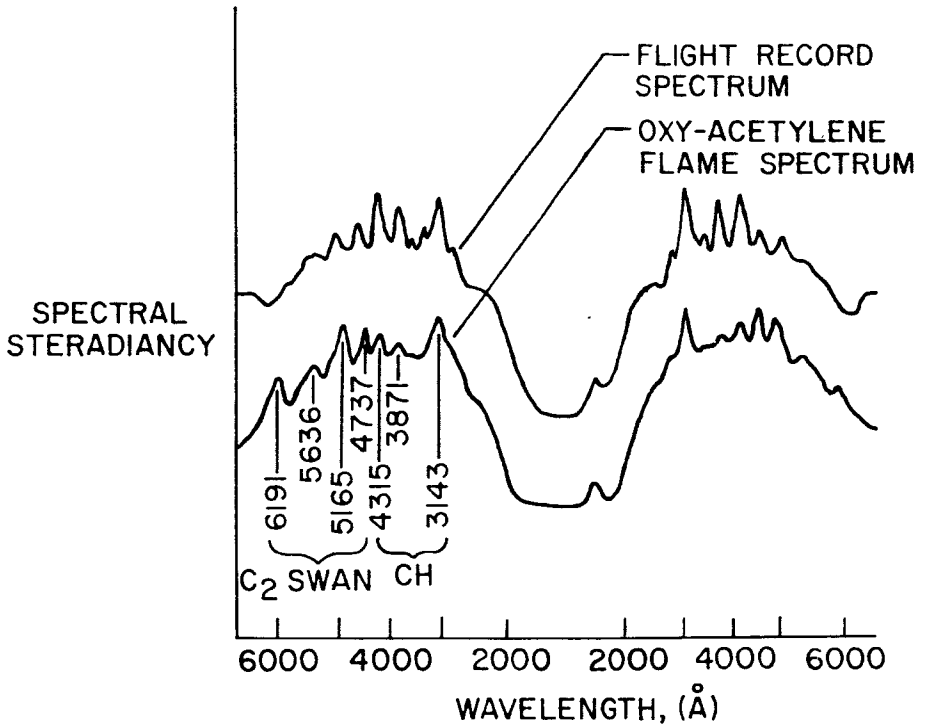

FIGURE 13. Comparison of a flight record spectrum with an oxy-acetylene flame spectrum. (Two adjacent scans of the same spectrum are shown.)

CONCLUSIONS

The flight spectroradiometer sensor performed as expected, recording the radiations it detected with good fidelity. Not all the design characteristics strived for in the sensor development were obtained. The spectral resolution was finally 100 Å instead of 75 Å due to the reduced frequency response. Although the sensor could detect a wavelength range from 2000 to 6000 Å, the energy calibration below 2500 Å was very poor due to insufficient radiation standards below 2500 Å. The final dynamic range of the sensor covered 4 decades of radiant energy instead of 5. Due to the rocket malfunction, the nose-window design was not tested. The

window survival problem for hypervelocity reentry radiative transfer measurements is very difficult to solve because no ground facilities are available to reproduce the heating rates that occur during reentry. There was hope this flight would provide window survival data for use on future reentry experiments.

The final accuracy in measuring wavelength and radiant energy is as expected. Wavelength can be measured to ± 50 Å on a final record. The radiant energy measurements have an uncertainty due to several instrument errors. The calibration standard lamp has a maximum uncertainty of ± 5 per cent. The spectroradiometer sensor calibration procedure results in a maximum uncertainty of ± 25 per cent. Another error in measuring the voltage output of the spectroradiometer through the telemetry system is ± 2 per cent of the full-scale reading. The maximum overall uncertainty in measuring the hot-gas steradiancy from a telemetry record is approximately ± 35 per cent.

REFERENCES

1. Keck, James C., Camm, John C., Kivel, Bennett, and Wentink, Tunis, "Radiation From Hot Air. II. Shock Tube Study of Absolute Intensities", *Ann. Phys.*, **7**, 1, 1–38 (1959).
2. Hochstim, A. R., "Gas Properties Behind Shocks at Hypersonic Velocities. I. Normal Shocks in Air", *Convair*, Rep. No. ZPh(GP)-002 (January 30, 1957).
3. Foster, W. G., "I. A Small Grating Monochromator, and II. Image Forming Properties of the Ebert Monochromator", *Opt. Soc. Amer.*, **42**, 9 (September, 1952).
4. Stair, R., Johnston, R. G., and Halbach, E. W., "Standard of Spectral Radiance for the Region of 0.25 to 2.6 Microns", *Jour. Res. Nat. Bur. Standards*, **64A**, 4, 291–296 (1960).

11. M. R. Denison and R. W. Ziemer: *Investigation of the Phenomena in Crossed-Field Plasma Accelerators*

The acceleration of a plasma by means of a crossed-field accelerator is beset by problems which as yet do not have adequate explanations. The experimentally observed effects include: the sudden drop in thrust with increasing magnetic field strength, extremely unsymmetrical electrode heating, and lack of acceleration in some closed-channel accelerators. These problems also have their counterparts in MHD generators.

In order to obtain a better understanding of the physical phenomena associated with $J \times B$ acceleration, an analytical and experimental diagnostic study was undertaken. A primary objective was to determine and understand the current density distribution in the discharge region.

A theoretical description of the current density distribution in a constant area $J \times B$ channel was developed, including the effects of both Hall currents and ion slip. Computer solutions for several values of the Hall parameter

$$C = \frac{\omega_e \tau_e}{1 + \omega_e \tau_e \omega_i \tau_i}$$

were obtained which exhibited the physically observed characteristics of high-current density concentrations at the upstream edge of the cathode and the downstream edge of the anode.

An experimental investigation of the phenomena occurring in a crossed-field accelerator was conducted using a confined jet-type accelerator, specifically designed and built for this basic study. The accelerator employed electrodes which were segmented transversely and longitudinally to the flow. These segments were electrically insulated, but at the same potential, and the current through each of the cathode and anode segments was individually measured.

In addition, electrode side wall potential measurements were made. Reproducible data were obtained which indicate the magnitude and distribution of the electric field in the core of the plasma as well as the

ED. NOTE: This work was performed at Electro-Optical Systems, Inc., Pasadena, California, under sponsorship of the Air Force Office of Scientific Research, Contract AF 49(638)-1063.

sheath potential drop on each electrode. Physical interpretations and evaluation of the observed phenomena are given and specific needs for more detailed diagnostic information are outlined.

INTRODUCTION

The purpose of the program of research discussed in this paper is to obtain a better understanding of the physical phenomena associated with magnetodynamic acceleration. Specifically, both the experiments and the analysis pertain to the phenomena which occur in a steady-state, crossed-field accelerator of uniform cross section. Pioneering work with such accelerators was carried out by Wood and Carter (**15**), and Demetriades and Ziemer (**16**). Since that time the number of such accelerators in this country has been steadily growing. It therefore appears that a closer look at the fundamental process is desirable. Presumably, when the nature of the interaction between the electromagnetic fields and the plasma is understood in detail some of the results will be applicable to other types of accelerators (or to generators), but in particular some of the difficulties encountered with crossed-field accelerators can be explained. These difficulties include electrode heating, thrust drop-off at high magnetic fields, and lack of acceleration in some closed-channel accelerators.

Most of these difficulties are linked to the current density distribution. For example, it is usually observed that the upstream end of the cathode and the downstream end of the anode glow brighter than other spots during the experiments and that damage due to heating occurs at these spots. Concentration of current might explain the heating. Furthermore, the general direction of the current is that which would be caused by the Hall effect. The resultant force vector due to the Hall effect is therefore at an angle to the direction of the channel. In addition, it is often argued that at high magnetic field the current density tries to seek a path of lower back EMF either by going through the boundary layer or by popping out of the magnetic field which is finite in extent.

In order to obtain some quantitative information on the current density distribution and other phenomena, a systematic series of experiments has been initiated using a crossed-field accelerator. The diagnostic techniques employed in the first series of experiments are relatively simple. However, these give very important information as to the overall problem and pinpoint specific needs for more sophisticated diagnostics in later experiments.

This paper contains a summary of the first series of experiments which have been carried out in less than a one-year period. One technique employed for obtaining information on the current density distribution consists of dividing both cathode and anode into nine segments. The nine segments are at the same potential but electrically isolated so that the current through each one can be measured independently. Another technique consists of side-wall potential measurements. These experiments are interpreted in light of a "weak interaction theory" which is summarized in this paper.

EXPERIMENTAL APPARATUS

A low-power, crossed-field ($J \times B$) accelerator was designed for the experimental study of the phenomena occuring during continuous electromagnetic plasma acceleration. The system consists of an arc jet plasma source followed by a 1-inch

square channel in which the plasma is accelerated by perpendicular electric and magnetic fields. Two water-cooled electrodes with a 1-inch square surface area are used to pass a current through the plasma normal to the flow direction and normal to a magnetic field generated by an electromagnet. A schematic diagram of the apparatus is shown in Figure 1. The arc jet and accelerator system is suspended

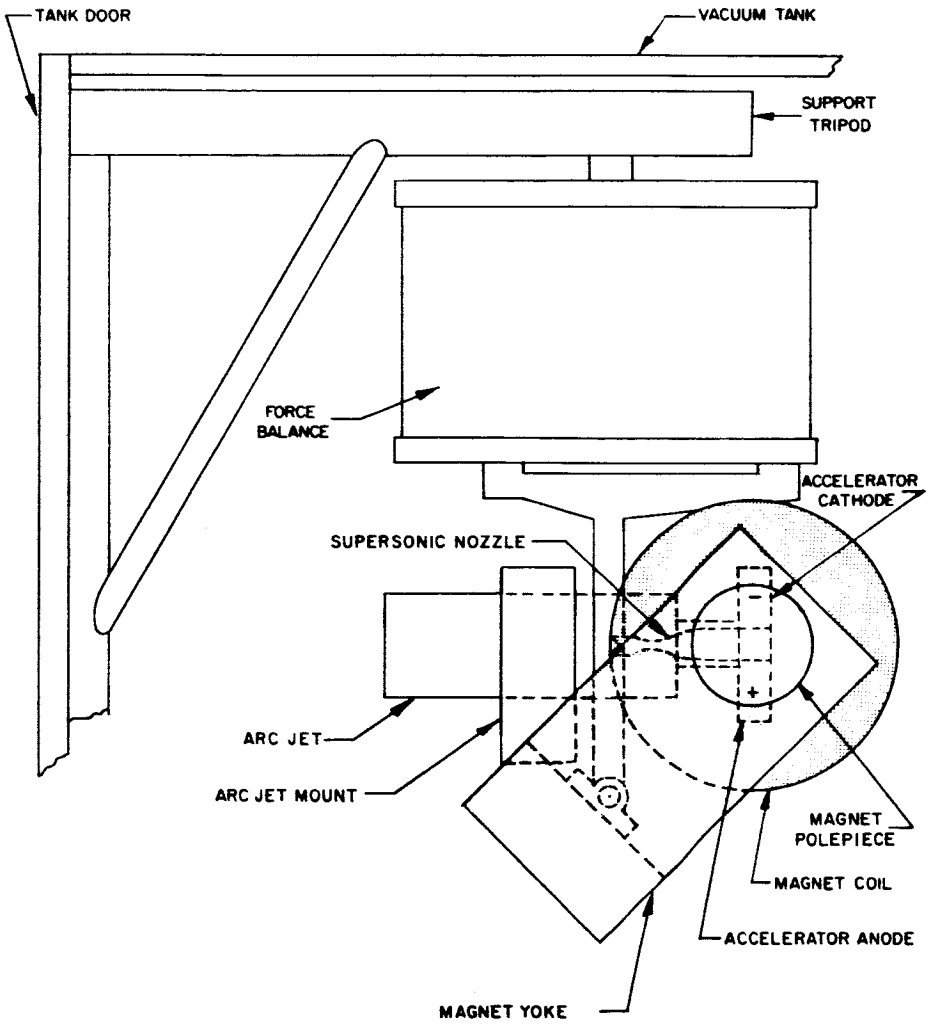

FIGURE 1. Schematic diagram of crossed-field accelerator experimental apparatus.

from a force measuring balance and is entirely enclosed within a vacuum tank. The accelerator magnet is mounted to the balance and the arc jet is, in turn, mounted to the magnet. Attached to the arc jet is a supersonic nozzle followed by the accelerator channel and electrodes. The nozzle and channel walls are made of boron nitride and are cooled by radiation. The arc jet mount contains a traversing mechanism so that the arc jet and accelerator as a unit can be moved back and forth with respect to the magnet. This feature permits the study of the effect of

magnetic field symmetry on the discharge phenomena. In addition, the ends of the magnet polepieces are replaceable so that various magnetic field distributions can be generated.

As indicated in the Introduction, the apparatus was designed for diagnostic studies. Current density distributions on the surfaces of the cathode and anode in longitudinal and transverse directions are measured by using electrodes which are divided into a number of segments. Each segment is electrically insulated from the others but is at the same potential. Therefore, by measuring the current through each segment, a current distribution is obtained. The accelerator electrodes were divided into nine segments as shown in Figure 2. (More finely divided segments can be used if greater resolution is desired in future experiments.) A divided electrode assembly is shown in Figure 3. Each segment is individually water-cooled. The water tubes conduct the current through each segment and also serve as a current-measuring shunt. The general experimental arrangement is shown in Figure 4, and a rear view of the entire apparatus is shown in Figure 5.

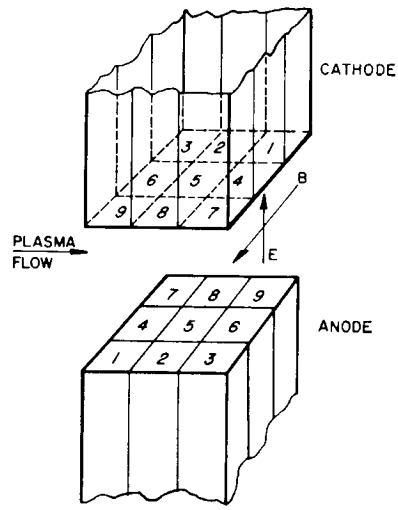

FIGURE 2. Arrangement and identification of divided electrode segments.

Incorporated into one side wall of the accelerator was an array of nineteen tungsten pins for the measurement of the potential distribution. Each pin was 0.040 inches in diameter and was set into a counterbored hole so that electrode material deposited on the side wall would not contact the pins and disturb the electrical measurement. The potential was measured with an oscilloscope through a motorized stepping switch which sampled the voltages at a rate of 20 per second.

In addition to the above measurements, direct measurements of the total momentum of the system were made. By measuring thrust and gas mass flow, measurement of effective exhaust velocity can be made. Direct visual and photographic observations also have been made by use of a mirror placed below the exhaust jet.

The arc jet is of rather conventional design and can be operated without a magnetic field to rotate the arc. This is required to avoid interference with the magnetic field of the accelerator. To increase the range of operating conditions of the arc jet, it is designed with an anode nozzle throat section which can be readily

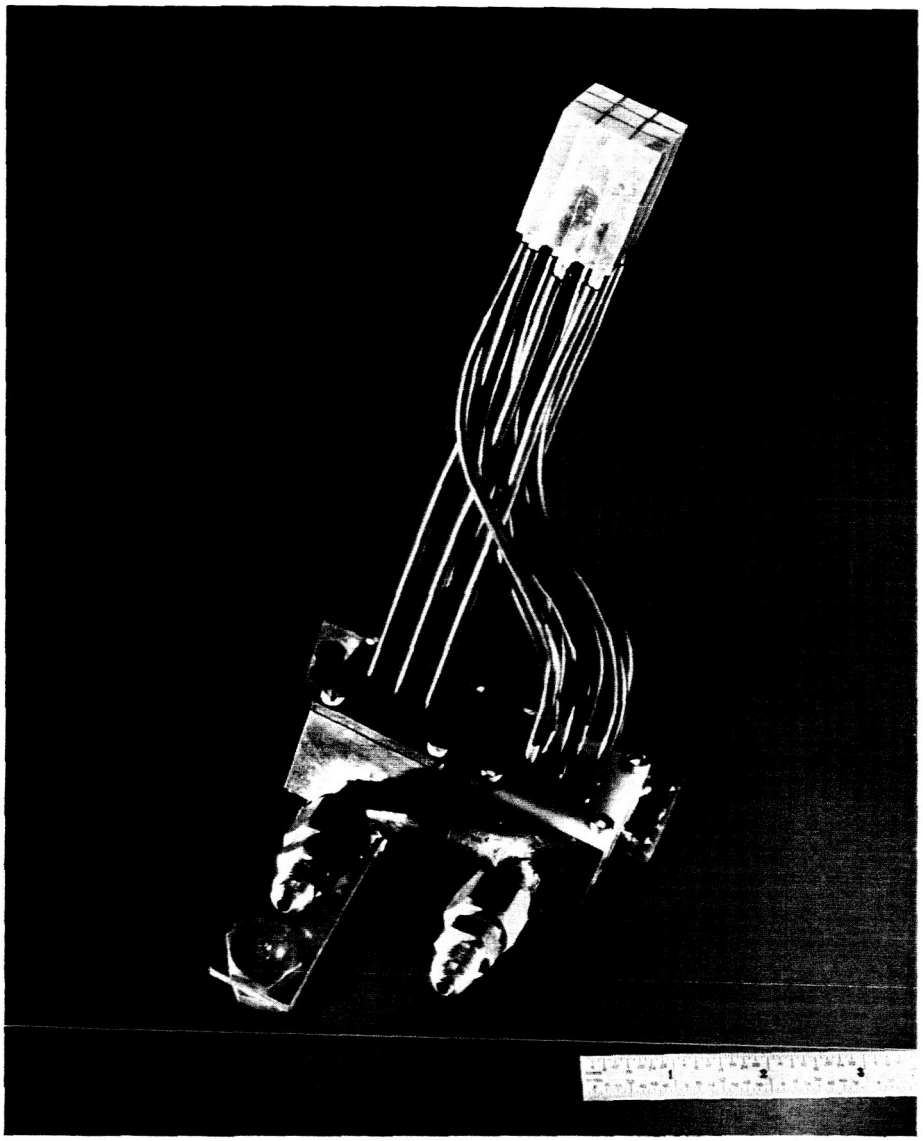

FIGURE 3. Divided electrode assembly.

replaced. This permits variation of the stagnation pressure and the nozzle area ratio. The arc jet is designed for a power input of up to 40 kw and a mass flow rate of 0.1 to 1 grams/sec.

To test for any magnetic interaction giving extraneous forces, the arc jet and accelerator electrodes were short circuited. Then the maximum currents were run through the arc jet, the accelerator, and the magnet, and the balance output was observed. A small net force from the arc jet current was observed but its magnitude was only 1 gram at 300 amps and 0.5 grams at 150 amps which is small for the thrust forces being imposed on the balance under normal operating conditions. In addition, the arc jet current is normally held constant for a series of tests. No

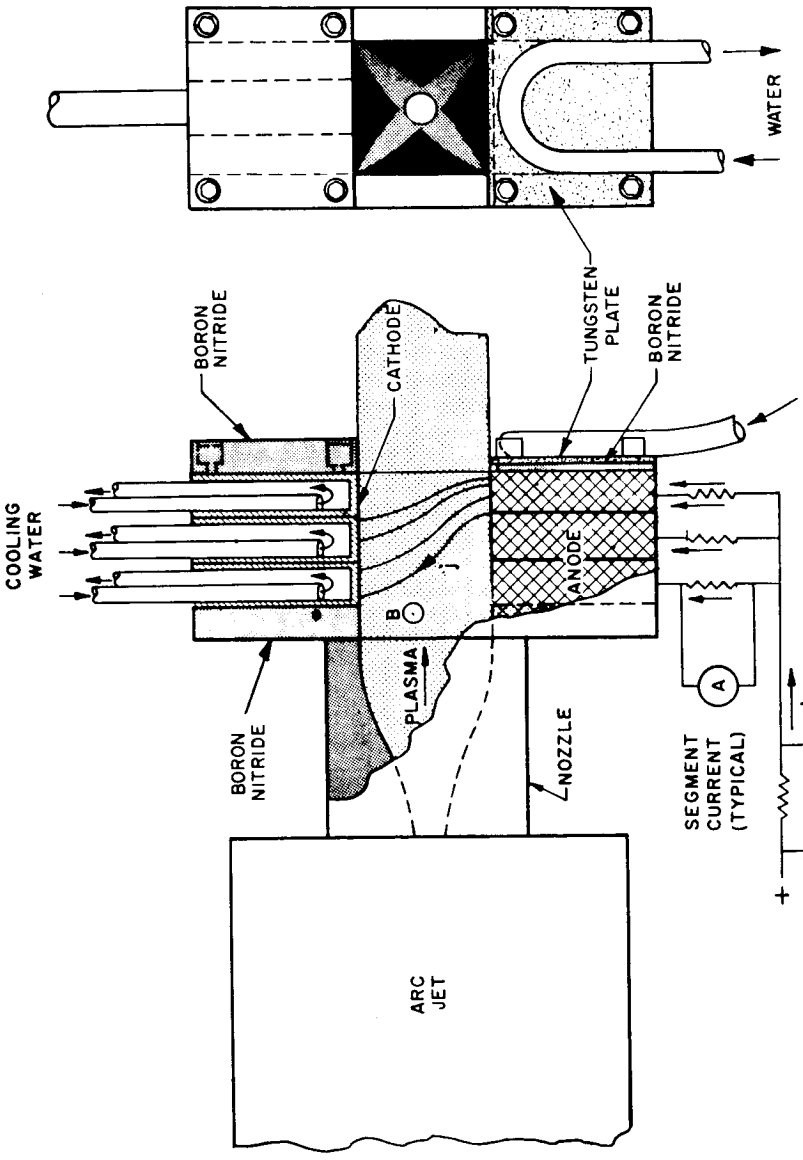

FIGURE 4. Accelerator assembly with divided electrodes.

appreciable force was observed from either the accelerator current or the electromagnet.

The general experimental procedure when thrust measurements were made was to first select the arc jet power level, mass flow rate, and vacuum tank ambient pressure. (The tank pressure was usually set at the level which yielded slight underexpansion of the flow, normally about 0.8 torr.) The arc jet was then operated at these conditions and measurements taken of current, voltage, and thrust. Next the accelerator current was turned on and measurements were taken of accelerator current, voltage, and thrust. Then, holding the accelerator current constant, the

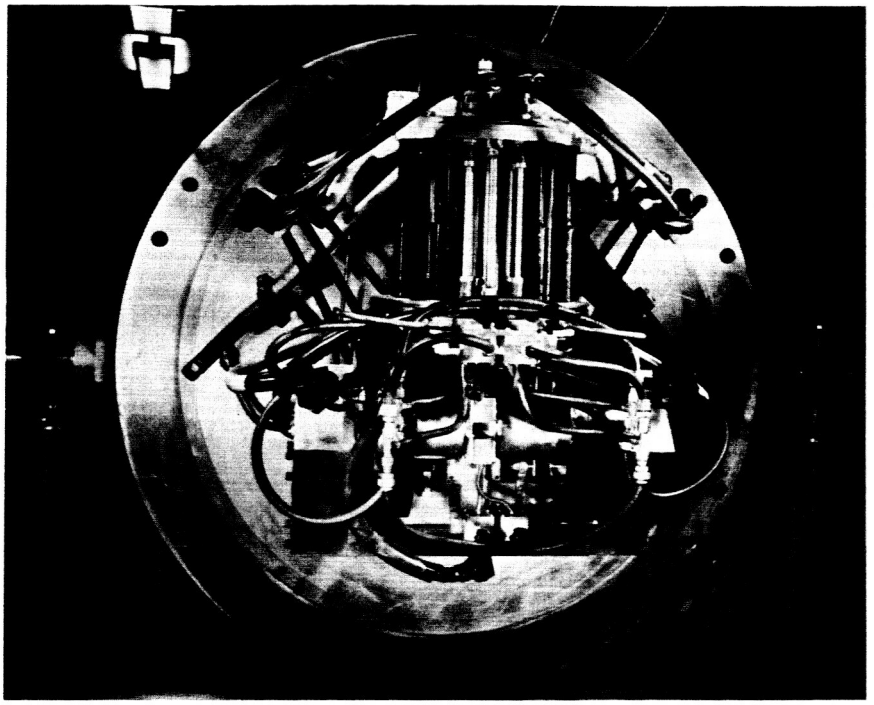

FIGURE 5. Rear view of accelerator and thrust balance mounted on vacuum tank door.

magnetic field was incrementally increased and measurements again taken at each magnetic field level. Measurements of all variables are observed on panel meters during the test and simultaneously recorded on a 36 channel high-speed oscillographic chart recorder for later reduction and evaluation. The frequency response of the recorder is from 150 to 8000 cps depending upon the particular galvanometers being used.

SUMMARY OF "WEAK INTERACTION THEORY"

In order to attempt interpretation of data it is necessary to have some sort of theoretical model and description of the process. Much of the early theoretical work was carried out because it was easy to solve, rather than because it aided in understanding experiments. Some insight into the performance can be obtained by means of one-dimensional analysis (**1, 2**). However, it has not been possible to apply these treatments to the correlation of experimental data. With respect to the crossed-field accelerator, the one-dimensional approach is deficient largely because of fringing electromagnetic fields and the Hall effect.

A striking experimental observation which cannot be explained by means of one-dimensional analysis is the tendency of the current to concentrate at the upstream end of the cathode and downstream end of the anode as shown by visual observation of bright spots. It appears that at least two-dimensional calculations are necessary before proper correlation between theory and experiment can be obtained.

An attempt has been made to develop a two-dimensional analysis for accelerators in reference (**3**). The analysis developed is specifically for the crossed-field accelerator although extension to other geometries is straightforward. It is in the category of a "weak interaction theory" because it is assumed that the interactions of the electromagnetic field with the gas through the Lorentz force and the power addition are both weak. Hence, constant gas properties can be assumed. It is shown that for constant plasma properties, small magnetic Reynolds number, and induced field small compared to applied field, the solution of Maxwell's equations and Ohm's law is reduced to the solution of Laplace's equation for the induced magnetic field.

The solution of this problem has been obtained in three ways: analytically, numerically, and approximately. The analytical solution is similar to the work of Sutton *et al.* (**4, 5**) developed for generators. However, the present analysis is for magnetic field geometries and plasma properties different from those studied previously. The numerical finite difference method was carried out because it is a first step toward development of a method for computing a "strong interaction theory" in which plasma properties vary. The importance of variable properties has been pointed out by Rosa (**5**).

ANALYSIS

The generalized expression of Ohm's law (**7, 8**) which was used is as follows:

$$\vec{j} = \sigma[\vec{E}+\vec{q}\times\vec{B}]-\frac{\omega_e\tau_e}{|B|}\vec{j}\times\vec{B}+\frac{\omega_e\tau_e\omega_i\tau_i}{|B|^2}\vec{j}\times\vec{B}\times\vec{B} \qquad (1)$$

This is a somewhat simplified version but it contains the important features of electron spiraling and ion slip.

Another simplification is to restrict attention to two dimensions. In the case of the crossed-field accelerator this corresponds to flow between infinite parallel plates with the direction of the entering fluid in the x direction. Let both the induced and the applied magnetic fields be in the z direction, perpendicular to the flow direction. In this way variations in the z direction can be neglected so that

$$\frac{\partial}{\partial z} = j_z = E_z = q_z = 0$$

In order for the plasma properties to be constant, it is necessary to restrict attention to the inviscid core of the gas. Even with weak interactions plasma properties vary across the viscous boundary layers and sheaths adjacent to the surface.

In the absence of surface currents the magnetic field is continuous across boundaries. The electric field, however, is not continuous because of surface charges in the sheaths. For these conditions the boundary conditions for the electric and magnetic fields are shown as follows:

	$B = B_1 \quad \vert \quad - \quad \vert \quad B = B_2$	
$\vec{E}_{-\infty} = -\vec{q}\times\vec{B}_1$	$E_x = 0$	$\vec{E}_{+\infty} = -\vec{q}\times\vec{B}_2$
$B_{-\infty} = B_1$	$E_x = 0$	$B_{+\infty} = B_2$
	$B = B_1 \quad \vert \quad + \quad \vert \quad B = B_2$	

where

$$B_1 = B_0+\frac{I_T\mu_0}{2}, \qquad B_2 = B_0-\frac{I_T\mu_0}{2}$$

The components of Maxwell's equations and Ohm's law in two dimensions are

$$j_x = \frac{1}{\mu_0}\frac{\partial B_z}{\partial y}, \qquad j_y = -\frac{1}{\mu_0}\frac{\partial B_z}{\partial x} \tag{2}$$

$$\frac{\partial E_x}{\partial y} - \frac{\partial E_y}{\partial x} = 0 \tag{3}$$

$$B_x = B_y = 0 \tag{4}$$

$$bj_x = \sigma[E_x + vB_z] - aj_y \tag{5}$$

$$bj_y = \sigma[E_y - uB_z] + aj_x \tag{6}$$

where $a = \omega_e\tau_e$, $b = 1 + \omega_i\tau_i\omega_e\tau_e$.

In order to solve these equations, the electric field is eliminated from equations (5) and (6) by means of equation (3) and the normalized induced magnetic field is defined as:

$$\bar{B} = \frac{2(B_z - B_0)}{I_T\mu_0}$$

If the induced magnetic field is small, $\mu_0 I_T/B_0 2l \ll 1$, and if the magnetic Reynolds number is small, $R_m = \sigma\mu_0 u_1 l \ll 1$, the resulting expression can be reduced to Laplace's equation for the induced magnetic field:

$$\nabla^2\bar{B} = 0 \tag{7}$$

The boundary conditions on the electrodes can be obtained from equation (5) when it is noted that the normal component of velocity is zero on all walls:

$$\frac{\partial\bar{B}}{\partial y} = C\frac{\partial\bar{B}}{\partial x} \quad \text{where} \quad C = \frac{\omega_e\tau_e}{1 + \omega_i\tau_i\omega_e\tau_e} \tag{8}$$

Once the induced magnetic field is obtained the potential difference can be determined by means of Gauss's theorem. If the volume is chosen such that the electrodes are the upper and lower surfaces and the cross section in the x-y plane is rectangular, then

$$\int\int \frac{\partial\phi}{\partial y}\,dy\,dx = -(\phi_+ - \phi_-)(x_2 - x_1) \tag{9}$$

Let $x_1 = -x_2$ to make use of the symmetry. Then it can be shown by use of equation (6) that

$$(\Phi_+ - \Phi_-) = uB_0h + \frac{1}{n_e e} I_T B_0 F(C) \tag{10}$$

where

$$F(C) = \frac{1}{2\bar{x}_2 C}\left[\int_0^1 \bar{B}(-\bar{x}_2, \bar{y})\,d\bar{y} + C\int_{-\bar{x}_2}^{\bar{x}_2} \bar{B}(\bar{x}, 0)\,d\bar{x}\right]$$

$$\bar{x} = \frac{x}{h}, \qquad \bar{y} = \frac{y}{h}$$

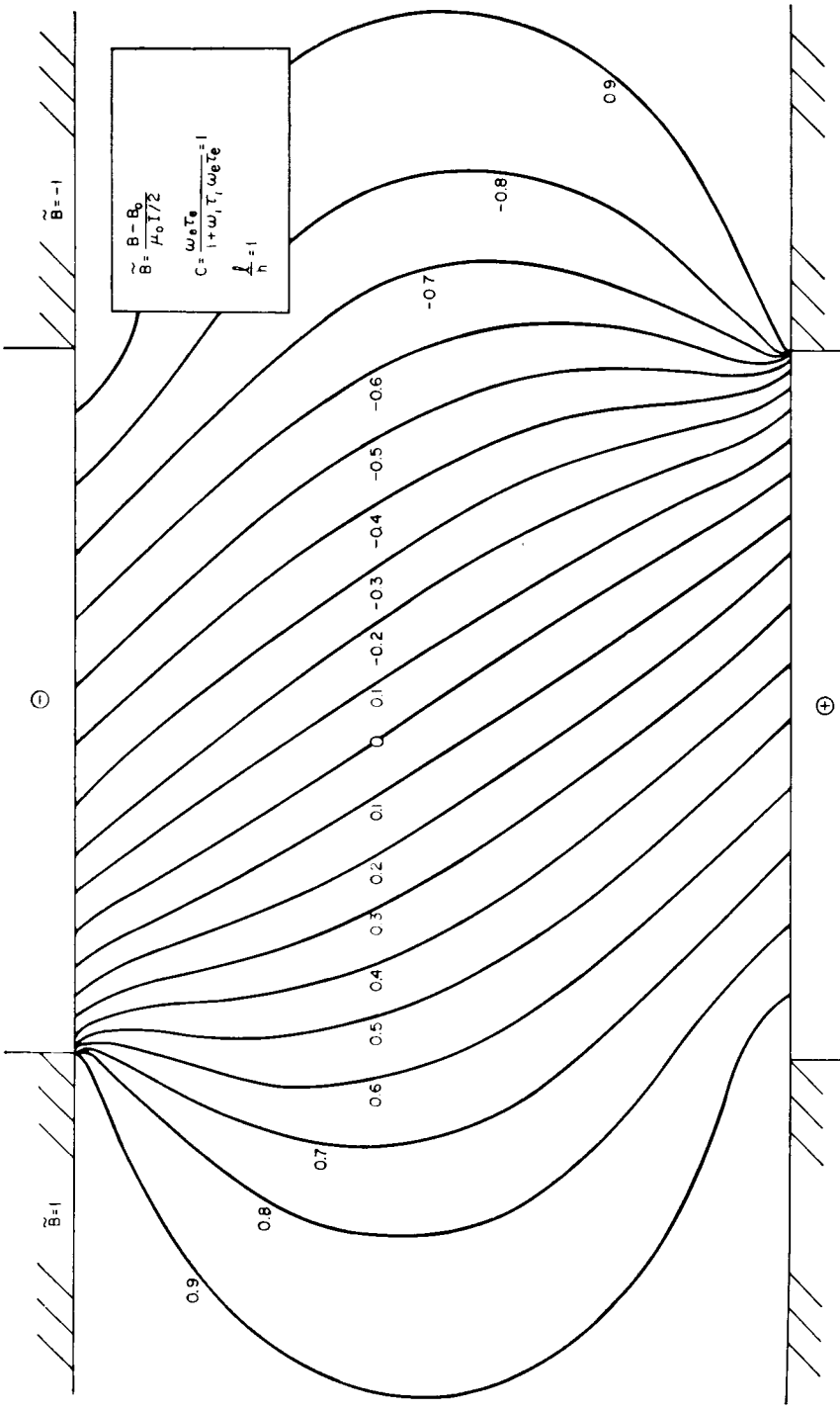

FIGURE 6. Induced magnetic field distribution obtained by finite difference method.

As mentioned previously, the advantage of the finite difference method is that it can later be extended to include variable properties and large induced fields since the character of the equations remains elliptic. Experience in overcoming numerical difficulties has been gained with this method, and a considerable number of cases for various values of the parameter C were run.

A typical induced field pattern computed by this method is shown in Figure 6. Current concentration at the upstream end of the cathode and the downstream end of the anode even at this modest value of C is evident, in agreement with experimental observations. It can be shown that when $C \to \infty$ the solution reduces to a source and sink at those locations. Note also that throughout much of the region the current path is straight at an angle given by the electrode boundary conditions. This suggests a possible approximate solution.

The approximate solution was obtained by assuming that equation (8) holds not only at the electrodes but in the entire region between the electrodes with the exception of the points on the electrodes where the gradients become steep. This is equilvalent to assuming the electric field is uniform and is in the y direction over most of the region between the electrodes. The boundary conditions on the

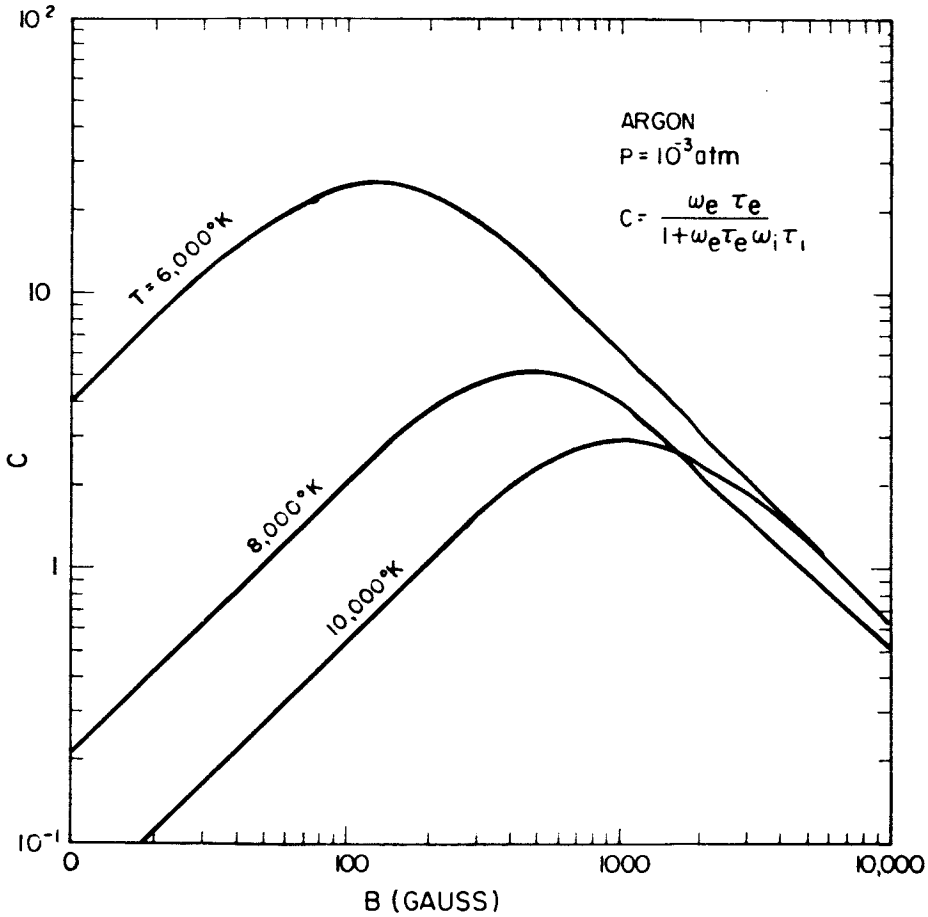

FIGURE 7. Effect of magnetic field strength on the parameter C for argon at several temperatures.

insulator were satisfied at the diagonally opposite corners of the electrodes which do not have steep gradients. The result is

$$\bar{B} = 1 - \frac{2(x+Cy)}{l+Ch} \tag{11}$$

where l is the electrode length and h is the gap. This approximate solution is very convenient for estimating the influence of the parameter C on measurable quantities such as voltage and current density distribution.

HALL PARAMETERS IN ARGON

The Hall parameters $\omega_e\tau_e/B$ and $\omega_i\tau_i/B$ can be obtained from expressions given by Cann (**8, 9**) to yield approximately the following:

$$\frac{\omega_e\tau_e}{B} \cong \frac{3}{4}e\left(\frac{\pi}{8m_eKT_e}\right)^{1/2}\left(\frac{n_eq_{ei}}{2}+n_aq_{ea}\right)^{-1} \tag{12}$$

$$\frac{\omega_i\tau_i}{B} \cong \frac{3}{4}e\left(\frac{\pi}{8m_iKT_i}\right)^{1/2}\frac{n_a}{(n_a+n_e)^2q_{ia}} \tag{13}$$

Cross sections were computed by Ziemer and Cann (**10**) assuming equilibrium. From this data the parameter C which is involved in the boundary conditions on the electrodes can be computed. The results for a pressure of 10^{-3} atmos, which is approximately the channel pressure used, are shown in Figure 7. At low field strengths C increases proportionally with respect to the magnetic field. The peak is

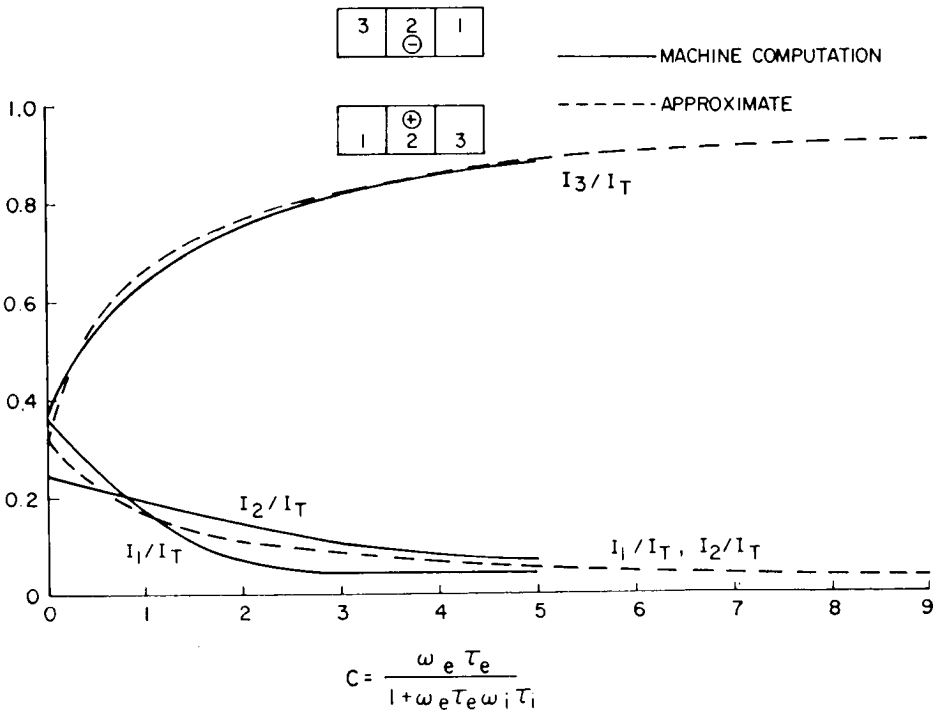

FIGURE 8. Distribution of current among electrode segments as a function of the parameter C.

reached when $\omega_e\tau_e$ cancels out and C is inversely proportional to B. Thus the current should spread out on the electrodes at high magnetic fields. This occurs at field strengths in the range of the experimental equipment. Although ion-slip controls in this region it does not follow that the ions do much spiraling; $\omega_i\tau_i$ is only of the order of 10^{-1}. Non-equilibrium effects will shift the peaks because of the change in the collision time for electrons. It is of interest to determine whether this spreading out of the current is observed experimentally.

CURRENT DENSITY AND VOLTAGE CALCULATIONS

For comparison with the divided electrode experiments, consider electrodes which are divided into three parts in the direction of flow with all parts at the same potential. The current distribution predicted for each segment as a function of the parameter C as calculated by the numerical analysis is shown in Figure 8. It can be seen that the approximate solution is rather good. Within the assumptions that have been made the distribution depends upon C only.

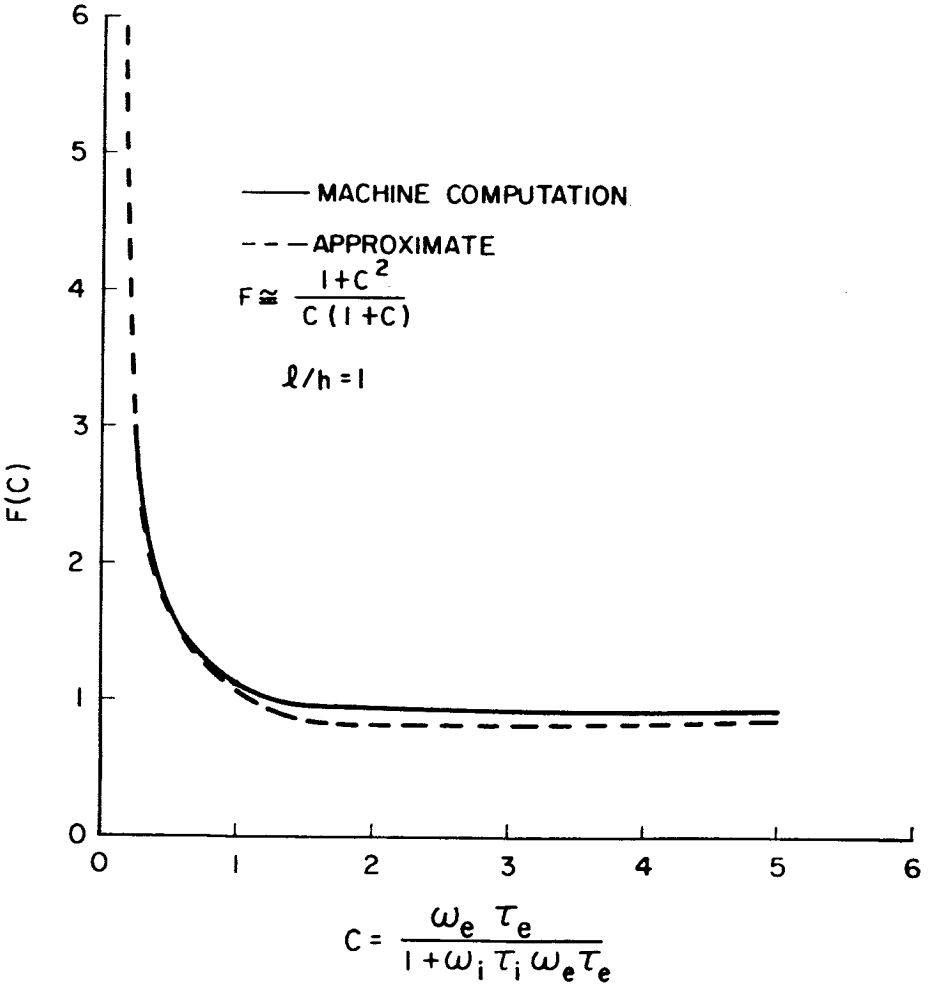

FIGURE 9. Variation of the potential function $F(C)$ with the Hall parameter C.

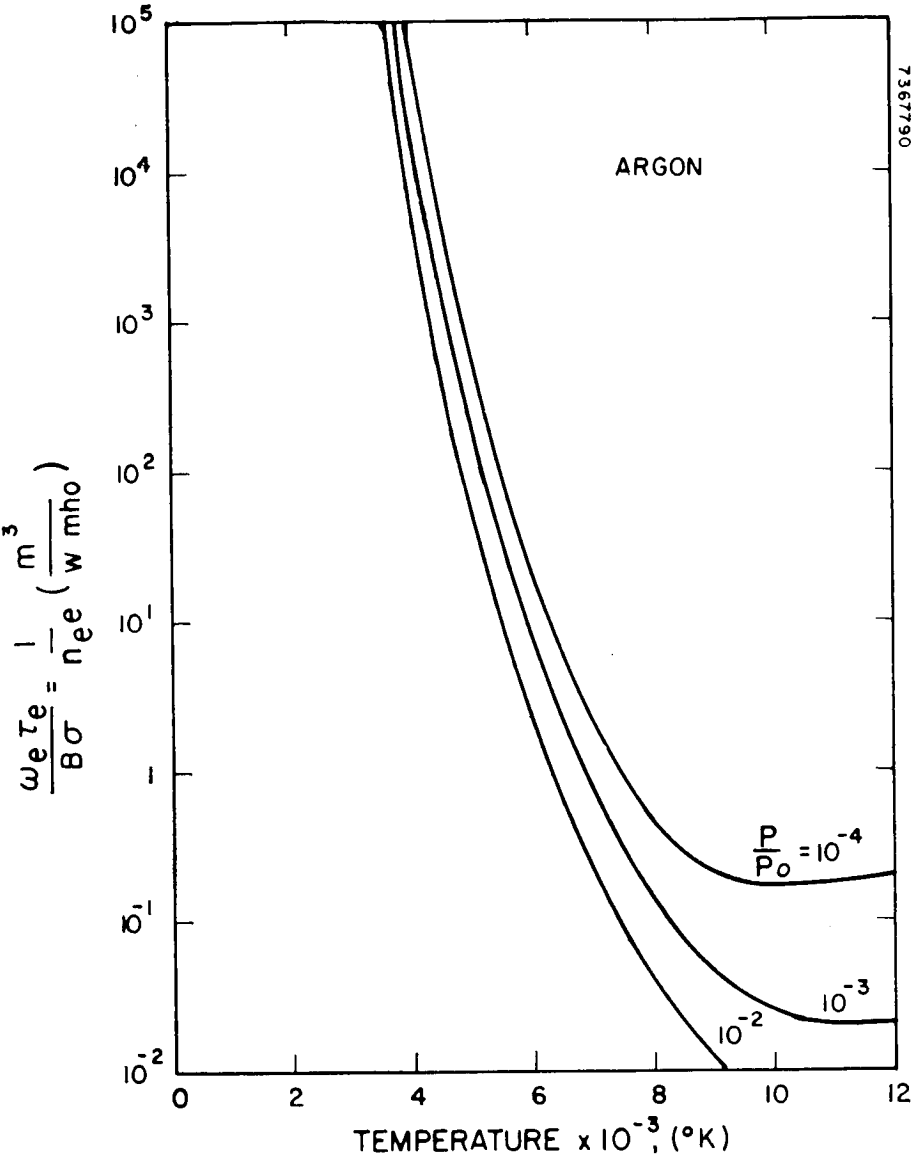

FIGURE 10. Hall coefficient for argon as a function of plasma temperature.

The influence of the current density distribution on the voltage is reflected in the function $F(C)$ of equation (10). Computation of $F(C)$ for various values of x_2 is a check on the numerical calculations since the results should be independent of $\bar{x}_2$. This was found to be true. A plot of $F(C)$ is given in Figure 9. It can be seen that again the approximate solution compares well with the machine computations. Note that at values of C greater than unity $F(C)$ itself approaches unity. Thus the only dependence of the potential difference on plasma properties is through the term $1/n_e e$. This quantity is a strong function of temperature if equilibrium conditions occur as shown in Figure 10. At low values of C, $F(C)$ is inversely proportional

to C so that the magnetic field cancels out of the second term or the right-hand side of equation (10). At low field strength under these conditions this term represents the scalar resistance of the plasma. These results will be referred to later when side-wall potential measurements are discussed.

EXPERIMENTAL RESULTS

PERFORMANCE

To aid in the interpretation of the current density and side-wall potential measurements and relate them to the accelerator operating conditions, the gross performance characteristics of the arc jet and accelerator should be known. In particular, it is important to know the effective plasma velocity and the velocity increment imposed by the accelerator.

Measurements were made of thrust with the force balance from which the apparatus was suspended and of the gas mass flow rate. In order to accurately determine the plasma velocity, measurement was also made of the channel exit and vacuum tank static pressures, and the velocity was computed from the relation

$$T = \dot{m}u_2 + (P_2 - P_3)A_2$$

in which subscript 2 refers to the channel exit and 3 refers to the ambient conditions. The results are shown in Figure 11 for the standard operating conditions of the arc jet.

From this data at various tank pressures with the arc jet alone operating and the accelerator channel present, the average exhaust velocity was determined. It was found to be 1000 to 1250 meters/sec, depending upon the mass flow rate and

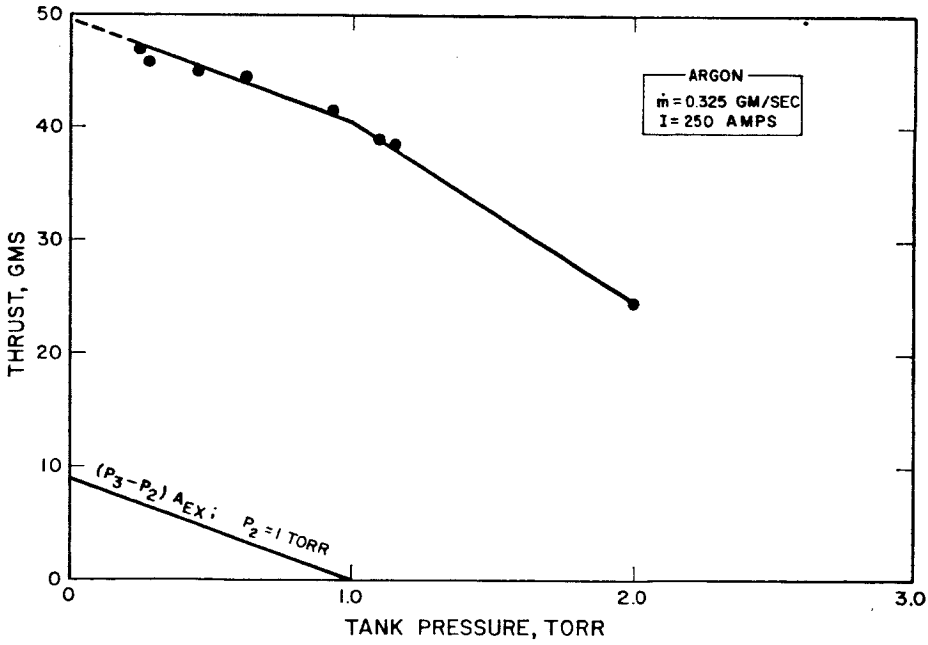

FIGURE 11. Measured thrust of arc jet with accelerator channel in place as a function of vacuum tank pressure.

power input. The higher figure corresponds to the conditions of the diagnostic experiments.

Measurements were also made of the velocity increment resulting from the $J \times B$ acceleration at conditions close to those for the subsequent studies. At an argon mass flow rate of 0.147 gm/sec and an arc jet power input of 3 kw, an arc jet thrust of 15.7 gm was obtained. Then operating the accelerator, a thrust ratio of up to 2.6 was obtained for a current of 62 amps and a magnetic field strength of 3450 gauss.

In later tests when the prime objective was current distribution or wall potential measurements, thrust measurements were not repeated in order to simplify the experiment. In this series of runs, the standard operating conditions for the arc jet were:

Gas	Argon
Mass Flow Rate	0.325 gm/sec
Power Input	5 kw
Total Pressure	145 mm Hg
Throat Area	$\sim$0.11 in^2
Channel Pressure	1.0 mm Hg
Gas Velocity	1250 m/sec (from thrust)

DIVIDED ELECTRODES

A pair of divided electrodes was constructed for use in the crossed-field accelerator to measure the current distribution over the cathode and anode surfaces; each electrode was divided into nine segments. All segments of an electrode were at the same potential but electrically isolated so that the current through each segment could be measured independently. One of the divided electrode assemblies is shown in Figure 3. The segments used in these first tests were water-cooled copper, insulated by an epoxy potting material. The numbering system for the segments used in describing the test data was shown in Figure 2.

The plasma source (arc jet) for these tests was run at a constant mass flow rate of argon of 0.325 gm/sec with a power input of about 5 kw yielding an average velocity of 1250 meters/sec. The accelerator was operated at a constant current of 50, 100, and 150 amps, and the applied magnetic field strength was varied incrementally from zero to 3400 gauss.

CATHODE DISTRIBUTION

The observed current distributions in general were unstable and sometimes oscillatory. More specifically, with no applied magnetic field, the cathode current was carried entirely by one segment, indicating a concentrated cathode attachment point. However, the cathode segment which carried the entire current was not always the same. The attachment point would be on one segment and then "instantaneously" jump to another segment, remain there for several tenths of a second or longer and jump to another segment. On some runs, the current would remain on one segment and not move for the duration of the test run. As the magnetic field was increased above 500 gauss, secondary discharges began to appear on other segments for durations of about 0.01 seconds, but still with the intermittent migration of the primary discharge region. At about 3000 gauss, the current became distributed over as many as four or five segments but still with short periods during which one segment carried the total current. In addition, the amplitude of the current waveform for each participating segment appeared to take

on the character of a random fluctuation. At these higher field strengths, there was a tendency for the cathode spots to confine their migration to the upstream segments. The general appearance of the discharge was considerably more steady with a magnetic field than without one.

The reasons for the observed current density distribution are as yet unknown. It is believed that the cathode distribution may be controlled by the cathode emission mechanism and that its behavior and cause is similar to that for other d-c arc cathode spots (without transverse flow and an applied magnetic field); this phenomenon is still not fully understood. One explanation for cathode spot migration is that the deposit or formation of a low work function material on the cathode surface such as an oxide occurs and the cathode spot moves to this region. Very rapidly this film is removed or destroyed and the cathode spot moves to a new portion of the film. This phenomenon occurs at a rate such that the cathode spot migrates over the cathode surface in a rapid and apparently random manner. Future tests will be run with tungsten electrodes instead of the copper ones used in these tests to determine if any effect can be attributed to the electrode material.

ANODE DISTRIBUTION

The character of the current distribution on the anode was quite different from that of the cathode. In general, the distribution measured on the anode was stable and more consistent among several runs. With no magnetic field, the current was carried predominantly by the trailing edge segments, 3, 6, and 9, but with some transverse asymmetry. There were a few runs, however, in which the current was carried largely by the center and upstream segments. As the magnetic field was increased, the current tended to concentrate on the three trailing edge segments as

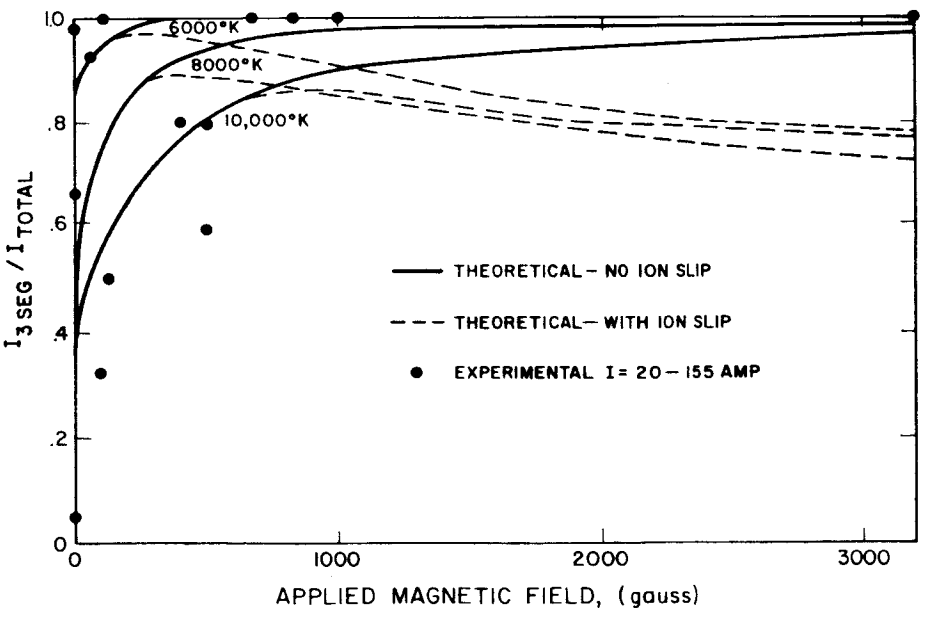

FIGURE 12. Comparison of theory and experiment for the fraction of current carried by the downstream third of the anode as a function of applied magnetic field strength.

predicted by theory. Above 700 gauss, the current was carried entirely by the trailing edge segments and the distribution among these three was uniform. Only very rarely was there observed any instability in the anode current distribution. When it did occur, the duration was about 0.05 to 0.2 seconds and then the previous stable distribution was re-established.

The anode current carried by the trailing third of the electrode, I_3/I_T, is compared with theoretical predictions in Figure 12. The theoretical predictions make use of the machine calculations for I_3/I_T as a function of C (presented previously in Figure 8) as well as equilibrium values of C for argon (which were presented in Figure 7). For the curves labeled "no ion slip" it was assumed that the cross section for ion-atom collision is sufficiently large to eliminate ion slip effects. Of all the cross sections used for the equilibrium calculations, this one is the least reliable. It can be seen from Figure 12 that the data agrees qualitatively with the predictions for "no ion slip" but with erratic behavior superimposed. No evidence was obtained of the current spreading out at high magnetic fields. This may be due to a faulty cross section for ion-atom collisions, or it may be that non-equilibrium conditions control. Independent measurement of plasma properties such as electron number density, electron temperature, and gas temperatures would shed some light on this question.

Much remains to be done with divided electrode measurements themselves. So far there is little data between 1000 and 3400 gauss. It is planned to carry out additional experiments in this region with tungsten electrodes instead of the copper ones used in these experiments. Hopefully, more reproducible data, which may permit more conclusive interpretation, can be obtained with such electrodes.

WALL POTENTIAL MEASUREMENTS

In order to obtain further correlation with theory, and in order to gain insight as to the behavior of the plasma, the potential distribution on the accelerator side wall was measured. If no appreciable current flows normal to the insulator side wall, the wall potential is indicative of the local plasma potential. This technique is similar to that employed by Louis *et al.* (**11**) for the generator.

A set of 19 tungsten pins was imbedded in one side wall of the accelerator, flush with the inner surface. The arrangement is shown in Figure 13. The pins were connected through a 2 pole stepping switch to a 502 Tektronix oscilloscope with a 10 megohm input impedance for voltage readout. With this system, the potential of the various pins was sampled and displayed two at a time with a sampling speed of 20 pairs per second. The oscilloscope display of two complete cycles was recorded photographically.

The first experiment to obtain the wall potential distribution was run with solid (not divided) water-cooled copper electrodes. After several series of tests, it was discovered that copper sputtered from the electrodes was depositing on the wall and was electrically interconnecting the pins. This resulted in very strange potential profiles. Even attempts to clean the wall after each test point failed to be adequate.

In order to eliminate this effect, two changes were made. First, the copper electrode surfaces were capped with a sheet of tungsten 0.060-inch thick to reduce the amount of material sputtered on to the wall; tungsten has a very low sputtering rate compared to copper. Secondly, the wall was counterbored at each pin so that the pin would not be in contact with the inner surface of the wall. If metal deposition did occur, the film could not easily bridge across to the tungsten pin insert.

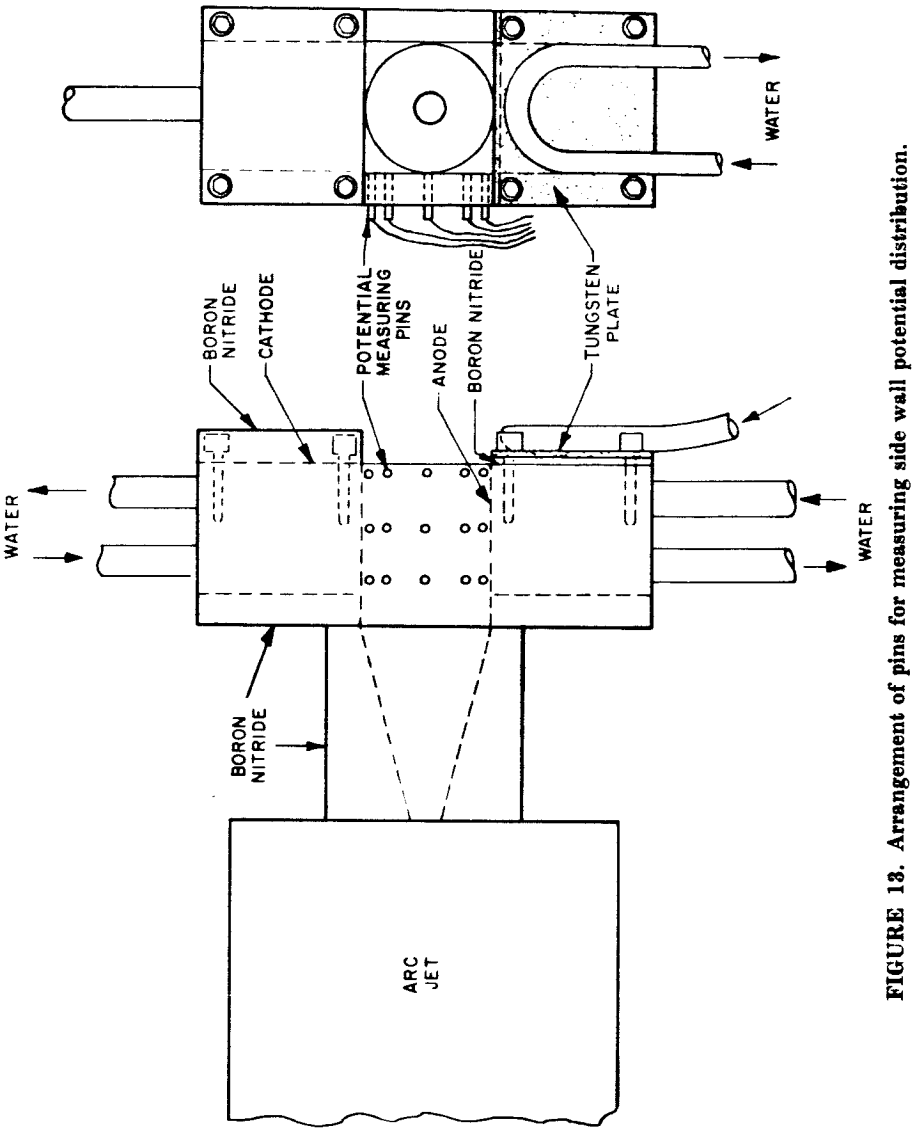

FIGURE 13. Arrangement of pins for measuring side wall potential distribution.

The above modifications proved successful and consistent measurements were obtained in subsequent tests.

The arc jet was operated at 5.2 kw input with an argon flow rate of 0.325 gm/sec. The accelerator was run at a constant current of 25, 50, and 100 amps with the magnetic field varied from zero to 5000 gauss. The measured wall potential for the 50-amp runs are plotted in Figures 14 to 16 as a function of the applied magnetic field strength for the distribution in the direction of the applied electric field at the upstream, middle, and downstream regions. The distribution normal to applied electric field is plotted for regions near the cathode (upper set), the mid-plane, and near the anode (lower set) in Figures 17 to 19. The effect of varying the current is indicated in Figure 20.

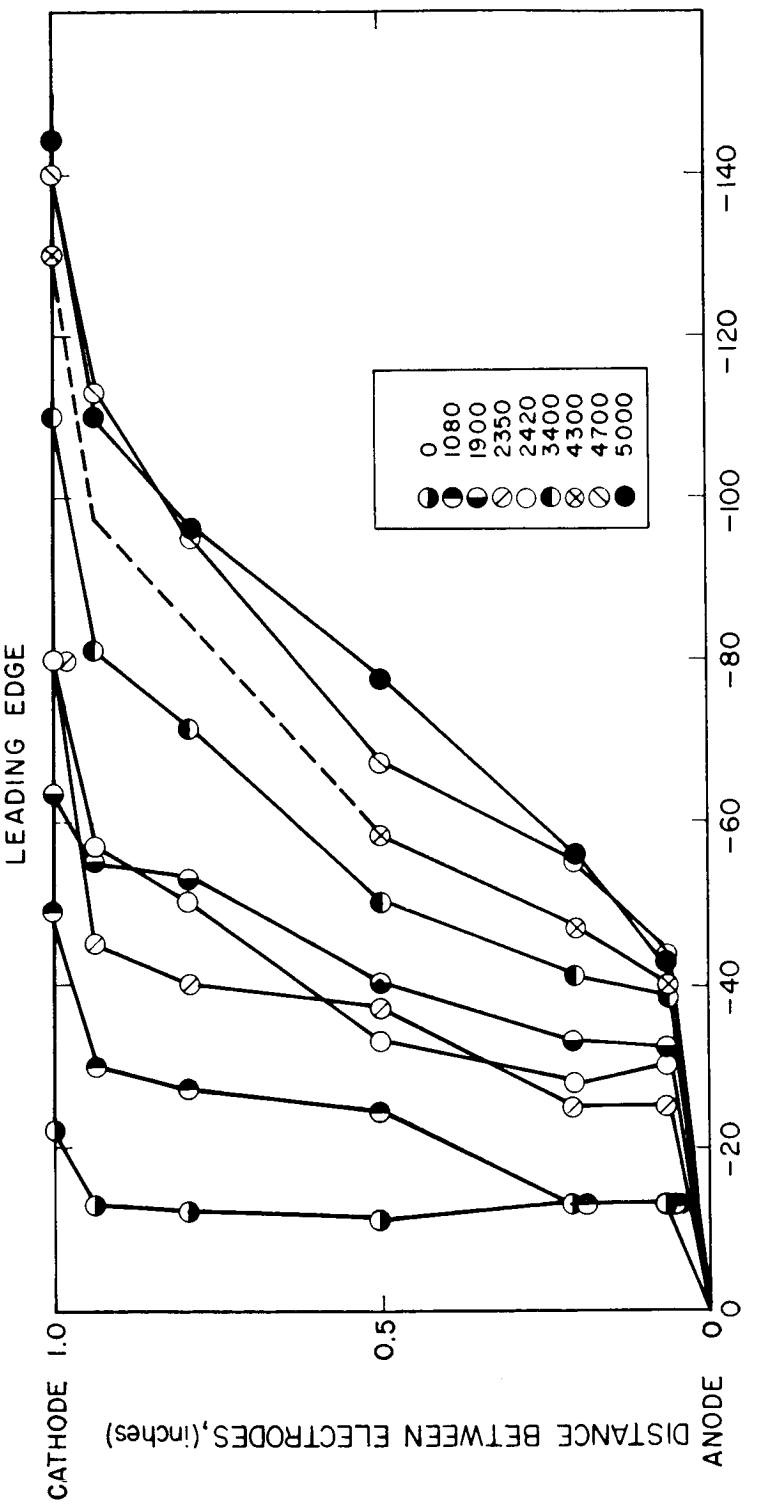

FIGURE 14. Measured potential distribution near leading edge of electrodes, $I = 50$ amps.

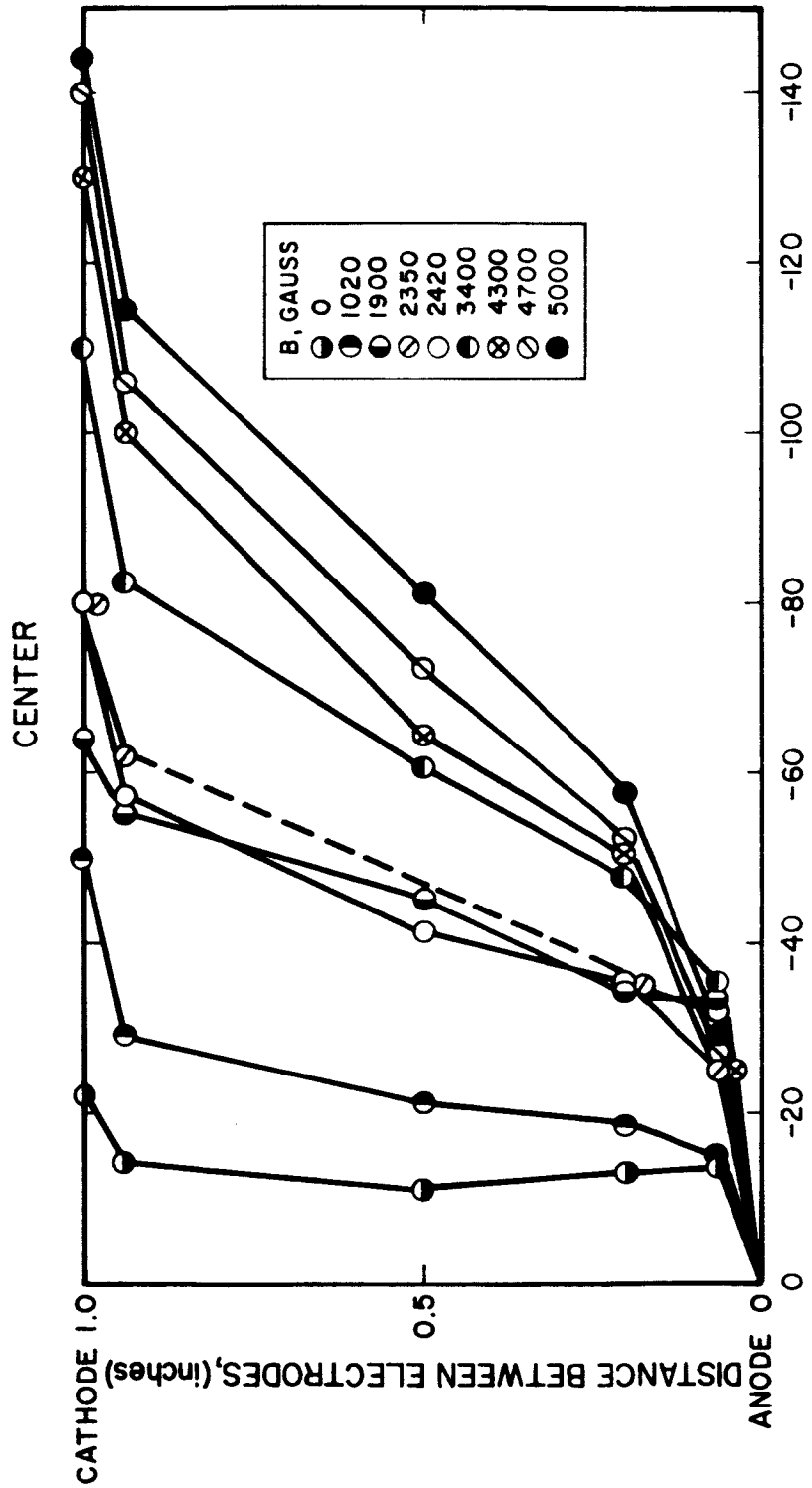

FIGURE 15. Measured potential distribution at center plane of electrodes, $I = 50$ amps.

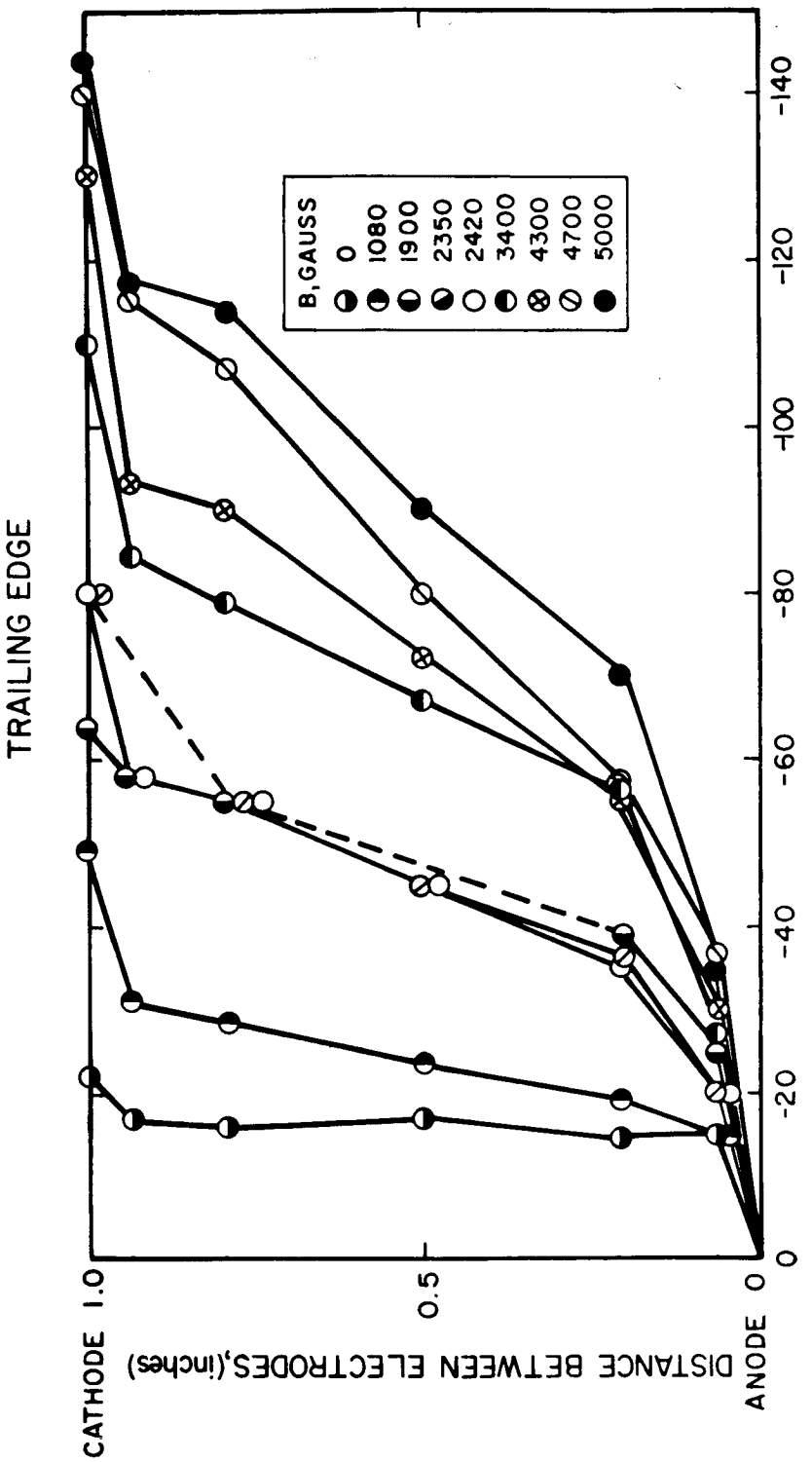

FIGURE 16. Measured potential distribution near trailing edge of electrodes, $I = 50$ amps.

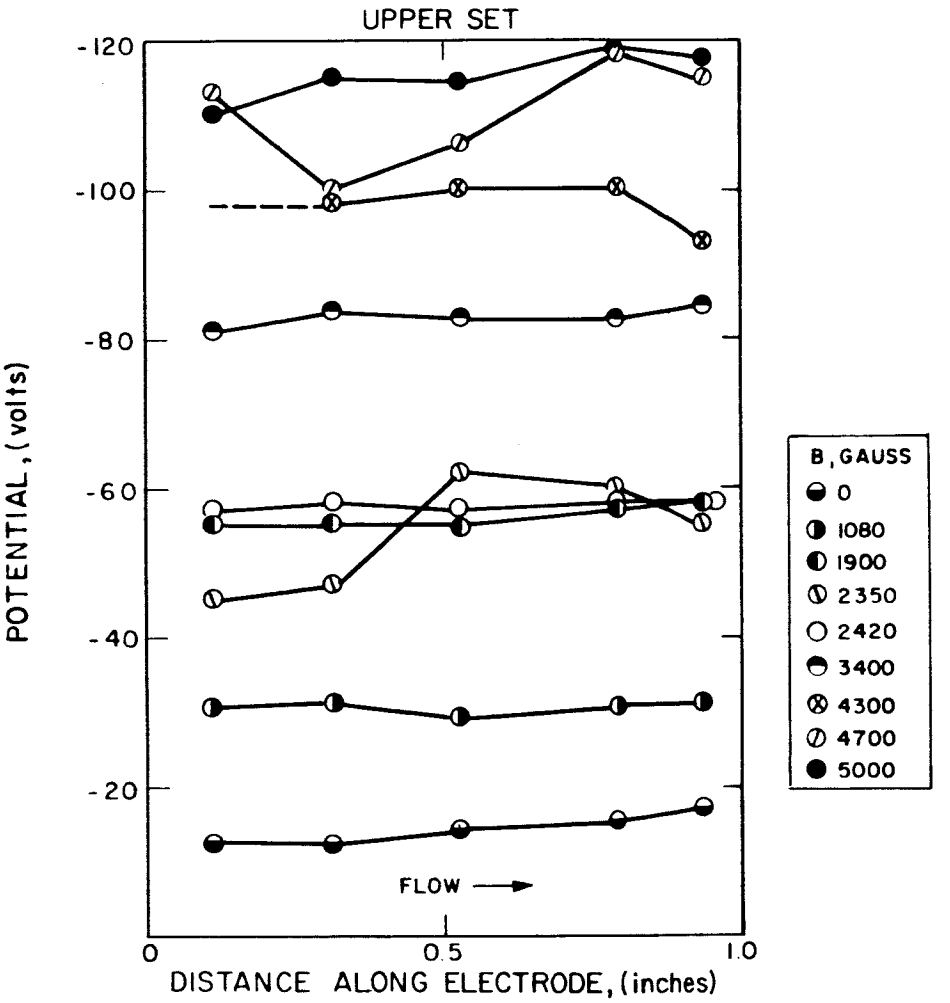

FIGURE 17. Measured potential distribution along plane near cathode, $I = 50$ amps.

ELECTRIC FIELD IN INVISCID CORE

The electric field in the inviscid core can be estimated from the slope in the central portion of the data presented in Figures 14 to 16. This is presented in Figure 21. It can be seen that there is no systematic variation in the data from leading edge to trailing edge. Furthermore, there is no systematic variation with applied current. Although there is scatter in the data, the reproducibility is very good. An average curve (almost a straight line) is plotted. The value of E/B from this line is approximately 6400 m/sec. Data from the total electrode potential is shown for comparison in which the field strength is determined by subtracting a constant electrode voltage drop of 20 volts and dividing by the electrode spacing. This data gives an equivalent value of E/B which is still higher. The difference is due to the effect of the magnetic field on the boundary layer or sheath potential drops which will be discussed later.

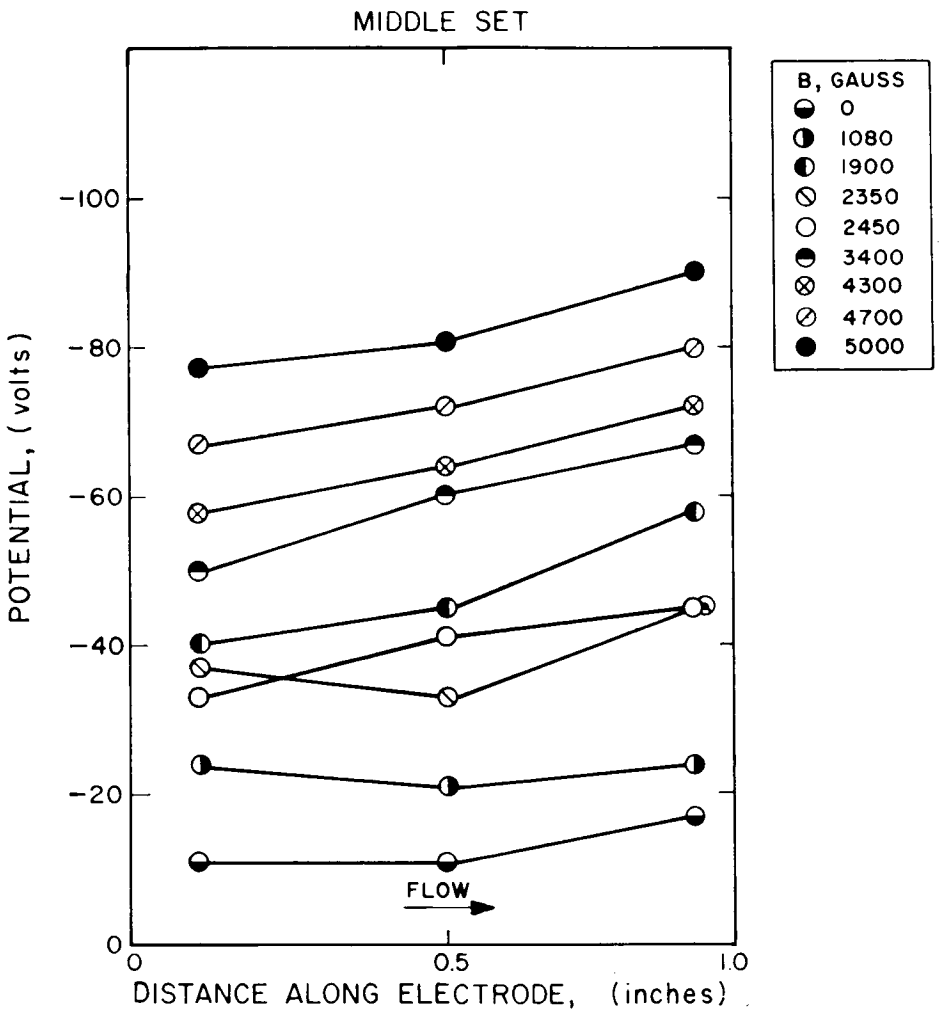

FIGURE 18. Measured potential distribution along middle plane, $I = 50$ amps.

From thrust measurements with pressure correction made with the arc jet connected to the accelerator section but with no second discharge, the velocity at the accelerator entrance, u_0, is 1250 m/sec. The average velocity in the accelerator can be expressed as

$$u_{av} = u_0 + \frac{BIh}{2\dot{m}}$$

if all of the Lorentz force is imparted to the gas. This is equivalent to a velocity of 2080 m/sec at 4000 gauss. Even with this correction, the velocity is far below that corresponding to the indicated value of E/B.

An additional increase in core velocity due to boundary layer effects can be introduced. It can be shown that for a square channel the thrust with the pressure correction divided by the mass flow is

$$\frac{T'}{\dot{w}} \cong u_c\left(1 - \frac{4\theta}{h}\right)$$

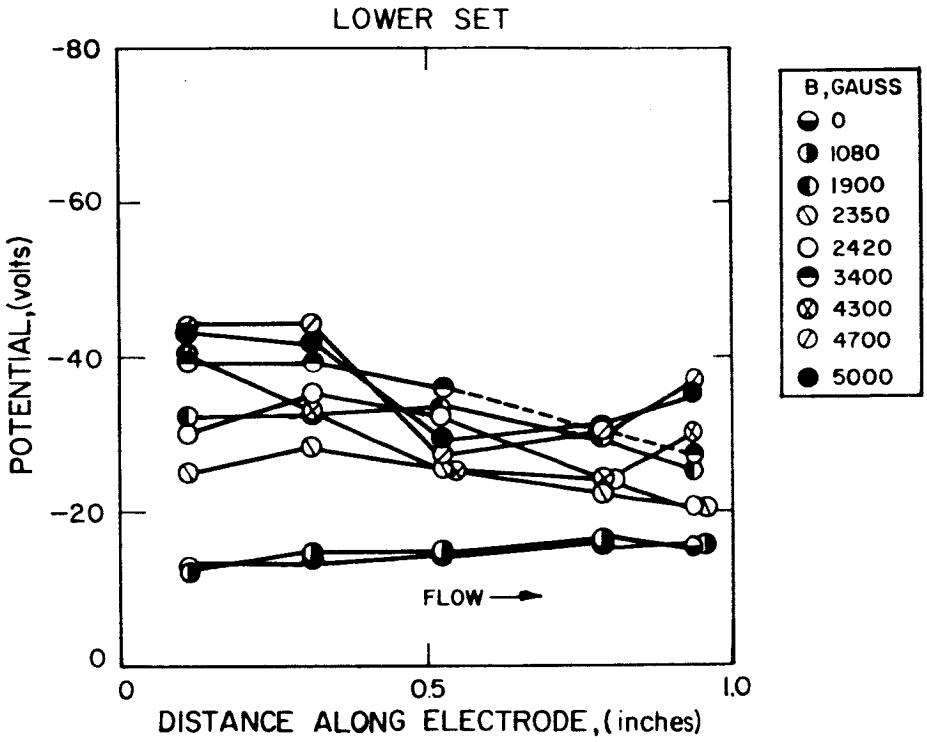

FIGURE 19. Measured potential distribution along plane near anode, $I = 50$ amps.

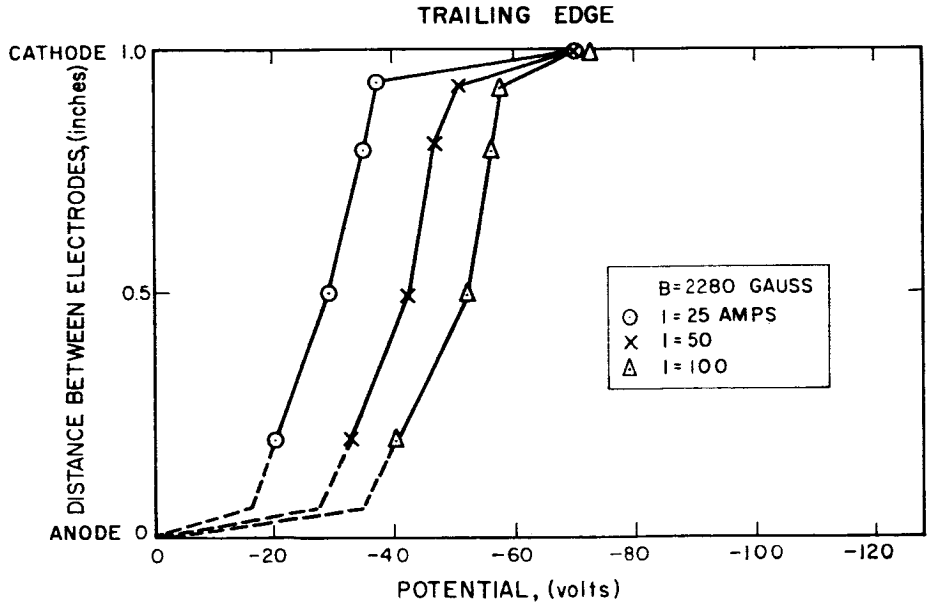

FIGURE 20. Measured potential distribution near trailing edge with variation of current, but constant magnetic field strength.

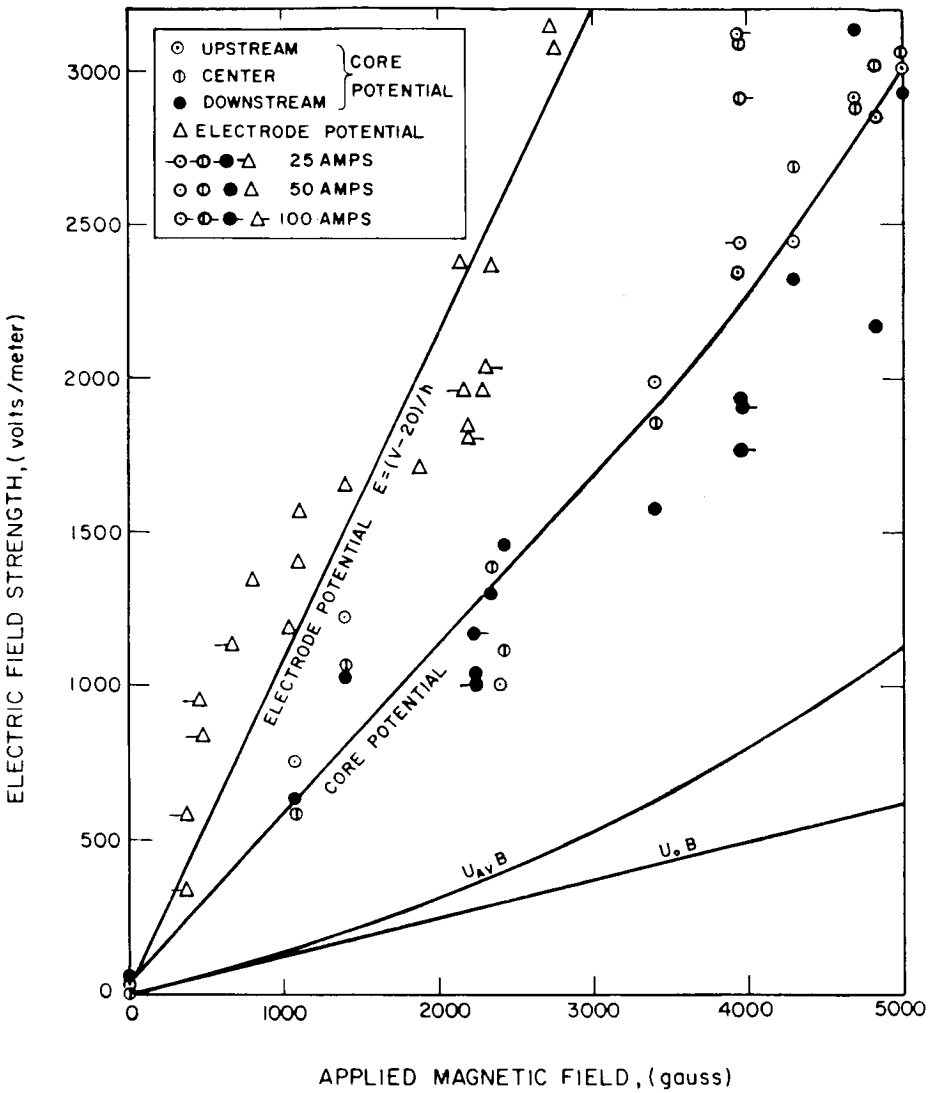

FIGURE 21. Measured electric field strength as a function of applied magnetic field.

where u_c is the core velocity, h is the electrode gap, and θ is the boundary layer momentum thickness. It can be seen that if the momentum thickness becomes as large as 10% of the gap, an error of close to a factor of two in estimating the velocity is possible when total thrust and mass flow are used.

An estimate of the momentum thickness can be obtained from hypersonic boundary layer theory from which

$$\frac{\theta}{x} = \frac{0.664}{Re^{1/2}}$$

This has the same form as the incompressible relation but the Reynolds number should be based on core properties. For a length, x, of 2 inches and a viscosity for

equilibrium argon (**12**) at about 8000°K, the Reynolds number turns out to be about 100. Hence, a value of θ on the order of a tenth of an inch is reasonable. The core velocity could then be increased by a factor of 1.7.

An alternate method of estimating the velocity in the accelerator section is from the power input to the arc jet and the mass flow. Under the conditions mentioned previously for these tests, and an estimated efficiency of 30%, the power into the gas represents a total enthalpy of $h_T/RT_0 = 85$. The corresponding measured total pressure is $P_T \cong 0.19$ atmos. Under these conditions the equilibrium degree of ionization in the chamber is only 1%. Therefore, modest supersonic Mach numbers, and a vacuum velocity of about 3000 m/sec, would be achieved. Use of the measured pressure in the accelerator section of 1 mm Hg with the measured total pressure leads to an accelerator inlet Mach number of 4.3. The area ratio would give the same results if the channel area were reduced by a displacement thickness of 6% for each side. This is not an unreasonable value of δ^* for a highly cooled boundary layer. This method, therefore, leads to velocities considerably closer to E/B. However, due to the nature of the arc column and the geometry of the arc head, the stagnation conditions are not accurately known.

The remaining portion of E/B may be explained by the resistance of the plasma including the influence of the Hall effect. In the analysis it was shown [equation (10)] that

$$\frac{E}{B_0} = u + \frac{I}{n_e e h^2} F(C) \quad \text{(note that } I_T = I/h\text{)}$$

For the Hall parameter C greater than unity, $F(C)$ is approximately unity. For a current of 50 amps at a gas temperature of 8500°K the second term would be as high as 4000 m/sec if the gas were in equilibrium, or as low as 450 m/sec if fully ionized. Such a temperature is not unreasonable considering the energy input to both arcs.

It is interesting to note that in spite of considerable thermal and kinetic energy addition, there was no detectable variation in the electric field from the leading edge to the trailing edge of the electrodes. It is possible, of course, that a significant fraction of the current is shunted around this portion of the core through the electrode boundary layers. This would reduce the value of I in the above expression so that the same value of the second term would correspond to a lower value of n_e.

The lack of a strong variation with applied current would seem to indicate non-equilibrium conditions if the electric fields observed are due to plasma resistance. Under equilibrium conditions the variations of $1/n_e e$ are exponential (Figure 10) with the changes in temperature which would result from changes in power input.

In order to obtain a more complete understanding of the data, it is obvious that further measurements are required. Direct measurement of velocity, temperature, and electron number density in the accelerator is desirable. In addition, non-equilibrium calculations along the lines of Kerrebrock's analysis (**13**) or that of Russell *et al.* (**14**) may help to explain the results. However, quantitative comparison cannot be expected since these theories are still not valid to closer than a factor of 10.

ELECTRODE VOLTAGE DROPS

From the wall potential measurements, the voltage drops near the surface of the cathode and anode can be determined. These voltage drops, which are due to electrode surface, electrode sheath, and cold boundary layer phenomena, are observed as regions of high electric field between the plasma core (where the electric field is constant) and the electrode surface.

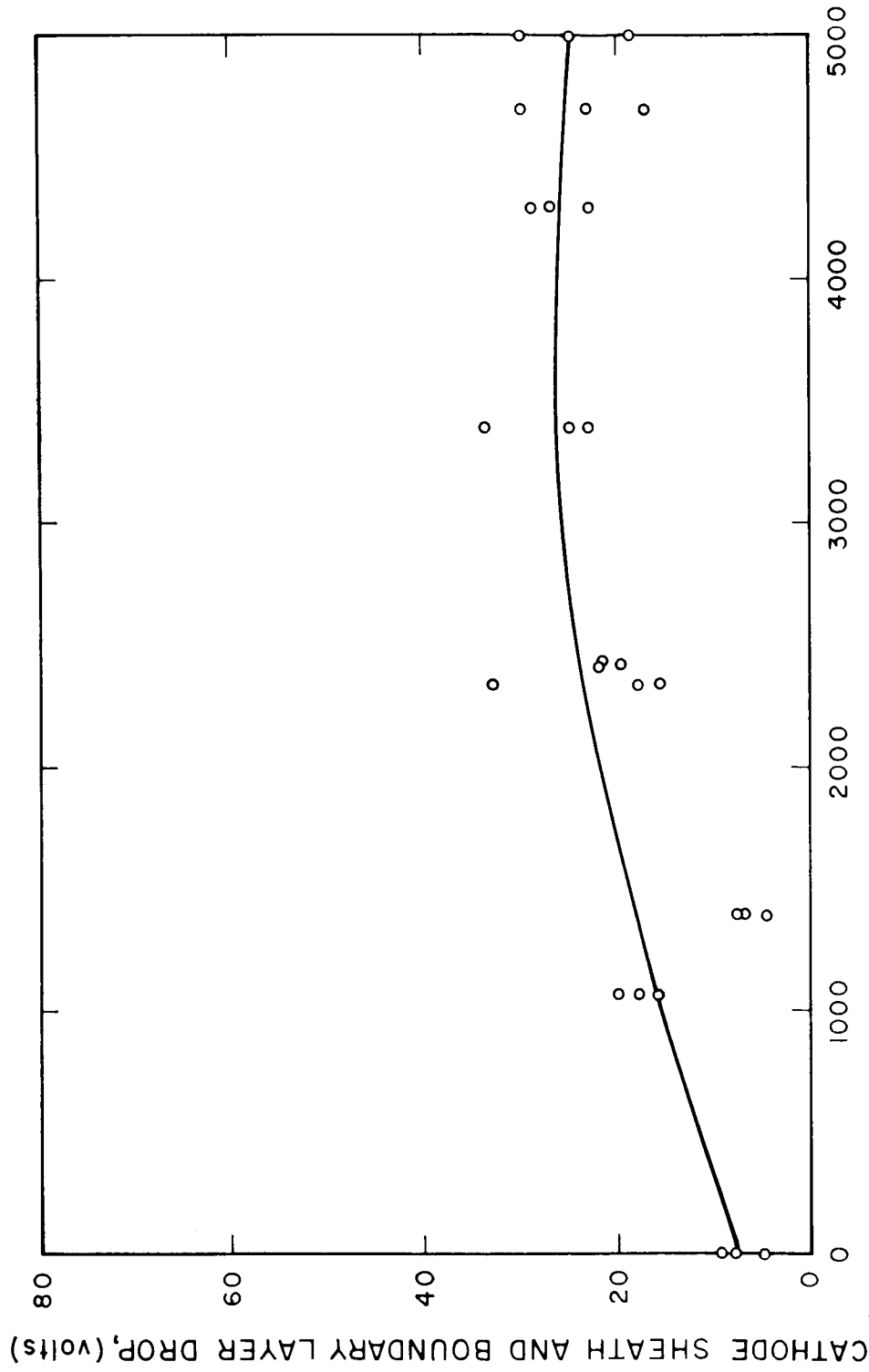

FIGURE 22. Cathode sheath and boundary layer voltage drop as a function of applied magnetic field strength.

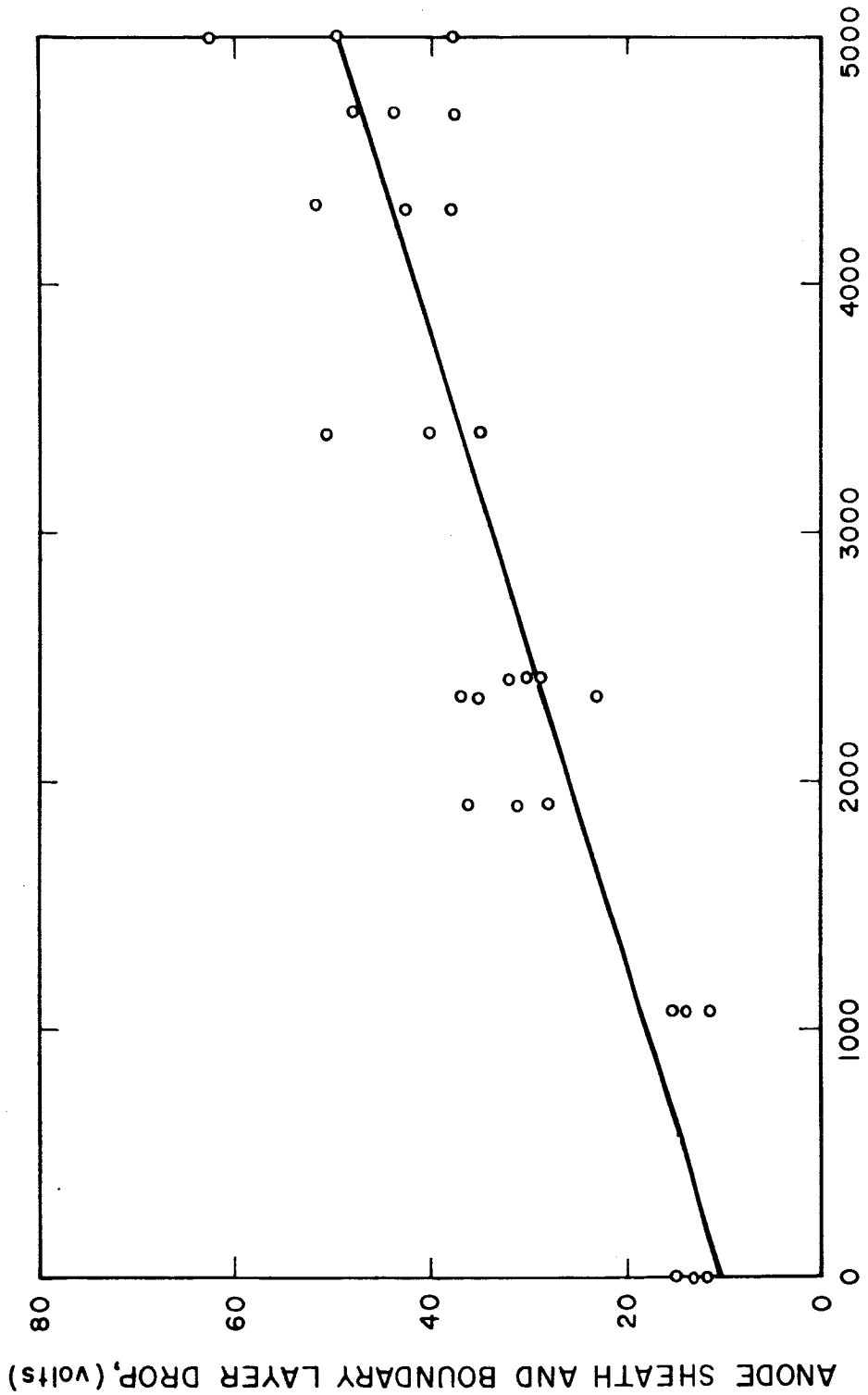

FIGURE 23. Anode sheath and boundary layer voltage drop as a function of applied magnetic field strength.

From Figures 17 and 19 it can be seen that, except for a few anomalous points, the potential along the electrodes is relatively constant. Thus the condition imposed in the analysis that for the inviscid region the potential is uniform along the electrodes appears to be justified, especially along the cathode.

It is observed that, with no magnetic field, the cathode drop is about 8 volts and the anode drop about 12 volts. As the magnetic field is increased, the electrode drops increase in the manner shown in Figures 22 and 23. At 5000 gauss, the cathode drop is about 25 volts and the anode drop is 50 volts.

Another interesting effect can be seen in Figures 14, 15, and 16. The thickness of the cathode drop region is constant. However, the anode sheath and boundary layer thickness increases at the center and trailing edge planes at about 2000 gauss and above. One possible explanation for this effect is that the Hall component of the Lorentz force, which is in the direction normal to the flow and the applied magnetic field, forces the gas away from the anode and towards the cathode. This pressure gradient across the stream would tend to compress the boundary layer on the cathode and thicken it on the anode. The voltage drop is further increased by a reduction of effective electrical conductivity in the boundary layer due to the Hall effect which can become very large in the cooler gas. Hence, the voltage drop across the boundary layer would tend to increase with increasing magnetic field strength.

The existence of these large electrode drops, particularly at the higher magnetic field strengths, represents a very large loss mechanism which is very detrimental to the overall accelerator efficiency.

CONCLUSIONS

The simple diagnostic techniques employed in these experiments have yielded interesting information about the behavior of the accelerator and qualitative correlation with theory.

Current concentration at the leading edge of the cathode and the trailing edge of the anode was confirmed with the divided electrodes in agreement with theory and visual observation. There was no evidence of the current spreading out at high magnetic fields as would occur if ion slip controls.

Reproducible data were obtained from side wall potential measurements. The magnitude of the electric field in the core cannot be explained by the back EMF alone. The resistance of the plasma appears to have a significant effect on the observed potential. The electric field was observed to be uniform from the leading edge to the trailing edge of the electrodes. Variation of the applied current by a factor of four had little effect on the core electric field. The anode sheath potential drops, on the other hand, increased with current but this was compensated by a reduction in cathode sheath drop. The magnitude of the sheath or boundary layer potential increased significantly with magnetic field. The potential along the electrodes at the edge of the boundary layer was relatively constant.

Although a considerable amount of information has been obtained with these simple diagnostic methods, and much remains to be done with these and similar techniques, the need for more sophisticated diagnostic tools has been demonstrated. Detailed information on electron density, electron temperature, gas temperature, and gas velocity would be very helpful in explaining the results. It appears that the phenomena which occur in such accelerators are sufficiently complex that a combination of diagnostic tools along with a realistic theory are required in order to obtain quantitative correlation and more complete understanding of the physical processes.

NOMENCLATURE

a	Hall parameter, defined in equation (6)
b	Hall parameter, defined in equation (6)
B	Magnetic field strength
B_0	Applied magnetic field
$\overline{B}$	Dimensionless induced magnetic field
C	Hall parameter, defined in equation (8)
e	Electronic charge
E	Electric field strength
h	Channel height
I_T	Total current per unit height
j	Current density
K	Boltzmann's constant
l	Electrode length
m_e	Mass of electron
m_i	Mass of ion
n_a	Number density of atoms
n_e	Number density of electrons
P	Pressure
q	Velocity
q_{ea}	Electron-atom cross section
q_{ei}	Electron-ion cross section
q_{ia}	Ion-atom cross section
T_e	Electron temperature
T_i	Ion temperature
u	x component of velocity
v	y component of velocity
w	z component of velocity
x	Distance along channel
y	Distance across channel in direction of electrodes
z	Distance across channel in direction of normal to electrodes
μ_0	Permeability of free space
ρ	Density
σ	Electrical conductivity
τ_e	Mean free time for electrons
τ_i	Mean free time for ions
ϕ	Electrical potential
ω_e	Gyration frequency for electrons
ω_i	Gyration frequency for ions

ACKNOWLEDGMENTS

The authors would like to thank Professor E. Zukoski of the California Institute of Technology for many valuable discussions.

REFERENCES

1. Resler, E. L., and Sears, W. R., "The Prospects for Magnetoaerodynamics", *J. Aero. Sc.*, **25**, 4, 235 (1958).
2. Kerrebrock, J. L., and Marble, F. E., "Constant Temperature Magnetogasdynamic Channel Flow", Reader's Forum, *J. Aero/Space Sci.*, **25**, 1, 78 (1960).

3. Denison, M. R., "A Two Dimensional Weak Interaction Theory for Crossed Field Accelerators", *Electro-Optical Systems RN–12* (April, 1963).
4. Sutton, G. W., "End Losses in Magnetohydrodynamic Channels with Tensor Electrical Conductivity and Segmented Electrodes", *J. Appl. Phys.*, **34**, 2, 396 (1963).
5. Hurwitz, H., Kibb, R. W., and Sutton, G. W., "Influence of Tensor Conductivity on Current Distribution in a MHD Generator", *J. Appl. Phys.*, **32**, 2, 205 (1961).
6. Rosa, R. J., "Hall and Ion-Slip Effects in a Non-uniform Gas", *Phys. Fluids*, **5**, 1081 (1962).
7. Cowling, T. G., *Magnetohydrodynamics* (New York: Interscience, 1957).
8. Cann, G. L., "Energy Transfer Processes in a Partially Ionized Gas", California Institute of Technology—*Hypersonic Research Memorandum No. 61* (June 15, 1961).
9. Cann, G. L., Teem, J. M., Buhler, R. D., and Branson, L. K., "Magnetogasdynamic Accelerator Techniques", *AEDC–TR–62–145* (July, 1962).
10. Ziemer, R. W., and Cann, G. L., "A Steady State Hall Current Accelerator", First Quarterly Progress Report, *Electro-Optical Systems Report 3160–1Q* (September 15, 1962).
11. Louis, J. F., Lothrop, J., and Brogan, T. R., "Studies of Fluid Mechanics using a Large Combustion Driven MHD Generator", *RR 145, AVCO-Everett Research Laboratory* (March, 1963).
12. Baum, E., "Transport Properties of Argon" (unpublished).
13. Kerrebrock, J. L., "Non-Equilibrium Effects on Conductivity and Electrode Heat Transfer in Ionized Gases", California Institute of Technology—*Guggenheim Jet Propulsion Center TN No. 4* (November, 1960).
14. Russell, G. R., Byron, S., and Bortz, P. I., "Performance and Analysis of a Crossed-Field Accelerator", paper presented at AIAA Electric Propulsion Conference, Colorado Springs, Colorado (March 11–13, 1963), *AIAA preprint 63–005.*
15. Wood, G. P., and Carter, A. F., "Consideration in the Design of a Steady DC Plasma Accelerator", in *Dynamics of Conducting Gases* (Evanston: Northwestern University Press, 1960).
16. Demetriades, S. T., and Ziemer, R. W., "Energy Transfer to Plasmas by Continuous Lorentz Forces", in *Magnetohydrodynamics, Proc. of the Fourth Biennial Gas Dynamics Symposium* (Evanston: Northwestern University Press, 1960).

12. Alan F. Klein: *A Survey of Optical Interferometry as Applied to Plasma Diagnostics*

The principles and techniques involved in the application of optical interferometry to plasma studies are reviewed. The assumptions and accuracy of the theoretical calculations are summarized. Experiments to date in the field are reviewed, and recent experiments at Aerospace Corporation are described in which monochromatic interferograms about two-dimensional, sharp and blunted bodies have been obtained using an image converter camera and an exploding wire light source. Resolution times down to 20 nanoseconds have been obtained while maintaining a conventional field of view. Using the multiple frames provided by the image converter camera, the flow fields have been studied as a function of time. White-light color interferograms of these flows have also been obtained at exposure times of 50 nanoseconds using a recently developed Kerr cell.

INTRODUCTION

The technique of optical interferometry has long been used in fluid mechanics and gas dynamics to measure gas density in nonionized flows in wind tunnels and shock tubes (**1**). However, not until the experiments of Alpher and White (**2, 3, 4**) was it successfully demonstrated that interferometry at optical wavelengths could be used to measure electron densities in plasmas.

Optical interferometry, as considered here, depends upon changes in the index of refraction of the test gas. In previous applications, when there were no changes in the chemical composition of the gas, the change in the index of refraction was just due to changes in the gas density. In the present application to plasma diagnostics, the change in the index of refraction is due to both neutral and charged particle-density changes. It will be seen that, usually, the only charged particle of importance in determining the index of refraction of the test gas is the electron. Under most conditions the interferograms reflect contributions due to both the neutral particles as well as the electrons, and additional techniques are required for separating the relative contributions. However, under some conditions, the changes in the index of refraction due to all but the electrons are negligible and the resulting interferograms then represent a direct mapping of the electron density in the flow field.

ED. NOTE: Mr. Klein is with the Aerospace Corporation, El Sequndo, California. This work was sponsored by the U.S. Air Force under contract No. AF04(695)-269.

The essential features of the optical system typically used in this work are indicated in Figure 1. The interferometer is of the Mach–Zehnder type, consisting of two fully-silvered mirrors, denoted by M, and two half-silvered mirrors, known as beam splitters, and denoted by S. Light from the light source is collimated by the lens L_1, and the parallel beam of light enters the interferometer and is divided into

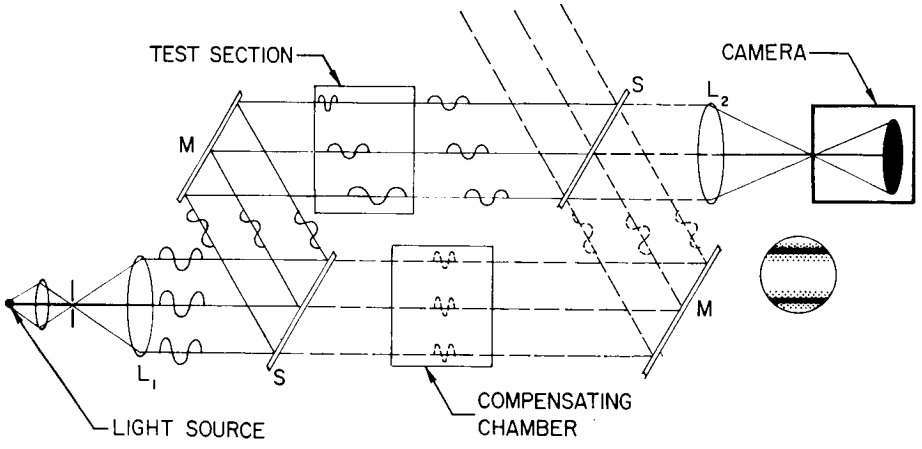

FIGURE 1. Schematic of optics.

two beams of equal amplitude by the first beam splitter. One beam passes through the test section and the other through a compensating chamber which compensates for the optical thickness of the test section windows and for the gas initially in the test section. At the second beam splitter the beams are recombined. The recombined beams are then focused onto the film plane of the camera by the lens L_2. Details of the construction and operation of such an interferometer are presented in reference (**1**).

Consider now the situation in which the collimated beam of light is a monochromatic beam of wavelength λ. If the optical lengths of the two beams are the same, and if the mirrors and beam splitters are all parallel, then the two beams will be in phase over the whole field when they recombine, and they will interfere constructively to produce a uniformly bright field. If the mirrors and beam splitters remain parallel, but the optical length of one beam is increased or decreased by $\lambda/2$ with respect to the other beam, then they will interfere destructively upon recombining and the field will be uniformly dark. If the optical lengths of the paths are the same, and one of the mirrors is rotated slightly, a linearly-changing path difference will be introduced across one beam relative to the other and, upon recombining, there will be alternate constructive and destructive interference, resulting in what is referred to as the initial or undisturbed fringe pattern. If a plasma is now introduced into the test section, further phase differences are introduced between the test and reference beams, causing fringe shifts relative to the undisturbed fringe pattern. These fringe shifts are just proportional to the change in index of refraction due to the presence of the plasma.

As is evident from Figure 1, changes in the index of refraction will be integrated across the width of the test section, and if local flow properties are to be obtained, it is necessary that properties be constant in this direction. Axisymmetric flows can also be treated, but the data reduction then involves an integral transformation. In addition, boundary layers, through which the test beam passes, are developed

at the walls and, under some conditions, these boundary layers can produce nonnegligible effects. Notice, too, that at the second beam splitter half of the recombined beam passes vertically out of the interferometer. This beam is generally not used, although in principle it could be.

THEORETICAL DISCUSSION

The theoretical aspects of both monochromatic and white-light interferometry have been discussed in detail in the literature (**3, 4, 5**). Aspects of the theory of monochromatic interferometry are summarized in this section, with recent additions to the theoretical picture included. Differences between monochromatic and white-light interferometry are discussed in a later section. Emphasis is placed on the case of shock-heated hydrogen, as this is particularly germane to the experiments that will be described in the next section.

The shift, S (in units of fringe spacing), of a fringe with respect to an undisturbed fringe is given by

$$S = \Delta(n-1)L/\lambda \tag{1}$$

where n is the index of refraction (the velocity of light in vacuo divided by the velocity of light in the test gas), L is the thickness of test gas traversed, and λ is the monochromatic observing wavelength. The quantity $(n-1)$ is the refractivity, and the fringe shift is proportional to $\Delta(n-1)$, or the change in refractivity with respect to some reference value.

If one considers the situation where a test section is initially filled with an undisturbed gas at room temperature and at some ambient pressure, and, at some later time, is filled with a plasma (for example, produced by the passage of a strong shock wave), then the fringe shift will be given by

$$S = [(n-1)_{\text{plasma}} - (n-1)_0]L/\lambda \tag{2}$$

where the subscript 0 refers to the gas initially in the test section.

The plasma refractivity can be made up of several components,

$$(n-1)_{\text{plasma}} = (n-1)_A + (n-1)_M + (n-1)_I + (n-1)_e + \cdots \tag{3}$$

The subscripts A, M, and I refer to atoms, molecules, and ions, respectively, in the ground state, and e refers to electrons. In addition, there may be contributions from such things as excited states. Any contribution from excited states will be neglected here; the justification is given in the next paragraph. In the following paragraphs each of the contributors to the plasma refractivity in equation (3) is considered briefly; its significance in particular examples is also discussed.

For atoms and molecules, the refractivity is given by

$$(n-1)_{A,M} = 2\pi N_{A,M}\alpha_{A,M} \tag{4}$$

where N is the number density of the molecular or atomic species and α is its polarizability. The polarizability is related to the separation between bound charges or the dipole moment, which can be induced in the atom or molecule per unit applied electric field. The larger the induced dipole moment, the more the test beam is retarded in passing through the medium, and the larger the phase difference between the test and reference beams when they are recombined. The polarizability is a function of wavelength, but in most cases there is little difference between the polarizability at optical wavelengths and the d-c or infinite wavelength polarizability. This is because optical frequencies are still small compared to the natural atomic frequencies. Table I contains values of the refractivity for molecular

hydrogen at standard temperature and pressure (S.T.P.) for several wavelengths (**6**). The results of some recent calculations of the refractivity of atomic hydrogen in the ground state (**7**) are also tabulated. Although the polarizability of an excited state of an atom, molecule, or ion is expected to be larger than the corresponding species in the ground state, the number density of particles in these excited states is generally so low that the contribution of these particles to the plasma refractivity can be neglected.

TABLE I. HYDROGEN REFRACTIVITIES

Refractivity	*Wavelength* (Å)		
	∞	5870	5461
$(n-1)_{H_2} \times 10^4$	1.358	1.388	1.392
$(n-1)_H \times 10^4$	1.132	1.173	1.179

Due to the lack of accurate values, most experimenters have assumed that, for hydrogen, the molecular and atomic refractivities are equal. Table I indicates there may be nonnegligible differences. Further experimental work is necessary to establish the validity of these differences. Infinite-wavelength polarizabilities for many atomic and molecular gases of interest are tabulated on page 86 of Allen (**6**).

The refractivity of the free electrons is calculated from dispersion theory. For an electron gas in which the electron-heavy particle collision frequency is much less than the observing frequency, the index of refraction is given by

$$n^2 = 1 - \omega_p^2/\omega^2 \tag{5}$$

where $\omega_p^2 = 4\pi N_e e/M_e$ is the square of the plasma frequency, and is the observing frequency. N_e is the number density of free electrons, e the electronic charge, and M_e the electron mass. Since $\omega_p^2/\omega^2 \ll 1$ for optical frequencies and for the electron density range of 10^{15} to 10^{18} cm^{-3}, one can write

$$(n-1)_e \approx \frac{-2\pi N_e e^2}{M_e \omega^2} \tag{6}$$

Putting in the appropriate constants,

$$(n-1)_e = -4.46 \times 10^{-14} \lambda^2 N_e \tag{7}$$

From equation (7), the contribution to the plasma refractivity of the free electrons is seen to depend only upon the wavelength and the electron number density, independent of the ambient gas. At a wavelength of 5461 Å, with a test-section thickness of 7.6 cm., from equations (1) and (7) it is seen that a shift of 0.1 fringe widths, due to electrons, corresponds to an electron density of 5.4×10^{15} cm^{-3}. Since a fringe shift of 0.1 fringe is considered a reasonable lower limit on the sensitivity of the technique, this places a lower limit of approximately 10^{15} cm^{-3} on the electron number density that can be measured with optical interferometry. It is possible to increase the sensitivity to 0.01 fringes and measure still lower electron densities (**8**).

For the case of the ions, both calculations and experiments are more difficult. It can be generalized that calculations and experiments are more difficult any time the state of the gas requires high temperature (e.g., ions and dissociated molecules). For argon, the ratio of the polarizability (hence the ratio of refractivities) of the

argon ion to the argon atom has been calculated by approximate quantum mechanical techniques, yielding a calculated value of 0.7 (**3, 5**). The accuracy of this value is questionable, but it is the best available. Since the value is of the same order as the atom value, the usual practice has been to set them equal. Since the fringe shift is proportional to the number density and since the electron refractivity, per particle, is generally much larger than the atom and ion refractivity, setting the ion polarizability equal to the atom polarizability results in no significant error, because the electron number density is always at least as large as the ion number density. In the case of hydrogen this uncertainty does not exist. The hydrogen ion, being a proton, is treated as an electron with a positive charge and a different mass. From equation (6), the electron refractivity is inversely proportional to the mass, so the ratio of electron refractivity to ion refractivity will be equal in magnitude to the ratio of proton mass to electron mass (approximately 10^3). The hydrogen ion refractivity is therefore completely negligible, since a free electron is always created with each ion.

Returning to the fringe shift equation (2) and inserting the appropriate expressions, one obtains

$$S = \left[\left(\sum_i 2\pi N_i\alpha_i - 4.46\times10^{-14}\lambda^2 N_e\right) - 2\pi N_0\alpha_0\right]\frac{L}{\lambda} \tag{8}$$

where the subscript i refers to the ith atomic, molecular, or ionic species in the plasma. The second term on the right of equation (8) is the free electron refractivity; the third term represents the refractivity of the reference gas (subscript 0). The density of free electrons in the reference gas is assumed to be negligible.

Consider now the case realized in the experiments to be described in later sections, where the undisturbed gas is room-temperature molecular hydrogen, and the plasma is generated by the passage of a strong shock wave. The plasma will then consist of free electrons, protons, and atomic hydrogen. It is assumed that the shock waves are strong enough to fully dissociate the hydrogen molecules.

Using the infinite wavelength refractivity values of Table I, equation (8) becomes

$$S = \frac{L}{\lambda}\left[(4.21\times10^{-25}N_{\mathrm{H}} - 4.46\times10^{-14}N_e\lambda^2) - 5.05\times10^{-25}N_{\mathrm{H_2}}\right] \tag{9}$$

where the protons have been neglected. The relaxation time for dissociation is much shorter than that for ionization, and short enough that dissociation appears as a discontinuity, so that immediately behind the shock front the gas will be fully dissociated, and N_e will be approximately zero. In addition, the gas will have been compressed by the shock. At this stage the fringe shift S will be given by the difference between the first and third terms of equation (9), and will be in the direction of increasing refractivity, inversely proportional to the observing wavelength. Behind the shock front, ionization will start and there will be a shift in the fringes in the direction of decreasing refractivity due to the second term in equation (9). The fringe shift due to the electrons is proportional to the wavelength, so that if the neutral particle density is also changing, one can separate the relative contributions to the net fringe shift by taking interferograms at two wavelengths. For a detailed discussion of this point see Alpher and White (**4**).

Since the fringe shift is proportional to the density N, conditions can be achieved where the ambient density is so low that, for the strongest shock waves, the fringe shift due to the compression and dissociation of the gas is less than 0.1 fringes. Under these conditions the interferograms represent a direct mapping of the electron density in the plasma.

TECHNIQUES

When optical interferometry was used mainly with steady-state devices such as wind tunnels, the light source/camera requirements posed few problems as one could use a long exposure time to photograph a comparatively large field of view, the extent of which was usually determined by the size of the interferometer optics. Many light sources of sufficient intensity and spectral distribution were available. For pulsed devices, such as shock tubes, one had to use an exposure time that was short enough to "stop" the motion of the shock wave. A brighter light source was thus required to expose films in these short exposure times. Shuttering was provided by either a fast mechanical shutter or, more commonly, the duration of the pulse from the light source itself. However, for application to many devices of interest today, the natural duration of these light pulses are too long to "stop" the motion and the light pulses are not bright enough to expose films in the extremely short times required. One way of circumventing these problems, as well as studying the time history of transient phenomena, is to use the technique of streak interferometry. In streak interferometry an image of the fringe pattern is swept across a film by a mirror rotating at high speed. However, instead of photographing a relatively large field of view as with conventional interferometry, only a very narrow strip of the test section is viewed. With this technique the effective resolution time is determined by the width of the strip of test section being viewed and by the speed at which the image is swept across the film. Typically, resolution times of ~ 0.1 μsec. are obtained. One now can use a long-duration pulsed light source of moderate intensity, and no shutter is necessary. The technique of streak interferometry was first reported by Bennett, Shear, and Burden, applying it to the study of axisymmetric, exploding-wire phenomena (**9**). Their white light work is mentioned again in the next section.

Most of the work that has been reported to date, applying optical interferometry to plasma diagnostics, has utilized the technique of streak interferometry (**10–14**). These experiments have involved electron density measurements in both two-dimensional and axisymmetric flows. Perhaps the most interesting of these are the experiments of Ramsden and McLean (**12, 13**) in which an attempt was made to compare the electron densities measured interferometrically with those measured

TABLE II. COMPARISON WITH SPECTROSCOPICALLY DETERMINED ELECTRON CONCENTRATIONS

1. Incident Shock Experiments

Interferometer $\times 10^{16}$ cm^{-3}	*Continuum* $\times 10^{16}$ cm^{-3}		*Line Width* $\times 10^{16}$ cm^{-3}	
	λ5200	λ4530	H_β	H_γ
4.5 ± 0.4	5.6 ± 0.7	5.4 ± 0.7	4.3 ± 0.6	4.8 ± 0.7

2. Reflected Shock Experiments

Interferometer $\times 10^{17}$ cm^{-3}	*Continuum* $\times 10^{17}$ cm^{-3}	H_β *Line Width* $\times 10^{17}$ cm^{-3}
2.9 ± 0.11	2.28	2.44

by spectroscopic techniques. Table II summarizes their results. In the first experiments, using an electromagnetic shock tube of the T type, with hydrogen as the test gas, electron densities were measured with the interferometer. The densities were also measured spectroscopically both by the absolute intensity of the continuum plasma emission at two different wavelengths and by the widths of Stark-broadened hydrogen Balmer lines. In the second experiments, working with the higher electron density gas behind the reflected shock wave in the same device, the interferometrically-determined electron densities were again compared with the spectroscopic values. Much better agreement, which the authors attribute mainly to the higher electron densities and hence the larger fringe shifts, was obtained in the second experiments.

If one is interested in studying, for example, the electron density distributions about bodies, or in the wakes of bodies, it then becomes necessary to photograph the whole test section, and not just a narrow strip. Hence, streak interferometry becomes unacceptable. In addition, for application to some of the devices of interest today, resolution times are required that are not attainable with streak interferometry.

Towards these ends, techniques have recently been developed at the Plasma Research Laboratory, Aerospace Corporation, for obtaining significantly better time resolution, at the same time maintaining a conventional field of view (**15**). Both monochromatic and color, white-light experiments have been conducted. The white-light experiments are discussed in the next section. In both the monochromatic and white-light experiments the plasma was generated in a conical-driver electromagnetic shock tube (**16**) using hydrogen as the working gas. This type of shock tube operates typically over the shock Mach number range of 20 to 60, at pressures from 5 microns to a few millimeters Hg. In all of the experiments an exploding tungsten wire was used as the interferometer light source. This light source was developed as part of the experimental program to provide a light pulse that was intense enough to enable one to expose conventional films in exposure times of ~ 0.01 μsec. The light source consists of a 5-mil tungsten wire, supplied by a 6000 joule capacitor bank, charged to 18 kV. Following a 6-μsec rise time, the resulting light pulse decays slowly back to zero over approximately 100 μsec. The light pulse is extremely bright and consists almost entirely of continuum radiation. The intensity is fairly uniform over most of the visible spectrum. The light source is thus suitable for both monochromatic and white-light interferometry. For the monochromatic experiments, a narrow pass-band interference filter is inserted in the light path. In the monochromatic experiments, the interferograms were photographed with a Space Technology Laboratories image converter camera. This camera provides three separate exposures per run, with individual frame exposure times down to 0.01 μsec, and any desired interval between each exposure.

Figure 2 is an overall view of the apparatus. In the left foreground is the conical discharge tube. The shock tube runs to the right, across the picture. Behind the interferometer, in the left background, the exploding wire light source and its associated optics can be seen. As shown in Figure 2, the wire itself is enclosed in the cylindrical can. This deflects the shock wave, which accompanies the explosion of the wire, away from the interferometer. The interferometer, visible in the center of the picture, has 6-inch diameter mirrors and beam splitters which can be adjusted remotely.

Figure 3 is a photograph of the test section as seen looking in through the interferometer. The aluminum shock tube has a 3-inch-by-3-inch cross section, and the diameter of the test section windows is 6 inches. A cylindrical model is shown in the photograph. Both a $\frac{3}{8}$-inch diameter cylindrical model and a 30° half-angle

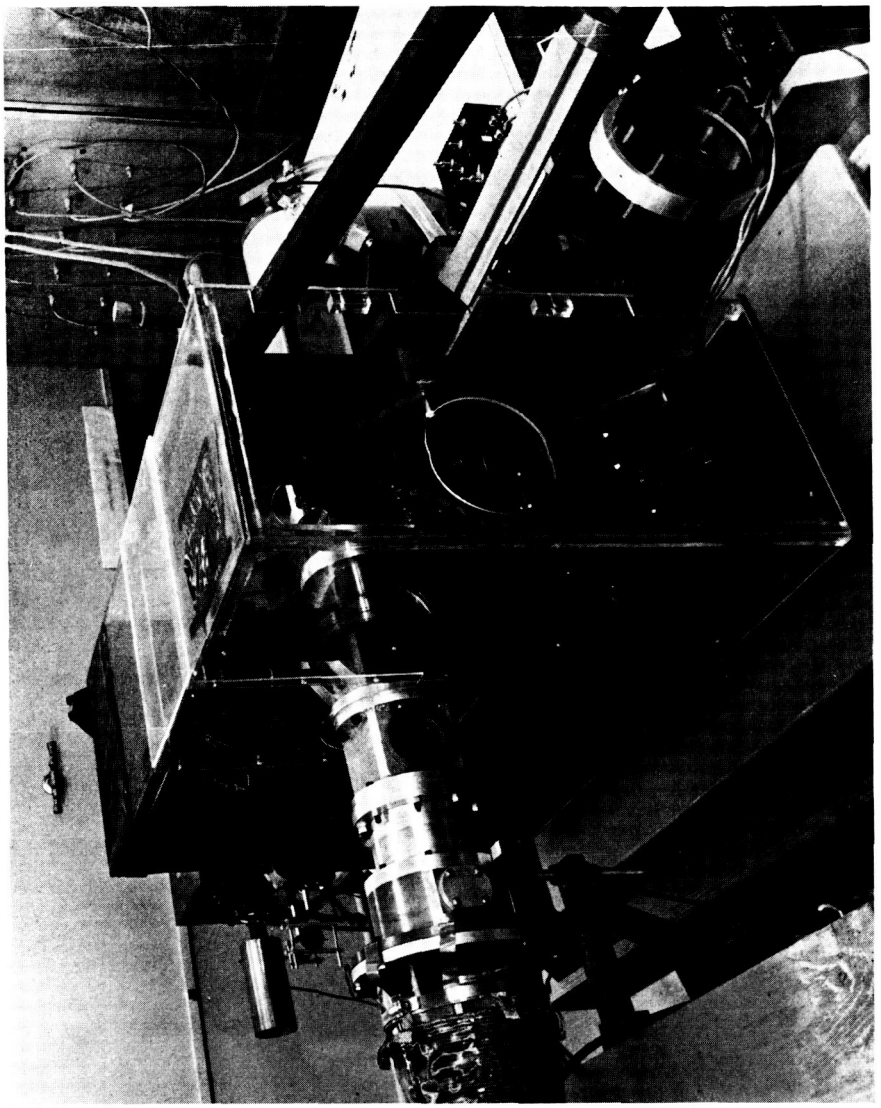

FIGURE 2. Overall view of apparatus.

wedge were used in these experiments. The models are supported by holes in the test section windows.

Figures 4 and 5 are monochromatic interferograms of the flow about the $\frac{3}{8}$-inch cylinder at 5461 Å, with both vertical and horizontal fringes. Figure 6 is a monochromatic interferogram, also at 5461 Å, with vertical fringes, of the flow about the 30° wedge. In each case the initial pressure of hydrogen is indicated in the picture. The arrow indicates the direction of flow in each of the frames. The time interval between successive frames, is indicated in microseconds by the time scale in each photograph; the exposure time of each frame is also indicated in microseconds. Notice that in the interferogram of the flow about the wedge the exposure time of each frame is 0.02 μsec. In each of the photographs the shock Mach number, at the test section, was approximately 20 to 30.

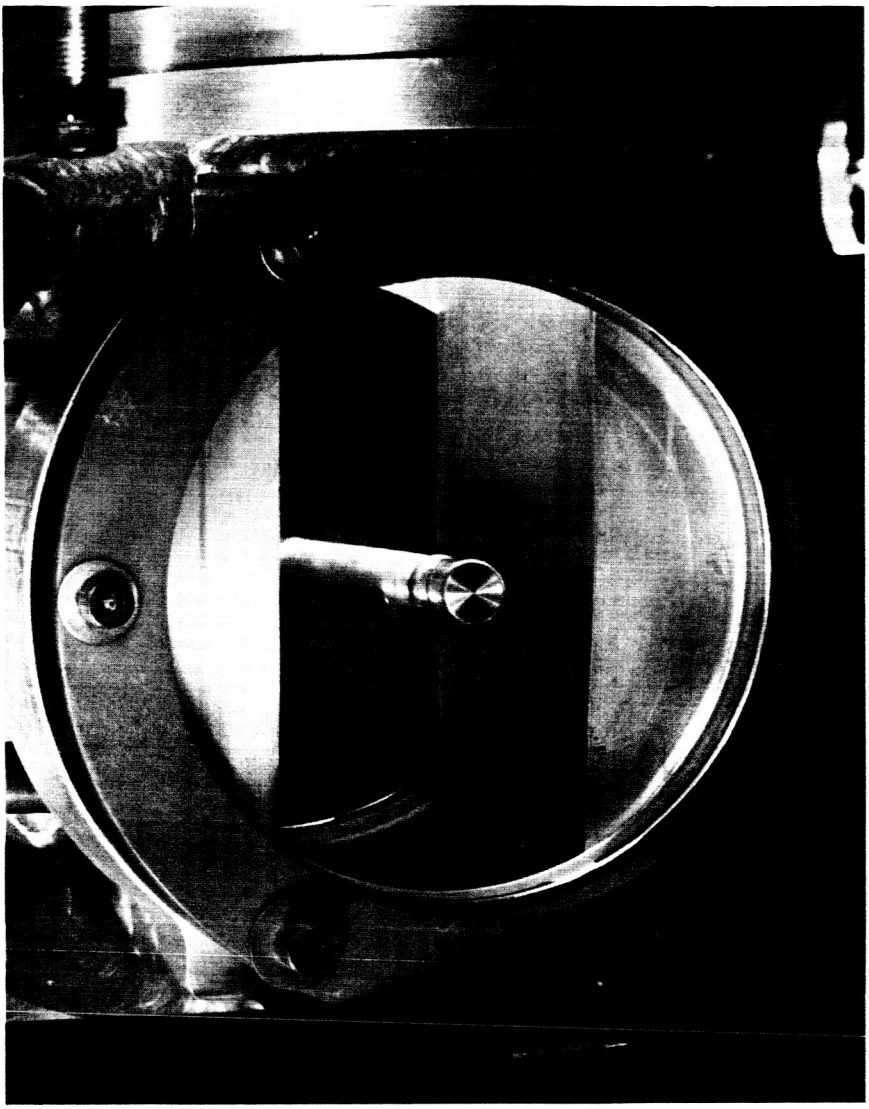

FIGURE 3. Shock-tube test section.

Little attempt has been made in these experiments to reduce the interferograms to give a point-by-point mapping of the electron density distribution in the flow field, although this could be done. The interferograms have only been analyzed qualitatively. This is due to the fact that the emphasis in the work to date has been on the development of the techniques. Also, the plasma generated in this type of shock tube is highly non-uniform and far from two-dimensional, so that the measured electron densities are not local properties of the flow field, but rather averages across the thickness of the test section.

WHITE-LIGHT INTERFEROMETRY

While a monochromatic fringe pattern is made up of many fringes, indistinguishable from one another, a white-light fringe pattern consists of approximately

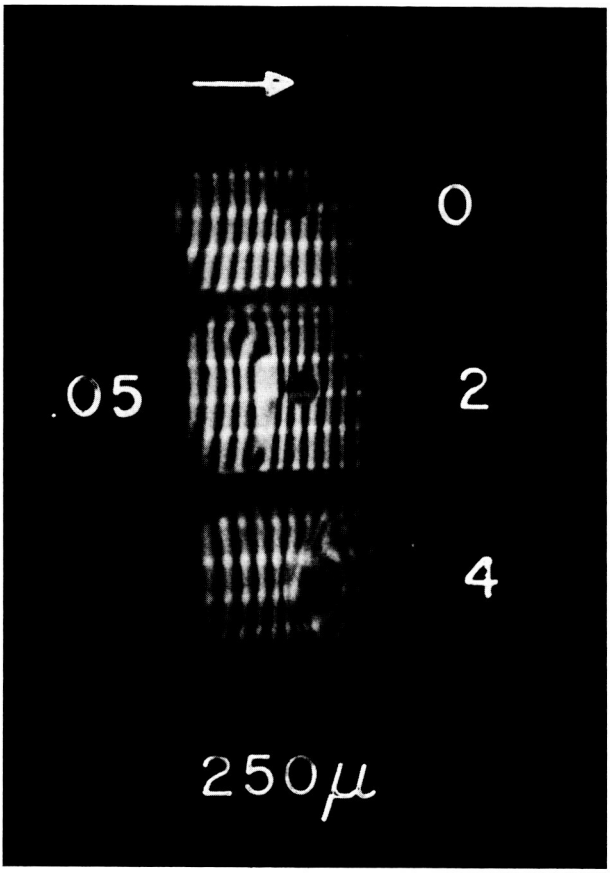

FIGURE 4. Monochromatic interferogram about $\frac{3}{8}$-inch-diameter cylinder at 5461 Å with vertical fringes.

10–20 fringes, each having its own color and, hence, distinguishable from the others. This property of the white-light fringes is of particular significance when there is a discontinuous shift in the fringe pattern, such as across a shock wave propagating into a non-ionized gas. In such a situation one cannot usually follow an individual fringe, in a continuous manner, through the shock. If the fringe shift is more than one full fringe width, an error of an integral number of fringe widths can result in the determination of the total fringe shift. However, this is not a problem when working with a white-light fringe pattern. The fringes are labeled by their color and the fringe shift is measured by connecting a fringe of a particular color with its counterpart on the other side of the shock.

As discussed by Alpher and White (**4**), there are several essential considerations that distinguish white-light interferometry from monochromatic interferometry. It now becomes necessary to distinguish between the phase index of refraction and the group index of refraction, and, hence, between the phase and group refractivities. The phase index of refraction, n_p, is the velocity of light in vacuo divided by the phase velocity in the medium, and the group index of refraction, n_g, is the velocity of light in vacuo divided by the group velocity of light in the medium. The shift of an individual fringe in either a monochromatic or white-light interferogram is determined by the phase refractivity, while the change in location of

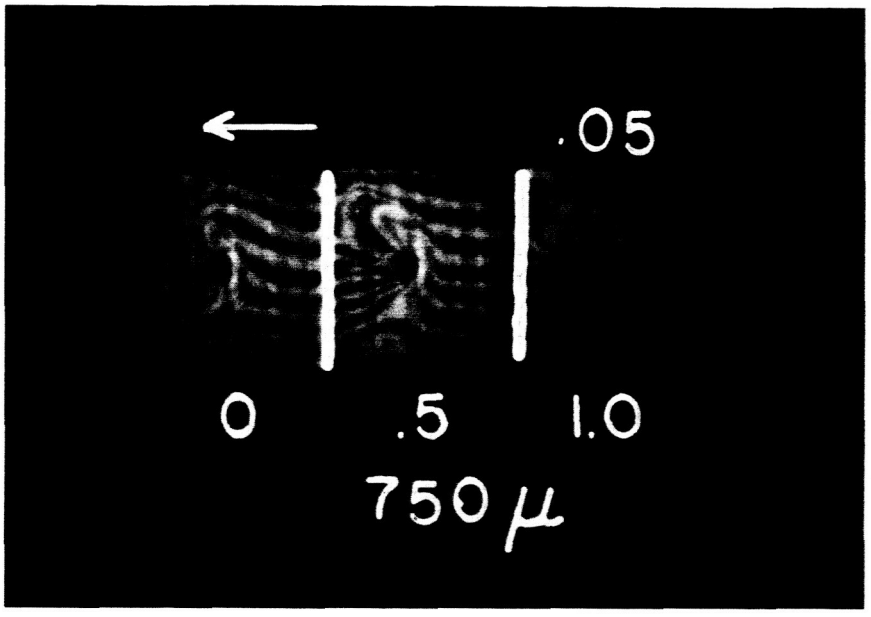

FIGURE 5. Monochromatic interferogram about $\frac{3}{8}$-inch-diameter cylinder at 5461 Å with horizontal fringes.

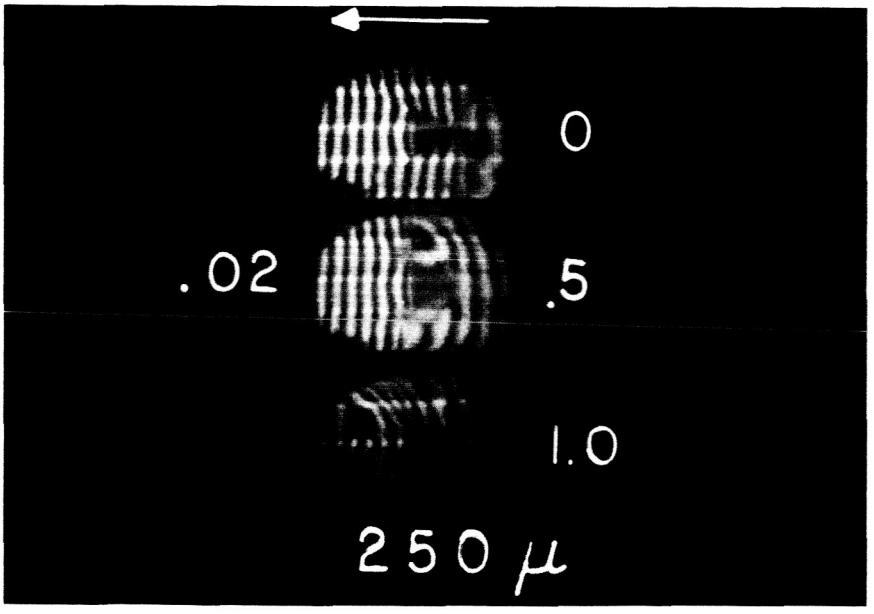

FIGURE 6. Monochromatic interferogram about 30° half-angle wedge at 5461 Å with vertical fringes.

the center of contrast of the white-light fringe pattern is determined by the group refractivity (see Alpher and White [**4**], p. 163). The center of contrast of a white-light interference pattern is where the monochromatic fringe patterns of all the

individual wavelengths making up the white light are in phase. When calculating the shift of the center of contrast by equation (1), λ is now a mean wavelength over the visible spectrum. The phase and group refractive indexes are related by

$$n_g = n_p - \frac{\lambda\, dn_p}{d\lambda} \tag{10}$$

at a wavelength λ. As illustrated by Alpher and White (**3–5**), for the non-ionized case there is usually a negligible difference between n_p and n_g, and there is then no observable difference between the shift of the center of contrast and the shift of the individual fringe. This is the property that allows one to follow the white-light fringes through a discontinuity. However, for electrons, the phase and group refractivities are equal in magnitude but opposite in sign. Hence, for the case of the ionized gas, where the free electrons have been seen to be the dominant species, the individual fringe shifts in one direction and the center of contrast shifts in the opposite direction by an equal amount.

Another aspect of white-light interferometry which has been used extensively by Bennett is known as single-fringe interferometry (**11**). In this case the spacing between fringes of the initial fringe pattern is increased until one fringe fills the entire test section. The fringe pattern that results from the presence of the plasma then represents lines of constant electron density. In the color, white-light work of Bennett (**11**), as in the monochromatic case, the technique of streak interferometry was used. Until now, no other color, white-light interferometry has been reported. This is due to the lack of a high-speed shutter that would transmit most of the visible spectrum without dispersion. Also adding to the difficulty has been the slow speed of color films and the lack of a suitable light source.

The recent development of a new Kerr cell, employing a fluid known as Kerrmax[17] instead of the usual nitrobenzene, coupled with the intensity of the exploding-wire light source and the fastest color films available has made possible color, white-light interferometry of the same flow fields which were described in the monochromatic section, with time resolution of 0.05 μsec.

Figures 7, 8, and 9 are typical color, white-light interferograms of the flow field with no model, the flow about the $\frac{3}{8}$-inch cylinder, and the flow about the 30° wedge, respectively. In each case the initial pressure was 0.5 mm Hg of hydrogen. As discussed earlier, this initial pressure is low enough so that the fringe shift due to the compression and dissociation of the hydrogen at the shock front will be too small to be resolved (less than 0.1 fringe), and the interferograms are a direct mapping of the electron density distribution. Since the fringe shift is only reflecting the presence of electrons, under these conditions one expects the center of contrast to shift in the opposite direction by an equal amount. This can readily be observed in Figure 7. The center of contrast is approximately the darkest of the three purple fringes in the undisturbed region of the flow (adjacent to the "whitest" bright fringe). Behind the shock front the fringes shift upwards, corresponding to a decrease in refractivity, while the dark purple coloring, characteristic of the center of contrast, shifts downward by an equal amount. (Note that in Figure 9 a shift upwards corresponds to an increase in refractivity.) The peak electron density is $\sim 5 \times 10^{16}$ cm^{-3}. In each of the color interferograms the exposure time was 0.05 μsec. The film used was Ansco Type FPC-132.

SUMMARY

The principles and techniques involved in the application of optical interferometry to plasma studies have been reviewed and summarized. Recent experiments

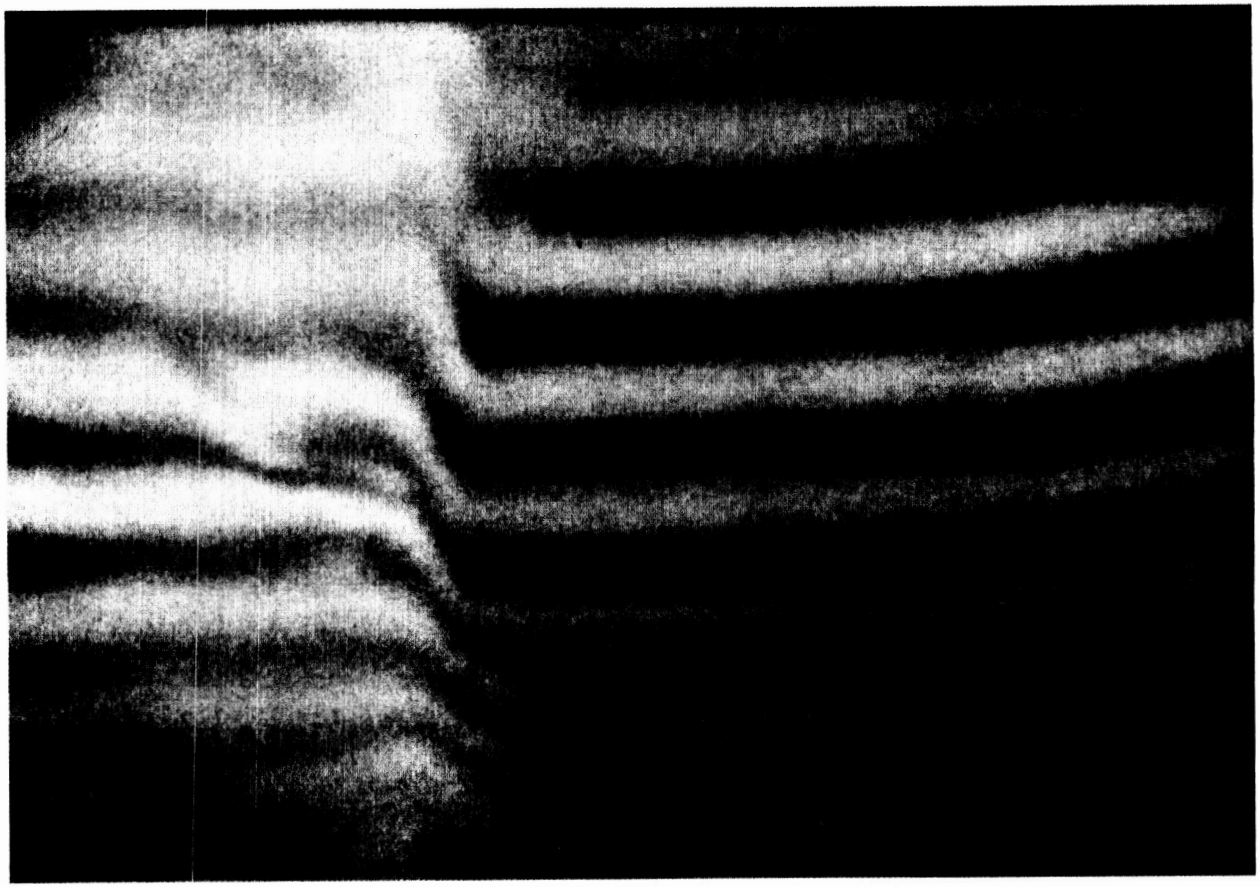

FIGURE 7. White-light interferogram of flow with horizontal fringes. Flow is from left to right. An upward shift of the fringes corresponds to a decrease in refractivity.

FIGURE 8. White-light interferogram of flow about ⅜-inch-diameter cylinder with horizontal fringes. Flow is from left to right. An upward shift of the fringes corresponds to a decrease in refractivity.

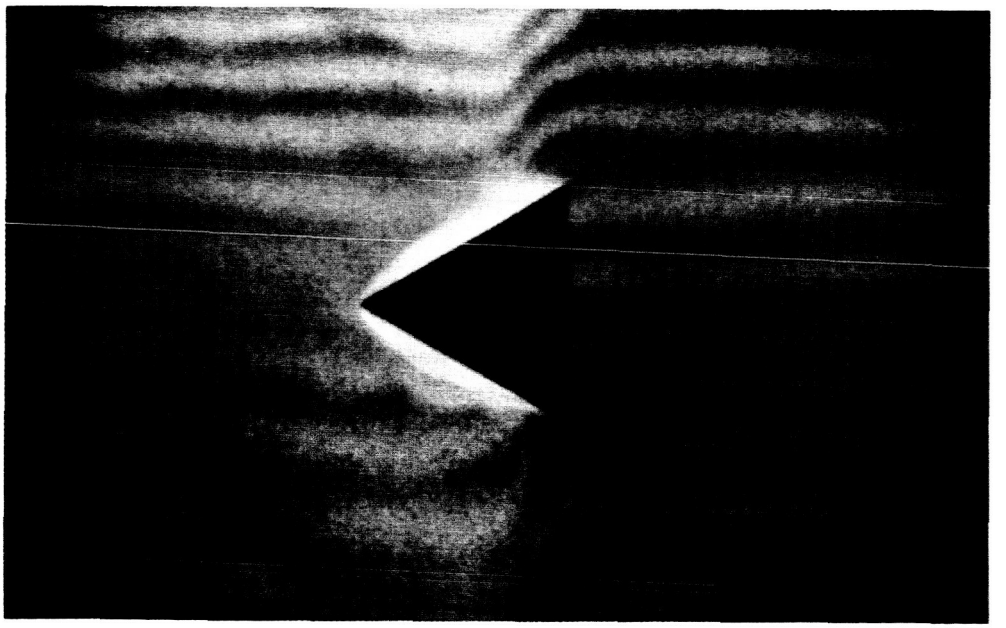

FIGURE 9. White-light interferogram of the flow about 30° half-angle wedge with horizontal fringes. Flow is from left to right. An upward shift of the fringes corresponds to an increase in refractivity.

at Aerospace Corporation have been described in which monochromatic interferograms have been obtained with significantly better time resolution than was previously available, while at the same time maintaining a conventional field of view. Techniques have been described by which it is possible to obtain color, white-light interferograms of entire flow fields, with good time resolution. The same color techniques could be applied to obtaining single-fringe interferograms of entire flow fields.

The technique of optical interferometry has been seen to provide measurements of the electron density in two-dimensional and axisymmetric, high electron density plasmas (10^{15}–10^{18} cm^{-3}). In a particular case, the electron densities obtained by spectroscopic techniques have been seen to agree quite well with the interferometrically-determined values.

ACKNOWLEDGMENT

The author would like to gratefully acknowledge the major contribution to the early stages of the research described in this paper, and the continuing support throughout the program, of Dr. Richard M. Head, Consultant, Aerospace Corporation.

REFERENCES

1. Ladenburg, R., *Physical Measurements in Gas Dynamics and Combustion* (Princeton: Princeton University Press, 1954).
2. Alpher, R., and White, D., "Interferometric Measurement of Electron Concentrations in Plasmas", *Phys. Fluids*, **1**, 452 (1958).
3. Alpher, R., and White, D., "Optical Refractivity of High-Temperature Gases, I. Effects Resulting from Dissociation of Diatomic Gases", *Phys. Fluids*, **2**, 153 (1959).
4. Alpher, R., and White, D., "Optical Refractivity of High-Temperature Gases. II. Effects Resulting from Ionization of Monatomic Gases", *Phys. Fluids*, **2**, 162 (1959).
5. Ascoli-Bartoli, U., De Angelis, A., and Martellucci, S., "Wavelength Dependence of the Refractive Index of a Plasma in the Optical Region", *Il Nuovo Cimento*, **18**, 1116 (1960).
6. Allen, C., *Astrophysical Quantities* (London: The Athlone Press, 1955).
7. Marlow, W., III, "Measurement of the Ground State Polarizability of Atomic Hydrogen", Ph.D. thesis, Stanford University, 1963, and *Bull. Am. Phys. Soc.*, **8**, 362 (1963).
8. Shukhtin, A., "Interferometric Method for the Determination of the Gas Density and Electron Concentration in Plasma", *Optics and Spectroscopy*, **10**, 222 (1961).
9. Bennett, F., Shear, D., and Burden, H., "Streak Interferometry", *J. Opt. Soc. Amer.*, **50**, 212 (1960).
10. Medford, R., Powell, A., Hunt, A., and Wright, J., "Interferometric Measurements of Electron Density in Deuterium Plasma", *Proc. Vth. Inter. Conf. on Ioniz. Phen. in Gases*, **2**, 2000 (1961).
11. Bennett, F., "Shock-Producing Mechanisms for Exploding Wires", *Phys. Fluids*, **5**, 891 (1962).
12. Ramsden, S., and McLean, E., "Optical Refractivity of Free Electrons", *Nature*, **194**, 761 (1962).

13. Ramsden, S., and McLean, E., "Optical Interferometric Measurement of Electron Density in an Electromagnetic Shock Tube", *Bull. Am. Phys. Soc.*, **7**, 157 (1962).
14. Klein, A., "Some Results Using Optical Interferometry for Plasma Diagnostics", *Phys. Fluids*, **6**, 310 (1963).
15. Klein, A., and Head, R., "Optical Interferometric Measurements about Bodies in a Hydrogen Plasma", *Bull. Am. Phys. Soc.*, **8**, 167 (1963).
16. Josephson, V., and Hales, R., "Parametric Study of the Conical Shock Tube", *Phys. Fluids*, **4**, 373 (1961).
17. Courtesy of Kappa Scientific Company, Sierra Madre, California.

13. Koichi Oshima: *Microwave Diagnosis of a Partly-Ionized Flow in the Presence of a Magnetic Field*

Starting with the conventional expression of tensor conductivity of a plasma, the interaction between a plane-polarized microwave and the plasma in the presence of a magnetic field is expressed analytically. Especially, this expression can give the angular dependence of the received power to the polarization plane. K-band and X-band microwave systems with a rotatable receiving horn to measure this angular dependence were developed and the measurements were carried out with supersonic flows of argon and nitrogen gas through a small wind tunnel.

The results with the K-band system were analyzed successfully by this analytical expression, but the analysis of the data with the X-band system was not conclusive. However, the measured angular dependence of the phase shift and attenuation showed qualitative agreement with the calculations.

INTRODUCTION

The application of microwave interferometry to plasma diagnostics, while it commands several technical advantages in principle, is somewhat limited in practice by the relatively narrow ranges of electron density and collision frequency in which any device of a given frequency can make effective measurements. For example, a 24-Gc interferometer, traversing a plasma 5 cm thick, can respond to electron densities between about 5×10^{10} and 2×10^{12} cm^{-3}. The possibility of extending the range of sensitivity of an interferometer through the introduction of an additional parameter—the electron cylotron frequency—would seem to be desirable and warrants specific assessment. Such an investigation would also have bearing on the problem of radio communication through the ionized gas surrounding a reentry vehicle.

In conventional microwave interferometry, two quantities are measured, phase shift and attenuation, which are related to two physical parameters in the plasma,

ED. NOTE: Dr. Oshima is now at the Aeronautical Research Institute, University of Tokyo, Komaba-Meguro-Ku, Tokyo, Japan.

The research reported in this paper was sponsored in part by the Aeronautical Systems Division, Wright-Patterson Air Force Base, under Contract No. AF 33 (657)-7760, and the Air Force Office of Scientific Research under Grant AF-AFOSR 55-63.

the plasma frequency (hence electron density) and electron-heavy particle collision frequency (hence electron temperature). While it yields no new information about the plasma, the presence of a magnetic field (which renders the plasma conductivity a tensor) does add a dimension of versatility and redundancy in the interferometric techniques. The present investigation is an attempt at assessing the practicality of such an approach to microwave diagnostics.

Two principal results are obtained, one from analysis and the other from experiments, which indicate severe limitations on the application of the magnetic-field technique to microwave interferometry. The theoretical study of the interaction of a plasma slab of finite depth with a microwave field having a magnetic field reveals a non-linear behavior with respect to the plasma thickness. The experimental study reveals that the properties of a plasma may be significantly altered by the presence of the magnetic field (beyond simply introducing gyration in the electrons) in ways that cannot be predicted by theory, thus rendering the diagnostic results ambiguous as to electron density and temperature.

MICROWAVE FIELD IN A PLASMA

We begin with the conductivity tensor σ of a plasma in a magnetic field as follows:

$$\sigma = \frac{\omega\eta}{4\pi j}\begin{pmatrix} L & jM & 0 \\ -jM & L & 0 \\ 0 & 0 & N \end{pmatrix} \tag{1}$$

$$L = \frac{1-j\beta}{(1-j\beta)^2-\gamma^2}, \qquad M = \frac{\gamma}{(1-j\beta)^2-\gamma^2}, \qquad N = \frac{1}{1-j\beta}$$

The z-axis is taken as the direction of the magnetic field, and, in the present experiment, is also the direction of the microwave propagation; ω is the angular frequency of the microwave; and

$$\eta = \left(\frac{\omega_p}{\omega}\right)^2, \qquad \beta = \frac{\nu}{\omega}, \qquad \gamma = \frac{\omega_c}{\omega} \tag{2}$$

ω_p, ν, and ω_c are plasma frequency, electron collision frequency, and electron cyclotron frequency, respectively.

$$\omega_p^2 = \frac{4\pi e^2 n_e}{m} = 3.18\times 10^9 n_e \ \text{((rad/sec)}^2\text{, 1/cm}^3\text{)}$$

$$\omega_c = \frac{e|\mathbf{B}_0|}{mc} = 1.76\times 10^7 |\mathbf{B}_0| \ \text{(rad/sec, gauss)} \tag{3}$$

where m, n_e, and e are electron mass, its number density, and its charge, respectively; $|\mathbf{B}_0|$ is the strength of applied field, and c is the speed of light. The Gaussian unit system is used.

To solve for the field in the plasma, one eliminates the terms involving the magnetic flux from the Maxwell equations to obtain

$$\nabla\times\nabla\times\mathbf{E} + \frac{1}{c^2}\frac{\partial^2\mathbf{E}}{\partial t^2} + \frac{4\pi\sigma}{c^2}\frac{\partial\mathbf{E}}{\partial t} = 0 \tag{4}$$

Time dependence of the electric field is $e^{-j\omega t}$. For a plane wave propagating in the z-direction, the space dependence is e^{jkz}, and the z-component of the field $\mathbf{E}$, $\mathbf{E}_z$,

is zero. Using the above expression of σ, the x- and y-component equations of $\mathbf{E}$, which are expressed as $E_x e^{-j(\omega t-kz)}$ and $E_y e^{-j(\omega t-kz)}$, are

$$\left\{k^2-\frac{\omega^2}{c^2}(1-\eta L)\right\}E_x-j\frac{\omega^2}{c^2}\eta M E_y=0$$
$$\left\{k^2-\frac{\omega^2}{c^2}(1-\eta L)\right\}E_y+j\frac{\omega^2}{c^2}\eta M E_x=0 \tag{5}$$

From the secular equation of these, two values of k are determined

$$k_1=\frac{\omega}{c}\sqrt{1-\frac{\eta}{1+\gamma-j\beta}} \qquad k_2=\frac{\omega}{c}\sqrt{1-\frac{\eta}{1-\gamma-j\beta}} \tag{6}$$

which correspond to the ordinary and extraordinary waves, respectively. The electric field components E_x, E_y, at a point where the microwave penetrates a plasma slab to depth z, may then be expressed as

$$E_x=E_+\exp(jk_1z)+E_-\exp(jk_2z) \qquad E_y=jE_+\exp(jk_1z)-jE_-\exp(jk_2z) \tag{7}$$

where E_+ and E_- correspond to the ordinary and extraordinary waves, respectively, and are determined by the incident condition.

Introducing the complex refractive index, n, and expressing the real and imaginary parts of k and n by a prime and double prime, respectively, we obtain

$$n_1'=\frac{c}{\omega}k_1'=\frac{1}{\sqrt{2}}\left[\left\{\left[1-\frac{(1+\gamma)\eta}{(1+\gamma)^2+\beta^2}\right]^2+\left[\frac{\beta\eta}{(1+\gamma)^2+\beta^2}\right]^2\right\}^{1/2}+\left[1-\frac{(1+\gamma)\eta}{(1+\gamma)^2+\beta^2}\right]\right]^{1/2}$$

$$n_1''=\frac{c}{\omega}k_1''=\frac{1}{\sqrt{2}}\left[\left\{\left[1-\frac{(1+\gamma)\eta}{(1+\gamma)^2+\beta^2}\right]^2+\left[\frac{\beta\eta}{(1+\gamma)^2+\beta^2}\right]^2\right\}^{1/2}-\left[1-\frac{(1+\gamma)\eta}{(1+\gamma)^2+\beta^2}\right]\right]^{1/2}$$

$$n_2'=\frac{c}{\omega}k_2'=\frac{1}{\sqrt{2}}\left[\left\{\left[1-\frac{(1-\gamma)\eta}{(1-\gamma)^2+\beta^2}\right]^2+\left[\frac{\beta\eta}{(1-\gamma)^2+\beta^2}\right]^2\right\}^{1/2}+\left[1-\frac{(1-\gamma)\eta}{(1-\gamma)^2+\beta^2}\right]\right]^{1/2} \tag{8}$$

$$n_2''=\frac{c}{\omega}k_2''=\frac{1}{\sqrt{2}}\left[\left\{\left[1-\frac{(1-\gamma)\eta}{(1-\gamma)^2+\beta^2}\right]^2+\left[\frac{\beta\eta}{(1-\gamma)^2+\beta^2}\right]^2\right\}^{1/2}-\left[1-\frac{(1-\gamma)\eta}{(1-\gamma)^2+\beta^2}\right]\right]^{1/2}$$

where the subscripts 1 and 2 represent the ordinary and extraordinary waves, respectively. Values of n' and n'' are shown for $0<\eta<5$ in Figure 1 for the case of $\beta=0.25$ and $\gamma=0.6$, 0.4, 0.2, and 0. In Figure 2 n is expressed in a complex plane, which may be useful for a general view of its character; that is, n_2'' is much larger than n_1'' for large values of η and γ, so the extraordinary wave decays rapidly in this case; and n_1' is nearly constant for $n>1$, so that the phase shift is independent of η.

Using equations (7) and (8), we obtain

$$E_x=E_+\exp(jn_1\tilde{z})+E_-\exp(jn_2\tilde{z}) \qquad E_y=jE_+\exp(jn_1\tilde{z})-jE_-\exp(jn_2\tilde{z}) \tag{9}$$

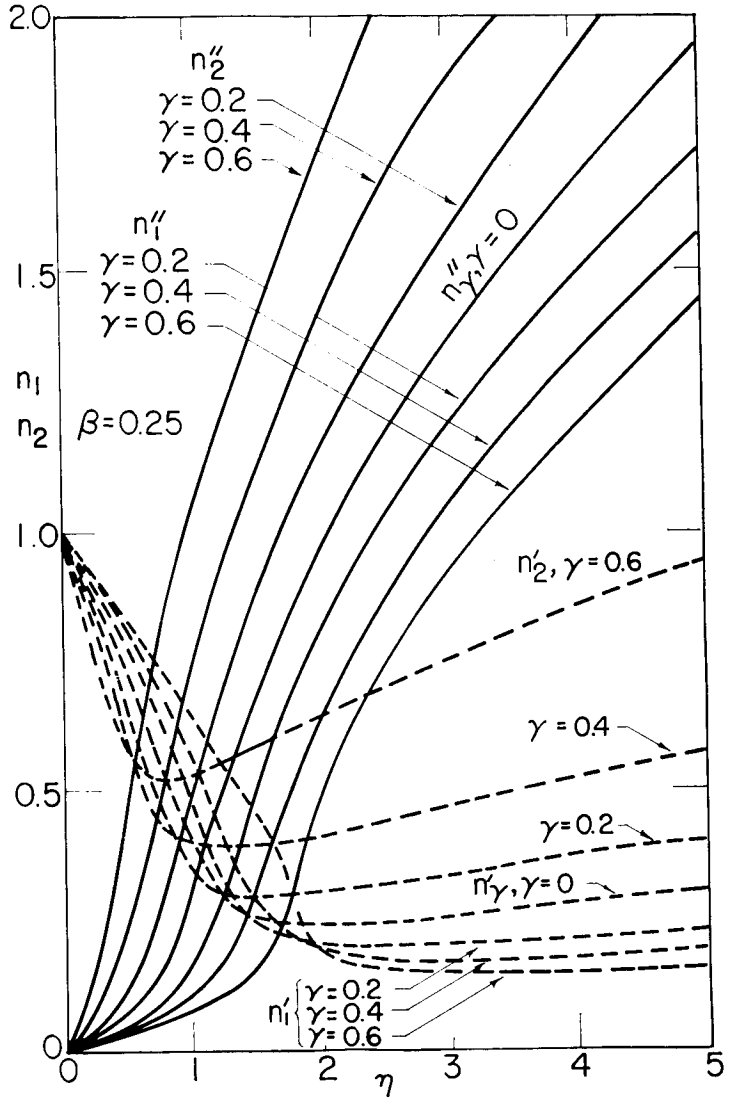

FIGURE 1. Values of n_1', n_1'', n_2', n_2'' at $\beta = 0.25$.

where $\tilde{z}$ is a non-dimensionalized plasma depth defined as

$$\tilde{z} = \frac{\omega}{c} z = \frac{2\pi}{\lambda} z \tag{10}$$

and λ is the wavelength of the microwave in vacuum.

PHASE SHIFT AND ATTENUATION DUE TO A PLASMA SLAB OF FINITE DEPTH

The incident, reflected, and transmitted waves through a plasma slab bounded by quartz slabs (of the same thickness as the plasma) are depicted in Figure 3. Rigorously, one should consider the five-slab configuration, since, unless the

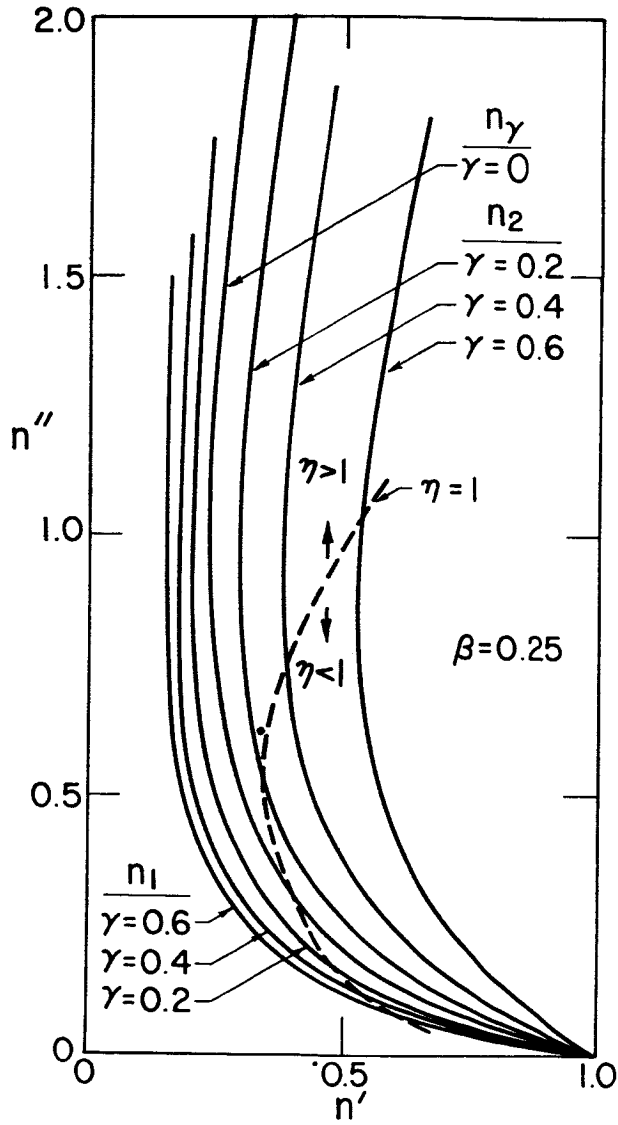

FIGURE 2. Values of n_1 and n_2 on a complex plane at $\beta = 0.25$.

microwave system is imbedded in the quartz, the quartz slabs are bounded by air (or vacuum). However, it has been found from experience (**1**) that a five-slab analysis introduces no significant alterations to the three-slab analysis, and thus does not warrant the significantly increased amount of algebra involved. With the amplitude E known, the other quantities, A, B, C, and D, can be determined by the boundary condition that the electric field strength and its space derivative must be continuous at the boundary. From this one obtains

$$B = E \frac{4nn_0 \exp\left[-j(n_0 - n)\tilde{d}\right]}{(n+n_0)^2 - (n-n_0)^2 \exp\left(2jn\tilde{d}\right)} \tag{11}$$

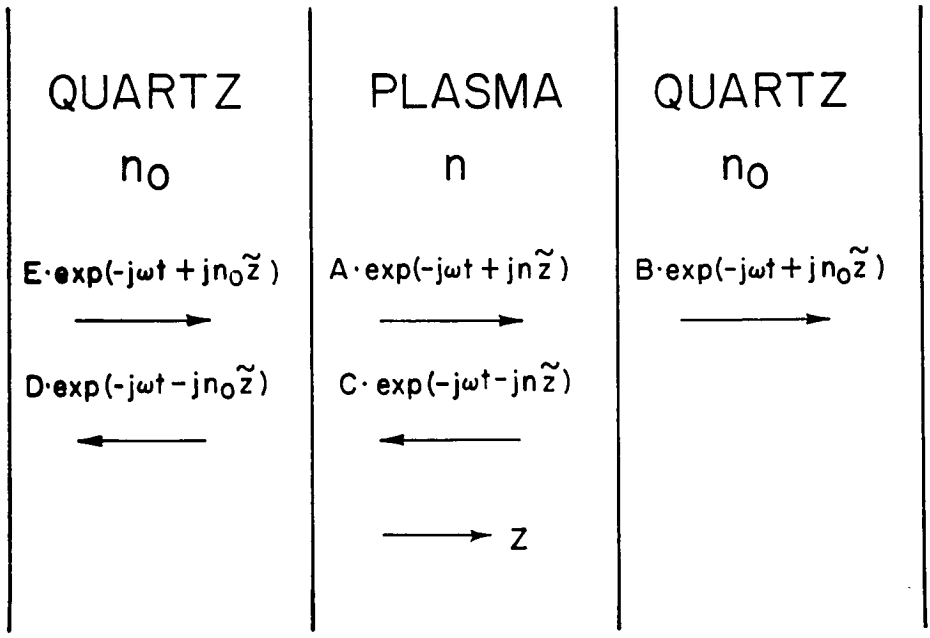

FIGURE 3. Propagation through a bounded plasma.

In the absence of the plasma, the value of B, denoted by B_0, is

$$B_0 = E \frac{4n_0 \exp[-j(n_0-1)\tilde{d}]}{(1+n_0)^2-(1-n_0)^2 \exp(2j\tilde{d})}$$

Thus the relative phase shift, Θ (in radians), and attenuation, A (in nepers), between two paths of the microwave, one through the plasma and the other through vacuum, can be expressed as

$$\exp(-j\Theta - A) = \frac{B}{B_0} = \frac{(1+n_0)^2-(1-n_0)^2 \exp(2j\tilde{d})}{(n+n_0)^2-(n-n_0)^2 \exp(2jn\tilde{d})} n \exp[-j(1-n)\tilde{d}] \quad (12)$$

Introducing an "effective refractive index", N, and Re and Im for the real and imaginary parts of the coefficient of the exponential term in equation (12), we obtain

$$\exp[-j(1-N)\tilde{d}] = (Re+Im)\exp[-j(1-n)\tilde{d}] \quad (13)$$

From equation (13)

$$N = n + \frac{1}{j\tilde{d}}\left[\frac{1}{2}\ln(Re^2+Im^2) + j\tan^{-1}\frac{Im}{Re}\right] \quad (14)$$

and

$$\Theta = (1-N')\tilde{d} \quad \text{or} \quad \theta = \frac{\Theta}{\tilde{d}} = 1-N' \quad (15)$$

$$A = N''\tilde{d} \quad \text{or} \quad \alpha = \frac{A}{\tilde{d}} = N'' \quad (16)$$

where N' and N'' are the real and imaginary parts, respectively, of N; and θ and α are normalized shift and attenuation, respectively.

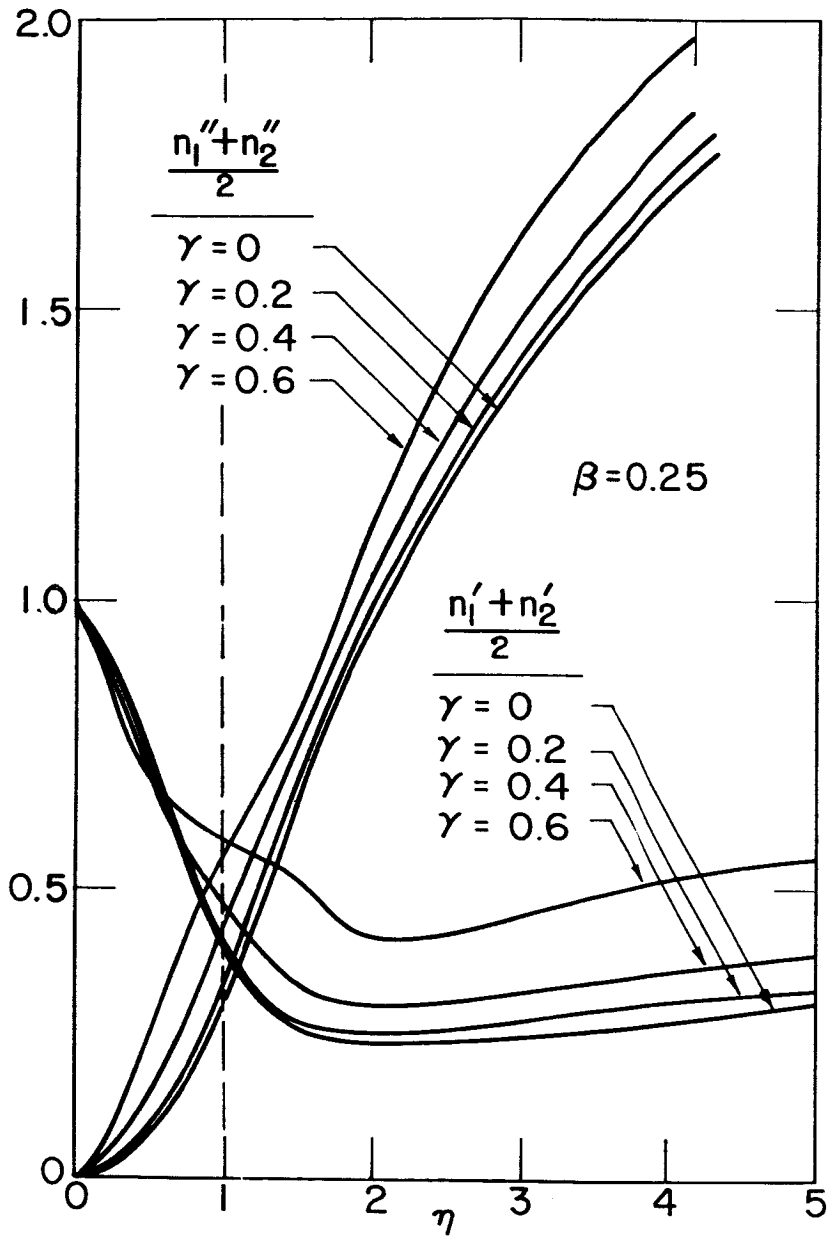

FIGURE 4. First-order terms in phase shift and attenuation.

In the presence of a magnetic field the polarization of a plane-polarized incident wave undergoes a rotation. If the receiving horn on the far side of the plasma is placed parallel to x, which is also the direction of polarization of the incident wave, then

$$\frac{B_x}{B_0} = \frac{1}{2}\{\exp[-j(1-N_1)\tilde{d}]+\exp[-j(1-N_2)d]\}$$

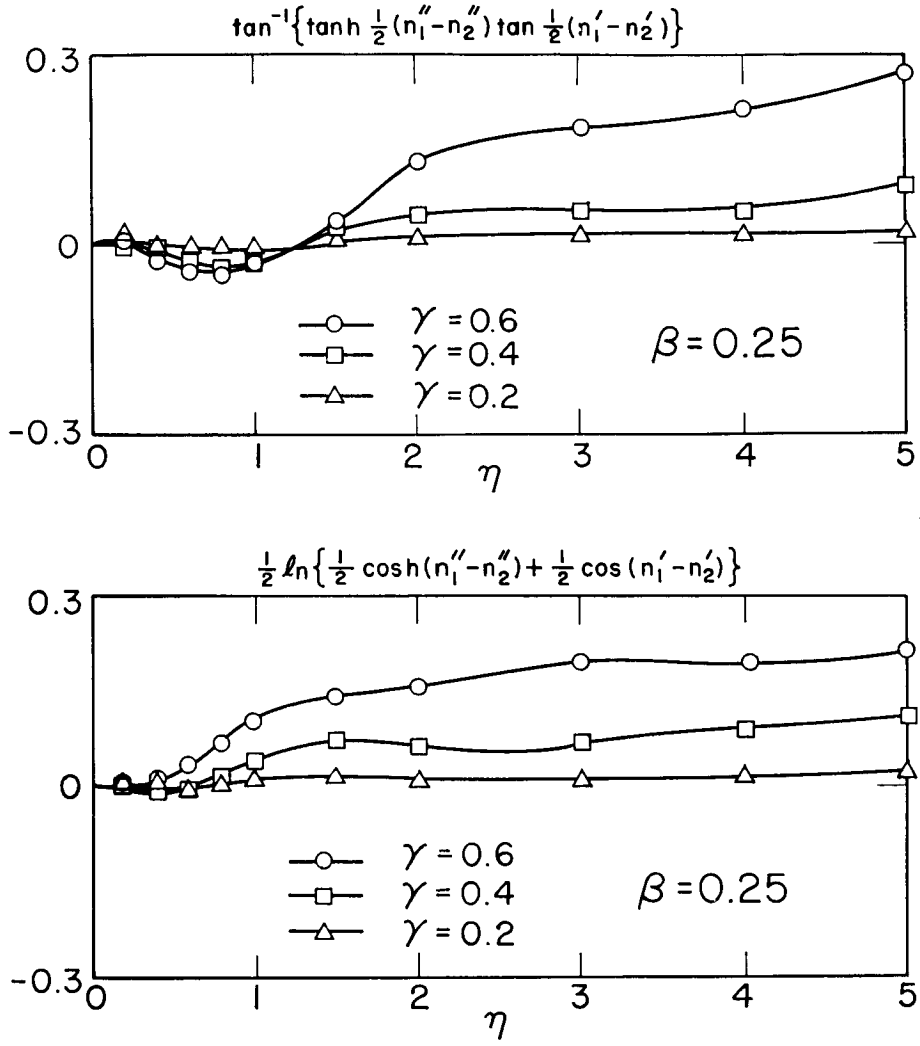

FIGURE 5. Zero-order, nonlinear terms in phase shift and attenuation.

and the resultant phase shift and attenuation are

$$\theta = 1 - \frac{N_1' + N_2'}{2} + \frac{1}{\tilde{d}} \tan^{-1} \left[\tanh \frac{N_1'' - N_2''}{2} \tilde{d} \cdot \tan \frac{N_1' - N_2'}{2} \tilde{d} \right] \tag{17}$$

$$\alpha = \frac{N_1'' + N_2''}{2} - \frac{1}{2\tilde{d}} \ln \left[\frac{1}{2} \cosh (N_1'' - N_2'')\tilde{d} + \frac{1}{2} \cos (N_1' - N_2')\tilde{d} \right] \tag{18}$$

The terms $(N_1' + N_2')/2$ and $(N_1'' + N_2'')/2$ represent first-order terms in the phase shift and attenuation, while the other terms indicate the nonlinear behavior. Assuming $N = n$ (which implies $\eta < 1$, as will be seen later), typical values of the first-order terms are shown in Figure 4; and, assuming further that $\tilde{d} = 1$, the nonlinear terms are shown in Figure 5. It is seen from Figure 4 that the first-order term (valid for $\eta < 1$), always results in increased attenuation with increasing

magnetic field, while the nonlinear term (Figure 5) tends to decrease the attenuation. In general, it is clear that the overall behavior in θ and α is a very complicated function of $\tilde{d}$ as well as η, β, and γ.

Small η Approximation

If $\eta < 1$ equation (18) simplifies to

$$\begin{aligned} n_1' &= 1 - \frac{1}{2}\frac{(1+\gamma)\eta}{(1+\gamma)^2+\beta^2} \\ n_1'' &= \frac{1}{2}\frac{\beta\eta}{(1+\gamma)^2+\beta^2} \\ n_2' &= 1 - \frac{1}{2}\frac{(1-\gamma)\eta}{(1-\gamma)^2+\beta^2} \\ n_2'' &= \frac{1}{2}\frac{\beta\eta}{(1-\gamma)^2+\beta^2} \end{aligned} \tag{19}$$

Further, if $\eta < 1$, $n \gtrsim 1$, so that equation (14) can be expanded in a power series in $(n-1)$

$$N = n + \frac{(Re' + j\,Im')}{j\tilde{d}}(n-1) + O[(n-1)^2] \tag{20}$$

where

$$Re' = -\frac{(1-n^4)\sin^2\tilde{d} + (1-n_0^2)\tilde{d}\sin\tilde{d}\cos\tilde{d}}{4n_0^2 + (1-n_0^2)^2\sin^2\tilde{d}}$$

$$Im' = \frac{2n_0(1-n_0^2)\sin\tilde{d}\cos\tilde{d} + (1-n_0)^2[2n_0 - (1+n_0)^2\sin^2\tilde{d}]\tilde{d}}{4n_0^2 + (1-n_0^2)^2\sin^2\tilde{d}}$$

If we retain only the zero order term in $(n-1)$ we obtain

$$N = n \tag{21}$$

If the first order term in $(n-1)$ is retained,

$$\begin{aligned} N' &= n' + \frac{Im'}{\tilde{d}}(n'-1) + \frac{Re'}{\tilde{d}}n'' \\ N'' &= n'' - \frac{Re'}{\tilde{d}}(n'-1) + \frac{Im'}{\tilde{d}}n'' \end{aligned}$$

from which n can be deduced from measured values of N' and N'', equations (15) and (16), as

$$n' = 1 + P(N'-1) + QN'' \qquad n'' = Q(N'-1) + P(N'') \tag{22}$$

where

$$P = \frac{Im'/\tilde{d}}{(1+Im'/\tilde{d})^2 + (Re'/\tilde{d})^2} \qquad Q = \left(\frac{Re'}{\tilde{d}}\right)\frac{1}{(1+Im'/\tilde{d})^2 + (Re'/\tilde{d})^2}$$

P and Q are shown in Figure 6. It is seen that the dependence of P and Q, and, consequently, of n, on $\tilde{d}$ is quite complex. The values of $\tilde{d}$ corresponding to a plasma thickness of 1 cm and with microwave at X-band and K-band are indicated in the figure. From these it is seen that X-band would be a poor choice, while at K-band the nonlinear effects are negligible.

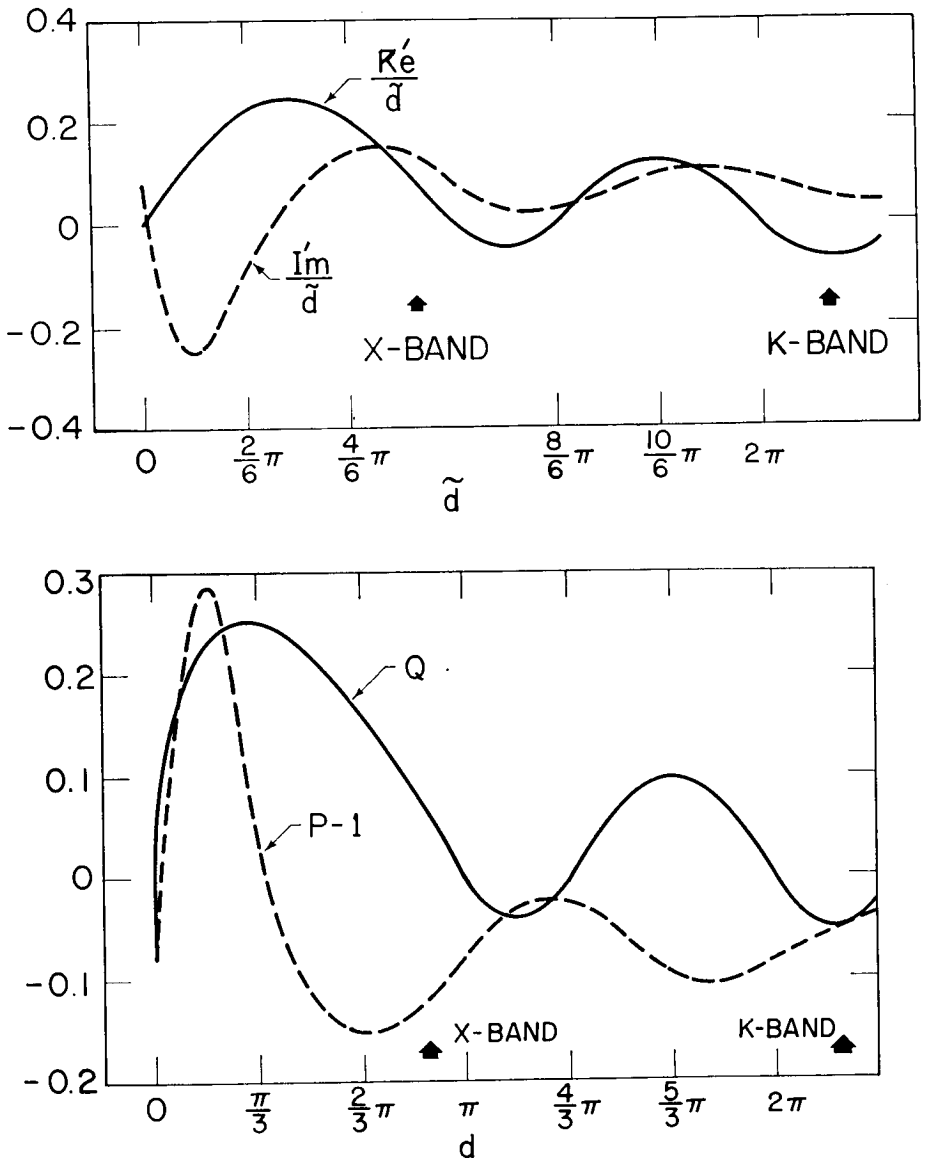

FIGURE 6. First-order, nonlinear effects in phase shift and attenuation.

EXPERIMENTAL STUDY

The experimental study is carried out with a plasma produced in a small supersonic wind tunnel (test section 16 mm in y-direction and 13 mm in z-direction) by the discharge from a 13-megacycle field imposed across the flow in the y-direction. The plasma is thus a nonequilibrium cold plasma. The static pressure in the flow (of nitrogen gas) is typically around 10 mm Hg, and the Mach number about 2. The magnetic field is produced by a pair of solenoids straddling the flow. The microwave propagates through the holes in the centers of the solenoids. Schematic

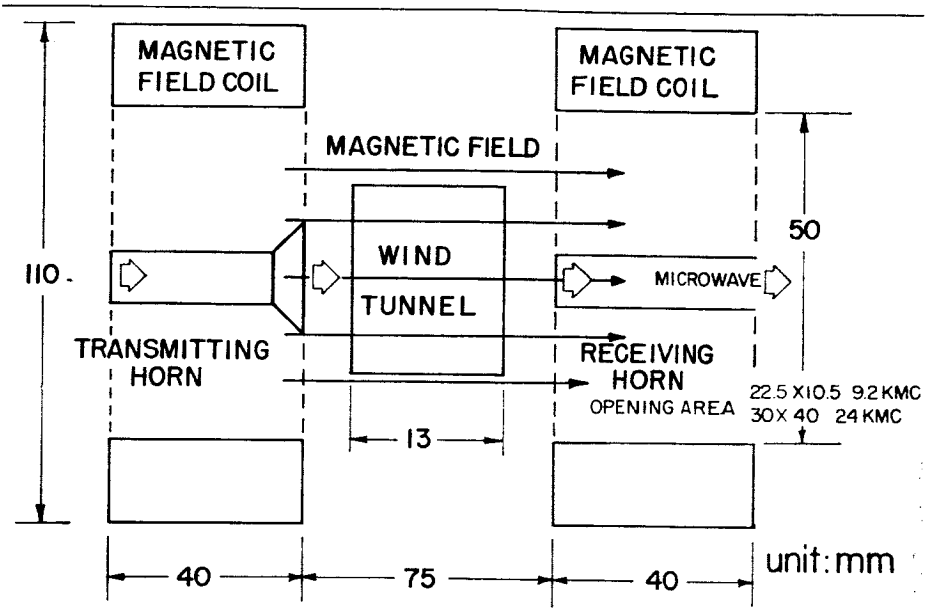

FIGURE 7. Wind tunnel and solenoids.

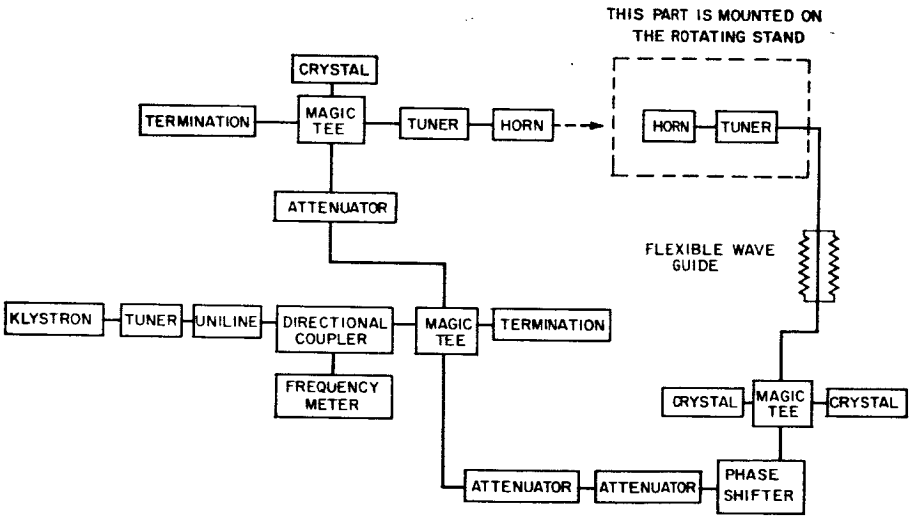

FIGURE 8. Microwave interferometer.

diagrams of the wind tunnel–solenoid combination and the microwave interferometer are shown in Figures 7 and 8. Figure 9 shows a photograph of the experimental set-up. Detailed descriptions of the experiments may be found in Oshima (**1**) and Pass (**2**).

In the experiments both K-band and X-band interferometers are used. The results with X-band, at a wavelength of 3 cm which is larger than the depth of the plasma, are quite unsatisfactory. The K-band results, with a wavelength of 1.2 cm, are deemed acceptable in the absence of the magnetic field. The slab height of 16 mm was shown in Oshima (**1**) to be an adequate approximation of an infinite

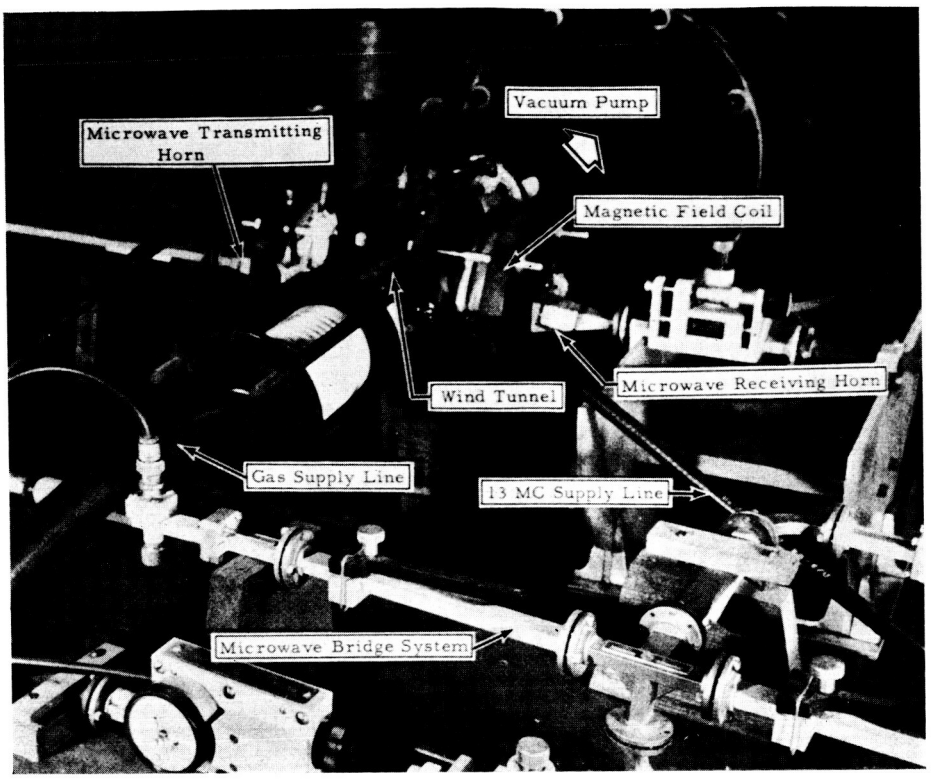

FIGURE 9. Experimental set-up.

slab. In Oshima (**1**) microwave measurements, utilizing the same apparatus as in the present work, with polystyrene sheets 30 cm × 30 showed results which were the same as those obtained with small sheets cut to fit the interior of the small wind tunnel test section. Typical results for zero magnetic field are shown in Table I. The notation "Heating Power" refers to the power in the 13-Mc exciting

TABLE I. ELECTRON DENSITY AND COLLISION FREQUENCY IN NITROGEN FLOW

Stagnation Pressure (cm Hg)	*Heating Power*	θ	α	n_e	ν
5	High	0.075	0.014	10.7×10^{11}	2.9×10^{10}
5	Low	0.043	0	6.2×10^{11}	0
10	High	0.083	0.028	12.2×10^{11}	5.1×10^{10}
10	Low	0.054	0	7.9×10^{11}	0
15	High	0.075	0.035	10.7×10^{11}	7.1×10^{10}
15	Low	0.040	0	5.7×10^{11}	0

field. At low power the attenuation is not detectable because of the fact that the plasma thickness is only about equal to the wavelength. The calculations leading to n_e and ν are based on equations (19) and (21), since $\eta < 1$.

In the measurements with magnetic field, results are quite inconclusive, for the following reasons:

At low magnetic field (less than 1 kilogauss) the measured values of phase shift and attenuation differ from those measured in the absence of the magnetic field with the same flow conditions and the 13-Mc input by very little, being of the order of the experimental scatter. At higher magnetic field (greater than 1 kilogauss) the conditions of the plasma are clearly affected by the presence of the magnetic field so that it is not possible to draw meaningful conclusions. Visually, the color of the plasma changes when the magnetic field is increased, and the highly luminous part of the plasma extends closer to the tunnel walls. Quantitatively, the static pressure in the flow, which increases when the 13-Mc power is turned on (due to the heating of the gas by the discharge), decreases when the magnetic field is increased, resulting in an apparent increase in the flow Mach number. This effect is shown by the data presented in Table II.

TABLE II. CHARACTERISTICS OF NITROGEN FLOW WITH MAGNETIC FIELD

Stagnation Pressure (cm Hg)	*Static Pressure* (mm Hg)	*Magnetic Field* (k/gauss)	*Input*† (kW)	*M*
5	5.5	0	0	2.096
5	10	0	1.6	1.444
5	9	1.2	1.6	1.549
10	8	0	0	2.300
10	11	0	1.75	1.912
10	10	1.2	1.75	2.023
10	8	0	0	2.300
10	15.5	0	2.0	1.546
10	14.5	1.2	2.0	1.616
15	10	0	0	2.416
15	15	0	2.0	1.913
15	14	1.2	2.0	1.991

† Energy input to the 13-Mc power tubes = plate current × plate voltage.

An explanation for the observed effect of the magnetic field may lie in the fact that the electron cyclotron radius for the experimental conditions is comparable to the electron mean free path (with respect to collisions with heavy particles), so that the presence of the magnetic field tends to reduce the collision frequency, which, in turn, reduces the decay rate in the nonequilibrium plasma used in the experiment. That this postulated mechanism is plausible is surmised from the decrease in the static pressure. Thus, the basic properties of the medium, with regard to density and temperature, are altered by the presence of the magnetic field, so that any apparent changes in propagation characteristics cannot be attributed to the magnetic field alone.

CONCLUSIONS

It is shown by analysis that the presence of a magnetic field in a plasma renders the effect of the thickness of the latter nonlinear with respect to the propagation of microwaves.

The changes in phase shift and attenuation due to the presence of the magnetic field are not monotonic with respect to the strength of the magnetic field, because of the nonlinear effect of the plasma thickness.

The properties of a plasma, especially a nonequilibrium plasma, may be so altered by the presence of a magnetic field as to render very difficult the interpretation of the measured results with a microwave interferometer.

REFERENCES

1. Oshima, K., "Microwave Measurements of Plasma Flow in a Supersonic Wind Tunnel", USCEC Rept. No. 83–208, AFOSR 1556, September, 1961.
2. Pass, H. R., "*K*-Band Microwave Interferometer Description and Initial Experiments in a Pilot-Model of the USC Low-Density Wind Tunnel", USCEC Rept. No. 56–217, AFOSR TN 60–1087, August, 1960.

14. Charles E. Shepard and Velvin R. Watson: *Performance of a Constricted-Arc Discharge in a Supersonic Nozzle*

The application of the wall-constricted electric arc to the heating of gas flowing through a DeLaval nozzle is discussed. It is shown that a direct-current arc can be maintained through the nozzle throat without disrupting the supersonic flow. High enthalpies are obtained by elongating the throat to form a constrictor tube. The behavior of the device can be described by the arc-column analysis of Stine and Watson in which radial conduction is assumed to be the only heat-loss mechanism. The measured radial and longitudinal enthalpy profiles are similar to those predicted by the theory.

INTRODUCTION

A new plasma generator has been developed at the Ames Research Center which produces a supersonic flow of gas at very high enthalpies. The design, based on the analysis of the constricted arc by Stine and Watson (**1**), has been successfully tested with mixtures of nitrogen and air and mixtures of nitrogen and carbon dioxide. The generator produces a steady supersonic gas stream, but the total enthalpy has a large gradient in the radial direction. With nitrogen, the average enthalpy of the stream is approximately 30,000 Btu/lb, whereas the centerline enthalpy was estimated to be 80,000 Btu/lb.

The purposes of this paper are to describe the new plasma generator, to present the experimental results obtained during recent testing, to compare the results with the theoretical analysis of Stine and Watson (**1**), and to discuss the pertinent arc-column scaling laws.

APPARATUS

The new plasma generator developed at Ames, called the constricted-arc supersonic jet, is shown schematically in Figure 1a. A conventional plasma generator for wind-tunnel use is shown for comparison in Figure 1b. In the conventional plasma generator, the gas is heated prior to entering the supersonic nozzle, but much of it bypasses the hot arc and remains cold. If the gas is allowed to reach a uniform temperature in a plenum chamber, additional heat is lost to the plenum chamber walls, and the energy of the gas in the test section is always far less than

ED. NOTE: Mr. Shepard and Mr. Watson are with the Ames Research Center, National Aeronautics and Space Administration, Moffett Field, California.

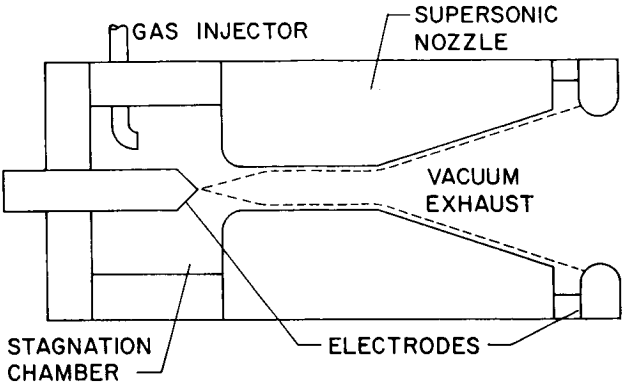

FIGURE 1a. Arc-heated supersonic jet, constricted arc.

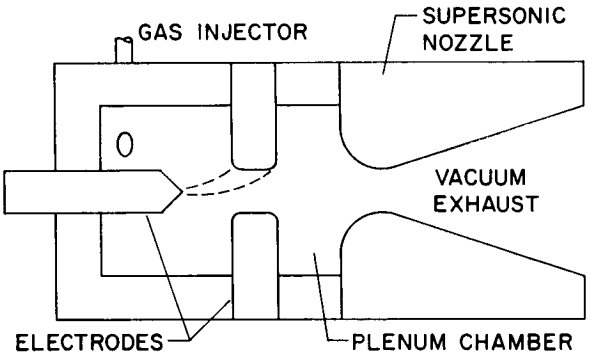

FIGURE 1b. Arc-heated supersonic jet, conventional arc.

the energy of the gas within or near the arc column. In the constricted-arc supersonic jet, however, the arc is forced completely through the nozzle, thus providing continuous heating of the gas up to the test section. All of the gas thus passes through or very near the arc column. Therefore, the energy of the gas in the test section of the constricted-arc supersonic plasma jet is much nearer the high energy of the gas within the arc column.

Two sizes of the constricted-arc supersonic jet were tested. The first had a $\frac{1}{4}$-inch-diameter throat and is shown in Figure 2a, and the second had a $\frac{1}{2}$-inch-diameter throat and is shown in Figure 2b. The three basic components of both units are the supersonic nozzle, the cathode at the upstream, or subsonic, end of the nozzle, and the anode at the supersonic end of the nozzle.

The nozzle has an extended throat to constrict the arc and provide high heating at relatively low arc currents. The throat must withstand the high heating rates developed at the edge of a constricted-arc column and must, at the same time, support the voltage gradient impressed along the arc. To meet the requirements for good thermal conductivity in the radial direction and good electrical insulation in the axial direction, the nozzle consists of water-cooled copper disks separated by boron nitride insulating wafers.

The cathode must be capable of carrying large currents without contaminating the test gas. A pointed, thoriated tungsten cathode, shielded by nitrogen, provides a steady attachment point for the arc column with negligible contamination. (If one is interested in heating air, oxygen-rich air can be added at the gas inlet to

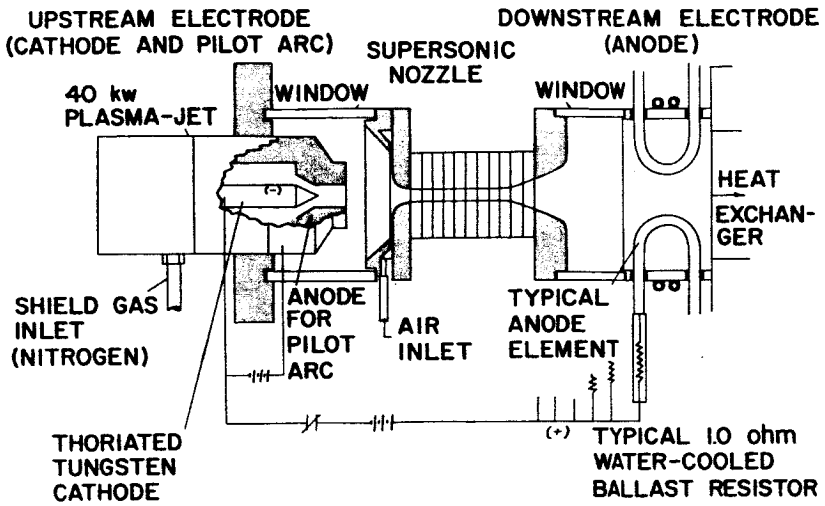

FIGURE 2a. Schematic diagram of constricted-arc supersonic jet, ¼-inch-diameter throat.

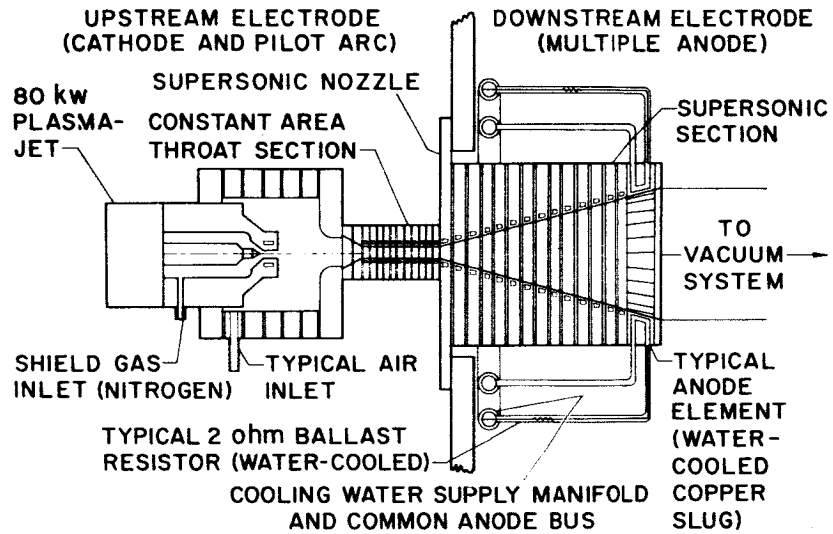

FIGURE 2b. Schematic diagram of constricted-arc supersonic jet, ½-inch-diameter throat.

produce the proper mixture in the test section.) A commercially available plasma torch is used in each unit as the cathode and shield.

The anode is in the low-pressure, supersonic end of the nozzle, so the arc attachment to the anode is diffuse. The anode can, therefore, withstand large currents with long lifetimes without a need for magnetically moving the arc attachment point. To assure a symmetric current distribution, the anode is segmented circumferentially, and each segment is connected to the power supply by means of a ballast resistance. In the ¼-inch-diameter unit, the segmented anode consists of six water-cooled loops of copper tubing placed downstream of the nozzle. In the ½-inch-diameter unit, the anode consists of 24 water-cooled copper blocks attached directly to the end of the nozzle. (See Figure 2.)

RESULTS

The results of the recent experimental testing of the plasma jets verified that the arc can be passed through the nozzle without disrupting the supersonic flow, and that very high enthalpies can be reached. Shock diamonds emerged from the nozzle as the current was increased from a very low value to the design current, indicating that the flow was supersonic. High-speed photographs indicated that the flow was very steady. Selected frames are shown in Figure 3.

Conventional steady-state instrumentation was used to measure current, voltage, cooling-water flow rates and temperature rises, gas flow rate, and plenum chamber pressure for the two units. Calculations of the power released to the gas and calculations of the power loss were carried out from the measurements of current, voltage, and cooling water flow and temperature-rise.

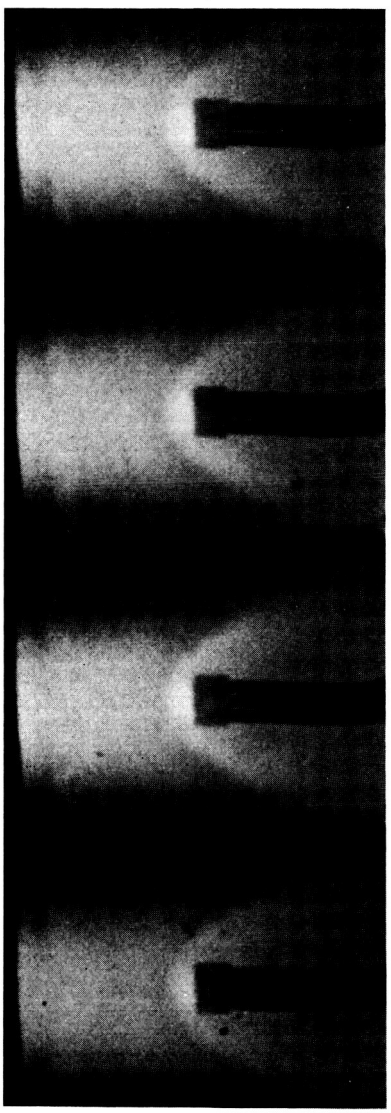

FIGURE 3. Movie sequence showing water-cooled impact pressure probe in supersonic jet ($\frac{1}{2}$-inch-diameter unit).

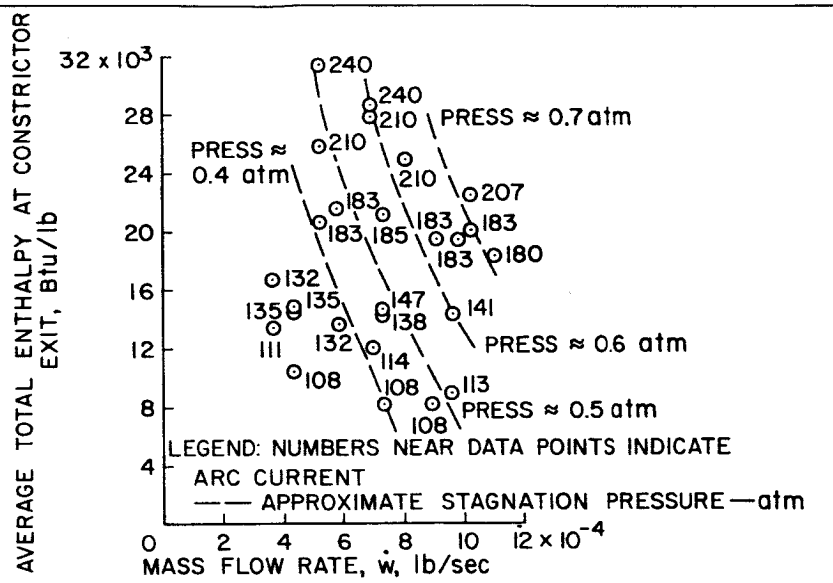

FIGURE 4. Average total enthalpy at the end of the constant area throat section in the ¼-inch constricted-arc supersonic jet as a function of nitrogen flow rate for various currents.

An average total enthalpy at the end of the constant-area throat section was determined by dividing the gas flow rate into the net power remaining in the gas at that location. Figure 4 shows enthalpy as a function of gas flow rate for various currents, together with the approximate plenum chamber pressure. Average total enthalpies in excess of 30,000 Btu/lb were obtained for the ¼-inch-diameter unit at about ½ atmosphere of pressure. The average total enthalpy for a few runs

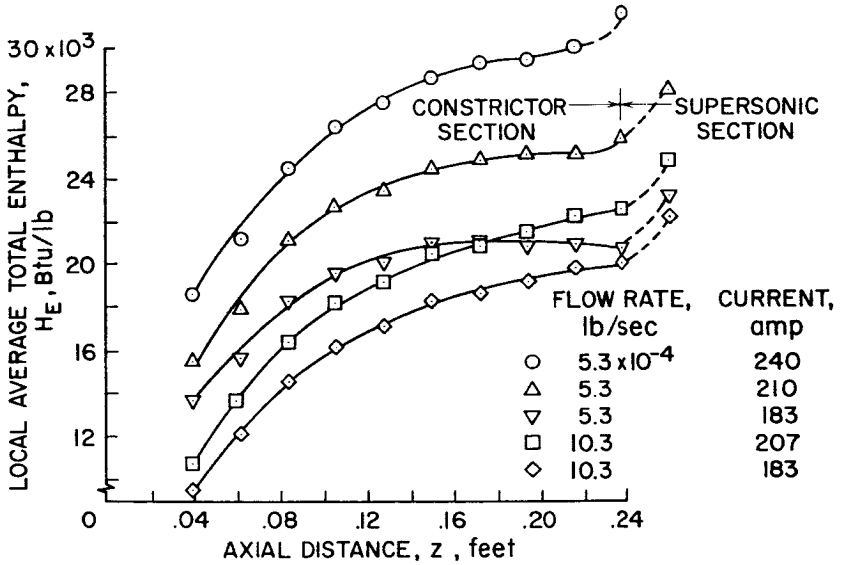

FIGURE 5. Throat section average total enthalpy versus axial distance for various arc currents and nitrogen flow rates.

was also determined in the test section of the $\frac{1}{4}$-inch-diameter unit from the power balance described above and the power absorbed in a tube and shell heat exchanger. It was found that the enthalpies obtained from the two methods agree within 12 per cent. The test section enthalpy was generally somewhat higher than the constrictor outlet enthalpy given in Figure 4.

Detailed measurements were made of the voltage drop between the cathode and the various constrictor-nozzle disks and of the power absorbed by each of the disks for the $\frac{1}{4}$-inch-diameter unit. Calculations were then made of the longitudinal distribution of power released to the gas, heat flux to the walls, and average total enthalpy. The buildup of average total enthalpy with longitudinal distance is shown in Figure 5 for several values of current and flow rate. The enthalpy level and the rate at which it increases is a function of the current and flow rate. The enthalpy rises more quickly at low flow rates and in some cases reaches an asymptotic value in the throat section. A further increase in enthalpy takes place as the gas leaves the constant-area section and enters the divergent (supersonic) region of the nozzle.

Profiles of impact pressure and stagnation heating rate to a $\frac{1}{2}$-inch-diameter, flat-faced calorimeter probe were measured in the test section of the $\frac{1}{2}$-inch unit. In order to deduce the enthalpy profile shown in Figure 6, it was assumed that the heat flux was proportional to the first power of enthalpy and to the square root of impact pressure. There was no region in the test section for which the enthalpy gradient was small; the center-line enthalpy was estimated to be 2.7 times the radially-averaged enthalpy of the test stream. Although the generator does not

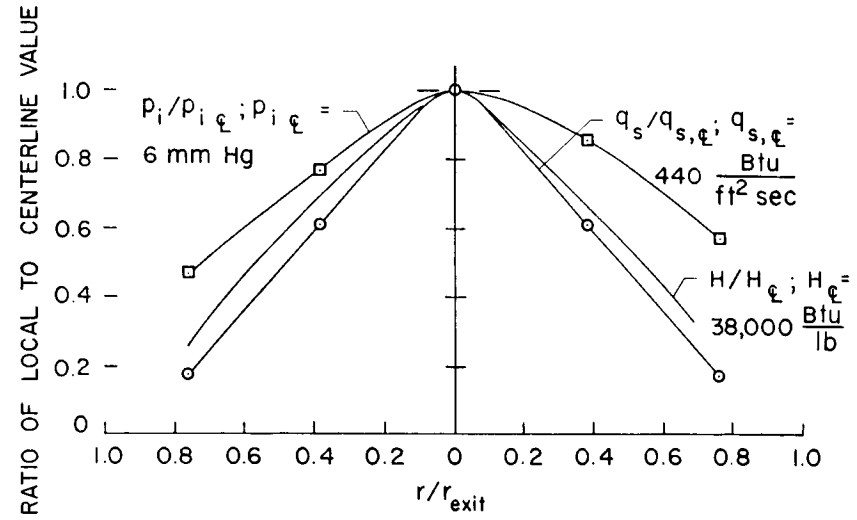

FIGURE 6. Typical radial profiles of impact pressure and stagnation-point heat transfer to a $\frac{1}{2}$-inch-diameter, flat-faced calorimeter probe and derived total enthalpy profile ($\frac{1}{2}$-inch unit).

provide a uniform stream for testing large models, it does provide high heating rates for small models. The gas used for most of the tests was nitrogen, but a few tests with air indicated that results were nearly the same for both gases. Both units were also operated with carbon dioxide (with a small amount of nitrogen shielding the cathode), and there was little change in the operating characteristics of the units; in other words, the flow was steady and supersonic.

COMPARING EXPERIMENT WITH THEORY

One of the features of the arrangement of the supersonic-arc plasma jet is that the gas heating process in the throat is amenable to analysis. In fact, the two plasma jets tested were designed with the aid of the theoretical analysis of the constricted-arc by Stine and Watson. Most of the heating takes place in the throat where the cross-section area is small; the simplified mathematical model of the arc column analyzed by Stine and Watson may be used to represent the arc column in the throat. The theoretical analysis presents the distribution of enthalpy and current in an axisymmetric arc column in which the dominant mechanism of energy loss from the column is radial conduction, and for which the specific mass flow, ρu, is constant. The relations between the state properties, enthalpy, electrical conductivity, and thermal conductivity potential, are linearized. The remaining characteristics of the column, such as voltage and heat flux, can be determined from the known enthalpy and current distributions.

To determine the degree to which the linear analysis can describe the arc-column characteristics, a series of comparisons was made between the experimental measurements and the predictions of the analysis.

Heat Flux

The analysis of Stine and Watson predicts that the heat flux to the elongated throat will be a function of enthalpy and will be independent of gas-flow rate. Figure 7 shows the experimental measurements of heat flux as a function of the average total enthalpy. The flow rates are also shown beside each data point. From this figure it can be seen that the heat flux is insensitive to the flow rate, but does correlate reasonably well with enthalpy, as predicted by the analysis. A straight line fitted to the data indicates that radiation is not important.

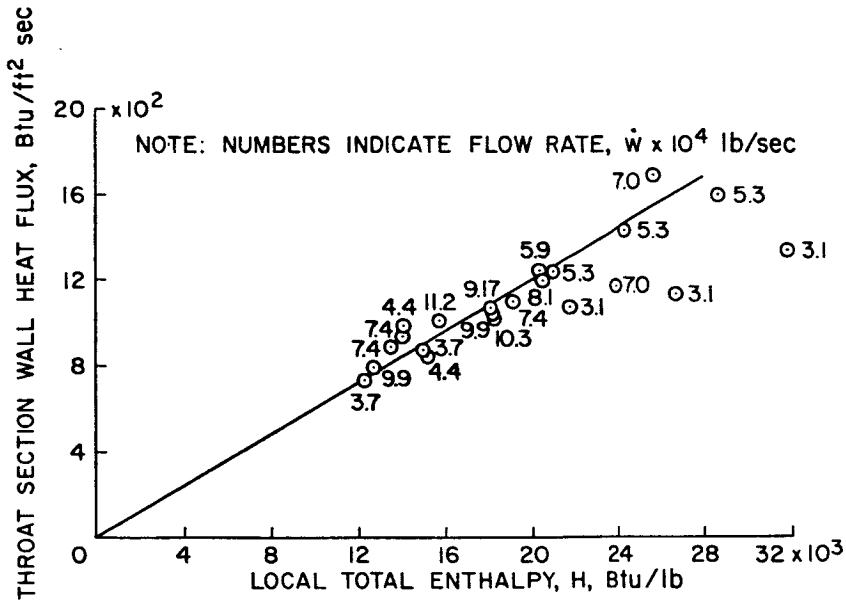

FIGURE 7. Throat section wall heat flux versus local average total enthalpy for various nitrogen flow rates; $z = 0.14$ feet ($\frac{1}{4}$-inch unit).

Voltage Gradient

The analysis also predicts that the voltage gradient will approach an asymptotic value as the gas-flow rate is decreased. The measured voltage gradient, shown in Figure 8, appears to approach an asymptotic value of about 500 volts/ft. Since the data are for a range of enthalpies, it appears that the voltage gradient is independent of enthalpy as predicted by the theory of Stine and Watson.

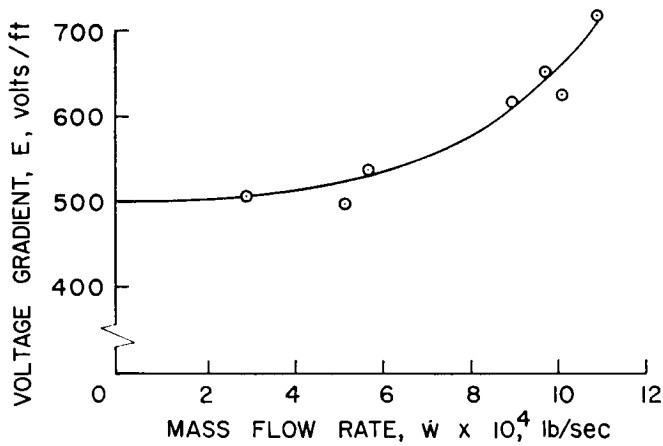

FIGURE 8. Voltage gradient as a function of nitrogen flow rate for the $\frac{1}{4}$-inch-diameter constricted-arc supersonic jet; $z = 0.15$ feet, $I = 183$ amperes.

Enthalpy Distribution

The analysis predicts that the increase of enthalpy with axial distance will be given by the equation,

$$h_E = h_{E,\infty}(1 - e^{-11.5\, z/z_0})^{1/2}$$

where

$$h_{E,\infty} = 4.08 \times 10^{-3}\left(\frac{c_p}{kA^{1/2}}\right)\left(\frac{I}{r_e}\right) \quad \text{and} \quad z_0 = \frac{\dot{w}c_p}{\pi k}$$

and the constants c_p/k and A represent the slopes of the straight-line approximations to the relationships between h and Φ and between σ and Φ, respectively; I is the current, r_e is the column radius, and $\dot{w}$ is the mass flow rate. The values of k and A are not known accurately, and, therefore, accurate predictions of enthalpy cannot be made from purely theoretical calculations. Furthermore, the relationships between h and Φ and between σ and Φ may be—in fact, probably are—nonlinear, so that the linear approximations will introduce further inaccuracy into the analysis. These relationships can be estimated from the theoretically-computed values of thermodynamic and transport properties, and electrical conductivity. The estimates shown in Figures 9 and 10 for air and nitrogen use the thermodynamic and transport properties from calculations by Hansen (**2**), and Ahtye (**3**), and electrical conductivity from calculations by Viegas and Peng (**4**), and Yos (**5**). The location of the straight line which best approximates each of these relationships is not obvious, and, unfortunately, a small change in the location of the line appreciably affects the value of the enthalpy predicted by the analysis. Nevertheless, one can deduce the locations of these lines from the data

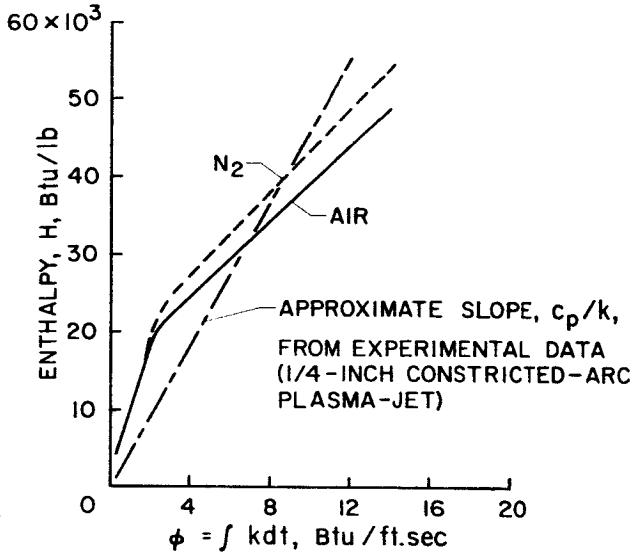

FIGURE 9. Enthalpy as a function of thermal conductivity potential for air and nitrogen at 1 atmosphere.

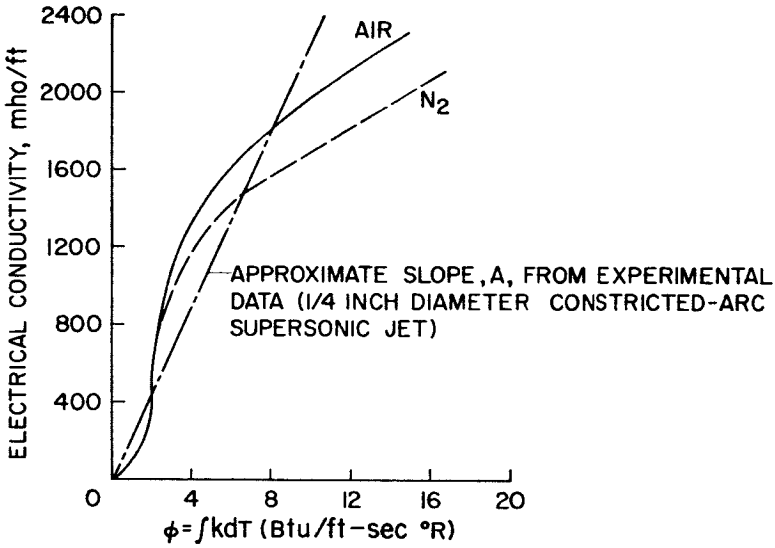

FIGURE 10. Electrical conductivity as a function of thermal conductivity potential for air and nitrogen at 1 atmosphere.

in Figures 7 and 8; in particular, a line drawn through the data in Figure 7 determines the line in Figure 9, and the value of E (of Figure 8) at zero mass flow determines the line in Figure 10. The prediction based on these deduced values of c_p/k and A is shown in Figure 11, and the experimental measurements are shown for comparison. The use of the values of c_p/k and A deduced from measurements made in the $\frac{1}{4}$-inch unit influences the agreement of the asymptotic enthalpy and the length required for the enthalpy to approach the asymptotic value for the

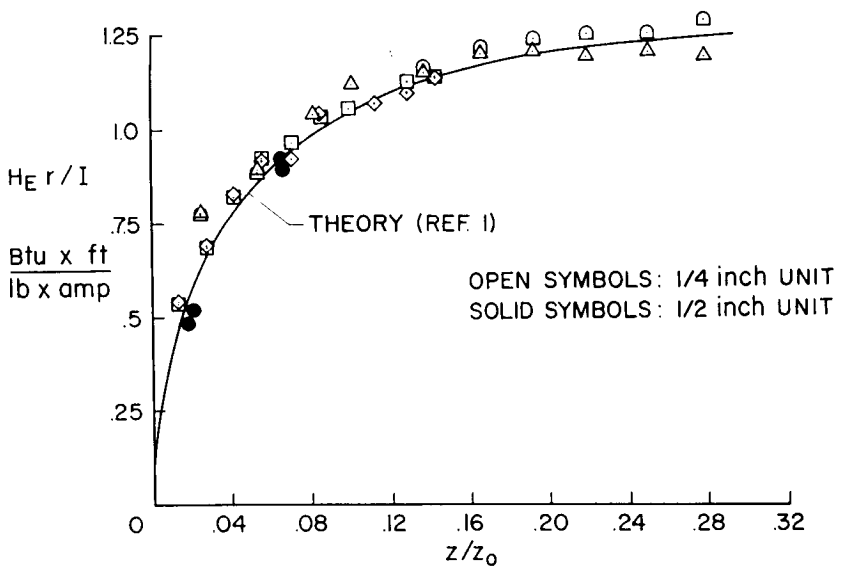

FIGURE 11. Comparison with theory (1) of experimentally determined enthalpy parameter, $H_E r/I$, versus dimensionless axial distance, z/z_0.

$\frac{1}{4}$-inch unit. However, the shape of the theoretical curve is not prescribed by the use of these values; the data therefore verify that the analysis predicts qualitatively the rate of increase of enthalpy with axial distance. Furthermore, the experimental data for the $\frac{1}{2}$-inch unit agree with this curve, so it appears that once the values of c_p/k and A are determined experimentally, the analysis predicts quantitatively the enthalpy for constrictors of all sizes.

Radial Enthalpy Profile

The analysis predicts that the radial profile of enthalpy in the constrictor will be a Bessel function of the first kind and of zero order. The ratio of center-line enthalpy to radially-averaged enthalpy would then be 2.3. The estimated ratio of center-line enthalpy to average enthalpy based on measurements at the end of the nozzle was 2.7 (see Figure 6). Therefore the enthalpy profile appears to be more peaked than the analysis predicts.

SCALING LAWS

Laws for scaling the constricted-arc supersonic jet can be deduced from the analysis for the range of throat sizes and pressures for which the flow remains laminar and for which the conduction heat loss is much larger than the radiation loss. The sizes and pressures for which the flow becomes turbulent are not known; however, theoretical calculations indicate that radiation losses become important in the $\frac{1}{2}$-inch unit at pressures over 10 atmospheres. Stine and Watson treat the scaling laws in detail, but we shall here present only the more interesting results.

Length and Flow Rate

The throat length and the mass flow rate do not affect the enthalpy independently. Only the ratio of $z/\dot{w}$ appears in the solution. Therefore, an increase in length is equivalent to a decrease in flow rate. For this reason, the dimensionless length, z/z_0, where $z_0 = \dot{w}c_p/\pi k$, is used hereafter.

Enthalpy

The radially averaged enthalpy is given by

$$h_E \propto \frac{I}{D} f\left(\frac{z}{z_0}\right)$$

where

$$f\left(\frac{z}{z_0}\right) = (1-e^{-11.5\ z/z_0})^{1/2}$$

For constant z/z_0, the enthalpy increases as the first power of current and increases with the inverse of the throat diameter.

Voltage Gradient

The voltage gradient is given by

$$E \propto \frac{1}{Df\left(\frac{z}{z_0}\right)}$$

and is independent of current.

Heat Flux

The heat flux to the throat wall is given by

$$q \propto \frac{I}{D^2} f\left(\frac{z}{z_0}\right)$$

or

$$q \propto \frac{h_E}{D}$$

For a given enthalpy, the heat flux decreases with increasing diameter. Therefore, assuming a given throat-cooling capability, the highest enthalpies should be obtained at the largest diameter for which the flow remains laminar and for which the radiation loss can be neglected.

CONCLUSIONS

We conclude, therefore, that an arc can be passed through a supersonic nozzle without disrupting the flow, that much higher enthalpies can be achieved by this process than from the more conventional plasma generator arrangements, and that the qualitative characteristics of the constricted-arc supersonic jet can be predicted from the analysis of Stine and Watson.

NOMENCLATURE

A	Parameter of the approximation $\sigma = A\phi$ used by Stine and Watson mho-sec/Btu
c_p	Specific heat at constant pressure, Btu/lb °F
D	Diameter
E	Voltage gradient, volt/ft
H	Local total enthalpy, Btu/lb (defined as zero at 530°R)
H_E	Mass average total enthalpy, Btu/lb (defined as zero at 530°R)
h_E	Radially averaged enthalpy, Btu/lb (defined as −3500 at 0°R)

I	Current, amperes
k	Thermal conductivity, Btu/ft °R sec
p	Pressure, atmospheres
p_i	Impact pressure, mm Hg
q	Heat flux, Btu/ft^2 sec
q_s	Stagnation-point heat flux, Btu/ft^2 sec
r_c	Radius of the current-carrying cylinder, ft
$\dot{w}$	Gas mass flow rate, lb/sec
z	Axial distance along the column (**1**), ft
z_0	$\dot{w}c_p/\pi k$ (**1**), ft
Φ	Conductivity function, $\int k\,dT$, Btu/sec ft (defined as -0.3 at 0°R)

Subscripts

$(\ )_\infty$	Value at large z/z_0
$(\ )_c$	Downstream end of constrictor
$(\ )_\mathfrak{q}$	Center-line value

REFERENCES

1. Stine, Howard A., and Watson, Velvin R., "The Theoretical Enthalpy Distribution of Air in Steady Flow Along the Axis of a Direct-Current Electric Arc", *NASA* TN D–1331, 1962.
2. Hansen, C. Frederick, "Approximations for the Thermodynamic and Transport Properties of High-Temperature Air", *NASA* TR R–50, 1959.
3. Ahtye, Warren F., and Peng, Tzy-Cheng, "Approximations for the Thermodynamic and Transport Properties of High-Temperature Nitrogen with Shock-Tube Applications", *NASA* TN D–1303, 1962.
4. Viegas, John R., and Peng, Tzy-Cheng: "Electrical Conductivity of Ionized Air in Thermodynamic Equilibrium", *ARS Journal*, **31**, 5, 654 (1961).
5. Yos, Jerrold M., "Transport Properties of Nitrogen, Hydrogen, Oxygen, and Air to 30,000°K", AVCO Corporation Technical Memorandum RAD-TM-63-7, March, 1963.

15. Philip Brockman, Robert V. Hess, and Richard Weinstein: *Measurements and Theoretical Interpretation of Hall Currents for Steady Axial Discharges in Radial Magnetic Fields*

Experiments for a Hall-ion accelerator are presented using axial electric fields and radial magnetic fields. Measurements of the variation of Hall currents with magnetic field for various constant axial currents are presented together with voltage variations. The pressures in the experiments vary from 15 *to* 40 μ, *the magnetic fields from* 0 *to* 500 *gauss, and the currents from* 1 *to* 40 *amperes. The Hall currents first increase with magnetic field and then decrease again as the magnetic field is increased. The variation can be interpreted in terms of Joule- and ion-slip losses for the partially-ionized plasma used in the experiments. The effect of transition to turbulence is also evaluated and the present state of the theory for turbulent conduction is discussed. Preliminary experiments for preionization and for the heating of ring-shaped cathodes to thermionic emission are discussed.*

INTRODUCTION

The research on acceleration of plasmas or ions in plasmas using azimuthal Hall currents and radial magnetic-field components has grown considerably since the early work on Hall current plasma accelerators at the NASA Langley Research Center (**1**), and the subsequent description of an added ion acceleration mechanism for improvement of a traveling wave accelerator by AVCO Everett Research Laboratory (**2**). The final grouping of the latter mechanism of ion acceleration under the principle of Hall-ion acceleration is based on the efforts of many research laboratories: Electro-Optics, General Electric, the Lewis and Langley Research Centers of NASA, and United Aircraft. A history of the development of Hall

ED. NOTE: Mr. Brockman, Mr. Hess, and Mr. Weinstein are with the NASA Langley Research Center, Langley Station, Hampton, Va. The research for this paper was performed in the Plasma Physics Section of the Magnetoplasmadynamics Branch. Part of the material in this paper has been presented by Mr. Brockman as a thesis in partial fulfillment of the requirements for the degree of Master of Arts at the College of William and Mary.

current accelerators is given in reference (**3**) in the section "Acceleration Using Hall Currents". (Note: one of the earliest contributions published in this field, reference (**17**), was omitted in this review.) The reason for the interest in Hall current accelerators is that they offer the possibility of magnetic containment, increased uniformity of discharges, reduction in electrode erosion, and operation over a very wide range of density and specific impulse.

There are several reasons for measuring Hall currents. One more or less obvious reason is that it gives an independent check of the thrust, which can be compared with direct thrust measurements. In this connection it should be noted that the total voltage drop must overcome the losses as well as accelerate the ions, so that this voltage drop is only a true measure of the acceleration of the ions if the losses are small.

The present measurements of Hall currents differ from those previously performed at the Langley Research Laboratory (**4, 5**), in that a much greater number of measurements were made at various axial currents and magnetic fields. By cross-plotting the results to indicate variation of Hall currents with magnetic field at a variety of constant axial currents, it was possible to establish more definite trends which were only suggested by the experiments in reference (**5**). Simultaneous measurements of the variation of axial voltage drop with magnetic field were also performed. In the present experiments measurements were also made over a wide current range for considerably lower pressures than previously reported by us. A special effort has been made to evaluate up to what point the novel effects can be interpreted through conventional loss mechanisms rather than through the popular field of plasma turbulence.

Finally, it should be pointed out that the Hall current apparently can provide vital information on certain anomalous or "turbulent" conduction effects which have recently received considerable attention. In the first (to our knowledge) study of instabilities and turbulent conduction effects in a Hall current accelerator which was conducted at the Langley Research Center (**6**), probes which were placed in the azimuthal direction of the Hall current indicated that although coaxial symmetry was imposed by the electrodes and the magnetic-field distribution, the plasma did not maintain symmetry under all conditions. At the same meeting Dr. Buneman independently emphasized in the Round Table Discussion, the importance of checking for plasma asymmetries in geometrically symmetric experimental arrangements. The azimuthal Hall current could be especially sensitive to deviations from symmetry and thus could offer a clue to the transition from conventional to turbulent conduction. Preliminary application of these concepts to the Hall-ion accelerator are discussed in the preprint with more details to be presented in the talk.

Experiments for the preionizer and the thermionically heated cathodes have to date been made in a separate test apparatus. The preionizer was designed and operated by J. Burlock and T. Collier, and the heated cathode by O. Jarrett. Details are given in Appendices B and C.

An experimental study of the influence of preionizers and heated cathodes on Hall currents, electric fields, and oscillations is being undertaken.

The major purpose of this paper is to gain an understanding of the acceleration mechanisms in a low-pressure Hall current accelerator. From a more fundamental viewpoint it is the aim to obtain an understanding of the mechanism of electric conduction across a magnetic field in the presence of ion motion.

Hall currents also have been measured for a high-power, high-pressure plasma Hall accelerator, and a Hall-ion accelerator operating in this range also has been constructed. Also note studies made at Electro-Optics (**7**).

APPARATUS

A schematic of the apparatus is given in Figure 1. The electrodes are 7.3-cm I.D. inserts within water-cooled holders. The inserts are copper at the anode and aluminum at the cathode in the experiments reported here, but these may be easily replaced by any other material. The edges of the electrodes and the glass are protected from the discharge by boron nitride insulators; these insulators leave 2.54 cm of the electrodes exposed to the discharge. The center glass is 7.3-cm I.D. and the discharge length is 22.86 cm. On either side of the discharge the electrode holders are connected to glass crosses. These crosses contain Hastings thermocouple vacuum gauges. The anode cross is connected to the gas input and the cathode cross leads to the vacuum system. The cathode cross also contains a cantilever support for a bakelite rod which, in turn, supports an iron bar in the center of the discharge. The iron bar is centered under the magnet and is 22.9 cm long, the bar is 3.16 cm O.D. and has a 1.27-cm hole through the center. This hole contains a teflon rod which is screwed to a boron nitride insulator at the anode end and to the bakelite rod at the cathode end. The iron bar is covered by a 38-cm pyrex tube. This cantilever arrangement was designed so that the accelerator can be mated with any type of preionizer at the anode and without changing the configuration or interfering with the flow from the preionizer. The magnet solenoid is 2.8 cm long and its center is 10.16 cm from the anode and 12.7 cm from the cathode. It is a 450-turn coil and is powered by ten 6-volt batteries; it is current controlled by means of a variable resistor. A search coil is mounted $4\frac{1}{2}$ cm from the center of the magnet on the cathode side. This is a 100-turn coil and is connected in series with a ballistic galvanometer. The arc power supply is a 700-volt, 1400-ampere motor-generator set and is connected to the electrodes through a 10.37-ohm ballast resistor. The pumping system consists of a cold trap, a 14-inch diffusion pump, and a Stokes vacuum pump. Figure 2 is a diagram of the magnetic field configuration for an average radial field of 100 gauss—a rapid increase of axial field strength occurs above 500 gauss due to saturation of the iron bar.

The investigations reported here are a study of the basic mechanisms of the discharge. The pumping system at this time is not adequate to remove the mass flow due to high ion currents. As a consequence, during operation there is a pressure rise at the pump entrance and a pressure drop at the gas inlet. This results in

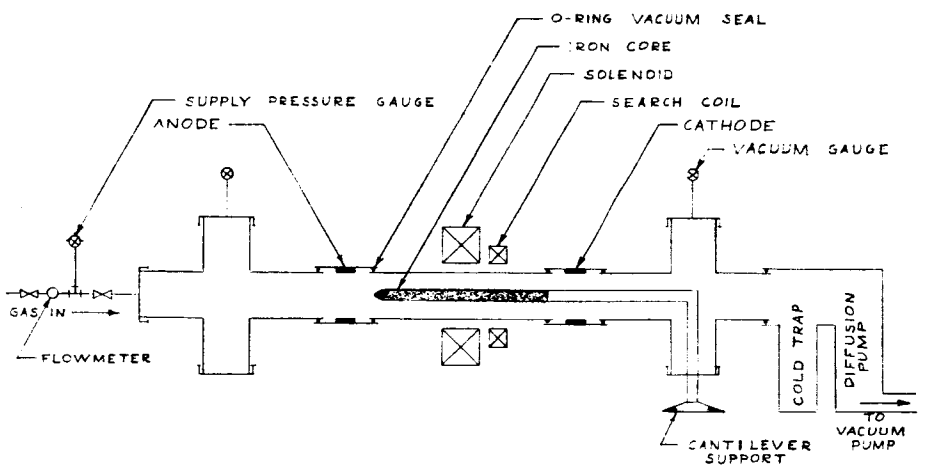

FIGURE 1. Schematic of apparatus.

a flow of neutral particles from cathode to anode. The back flow or circulation of neutrals permits the maintenance of high ion currents. A larger vacuum system (four 35-inch diffusion pumps) is now under construction, to be used for experiments at high specific impulse.

OPERATION OF DISCHARGE AND MEASUREMENTS

As the solenoid is in the center of the discharge, the radial magnetic field reverses direction from the anode side to the cathode side of the discharge. This will also reverse the direction of the Hall current and of any gas rotation as these are functions of $\vec{v} \times \vec{B}$. However, the forces will remain in the same direction as these, in turn, are functions of $(\vec{v} \times \vec{B}) \times \vec{B}$. Thus, the reversing magnetic field has the advantage of tending to destroy any gas rotation which may build up on one side

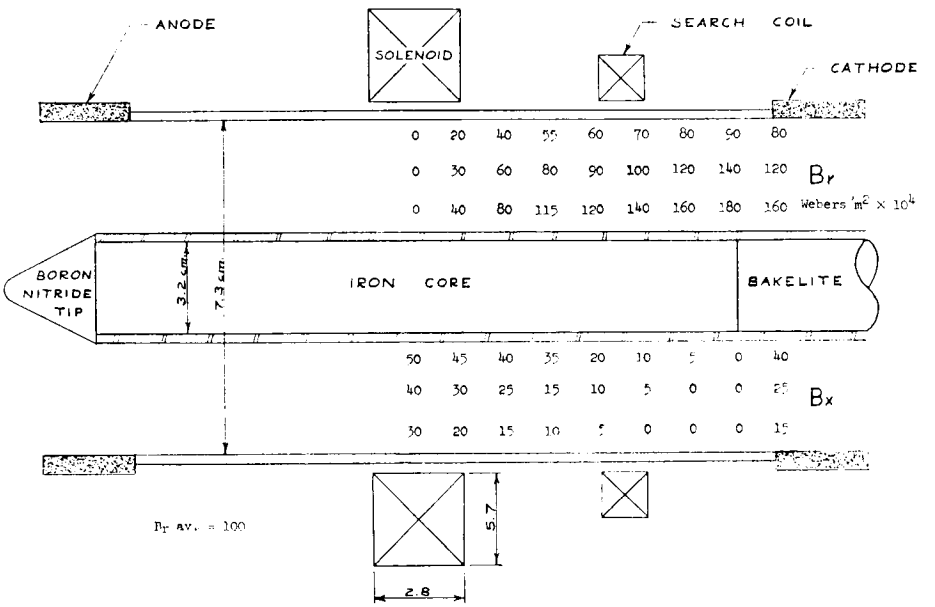

FIGURE 2. Schematic of magnetic field configuration.

of the magnet. On the cathode side of the discharge the gas will enter with any rotation that has built up; on the anode side the rotating force will then be reversed and the average rotation on the cathode side should be close to zero.

The discharge for these experiments was operated with no preionizer. Thus, all ionization was supplied by the electric field. Starting ionization was supplied by a Tesla coil, but this was turned off before any measurements were taken. Voltage and current were monitored on standard meters and also recorded on a Consolidated Electric Co. oscillograph. Pressure was monitored on two Hastings thermocouple gages and also recorded on the oscillograph. Hall current was measured by means of a 100-turn search coil and ballistic galvanometer. The discharge was turned off and the collapsing magnetic field of the Hall current induced an EMF in the search coil. The search coil was connected in series to the ballistic galvano-

meter through a 15-ohm resistance; the current through this circuit was integrated by the ballistic galvanometer giving the total charge. This charge is proportional to the original Hall current. The ballistic galvanometer was calibrated by placing two 80-turn coils in place of the Hall current. These coils were 5.3 cm in diameter and 7 cm in length. The ballistic galvanometer was calibrated by running various currents through the coils. The direction of current was reversed in the two coils to represent the Hall current. When the current was turned off, the reading on the galvanometer was taken. The calibration was retaken at several magnetic field strengths in order to see if any saturation of the iron bar was affecting the readings. A slight drop in reading was noted at 550 gauss but this drop was within reading error. However, the sudden increase of the axial field at saturation may explain the sharp dropoff in Hall current. This effect is negligible below 550 gauss. The ballistic galvanometer was calibrated in amperes and the area of the Hall current was estimated at 17.79 cm^2. According to visual observation the discharge area did not vary much above a magnetic field of ~ 10 gauss. The current was multiplied by $10^4/17.79$ to give amperes/m^2. The axial current was multiplied by $10^4/30.59$ to give amperes/m^2 and the arc voltage multiplied by 100/22.86 to give volts/meter. Mass flow was measured by a tri-flat flow tube and a standard pressure meter. Magnetic field was calibrated versus current in magnet by a gauss meter. Magnet current was set with a standard ammeter.

In operating the discharge, pressure was set using a variable leak; the voltage across the electrodes and the magnetic field were preset. The discharge was started with the Tesla coil and when voltage and current oscillations as observed on the meters had settled out, the oscillograph was started and the switch controlling the ballistic galvanometer was depressed. The discharge was then turned off and the reading on the ballistic galvanometer taken by hand. Ideal operation would have been to operate the discharge at constant current for various magnetic-field strengths. However, as the power supply was not current controlled it was both difficult and time consuming to adjust the current during each run. At each magnetic-field strength the discharge was started at various voltages; the running voltage and current were allowed to adjust themselves. After preliminary data reduction, more data were taken in regions of interest. In order to extend the range of currents at high magnetic-field strengths, it was sometimes necessary to start the discharge and then decrease the voltage. Data were taken at 15, 30, and 40 microns and these data are presented in the form of arc voltage in volts/meter and Hall current in amperes/m^2 plotted versus arc current in amperes/m^2 for various magnetic-field strengths.

The data were then cross-plotted to give arc voltage and Hall current versus magnetic-field strength for various arc currents. These curves are presented in Figures 3 through 6.

The primary purpose of this study was to measure the Hall currents. Making a survey of any parameter is time consuming and thus several measurements which are needed for a complete analysis have not yet been made. A program has been active for some time to measure local voltage drop with floating probes and to make some measurements of ion density and electron temperature with Langmuir probes and double probes. The floating probe errors should cancel if the probes are close together so that the plasma conditions are equal at both probes. However, the magnetic field will influence the electron temperature and ion density measurements to some extent (**8**). The variation of these parameters should be comparable at any constant magnetic-field strength, but there is some question in comparing measurements taken at different magnetic-field strengths. An attempt will also be made to measure velocities and forces in the accelerator.

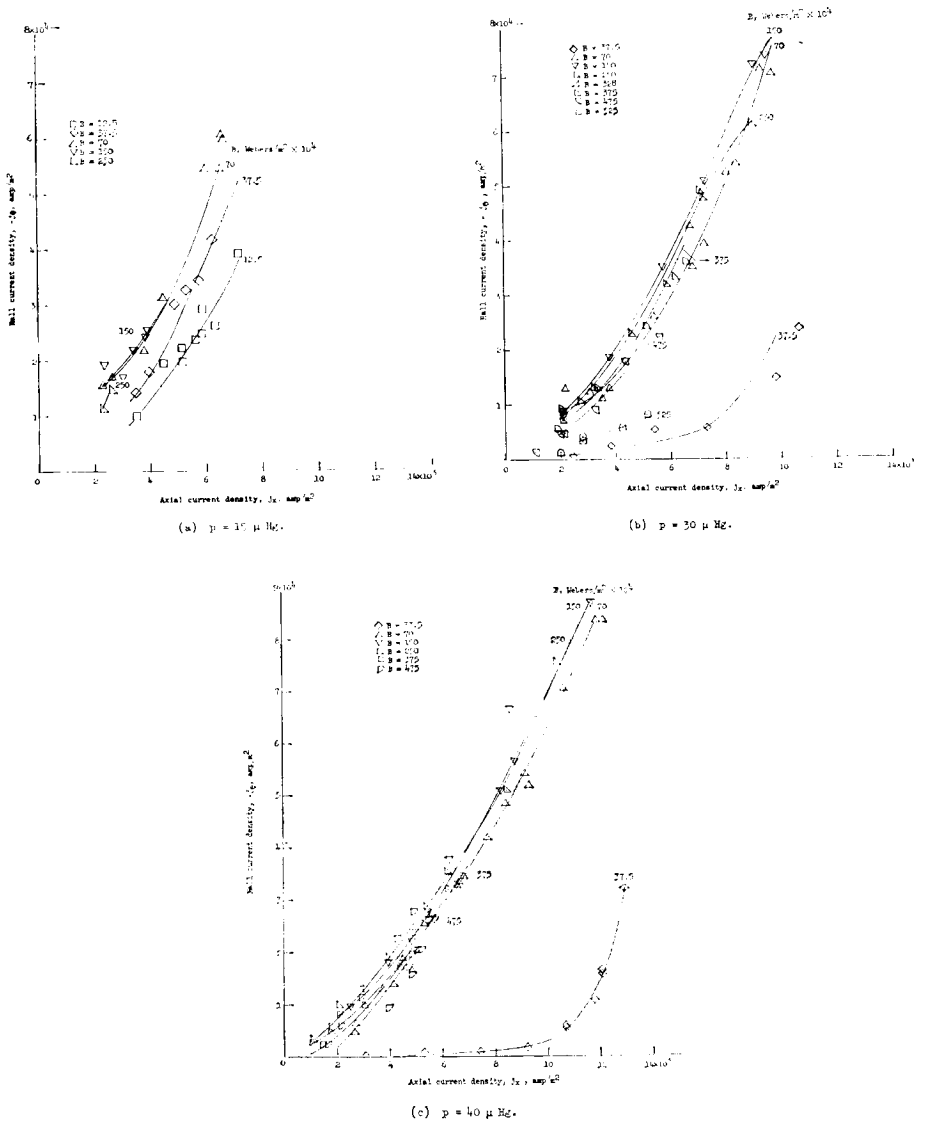

FIGURE 3. Hall current density versus axial current density for various magnetic flux densities.

A few basic measurements of oscillations in the discharge have been made with a simple metal plate capacitively coupled to the discharge through the glass. A survey of oscillations with probes placed in the plasma will be reported.

INTERPRETATION OF RESULTS

The most striking result found is the increase, peaking, and decrease of Hall current with increase of magnetic field at constant axial current. The initial increase of the Hall current with increasing axial current at constant magnetic field and the form of the arc voltage versus axial current curves at constant

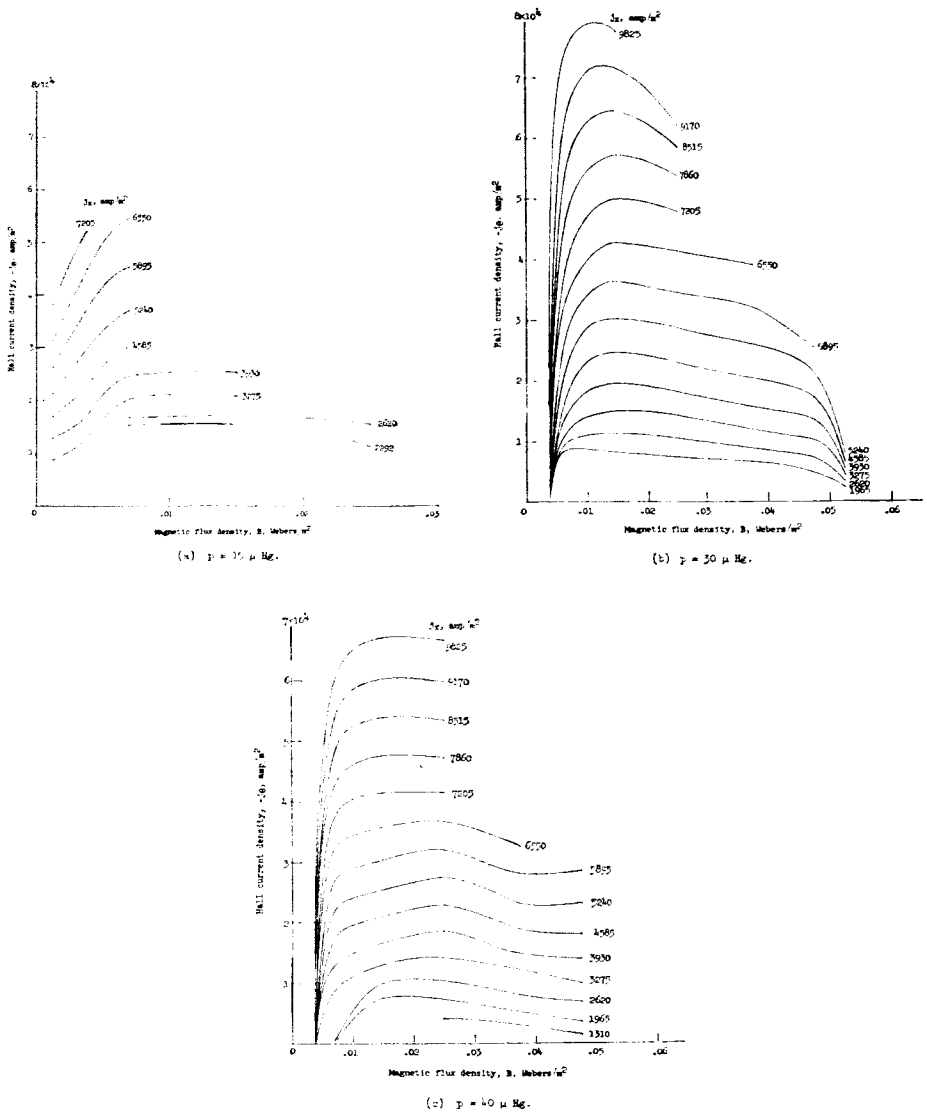

FIGURE 4. Hall current density versus magnetic flux densities for various axial current densities.

magnetic field has been previously reported (**4**). The shape of the curves of arc voltage versus magnetic-field strength are different in certain regions than those normally reported in, for example, references (**9**) and (**10**), but this may be due to the inherent errors in measuring total arc voltage rather than local electric field, or it may be due simply to our particular operating conditions.

Since the experiments are concerned with a partially ionized-plasma in a magnetic field and include the motion of ions with respect to neutrals, it is of interest to see to what extent the experiments can be interpreted in terms of the conventional generalized Ohm's law including ion slip. The influence of turbulence is discussed in a later section.

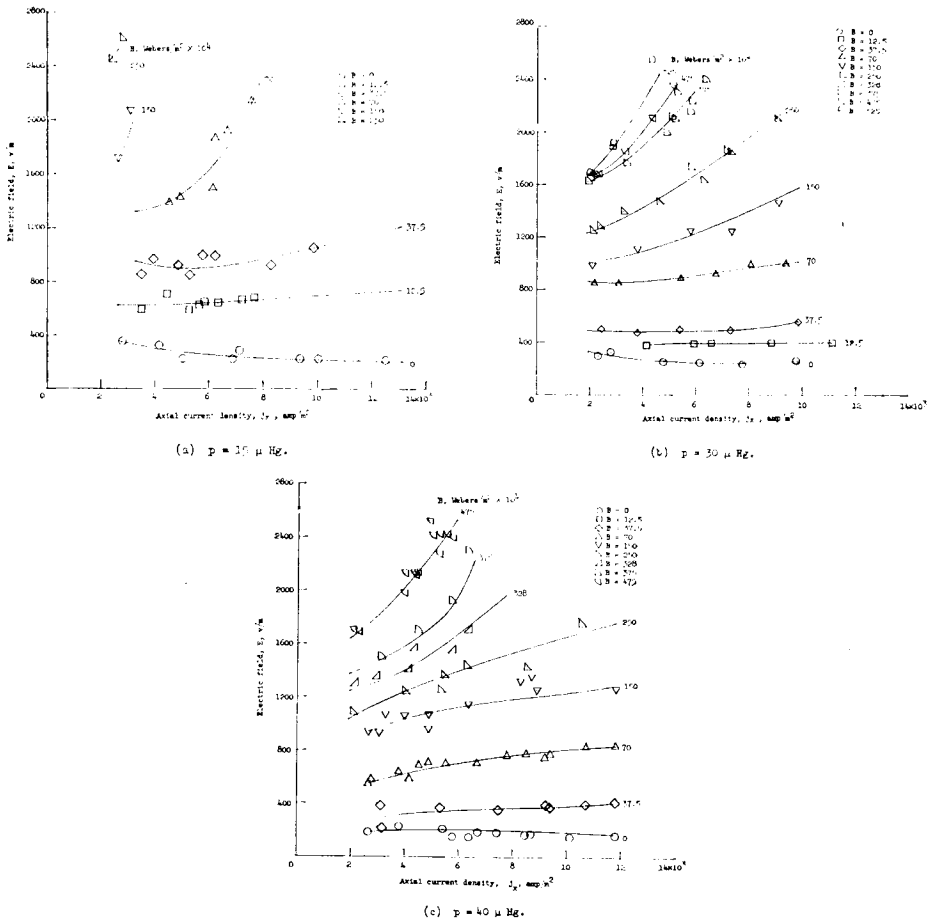

FIGURE 5. Electric field versus axial current density for various magnetic flux densities.

Repeating equation (A4) from Appendix A, which is the complete equation for j_θ including motion of ions and neutrals but not turbulence,

$$-j_\theta = \frac{1}{W}(j_x - n_e e v_x) \tag{1}$$

The inclusion of $2\omega_i\tau_i\omega_e\tau_e$ in the term

$$W = \frac{1+2\omega_e\tau_e\omega_i\tau_i}{\omega_e\tau_e}$$

gives the influence of ion slip. The ion slip term will increase W and, therefore, decrease j_θ at constant magnetic field. However, solving equation (A2) for E'_x,

$$E'_x = \frac{1+W^2}{W}\frac{j_x B}{n_e e} - \frac{v_x B}{W} \tag{2}$$

The effect of ion slip on E'_x is more complicated than on j_θ. The term

$$\frac{1+W^2}{W} = \frac{1}{W} + W = \frac{\omega_e\tau_e}{1+2\omega_e\tau_e\omega_i\tau_i} + \frac{1+2\omega_e\tau_e\omega_i\tau_i}{\omega_e\tau_e} \tag{3}$$

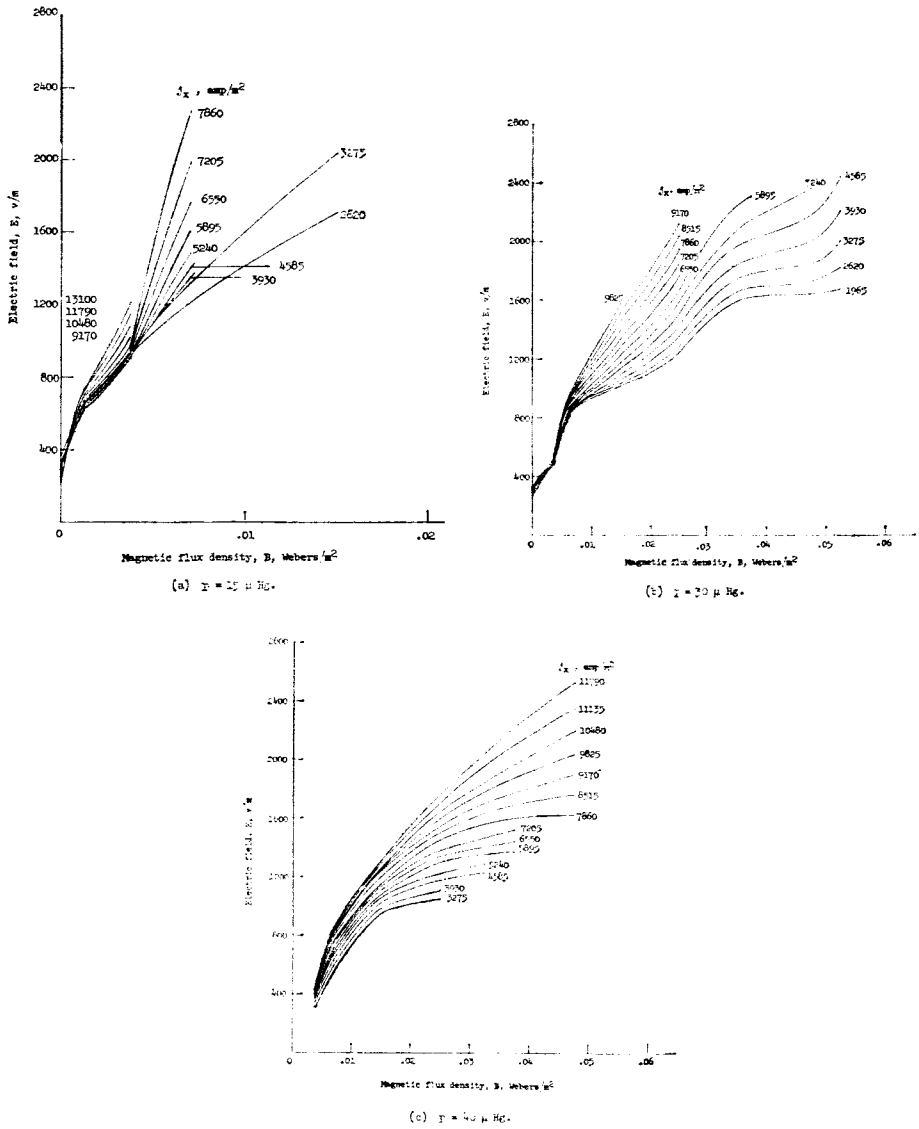

FIGURE 6. Electric field versus magnetic field strength for various axial current densities.

Thus for $W \ll 1$ an increase in $\omega_i \tau_i$ will decrease E'_x (through an increase in ion current) but for $W \gg 1$ an increase in $\omega_i \tau_i$ will increase E'_x (neglecting v_θ). For constant j_x the increase then decrease of $-j_\theta$ is due either to variations of W, v_x or n_e with B. At the particular conditions that we operate n_e is probably small and v_x the average (or center-of-mass) plasma velocity is limited, as pointed out in the section on apparatus. It, therefore, seems that the effect of $n_e e v_x$ can be neglected, for the present case.

A simple explanation of the variation of Hall current with magnetic field can be based on the variation of W with magnetic field. The following assumptions were made: first, that $n_e e v_x$ was negligible compared to j_x, and, second, that τ_e and τ_i

were constant for j_x constant. This second assumption is based on the condition that τ_e and τ_i are not explicit functions of E'_x or B. The calculated values of $\omega_e\tau_e/B$ and $\omega_i\tau_i/B$ in the literature usually depend on the equivalency of electron and ion temperatures; we know that our low-pressure operation does not justify this assumption. In order to generate some theoretical curves for j_θ versus B, equation (1) is rewritten in the form

$$W = \frac{j_x}{-j_\theta} \tag{4}$$

and then for a particular experimental curve a calculation is made of the minimum value of W, as $W_{\min} = j_x/-j_{\theta,\max}$. The values of $\omega_e\tau_e/B$ and $\omega_i\tau_i/B$, at $j_{\theta,\max}$, were then calculated for this case using equations (A11) and (A12).

These values were then divided by the magnetic-field strength at the maximum j_θ point. The resultant values of $\omega_e\tau_e$ and $\omega_i\tau_i$ were used with equation (A7) to calculate W as a function of B. Typical plots of $1/W$ versus B and $(1+W^2)/W$ are given in Figure 7. Equation (4) was then used to calculate theoretical values of j_θ versus B. Equation (2) was used to calculate values of $n_e e E'_x$ versus B. The sheath voltage was assumed to be equal to the experimental voltage at $B=0$, and

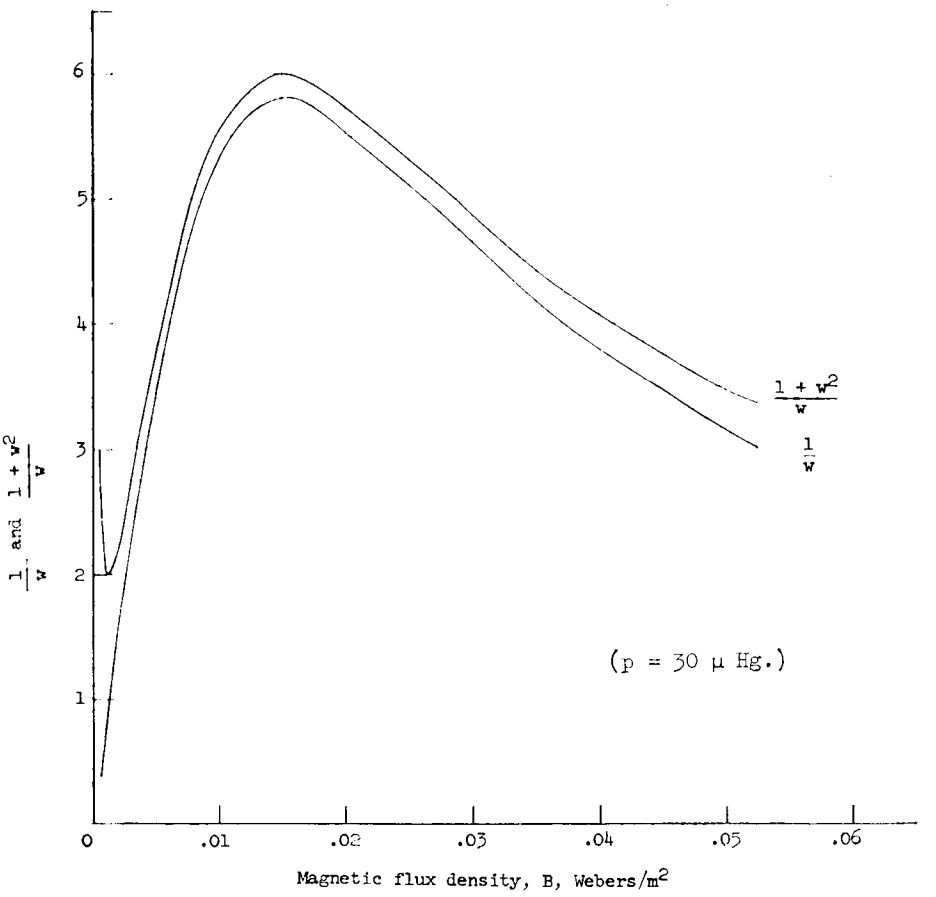

FIGURE 7. Variation of $\frac{1}{W}$ and $\frac{1+W^2}{W}$ with magnetic flux density.

it was also assumed that n_e was constant; for constant j_x a value of n_e was chosen so that the highest point of the experimental and theoretical E'_x versus B curves would match and the assumed sheath voltage was added to the theoretical curves so that the bottom points would also match. Thus, only the shape of these curves can be compared. The method of calculating W_{min}, of course, forces the experimental and theoretical Hall current curves to match at $j_{\theta,max}$. In Figure 8 experimental and theoretical curves of j_θ versus B are compared for $j_x=3930$, 5240, and 9170 amp/m^2; at $j_x=3930$ amp/m^2, $W_{min}=0.2$, $B=0.015$ web/m^2, $\omega_e\tau_e/B=668$, $\omega_i\tau_i/B=3.32$; at $j_x=5240$, $W_{min}=0.1158$, $B=0.015$ web/m^2, $\omega_e\tau_e/B=772$, $\omega_i\tau_i/B=2.9$; at $j_x=9170$, $W_{min}=0.1274$, $B=0.0125$, $\omega_e\tau_e/B=1256$,

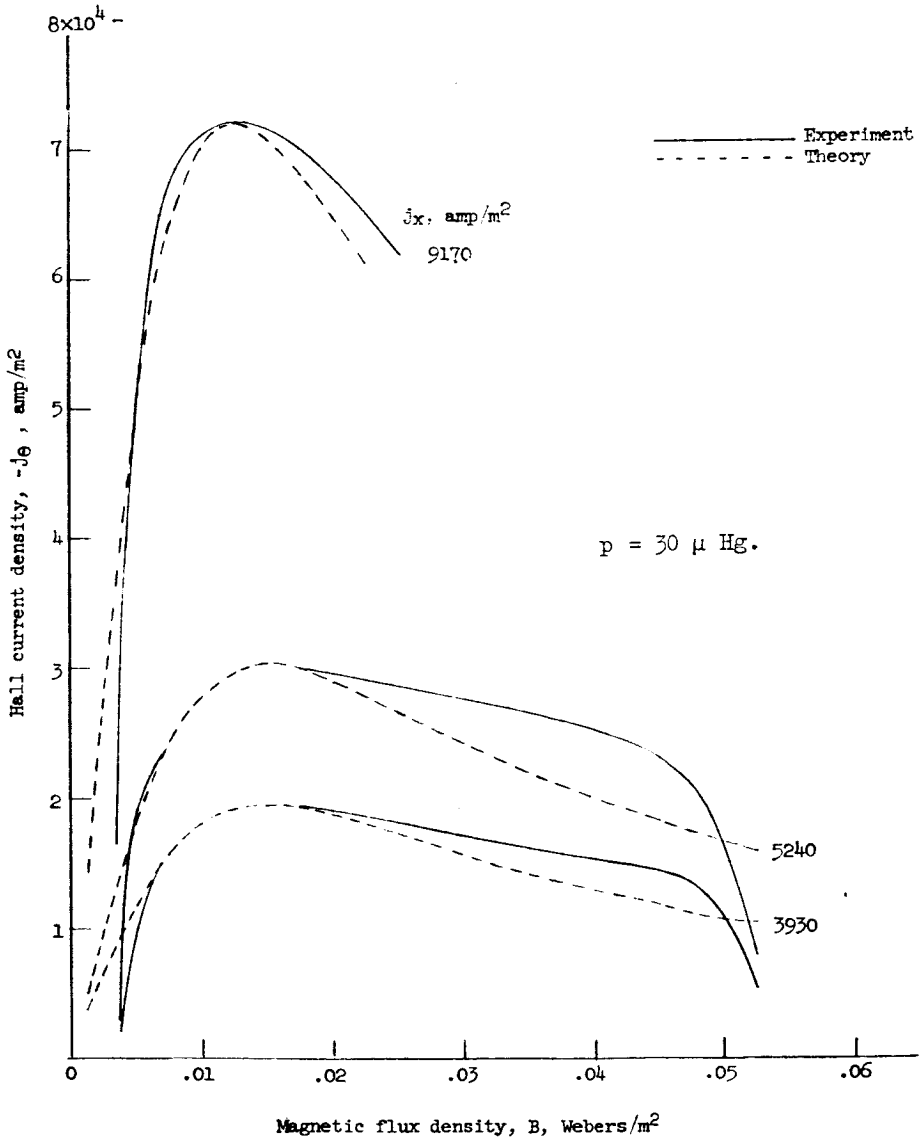

FIGURE 8. Comparison of theory and experiment (Hall current density versus magnetic flux density).

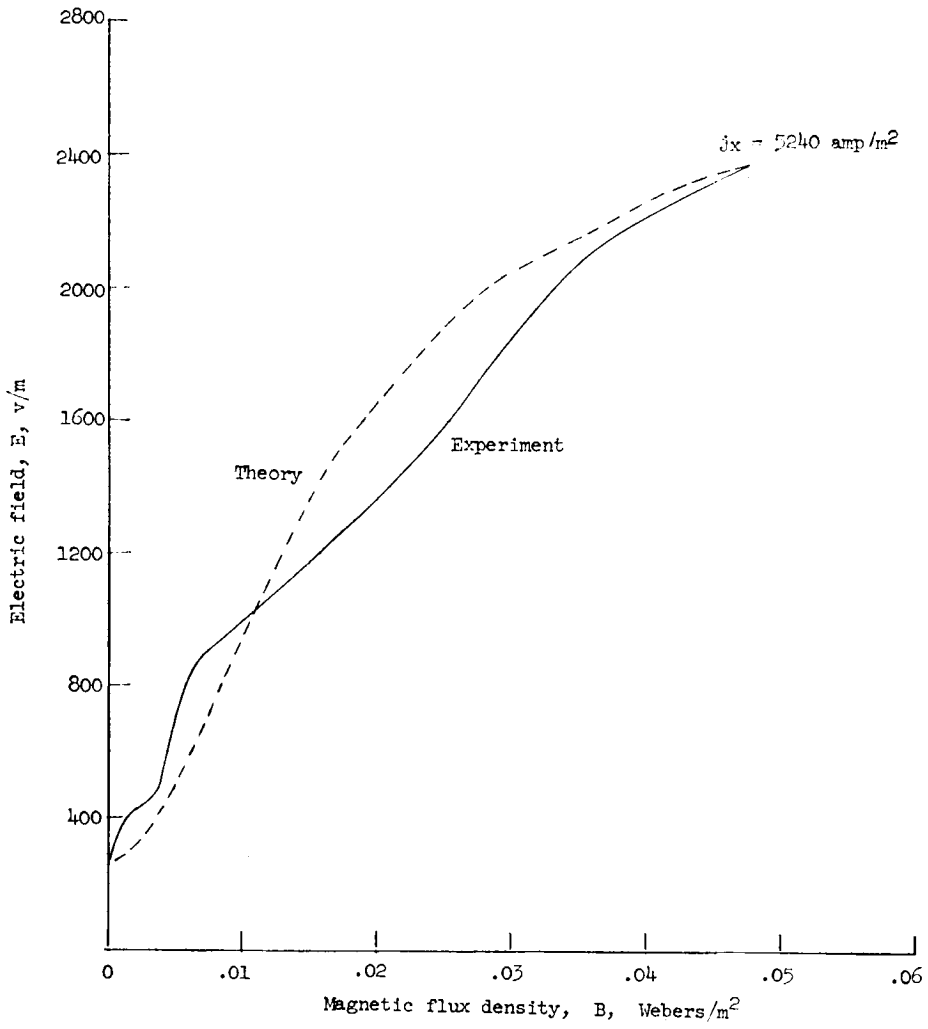

FIGURE 9. Comparison of theory and experiment (electric field versus magnetic flux density).

$\omega_i\tau_i/B = 2.55$. In Figure 9 the theoretical and experimental curves of E'_x versus B are compared for $j_x = 5240$ at 30 microns Hg. We added 247 volts/m to the theoretical curve to account for sheath voltage at $B = 0$; for curve matching n_e was adjusted to be 2.67×10^{18} particles/m^3. This corresponds to a very reasonable low percentage ionization. The values of $\omega_i\tau_i/B$ show good agreement with theory if the cross sections, $Q_{in,ex}$, for resonant charge exchange (**18**) are used in the expression for $\tau_i = \lambda_{in}/\bar{c} = 1/(n_n Q_{in,ex}\bar{c})$. The mean free path λ_{in} is at least of an order of magnitude smaller than the length of each accelerating section so that sufficient collisions of ions with neutrals can take place to develop friction between the two species characteristic of the ion-slip concept. This should even be true when the directed ion velocities exceed $\bar{c}$. Detailed calculations of $\omega_i\tau_i$ depending on random (temperature), or directed-ion energies, neutral temperatures, and densities will be presented elsewhere. Ion-wall collisions must also be considered at pressures slightly below those reported here. Calculations for $\omega_e\tau_e/B$ for a variety of electron temperatures

considerably in excess of ion temperatures and for various charged-particle concentrations also show good agreement. The Hall current curves match quite well and seem off by only a slight rotation. This can be due to the error involved in neglecting various effects when calculating $W_{\min}$. The E_x' does not match as well except at the low- and high-magnetic-field strengths, where the general curvature is the same.

In matching theory with experiments, one must also be reminded that the values for E_x' in Figures 5 and 6 are based on averaging the voltage drop over the length of the apparatus including sheath drop. Only isolated measurements have been made so far of the voltage distribution in the accelerator. A complete survey is, however, necessary to obtain a more detailed account of the contribution in sheath drop with varying magnetic field. One should also be reminded that the electric field appearing in the equations is given by $E_x'=E_x-v_\theta B$ where E_x is the measured quantity.

Although special care has been taken to reverse B in the acceleration process, a certain amount of rotation will exist. The effect of rotation can also reduce j_θ/j_x, but it appears unlikely that it would be the sole effect since the drop in j_θ begins at values of $\omega_i\tau_i$ (which approximately equals λ_i/r_{Li}) considerably below unity and the center-of-mass velocity is small. Preliminary observations of the rotational speed of the discharge also indicate that it is low.

Before it can be stated with assurance that ion slip is the main contributor, and not turbulence (see next section), several additional measurements are necessary. These include measurements of n_e, v_x, local measurements of E_x, and measurements of turbulent effects. Also, measurements of electron and gas temperatures would be helpful in directly calculating values of τ_e and τ_i.

COMPARISON WITH OTHER THEORETICAL APPROACHES

NEGLECT OF ION SLIP AND LOSS-FREE CASE

For negligible values of $\omega_e\tau_e\omega_i\tau_i$ the ion-slip losses can be neglected and equation (A4) in Appendix A changes from

$$-j_\theta = \frac{\omega_e\tau_e}{1+2\omega_e\tau_e\omega_i\tau_i}(j_x-n_cev_x)$$

to

$$-j_\theta = j_x\omega_e\tau_e\left(1-\frac{n_eev_x}{j_x}\right) \tag{5}$$

where the center of mass velocity v_x in equation (5) does not include the motion of neutrals. For small values of ion flow, equation (5) assumes the familiar form

$$-\frac{j_\theta}{j_x} = \omega_e\tau_e \tag{6}$$

Equation (A2) for j_x changes for negligible ion slip from

$$j_x = n_ee\frac{\dfrac{1+2\omega_e\tau_e\omega_i\tau_i}{\omega_e\tau_e}\dfrac{E_x'}{B}+v_x}{1+\left(\dfrac{1+2\omega_e\tau_e\omega_i\tau_i}{\omega_e\tau_e}\right)^2}$$

to

$$j_x = \left(n_eev_x+\frac{n_ee}{\omega_e\tau_e}\frac{E_x'}{B}\right)\left[\frac{1}{1+\left(\dfrac{1}{\omega_e\tau_e}\right)^2}\right] \tag{7}$$

Solving equation (7) for v_x and substituting into equation (5) for j_θ gives

$$-j_\theta = n_e e \frac{E'_x}{B} - \frac{j_x}{\omega_e \tau_e} \tag{8}$$

Equation (1) indicates that the inclusion of ion motion will reduce the value of j_θ/j_x below $\omega_e\tau_e$ and equation (8) shows that with increasing $\omega_e\tau_e$

$$-j_\theta \to n_e e \frac{E'_x}{B} \tag{9}$$

Noting that for large $\omega_e\tau_e$ values j_x in equation (7)

$$j_x \to n_e e v_x \tag{10}$$

the limiting value for j_θ/j_x is

$$-\frac{j_\theta}{j_x} \to \frac{E'_x}{B}\frac{1}{v_x} \tag{11}$$

Since for the loss-free case the ions are electrostatically accelerated,

$$v_x = \sqrt{\frac{2eV}{m_i}}$$

Assuming $E'_x l = V$,

$$-\frac{j_\theta}{j_x} \to \sqrt{\frac{E'_x}{l}}\frac{1}{B}\sqrt{\frac{m_i}{2e}} \tag{12}$$

Equation (12) shows how much j_θ/j_x will be reduced below the increasing $\omega_e\tau_e$ as the losses decrease with increasing B, if an increase in the flow of ions is allowed. The transition to smaller losses as B increases beyond the Hall current peak in Figure 4 is, however, most unlikely in the present experiment.

Another possibility for a decrease in j_θ/j_x with B after the peak, for a constant j_x, can be explained from equation (8) in terms of a decrease in τ_e or a decrease in n_e with increasing B (assuming that E'_x/B is constant or increases). Since

$$\tau_e = \frac{\lambda}{\bar{c}} = \frac{1}{\sum nQ}\frac{1}{\bar{c}}$$

a decrease in τ_e, barring an increase in n_e (which would also decrease j_θ), would require an increase in the collision cross section. The possibility of such a decrease will depend very much on T_e and the degree of ionization, which help to determine whether elastic collisions of electrons with neutrals, or with ions (Coulomb collisions) predominate. Of course, a check has to be performed if such changes in τ_e and n_e could agree with the experimental variation of E'_x with B for high values of j_x = constant, when ion-slip losses become negligible. The neglect of ion-slip losses applies when the friction force, $\frac{1}{2}m_i\nu_i(v_i - v_n)$, between ions and neutrals is small. See equations of motion in reference (**6**). This is true for dense plasmas with low percentage ionization and slow acceleration where v_n differs little from v_i, as well as for fully-ionized plasmas where with vanishing of neutrals the collision frequency ν_i, between ions and neutrals, approaches zero. Neglect of ion-slip losses may also apply to the acceleration of very low-density plasmas in the Hall accelerator, when collisions between (approximately) axially moving ions and neutrals are scarce, but the collisions of electrons, moving in a spiral path, with ions or neutrals, are more frequent. Experiments using accelerators with length below λ_{in} will be useful in checking the various mechanisms.

In looking for simple effects the influence of rotation also has to be considered. For the neglect of ion slip the rotation appears only in the term $E'_x = E_x - v_\theta B$. It must be remembered again that E_x is the measured quantity so that $v_\theta B$ could reduce j_θ with increasing B. The effect of rotation alone, however, does not seem well suited to explain the pronounced increase and decrease of j_θ with B. Integration of the simultaneous equations of motion for the ions, electrons, and neutrals is in progress to check if there exists a density range where rotation must be considered. Experiments with plasmas for which the ion slip is known to be small will be performed using injection of low-density, highly-ionized plasmas.

EFFECT OF TURBULENT CONDUCTION MEANING OF LINEAR VARIATION OF E'_x VERSUS B FOR TURBULENT AND CONVENTIONAL CONDUCTION

In the theory for turbulent conduction (**11**) adapted to the present case in references (**9**) and (**3**), two basic assumptions are made. One is that the ions are assumed at rest, and, second, the influence of turbulence on j_θ and the possibility of polarization of the oscillations is not taken into account. The neglect of ion motion limits the theory to high-frequency oscillations with frequency larger than the ion cyclotron frequency. The applicability of this restricted theory to the interpretation of comparatively low frequencies at high magnetic fields (**9**) thus must be examined in detail. Recently the theory developed in reference (**11**) has been extended in reference (**12**) to include ion motion, and the result was obtained that ion motion greatly reduces the effect of turbulent conduction. This result seems in contrast to the discussion of the growth of other instabilities of plasmas in magnetic fields in reference (**12**) and of the relevant stabilities discussed in references (**6**), (**13**), (**19**), and to one unpublished discussion of instability of hollow cathode discharges by D. L. Morse of M.I.T. where the presence of ion motion is essential for such growth. Detailed measurements have to be performed to understand to what extent the ions influence the turbulent conduction process and to decide which instability has the greatest effect in producing the turbulent state. Also, a careful separation has to be made between the effects of ion slip and turbulence since both may reduce j_θ/j_x.

Next, the influence of turbulence on the azimuthal Hall current j_θ is evaluated. For this purpose, the basis for the development of the theory for turbulent conduction in reference (**11**) has to be briefly discussed. The theory deals in essence with turbulent conduction and diffusion assuming isotropic turbulence. It can be regarded as a limiting case for small random non-uniformities of the theories of conduction in plasmas with distributed non-uniformities in the presence of Hall effects; these theories were independently developed (**6, 14**). Since non-uniformities affect the Hall current it appears proper to include their influence also in a theory for turbulent conduction, especially since it was shown experimentally (**6, 19**), that the instabilities have their origin in azimuthal phenomena.

Since the effect of turbulence on the Hall current has not been considered in the literature, an attempt is made here to introduce it formally in analogy to the effects of turbulence on the axial current. (Note that in this attempt we have avoided the inclusion of the important ion oscillations which may even affect v_x.)

$$j_x = \alpha n_e e \frac{E'_x}{B} + n_e e v_x \tag{13}$$

where α under the neglect of ion motion is given by

$$\alpha = \tfrac{1}{4}\pi[(n_e - n_{0e})^2]_{\text{avg}}/n_{0e}^2$$

Comparison with equation (7) for the fully-ionized case indicates that $\omega_e\tau_e$ has been replaced by a constant $1/\alpha$. The quantity α is assumed to be about $\frac{1}{15}$ in references (**11**) and (**9**). The possibility also must be considered that the reduction of j_θ with B could be influenced by transition to turbulent conduction. Experiments for a highly-ionized plasma, using a pre-ionizer, should help to emphasize the turbulent effects by keeping ion slip small.

The turbulent losses could be introduced into j_θ in formal analogy with equations (5) and (8) for the fully ionized case, with the result

$$-j_\theta = j_x \frac{1}{\alpha}\left(1 - \frac{n_e e v_x}{j_x}\right) \tag{14}$$

and

$$-j_\theta = n_e e \frac{E'_x}{B} - \alpha j_x \tag{15}$$

While such a theory would indicate a reduction in j_θ from the non-turbulent case, an increase in α with B would be necessary to explain the decrease in j_θ/j_x. Since an increase in α with B would also influence the E'_x versus B relation in equation (13), the important question also arises as to whether the turbulence differs in the axial and azimuthal direction, that is, is polarized in the magnetic field rather than isotropic. The possibilities that the oscillations may not develop into fully-turbulent flow because of finite dimensions or that the oscillations can cause an increase in resistivity without changing the proportionality of E_x to B^2 (**19**) must be considered also.

Finally, a brief evaluation of the influence of turbulent conduction on the variation of E'_x versus B is made. In the absence of ion motion the conventional conduction across B changed from [see equation (7)]

$$j_x = \frac{n_e e}{\omega_e \tau_e}\frac{E'_x}{B} = \frac{n_e m_e}{\tau_e}\frac{1}{B^2}E'_x \tag{16}$$

to [see equation (13)]

$$j_x = \alpha n_e e \frac{E'_x}{B} \tag{17}$$

Assuming constant values for n_e, τ_e, α, and j_x, for conventional conduction

$$E'_x \propto B^2 \tag{18}$$

while for turbulent conduction

$$E'_x \propto B \tag{19}$$

It should be noted in this connection that some curves in Figure 6 representing the variation of E'_x versus B could, with a little imagination, be interpreted as showing transition from square to linear dependence for the higher currents. This transition seems to occur approximately for values of B where the Hall current begins to drop in Figure 4. As noted before, however, since the drop in Hall current does not seem to fit into existing turbulent theory, excluding the influence on j_θ, the possibility of polarization and the effect of ion motion would have to be studied to evaluate what could be very important effects in turbulence. The effect of ion

motion has also a very simple influence for $n_e e v_x = \text{constant}$, since as v_x increases n_e is decreased, which in turn can change the term $\alpha n_e e E_x'/B$ and thus the variation of E_x' with B.

Hence, the importance of obtaining a better theory and more measurements for turbulent conduction, including ion motion across B in the presence of neutrals, and for turbulence in the azimuthal direction of the Hall current is very evident. Before such advances are made, the influence of turbulence is difficult to assess, except with many more careful measurements. This, of course, does not mean that means for delaying transition to turbulence may not be found before turbulence is fully understood. Theoretical reasoning (**3**) and experiments and theory for other discharge-magnetic-field instabilities (**15**) suggest that preionization, with resulting reduction in E_x', should give such a delay. Proof must wait for experimental results.

The question also arises as to whether the change from square to linear dependence of E_x' on B can be explained by mechanisms other than the transition from conventional to turbulent conduction. A deviation from the parabolic characteristic can also be interpreted in terms of ion slip, since the latter is a loss which reduces the impedance due to high Hall currents alone, which is the basis for the parabolic characteristic. This reduction in impedance occurs, in essence, for $\omega_i\tau_i \leqq 1$, since for $\omega_i\tau_i > 1$ a related increase in impedance as occurred originally due to $\omega_e\tau_e > 1$ sets in, with resulting tendency again toward $E_x' \propto B^2$. (Note that $v_\theta B$, due to rotation, can modify the effect.) Since most of the experiments performed so far in the Hall accelerator are in the range of $\omega_i\tau_i \leqq 1$, the change from square dependency and even a transition to approximately linear dependency could be possible, especially if the possibility of variations in τ_e, T_i, and n_e are also included.

The question also arises as to what extent a linear variation of E with B could be explained through ionization and diffusion. The various possibilities of influencing the conduction across a magnetic field for partially-ionized plasmas, with predominance of electron-neutral collisions or electron-ion collisions are discussed in reference (**20**). In accordance with equation (16), if $n_e/\tau_e \propto B$, $j_x \propto E_x'/B$, or for $j_x = \text{constant}$, then $E_x' \propto B$. Experiments with high-density plasmas where oscillations and ion-slip losses are small showed $E \propto B$, meaning that effects other than oscillations can cause $E \propto B$. The calculation of the variation of the ionization with B requires the use of the energy equation. Preliminary studies of the energy balance were reported in reference (**16**). A detailed study of the energy balance including non-equilibrium effects (since $T_e \gg T_i$) and radiation was in progress at the time of the publication of reference (**20**), and will be reported elsewhere. Finally, it would be of great interest to study the effect of random non-uniformities or turbulence on non-equilibrium ionization.

Appendix A

EQUATIONS FROM OHM'S LAW

Ohm's law in the presence of a magnetic field can be written (**6, 7**) in the following manner where the factor 2 with the term $2\omega_e\tau_e\omega_i\tau_i$ is included in τ_i (**7**):

$$\vec{j} = \frac{\sigma_0}{(\omega_e\tau_e)^2 + (1+2\omega_e\tau_e\omega_i\tau_i)^2}\left\{(1+2\omega_e\tau_e\omega_i\tau_i)\vec{E'} - \frac{\omega_e\tau_e}{B}(\vec{E'}\cdot\vec{B}) + \left[\left(\frac{\omega_e\tau_e}{B}\right)^2 + \frac{\omega_e\tau_e\omega_i\tau_i}{B^2}(1+2\omega_e\tau_e\omega_i\tau_i)(\vec{E'}\cdot\vec{B})\vec{B}\right]\right\} \tag{A1}$$

In the linear Hall accelerator E_r, E_θ, v_r, B_x, and B_θ are all taken as zero. Noting that

$$\frac{\sigma_0}{\omega_e\tau_e} = \frac{n_e e}{B}$$

and defining

$$W = \frac{1+2\omega_e\tau_e\omega_i\tau_i}{\omega_e\tau_e} = \frac{1}{\omega_e\tau_e}+2\omega_i\tau_i$$

The expressions for j_x and j_θ are

$$j_x = n_e e \frac{W\dfrac{E'_x}{B}+v_x}{1+W^2} \tag{A2}$$

$$-j_\theta = n_e e \frac{\dfrac{E'_x}{B}-Wv_x}{1+W^2} \tag{A3}$$

We use $-j_\theta$ since the Lorentz force in the axial direction is $-j_\theta B_r$. Three other expressions for $-j_\theta$ can be found by eliminating E'_x, v_x, and n_e from the above equations:

$$-j_\theta = \frac{1}{W}(j_x - n_e e v_x) \tag{A4}$$

$$-j_\theta = n_e e \frac{E'_x}{B} - Wj_x \tag{A5}$$

$$-j_\theta = \frac{\dfrac{E'_x}{B}-Wv_x}{W\dfrac{E'_x}{B}+v_x} j_x \tag{A6}$$

If for j_x constant, τ_e and τ_i are also assumed constant, W will be a function of B only,

$$W = \frac{1}{\dfrac{e\tau_e}{m_e}B} + \frac{2e\tau_i}{m_i}B \tag{A7}$$

and

$$\frac{dW}{dB} = -\frac{1}{\dfrac{e}{m_e}\tau_e B^2} + \frac{2e}{m_i}\tau_i \tag{A8}$$

$$\frac{d^2W}{dB^2} = \frac{2}{\dfrac{e}{m_e}\tau_e B^3} \tag{A9}$$

Thus W will have a minimum value at

$$2\frac{e\tau_e}{m_e}B\frac{e\tau_i}{m_i}B = 1$$

or

$$2\omega_e\tau_e\omega_i\tau_i = 1 \tag{A10}$$

and at this minimum value

$$W_{\min} = \frac{2}{\omega_e \tau_e} \tag{A11}$$

and

$$2\omega_i \tau_i = \left.\frac{1}{\omega_e \tau_e}\right|_{W = \min} \tag{A12}$$

Appendix B

METHODS OF PREIONIZATION

REASONS FOR PREIONIZATION

As pointed out in the discussion of turbulent conduction in the body of the paper, the effect of preionization is not only to increase the number of ions being accelerated over the full length, its function is also to delay the onset of instabilities and transition to turbulent conduction by reduction of the voltage which provides energy for the growth of instabilities and turbulence. Two methods of preionization will be discussed. One makes use of a coaxial preionizer with magnetic field which injects a plasma stream into the accelerator. Such a preionizer has been designed and operated. The second method of preionization is actually a method for supplementary ionization in the accelerator region itself. Such an approach has been tried for delaying the onset of instabilities of an arc column in an axial magnetic field (**15**) and will be applied to the present Hall-ion accelerator.

DESIGN AND OPERATION OF ARC PREIONIZER

J. Burlock and T. Collier

Method and Design

Most preionizers for the low-density plasma accelerators consist of some form of PIG discharge with externally-heated, thermionically-emitting cathodes. In order to obtain a highly-ionized plasma, the use of high currents in the preionizer becomes desirable; for that purpose it has to operate in the arc mode. For injection into the Hall-ion accelerator with a center core it is, furthermore, desirable to produce a plasma stream which is concentrated, more or less, in a cylindrical annulus.

These various requirements suggested the use of a tungsten disk cathode self-heated by the arc discharge inside a ring anode. The design is shown in Figure 10. The arc discharge establishes itself mainly in the space between the edges of the disk and the anode and is blown into the accelerator. The edges of the disk can act as an electric field concentrator and facilitate the starting and act to maintain the discharge in this position. The magnetic field can be purely axial or somewhat slanted giving the effect of a Hall current plasma accelerator. The disk cathode was supported by a center sting with much smaller diameter, which resulted in uniform heating of the cathode disk, since only a small ($\frac{1}{8}$-inch) spot was cooled by presence of the rod. The major mechanism for removal of heat from the disk was radiation.

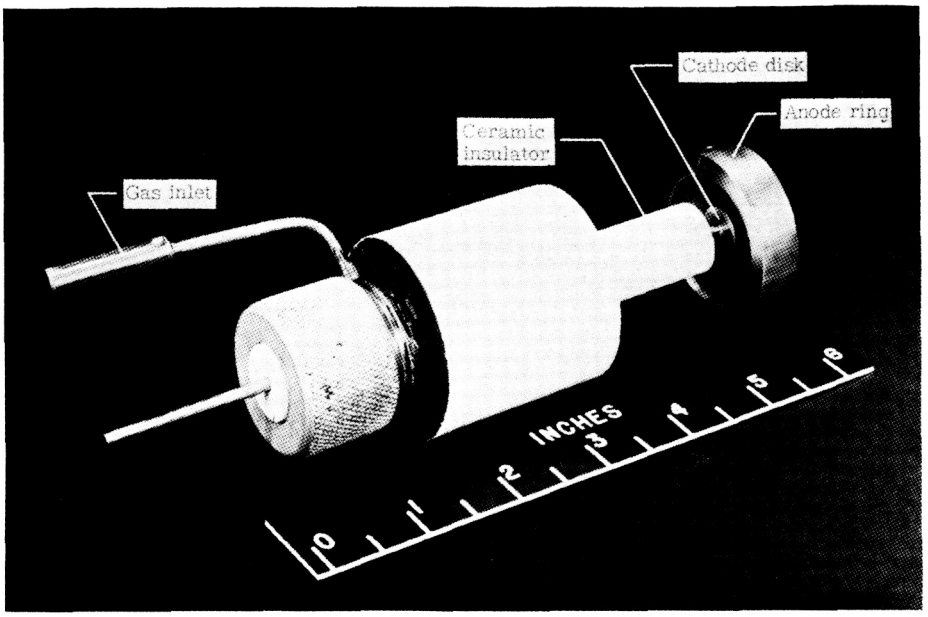

FIGURE 10. Arc preionizer.

Operation

A high-voltage, low-current glow discharge produces the initial heating. A rapid shift to high-current operation follows as the cathode reaches emitting temperature. The cathode disk appears uniformly heated except for the central region, where the supporting rod is welded. Operation appeared quite smooth except for the occasional appearance of anode spots. (Operation in this instance was in argon at 30 microns pressure, and 15 to 18 amperes at several hundred volts in a magnetic field of 5000 gauss.)

METHODS FOR SUPPLEMENTARY IONIZATION IN ACCELERATOR

The basic requirement for any technique of ionization enhancement is that the Hall current accelerator mechanism should not be disturbed. Several possible techniques for obtaining the desired ionization will be discussed briefly.

Electrostatic coupling of high-frequency energy directed radially along the flux lines could be used. For frequencies much below plasma frequency, it would be necessary to minimize the impedance of any dielectric intervening between the electrodes and plasma because of the relatively low impedance of a highly overdense plasma. However, if leads through the structure are permissible, the electrode could be placed inside, and the dielectric problem would not occur. Electrode cooling in this case would also protect the glass wall.

Inductive coupling of high-frequency energy by means of a solenoid has been used to increase ionization and reduce the axial electric field. The presence of the radial magnetic field of the Hall accelerator transverse to the induced azimuthal electric field hinders the coupling of energy, and relatively high powers are required

to produce appreciable changes in conductivity and axial electric field. Operation at electron cyclotron resonance frequency would provide an important coupling enhancement. For this operation the magnetic fields of interest for the acceleration process, with intensities of hundreds of gauss and higher, would call for power at frequencies to the order of hundreds to several thousand megacycles. A reasonable upper limit for the resonance technique could be at between one and two thousand gauss, where high power at the corresponding cyclotron resonant frequencies (in the kilomegacycle range) is still reasonably available. Since the electron motion is bidirectional, it should probably not interfere with the undirectional fields and current flows of the accelerating process. It could perhaps provide additional stabilization (**3**).

One other possible means of enhancing ionization would be the use of electron ionizing beams, which have proved successful in generating plasmas of reasonably high densities (**20**) and hollow cathode plasma injection.

Appendix C

DESIGN AND OPERATION OF AN EXTERNALLY-HEATED RING CATHODE

Olin Jarrett

Most designs for externally-heated cathodes for thermionic emission use either a tungsten filament heated by Joule losses due to resistance or a tungsten disk heated by electron bombardment. Since in the Hall accelerator the use of axially-symmetric cathode shapes, especially ring cathodes, is highly desirable, another method of cathode heating was tried which ideally seems to suit this purpose. This method of heating also avoids the necessity of vacuum seals for hot external leads.

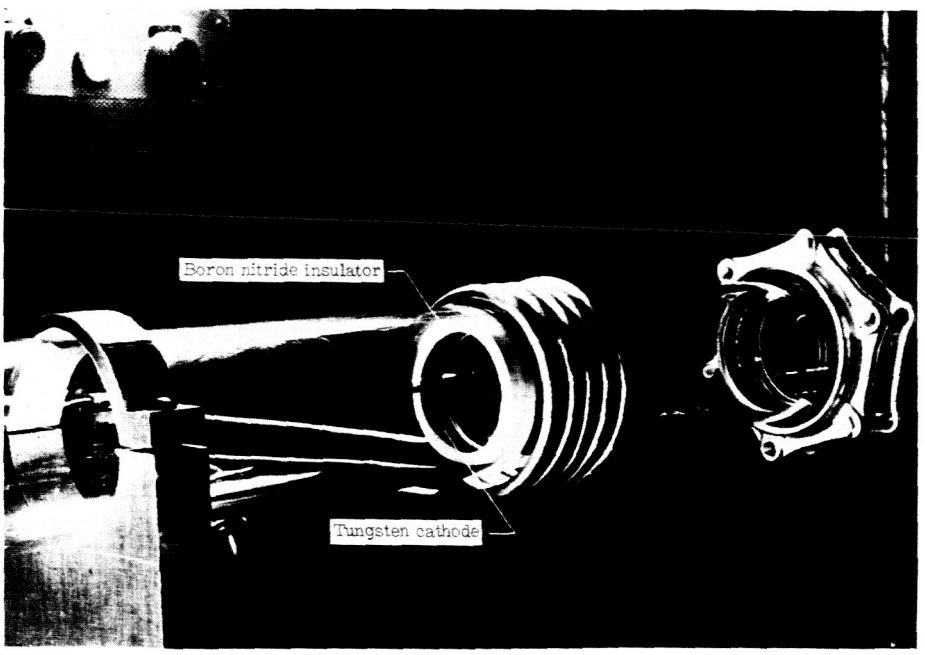

FIGURE 11. Inductively-heated cathode.

A RF-heated ring cathode has been constructed and tested. The heated cathode (Figure 11) consists of a tungsten ring placed inside of a boron nitride holder which fits into a vycore or quartz tube, inside of which the low pressure is maintained. A connection to the direct-current power supply for operation of the Hall-ion accelerator is provided.

Tests of this device showed that the cathode is uniformly heated to thermionic emission temperature. Since a 20-kw, 450-kc power supply has been available to us, the heating is done with power to spare. The cathode has been installed in an accelerator and the effect on the discharge characteristics will be tested in the near future. Various methods of avoiding possible disturbances of Hall current measurement during such heating have been considered, such as choking the Hall current diagnostic coil, or providing a cathode thick enough to provide sufficient heat capacity for the duration of the Hall current measurement.

The use of a RF-heated cathode should also prove very useful in preionizers or axially symmetric plasma accelerators in general.

Tests are also in progress with thick, resistance-heated ring filaments, such as those used in induction furnaces.

NOMENCLATURE

$\vec{B}$	Magnetic flux density
$\bar{c}$	Mean thermal velocity
e	Charge on singly-ionized ion
$\vec{E}$	Electric field strength
$\vec{E'}$	$\vec{E'} = \vec{E} + \vec{v} \times \vec{B}$
$\vec{j}$	Current density
l	Length
m_e, m_i	Mass of electron and ion
m	Meter
n	Particle density
p	Pressure
Q	Collision cross section
r_L	Larmor radius
t	Time
T	Temperature
$\vec{v}$	Center of mass velocity
V	Voltage
W	$W = \dfrac{(1+2\omega_e\tau_e\omega_i\tau_i)}{\omega_e\tau_e}$
α	Quantity defined in equation (13)
λ	Mean free path
μ	Microns
ν	Collision frequency
σ_0	Conductivity in the absence of a magnetic field, $\sigma_0 = \dfrac{n_e e^2 \tau_e}{m_e}$
τ	Mean free time between particle collisions
ω_e, ω_i	Cyclotron frequency, $\omega_e = \dfrac{eB}{m_e}$, $\omega_i = \dfrac{eB}{m_i}$

Subscripts

e	Electron
i	Ion
n	Neutral
r, θ, x	Refer to cylindrical coordinate system

Superscript

$\vec{(\ )}$	Vector quantity

REFERENCES

1. Hess, R. V., "Experiments and Theory for Continuous Steady Acceleration of Low Density Plasmas", in *Proc. XI Internatl. Astronautical Congress, August 1960* (Vienna: Springer Verlag, 1961), I, 404–411.
2. Bratenahl, A., Janes, G. S., and Kantrowitz, A. R., "Plasma Acceleration in the Electromagnetic Region II", *Bull. Amer. Phys. Soc.*, Series II, **6**, 4, 379 (1961).
3. Hess, R. V., "Fundamentals of Plasma Interaction with Electric and Magnetic Fields", *NASA-University Conference on the Science and Technology of Space Exploration*, **2**, Paper 59, Chicago (November, 1962).
4. Rigby, R. N., "Some Physical Properties of an Axial Electric Arc in a Radial Magnetic Field" (M.A. thesis, The College of William and Mary, August, 1962).
5. Hess, R. V., Rigby, R. N., and Weinstein, R. H., "Observation of Hall Currents for a D-C Axial-Arc Discharge in a Radial Magnetic Field", *Bull. Amer. Phys. Soc.*, Series II, **8**, 2, 168 (1963).
6. Hess, R. V., Burlock, J., Sevier, J. R., and Brockman, P., "Theory and Experiments for the Role of Space Charge in Plasma Acceleration", Symposium on Electromagnetics and Fluid Dynamics of Gaseous Plasma, April, 1961; published in *Microwave Res. Inst. Symposia Ser.* (Brooklyn: Brooklyn Polytechnic Press, 1962), XI, 269–305.
7. Cann, G. L., Ziemer, R. W., and Marlotte, G. L., "The Hall Current Plasma Accelerator", presented at the ARS Electric Propulsion Conference, Colorado Springs, Colorado (March, 1963).
8. Chen, F. F., "A Time Resolved Probe Method", *MATT 62*, Plasma Physics Lab., Princeton University (February, 1961).
9. Janes, G. S., Dotson, J., and Wilson, T., "Electrostatic Acceleration of Neutral Plasmas. Momentum Transfer Through Magnetic Fields", *Avco-Everett Res. Lab. AMP 88* (September, 1962).
10. Salz, F., Meyerand, R. G., Jr., and Lary, E. C., "Ion Acceleration in a Gyro-Dominated Neutral Plasma Experiment", *Bull. Amer. Phys. Soc.*, Series II, **7**, 7, 441 (1962).
11. Yoshikawa, S., and Rose, D. J., "Anomalous Diffusion of a Plasma Across a Magnetic Field", *Phys. Fluids*, **5**, 10, 1272 (1962).
12. Kadomtsev, B. B., "Turbulent Plasma in a Strong Magnetic Field", *J. Nuclear Energy*, Part C (Plasma Physics), **5**, 31–36 (1963).
13. Velikhov, E. P. "Hall Instability of Current Carrying Slightly Ionized Plasmas", Symposium on Magnetoplasmadynamic Electrical Power Generation, Newcastle, England, September, 1962.
14. Rosa, R. J., "Hall and Ion-Slip Effects in a Nonuniform Gas", *Phys. Fluids*, **5**, 9, 1081–1090 (1962).

15. Gierke, G., and Wöhler, K. H., "On the Diffusion in the Positive Column in a Longitudinal Magnetic Field", *Nuclear Fusion Journal of Plasma Physics and Thermonuclear Fusion*, 1962 Supplement, Part 1, 47–53 (1962).
16. Chubb, D. L., "Hall Current Ion Accelerator", Fourth Symposium on the Engineering Aspects of Magnetohydrodynamics (10-minute paper, only oral presentation), April, 1963.
17. Haines, M. G., "A Mechanism for the Acceleration of Positive Ions in a Pinched Plasma", Conference on Plasma Physics and Controlled Nuclear Fusion Research, Salzburg (September 4–9, 1961).
18. Hasted, J. B., "Charge Changing Collisions", Vth Inter. Conf. on Ionization Phen. in Gases, Munich (August 28–September 1, 1961).
19. Lary, E. C., Meyerand, R. G., and Salz, F., "Fluctuations in Gyrodominated Plasma", VIth Inter. Conf. on Ionization Phen. in Gases, Paris (July 8–13, 1963).
20. Smullin, L. D., and Getty, W. D., "Generation of a Hot, Dense Plasma by a Collective Beam-Plasma Interaction", *Phys. Rev. Letters*, **9**, 1 (July 1, 1962).

16. Sterge T. Demetriades: *Momentum Transfer to Plasmas by Lorentz Forces*

"Entia non sunt multiplicanda praeter necessitatem"
(*Occam's Razor*, William of Occam, ca. 1340 A.D.)

A theoretical and experimental study of momentum transfer to plasmas by Lorentz forces is described. A generalized Ohm's law is used to predict changes in the direction and magnitude of the momentum of a stream of plasma and other observable macroscopic effects in a crossed-field accelerator in terms of species temperatures and concentrations and other plasma parameters. The assumption of local thermal equilibrium is not required in this approach. Measurements of momentum change and other effects are presented that are substantially in agreement with theory. Gross mean estimates of the plasma parameters in the cross-arc region are obtained from the measured momentum changes and power input.

INTRODUCTION

A large number of laboratories are engaged in research and development of plasma accelerators using a wide variety of devices to accelerate a plasma by Lorentz forces. One of the most popular of these devices appears to be the *d-c linear shunt* plasma accelerator. It operates by the application of an externally-supplied current across a usually preionized gas stream in a region where an external magnetic field can be applied in a direction which is, more or less, perpendicular to both the discharge and the flow direction. This type of accelerator is usually called a *crossed-field plasma accelerator*. At last count, these devices were in use in at least nine industrial organizations and three government laboratories. Needless to say, the author finds this situation very flattering.

Progress in understanding the processes of the conduction of electric current in a plasma in the presence of electric and magnetic fields (**1–8**) has yielded valuable insight into the operation of crossed-field accelerators (**8–19**).

Since the most important results of the most promising projects are not yet openly available, it is rather difficult to carry out a comparative evaluation of the various programs at this time. However, the author has carried out experiments with multiple-electrode accelerators with each electrode pair powered by a separate power supply. Three-, four-, and seven-electrode-pair accelerators were built and tested. The four-electrode-pair accelerators were tested with uncooled as well as water-cooled electrodes. Power levels of approximately 750 kw have

ED. NOTE: Mr. Demetriades is with Rocket Power, Inc., Pasadena, California. This work was supported by the U.S. Air Force through the Propulsion Division, Directorate of Engineering Sciences, Office of Aerospace Research, Air Force Office of Scientific Research, under Contract AF 49(638)-1160.

been attained at flow rates for argon as low as 1.5 gm/sec. Velocities of approximately 8×10^3 m/sec have been achieved with air. Large accelerators (> 10 Mw) for wind-tunnel application are under development (**20, 21, 22**). Most of the power supplied to these accelerators goes into the gas.

Early continuous, crossed-field accelerators suffered from considerable side-wall and electrode erosion. Experiments by the author have shown that side-wall insulator erosion can be effectively stopped under certain conditions by the use of a metal stud side-wall design similar to the peg side-wall used in AVCO's MHD power generators (**20**). In the author's segmented (stud or peg) side-wall design, each water-cooled segment is made of metal (copper) and is insulated electrically from the other segments. This "mosaic" of water-cooled segments is mounted firmly on a transite slab and the interstices (0.15 to 0.50 cm wide) between the segments are filled with a slurry of alumina or zirconia insulator. The slurry is baked to give a firm matrix. However, the insulator matrix does not carry any stress since the copper segments are firmly mounted on the transite slab. The surface of the copper studs or segments (approximately 1 cm × 1 cm to 1.5 cm × 5 cm) is exposed to the plasma. The cooling-water connections are on the other side of the slab facing the magnet poles. These side-walls can remove between 1 and 4 kw per cm^2 of surface. Under certain circumstances these side-wall losses can be unacceptable and other methods of containment (e.g., magnetic or cold-gas) may be necessary. The electrode erosion and melting problems were solved by using multiple electrodes powered by separate power supplies (i.e., by passing only a fraction of the total current through each electrode) and by proper design of the electrode cooling passages so that wiping speeds in excess of 6 m/sec and high cooling rates (> 5 kw/cm^2) can be achieved. Accelerator electrodes can now be operated for long periods of time (> 1 hr) with very little erosion.

Sufficient progress has been made on component development during the last year at Northrop Plasma Laboratories and elsewhere to ensure that crossed-field accelerators of high performance and long life for wind-tunnel, enthalpy booster, space propulsion, and many other applications will be available soon *if the present rate of progress is not interrupted.*

The space propulsion applications of these relatively low-voltage accelerators will have to meet very tough competition from other devices (notably the high-voltage electrostatic accelerators and low-pressure electrothermal engines) that are more advanced in development and are presently favored despite the power-conditioning problems imposed by the required high voltages. In any case, the deplorable lack of vision and progress in planning and developing suitable power supplies for space applications such as electric propulsion will certainly effect a delay, perhaps fatal, in the use of crossed-field accelerators for space propulsion.

Thus, it appears that the major engineering problems involved in crossed-field accelerators for conventional applications are not only well understood, but also well on the way to solution. Despite these formidable problems, the crossed-field accelerator is the first plasma accelerator to be put into practical use, as for reentry simulation (**17, 20, 22**).

The questions now become: What are the possibilities of crossed-field accelerators for less conventional applications? If enthalpies of the order of 10^9 joules/kg can be achieved in these devices with such relative ease and on a continuous basis, why not hope for enthalpy levels of 10^{12} or 10^{14} joules/kg through further development of these machines? Can these devices be used as radiation sources? If strong Lorentz forces can be developed by the applied-current, applied-magnetic-field technique, why not use the same technique for the containment of the dense and very hot plasmas that these devices appear capable of generating?

To answer these questions will require considerably more understanding of the detailed processes that take place in these accelerators, including electrode emission, electrode fall, ionization, radiation, chemical reaction, transport and thermodynamic processes in the presence of electric and magnetic fields, energy and momentum transfer by Lorentz forces, and many other important phenomena. These are essentially scientific problems that require additional effort.

Engineering progress in crossed-field accelerators is thus stimulating scientific investigations that may lead to the answer of many important scientific problems in plasma physics, and this in turn may lead into accelerated engineering progress in plasma technology.

To illustrate, we shall consider some experiments on the momentum transfer to plasmas by Lorentz forces carried out in the course of the engineering development of crossed-field plasma accelerators and their effect on our understanding of the processes governing the transport of electric charge (generalized Ohm's law) in a plasma in the presence of electric and magnetic fields.

Another objective of this study will be to measure macroscopic momentum-change effects and to relate them to those microscopic plasma properties that are significant in momentum exchange processes in a plasma; and conversely, to relate microscopic plasma parameters to measurable macroscopic momentum changes. In this investigation, measurements are obtained of changes in the direction and magnitude of the momentum of a stream of plasma in a crossed-field accelerator with increasing magnetic induction at different power levels by mounting the entire accelerator assembly on a sensitive balance and observing (1) the forces due to interaction between the applied fields and the plasma stream, and (2) the deflection of the jet of plasma. The accelerator is operated in the free-jet mode in order to simplify the analysis. The close agreement between free-jet and fully-confined experiments has been confirmed by Burkhard *et al.* at AVCO/RAD (**16, 17**).

THEORY

To compute the momentum transfer to a plasma by Lorentz forces, one needs to know the force per unit volume $\vec{F}_v$ acting on the plasma. The local magnitude of this force is given by the relation

$$\vec{F}_v = \vec{J} \times \vec{B} \tag{1}$$

where $\vec{J}$ is the local current density and $\vec{B}$ is the local magnetic induction. When the magnetic induction is externally applied and the induced magnetic field is relatively small (as is usually the case in crossed-field accelerators), the local value of $\vec{B}$ can be estimated with considerable precision. Thus, the problem of computing $\vec{F}_v$ reduces to the problem of determining $\vec{J}$.

For low-frequency oscillations and therefore also for a quiet or non-turbulent plasma where the local small-scale density fluctuation can be neglected, it can be shown (**1**) that the generalized Ohm's law in the first approximation (i.e., neglecting viscosity) has the form

$$\begin{aligned}\vec{E}' = {} & \eta^{(1)}\vec{J} + \sum_{\mu} \beta_{\mu}{}^{(1)} \nabla p_{\mu} + \theta^{(1)} \nabla T \\ & + [\eta^{(2)}\vec{J} + \sum_{\mu} \beta_{\mu}{}^{(2)} \nabla p_{\mu} + \theta^{(2)} \nabla T] \times \vec{B} \\ & + [\eta^{(3)}(\vec{J} \times \vec{B}) + \sum_{\mu} \beta_{\mu}{}^{(3)} (\nabla p_{\mu} \times \vec{B}) + \theta^{(3)} (\nabla T \times \vec{B})] \times \vec{B}\end{aligned} \tag{2}$$

In equation (2) $\vec{E}'=\vec{E}_0+\vec{U}\times\vec{B}$, $\vec{E}_0$=applied electric field, $\vec{U}$=plasma streaming velocity, T=plasma temperature, p_μ=partial pressure of species μ, and the coefficients $\eta^{(i)}$, $\beta^{(i)}$, and $\theta^{(i)}$ are functions of species concentrations, charge of each component, collision cross-sections for momentum transfer between components, temperature of each component, mass of each component, thermal diffusion coefficients, etc., as defined by Polovin and Cherkasova (**1**). Strictly speaking, equation (2) is valid for a multicomponent plasma where all the components are at the same temperature, T. However, when the temperature gradients can be neglected, it can be shown that equation (2) is also valid for a two-temperature plasma where the electron temperature T_e is different from the atom or ion temperature $T_a=T_i$, provided the electron drift velocity v_d is small compared to the electron random thermal velocity in the plasma, v_e (**2**). Assuming that the current is carried by the electrons only, the inequality $v_d\ll v_e$ is satisfied when

$$v_d = J/(en_e) = 6.25\times10^{18}J/n_e \ll 6.2\times10^3 T_e^{1/2} = v_e \tag{3}$$

where J=amp/m^2, n_e=electrons/m^3, T_e=°K, and the velocities are given in m/sec. Thus, for $n_e=10^{21}$ electrons/m^3 and $T_e=10^4$ °K, the current density must be considerably less than 10^8 amps/m^2 in order that equation (2) may be used for a two-temperature plasma with negligible temperature gradients. When the temperature gradients cannot be neglected, it can be shown that equation (2) is still valid provided $m_eT_e/m_a\ll T_a\leq T_e$. In both cases all magnitudes in equation (2), except τ_{ia}, should be determined at T_e. The modifications of equation (2) required when these conditions are not fulfilled are beyond the scope of this paper. Yoshikawa and Rose (**3**) and several other authors have shown that when the temperature gradients are negligible, local small-scale plasma turbulence leads to different values of the coefficients $\eta^{(i)}$ and $\beta^{(i)}$. Their work confirms the "anomalous diffusion" theory proposed by Bohm (**4**). However, since anomalous diffusion takes place when the pressure is low ($p<100$ μ Hg, $n<10^{20}$ particles/m^3) and the magnetic field is high ($\omega_e\tau_e\gg1$, $\tau_e=\tau_{ea}\tau_{ei}/(\tau_{ei}+\tau_{ea})$), the values of the coefficients $\eta^{(i)}$ and $\beta^{(i)}$ given by Polovin and Cherkasova (**1**) apply in the experiments described here where $n>10^{20}$ particles/m^3 and $\omega_e\tau_e<10$. It can be shown that the general form of Ohm's law given by equation (2) leads to the special cases derived by Cowling (**5**), Schlüter (**6**), Lehnert (**7**), and Liubimov (**2**). Thus, when the plasma consists of electrons (e), one species of singly charged ions (i), and one species of neutrals (a), and temperature gradients and space charge concentrations are negligible ($n_e=n_i$), while the inequality $\frac{1}{2}m_iq_{ia}v_{ia}=eB/(2\omega_i\tau_{ia}n_a)\gg m_eq_{ea}v_{ea}=eB/(\omega_e\tau_{ea}n_a)$ is valid, equation (2) reduces to

$$\vec{E}' = \left(\frac{n_e\lambda_{ei}+n_a\lambda_{ea}}{n_ee^2}\right)\vec{J}+\frac{1}{en_e}\left((\vec{J}\times\vec{B})-\nabla p_e\right) + \frac{n_a}{n_e\lambda_{ia}(n_e+n_a)^2}\left[\nabla(p_e+p_i)-\frac{n_e}{n_a}\nabla p_a-(\vec{J}\times\vec{B})\right]\times\vec{B} \tag{4}$$

where $\lambda_{ea}=m_eq_{ea}v_{ea}$, $\lambda_{ei}=m_eq_{ei}v_{ei}$, $\lambda_{ia}=\frac{1}{2}m_iq_{ia}v_{ia}$, m_e=electron mass, m_i=ion mass; v_{ea}, v_{ei}, v_{ia}=relative velocities between electrons and atoms, electrons and ions, and ions and atoms, respectively; q_{ea}, q_{ei}, q_{ia}=collision cross-sections for momentum transfer between electrons and atoms, electrons and ions, and ions and atoms, respectively; n_e, n_a=electron and atom concentrations, respectively; e=electronic charge, $\omega_e=eB/m_e$, $\omega_i=eB/m_i$; τ_{ea}, τ_{ei}, τ_{ia}=inverse of collision frequencies for collisions between electrons and atoms, electrons and ions, and ions

and atoms, respectively. For $\tau_{ea} \gg \tau_{ei}$ (i.e., $n_i \lambda_{ei} \gg n_a \lambda_{ea}$), equation (4) reduces further to

$$\vec{E''} = \frac{1}{\sigma_0} \vec{J} + \chi(\vec{J} \times \vec{B}) - \psi(\vec{J} \times \vec{B}) \times \vec{B} \tag{5}$$

where

$$\vec{E''} = \vec{E'} + \chi \nabla p_e + \psi \left[\frac{n_e}{n_a} \nabla p_a - \nabla(p_e + p_i) \right] \times \vec{B} \tag{6}$$

and

$$\chi = \frac{1}{en_e}, \psi = \frac{n_e e B (n_e + n_a)^2}{2\omega_i \tau_{ia} n_a^2} \quad \text{and} \quad \sigma_0 = \frac{e^2 n_e \tau_{ei}}{m_e} \tag{7}$$

Equation (5) can also be written

$$\vec{J} = \overleftrightarrow{\sigma} \vec{E''} \tag{8}$$

Equation (4) is identical with Liubimov's version of the generalized Ohm's law (**2**) and is equivalent to the Cowling-Schlüter version (**5, 6**), with the additional terms ∇p_i and $-(n_e/n_a)\nabla p_a$. The coefficients of the terms $\vec{J}$, $\vec{J} \times \vec{B}$, ∇p_e, and $(\vec{J} \times \vec{B}) \times \vec{B}$ of these authors, including Lehnert (**7**), are identical with the coefficients derived by Polovin and Cherkasova (**1**) even when λ_{ea} and τ_{ei} are not negligibly small compared with λ_{ia} and τ_{ea}, respectively. The work of all these authors leads to a generalized Ohm's law similar to equation (5). Finally, the components of the tensor $\overleftrightarrow{\sigma}$ of equation (8), the equivalent of equation (5), were given by Demetriades (**8, 9**).

The assumptions leading to equations (2) and (4) are enumerated and discussed by Polovin and Cherkasova (**1**), and Liubimov (**2**).

As shown in an earlier publication (**10**), equation (2) or equation (4) can be used in an attempt to relate the magnitude of the components of the current density (and also the components of the conductivity tensor and therefore the collision cross-sections for momentum transfer between electron, ion, and neutral gases as well as other plasma parameters) to the observable changes in magnitude and direction of the momentum of a stream of plasma in the Mark II (**8, 9**) crossed-field plasma accelerator operating in the free-jet mode. The changes in the momentum of the stream of plasma due to the Lorentz force per unit volume, $\vec{J} \times \vec{B}$, can be measured by mounting the entire accelerator assembly on a sensitive balance in a vacuum tank and observing the thrust (or drag) and the angle of deflection, ϕ, of the jet. It should be stressed that the results of this approach can be as precise as the analysis is sophisticated. However, in order to make the analysis tractable, it will be necessary to make simplifying assumptions that may introduce an error of as much as a factor of 3 or 4 in the mean values of some of the plasma parameters, temperatures, and concentrations obtainable by this method.

The assumptions made in the derivation of equation (4) limit its applicability to experiments where boundary layer and transition layer effects are negligible. These conditions are most nearly satisfied in the core of the cross-arc of the Mark II plasma accelerator when it is operated in the free-jet mode. The phenomena associated with the cross-arc of this accelerator were described in an earlier publication (**11**).

Since the distribution of the magnetic induction $\vec{B}$ can be established and $\vec{J}$ can be obtained from equation (5), precise expressions for the forces acting on the plasma in the x and y directions can be computed in principle. If, in order to simplify the

computation, it is assumed that $\vec{E}'=(E'_x, E'_y, 0)$, $\vec{B}=(0, 0, B_z)$, and $\vec{U}=(U_x, 0, 0)$, the current density components in the region of influence of the magnetic field are given by

$$J_{1x} = \frac{\sigma_0[(1+\Omega_2^2B^2)E'_x-\Omega_1BE'_y]}{(1+\Omega_2^2B^2)^2+(\Omega_1B)^2} \tag{9}$$

and

$$J_{1y} = \frac{\sigma_0[(1+\Omega_2^2B^2)E'_y+\Omega_1BE'_x]}{(1+\Omega_2^2B^2)^2+(\Omega_1B)^2} \tag{10}$$

where

$$\Omega_1^2 \equiv e^2\tau_{ei}^2/m_e^2 = \sigma_0^2\chi^2 \tag{11}$$

and

$$\Omega_2^2 \equiv 2e^2\tau_{ia}\tau_{ei}(1-\alpha)^2/m_em_i = \sigma_0\psi \tag{12}$$

The ohmic heat dissipated per unit volume is

$$\vec{J}\cdot\vec{E}' = J_xE'_x+J_yE'_y = \frac{\sigma_0(1+\Omega_2^2B^2)(E')^2}{(1+\Omega_2^2B^2)^2+(\Omega_1B)^2} = \left[\frac{1+\Omega_2^2B^2}{\sigma_0}\right]J^2 \tag{13}$$

The total electrical power per unit volume of plasma in the accelerator is given by

$$\vec{E}_0\cdot\vec{J} = \left(\frac{1+\sigma_0\psi B_z^2}{\sigma_0}\right)(J_x^2+J_y^2)+(J_yU_xB_z-J_xU_yB_z) \tag{14}$$

When $E'_x=E_{0x}+U_yB_z=0$, $B_z=B$, the total power supplied to the plasma per unit volume is given by

$$E_{0y}J_y = \left(\frac{1+\sigma_0\psi B^2}{\sigma_0}\right)\left[1+\frac{\sigma_0^2\chi^2B^2}{(1+\sigma_0\psi B^2)^2}\right]J_y^2+U_xBJ_y \tag{14a}$$

and when $J_x=0$ ("staggered" electrodes), the total power supplied to the plasma per unit volume is given by

$$E_{0y}J_y = \left(\frac{1+\sigma_0\psi B^2}{\sigma_0}\right)J_y^2+U_xBJ_y \tag{14b}$$

When $E_{0x}=0$ (i.e., "symmetrical" electrode positions, long electrodes, no end effects), equation (14) becomes

$$E_{0y}J_y = \frac{1}{\sigma_0}(1+\sigma_0\psi B^2)J_y^2-\chi B_zJ_yJ_x+U_xB_zJ_y \tag{14c}$$

since

$$E'_x = \frac{1}{\sigma_0}\{(1+\sigma_0\psi B^2)J_x+(\sigma_0\chi)J_y\}$$

and

$$E'_y = \frac{1}{\sigma_0}\{(1+\sigma_0\psi B^2)J_y-(\sigma_0\chi)J_x\}$$

Note that J_x in equation (14c) is negative. The first term on the right-hand side of equations (14a), (14b), and (14c) is the ohmic heating term and the other terms on the right-hand side are the acceleration power. Note that equations (14b) and (14c)

yield lower values of E_{0y} than equation (14a) for the same values of J_y, U_x, σ_0, ψ, and B. Note also that as the degree of ionization approaches unity, ψ approaches zero and the ohmic heating decreases.

Equations (13) to (14c) demonstrate the need to know the magnitude of the quantities χ and ψ (or Ω_1 and Ω_2) in order to determine accelerator performance.

When single electrodes (one anode and one cathode) are used in a symmetrical configuration (i.e., no stagger; their centerlines on the same line normal to the flow direction), the axial electric field E'_x is negligible because the increase of conductivity with axial distance x is equivalent to longer electrodes with constant conductivity and therefore $E_{0x} \approx 0$ and $U_y B_z \approx 0$ over most of the interaction region as shown by Denison (**19**) and Hurwitz *et al.* (**27**). Thus it can be assumed that the plasma is at approximately the same potential at the inlet and at the exit of the inter-electrode region ("shorted axially") and $E'_x = 0$. Then the current density components in the region of influence of the magnetic field where the electric field is E'_{1y} become (**9**)

$$J_{1x} = -\frac{\sigma_0 E'_{1y}(\Omega_1 B)}{(1+\Omega_2^2 B^2)^2 + (\Omega_1 B)^2} \tag{15}$$

and

$$J_{1y} = \frac{\sigma_0 E'_{1y}(1+\Omega_2^2 B^2)}{(1+\Omega_2^2 B^2)^2 + (\Omega_1 B)^2} \tag{16}$$

If, in addition, it is assumed (1) that the magnetic field in the accelerator is constant in the region between the electrodes and zero elsewhere, (2) that the current density is constant with x in the region between the electrodes while it is zero upstream of the electrodes and of some undefined form in the region downstream of the electrodes, and (3) that (when the applied current is kept constant) the electric field in the plasma between the electrodes with the magnetic field on, $E'_{1y} = E_0 - U_x B_z$, is equal to the applied electric field at zero magnetic induction $(E_0)_{B=0}$, it can be shown (**9**) that the components of the forces acting on the plasma (equal and opposite to the thrust on the accelerator) are given by

$$\Theta_x = \int_V J_{1y} B_z \, dV = \frac{hBI_{0c}(1+\Omega_2^2 B^2)}{(1+\Omega_2^2 B^2)^2 + \Omega_1^2 B^2} \tag{17}$$

$$\Theta_y = -\int_V J_{1x} B_z \, dV = \frac{hBI_{0c}(\Omega_1 B)}{(1+\Omega_2^2 B^2)^2 + \Omega_1^2 B^2} \tag{18}$$

where h = electrode gap, I_{0c} = total applied current, and V = volume.

To determine the validity of equations (9) to (18) and, consequently, the validity of the generalized Ohm's law, equation (5), it is necessary to devise some tests of these equations on the basis of easy-to-observe macroscopic effects and simple measurements. In particular, it was decided to perform critical experiments to determine whether, for example, the deflection of the jet of plasma by the action of $\vec{J} \times \vec{B}$ forces was due to the "blowing-out" of the discharge as a result of the high plasma velocity (i.e., due to a more pronounced skewness or "distortion" of the discharge in the accelerator resulting from higher plasma velocities) or due to a higher Hall current (i.e., to higher values of the axial current resulting from the higher magnetic field).

Note that a simple momentum-vector diagram for the deflection angle ϕ gives

$$\tan \phi = \frac{\Theta_y}{\dot{m}U_1 + \Theta_x} \tag{19}$$

where $\dot{m}U_1$ is the rate at which momentum enters the inlet of the accelerator (called inlet momentum in the following text). The quantities $\tan \phi$, Θ_x, and $\dot{m}U_1$ can be easily measured (**8–12**). The geometry of this analysis is shown in Figure 1.

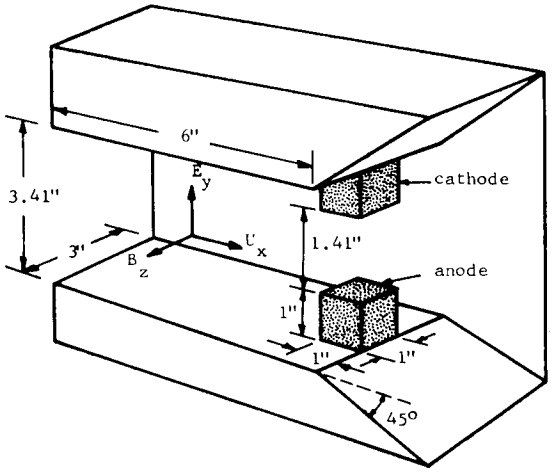

FIGURE 1. Schematic diagram of one electrode-pair Mark II-A $J \times B$ accelerator showing dimensions and coordinates.

Now equations (9) to (19) predict the following effects:

1. If the polarity (direction) and magnitude of the total applied current is kept constant while the polarity of the magnetic field is reversed ($B_z = -B$), equations (17), (18), and (19) predict that:
   - 1.1 The jet deflection remains in the same direction (i.e., $\tan \phi$ does not change sign).
   - 1.2. The deflection angle ϕ increases:
     - 1.2.1. By a small amount if $\dot{m}U_1 \gg \Theta_x$,
     - 1.2.2. By a large factor if $\dot{m}U_1$ is only slightly larger than Θ_x.

   This is shown schematically in Figure 2**a**.
2. If the polarity of both the applied B and applied I_{0c} are reversed, the angle ϕ changes sign (i.e., the deflection is in the opposite direction). This is shown in Figures 2a and 2b.
3. An increase of inlet momentum ($\dot{m}U_1$) while all other parameters remain constant decreases the magnitude of $\tan \phi$.
4. An increase of the degree of ionization by increasing the power (energy content) of the plasma jet entering the inlet of the accelerator (e.g., by an increase of arc jet power) brings about a decrease of the magnitude of $\tan \phi$. This is due to the decrease of the Hall coefficient (which is proportional to $1/n_e$) and therefore of J_x and Θ_y. Note that an increase in arc jet power increases U_i and decreases τ_{ei}, and therefore the observed decrease of

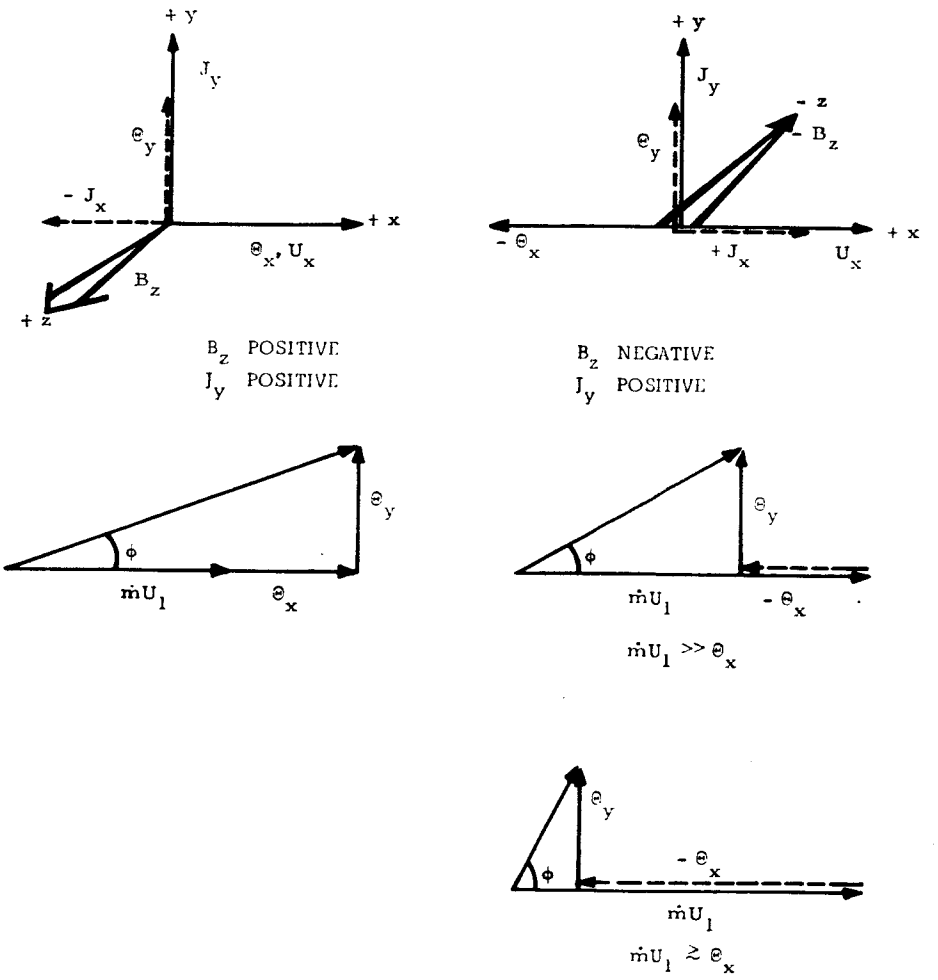

FIGURE 2a. Effect of magnetic field polarity on deflection angle ϕ when $\dot{m}U_1 \gg \Theta_x$ and $\dot{m}U_1 \gtrsim \Theta_x$ ($J = J_y$, $B = B_z$ and $J = J_y$, $B = -B_z$).

$\tan\phi$ by the combined effects should be more than that predicted for each effect alone. This is shown in Figure 3 where the experimental and theoretical results of the jet deflection angle ϕ are presented as a function of the arc jet power input. The theoretical curve was computed assuming I_{0c} = constant, B = constant, and

$$\Theta_y = \Theta_x\left(1+\frac{\dot{m}U_1}{\Theta_x}\right)\tan\phi = \text{constant} \tag{20}$$

in equation (19). Thus

$$\tan\phi = \frac{\left[\Theta_x\left(1+\frac{\dot{m}U_1}{\Theta_x}\right)\tan\phi\right]_{\min}}{\dot{m}U_1+\Theta_x} \tag{21}$$

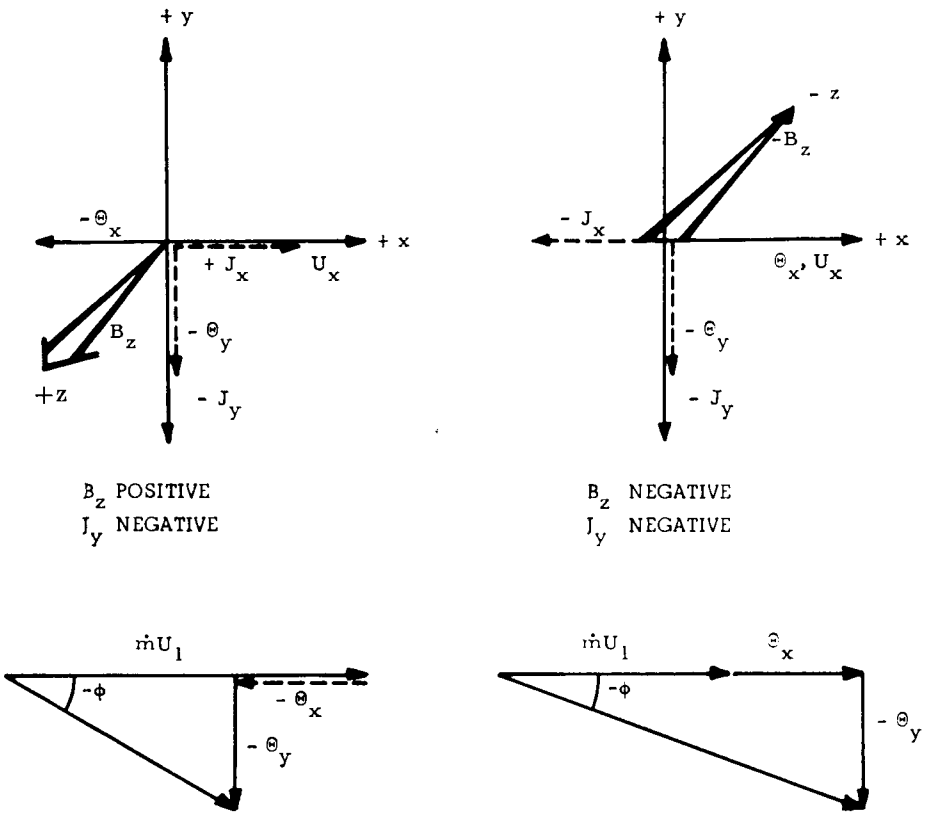

FIGURE 2b. Effect of electric and magnetic field polarity on deflection angle ϕ ($J = -J_y$, $B = B_z$ and $J = -J_y$, $B = -B_z$).

where the subscript min denotes evaluation of the term in the brackets at the minimum arc jet power point on the experimental curve. However, from equations (17), (18), and (19), it follows that

$$\frac{\Theta_y}{\Theta_x} = \left(1 + \frac{\dot{m}U_1}{\Theta_x}\right) \tan \phi = \frac{\Omega_1 B}{1 + \Omega_2^2 B^2} \tag{22}$$

or

$$\tan \phi = \frac{\tau_{ei}}{\Theta_x + \dot{m}U_1} \left[\frac{1.76 \times 10^{11} \Theta_x B}{1 + \Omega_2^2 B^2}\right] \propto \frac{1}{n_e} \tag{23}$$

where

$$\frac{1.76 \times 10^{11} \Theta_x B}{1 + \Omega_2^2 B^2} \approx \text{constant} \tag{24}$$

Note that the experimental $\tan \phi$, when compared with the theoretical curves computed by the increase in the $\dot{m}U_1$ alone, appears to decrease faster for argon than it does for helium. This is due to a comparatively smaller decrease in τ_{ei} for helium with increasing *arc jet* power.

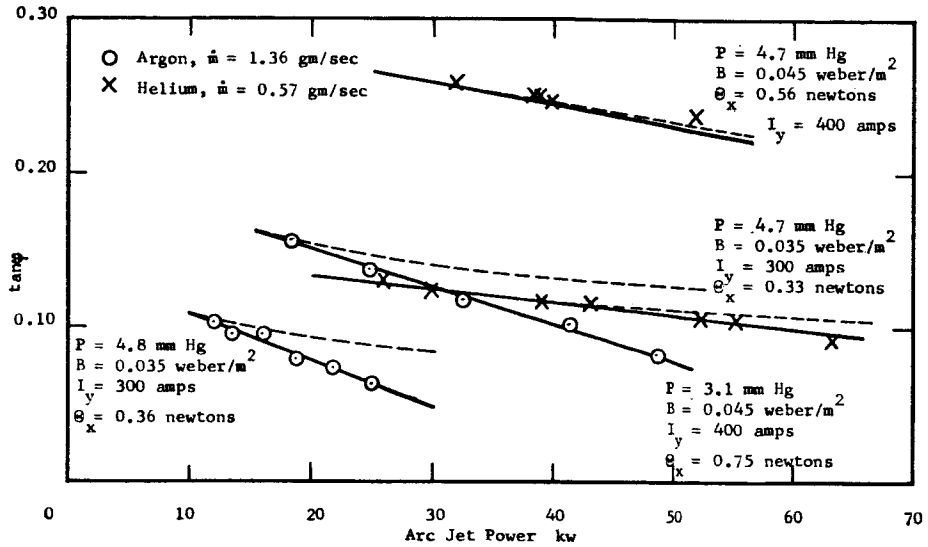

FIGURE 3. Experimental and theoretical results of jet deflection angle ϕ as a function of arc-jet power input. Dashed lines represent computations of tan ϕ from equation (21) under assumption of constant Θ_y.

5. At moderate values of B ($0<B<0.2$ weber/m^2), an increase in B (the applied magnetic field) brings about an increase in the deflection angle. Note that from equations (17), (18), and (19),

$$\tan\phi = \frac{\Omega_1 B^2 h I_{0c}}{hBI_{0c}(1+\Omega_2^2B^2)+\dot{m}U_1[(1+\Omega_2^2B^2)^2+\Omega_1^2B^2]} \tag{25}$$

6. The quantity $\Theta_y/\Theta_x=\Omega_1 B/(1+\Omega_2^2B^2)=[1+(\dot{m}U_1/\Theta_x)]\tan\phi$ is proportional to B as $B\to 0$. At the same time at $B=0$, $d(\Theta_y/\Theta_x)/dB=\Omega_1$, $\tan\phi=0$, and $d(\tan\phi)/dB=0$. Moreover, as $B\to 0$, $\tan\phi$ becomes proportional to B^2, $d(\tan\phi)/dB$ becomes proportional to B, and $[1+(\dot{m}U_1/\Theta_x)]$ becomes proportional to $1/B$.
7. An increase of the *accelerator* power at constant B decreases the magnitude of tan ϕ as a result of:
   7.1. An increase of I_{0c} and consequently Θ_x,
   7.2. An increase of n_e and consequently a decrease in Θ_y.
8. A decrease of pressure (or density) in the plasma jet at constant I_{0c} and B brings about an increase in the magnitude of tan ϕ as a result of an increase in τ_{ei}.
9. An increase in B while I_{0c} remains constant brings about a decrease of the transverse conductivity σ_y and an *increase* in the total power required to push the current I_{0c} through the plasma.
10. Staggering the electrodes by an appropriate amount so as to introduce an *axial* electric field eliminates the axial (Hall) current, $J_x=0$ in equation (9), and the jet deflection. It also *decreases* the accelerator *power required* to drive the same current I_{0c} across the electrode gap at any given magnetic field. In other words, the required voltage (electric field) for a given applied current at a given applied magnetic induction is substantially reduced and the efficiency of the accelerator is improved.

11. The required stagger, $J_x=0$ in equation (9), is such that the anode should be placed upstream of the cathode at a distance $d=h\sigma_0\chi BJ_y/[(1+\sigma_0\psi B^2)J_y+UB\sigma_0]\approx h\Omega_1 B/(1+\Omega_2^2B^2)$, where h is the electrode gap along the y-axis and U is an average velocity.
12. At constant B, an increase of the applied current I_{0c} brings about an increase in the transverse conductivity σ_y (since n_e increases and Ω_1 and Ω_2 decrease). Moreover, the transverse conductivity initially increases rather rapidly with increasing applied current (or increasing cross-arc power) as both Ω_1 and Ω_2 decrease. The *rate* of increase of σ_y decreases as the power level increases, and when Ω_1 and Ω_2 both become negligible, σ_y levels out. As the power level increases, σ_y changes at a rate specified by the electron temperature.
13. As the cross-arc power level increases, the electron concentration n_e also increases. Therefore, the value of τ_{ei} decreases.
14. Since the currents in the accelerator will tend to avoid regions of (a) low conductivity, (b) high back EMF, (c) high magnetic field, (d) low pressure or density, and (e) high velocity (where the static pressure drops and the back EMF increases simultaneously), it is clear that a magnetic plug (i.e., a local maximum of the magnetic field in a region of decreasing pressure) can be

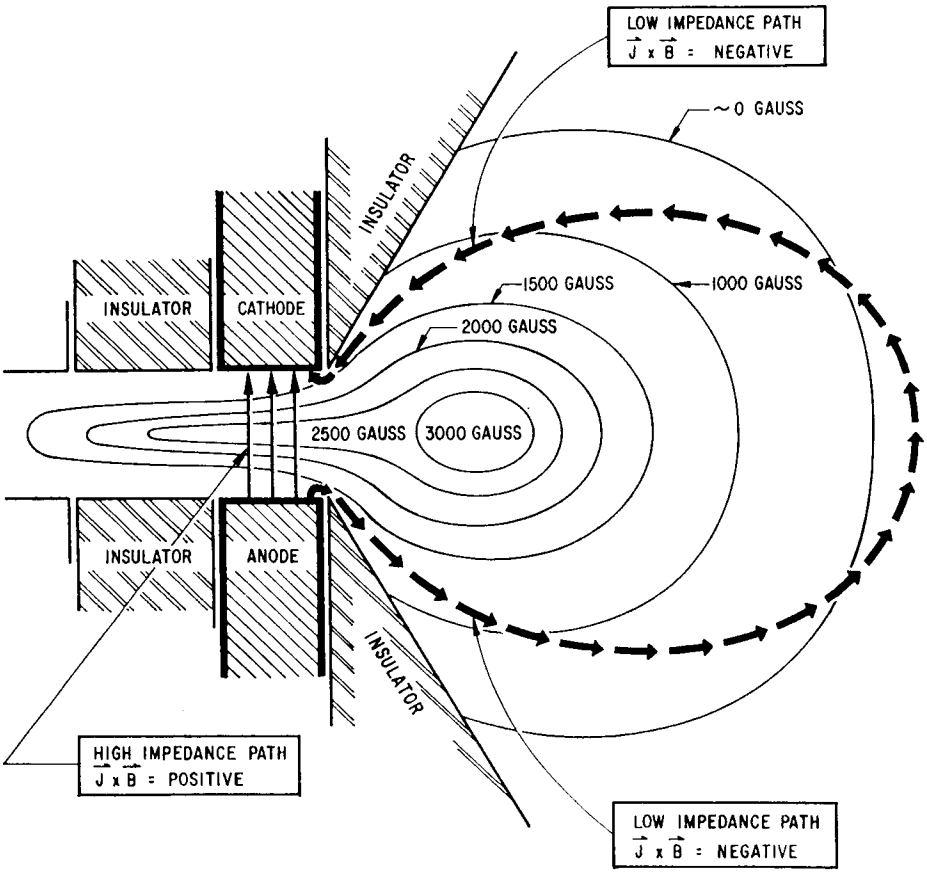

FIGURE 4. Schematic of thrust-configuration plasma accelerator operating in the decelerating mode. Magnetic field normal to page and directed from page to reader.

made to divert the current in such a manner that an accelerator in the thrust configuration (thrust-producing polarity of $\vec{J}$ and $\vec{B}$) can be made to produce *drag* by passing most of the current from one electrode to the other in a negative (decelerating) direction as shown schematically in Figure 4 by the dashed arrows.

15. At low B ($B<0.2$ weber/m^2), the magnitude of the reduced thrust $\Theta_x/\hbar I_{0c}$ should be proportional to B. As B increases, $\Theta_x/\hbar I_{0c}$ goes through a maximum and then begins to decrease.
16. The power dissipation (ohmic heating) in the plasma should be given by equation (13). The power dissipation at high magnetic inductions and constant applied current (equal to the difference between the total power into the accelerator and the sum of the power going into acceleration and the power going into the electrodes and confining walls) should be proportional to B^2 when Ω_2 remains constant with increasing B.
17. When there is no applied current and $E_{0x}=E_{0y}=0$, the current density components are given by $J_{1x}\approx\sigma_0(\Omega_1 B)U_x B/A$ and $J_{1y}\approx-\sigma_0(1+\Omega_2^2B^2)U_x B/A$ where $A=(1+\Omega_2^2B^2)^2+(\Omega_1 B)^2$ and $B=B_z$. Then for $U_x\approx U_1=$constant,

$$\Theta_x \approx -\sigma_0(1+\Omega_2^2B^2)U_1B^2\hbar/A \quad \text{and} \quad \Theta_y \approx -\sigma_0(\Omega_1 B)U_1B^2\hbar/A$$

Since these induced currents will be usually small, there will be only a slight slowing-down and a slight downward deflection of the jet when the electrodes are shorted externally. These effects will manifest themselves in a decrease of the diameter of the supersonic jet in the region between the pole pieces and a slight exhaust jet deflection. When there are no electrodes, the jet will still deflect—perhaps in a complicated way—because the current loops will have to close within the plasma. Note the dependence of Θ_y on B^3. The deflection angle, in this case, changes sign with B. This effect is the opposite of the effect described in item 1 (Figure 2a) and was observed by Warder (**24**). Note also that the induced electric field (back EMF) is sufficient to cause electron heating and a non-linear Ohm's law even in the absence of applied electric fields.

18. At high pressures ($p_a\gtrsim 1$ atmos) and low degrees of ionization in the pre-ionized gas stream [$\alpha=n_e/(n_e+n_a)\lesssim 0.01$], $n_e\lambda_{ei}\ll n_a\lambda_{ea}$ and equation (4) reduces to $\vec{J}=[n_e e^2/(n_a m_a q_{ea} v_{ea})]\vec{E}'$. Then the conductivity of the gas at the accelerator inlet will be of the order of 100 mhos/m and the high particle density would *prevent* the electrons from picking up enough energy between collisions in the cross-arc to cause a large increase in ion pairs more or less uniformly over the entire region between the electrodes. The electron temperature will increase only slightly above the ion and atom temperatures ($T_e\geq T_a=T_i$). The combined effect of non-equilibrium ionization and elevated electron temperature will still cause the Ohm's law in the plasma to be non-linear. However transition region, boundary layer, and other aerodynamic phenomena are no longer negligible, and the simple theory outlined above would not apply. At high pressure, relatively "cold" gas flow (low n_e), and relatively low applied currents ($<10{,}000$ amps), the discharge will tend to be of the thin filament type investigated by Thiene, Chambers, and Jaskowsky (**23**), and it would tend to blow out by aerodynamic forces. The discharge would then be unstable. It would ignite close to the leading edge of the electrodes, and would be blown downstream to the trailing edge where it would bulge out until it became extinguished, only to re-ignite at the leading edge. The application of the magnetic field would

not significantly alter these events, although it might increase their frequency and regularity. The bulging-out of the discharge would be enhanced by the magnetic field of the proper polarity and the increased discharge length would drive up the required voltage with increasing B, perhaps at a rate faster than that demanded by the increase in the induced electric field UB. The bulging current paths would then react with the magnetic field to smear out the jet instead of simply deflecting it in a well-collimated beam.

Other observable effects could be predicted by this simple treatment [equations (15) to (19)] if sufficient control is possible in designing and performing the experiments. For example, if the expellant is changed while the electron concentration and collision cross sections remain the same, one should expect the magnetic field B at which the reduced thrust Θ_x/hI_{0c} reaches a maximum to be roughly proportional to $m_i^{3/4}$ and $(\Theta_x/hI_{0c})_{\max}$ to be proportional to $m_i^{-1/4}$.

Since the observable effects will give a good estimate of the magnitude of the components of the tensor conductivity, it is possible, in principle, to obtain estimates of the values of some of the parameters of the plasma in the region of the interaction of the cross-arc with the magnetic field. These parameters include the electron, ion, and atom concentrations, temperatures, and partial pressures, and the electron-ion and ion-atom collision cross sections. Gross mean values of these parameters can be obtained from the following set of equations (in mks units):

$$p_e = n_e k T_e \tag{26}$$

$$p_a = n_a k T_a \tag{27}$$

$$p_i = n_i k T_i, \quad T_a = T_i, \quad n_e = n_i \tag{28}$$

$$P = p_e + p_a + p_i \tag{29}$$

$$\dot{m} = (n_e m_e + n_a m_a + n_i m_a) A_{ej} U_{ej}, \quad m_i = m_a \tag{30}$$

$$q_{ei} = 5.85 \times 10^{-10} T_e^{-2} \ln \Lambda \tag{31}$$

$$\Lambda = 1.23 \times 10^{7} T_e^{3/2} n_e^{-1/2} \tag{32}$$

$$\sigma_y = \frac{I_{0c} h_{ep}}{V_{ep} A_{ep}} = \frac{(1+\Omega_2^2 B^2) \times 7.7 \times 10^{-3} T_e^{3/2} (\ln \Lambda)^{-1}}{(1+\Omega_2^2 B^2)^2 + (\Omega_1 B)^2} \tag{33}$$

$$q_{ei} = 2.84 \times 10^{7} (n_e \Omega_1)^{-1} T_e^{-1/2} \tag{34}$$

$$q_{ia} = \frac{3.2 \times 10^{-19} \pi^{1/2} n_a \Omega_1}{(n_e + n_a)^2 m_i^{1/2} (8kT_i)^{1/2} \Omega_2^2} \tag{35}$$

where

$$\Omega_1 = \left[1 + \frac{\dot{m} U_1}{\Theta_x}\right] \frac{\tan \phi (1 + \Omega_2^2 B^2)}{B} \tag{36}$$

and

$$\Omega_2^2 = \frac{d}{dB}\left[-\frac{1}{B}\frac{\Theta_y}{\Theta_x}\right] \Big/ \frac{d}{dB}\left[B \frac{\Theta_y}{\Theta_x}\right] \tag{37}$$

while A_{ej} = effective jet cross-sectional area, U_{ej} = effective jet velocity, h_{ep} = effective discharge length, V_{ep} = effective voltage drop in plasma, A_{ed} = effective discharge cross-sectional area, and $\dot{m}$ = flow rate at accelerator inlet. In principle, the magnitude of these effective quantities can be obtained by determining the distribution of current density, electric field, flow velocity, etc., in the cross arc.

Then the simultaneous solution of equations (26) to (37) would yield values of p_e, p_a, p_i, n_e, n_a, T_e, T_i, q_{ei}, q_{ia}, Ω_1, and Ω_2 in terms of tan ϕ, Θ_x, B, $\dot{m}U_1$, m_i, and these effective quantities.

EXPERIMENTAL INVESTIGATION

This work is a continuation of earlier experiments (**8, 10, 22**). The apparatus used has been described in detail in earlier publications (**8–14, 22**). In the experiments reported here, the Mark II-A accelerator (shown in Figure 1) was operated in the free-jet mode (**8**). Some ambient gas entrainment occurred and the accelerator inlet momentum $\dot{m}U_1$ used in equation (19) should, strictly speaking, be measured in a manner such as to include the increase in inlet momentum due to the suction generated by the operation of the accelerator. The flow rate $\dot{m}$ in equation (30) should likewise be corrected for entrainment. The increase of the inlet momentum with the accelerator on was measured by means of static pressure, total pressure, and vane-deflection measurements at various places in the inlet. These measurements proved that the increase in inlet momentum due to accelerator-induced entrainment was negligible as long as the accelerator operated at $\Theta_x < 2.5$ newtons and the geometry was essentially as described in reference (**8**) (i.e., the inlet was within a few mm of the arc-jet exit).

Plasmas of argon and helium were used and measurements were made of the deflection angle ϕ, the axial thrust Θ_x, the plasma generator flow rate $\dot{m}$, the inlet momentum $\dot{m}U_1$, the magnetic field B, the current-voltage characteristics of the cross-arc discharge with and without magnetic field, the tank pressure p, the plasma generator (arc-jet) power input, the power absorbed by the arc-jet coolant, the power added to the argon and helium plasmas by the plasma accelerator, etc. The axis of the luminous jet was found to coincide with the flow axis in all cases.

In the course of these experiments, all the predicted effects (1 to 17, listed in the previous section), with the exception of item 18, were observed. No experiments were performed at $p \approx 1$ atmos. Experiments concerned with item 17 were recently also performed by Warder (**24**). The experimental results presented in Figures 2a to 20 indicate that the description of momentum transfer to plasmas in these experiments given by the above analysis includes all major effects. Experimental verification of most of the theoretical predictions instills a measure of confidence in the use of the generalized Ohm's law given by references (**1**) through (**7**) and increases the probability that the momentum-change technique, with further elaboration, can be made to yield valuable information on basic plasma properties. It is left to the readers to explain how, in spite of the numerous assumptions, reasonable answers were obtained.

Additional work is required to examine in detail the magnitude and effect of the coefficients $\beta^{(i)}$ and $\theta^{(i)}$, to formulate an energy balance that allows for ionization and recombination and provides information on the current density, electric field, velocity, species concentration, pressure, and temperature distributions.

Figures 2a and 2b show qualitatively the predicted deflection of the jet (identified as the resultant) with various combinations of magnetic field and applied current polarity for $\dot{m}U_1 \gg \Theta_x$ and $\dot{m}U_1 \gtrsim \Theta_x$. These deflections (items 1 and 2 of the theoretical discussion in the last section) were indeed observed. Observations of the discharge were described in reference (**11**).

Figure 3 shows the experimental results obtained for tan ϕ as a function of arc-jet power at constant I_{0c} and B for helium and argon. The results of Figure 3 confirm the predictions of items 3 and 4 of the theoretical section. The theoretical curves for constant Θ_y were obtained in the manner discussed (item 4). The

decrease of tan ϕ with increase in gas enthalpy is not as marked for helium as it is for argon because the degree of ionization (electron concentration) increases faster for argon than for helium at these enthalpy levels. The ratio of the temperature increase of argon over the temperature increase of helium is approximately equal to $(\dot{m}C_p)_{He}/(\dot{m}C_p)_A \approx 4$, where C_p = specific heat at constant pressure. The power into the gas at the arc jet can be estimated from Figure 5. It shows the power into the arc-jet coolant as a function of total arc-jet power for helium and argon. The heat input to the arc-jet coolant is determined by measuring the flow rate and temperature rise of the water coolant flowing through the plasma generator cooling jacket.

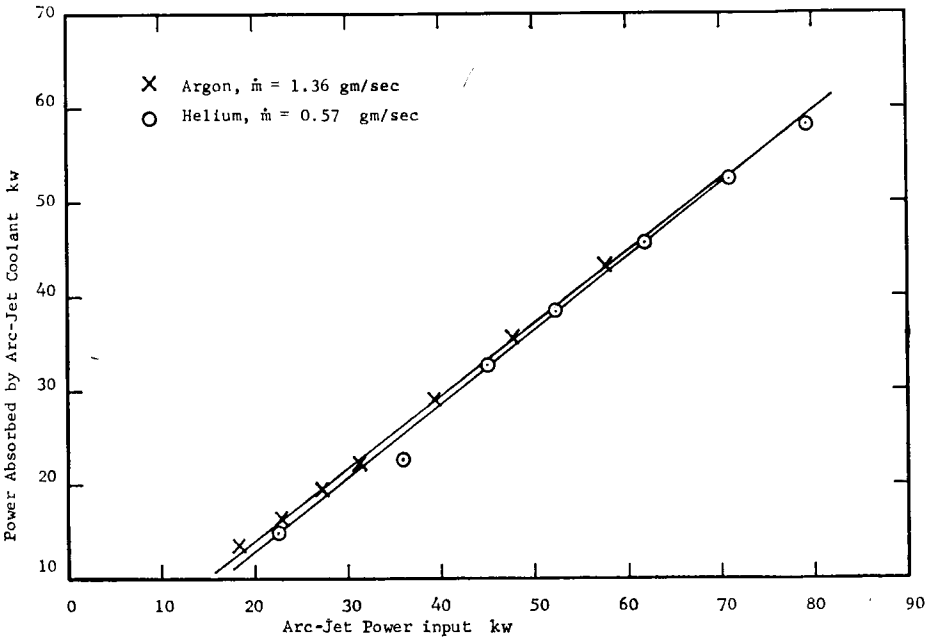

FIGURE 5. Arc-jet power absorbed by coolant as a function of total power input.

Figure 6 shows the axial thrust increment obtained for argon and helium plasmas as a function of magnetic flux density for constant cross-arc current and three arc-jet total inputs of 24, 32, and 40 kw. The results were corrected for magnetic interference by careful calibration of the thrust balance. The data indicate that within the region covered by these experiments the recorded thrust is independent of the arc-jet power level and the type of plasma used. The data agree with the theoretically-predicted values to within a few per cent.

Figure 7 shows the accelerator inlet momentum $\dot{m}U_1$ for argon and helium plasma jets as a function of arc-jet power input. The measurements were made by mounting a flat steel plate on a negligible-displacement pendulum balance. The flat steel plate was perpendicular to the arc-jet flow axis. Great care was exercised to have the normal to the plate correctly aligned with the plasma jet axis. The plate was placed approximately where the accelerator electrodes were normally located ($\sim$14 cm downstream of the arc-jet exit). Running time was also found to be an important factor. In order to prevent the hot plasma from deforming the 2.5-cm-thick steel plate and from moving the center of mass of the pendulum

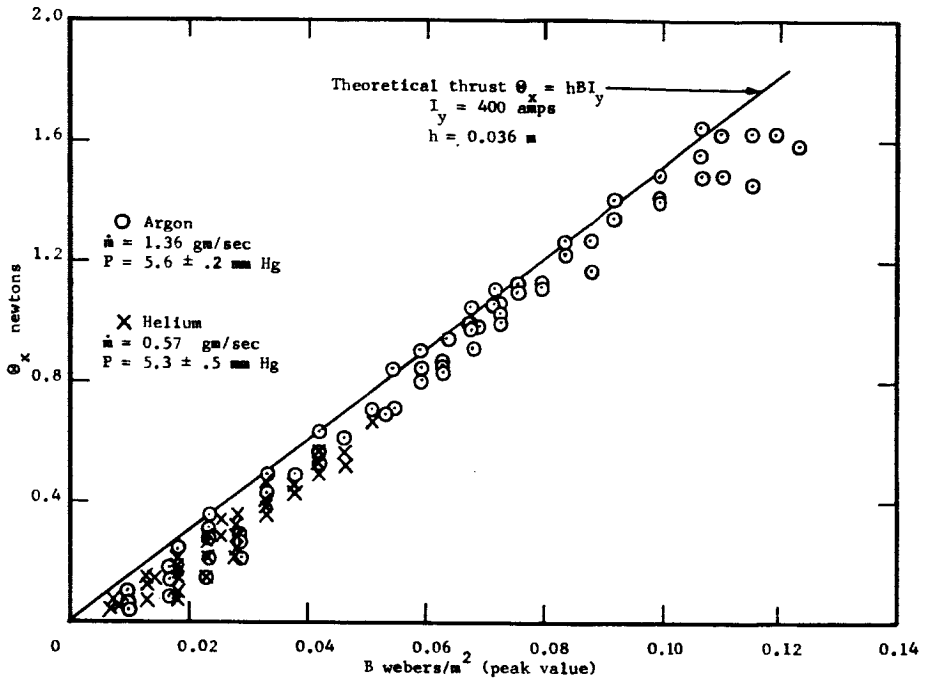

FIGURE 6. Argon and helium axial-thrust increment as a function of magnetic flux density.

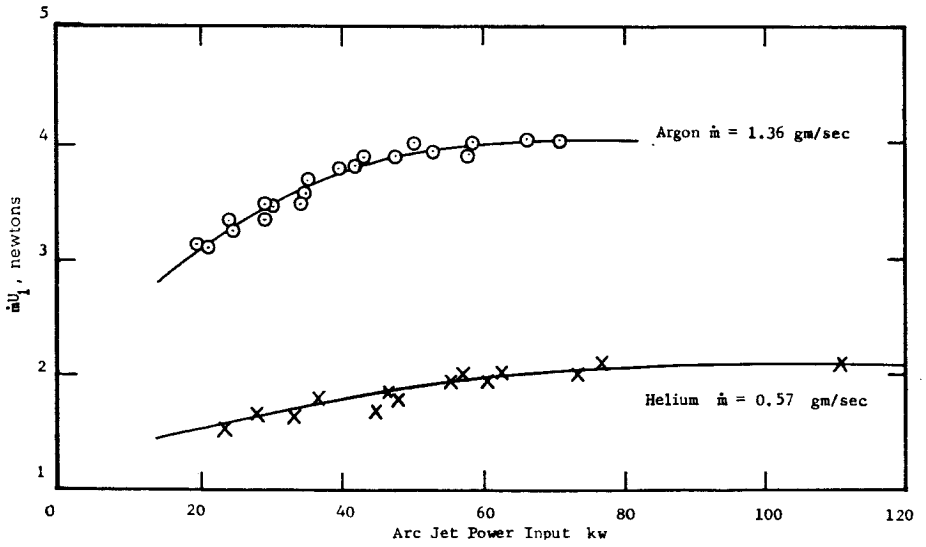

FIGURE 7. Argon and helium inlet momentum as a function of arc-jet power input.

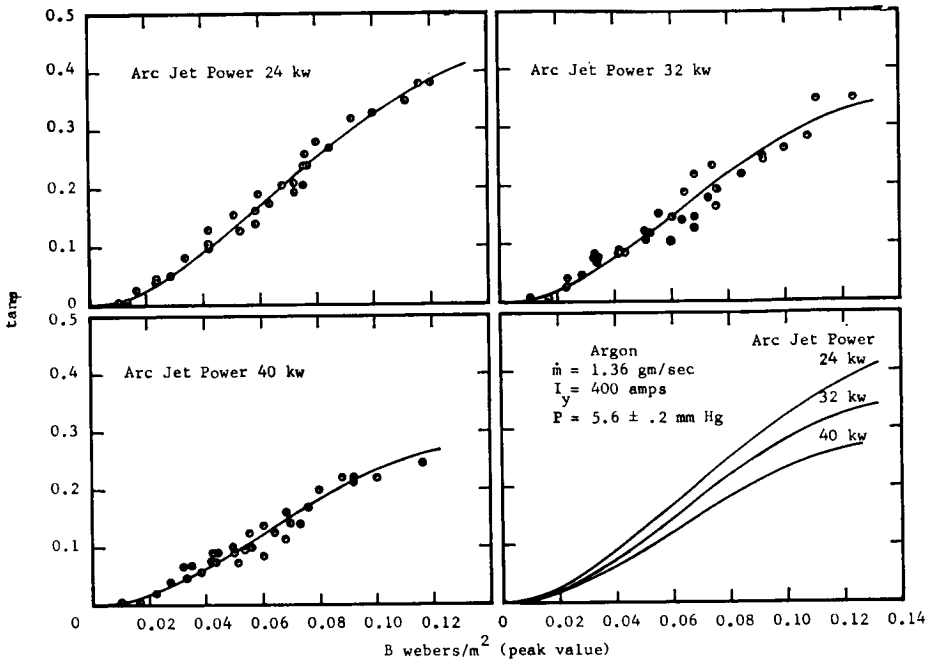

FIGURE 8. Argon jet deflection angle as a function of magnetic flux density and arc-jet power input.

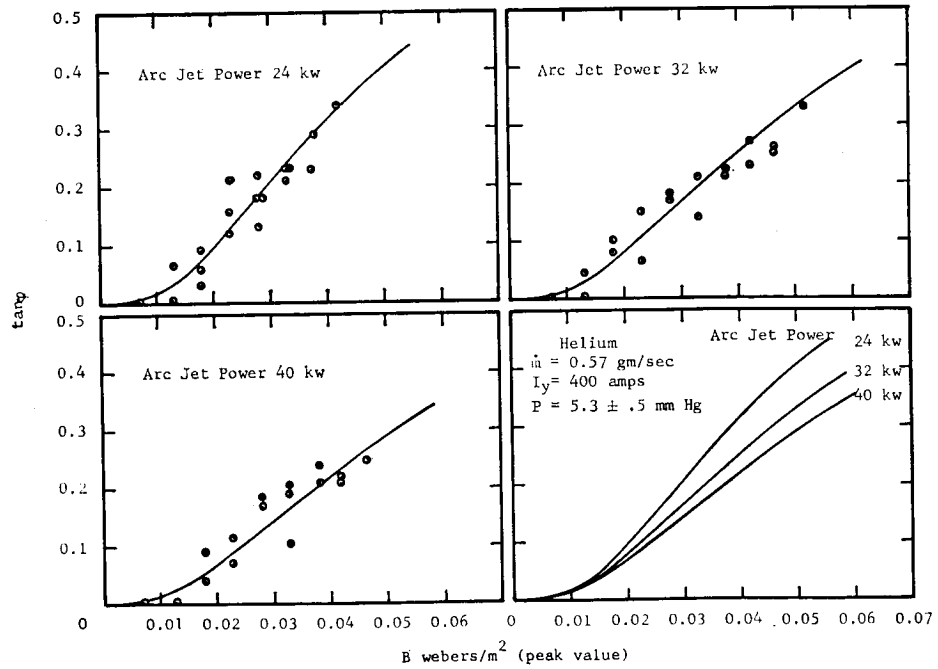

FIGURE 9. Helium jet deflection angle as a function of magnetic flux density and arc-jet power input.

system (by expansion), each run was limited to a few seconds, and only those runs where the balance returned exactly to the null point were retained. A recalibration of the thrust balance immediately after each run was also performed.

Figures 8 and 9 show the jet deflection angle for argon and helium, respectively, as a function of the magnetic flux density for constant cross-arc current and for three different arc-jet power levels. The deflection angle was determined by double-exposure pictures of the deflected and undeflected jet. The results are in agreement with the qualitative theoretical predictions discussed earlier (items 4 through 7 in the theoretical discussion). Examples of the double exposure pictures obtained were given in references (8) and (25).

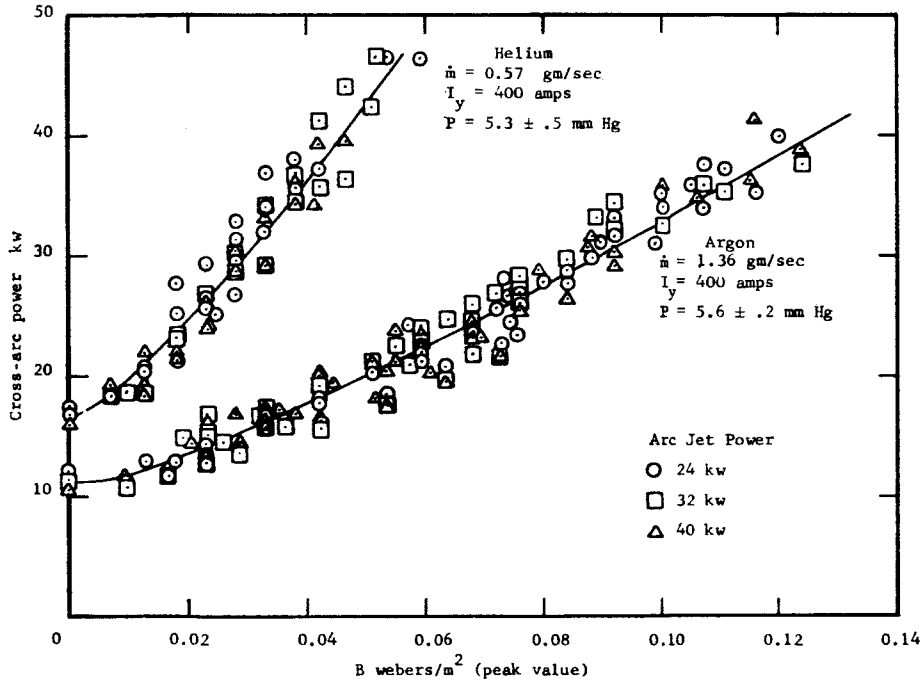

FIGURE 10. Cross-arc power input into argon and helium plasma as a function of magnetic flux density at constant cross-arc current.

Figure 10 shows the cross-arc input power required to pass a given amount of current across argon and helium plasma streams for three different arc-jet power levels with increasing magnetic flux density. The data seem to indicate that the cross-arc power is independent of the arc-jet power level. This is generally not true. However, the difference in static enthalpy of the plasma stream between the three arc-jet power levels used in our experiments is not large enough to produce any appreciable difference in the results.

Figure 11 shows the dependence of $\Theta_y/\Theta_x=[1+(\dot{m}U_1/\Theta_x)]\tan\phi$ for argon and helium on the magnetic induction as computed from the data presented in Figures 6 to 9 for three different arc-jet power levels. It is of interest to note that the Hall thrust, and therefore the Hall current, may well exceed the axial thrust and the transverse current respectively.

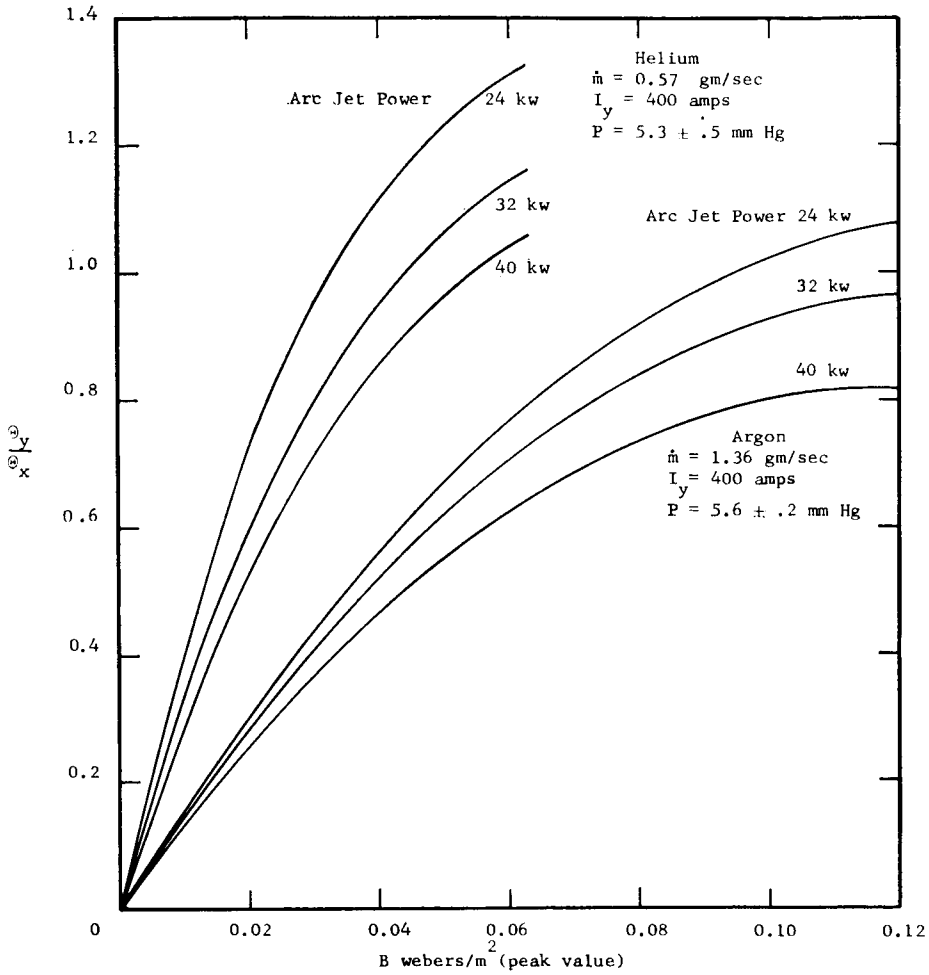

FIGURE 11. Ratio of Hall-thrust to axial-thrust increment for argon and helium as a function of magnetic flux density and arc-jet power [values from equation (19)].

Figure 12 shows the apparent efficiency, $\eta_{app}=\{[\Theta_x^2+\Theta_y^2]/2\dot{m}+U_1\Theta_x\}/(\pi_e+\pi_m)$ where π_e = electrical power input to the cross-arc and π_m = power to the magnet, of the unconfined accelerator operating with argon and helium plasmas as a function of the magnetic induction and three arc-jet power levels. These results were computed from the data presented in Figures 6 to 10, and they indicate an increase in efficiency with increasing arc-jet power. Figure 13 shows the total apparent specific impulse $[\Theta_y^2+(\Theta_x+\dot{m}U_1)^2]^{1/2}/\dot{m}g_c$ of the unconfined accelerator operating with argon and helium plasmas as a function of the magnetic induction and three arc-jet power levels. These results were computed from the data presented in Figures 6 to 9, and they indicate an increase in specific impulse with increasing arc-jet power level. The flow rate $\dot{m}$ used in these computations was the arc-jet flow rate and $g_c=9.81$ newtons/kg.

During these experiments, it was observed that a decrease of tank pressure at constant I_{0c} and B brought about an increase in the magnitude of tan ϕ, while an increase in B (when I_{0c} and the pressure remained constant) brought about an

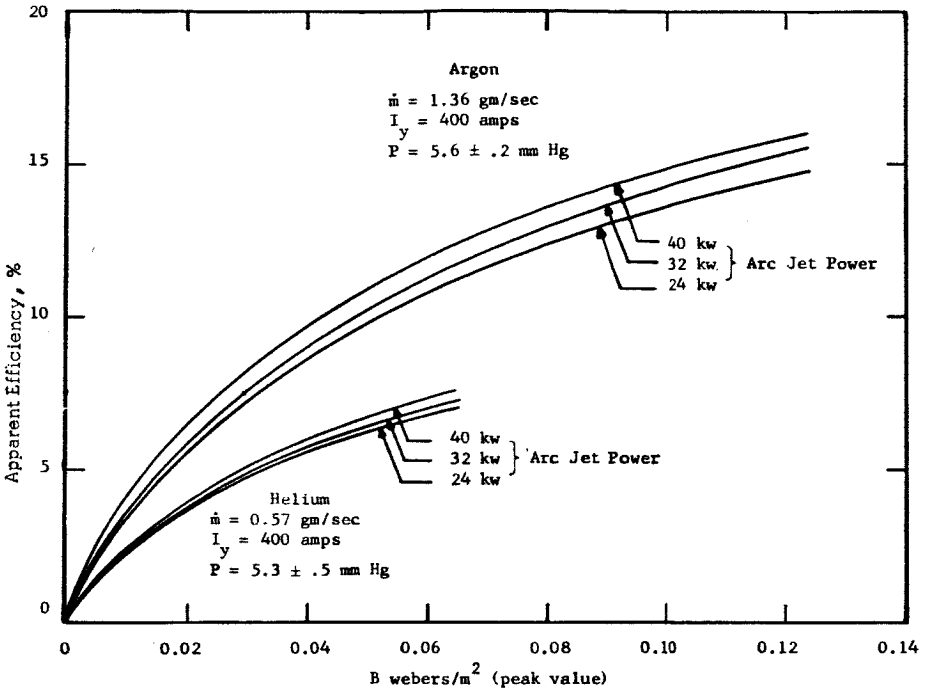

FIGURE 12. Apparent efficiency of an unconfined accelerator as a function of magnetic flux density and arc-jet power.

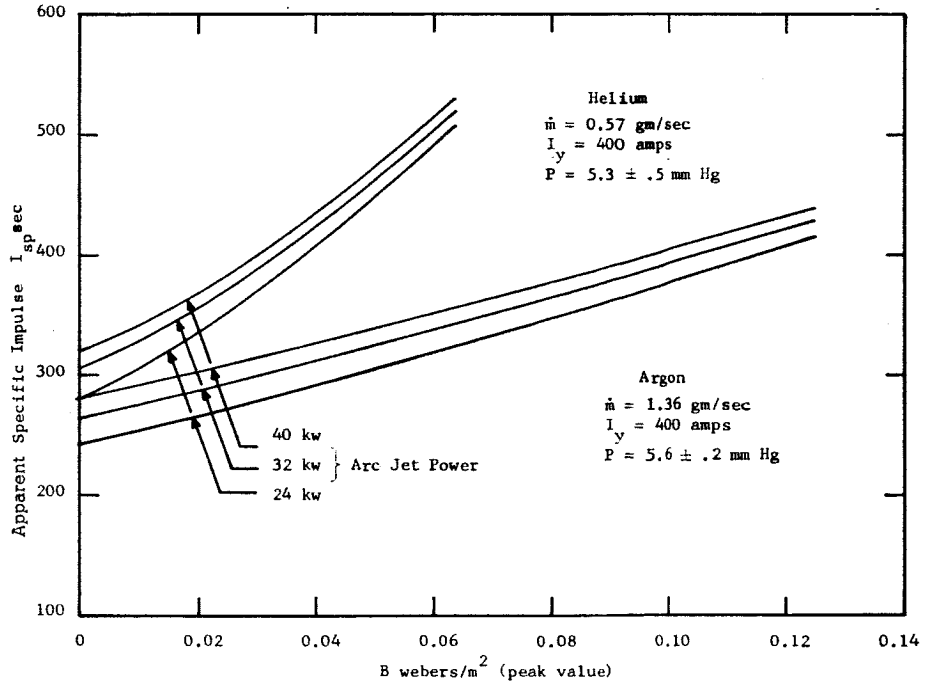

FIGURE 13. Apparent specific impulse as a function of magnetic flux density and arc-jet power.

increase in the total power required to push the current I_{0c} through the plasma (i.e., an increase in the applied voltage). The effects described by items 8 and 9 of the theoretical discussion were thus observed to occur (**8, 9, 11, 13, 14**). The electrode stagger effect predicted by items 10 and 11 of the theoretical discussion was also observed as described in references (**8**), (**11**), (**13**), and (**14**). The effects described by items 12 to 17 were also observed to occur and are described in references (**9**), (**11**), (**14**), and (**18**). In particular, an accelerator with a field geometry approximately as depicted in Figure 4 was built and the drag effects described by item 14 were observed. At constant B, the quantity dV_0/dI_{0c}, where V_0 is the applied voltage, is proportional to $1/\sigma_y$. This quantity was found to behave as described by item 12 (**9, 14, 18**). The cross-arc power increases as either I_{0c} or B, or both, increases. In that case, the quantity χ (Hall coefficient) was found to decrease, and therefore n_e increased while τ_{ei} decreased (**14**), as described by item 13. This effect is also shown in Figure 14, where typical values of Ω_1 [given by equation (36)] are plotted as a function of B for argon and helium. The effect predicted by item 15 was observed as already described in reference (**9**). The effect described by item 16 was also observed and may be obtained from the data presented in Figures 10 and 12, together with the electrode power losses presented in references (**9**), (**13**), and (**14**). Note that Ω_2, as obtained from equation (37), is indeed nearly constant with B for argon (Figure 15), and that Ω_1 decreases markedly for helium but only slightly for argon as B increases. This behavior of Ω_1 appears to indicate that the argon is already highly ionized by the application of the cross arc at $B=0$, and an increase of B (and of cross-arc power, see Figure 10) brings about a small increase in n_e. For helium, however, an increase of B (and of cross-arc power) brings about a significant increase of the degree of ionization.

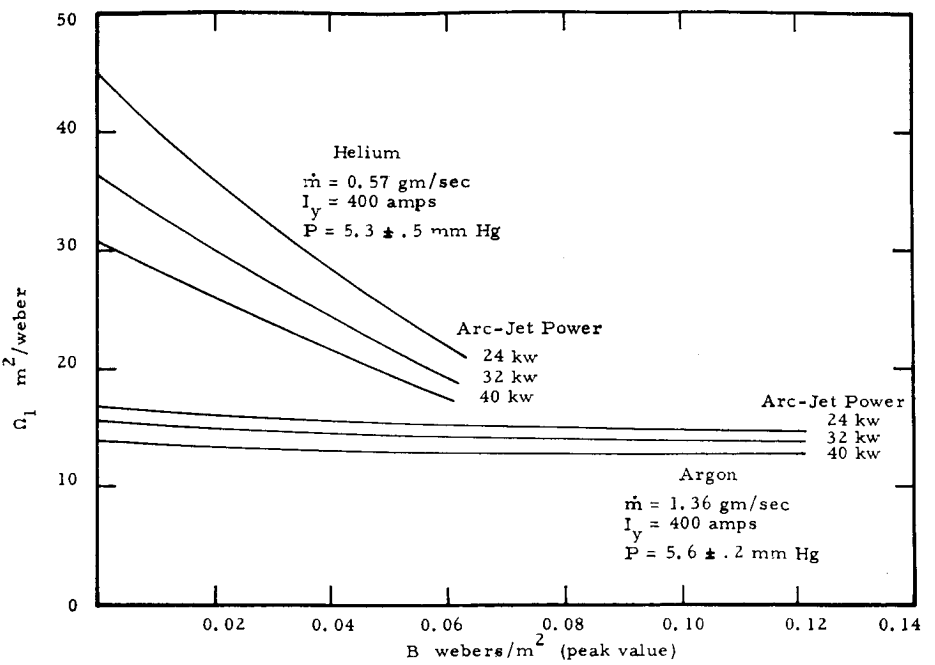

FIGURE 14. The value of Ω_1 for argon and helium as a function of magnetic flux density and arc-jet power.

The corresponding behavior of typical values of Ω_2 is shown in Figure 15. The values of Ω_2 decrease slightly with increasing B for argon, while they first increase and then decrease for helium. Since, in mks units,

$$\Omega_1 = \sigma_0 \chi = 4.84 \times 10^{16} \frac{T_e^{3/2}}{n_e \ln \Lambda} \tag{38}$$

and

$$\Omega_2^2 = \sigma_0 \psi = 2.6 \times 10^9 \frac{T_e^{3/2} n_a}{n_e (n_e + n_a)^2 q_{ia} T_i^{1/2} m_i^{1/2} \ln \Lambda} \tag{39}$$

the initial increase of Ω_2 for helium cannot be easily explained on theoretical grounds. It is possible that the scatter in the observed values of Θ_x and $\tan \phi$ at low values of B do not permit an accurate determination of Ω_2 from equation (37) for helium. The effect described by item 17 was also observed by Warder (**24**). The values of Ω_1 and Ω_2 plotted in Figures 14 and 15 were obtained by assuming a uniform current density distribution.

Figures 16 to 18 are presented lest we forget that some very crude assumptions are made in the analyses given here.

Figure 16 presents two photographs of the argon spectrum in the interelectrode region. In both exposures, the top of the figure represents the upstream edge of the region observed. Approximately 5 cm along the axis of the jet of plasma was focused onto the spectrograph slit to produce these spectra. The electrode axis coincided with the center of the 5-cm length focused on the slit and the electrodes were equidistant from the jet axis. The top exposure presents the spectrum of the

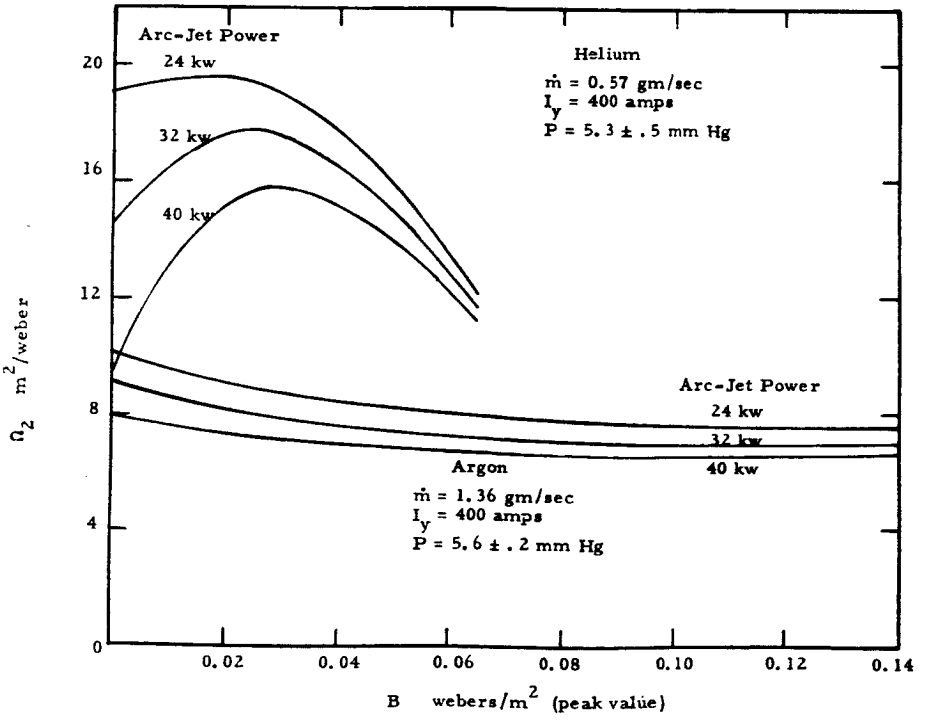

FIGURE 15. The value of Ω_2 for argon and helium as a function of magnetic flux density and arc-jet power.

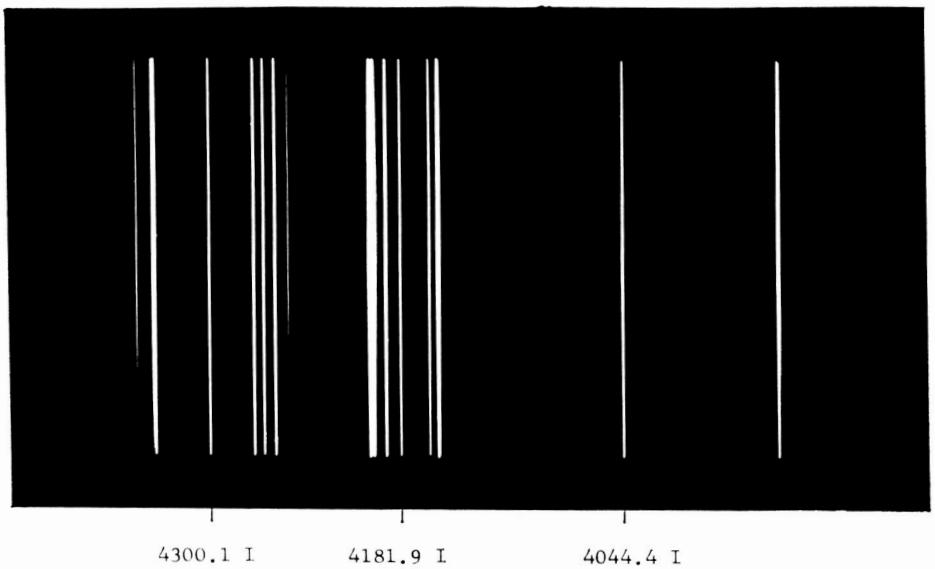

FIGURE 16a. Argon spectrum: arc-jet power = 32 kw; no cross-arc power; no magnetic field.

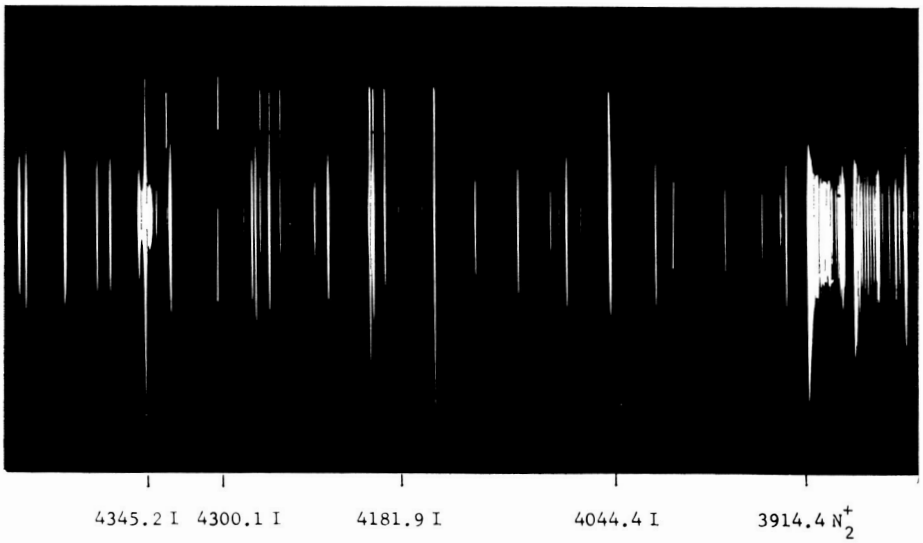

FIGURE 16b. Argon spectrum: arc-jet power = 32 kw; cross-arc power = 16.5 kw; magnetic induction $B = 0.033$ weber/m^2.

plasma stream generated by the arc jet in the absence of a cross arc and with no magnetic field. The bottom picture is the spectrum of the same region with the cross-arc power on (16.5 kw) and a magnetic field of 0.033 weber/m^2 applied. In the upper exposure, only atomic lines are observed, and this suggests that the radiation might be the result of metastable atoms that are excited in the arc region of the plasma generator. The ions have to a large extent recombined by the time

they reach the region in focus. The atomic radiation shown in the upper exposure is augmented in the lower exposure by many lines from singly-ionized atoms (e.g., 4383 Å, II) and additional neutral atom lines. Some neutral lines have disappeared almost completely (4300.1 Å, I). It is important also to note that in the lower exposure the atom lines get stronger in the interelectrode region where a high cross-arc current density is present. Similarly, the ion radiation is weak in the upstream (top edge) and downstream (bottom edge) of the figure but increases in the space between the electrodes (center of lower picture). Thus, in the inter-electrode region, an increase in either the ion and electron concentrations or the electron temperature, or both, appears to take place. Finally, the presence of

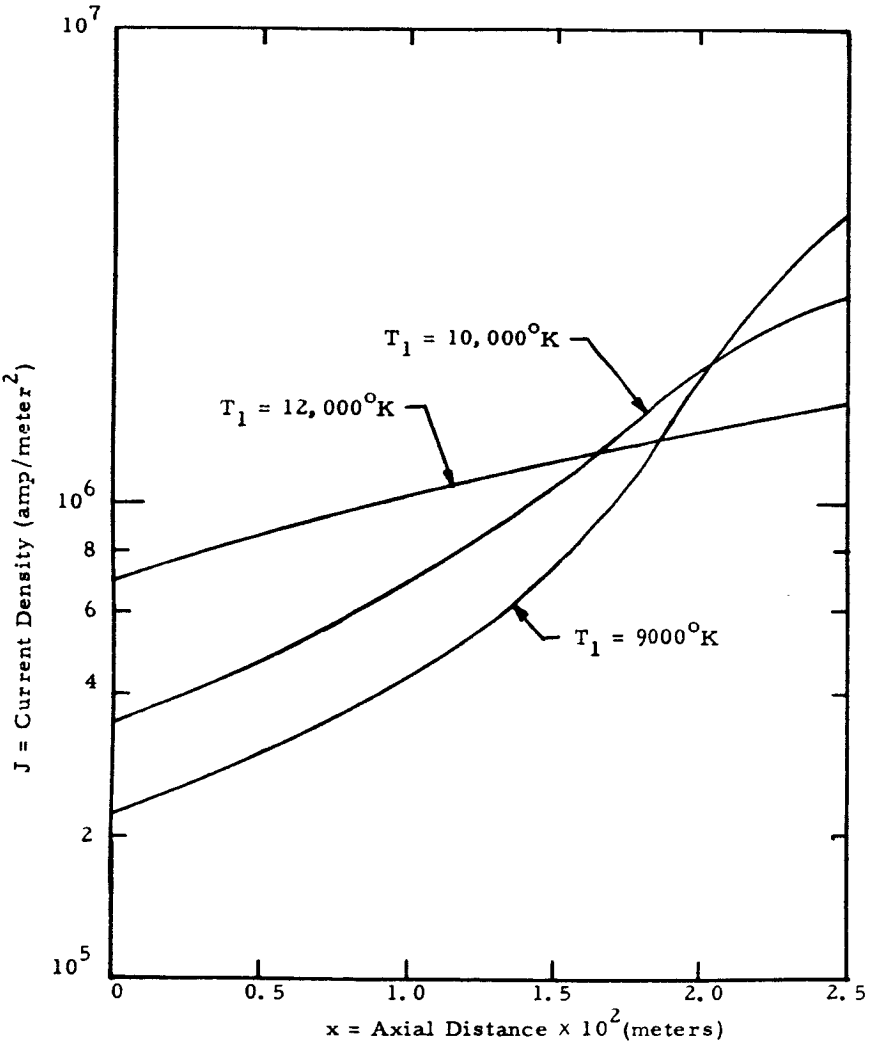

FIGURE 17. Theoretical transverse current density distribution in argon for three inlet temperatures, T_1, obtained by Lenn (14) using an analysis that allows for variable conductivity but assumes local thermal equilibrium (L.T.E.). Discharge characteristics are: $I_{0c} = 1000$ amperes, $B = 0.1$ weber/m^2, electrode length $= L = 0.025$ m, electrode width $= W = 0.025$ m, discharge cross-section $= WL$.

N_2^+ bands indicates strong deviations from local thermal equilibrium, but does not positively rule out equilibrium ionization and excitation at the electron temperature, despite the effect of the electric field.

Figure 17 is a theoretical computation of the current density as a function of electrode length for a geometry similar to Figure 1. This computation was carried out by Lenn (**14**). It appears to indicate that the current density increases towards the trailing edge of the electrodes. This increase becomes more pronounced for low inlet temperatures. Figure 18 presents the current-voltage characteristics for an electrical discharge across preheated (and preionized) argon and helium supersonic jets at $B=0$. These cross-arc characteristics indicate that the transverse conductivity $\sigma_y = dI_{0c}/dV_0$ of helium is considerably lower than that of argon. The observed behavior of the current-voltage cross-arc characteristics with $B=0$ at low applied current is not easy to explain. These jets of argon and helium plasma were produced by the equipment described in references (**9**), (**11**), and (**22**).

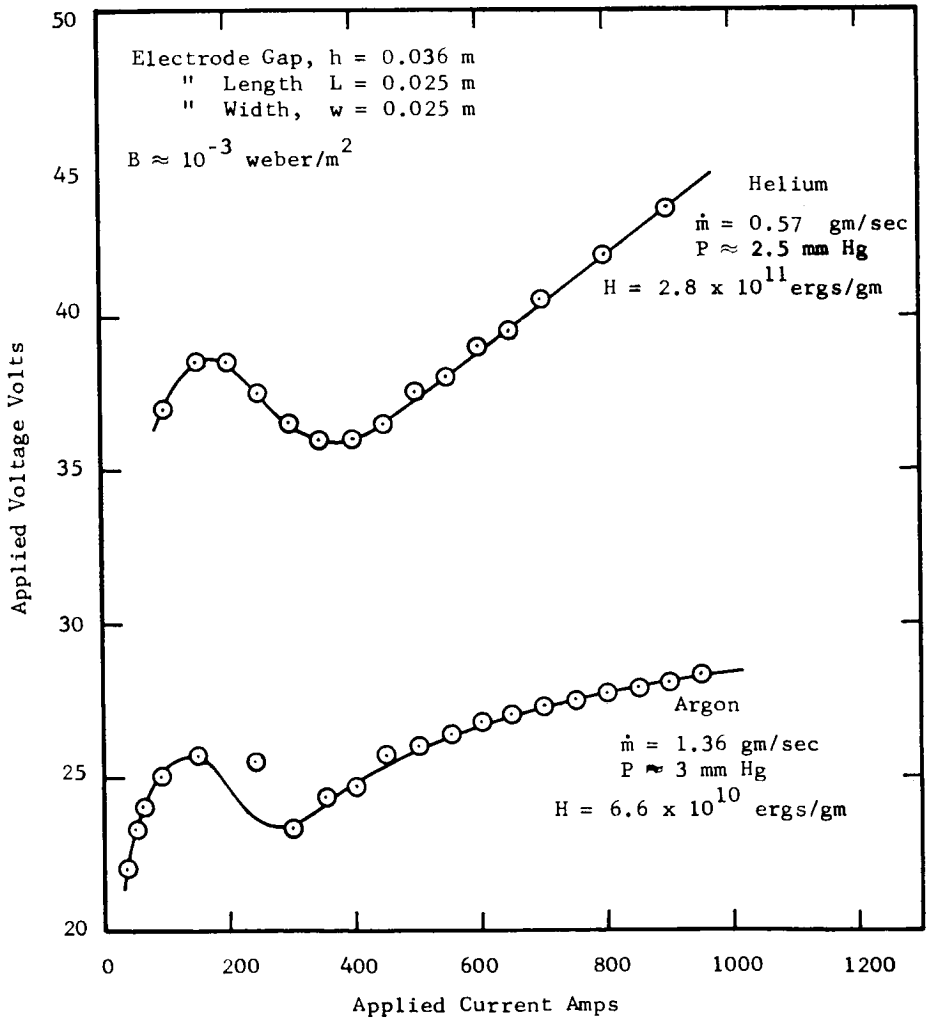

FIGURE 18. Current-voltage characteristics for an electrical discharge across a preheated plasma stream.

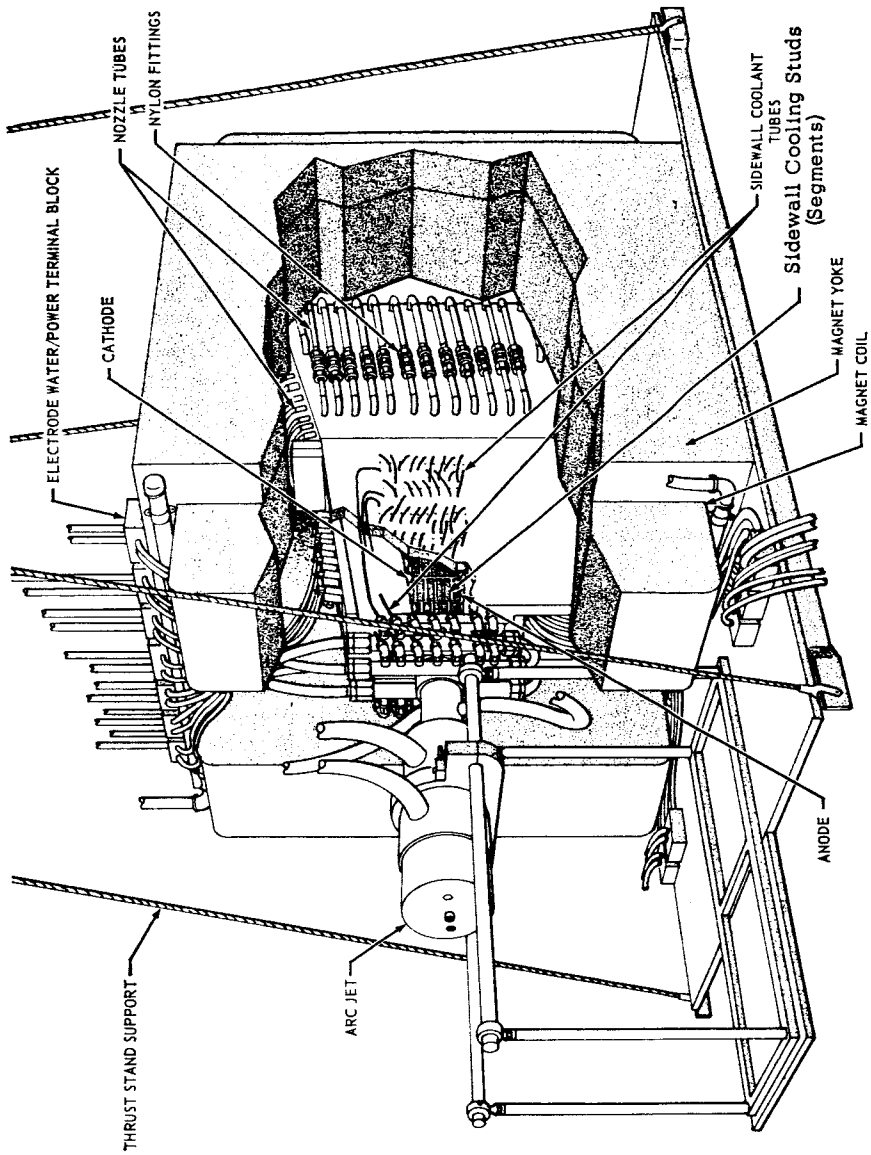

FIGURE 19. Cutaway sketch of Mk. CA-1 accelerator and arc-jet shown mounted on thrust stand. Accelerator section is shown in greater detail in Figure 20. (Momentum change of stream is measured by observing the thrust change on strain gauges.)

Typical values of the gross mean plasma parameters obtained by using these experimental results to solve the system of equations (26) to (37) are (for argon): $T_e \approx 12{,}000$ to $29{,}500°K$, $T_a = T_i \approx 7000$ to $4000°K$, $n_e \approx 6 \times 10^{20}$ to 8.6×10^{20} electrons/m^3, $n_a \approx 7 \times 10^{21}$ to 6.2×10^{21} atoms/m^3, and, using the values corresponding to the highest T_e, $p_e \approx 2.65$ mm Hg, $p_a \approx 2.6$ mm Hg, $p_i \approx 0.36$ mm Hg, $q_{ei} \approx 5.2 \times 10^{-18}$ m^2, $q_{ia} \approx 1.9 \times 10^{-19}$ m^2, $v_d \approx 6.7 \times 10^3$ m/sec, $\chi \approx 0.007$, $\psi \approx 0.016$, $\sigma_0 \approx 5100$ mhos/m, $\sigma_y \approx 1100$ mhos/m, $\tau_{ei} \approx 2.1 \times 10^{-10}$ sec, $\tau_{ia} \approx 5.7 \times 10^{-7}$ sec, $\omega_e \tau_{ei} \approx 2$, $\omega_i \tau_{ia} \approx 0.07$. Typical values of the same quantities for helium are given by: $T_e \approx 19{,}500°K$, $T_a = T_i \approx 2000°K$, $n_e \approx 2.8 \times 10^{20}$ electrons/m^3, $n_a \approx 2.4 \times 10^{22}$ atoms/m^3, $p_e \approx 0.55$ mm Hg, $p_i \approx 0.05$ mm Hg, $p_a \approx 4.64$ mm Hg, $q_{ei} \approx 1.2 \times 10^{-17}$ m^2, $q_{ia} \approx 2.5 \times 10^{-19}$ m^2, $v_d \approx 2 \times 10^4$ m/sec, $\chi \approx 0.02$, $\psi \approx 0.05$, $\sigma_0 \approx 2700$ mhos/m, $\sigma_y \approx 400$ mhos/m, $\tau_{ei} \approx 3.4 \times 10^{-10}$ sec, $\tau_{ia} \approx 5 \times 10^{-8}$ sec, $\omega_e \tau_{ei} \approx 3$, $\omega_i \tau_{ia} \approx 0.006$.

These values were obtained at $B = 0.05$ weber/m^2, $I_{0c} = 400$ amps, arc-jet power = 32 kw (for argon—4.7 kw into kinetic energy, 4.1 kw into static enthalpy, remainder into coolant; for helium—2.5 kw into kinetic energy, 6.8 kw into static enthalpy, remainder into coolant), cross-arc power = 20 kw for argon (2.3 kw into kinetic energy, 7.1 kw into static enthalpy, 10.6 kw into coolant) and 42.5 kw for helium (3.4 kw into kinetic energy 21.1 kw into static enthalpy, and 18.0 kw into coolant); total static enthalpy into gas = 8.2×10^6 joules/kg for argon and 4.9×10^7 joules/kg for helium, $\dot{m} = 1.36 \times 10^{-3}$ kg/sec for argon and 0.57×10^{-3} kg/sec for helium, $\Theta_x = 0.70$ newtons, $\Theta_y = 0.43$ newtons for argon and 0.75 newtons for helium,

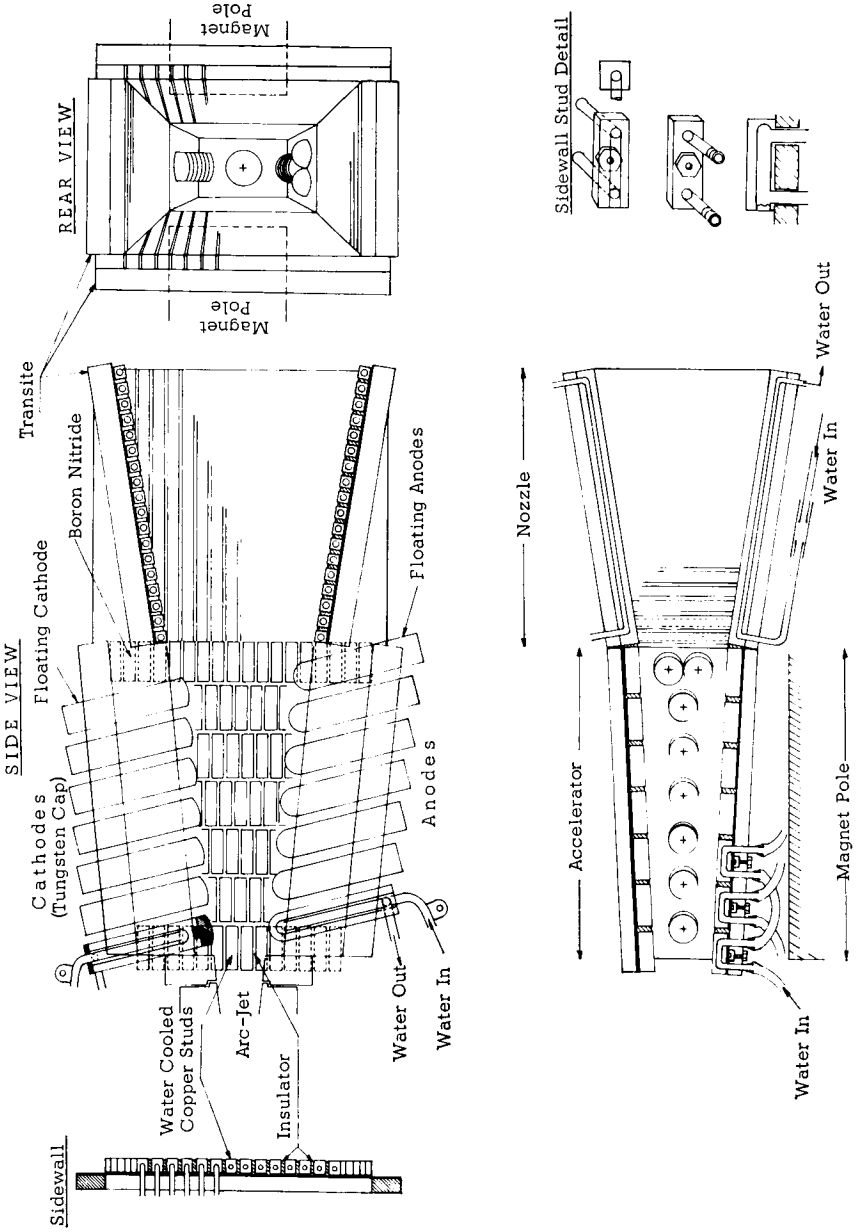

FIGURE 20. Schematic of seven-electrode crossed-field accelerator for wind-tunnel applications.

$V_0 = 50$ volts for argon and 106 volts for helium, and $\dot{m}U_1 = 3.56$ newtons for argon and 1.7 newtons for helium. A linear current-density distribution was assumed in these computations and the evaluation of the various parameters was carried out at the point x where $\frac{1}{2}I_{0c} = \int_0^x J_y w dx$. Note that the degree of ionization for helium is low enough to make $n_a\lambda_{ea} = 5.2 \times 10^8$ only slightly smaller than $n_e\lambda_{ei} = 27 \times 10^8$. Note also that it takes a minimum of 51.2 kw to ionize 1.36×10^{-3} kg/sec of argon and a minimum of 335 kw to ionize 0.57×10^{-3} kg/sec of helium. It appears that the static enthalpy for argon measured calorimetrically is in good agreement with the static enthalpy (including ionization) obtained by the momentum-change technique. The agreement is not so good for helium. It is entirely possible, however, that the probable error in the helium static-enthalpy estimate obtained from the scant calorimetric data available on helium can account for the discrepancy. In any case, the assumptions made in obtaining these estimates of species temperatures, concentrations, and collision cross sections do not justify expectations of accuracy better than within a factor of two or three. Some refinements of the theory have recently been carried out by Kontaratos (**26**).

The information obtained in these and previous experiments (**8–18, 22**), notably the early results of Demetriades (**22**) and the more recent results of Burkhard *et al.* (**16, 17**), were used to design a crossed-field plasma accelerator for wind-tunnel applications (Figures 19 and 20). The objective of this accelerator was to produce a stream of air with a velocity of approximately 8×10^3 m/sec and a static pressure of 1 to 10 mm Hg. The design and testing of accelerator Mark CA-1 was carried out under subcontract from MHD Research, Inc., for NASA/ Ames Research Center, Contract No. NAS 2–1170.

CONCLUSIONS

Momentum transfer to plasmas by Lorentz forces away from boundary and transition regions can be described quantitatively by means of a generalized Ohm's law for multicomponent, two-temperature plasmas expressed in terms of the plasma properties and species temperatures and concentrations. The assumption of local thermal equilibrium is not required in this approach.

Observations and measurements of momentum change and other effects are reported that are substantially in agreement with theory. This experimental verification of the theoretical predictions instills confidence in the use of the generalized Ohm's law to describe the conduction of electrical current through plasmas in the presence of magnetic fields and appears to justify most of the assumptions made in this crude analysis.

The measurement of momentum change effects brought about by the interaction of the cross arc with the magnetic field yields valuable information on plasma properties and species temperatures and concentrations in the absence of local thermal equilibrium.

Preliminary independent measurements of some of these parameters appear to be in agreement with the results obtained by momentum-change techniques. Refinement of the theory is required to improve the accuracy of these measurement techniques.

ACKNOWLEDGMENTS

I want to thank the Air Force Office of Scientific Research for making funds available for this study under Contract AF 49(638)–1160 at the Plasma Laboratories of Northrop Corporation. I also want to thank Dr. A. N. Kontaratos, who

helped perform the experiments and reduce the data; the laboratory technicians J. Superata and L. Goltra, who helped assemble, maintain, and operate the apparatus known as accelerators Mark I, II, and II-A, Mark III, and Mark CA-1 in tanks "A", "B", and "C", respectively, at the Plasma Laboratories of Northrop Corporation; Mr. C. F. Knopp and Mr. L. R. Dawson, who assembled the spectroscopic equipment and obtained useful spectroscopic data; and the other members of the staff of the Plasma Laboratories of Northrop Corporation, including Dr. J. R. Bodoia, Dr. P. D. Lenn, Dr. C. L. Maldonado, Dr. J. J. McClure, Dr. H. N. Olsen, Dr. J. B. Wilkinson, Mr. G. L. Hamilton, and Mr. D. Ward, for their comments.

Finally, I want to thank Professor A. B. Cambel and Mr. R. W. Springer for making the presentation of this paper possible.

REFERENCES

1. Polovin, R. V., and Cherkasova, K. P., "Magnetohydrodynamic Description of a Plasma", *Zhurnal Tekhnicheskoi Fiziki*, **32**, 6, 649–656 (June, 1962) [translation in Soviet Physics—*Technical Physics*, **7**, 6, 475–479 (December, 1962)].
2. Liubimov, G. A., "On the Form of Ohm's Law in Magnetohydrodynamics", *Prikladnoi Matematika i Mekhanika*, **25**, 4, 611–622 (July, 1961) [translation in Soviet Mathematics: *Applied Mathematics and Mechanics*, **25**, 4, 913–929 (February, 1962)].
3. Yoshikawa, S., and Rose, D. J., "Anomalous Diffusion of a Plasma Across a Magnetic Field", *Phys. Fluids*, **5**, 3, 334–340 (March, 1962).
4. Bohm, D., Chapter 3 in *The Characteristics of Electrical Discharges in Magnetic Fields*, ed. A. Guthrie and R. K. Wakerling (New York: McGraw-Hill, 1949).
5. Cowling, T. G., *Magnetohydrodynamics* (New York: Interscience Publishers, 1957); also, "The Electrical Conductivity of an Ionized Gas with Applications to the Solar Atmosphere", *Proc. Roy. Soc. (London) A.*, **183**, 453–478 (1945).
6. Schluter, A., "Dynamik des Plasmas I", *Z. Naturforschung*, **5a**, 72 (1950); **6a**, 73–78 (1951).
7. Lehnert, B., "Plasma Physics on Cosmical and Laboratory Scale", *Suppl. Nuovo Cimento*, Series 10, **13**, 1, 59–110 (1959).
8. Demetriades, S. T., "Experiments with a High Specific Impulse Crossed-Field Accelerator", *NSL–62–130*, Northrop Space Labs, Northrop Corp., Hawthorne, California; presented at Third Symposium on Engineering Aspects of Magnetohydrodynamics, University of Rochester, March 28–30, 1962 (to be published by Gordon and Breach Science Publishers, Inc.).
9. Demetriades, S. T., Hamilton, G. L., Ziemer, R. W., Jarl, R. W., and Lenn, P. D., "Three-Fluid Non-Equilibrium Plasma Accelerators, Part I", *ARS Preprint No. 2375–62*, ARS Electric Propulsion Conference, Berkeley, California, March 14–16, 1962; published in *Progress in Astronautics and Aeronautics*, ed. E. Stuhlinger ["AIAA Series" (New York: Academic Press, Inc., 1963)], **9**, 461–511.
10. Demetriades, S. T., "Novel Method of Measurement of Plasma Properties by Momentum-Change Techniques", *Phys. Fluids*, **4**, 12, 1569–1570 (December, 1961).
11. Demetriades, S. T., and Lenn, P. D., "Electrical Discharge Across a Supersonic Jet of Plasma in Transverse Magnetic Field", *AIAA Journal*, **1**, 1, 234–236 (January, 1963).
12. Demetriades, S. T., and Ziemer, R. W., "Energy Transfer to Plasmas by Continuous Lorentz Forces", *ARS Preprint 2002 61*, IVth Biennial Gas

Dynamics Symposium, Northwestern University, Evanston, Illinois (August 23–25, 1961); published in *Magnetohydrodynamics*, eds. A. B. Cambel, T. P. Anderson, and M. M. Slawsky (Evanston: Northwestern University Press, 1962), 185–205.

13. Lenn, P. D., Bodoia, J. R., Ward, D. L., Hamilton, G. L., and Demetriades, S. T., "Three-Fluid Non-Equilibrium Plasma Accelerators, Part II", *AIAA Preprint No. 63047*, AIAA Electric Propulsion Conference, Colorado Springs, Colorado, March 11–13, 1963 (to be published).
14. Demetriades, S. T., *et al.*, "Experimental and Analytical Investigations of Crossed-Field Plasma Accelerators", NSL–62–113–10, Northrop Space Labs., Northrop Corporation, Hawthorne, California (June, 1963).
15. Blackman, V. H., and Sunderland, R. J., "The Experimental Performance of a Crossed-Field Plasma Accelerator", *ARS Preprint No. 2633–62*, ARS 17th Annual Meeting and Space Flight Exposition, Los Angeles, California, November 13–18, 1962.
16. Burkhard, K., Devine, R., Hogan, W. T., and Kessler, R., "Experimental Investigation of a Crossed-Field Accelerator for High-Enthalpy Re-entry Simulation", IVth Symposium on Engineering Aspects of Magnetohydrodynamics, University of California, Berkeley, California, April 10–11, 1963.
17. Burkhard, K., Devine, R., Hogan, W. T., and Kessler, R., "A Continuous Crossed-Field Gas Heater for Re-entry Simulation", *AIAA Preprint No. 63–203*, AIAA Summer Meeting, Los Angeles, California, June 17–20, 1963.
18. Russel, G. R., Byron, S., and Bortz, P. I., "Performance and Analysis of a Crossed-Field Accelerator", *AIAA Preprint No. 63–005*, AIAA Electric Propulsion Conference, Colorado Springs, Colorado, March 11–13, 1963.
19. Denison, M. R., "A Two-Dimensional Weak Interaction Theory for Crossed-Field Accelerators", *Research Note RN–12*, Electro-Optical Systems, Inc., Pasadena, California (April, 1963); also "Physical Phenomena Associated with Magnetogasdynamic Acceleration", co-author R. W. Ziemer, AFOSR Contract No. AF 49(638)–1063, presented at Sixth Annual AFOSR Contractors' Meeting on Ion and Plasma Acceleration, Northwestern University, Evanston, Illinois, March 14–15, 1963.
20. Kantrowitz, A., AVCO-Everett Research Laboratory, Everett, Massachusetts, private communication.
21. Wood, G. P., NASA/Langley Research Center, Langley, Virginia, private communication.
22. Demetriades, S. T., "Experimental Magnetogasdynamic Engine for Argon, Nitrogen and Air", Second Symposium on Engineering Aspects of Magnetohydrodynamics, Philadelphia, Pa., March 9–10, 1961; *Engineering Aspects of Magnetohydrodynamics*, eds. C. Mannal and N. W. Mather (New York: Columbia University Press, 1962), 19–44.
23. Thiene, P. G., Chambers, J. E., and Jaskowsky, W., "Experimental Investigation of the Behavior of an Arc Positive Column in the Presence of Forced Convection", *Report No. T–4TN031–334*, AFOSR–682, Contract No. AF 49(638)–334, ASTIA Document No. AD–260648, Plasmadyne Corp., Santa Ana, California (April 29, 1961).
24. Warder, R. C., Jr., Northwestern University, Evanston, Illinois, private communication, also "Microwave Diagnostics of Arc Heated Argon Plasma Flows" (Ph. D. thesis, Northwestern University, April, 1963), NU–GDL Report No. B–1–63.
25. Demetriades, S. T., "Plasma Propulsion, Parts I and II", *Astronautics*, **7**, 3 and 4, 21 and 40 (March and April, 1962).

26. Kontaratos, A. N., Rocket Power, Inc., Research Laboratories, Pasadena, California, private communication.
27. Hurwitz, H. Jr., Kilb, R. W. and Sutton, G. W., "Influence of Tensor Conductivity on Current Distribution in a MHD Generator", *J. App. Phys.*, **32**, 2, 205–216 (February, 1961).

17. L. J. Krzycki, H. M. Larsen, and W. M. Byrne, Jr.: *Magnetohydrodynamic Power Generation from a Supersonic Rocket Exhaust*

A theoretical and experimental feasibility investigation of an MHD electrical power generator using a supersonic rocket exhaust (Mach 2.3, 2160 m/sec) as the working fluid was conducted at the Naval Ordnance Test Station, China Lake, California. Theoretical calculations of thermal ionization and gas conductivity, using a digital computer, indicated that a supersonic gas source had definite advantages over a subsonic one. Experimental firings of a liquid rocket-MHD power generator proved the feasibility of the concept and indicated areas of developmental difficulty.

INTRODUCTION

Theoretical and experimental studies have indicated that the MHD generator, in which electrical power is generated without the use of moving parts from the magnetohydrodynamic interaction of a partially-ionized gas and an external magnetic field, is one of the few systems potentially capable of satisfying the unique power requirements of present and future weapons systems (**1**). Further study indicated that supersonic MHD power generation using a solid-fuel plasma source would be an ideal method of generating large amounts of electrical energy for short periods of time. MHD power generation systems were envisioned which had high power densities, long shelf life, and rapid start capabilities.

At the time the project reported herein was initiated, little theoretical, and no experimental, work had been reported on MHD power generation from a supersonic gas stream. It was deemed advisable, therefore, to determine by means of a theoretical and experimental program at least some of the difficulties associated with supersonic MHD power generation.

THEORY

MHD POWER GENERATION

The mechanism of MHD power generation is similar to that of conventional rotating generators, in that an electrical conductor is moved across a magnetic field and a potential difference is induced along the conductor. In the conventional mechanical generator, an external power source causes a metallic conductor to

ED. NOTE: Mr. Krzycki, Mr. Larsen, and Mr. Byrne, are with the Propulsion Development Department, U.S. Naval Ordnance Test Station, China Lake, California.

rotate in a magnetic field. In the MHD generator the metallic conductor is replaced by an ionized gas and the external power source by a pressure differential. The gas flows through a region which is subjected to a strong magnetic field perpendicular to both the gas flow and to electrodes in contact with the moving, ionized gas. An external load connected to the electrodes draws energy from the gas stream which in turn suffers a reduction of enthalpy as a result of the power extraction. Figure 1 shows a simplified rocket-MHD (RMHD) generator in which a chemical rocket engine furnishes the partially-ionized gas to the MHD power channel.

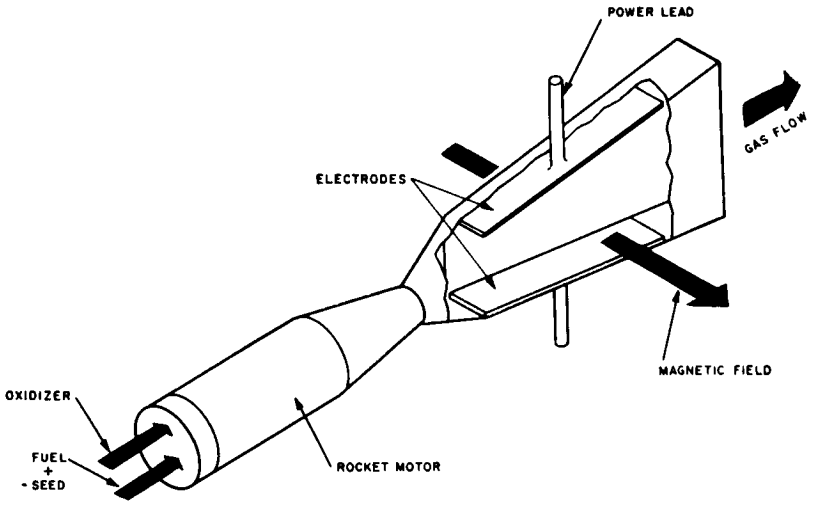

FIGURE 1. Schematic diagram of RMHD generator.

The equations describing the operation of MHD power generators are well documented; see (**2**), for example. For initial engineering calculations, the following equations can be used (**2**).

$$\begin{aligned} &(a) \quad V_{oc} = uBW \\ &(b) \quad I_{sc} = \sigma uBDL \\ &(c) \quad \Pi = \frac{\sigma u^2 B^2}{4} \end{aligned} \tag{1}$$

The electrical conductivity of the gas, σ, is a function of both pressure and temperature for a given chemical composition. The electrical conductivity of seeded equilibrium combustion gases rapidly reaches a maximum on the order of tens of mhos per meter. The magnetic field, B, is a separate variable which, in most cases, can be varied independently of the gas. (As we shall see later, the strength of the magnetic field can affect the gas conductivity.) The velocity of the fluid may be widely varied depending upon whether the flow is subsonic or supersonic. The dependence of the maximum generated power density on the term u^2 means that a reduced electrical conductivity due to the expansion of the gas can be more than compensated for by the increased gas velocity associated with that expansion. For this reason, MHD power generation using a supersonic combustion gas is very attractive from the point of high generated power density.

THERMAL IONIZATION

To obtain the functional dependence of σ on the thermodynamic variables and constitution of the gas, it was first assumed that the electric current in the gas was due to the motion of free electrons under the influence of the electric field,

and further, that these electrons were produced by thermal ionization of seed gas atoms. An expression was required which related the equilibrium number density of electrons to the neutral particle number density, in terms of the thermodynamic variables of the gas. The equilibrium degree of thermal ionization of a gaseous species is given by the Saha equation (**3**, **4**)

$$\log \frac{Px^2}{1-x^2} = \frac{23070\phi}{4.573T} + 2.5 \log T + \log \frac{g_i g_e}{g_0} - 6.491 \tag{2}$$

where x is the degree of ionization, P is the gas pressure in atmospheres, ϕ is the ionization potential of the species, and T is the Kelvin temperature. The constants g_i, g_e, and g_0, refer to the multiplicity of energy states of the ion, electron, and neutral atom, respectively. Suitability arguments have been formulated which justify the application of the Saha equation to a complex system such as a combustion product gas. In the temperature and density regime typical of chemical rocket engines, the degree of ionization of the gas is relatively low; however, with the addition of a small amount of an alkali metal or its salt, the number density of electrons can be greatly increased. In this case, the Saha equation can be written

$$\ln \frac{x^2}{1-x^2} = \frac{k_1}{T} + 2.5 \ln T - \ln P_s + k_2 \equiv \eta \tag{3}$$

where $k_1 = -1.1616\phi \times 10^4$, $k_2 = -14.946$, and P_s is the partial pressure of the monatomic form of the seed gas in atmospheres. For the case of macroscopic electrical neutrality, equation (3) can be solved for the degree of ionization of the alkali metal seed

$$n_e/n_s = (e^{-\eta}+1)^{-1/2} = x \tag{4}$$

where n_s is the number density of seed atoms initially present in the gas mixture. The particle density of species j is related to its partial pressure by

$$n_j = P_j/kT \tag{5}$$

where k is the Boltzmann constant. Implicit in equation (5) is the assumption of a Maxwellian velocity distribution—a valid assumption for the collision-dominant case of ordinary chemical rocket processes. If the molar concentration of species j is denoted by X_j, equation (5) can be rewritten as

$$n_j = k_3 X_j/T \tag{6}$$

where k_3 takes the constant value $1.013(\mathrm{AAA}) \times 10^5/k$. (AAA) is a conversion factor for molar concentration to partial pressure and is printed on the output sheets of the NOTS Propellant Evaluation Program (**5**)†. Equations (4) and (6), when combined, give the free electron density of the gas as

$$n_e = xk_3 X_s/T \tag{7}$$

where X_s is the molar concentration of monatomic seed material.

ELECTRICAL CONDUCTIVITY

The d-c electrical conductivity, σ, of a gaseous mixture can be written as (**6**, **7**)

$$\sigma = \frac{4.5 \times 10^{-12} n_e}{T^{1/2} \sum_j n_j Q_j} \tag{8}$$

† The NOTS Propellant Evaluation Program is a computer program (IBM 7090) used to determine the thermodynamic parameters of a propellant combination. The temperature, enthalpy, entropy, ratio of specific heats, molecular weight, and gram-moles of the constituents at equilibrium are calculated for both the combustion chamber and the exhaust. The expansion process assumes shifting equilibrium and dissociation of the combustion products.

where Q_j is the elastic scattering cross section of species j with electrons. The various terms involved in the summation refer to the interaction of electrons with electrons, ions, seed atoms, and typical combustion-product molecules. For a macroscopically neutral plasma, equation (8) can be rewritten with the aid of equations (4) and (5) as

$$\sigma = \frac{4.5 \times 10^{-12}}{T^{1/2}(Q_e + Q_i + Q_s/x + PQ_0/xP_s)} \tag{9}$$

where the subscripts e, i, s, and 0 refer respectively to electrons, ions, seed atoms, and typical combustion molecules.

The electron–electron cross section as given by Fay (**7**) is

$$Q_e = 2.1 \times 10^{-10} T^{-2} \ln \left[\frac{1.24 \times 10^7 T^{3/2}}{n_e}\right] \tag{10}$$

Using equation (7) this may be written as

$$Q_e = 2.1 \times 10^{-10} T^{-2} \ln \left[\frac{1.24 \times 10^7 T^{5/2}}{x k_3 X_s}\right] \tag{11}$$

The electron–ion cross section (**8**) can be written in c.g.s. units as

$$Q_i = 8.1 b^2 \ln (h/b) \tag{12}$$

where h is the Debye length† and b is the impact parameter for 90° scattering‡. By the same method as was used to obtain equation (11), and converting to m.k.s. units, the cross section can be written as

$$Q_i = 1.25 \times 10^{-10} T^{-2} \ln \left[\frac{1.54 \times 10^{14} T^4}{x k_3 X_s}\right] \tag{13}$$

The d-c electrical conductivity of seeded rocket exhaust gases is given by equation (9) in terms of the thermodynamic variables of the gas. The interaction terms, Q_e and Q_i, are given in terms of the thermodynamic variables of the gas by equations (11) and (13). Terms Q_s and Q_0 are constants. For the electron energy range involved, a value of 4×10^{-18} square meters may be assumed for Q_s (**9**) while a representative value of Q_0 would be 2×10^{-19} square meters (**7**).

MAGNETIC FIELD EFFECTS

The design of MHD generators using strong magnetic fields is complicated by the fact that the electrical conductivity is not merely a scalar function of the temperature and pressure, but is also a tensor function of the magnetic field. This tensor quality reduces σ in a direction perpendicular to the magnetic field (**10**) as

$$\sigma_\perp = \frac{\sigma}{1 + \omega^2 \tau^2} \tag{14}$$

where ω is the gyromagnetic frequency of the electron (a function of B only) and τ is the electron collision period (a function of the thermodynamic variables of the gas). In addition, the current density in the gas is no longer parallel to the electric field (Hall effect), but has a component along the axis of the generator channel.

† $h = (kT/4\pi n_e e^2)^{1/2}$
‡ $b = e^2/3kT$

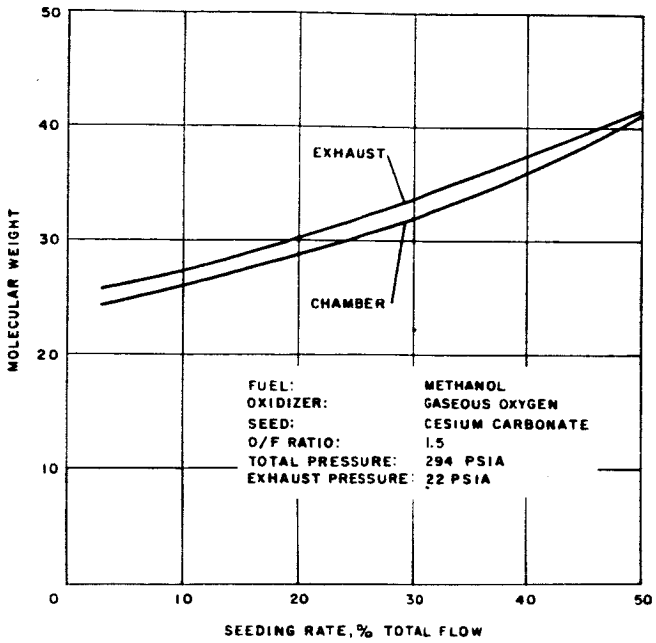

FIGURE 3. Variation of molecular weight with seeding rate.

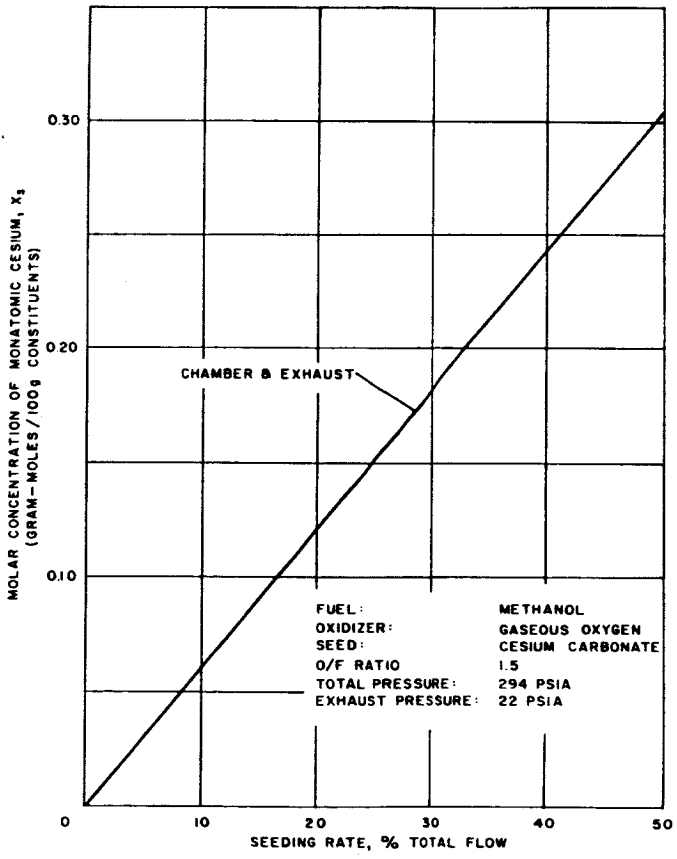

FIGURE 4. Molar concentration of monatomic cesium for various seeding rates.

The value of $\omega\tau$ is given by

$$\omega\tau = 1.3 \times 10^3 (B/P)(T)^{1/2} \tag{15}$$

The derivation of this relationship is given in **Appendix A.** A constant value for the gas-particle collision cross section of 3×10^{-19} square meters (**6**) has been chosen for the energy range and species appropriate to the systems under consideration.

MICROWAVE DIAGNOSTICS

For an experimental verification of the programmed conductivity expression, a series of microwave experiments was performed to determine the electron density in the supersonic exhaust of the rocket engine which was used in the power generation experiments. The results of this study, which indicated good agreement with the electron densities predicted by the programmed expression, are presented in (**11**).

THEORETICAL CALCULATIONS

The equations describing the thermal ionization and electrical conductivity of seeded combustion products were programmed for digital computer (IBM 7090) solution. Figures 2 through 9 show the variation of some of the parameters and equations discussed under **THEORY**. These figures were theoretically determined using conditions that were typical of those used in the experimental investigation. Figures 2 through 9 are all plotted against a common abscissa which indicates a wide range of cesium carbonate seed rates. Figures 10 and 11 are plots of the electron density and electrical conductivity at the entrance of the MHD channel for conditions of interest other than those actually used in the power-generator experiments. A sample calculation of the thermal ionization and electrical conductivity in a rocket engine exhaust is presented in **Appendix B.**

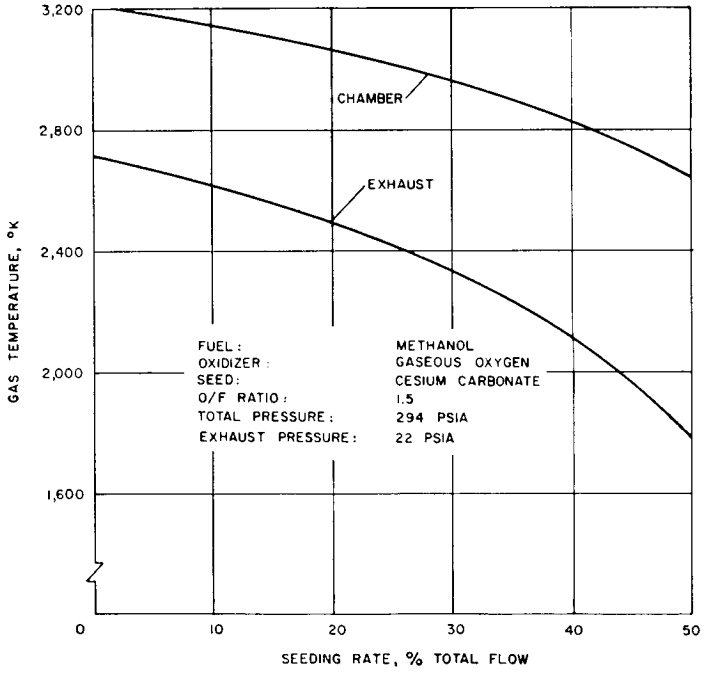

FIGURE 2. Variation of gas temperature with seeding rate.

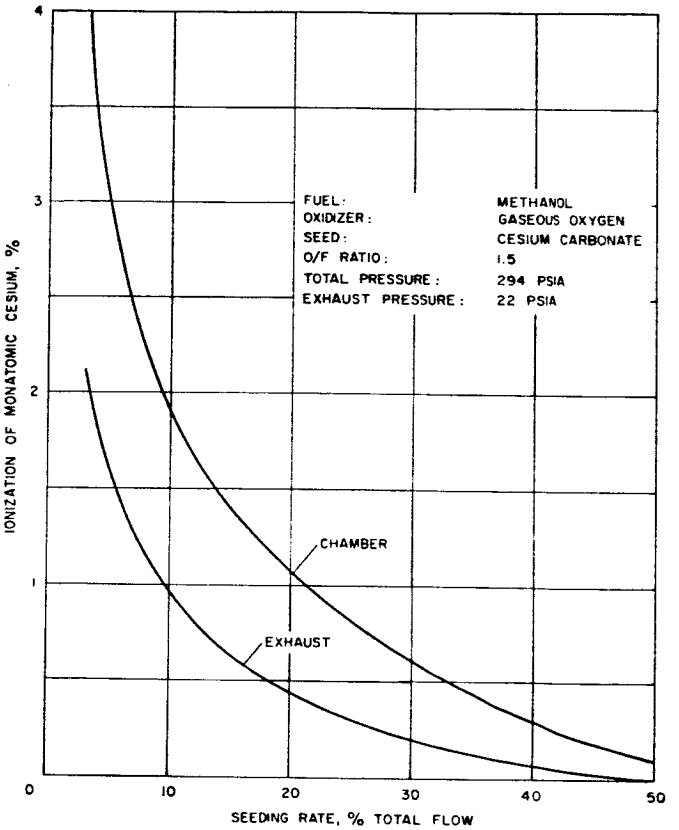

FIGURE 5. Per cent ionization of monatomic cesium for various seeding rates.

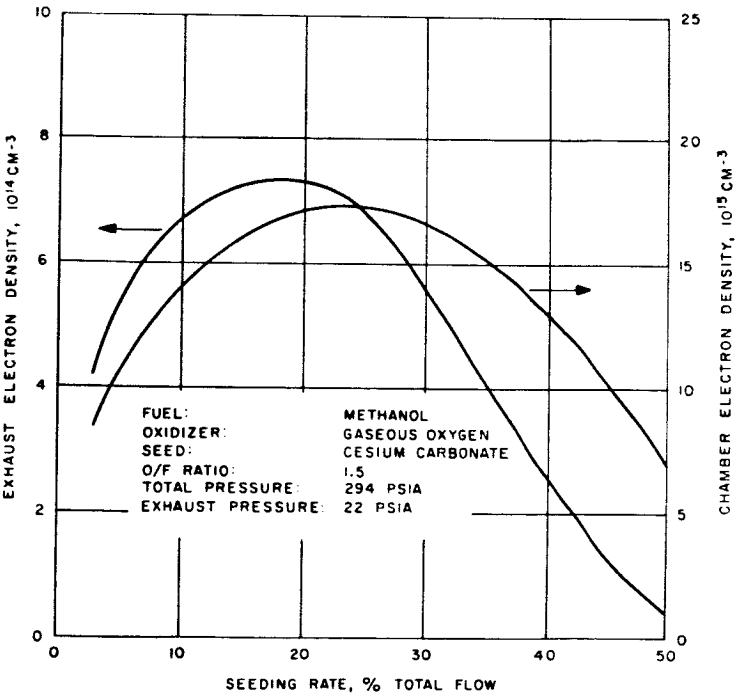

FIGURE 6. Electron density versus seeding rate.

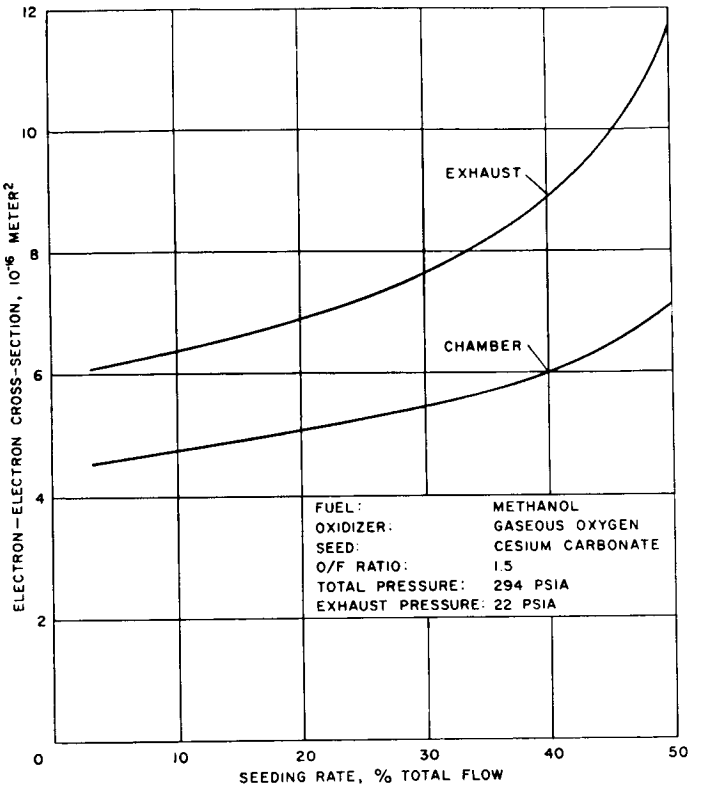

FIGURE 7. Electron–electron collision cross-section versus seeding rate.

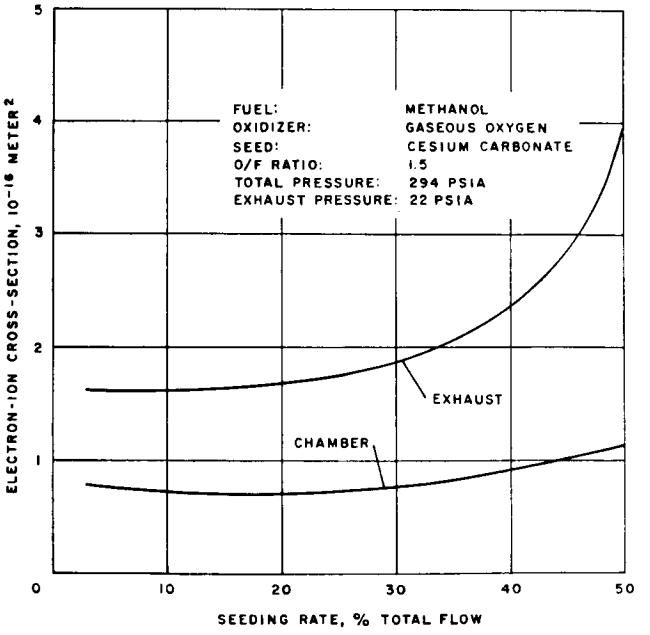

FIGURE 8. Electron–ion collision cross-section versus seeding rate.

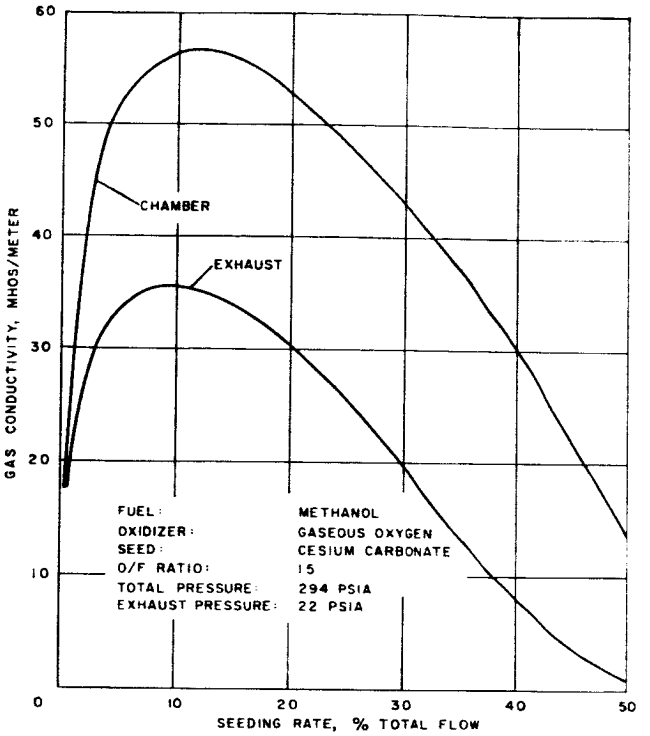

FIGURE 9. Electrical conductivity versus seeding rate.

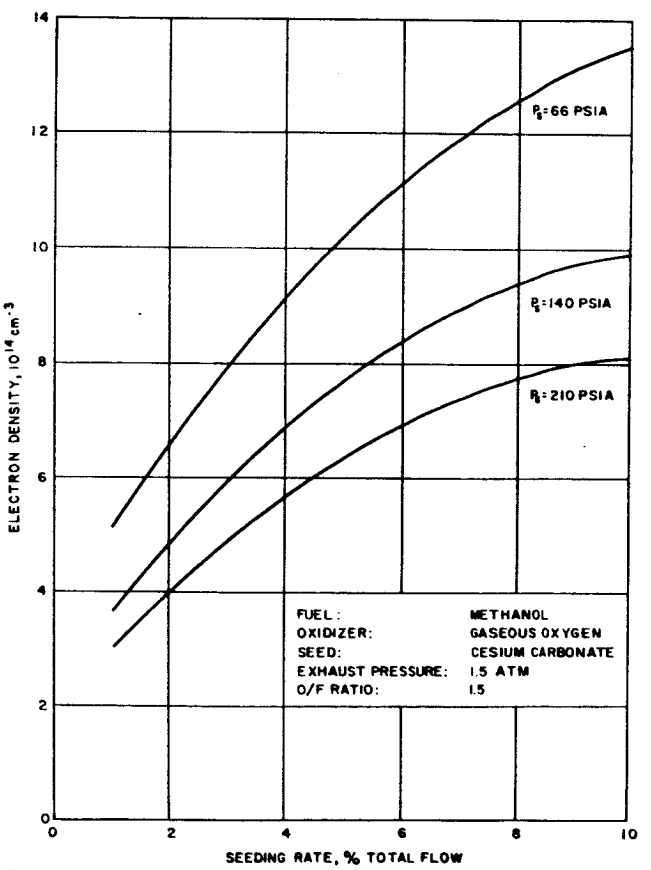

FIGURE 10. Electron density at nozzle exit versus seeding rate for various chamber pressures.

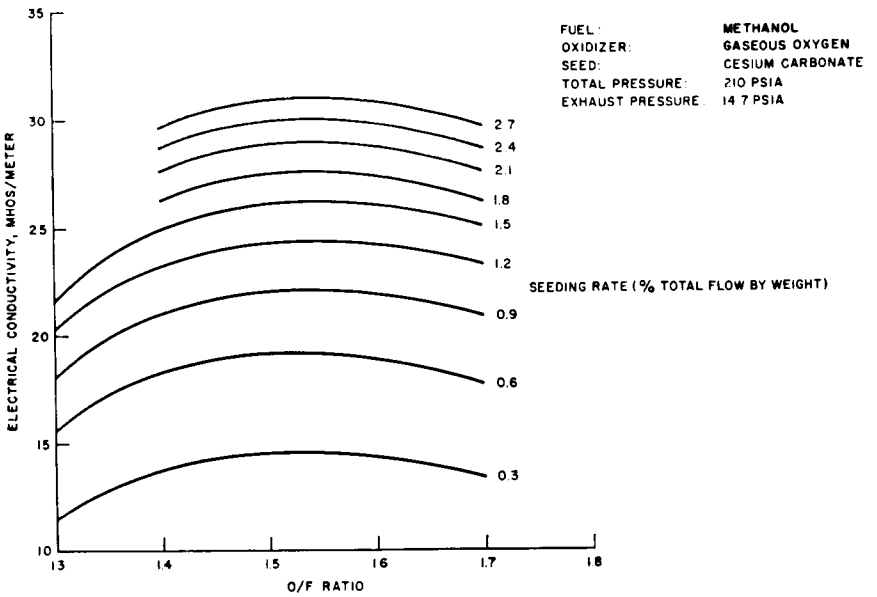

FIGURE 11. Electrical conductivity at nozzle exit versus o/f ratio for various seeding rates.

POWER GENERATION APPARATUS

LIQUID-FUEL ROCKET ENGINE

The NOTS rocket-MHD experiments utilized a small research rocket engine which burned gaseous oxygen and methyl alcohol. Seed material was caesium carbonate which was dissolved in the alcohol prior to the experiment. The NOTS Propellant Evaluation Program (**5**) was used to calculate the thermodynamic properties of the rocket combustion process.

The nozzle exit Mach number (the MHD channel entrance Mach number) was selected on the basis of an optimization study employing the NOTS Propellant Evaluation Program and the NOTS Electrical Conductivity Program. The results of this optimization study are shown in Figures 12 and 13. The goal of the study was to determine the channel Mach number and seeding rate which would give the highest generated electrical power density based on equation (1c). The Mach number thus chosen was 2.3 and the seeding rate was eight per cent cesium carbonate by weight of the total propellant and seed flow through the generator.

The initial design of the RMHD rocket engine (design "A") used a nozzle with a 22-degree expansion half-angle. This abnormally large angle was necessary because of the fabrication technique used in the construction of the square-throat, rectangular-exit nozzle. Flow separation and extreme erosion of the power-channel-insulating side plates were experienced with this nozzle. However, numerous tests were conducted and electrical power was generated through its use. This engine was also used in the microwave diagnostics study (**11**).

Because of the flow separation and channel erosion experienced with engine design "A", an advanced design was formulated (design "B") using a different fabrication and assembly technique which reduced the expansion half-angle of the nozzle to 10 degrees. A constant-area, water-cooled, flow-straightener section, 1 inch long, was attached to this nozzle exit, turning the flow into a parallel

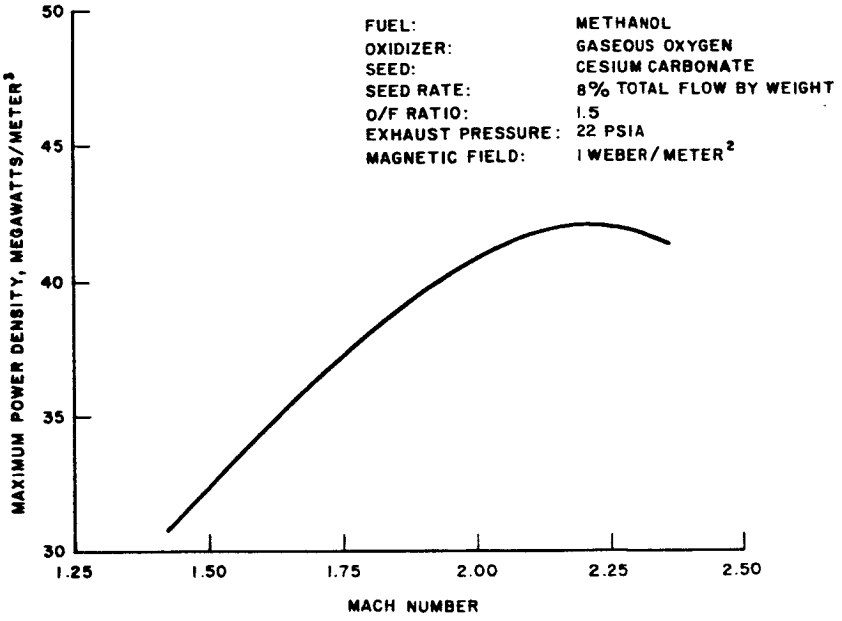

FIGURE 12. Maximum generated power density versus Mach number.

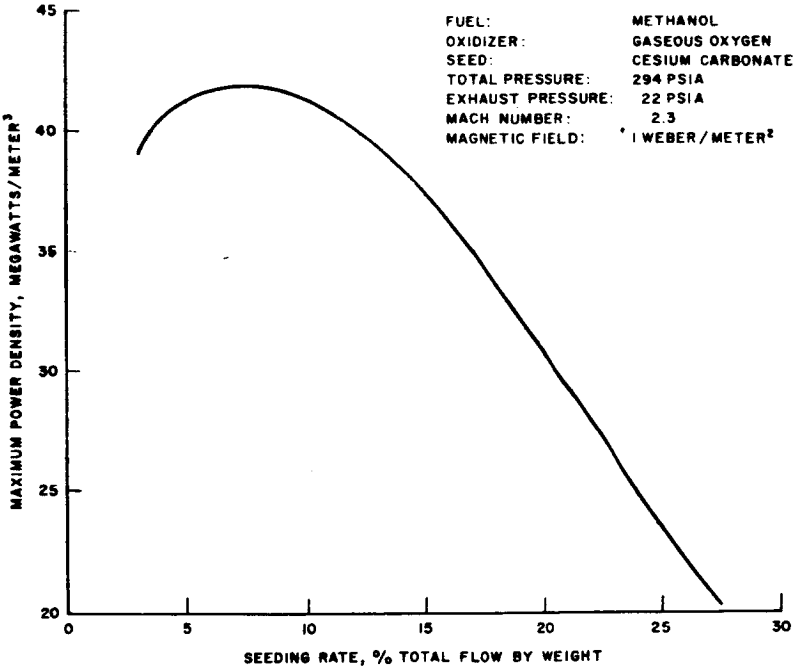

FIGURE 13. Maximum generated power density versus seeding rate.

stream. A nozzle-exit pressure line for measurement of the static pressure immediately upstream of the power channel entrance was attached to the flow straightener section. This engine design resulted in improved flow characteristics and reduced the erosion problem of the channel-insulating side wall.

Specifications and operating parameters for the water-cooled copper rocket engine were:

Sonic throat	0.50×0.50 inches (square)
Nozzle exit	0.50×1.35 inches (rectangular)
Combustion chamber pressure	294 psia
Combustion chamber temperature	3159°K (8 per cent seed rate)
Nozzle exit pressure	22 psia
Nozzle exit temperature	2550°K
Nozzle exit Mach number	2.3 (2160 m/sec)
Total propellant flow	0.42 lb/sec
Cooling water flow	2–3 lb/sec
Energy loss to coolant	60 kilowatts

The injector used for all RMHD rocket engine operations was of the impinging-stream type with nine triplet combinations. Injector and combustion chamber lifetimes were normally measured in terms of hours of actual firing time.

POWER CHANNEL

The NOTS RMHD generator used a constant-area supersonic power-extraction channel. This structure presented a great number of material and operational problems. Both continuous and segmented electrode configurations were used. The experimental results discussed in this report are from the continuous electrode configuration only. Several designs of segmented electrodes were tried. Each design was rejected after hot firings because of failure to maintain either electrical or structural integrity over even a short time period.

The RMHD power channel consisted of two water-cooled, non-magnetic stainless-steel, backing plates supporting the electrically-insulating material. This assembly formed the walls of the channel normal to the applied magnetic field. The electrodes, which were fitted between the side walls, were water-cooled copper. The electrode surface exposed to the hot gas flow was knurled to break up the boundary layer; it was hoped that this would permit better contact between the electrode and the ionized gas. The electrode area was 0.50×4.2 inches. The short generator length was determined by the length of the magnet-pole pieces and did not represent any appreciable fraction of the total generator length that might have been used had a more suitable magnet been available to the project. Immediately downstream of the power generating section the flow was rapidly expanded to lower its conductivity and reduce end losses. Electrode-cooling water was dumped into the hot exhaust at the end of the power channel. Electrical connections to the electrodes were made through the electrode water coolant lines. The channel was assembled with nonmagnetic stainless-steel cap screws and micarta insulating sleeves. Epoxy resins and Sauereinsen high-temperature cements proved helpful in channel component assembly and sealing, and appeared to endure the operational environment well.

Magnesium oxide (MgO) in two different grades and Vycor glass in rolled form were used with partial success as materials for the insulating side walls of the power channel. These walls were required to have electrical resistance orders of magnitude greater than the ionized gas resistance yet they were directly exposed to the hot (2550°K), high-velocity (2160 m/sec) gas stream.

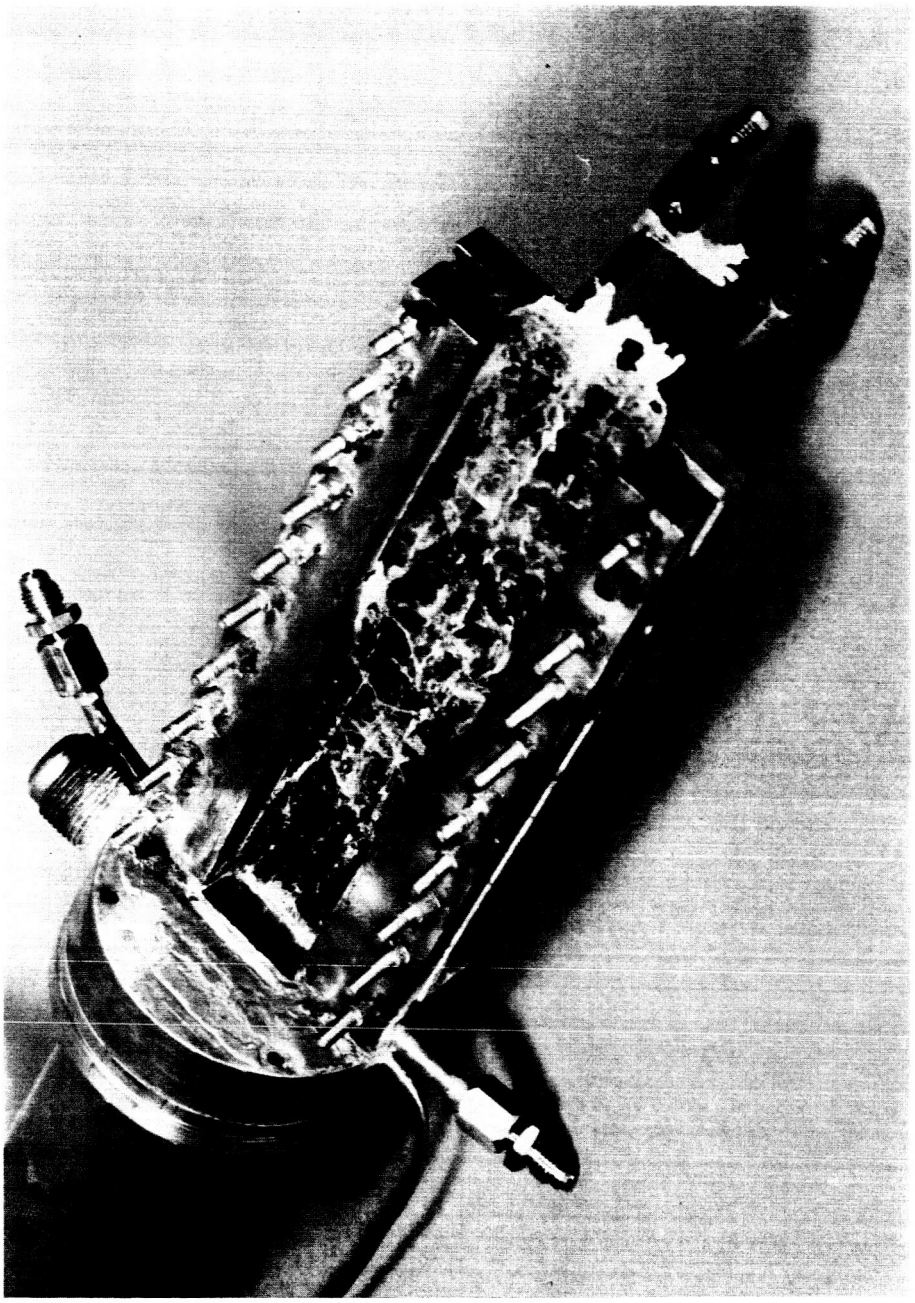

FIGURE 14. RMHD channel with Vycor insulating plates after 41-second firing.

Norton Magnorite fused MgO in $\frac{1}{8}$- and $\frac{1}{4}$-inch-thick slab form and Lofero HM MgO brick (cut and ground to the required size for use in the power channel) in $\frac{1}{4}$-inch-thick slab form were the two MgO materials used. In the initial experiments the $\frac{1}{8}$-inch-thick Magnorite plates were used but this thickness was found difficult to handle in assembling the power channel because of its brittleness. Thereafter, all MgO insulating plate thicknesses were $\frac{1}{4}$-inch. The Lofero HM brick was

97 per cent MgO with small amounts of other oxides. Results from the power generation runs indicated that the fused MgO was able to endure the hot, high-velocity gas stream better than the 97 per cent MgO.

Both $\frac{1}{8}$- and $\frac{1}{4}$-inch-thick Corning Vycor glass plates were used in the generator experiments. Again, because of assembly difficulties with the $\frac{1}{8}$-inch thickness in

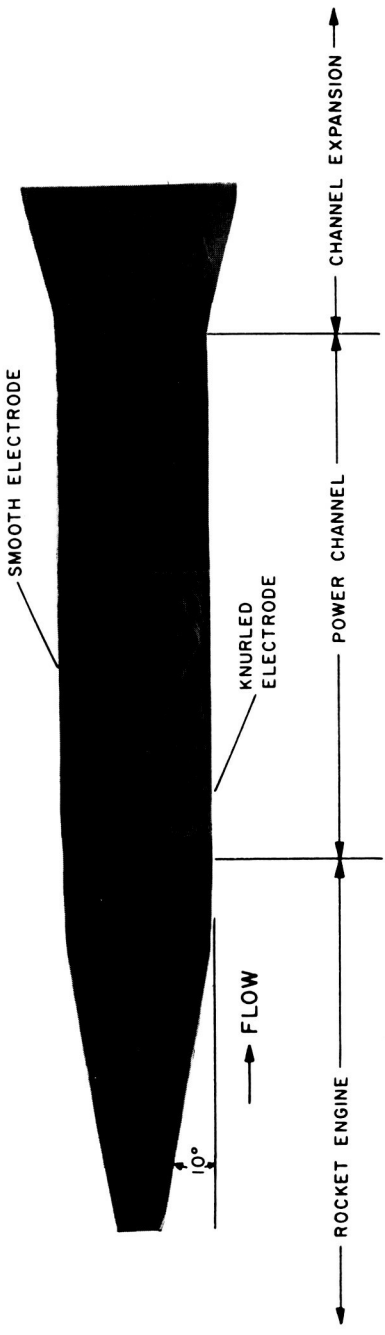

FIGURE 15. RMHD channel flow visualization.

the initial experiments, all succeeding runs were made with the $\frac{1}{4}$-inch thickness. The Vycor glass had a tendency to flow during the experiment and after a firing of 30 or more seconds about half of the $\frac{1}{4}$-inch-thick plate would be gone. Figure 14 is a photograph of the RMHD power channel attached to engine design "B" after a power generation run of 41 seconds. Vycor glass was used as the insulating material and the roughened surface and flow of glass is noticeable in the photo.

FLOW VISUALIZATION

The flow pattern occurring within the power channel of the RMHD generator was of interest because of the possibility of shocks due to the supersonic gas stream. Subsonic-flow MHD power generators are not subject to this phenomenon, although flow patterns through them also are important. Spark shadowgraph photographs were taken of a gaseous nitrogen flow through transparent-walled devices which duplicated in dimension and configuration the RMHD power channel with continous electrodes. In the cold flow studies the continuous electrode configuration was used with one electrode surface knurled while the other remained a smooth, machined surface. Nitrogen plenum conditions were adjusted so that the channel static pressure matched that experienced in the hot-fired experiments. The cold flow channel Mach number was 2.5, while the hot flow case was 2.3. Figure 15 is a composite of three spark shadowgraph photographs indicating the shock structure in the RMHD channel with engine design "B". The knurled electrode surface clearly perturbs the flow and yields the desired mixing action. Comparison of the cold-flow shock locations and the erosion pattern observed on the MgO and Vycor insulating plates which had been subjected to hot firings indicated a striking similarity. The conclusion to be made from the flow-visualization studies is that contoured nozzles designed to give shock-free and parallel flow at the nozzle exit are required for acceptable flow in a supersonic MHD power channel.

MAGNET

An uncooled d-c laboratory magnet with adjustable pole gap was used in the NOTS RMHD experiment. The limitations imposed because of the small field volume of the magnet were many. Foremost was the influence on power channel design. When the $\frac{1}{8}$-inch-thick insulating plates were used in channel fabrication, it was possible, by operating the magnet at overload conditions, to maintain a 10,000-gauss field across the power channel. However, when the $\frac{1}{4}$-inch-thick plates were used, this field was reduced to 5700 gauss.

LOAD ELEMENT

The load element for the RMHD generator was an air-cooled, 16-ohm, manually-operated rheostat. The potential across it and the current through it were recorded on an optical galvanometer oscillograph. A wattmeter was used to determine the maximum power point for the generator when it was under load.

POWER GENERATION EXPERIMENTS

TEST ARRANGEMENT

The RMHD experiments were performed in the magnetofluids experimental bay at the Applied Research Laboratory, NOTS.

Gaseous oxygen was regulated by remotely-loaded dome regulators. The flow was controlled by two remotely-operated ball valves; flow rate was measured with an ASME thin-plate orifice. Differential pressure was measured by a high-pressure manometer.

Methyl alcohol and cesium carbonate seed were premixed before the experiment and then stored in a high-pressure, stainless-steel fuel tank. The fuel was pressurized by gaseous nitrogen regulated by remotely-loaded dome regulators. Fuel flow rate was measured with an ASME thin-plate orifice and a mercury manometer. An empirical calibration curve was used for the liquid fuel flow (with seed material), while flow curves were calculated for the gaseous oxidizer. All pertinent differential and line pressures were photographically recorded from a gauge panel. All dome handloaders and valve controls were located in one console in full view of the gauge panel, so that chamber pressure and oxidizer-fuel ratio could be monitored —and controlled—during a run.

Ignition of the primary propellants was accomplished by heating a carbon rod to incandescence in an oxygen and propane flame inside the chamber. When the rod was incandescent, the primary propellant flow was initiated. The hot carbon rod ignited the propellants and was then blown from the engine by the exhaust.

The rocket engine test stand was an integral unit which also contained a support for the MHD power channel. An over-head view of this experimental arrangement is shown in Figure 16.

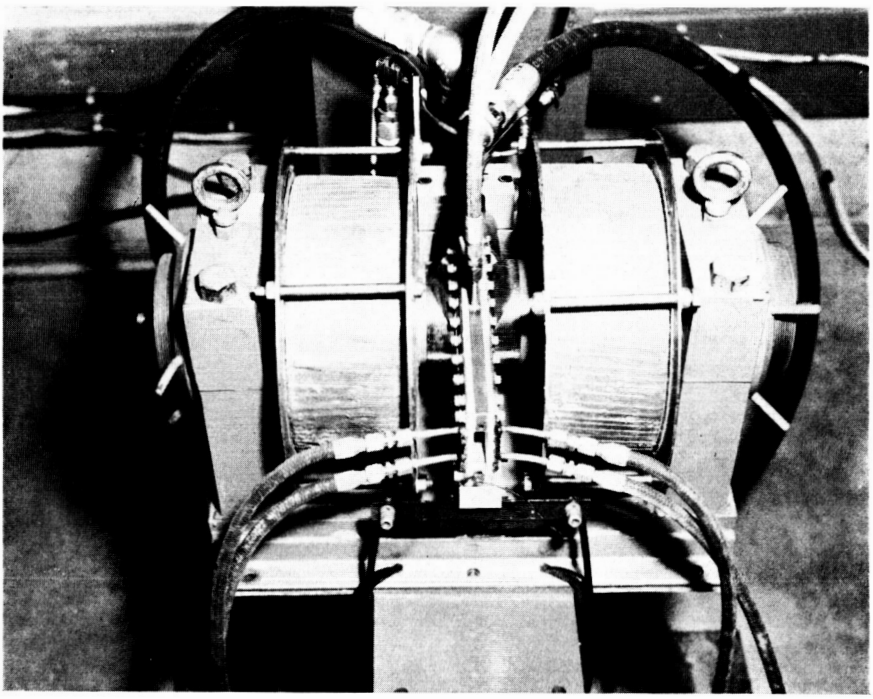

FIGURE 16. RMHD generator and magnet.

EXPERIMENTAL PROCEDURE

The usual operating procedure for an RMHD power generation run follows. With all facility equipment and recording apparatus operational, the cooling water flow for the rocket engine, the backing plates, and the electrodes was started.

The magnet current was gradually increased to operating value while, simultaneously, the pilot flows of propane and oxygen were ignited and the carbon rod heated to incandescence. The oscillograph was started and the primary propellants were injected into the combustion chamber. After primary-propellant ignition the chamber pressure would build smoothly to the desired value in about four seconds. During this initial phase only the open-circuit voltage was being recorded. Small changes were made in the propellant flow rates to bring chamber pressure and oxidizer-fuel ratio to design values. At this point the RMHD generator was alternately switched from the open-circuit condition to the short-circuit condition. Then the load resistor was cycled through its full range to obtain a voltage-current characteristic. When maximum power conditions were obtained (as indicated by a wattmeter) the motor-generator powering the magnet was cut and the magnet current allowed to slowly decrease. This entire test procedure was repeated for the duration of the firing. When the run was terminated an automatic nitrogen flush system purged the rocket engine and power channel. A photograph of the RMHD generator during a hot firing is shown in Figure 17.

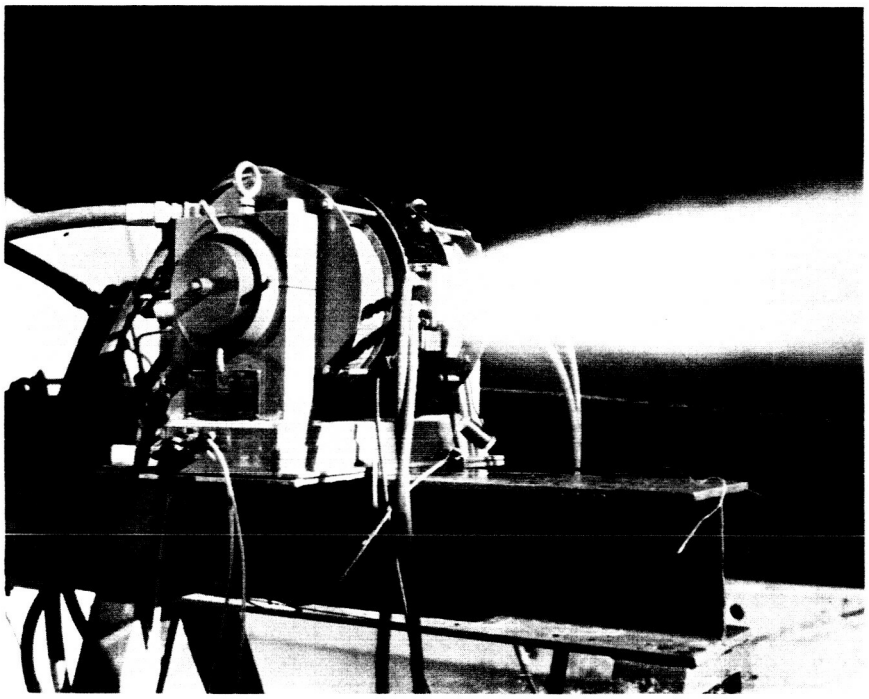

FIGURE 17. RMHD generator in operation.

EXPERIMENTAL RESULTS

Experimentally measured voltage and current and the computed power for the seven successful firings of the RMHD generator (April through December of 1962) are tabulated in Table I. The theoretical values for the first two firings are approximations due to the rocket engine operating far from desired conditions (due to the short run time); conductivity data was lacking in this regime. All values in the rows marked "Per cent Theoretical" refer to the measured percentage of

TABLE I. SUMMARY OF EXPERIMENTAL RMHD GENERATOR RESULTS

Experiment Number	1	2	3	4	5	6	7
Open-circuit voltage							
Measured (volts)	34.9	29.0	31.8	18.2	28.1	17	13.6
Per cent theoretical	47.2	40	44	43	66.4	40	32.3
Short-circuit current							
Measured (amperes)	3.4	6.3	3.6	2.5	2.9	2.34	2.53
Per cent theoretical	4.6	9	4.2	5.4	6	5	5.5
Maximum Power							
Measured (watts)	3.5	6.1	18.2	9.1	23.7	12.8	5.38
Per cent theoretical	0.26	0.48	1.2	1.9	4.7	2.6	1.1
Seeding rate (per cent)	4	8	8	8	8	4	8
Magnetic field (gauss)	10,000	9800	9800	5700	5700	5700	5700
Gas conductivity (mhos/meter) [*see equation* (14)]	25.4	24.5	30	27.8	28.7	27.8	27.7
Experiment duration (seconds)	7.2	32.3	7.1	41.4	83.8	253	244

the theoretical maximum predicted under the operating conditions at the time the experimental measurement was made. The MHD channel equations given by equation (1) were used in calculating the theoretical maximums. The gas conductivity was obtained from the programmed electrical conductivity expression and corrected for the effect of the magnetic field, equation (14). **Appendix C** presents a sample calculation of the MHD generator characteristics.

Figures 18 and 19 contain the external characteristics and power curves for two of the RMHD generator firings. For the run represented by Figure 18 Vycor glass insulating side plates were used and the cesium carbonate seed rate was 8 per cent. For the run represented by Figure 19 fused MgO insulating plates were used and the seeding rate was 4 per cent. The curves indicate that the same general trends apply to both runs.

The data for Figure 18 were taken in a 14-second elapsed time interval beginning 23 seconds after engine ignition by varying the load rheostat from open to short circuit. The voltage decreased linearly from the open-circuit to the short-circuit condition. The power curve indicates that the maximum point occurred at a current of 1.6 amperes and a potential of 13.5 volts. The load resistance under these conditions is 8.4 ohms. From simplified theory (7) maximum power is drawn when the external and internal resistances of the generator are matched. Therefore, the effective internal resistance of the generator is 8.4 ohms.

The data for Figure 19 were taken in a 7-second elapsed time interval beginning 15 seconds after engine ignition. Desired flow rates and stable engine operation were achieved 13 seconds after engine ignition. The voltage decreased almost linearly from the open-circuit to the short-circuit condition. A slight decrease in dV/dI appeared as the current increased. The open-circuit voltage maximum changed 9.3 per cent during the 7-second recording interval. The power curve indicates that the maximum power point occurred at a current of 0.9 amperes and

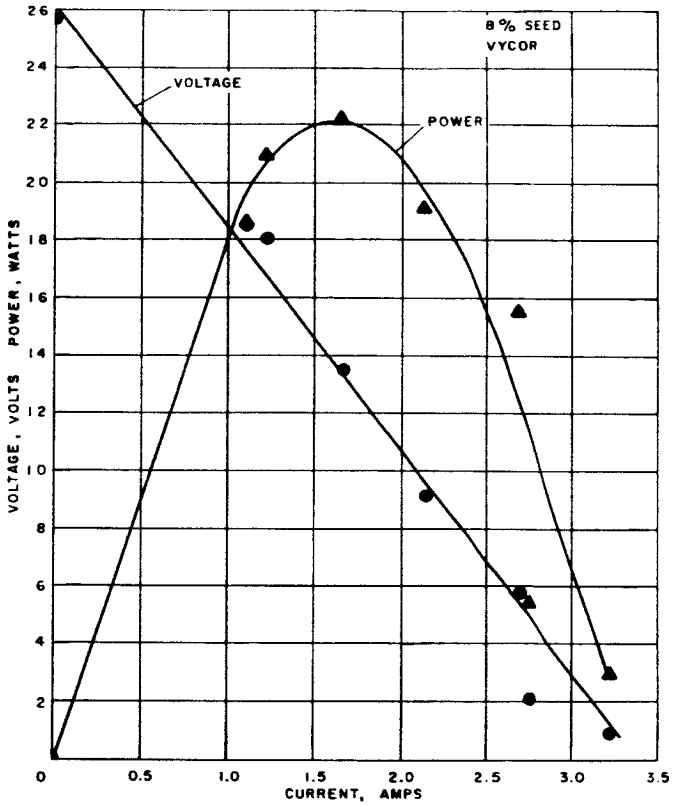

FIGURE 18. Performance characteristics of RMHD generator.

a potential of 9 volts. The load resistance is therefore 10 ohms. In a similar measurement, taken 165 seconds after ignition, the resistance was calculated as 9.4 ohms. Since the internal and external resistances are the same at the maximum power point, the voltage drop is the same and, therefore, the open-circuit voltage is twice the maximum power-point voltage. This value of 18 volts demonstrates good agreement with the measured open-circuit voltage of 17 volts.

According to simplified theory the internal resistance of the generator is given by (7)

$$R = \frac{W}{\sigma_{\perp} DL} \tag{16}$$

From known dimensions of the power channel and a measured internal resistance of 10 ohms, the conductivity of the gas is found to be 2.5 mhos/meter. The short-circuit current is given by equation (1b). Using this equation and a value of 2160 meters/sec for the gas velocity (this velocity is given as part of the NOTS Propellant Evaluation Program) the gas conductivity is computed to be 1.8 mhos/meter. Using the calculation procedure of Appendix B, the gas conductivity is found to be 27.8 mhos/m.

For the ideal generator the maximum power produced by the generator may be given by (7)

$$\mathrm{P} = \frac{(V_{oc})(I_{sc})}{4} \tag{17}$$

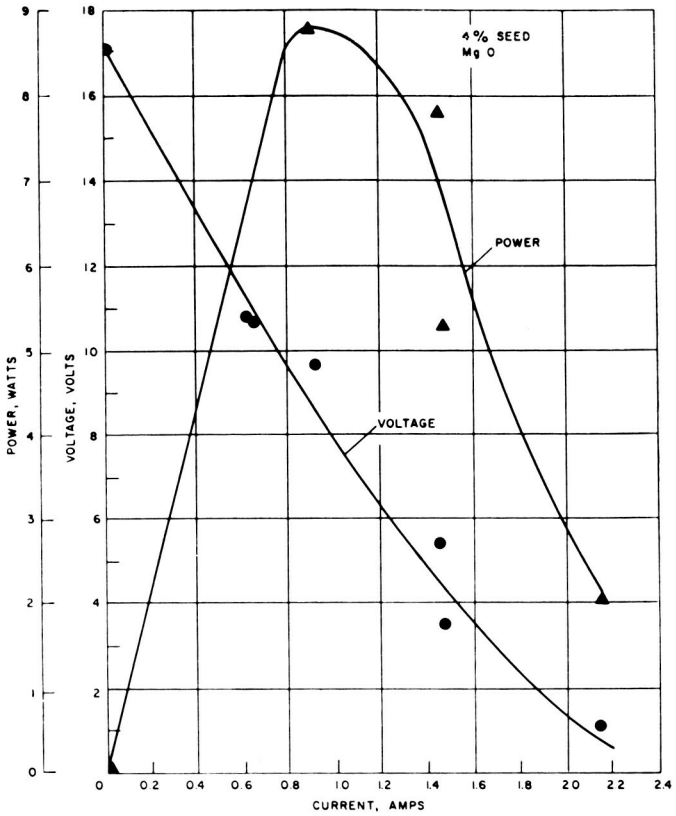

FIGURE 19. Performance characteristics of RMHD generator.

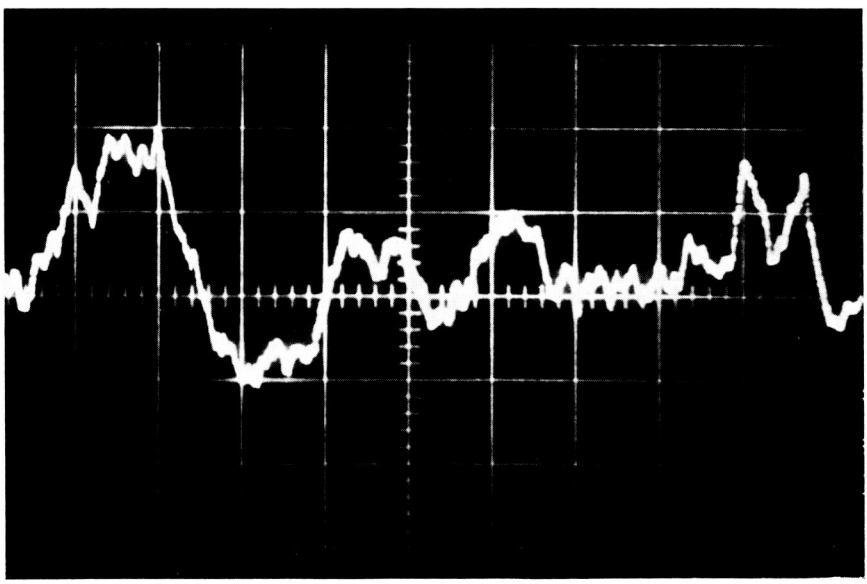

FIGURE 20. RMHD voltage noise (gain, 0.5 volts/cm; sweep, 0.0002 sec/cm).

From Figure 19 one finds that the maximum power point is 95 per cent of the theoretical power available, based on the measured values of the open-circuit voltage and the short-circuit current.

The optical galvanometer oscillograph traces of the RMHD generator potential and current showed that these parameters had alternating components about 10 per cent of the d-c levels. Actual cyclic phenomena were almost impossible to interpret, but oscilloscope photographs of the open-circuit voltage indicated several frequency modes (360, 1250 cps and others). A photograph of this voltage oscillation is shown in Figure 20. This type of MHD generator behavior has been reported by other investigators (**12**).

CONCLUSION

Electrical energy was generated from an MHD interaction with an electrically conducting supersonic combustion gas. The small scale of the experiment precluded diagnostics within the MHD channel. The external experimentally determined characteristics of the generator agreed well with idealized MHD channel theory. The electrical conductivity of the supersonic gas within the channel showed some variance with the values predicted by programmed thermal ionization and gas conductivity equations.

It was found that the 2160-meters/sec gas stream created an environment of severe heat transfer and drag on the structural elements of the power channel. Segmented electrodes were not successful in this environment; however, further design would probably have resulted in a suitable configuration. Knurling of the continuous water-cooled copper electrode surfaces to break up the boundary layer resulted in increased power output from the generator. Inspection of the electrode surfaces and the insulating wall material after hot firings revealed that the boundary layer may have been $\frac{1}{8}$-inch thick; the reduction of electrode area would be about one-half. Cold flow visualization studies and inspection of the insulating wall material after hot firings indicated that contoured expansion nozzles are necessary for supersonic MHD generator channels to prevent shocks and material erosion.

ACKNOWLEDGMENT

The authors are indebted to James B. Lee for assistance in designing, operating, and maintaining the electrical instrumentation.

NOMENCLATURE

AAA	Conversion factor (**5**)
B	Magnetic field strength, webers/m^2
b	Impact parameter, cm
D	Width of electrode, meters
e	Electron charge, 4.803×10^{-10} esu
g	Multiplicity of energy states, dimensionless
h	Debye length, cm
I	Current, amperes
k	Boltzmann constant, 1.3804×10^{-23} joule/°K
k_1	Constant, $-1.1616\phi \times 10^4$
k_2	Constant, -14.946
k_3	Constant, $1.013\ (\mathrm{AAA}) \times 10^5/k$

L	Length of electrode, meters
M	Mach number, dimensionless
m_e	Mass of electron, 9.1085×10^{-31} kg
n	Particle density, particles/volume
P	Pressure, units as indicated
Q	Collision cross section with electrons, m^2
R	Internal resistance of MHD generator, ohms
T	Temperature, degrees Kelvin
u	Velocity, meters/sec
V	Voltage, volts
v	Electron thermal velocity
W	Distance between electrodes, meter
X	Molar concentration, gram-moles/100 grams
x	Degree of ionization, dimensionless
η	Parameter in equation (3)
λ	Mean-free-path, meters
Π	Maximum power density, watts/m^3
P	Power, watts
σ	Electrical conductivity, mhos/meter
τ	Electron collision period, seconds
ϕ	Ionization potential, volts
ω	Electron gyromagnetic frequency, radians/sec

Subscripts

e	Electron
i	Ion
j	jth species
o	Neutral atom
oc	Open circuit
s	Seed
sc	Short circuit
$\perp$	Magnetic field dependency

Appendix A

SIMPLIFIED EXPRESSION FOR $\omega\tau$ IN PARTIALLY-IONIZED GASES

The degree to which the transport coefficients of a partially ionized gas are modified by a magnetic field is a function of the product $\omega\tau$, where ω is the gyromagnetic frequency of the electron and τ is the mean time between collisions of electrons with atomic and molecular particles. For seeded combustion gases assumptions may be made which lead to a simplified expression for $\omega\tau$.

The gyromagnetic frequency of an electron is

$$\omega = eB/m_e$$

where e is the electronic charge, m_e is the mass of an electron and B is the magnetic field.

To calculate the collision period the assumption is made that the combustion gas is seeded with small amounts of materials which are easily ionized and that the fluid is a perfect gas in thermodynamic equilibrium and exhibits a small degree of ionization. The electron collision period is

$$\tau = \lambda/v$$

where λ is the mean-free-path for electrons and v is the electron thermal speed which is given from kinetic theory considerations as

$$v = (8kT/\pi m_e)^{1/2}$$

The mean-free-path for electrons is

$$\lambda = 1/nQ$$

where n is the gas particle density and Q is the gas particle collision cross section. The gas particle density is

$$n = P/kT$$

Combining the above relations one obtains the expression

$$\omega\tau = (e/Q)(\pi k/8m_e)^{1/2}(B/P)(T)^{1/2}$$

Substituting the values of the electron charge and mass and assuming a value for the collision cross section of 3×10^{-19} square meters (**6**) one obtains

$$\omega\tau = 1.3 \times 10^3(B/P)(T)^{1/2}$$

Appendix B

CALCULATION OF ELECTRICAL CONDUCTIVITY

To illustrate the procedure used in calculating the degree of ionization, the free electron density, and the electrical conductivity in a rocket engine exhaust, a sample calculation will be made. The rocket engine burns gaseous oxygen and methyl alcohol at an oxidizer-fuel ratio of 1.45 with a combustion chamber pressure of 177 psia. The propellant is seeded with cesium carbonate to the amount of 1 per cent by weight of total mass flow. The values of the thermodynamic parameters at the nozzle exit for an isentropic expansion to 14.7 psia with shifting equilibrium, as given by the NOTS Propellant Evaluation Program (**5**), are

$$\begin{aligned} T &= 2585°\text{K} \\ P_s &= 1.563 \times 10^{-3} \text{ atmospheres} \\ \text{AAA} &= 0.2562 \\ X_s &= 6.1 \times 10^{-3} \text{ gram-moles/100 grams} \end{aligned}$$

The ionization potential for cesium is 3.87 volts, so that equation (3) becomes

$$\eta = -\frac{(1.1616 \times 10^4)(3.87)}{2585} + 2.5 \ln (2585) - \ln (1.563 \times 10^{-3}) - 14.946$$

$$\eta = -6.238$$

The degree of ionization of the seed material is now given by equation (4) as

$$x = (e^{6.238} + 1)^{-1/2} = 0.0442$$

The monatomic cesium gas is ionized to the degree of 4.42 per cent. The value of k_3 is found to be 1.881×10^{27}, so that the electron density in the rocket exhaust gases is found from equation (7) to be

$$n_e = \frac{(0.0442)(1.881 \times 10^{27})(6.1 \times 10^{-3})}{2585}$$

$$n_e = 1.96 \times 10^{20} \text{ electrons/m}^3$$

The electron–electron cross section is found from equation (11)

$$Q_e = 5.85 \times 10^{-16}\ \mathrm{m}^2$$

and the electron–ion cross-section is found from equation (13)

$$Q_i = 1.78 \times 10^{-16}\ \mathrm{m}^2$$

From equation (9) the electrical conductivity is found to be

$$\sigma = 24\ \text{mhos/meter}$$

Appendix C

CALCULATION OF MHD GENERATOR PERFORMANCE

The NOTS Propellant Evaluation and Electrical Conductivity Programs were used to obtain the MHD channel-entrance parameter values. For a typical MHD generator firing these values were:

Temperature	2550°K (calculated)
Pressure	17.33 psia (measured)
Seed rate	8 per cent (measured)
Magnetic field	5700 gauss (measured)
Gas velocity	2160 meters/sec (calculated)
Gas conductivity	35.4 mhos/m (calculated)
W	1.35 inches
D	0.50 inches (measured)
L	4.20 inches

Since continuous electrodes were used in this typical experiment the value of $\omega\tau$ must be considered. From equation (15) one finds

$$\omega\tau = \frac{(1.3 \times 10^3)(0.57)(2550)^{1/2}}{(17.33/14.7)(1.013 \times 10^5)}$$

$$\omega\tau = 0.312$$

where the channel-entrance pressure has been converted to newtons/m^2. The effective electrical conductivity of the exhaust gases is given by equation (14) as

$$\sigma_\perp = \frac{35.4}{1+(0.312)^2} = 32.2\ \text{mhos/meter}$$

The open circuit potential, V_{oc}, is computed from equation (1a) as

$$V_{oc} = uBW = (2160)(0.57)(0.0343) = 42.3\ \text{volts}$$

The short circuit current is given by equation (1b) as

$$I_{sc} = \sigma_\perp uBDL = (32.3)(2160)(0.57)(0.0127)(0.1067)$$
$$I_{sc} = 53.8\ \text{amperes}$$

The maximum power density is given by equation (1c) as

$$\Pi = \sigma_\perp u^2 B^2/4 = (32.2)(2160)^2(0.57)^2/4$$
$$\Pi = 12.2\ \text{megawatts/m}^3$$

From this value, the maximum generated power of the RMHD generator is

$$\mathrm{P} = \Pi \times (\text{volume of channel}) = (12.2 \times 10^6)(0.0343)(0.0127)(0.1067)$$
$$\mathrm{P} = 565\ \text{watts}$$

REFERENCES

1. Huth, J. H., "A Brief Study of Rocket-Powered Magnetohydrodynamic Generators and Energy-Storage Devices", ARPA Order No. 91–59, The Rand Corporation (May, 1960).
2. Sutton, G. W., "Design Considerations of a Steady D.C. Magnetohydrodynamic Electrical Power Generator", General Electric Report No. R59 SD 432 (September, 1959).
3. Zemansky, M. K., *Heat and Thermodynamics* (New York: McGraw-Hill, 1957), 439.
4. Francis, G., *Ionization Phenomena in Gases* (London: Butterworth, 1960), 46.
5. Browne, H. N., *et al.*, "The Theoretical Computation of Equilibrium Compositions, Thermodynamic Properties and Performance Characteristics of Propellant Systems", NAVWEPS Report 7043, NOTS TP 2434, China Lake, California (June 8, 1960).
6. Goldberg, P. A., "Electrical Properties of High-Altitude Ionized Shock Waves", in *Plasma Physics*, ed. J. E. Drummond (New York: McGraw-Hill, 1961), 245.
7. *Engineering Magnetohydrodynamics*. Massachusetts Institute of Technology, Summer Session Notes (June, 1961).
8. Basu, S., "Ionization in Seeded Detonation Waves", *Phys. Fluids*, **3**, 456 (1960).
9. Brown, S. C., *Basic Data of Plasma Physics* (New York: Technology Press of MIT and John Wiley and Sons, Inc., 1959).
10. Pai, S. I., *Magnetohydrodynamics and Plasma Dynamics* (New Jersey: Springer-Verlag/Prentice-Hall, 1962), 164.
11. Larsen, H. M., and Turner, C. H., "Microwave Measurements of Electron Density in Seeded Rocket Exhaust Gases", NAVWEPS Report 8059, NOTS TP 3062, China Lake, California (September 21, 1962).
12. Blackman, V. H., *et al.*, "MHD Power Generation Studies in Rectangular Channels", in *Proceedings of the 2nd Symposium on the Engineering Aspects of Magnetohydrodynamics* (New York: Columbia University Press, 1962), 180.

18. A. I. Carswell, M. P. Bachynski, and G. G. Cloutier: *Microwave Measurements of Electromagnetic Properties of Plasma Flow-fields*

Measurements of the transmission, reflection, and radiation of microwave energy by a flowing plasma can, in principle, lead to an understanding of the electromagnetic properties of the plasma. This paper deals with (1) *the limitations in setting up theoretical models which will allow the interpretation of the measurements, and* (2) *the difficulties and techniques in setting up experiments which lend themselves to theoretical interpretation.*

The importance of such effects as near- and far-field diffraction, refraction, multiple-reflection, and stray scattering are illustrated by a series of measurements conducted on a typical experimental arrangement. A high time-resolution microwave technique for obtaining simultaneous information on the phase and amplitude of the probing microwave signal has been developed and its use for the measurement of rapidly varying plasmas illustrated. Considerations on the possibilities and the limitations of improving spatial resolution are also outlined.

Laboratory investigations of the reflection of microwaves from supersonic plasma flow streams are described. Back-scattering measurements at frequencies of 9.4 Gc and 24 Gc on laminar and turbulent supersonic plasma streams and the effects of turbulence in the flow and polarization of the incident microwave fields on the scattering properties of the plasma have been studied.

INTRODUCTION

Because of the present interest in the reentry environment, a need exists to examine the properties of gas-dynamic flow-fields in which there is a significant degree of ionization. Among the many possible methods available for studying these plasma systems (**1**), microwave "probing" techniques offer many apparent advantages.

The use of microwaves for plasma diagnostic purposes has, in recent years, been the subject of detailed investigation by many workers (**2**); considerable

ED. NOTE: Dr. Carswell, Dr. Bachynski, and Dr. Cloutier are at the Research Laboratories, RCA Victor Company, Ltd., Montreal, Quebec, Canada.

progress has been made. The purpose of the present paper is to discuss the application of the various microwave techniques to the study of plasma properties in the presence of a (supersonic) flow-field. Since the detailed properties of such plasma systems are, in general, extremely complex because of the large number of phenomena taking place simultaneously, it is desirable to examine the "conventional" microwave diagnostic methods in the light of these additional effects.

In this paper the material will be somewhat restricted in that we shall orient the discussion towards the types of plasmas encountered in the laboratory facilities used for the generation of high-velocity plasma flow-fields, i.e., the plasma tunnel, the shock tube, and the ballistic range (**3**). This area encompasses a large portion of recent work on plasma flow effects and should serve to illustrate the essential factors involved in the microwave study of any "moving" plasma. An attempt has been made to examine the more practical aspects of the work with the main emphasis being on an examination of the problems involved in making meaningful measurements and in understanding their limitations. Experiments in our laboratories have indicated the importance of these problems, and results from these investigations will be used as illustrations.

Before discussing in detail the factors relating to the microwave measurements it is worth examining briefly the general situation which faces research workers at present in this field. We have attempted to summarize these in the simple block diagram of Figure 1. As shown in the diagram, the determination of the properties of any real plasma system depends on two factors, namely the avail-

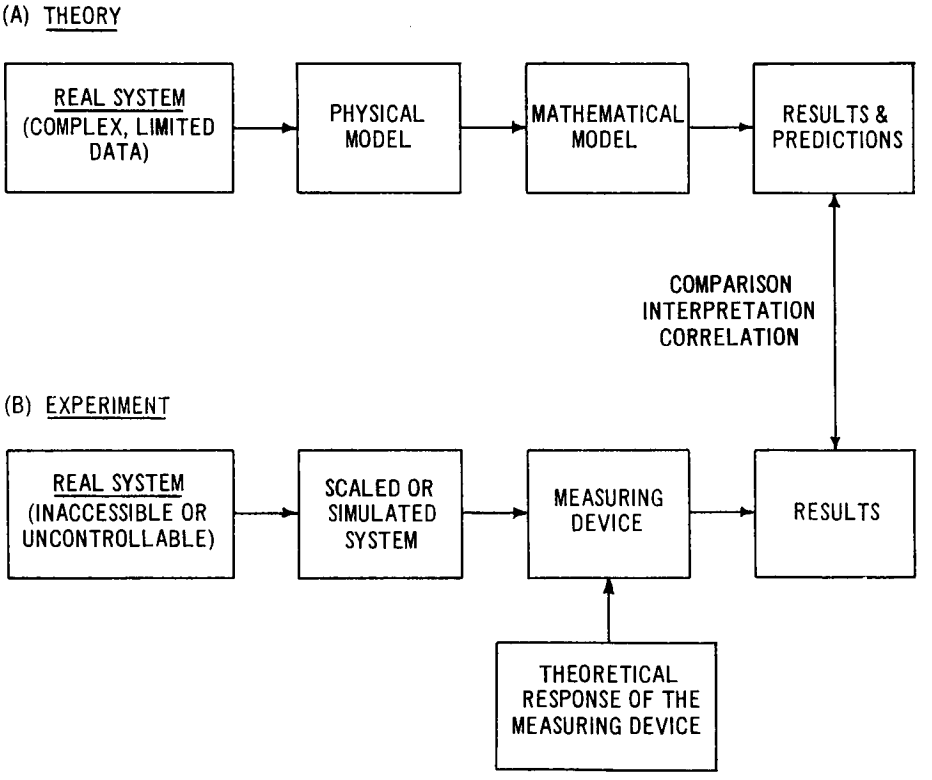

FIGURE 1. Block diagram showing the various considerations involved in studying plasma flow-fields.

ability of a theory which can adequately describe the physical situation, and an experimental capability to make measurements of the quantities described by the theory. It is essential to remember that the theory and experiment are interdependent and complementary. Because of the complexity of "flowing" plasma systems it is often difficult to make a direct and meaningful comparison between theory and experiment.

Usually the theoretician is restricted in his analysis not only by the complexity of the problem but also by a lack of good quantitative experimental data which he can use as a guide. In order to handle any problem analytically it is necessary to select a suitable physical model to describe the particular plasma system of interest. In most instances this step involves assumptions and simplifications that may limit the amount of quantitative information about the real system which can be deduced from the model. Usually it is necessary to make a compromise between a model which is accurate (and hence very complicated both physically and mathematically) and one which is less exact but is mathematically tractable. Thus it is essential for the experimentalist, who is endeavouring to compare his results with the theory, to be aware of the limitations of the particular theoretical analysis with which he is dealing.

From the experimental point of view an entirely different set of difficulties arises. First, in many laboratory studies, one is trying to simulate conditions which exist elsewhere in some "full-scale" situation (e.g., the simulation of a reentry environment). In this case the main interest is in obtaining more information about the "full-scale" system from the laboratory measurements on the simulated system. This means that for any useful information to be derived, the simulation must at some stage allow a comparison of the laboratory "numbers" with the full-scale system. In the simulation of supersonic plasma flow-fields this step is by no means trivial.

First of all, any attempt at "simulation" tacitly assumes that a detailed knowledge of the full-scale system exists and, in general, this is not true (**4**). Secondly, it is not difficult to show that because of the complexity of the full-scale system (in the reentry case) it is impossible to simulate in the laboratory all of the full-scale plasma parameters exactly in a single device or experiment (**5, 6, 7**). Hence in a laboratory simulation, the experimentalist is forced to be satisfied with something less than an exact "scaling" of the real system.

Once the laboratory system has been established to optimize the scaling requirements, the major experimental problem lies in making meaningful measurements of the very complicated plasma flow-field structure. Although there is a rather large body of experimental work on plasma diagnostics, the art of applying these methods to obtain quantitative measurements in the various supersonic plasma flow facilities of interest is still only at a very early stage of development. Because of this inability to relate the "measurables" in an experiment to the "plasma physics", the experimentalist is at present in the position of having to design and calibrate each diagnostic tool for each specific measurement. Under these conditions it is not surprising that discrepancies often arise between some of the measurements.

In the remainder of this paper we shall discuss the microwave techniques for plasma diagnostics within the general framework indicated in Figure 1.

THEORY OF MICROWAVE INTERACTION WITH PLASMA

From the point of view of employing microwave techniques for plasma diagnostics, the ultimate aim of the "theoretical" analysis is to provide meaningful

expressions for the various plasma parameters of interest (e.g., the electron density, electron temperature, collision frequency, etc.) in terms of the microwave measurables (e.g., amplitude, phase, frequency, polarization, etc.). To do this properly requires a general discussion of the interactions of electromagnetic waves with plasma. An analysis of this type can be achieved in a rigorous manner only through a study of the statistical mechanics of irreversible processes in systems containing mixtures of electrically charged and uncharged particles (**8, 9**). As yet this rigorous approach is incapable of supplying quantitative predictions which can be readily compared with experimental measurements.

In spite of this limitation, however, great progress has been made by employing less accurate descriptions of the interaction. One of the most useful descriptions of the plasma is given in terms of its effective dielectric coefficient (**10**). By considering the kinetics of the "particles" in the plasma under the influence of the field of an electromagnetic wave, it is possible to obtain expressions for the effective dielectric coefficient in terms of the plasma parameters. In general, the effective dielectric coefficient of a plasma is a complex quantity of the form (**11**)

$$K = K_r - iK_i \tag{1}$$

where K_r and K_i are the real and imaginary parts of the complex dielectric coefficient K.

Hence, using this approach, the problem of electromagnetic wave propagation in a plasma reduces to one of wave propagation in a medium of complex dielectric coefficient (**12**). For a plane wave with harmonic time variation ($e^{i\omega t}$) propagating in the x-direction in such a medium, the electric field variation may be written as

$$\mathbf{E} = \mathbf{E}_0 \, e^{i\omega t} \, e^{-\gamma x} \tag{2}$$

where γ is the propagation constant given by

$$\gamma = ikK^{1/2} \tag{3}$$

and $k = 2\pi/\lambda$, λ = free space wavelength.

In general, γ may be written in the form

$$\gamma = \alpha + i\beta \tag{4}$$

where

$$\alpha = k\left[\frac{(K_r^2 + K_i^2)^{1/2} - K_r}{2}\right]^{1/2} \tag{5}$$

$$\beta = k\left[\frac{(K_r^2 + K_i^2)^{1/2} + K_r}{2}\right]^{1/2} \tag{6}$$

with α and β being termed the attenuation and phase constant, respectively. The attenuation of the wave (in decibels) in traveling a distance d in the medium is given by

$$A = 20 \log_{10} \frac{\mathbf{E}_0}{\mathbf{E}} \tag{7a}$$

or

$$A = 8.68\left(\frac{\alpha}{k}\right) 2\pi \left(\frac{d}{\lambda}\right) \tag{7b}$$

The phase shift (over a path length d) arising from the presence of the plasma is given by

$$\Delta\Phi = kd - \beta d \tag{8a}$$

$$\Delta\Phi = 2\pi \frac{d}{\lambda}\left[1 - \frac{\beta}{k}\right] \text{ radians} \tag{8b}$$

If the values of α and β from equations (5) and (6) are inserted in equations (7) and (8) the resulting expressions for the attenuation and phase shift are given by

$$A = 54.6\left(\frac{d}{\lambda}\right)\left[\frac{(K_r^2+K_i^2)^{1/2}-K_r}{2}\right]^{1/2} \tag{9}$$

$$\Delta\Phi = 6.28\left(\frac{d}{\lambda}\right)\left\{1-\left[\frac{(K_r^2+K_i^2)^{1/2}+K_r}{2}\right]^{1/2}\right\} \tag{10}$$

As they stand, these equations are purely a formal result of the solutions of Maxwell's equations for a plane wave in a medium with a complex dielectric coefficient, giving expressions for the measurable quantities A and $\Delta\Phi$ in terms of the dielectric coefficient. For plasma diagnostics by microwaves it is necessary to have explicit expressions for K_r and K_i in terms of the plasma parameters and in the derivation of these it is necessary to introduce a specific model of the plasma.

UNBOUNDED PLASMAS

One of the models widely used in diagnostic applications considers the motion of an "average" electron in an unbounded homogeneous plasma. This results in an effective dielectric coefficient of the plasma which is given by (**10**)

$$K = \left[1-\left(\frac{\omega_p}{\omega}\right)^2\frac{1}{1+(\nu/\omega)^2}\right]-i\left[\left(\frac{\omega_p}{\omega}\right)^2\frac{(\nu/\omega)}{1+(\nu/\omega)^2}\right] = K_r-iK_i \tag{11}$$

where $\omega_p^2=ne^2/m\epsilon_0$ is the "plasma frequency", n=electron density, e=electron charge, m=electron mass, and ν=effective electron collision frequency.

By inserting the values of K_r and K_i from equation (11) into equations (9) and (10), a direct relationship is obtained between the measurable quantities, A and $\Delta\Phi$, and the plasma parameters, n and ν.

From the form of equation (11) it is evident that for $\nu=0$ microwaves will only propagate in the plasma for $\omega>\omega_p$. This so-called "cut-off" of propagation occurs for $K=0$ and this fact is often used to determine the electron density in the plasma at "cut-off" from the relationship

$$\omega = \omega_p \quad \text{or} \quad f \approx 9000\sqrt{n} \tag{12}$$

where f is in units of $(\text{sec})^{-1}$ and n is in units of electrons/cm^3. If the collision frequency differs from zero, however, the concept of a "cut-off" is not really valid since for any nonzero collision frequency propagation can occur even when $\omega_p>\omega$.

Also, for $\nu \approx 0$ it is evident from equation (10) that

$$\Delta\Phi = 2\pi\frac{d}{\lambda}\left[1-\left(1-\frac{\omega_p^2}{\omega^2}\right)^{1/2}\right] \tag{13}$$

and this expression is often utilized in the study of plasmas by microwave interferometry techniques (**13**). For $\omega_p \ll \omega$ equation (13) reduces to

$$\Delta\Phi = \frac{\pi d}{\lambda}\frac{ne^2}{m\epsilon_0\omega^2} \tag{14}$$

showing that in this approximation the phase shift caused by the plasma is proportional to the electron density.

At present, the simple theory outlined above is often used for microwave studies of plasma systems. To examine the complex plasmas in gas-dynamic flow systems, however, this analysis is not sufficiently realistic for most cases of practical interest.

It is not possible in the space available to describe the limitations in detail but it is hoped that a brief summary of them will serve to emphasize the fact that the errors introduced by the application of an over-simplified theoretical model are not negligible.

It should be mentioned, at first, that one of the basic parameters used in the definition of the plasma, i.e., the effective collision frequency, ν, is in fact, not a simple entity, but a lumped parameter describing the interaction of the electrons with each of the species (ions, electrons, neutrals) in the plasma. Since the definition of this parameter can vary depending on the interactions which are included in the theory, restrictions which are not readily apparent may be placed on the final results. The definition of "a collision frequency" in complex systems requires care, especially if the plasma is undergoing "chemical-kinetic" reaction and if the conditions are far removed from the idealized "equilibrium" situation.

In addition, the theory outlined above is based on the assumption of an unbounded, homogeneous plasma. In practice, any plasma used for laboratory studies is neither unbounded nor homogeneous, so it is necessary to re-examine, from the practical point of view, the various relations derived.

For an unbounded plasma the foregoing theory can be modified to incorporate inhomogeneities by allowing the various plasma parameters to depend on the spatial coordinates. Strictly speaking, in this situation, one should also consider the effects of diffusion currents which necessarily exist in the plasma, but these effects are usually small and are generally neglected in comparison with the electron "conduction" current.

The basic wave equations for the non-homogeneous plasma are of the form (**10, 14**)

$$\nabla^2\mathbf{E}+k^2K\mathbf{E} = -\nabla\left(\mathbf{E}\cdot\frac{\nabla K}{K}\right) \tag{15a}$$

$$\nabla^2\mathbf{H}+k^2K\mathbf{H} = -\frac{\nabla K}{K}\times(\nabla\times\mathbf{H}) \tag{15b}$$

where the plasma permeability is assumed equal to the free space permeability μ_0 (which is, in most cases, a legitimate assumption). The behavior of an electromagnetic wave in a nonhomogeneous plasma is obtained from a solution of equations (15a) and (15b). In order to proceed with such calculations it is necessary to assume specific spatial variations of the plasma dielectric coefficient (**15, 16, 17**) and often for practical problems this variation is not known or is too complicated to allow anything but machine calculations of the problem.

In the presence of an external magnetic field a plasma becomes an anisotropic medium and as a result, the effective dielectric coefficient is no longer a scalar quantity but must be expressed as a tensor. In this case the formal mathematical analysis involves the propagation of electromagnetic waves in a medium possessing a tensor dielectric coefficient (**18, 19**). The specific form of the dielectric coefficient tensor depends on the plasma variables (particle densities and collision frequencies, etc.) as well as the magnetic field strength and orientation with respect to the electromagnetic wave field. If the plasma is nonhomogeneous as well as anisotropic, the elements of the tensor are functions of position and again any detailed analysis involves specific spatial variations of these quantities. In general, the wave equations are very difficult to solve, with solutions being available only for specific cases, and no further discussion will be given here (**18, 19, 20**).

FINITE PLASMAS

The discussion thus far has been concerned only with the propagation of electromagnetic waves inside a plasma. Any effects of boundaries on the problem have been ignored so all of the preceding treatment is only applicable to unbounded plasmas. In order to make any meaningful comparison with experiment it is necessary to take into account the effects of boundaries on the wave propagation. Using again the "dielectric" concept of the plasma, this is usually achieved by matching the fields on both sides of a boundary in the conventional manner of electromagnetic theory (**21**). This approach involves the inclusion of a reflected wave at any interface, and for multiple boundaries the reflections become increasingly important.

In a recent report (**22**) Bachynski *et al.* have considered in detail some of the problems encountered when making microwave diagnostics of finite plasmas. It is shown that the presence of boundaries can cause very significant changes in the attenuation and phase measurements on a plasma and can lead to errors ranging up to factors of ten or larger in the plasma parameters deduced on the basis of the "unbounded" theory.

For example, it is shown that for a uniform plasma slab bounded by dielectric plates (a configuration closely approximating many experimental arrangements) the signal transmitted through the system can be greater with the plasma than that with no plasma in the container. This apparent negative attenuation simply shows that the container (the parallel dielectric plates) reflects more signal when the electron density is zero than in the presence of the plasma. The reason for this is that the varying refractive index of the plasma can "match" the two dielectric plates causing less reflected signal. It is interesting to note that recent measurements in a plasma flow facility have produced this same effect (**23**).

A second important effect encountered when dealing with finite plasmas is that of refraction. Since the refractive index of the plasma ($\mu = K^{1/2}$) is in general different from its bounding medium (e.g., free space, or a dielectric container), refraction will occur at each interface, if the angle of incidence differs from zero. The net result of the refraction is that the nature of the incident beam of energy is altered. The plasma can be considered to act as a lens of refractive index less than unity. Hence in any measurement of microwaves transmitted through a plasma the energy density in the transmitted beam is changed not only by the amount of energy absorbed in the plasma but also by the amount of focusing or defocusing which has taken place.

Using the concepts of geometrical optics (i.e., plasma dimensions large compared to wavelength, losses in the plasma small, etc.) it is possible to make estimates of the refractive effects for plasmas of simple geometric shape. These calculations require specific assumptions concerning the plasma geometry, the spatial variation of the electron density, and the nature of the incident microwave beam (i.e., whether it is parallel, convergent, or divergent) and for details the reader is referred to the literature on this subject (**22, 24**). As would be expected, the calculations show that under certain conditions the refractive effects can be very large and in general it is preferable in most experimental arrangements to try to remove the effect of refraction by maintaining the microwave beam normal to the interfaces of interest.

For plasmas which are only of the order of a few wavelengths in size (as is usually the situation in the laboratory) it is also necessary to consider diffraction effects. Again, the geometry of the plasma and the nature of the incident wavefront must be specified to allow solution of these problems. In some cases it is possible

to employ the Kirchhoff scalar diffraction theory (**25**) to provide useful results (**26**).

For simple geometric shapes (e.g. cylinders and spheres) the problem can be treated as a scattering problem (**27, 28**) wherein the electromagnetic field is considered to be composed of an incident (plane) wave and an outgoing scattered wave possessing either cylindrical or spherical symmetry. By knowing the spatial dependence of the dielectric coefficient of the plasma scatterer, it is then possible to apply the usual boundary conditions and obtain a solution (**16**). Again, all but the simplest problems require computer analysis to obtain numerical results (**29**).

"FLOWING" PLASMAS

In the foregoing analysis of the interaction of microwaves with plasma, there has been no specific consideration of systems possessing a "bulk" flow velocity. The only motions accounted for have been the thermal motions of the particles and the motions induced by the applied electromagnetic fields. That this analysis is valid even for the hypersonic velocities generated in modern gas-dynamic test facilities can be seen by examining the magnitudes of the various parameters involved.

First of all, if we consider the $\underset{\sim}{U} \times \underset{\sim}{B}$ force arising from the interactions of the electrons (possessing the mean flow velocity $\underset{\sim}{U}$) with the magnetic component of the microwave field it is seen that this force is of the order of U/c smaller than the microwave electric field force acting on the electrons (**12**) (where c is the velocity of light). Hence for the nonrelativistic fluid velocities of interest, this magnetic interaction is negligible.

Secondly, if $U \ll c$ the electromagnetic wave sees an essentially stationary gas. The correction for the relative motion of the fluid and the microwave field is again of significance only for relativistic fluid velocities, and can be neglected for the systems of gas-dynamic interest.

In addition, it is apparent that since the microwaves are predominantly affected by the electron component of the plasma, any direct effects of fluid flow would not be expected to appear when $U < V$, the average thermal velocity of the electrons in the plasma. Since the electron thermal velocity is of the order of 10^7 cm/sec, most of the velocities of current experimental interest are not sufficiently large to impose any significant velocity contribution to the existing motions of the electrons in the plasma.

Hence, insofar as the electromagnetic theory of microwave propagation in plasmas is concerned, the presence of nonrelativistic flow velocities in the system introduces basically no new concepts. There are, however, serious "secondary" complications introduced by the fluid flow. These arise from the presence in a supersonic flow-field of the space- and time-dependent nonhomogeneities in the plasma properties. The existence of shock fronts, boundary layers, turbulence, and chemical-kinetic reactions in the flow-field make any realistic computation of the effective dielectric coefficient of the plasma virtually impossible, and hence it is very difficult to provide realistic expressions for the measurable quantities. It is for this reason that the flow effects do introduce significant complications in the application of microwave diagnostic techniques to supersonic flow facilities.

MICROWAVE TECHNIQUES FOR PLASMA DIAGNOSTICS

Experimentally, the application of microwave techniques for plasma diagnostics involves essentially a measurement of the effective dielectric properties of the plasma by microwave methods. Hence, in principle, one could employ any of the conventional microwave methods described in the literature (e.g. [**30**]) for measuring such properties.

For plasmas, however, certain limitations arise which often greatly reduce the number of techniques which can be applied. As already indicated, any microwave probing of plasmas must employ a frequency of the order of the electron plasma frequency of the system of interest. This consideration thus establishes the range of wavelengths which can be usefully employed in any experiment and usually places a strong limitation on the spatial resolution of the measurement. In addition, if the diagnostic technique is to be of general value it should be capable of examining plasmas of rather arbitrary geometry and composition over a wide range of experimental conditions.

Broadly speaking, the possible microwave diagnostic methods for plasmas may be divided into three separate classifications. The first involves the propagation of microwaves in bounded structures, such as resonant cavities or waveguides, which contain plasmas. The second is usually termed the free-space propagation method in which a microwave "beam" is directed through the plasma of interest. Finally, there are the techniques involving the insertion of microwave probes or antennas into a plasma to measure the effects of the plasma environment on the "impedance" of the antenna. The classification into these three types of measurement is, of course, somewhat arbitrary since the distinction between them is not rigorously defined and is dependent in many cases on the size and geometry of the system and on the approach of the investigator.

When these methods are considered for diagnostics of the aerodynamic systems of current interest, it is apparent that the free-space propagation method shows the greatest possibilities. Although the cavity and waveguide techniques have been widely used in laboratory studies of plasmas and have been developed to a high degree of refinement and reliability (**31–34**), they are of limited usefulness in flow systems where the plasma geometry can generally not be tailored to fit inside the microwave enclosure. The method has been used with some success in both shock tube and ballistic studies of plasma flow-fields (**35**). In shock tube studies it is possible to use the shock tube itself as a portion of the waveguide and in this way propagate signals through the shock front. In this application, however, the usable microwave frequency range is limited by the dimensions of the shock tube. Measurements in ballistic ranges have been reported (**35**) in which the projectiles have been fired through cavities and waveguides but in view of the experimental and analytical difficulties, this approach appears to be of limited usefulness. However, a recent application of "resonant structure" techniques involving Fabry-Perot-type interferometry in a ballistic range (**36**) may have promise for future studies.

An example of the results which can be obtained using waveguide techniques for studies of continuous supersonic plasma flow streams is shown in Figure 2 (**37**). These results were obtained by passing a small plasma jet (enclosed in a glass tube) through a hole in a section of X-band waveguide as shown and measuring the attenuation and phase shift of the transmitted signal. As the sample results show, quite consistent and reproducible results can be obtained, but to derive the plasma parameters from these requires some rather "over-simplifying" assumptions about the plasma properties.

The microwave or radio frequency probing techniques using antennas immersed directly in plasma systems have been studied by several workers recently (**38–41**). Since very small radiating surfaces can be used, the method offers the possibility of improving the spatial resolution of the microwave measurements. In general, however, the measurements of the plasma properties by this method are only semi-quantitative, and much more work is required before this method can be fully utilized. For applications to the study of flowing plasmas, this method

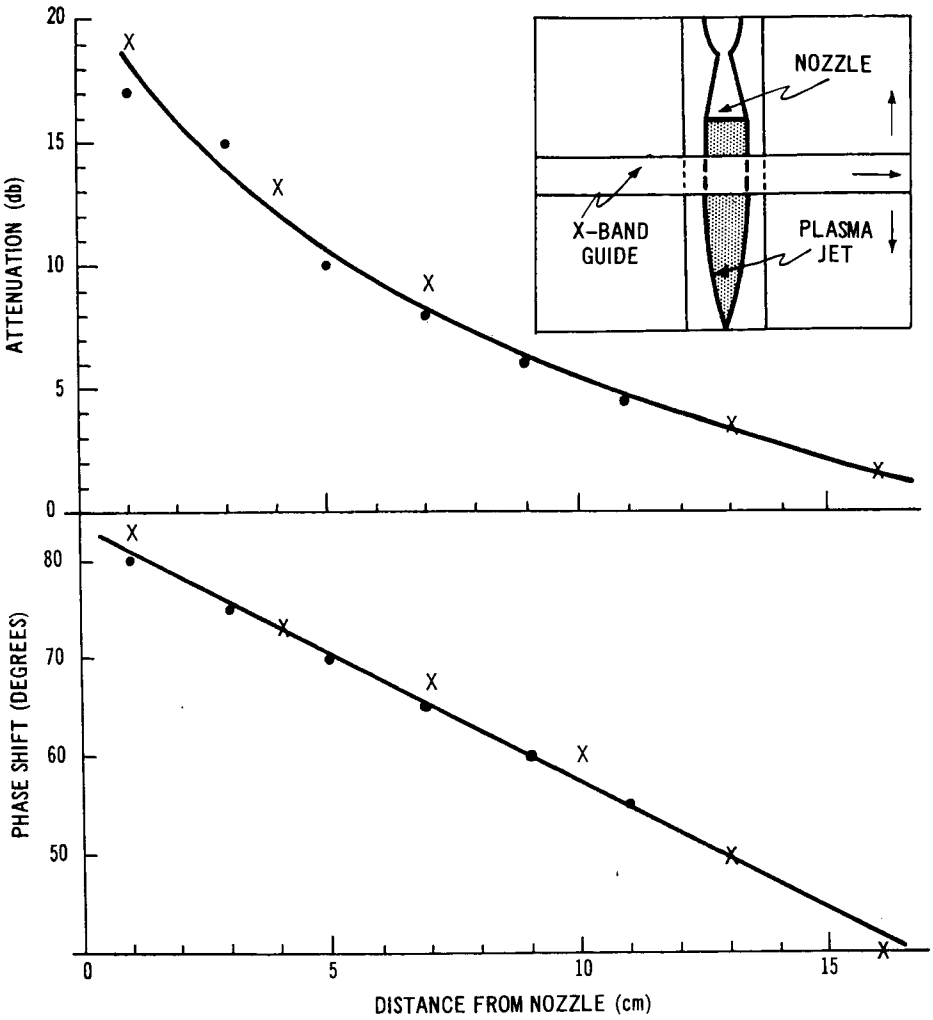

FIGURE 2. Sample results showing the phase shift and attenuation of a 9.2 Gc signal passing through a supersonic argon plasma jet as shown in the inset. The results for two separate measurements show the reproducibility obtained.

suffers from the usual disadvantage associated with the probing of supersonic flow streams. The disturbances introduced into the flow are difficult to assess and the interpretation of the measurements is thus complicated.

The free-space propagation method is particularly attractive for plasma diagnostics in conventional flow facilities. It can be readily adapted to suit existing plasma geometries and the plasma stream can be observed with no perturbations other than those caused by the microwave signal itself which are negligible for the low microwave power levels used. In the remainder of this paper the free-space propagation techniques will be discussed in more detail.

FREE-SPACE PROPAGATION MEASUREMENTS OF PLASMA FLOW-FIELD PROPERTIES

Because of its greater versatility of application, the free-space propagation method has been used in conjunction with a wide range of gas-dynamic facilities

(**35, 37, 42–54**). Although a variety of experimental arrangements is possible, they may all be summarized under the four basic arrangements shown in Figure 3, i.e., the measurements involve a study of: (a) transmission, (b) reflection, (c) scattering, or (d) radiation by the plasma flow-field. By using the appropriate theoretical model and experimental system, each of these microwave methods can be used to deduce information about the plasma. The direction of microwave

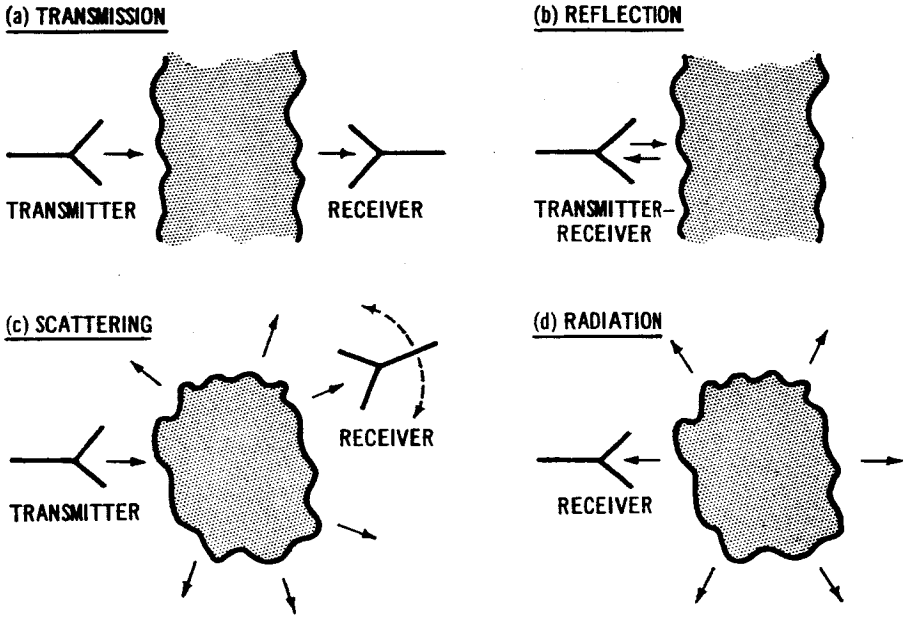

FIGURE 3. Schematic diagram showing the four basic experimental arrangements for microwave diagnostics of plasma by the free-space propagation method.

propagation can be at any angle to the direction of plasma flow, but in most cases only the parallel and transverse orientations are employed since for these arrangements the interpretation of the results is generally somewhat simpler. In all cases the measured parameters are the amplitude and phase (with respect to an arbitrary reference point) of the microwave signal. In some instances, particularly when external magnetic fields are involved, the polarization of the microwave field can also be used to study certain properties of the plasma (**55**), but these cases will not be discussed here.

In any of the experimental arrangements of Figure 3 it is desirable to be able to probe the plasma with good spatial and temporal resolution. Unfortunately, the spatial resolution of the microwave method is rather poor in comparison with other methods (e.g., optical or probe studies) since even with focusing techniques, the resolution is limited to distances of the order of the wavelength employed (**56, 57**), which generally varies from a few millimeters to a few centimeters. Since the usable wavelength is dictated by the electron density in the plasma, as mentioned previously, it is not, in general, possible to improve the spatial resolution by arbitrarily reducing the wavelength. In addition, the propagation method always involves a "line of sight" integration of the plasma properties, and the parameters deduced from the microwave measurements represent only an average over the plasma volume within the microwave beam. For flow systems in which

large spatial variations exist this is a great disadvantage and for these systems it is essential that supplementary measuring techniques with better spatial resolution be employed (**53, 58**).

Until recently the time resolution of microwave plasma measurements was rather poor. This was caused by the fact that although microwave signal amplitudes could be measured very rapidly, the measurements of the phase were rather slow. The phase measurement involves a comparison of the unknown wave with some fixed phase reference, and the usual microwave bridge techniques (**30**) involve slow "balancing" operations. However, several new systems (**59, 60, 61**) have been developed specifically for plasma studies so that now the phase measurements can be made in times of the order of 10^{-7} sec which is sufficiently rapid for most requirements.

A system of particular usefulness is the "multiple-probe" device recently described by Osborne (**60**). In this system the "unknown" microwave signal is combined with a reference signal to produce a standing wave in a waveguide section. This standing wave is then sampled by four detectors (probes) at one-eighth guide wavelength intervals and the instantaneous phase and amplitude of the unknown wave are displayed on an oscilloscope simultaneously as the orientation and length, respectively, of a vector in a polar plot. One of the arrangements for utilizing this device is shown in Figure 4. Using trace brightening, only the tip of the vector can be made visible and hence the value of the amplitude and phase of the "unknown" microwave signal can be displayed as a single point on the oscilloscope screen.

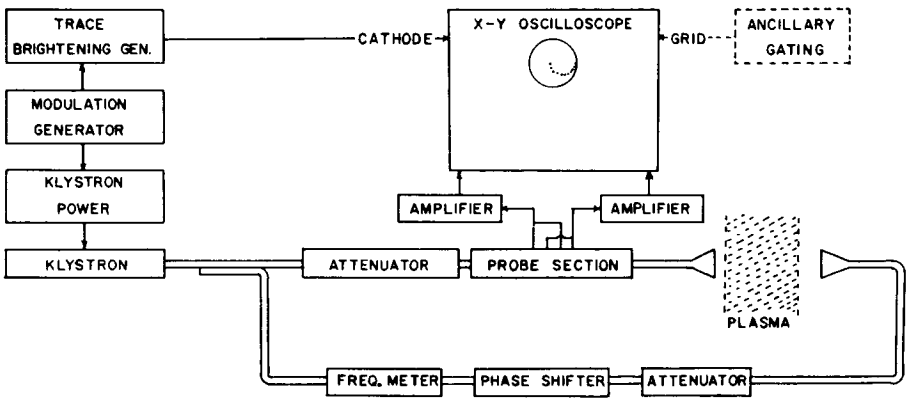

FIGURE 4. Block diagram of the multiple-probe system used for transmission measurements.

Apart from the obvious advantage of providing both phase and amplitude information, this device provides phase measurements accurate to within a few degrees and unambiguous even for phase variations greater than 360°. It has also been operated with sampling times of the order of 10^{-7} sec.

TRANSMISSION MEASUREMENTS

The transmission technique is probably the most widely used at present for plasma flow diagnostics. Experimentally the method is attractive because the necessary microwave apparatus can be kept quite simple, and it can be readily appended to existing flow systems. By transmitting the microwave beam across

the test section of a "plasma tunnel" or a shock tube, or through the plasma generated by a hypersonic projectile in a ballistic range, it is very simple to measure the phase and amplitude of the transmitted signal. Basically, this method can be applied whenever the condition $\omega \geq \omega_p$ is satisfied in the portion of the plasma examined, although detailed calculations are required to accurately define the useful range (**42**). In general, the theory for unbounded, homogeneous plasma outlined in an earlier section is utilized to obtain values for the electron density and the collision frequency employing formulas such as those given by equations (7) through (14). Some of the theoretical difficulties encountered in applying such equations to real systems have already been outlined and the required corrections indicated. Experimentally, additional problems are encountered in trying to satisfy the necessary criteria in the apparatus. One of the most important of these is the nature of the incident wave front. Ideally this should be plane, but in fact, unless considerable care is exercised, this condition is very poorly satisfied and large errors can result (**22, 26, 53**). By using lenses, far-field radiation from a simple horn antenna, or other techniques, it is generally possible to minimize this error (**22**). Very often, however, there is a great temptation to ignore this effect and simply place a pair of microwave horns on opposite sides of the apparatus when the separation is often only of the order of a few wavelengths. It is not surprising that in such cases inconsistent measurements are often found.

The problems of refraction and diffraction have already been mentioned and in any transmission measurements the error introduced by these effects must be taken into account. This often involves the "calibration" of the apparatus by

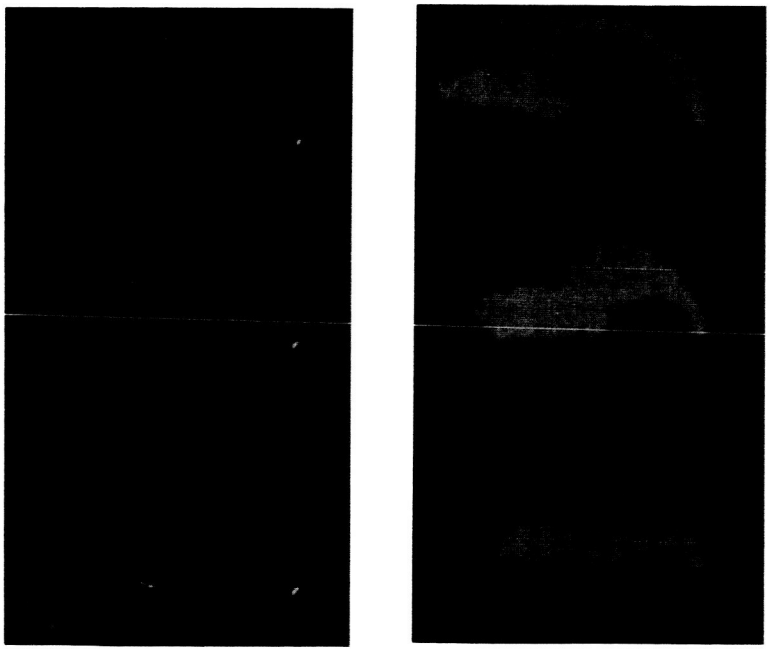

FIGURE 5. Sample results showing the difference in a multiple-probe display between a stationary plasma and a turbulent flowing plasma: (a) a stationary argon plasma excited at 60 c/sec with a sampling rate of 10^4/sec for a period of approximately 3 msec; (b) a turbulent (Mach 2) argon plasma with a sampling rate of 5×10^6/sec for a period of ~ 0.5 sec.

using samples of known geometry and dielectric properties in place of the plasma (**23, 51, 53**).

In transmission measurements it is also necessary to consider the effects of multiple reflections in the apparatus since these can introduce spurious signals at the receiving antenna. Apart from the obvious reflections from the walls of the vacuum system, it has been found that in some cases reflections arising from the receiving antenna itself can cause significant alterations in the measurements (**22**).

Apart from these considerations which mainly concern the apparatus limitations, one is confronted with the inherent complexities of the plasmas which are generated in the flow systems. In addition to the presence of spatial irregularities, the plasma often displays the randomly fluctuating properties characteristic of turbulent flow. In Figure 5 an illustration is given of the complications introduced into microwave measurements by such plasma turbulence (**37**).

The two photographs show the multiple probe display (see Figure 4) of a 9.2 Gc microwave signal transmitted through time-varying plasmas. In Figure 5a the signal is transmitted through a non-flowing argon plasma excited by a 60 c/sec source and in Figure 5b the signal is transmitted through a supersonic argon plasma stream. In both cases a time exposure was used so that the time development of the plasma could be photographed. In the first case only the variation during a quarter cycle of the excitation voltage is shown for a 10^4/sec sampling rate and in the second, a time exposure of about one-half second is used with a sampling rate of 5×10^6/sec. Since each spot on the screen gives the amplitude and phase of the transmitted microwave signal at a particular instant of time, such a time-integrated display shows the degree of variation (fluctuation) and the frequency of occurrence of the plasma parameters. This is shown by the spread and number density of the spots respectively in any region of the display. This comparison of Figures 5a and 5b shows clearly the problems involved in making meaningful measurements of complex plasma flow systems.

REFLECTION MEASUREMENTS

Many of the comments made concerning the instrumentation for transmission measurements apply equally well in the case of reflection studies. One major difference, of course, exists in the fact that reflection measurements are, in general, limited by the condition that $\omega \leq \omega_p$ must be satisfied to provide reflected signals of reasonable magnitude. Thus for a given plasma one is again limited in the range of wavelengths which can be utilized.

Whereas transmission measurements can be used to measure the properties of a plasma in a given volume, reflection measurements tend to examine "surface" effects since they are only able to penetrate the plasma until the electron density is such that $\omega_p = \omega$ (again assuming $\nu \ll \omega$). Any changes in electron density within the plasma beyond this region are not detectable in the reflected microwave signal. This difficulty can, in principle, be alleviated to some extent by using several frequencies (**13**) so that the "reflection" can be made to occur at different regions in the plasma, but this procedure is usually limited by the cost and bulk of the apparatus required.

Stray reflections from the apparatus are a serious problem in reflection measurements since they can often be of greater magnitude than the useful signal and it is difficult to separate the "useful" from the "stray". Matching techniques which involve the introduction of additional reflections to "tune out" the unwanted stray signals must be employed with considerable caution. Often the stray signal reaching the detector when there is plasma in the apparatus is quite different

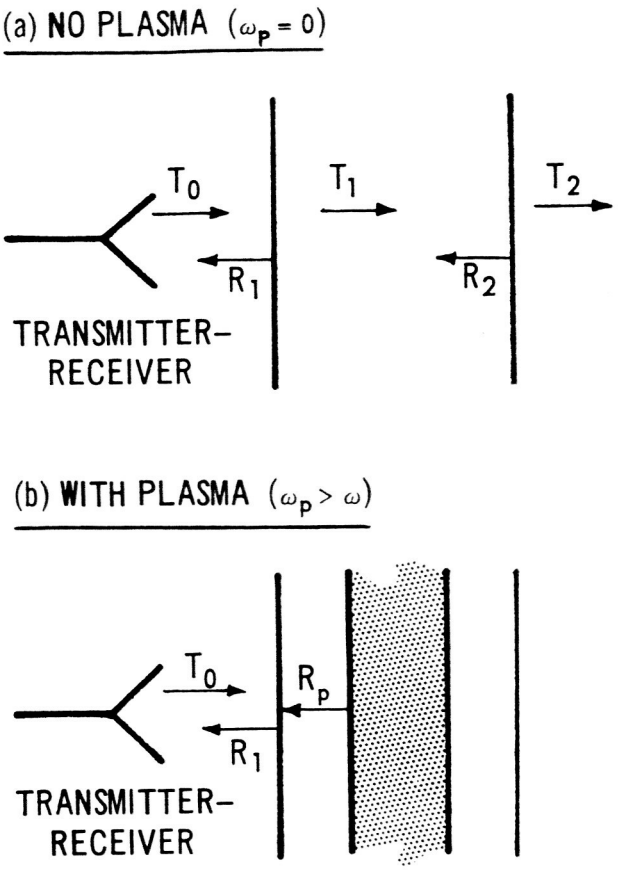

FIGURE 6. Schematic diagram to illustrate the change in "matching" conditions in a microwave reflection system as the plasma density changes. T represents transmitted signals, R reflected signals.

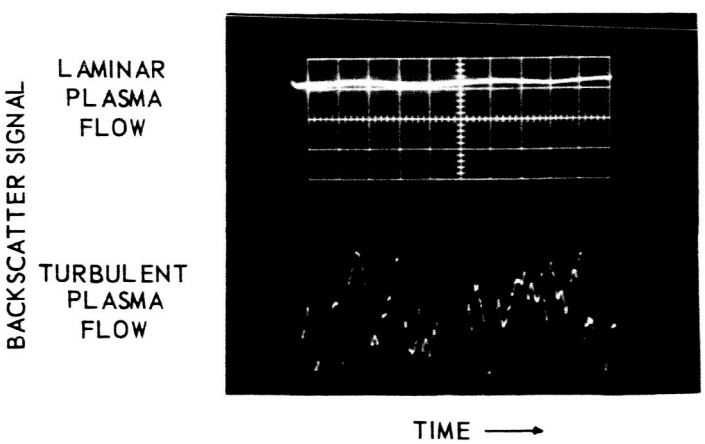

FIGURE 7. Comparison between the signal amplitudes of microwaves reflected from a laminar and a turbulent plasma flow-field. Time scale: 1 msec/div.

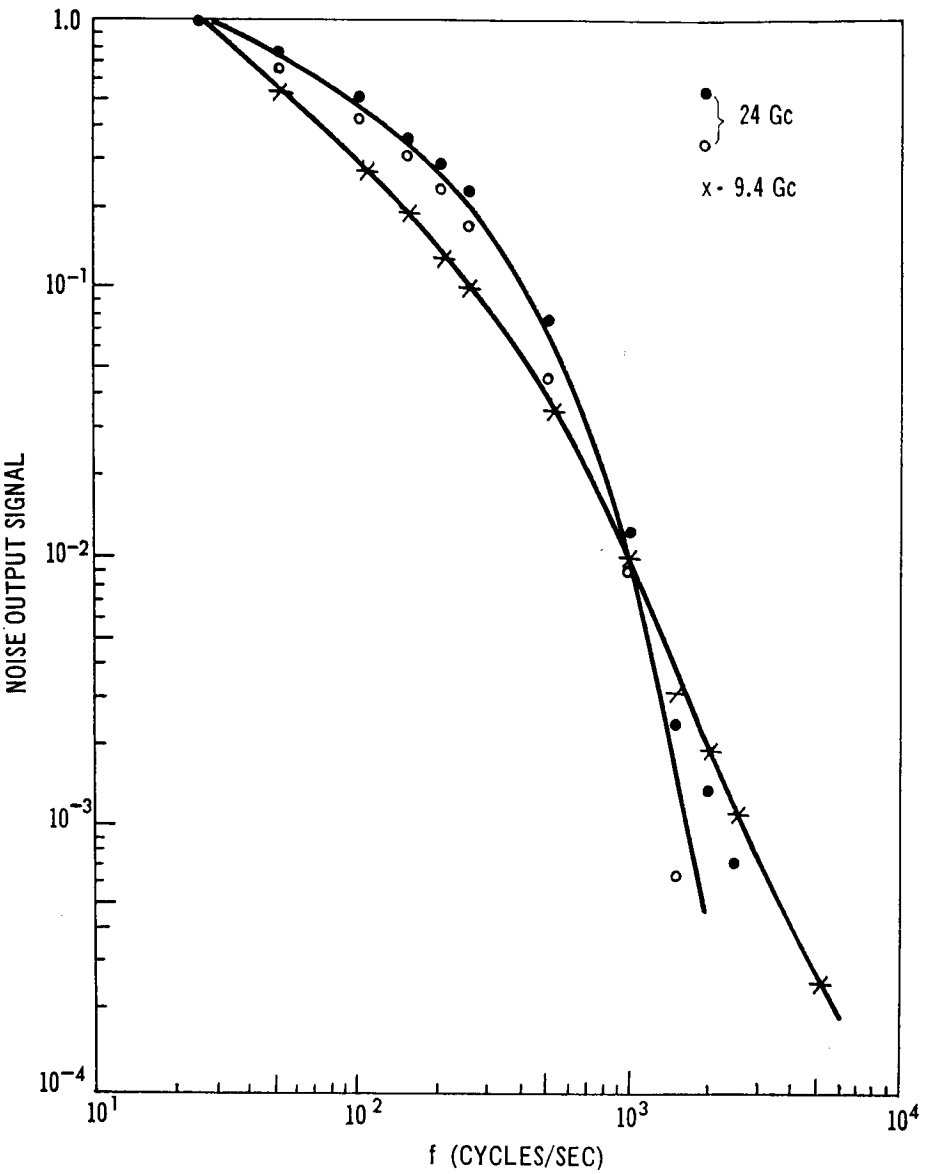

FIGURE 8. Frequency content of the fluctuating microwave signal (X and K band) reflected from a turbulent plasma stream. The results have been normalized to unity at 25 c/sec.

from that obtained with no plasma in the apparatus. Hence the matching of the system in the absence of a plasma (as is usually done experimentally) does not assure a matching when the plasma is present.

This fact can be readily illustrated by the simple example shown in Figure 6 in which a plasma is shown to be enclosed between two (dielectric) bounding walls. In the absence of plasma in the apparatus the stray signal reaching the receiver has contributions arising from both walls of the plasma container. If a plasma is introduced, however, the stray signal from the back wall is reduced to zero as ω_p

increases above ω. In this case the stray signal from the container now comes only from the first dielectric wall and the necessary matching condition is quite different. This case is very often encountered in many simple reflection measurements.

As with transmission measurements, time-dependent variations of the plasma properties can cause difficulties in the interpretation of the measurements. Figure 7 shows a sample photograph of the amplitude of a 9.4 Gc signal reflected from a supersonic plasma flow-field for both laminar and turbulent flow conditions as a function of time (**53**). In the laminar case the return is quite steady, whereas in the turbulent case the signal exhibits random fluctuations in amplitude. An analysis of the frequency content of this signal can be made with the aid of a wave analyzer and the results for two microwave frequencies (9.4 Gc and 24 Gc) reflected from the same plasma jet are shown in Figure 8 (**53**). It is seen that the spectrum has a frequency content similar to that measured for velocity fluctuations in turbulent flows (**62**). The full significance of these measurements is not as yet clear but the results serve to indicate some of the problems encountered in flowing plasmas as well as the applications of microwave techniques to the study of turbulence in plasma flow systems.

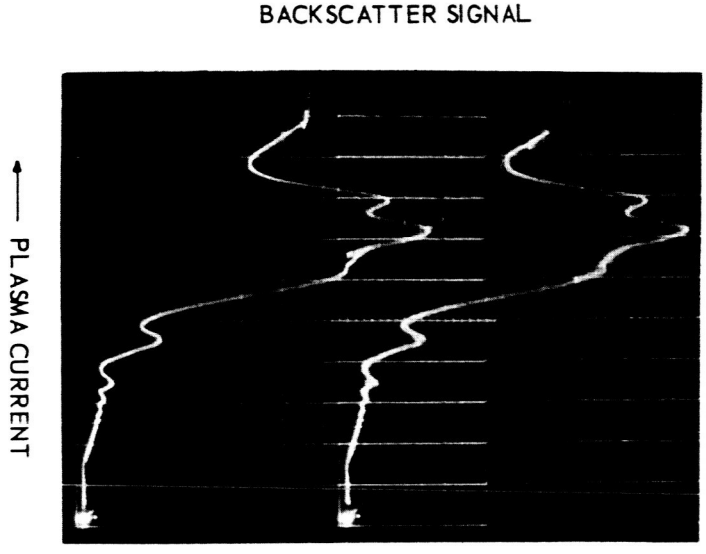

FIGURE 9. Sample resonance patterns for 9.4 Gc microwave scattered from a 5 mm diameter plasma column (mercury discharge tube).

Another quite different microwave reflection method involves the use of Doppler techniques to measure the velocities of moving plasma surfaces (**57, 63**). Using these techniques accurate measurements can be made of the motion of the effective "reflecting surface" in the plasma and this method has been used by various workers in both shock tube and ballistic range studies. It is also possible to employ pulsed "radar" techniques to define the plasma geometry to some extent by the time delay and shape of pulses reflected from plasma systems. Some laboratory measurements of this type have been reported (**47, 48**), but because of the small distances encountered in laboratory studies, these measurements require rather specialized equipment involving nanosecond pulse gear.

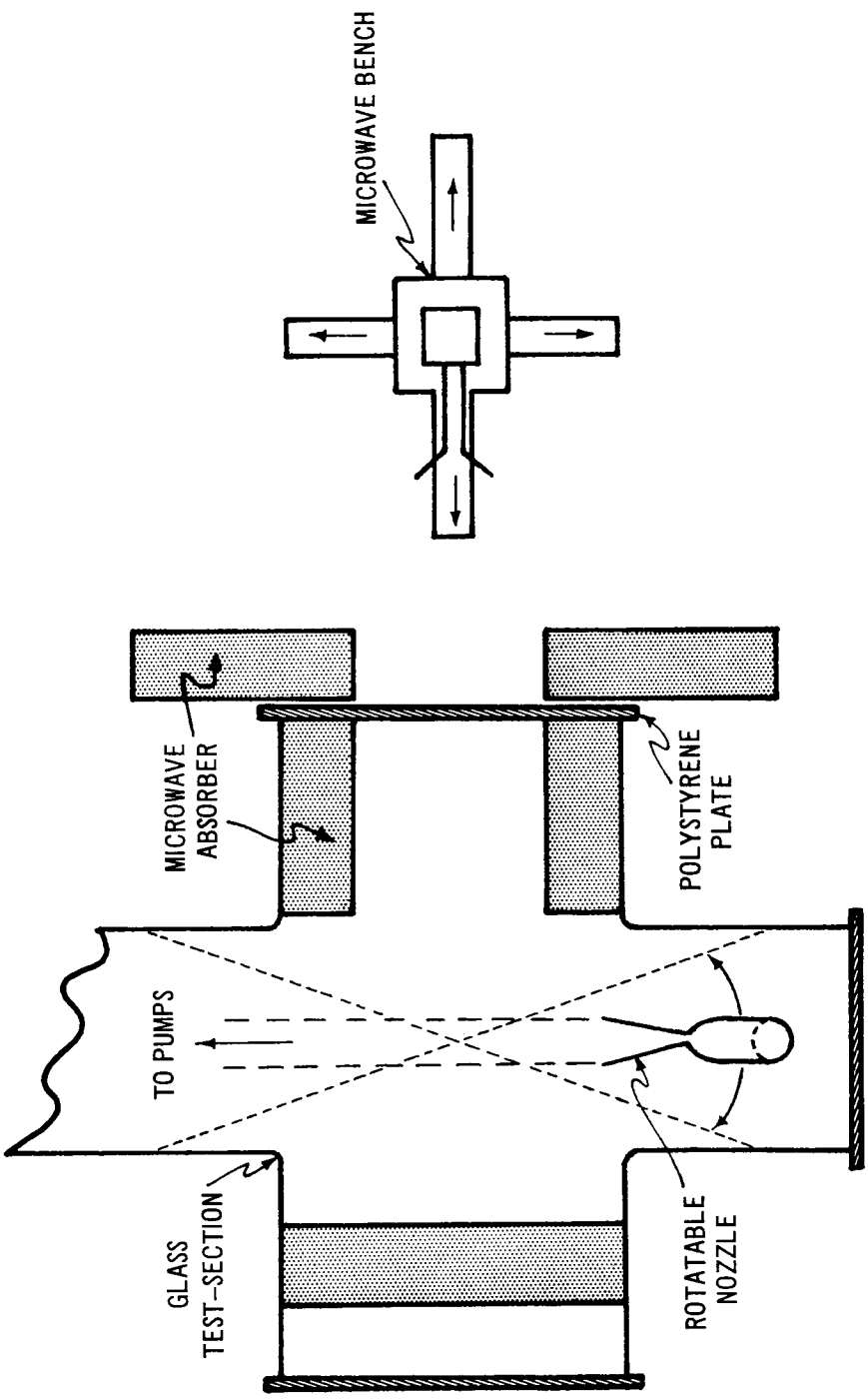

FIGURE 10. Schematic diagram of the apparatus used in the scattering studies.

SCATTERING MEASUREMENTS

As already mentioned, the concepts of "transmission" and "reflection" of microwaves by plasma become less clear if the plasma geometry differs appreciably from the simple quasi-slab approximations indicated in Figures 3a and 3b. In such cases it is often simpler to apply the analysis of conventional scattering theory (**16**), and the transmitted and reflected components of the wave field are then merely the "forward" and "backward" components in the scattered field. Because of the theoretical and experimental problems involved in measurements of such plasmas by microwaves, only a limited amount of laboratory investigation has been attempted—even for the simpler case of stationary plasmas in gas discharge tubes. Much of this work in recent years has been concerned with the scattering of microwaves by cylindrical plasma geometries with the emphasis being placed on the examination of the still unexplained resonance phenomena which occur for certain conditions of the incident wave fields and plasma properties (**64–68**). Figure 9 is a sample photograph (**53**) of the "resonances" obtained in the microwave signal backscattered from a cylindrical plasma as the discharge current (electron density) varies.

Scattering techniques can be extended to allow examination of the properties of flowing plasmas although they are somewhat limited in scope. In a recent investigation our laboratory has undertaken to examine some of the characteristics of microwave scattering from supersonic plasma jets (**53**).

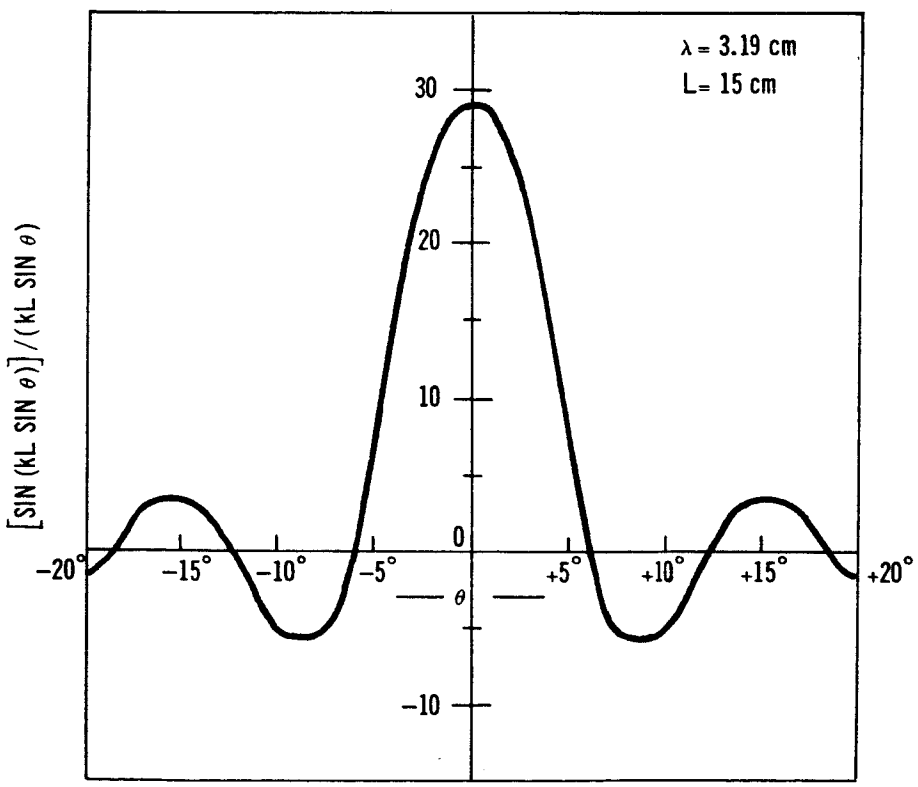

FIGURE. 11a. Theoretical aspect-angle dependence of the microwave signal backscattered from a metal cylinder of length *L*.

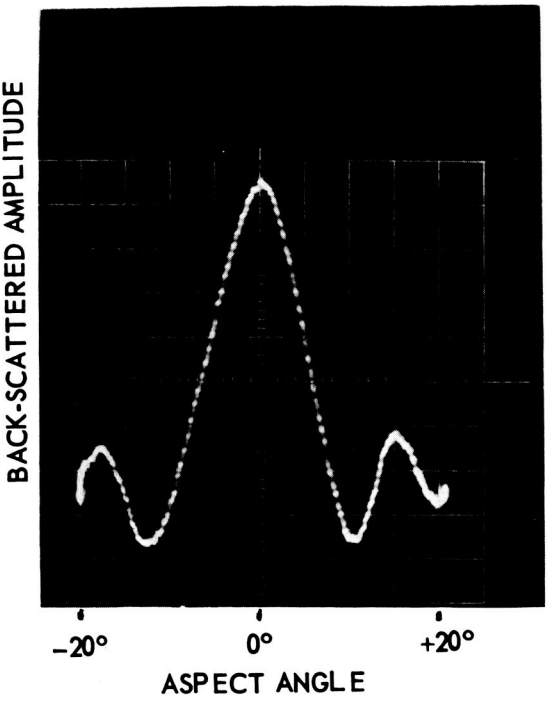

FIGURE 11b. Measured aspect-angle dependence of the microwave signal (9.4 Gc) back-scattered from an 0.5-inch diameter metal rod mounted in the tunnel (Figure 10) in place of the plasma.

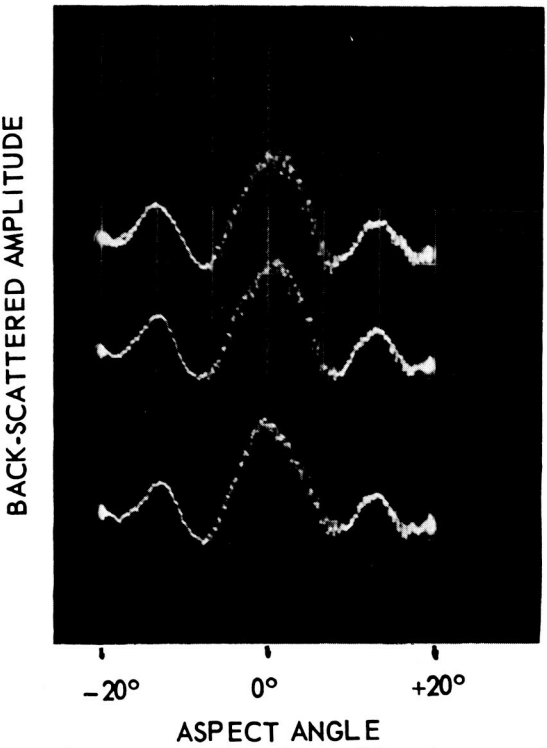

FIGURE 11c. Measured aspect-angle dependence of the microwave signal (9.4 Gc) back-scattered from a Mach 2 plasma jet in the tunnel.

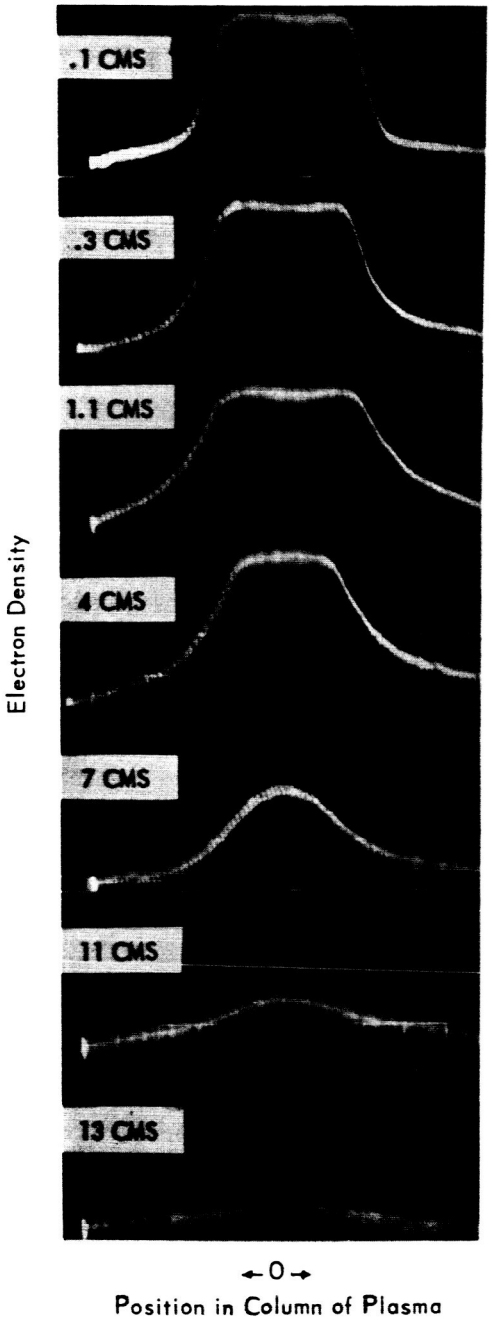

FIGURE 12a. Sample probe sweeps in the plasma jet showing the variation of the electron density in the flow-field at various distances from the nozzle.

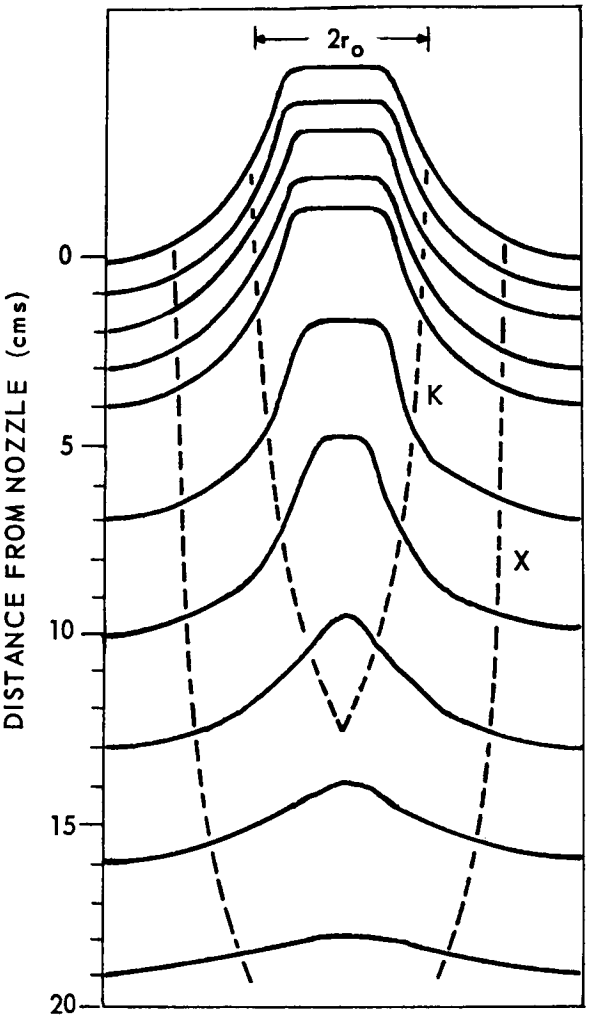

FIGURE 12b. A contour-type display of the electron density in the flow-field showing the effective reflecting surfaces ($K = 0$ surfaces) of the plasma for both X and K band microwaves (i.e., 9.4 and 24 Gc). The nozzle exit diameter, $2r_0$ is also indicated.

The apparatus (**69**) shown in Figure 10 was specifically constructed for this work and hence the techniques are not generally applicable to conventional flow facilities. Using the rotatable nozzle in this continuous flow device it is possible to examine the scattering of microwaves from the (cylindrical) plasma stream at various angles of incidence.

In Figure 11 results are shown for back-scattering (reflection) measurements using this system. In Figure 11a the theoretical results (**28**) of the variation of the amplitude of the back-scattered signal from a metal rod as a function of aspect angle are shown, and in Figure 11b and Figure 11c sample scattering results are shown for both a metal rod and a plasma jet. The electron density in the jet as derived from probe measurements is shown in Figure 12a. From such measurements considerable information concerning the plasma may be obtained. The plasma used in obtaining Figure 11 had very little axial variation of the electron density

in the portion of the jet probed by the signal (*X*-band curve in Figure 12b) hence the shape of the amplitude-versus-angle plot is very similar to that of the uniform metal cylinder.

The effects of axial gradients in the electron density can be seen in Figure 13 in which the amplitude-versus-angle plot is no longer symmetric about the "broadside" position. Measurements show that this curve is similar in form to that obtained by scattering from a tapered metal cylinder. Using this method it is thus possible to obtain some information as to the spatial variations of the plasma within

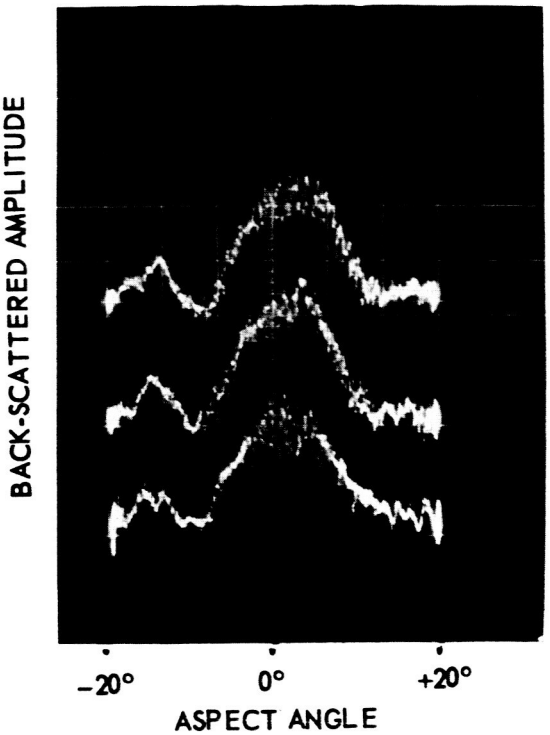

FIGURE 13. Aspect-angle dependence of the back-scattering from a turbulent plasma jet. The asymmetry of the curve is due to the large axial gradient of electron density in the stream and the "noisy" fluctuations of the signal are due to stream turbulence.

the microwave beam, but in all of this work it has been found essential to supplement the microwave measurements with probe diagnostics of the plasma (**53, 58**)

In addition, by using incident microwave signals polarized in a direction perpendicular to the axis of the plasma jet it has been possible to observe (**53**) in the streams the resonance effect mentioned above. Since these resonances are intimately related to the ratio of ω/ω_p it is possible that future findings may permit their use as a diagnostic technique (**70**).

RADIATION MEASUREMENTS

In principle, microwave radiation measurements are ideal for plasma studies since they introduce no perturbation of the plasma. The radiation, by the electrons in a plasma, of electromagnetic energy over a wide frequency range is a well-known fact and has led to the application of microwave radiometry for the measurement of electron temperature in plasmas (**1, 2**).

If the radiation received from the plasma is in a frequency range which is higher than the plasma frequency, the plasma is then essentially transparent to the radiation. Under these conditions the intensity of the radiation emitted can be expressed in terms of the emissivity of the plasma as computed from the basic radiation processes such as *bremsstrahlung*, recombination, and Cherenkov radiation. When the observed radiation is in the range of frequencies which corresponds to the plasma frequency, the absorptivity of the plasma to the microwaves is appreciable and one can use (assuming thermodynamic equilibrium) the generalized form of Kirchhoff's law (**71**) of thermal radiation for relating the intensity of emitted radiation to the electron temperatures. If the emitted radiation is at a frequency lower than the plasma frequency, then the reflectivity of the plasma to the electromagnetic radiation must be taken into account. In this case, the absorptivity of the plasma as appearing in Kirchhoff's law is reduced by the reflectivity of the plasma at that frequency.

When measuring radiation from plasmas which are not confined in a waveguide, particular care must be given to account for the directivity of the receiving antenna and the solid angle subtended by the plasma. This problem has been considered by Bachynski *et al.* (**72**). In all cases it is found that the power level of the microwave radiation emitted by plasmas is very low and consequently microwave receivers of very low noise level must be used. Microwave radiometers with the required sensitivity can be easily designed (**73**) for examining stationary plasmas (**74, 75**) but difficulties arise when one desires to observe rapidly time-varying and nonrepetitive plasmas (**46, 76**). In order to meet this requirement one needs to use a wide-band, low-noise receiver and at microwave frequencies this requires rather elaborate and expensive systems. As yet a very limited number of measurements have been reported on flowing plasmas and the results are rather unsatisfactory. There is no doubt that the measurement of the microwave radiation emitted by a plasma can be of great value in determining the temperature of the electrons in the plasma. It is felt that a concentrated effort should be made (**74**) to develop a reliable technique for measuring microwave radiation from nonrepetitive, time-varying plasmas and to correlate such measurements with the transmission, reflection, and scattering measurements.

CONCLUSION

Microwave techniques have proven to be of considerable value in the study of "simple" plasma systems. A high degree of accuracy is possible in the determination of the microwave parameters (phase, amplitude, frequency, etc.) with time resolutions of up to 10^{-7} sec and space resolution of the order of a radio frequency wavelength.

A major difficulty exists, however, in relating the measurable microwave parameters to the detailed properties of the plasma. This is particularly true in gas-dynamic flow studies since such plasma systems are inherently quite complex. The studies undertaken to date do not permit one to deduce the plasma parameters from microwave measurements with a precision approaching that of the microwave data.

A greater emphasis should, therefore, be placed on theoretical analyses which will take into account the significant influence of the practical experimental microwave techniques and upon the design of experiments which can approach more closely the requirements of the idealized theory. It is in this way that meaningful advances will be made.

REFERENCES

1. (a) Wharton, C. B., "International Summer Course in Plasma Physics", Danish Atomic Energy Commission, Risö, Denmark (August, 1960).
   (b) Wharton, C. B., "A Survey of Plasma Instrumentation", *IRE Trans.* NS-8, No. 4, 56 (1961).
2. Drummond, J. E. (ed.), *Plasma Physics* (New York: McGraw-Hill, 1961), III.
3. Cordero, J., Diederich, F. W., and Hurwicz, H., "Aerothermodynamic Test Techniques for Re-entry Structures and Material", *Aerospace Eng.*, **22**, 166 (1963).
4. Beiser, A., and Raab, B., "Hydromagnetic and Plasma Scaling Laws", *Phys. Fluids*, **4**, 177 (1961).
5. Chuan, R. L., "Experimental Investigation of Electromagnetic Propagation Through the Plasma Sheath in a Hypersonic Low Density Wind Tunnel" in *Electromagnetic Effects of Re-entry* (New York: Pergamon Press, 1961), 180.
6. Chopra, K. P., "Interactions of Rapidly Moving Bodies in Terrestrial Atmosphere", *Rev. Mod. Phys.*, **33**, 153 (1961).
7. Glick, H. S., "Interaction of Electromagnetic Waves with Plasmas of Hypersonic Flows", *ARS Jour.*, **32**, 1359 (1962).
8. Chapman, S., and Cowling, T. G., *Mathematical Theory of Non-Uniform Gases* (New York: Cambridge University Press, 1958), Chapter 18.
9. Guernsey, R. L., "The Kinetic Theory of Fully Ionized Gases", University of Michigan Tech. Report, Proj. 03114 (July 1960).
10. (a) Bachynski, M. P., Shkarofsky, I. P., and Johnston, T. W., "Plasmas and the Electromagnetic Field", RCA Victor Rep. No. 7-801-2 (1958).
    (b) Whitmer, R. F., "Microwave Interactions with Ionized Media", *Microwave Jour.*, **2** (February-March 1959).
11. Bachynski, M. P., Johnston, T. W., and Shkarofsky, I. P., "Electromagnetic Properties of High Temperature Air", *Proc. IRE*, **48**, 347 (1960).
12. Stratton, J. A., *Electromagnetic Theory* (New York: McGraw-Hill, 1941).
13. Wharton, C. B., and Slager, D., "Microwave Determination of Plasma Density Profiles," *J. Appl. Phys.*, **31**, 428 (1960).
14. Klein, M. M., Greyber, H. D., King, J., and Brueckner, K., "Interaction of a Non-Uniform Plasma with Microwave Radiation", in *Electromagnetic Effects of Re-entry* (New York: Pergamon Press, 1961), 105.
15. Albini, F. A., and Jahn, R. G., "Reflection and Transmission of Electromagnetic Waves at Electron Density Gradients", *J. Appl. Phys.*, **32**, 75 (1961).
16. Carswell, A. I., Nuttall, J., and Paquette, G., "Electromagnetic Wave Scattering by Plasma Systems with Applications to the Re-entry Problem", RCA Victor Res. Rep. 7-801-05; also DAMP Tech. Mono. No. 62-24 (December, 1962).
17. Bachynski, M. P., "Nature of Electromagnetic Waves in Non-Homogeneous Anisotropic Plasma", RCA Victor Res. Rep. 7-801-7 (June, 1960).
18. Budden, K. G., *Radio Waves in the Ionosphere* (New York: Cambridge University Press, 1961).
19. Ratcliffe, J. A., *Magneto-Ionic Theory and the Atmosphere* (New York: Cambridge University Press, 1959).
20. Ginzburg, V. L., *Propagation of Electromagnetic Waves in Plasma* (Amsterdam: North-Holland, 1961).
21. Panofski, W., and Phillips, M., *Classical Electricity and Magnetism* (Reading, Massachusetts: Addison-Wesley, 1956).
22. Bachynski, M. P., Cloutier, G. G., and Graf, K. A., "Microwave Measurements of Finite Plasmas", AFCRL-63-161 (May, 1963).

23. (a) Warder, R. C., Jr., Brodwin, M., and Ali Bulent Cambel, "Electron Density and Collision Frequency of Arc-Heated Argon Plasma", ASTIA AD-276-909 (January 1962).
(b) Warder, R. C., Jr., Brodwin, M., and Ali Bulent Cambel, "Sources of Error in the Microwave Diagnostics of Plasmas", *J. Appl. Phys.*, **33**, 2868 (1962).
24. Heald, M. A., "The Application of Microwave Techniques to Stellerator Research", Princeton University Rep. MATT-17 (August, 1959).
25. Born, M., and Wolf, E., *Principles of Optics* (New York: Pergamon Press, 1959).
26. Cloutier, G. G., Bachynski, M. P., and Graf, K. A., "Antenna Properties in the Presence of Ionized Media", AFCRL-62-191 (1962).
27. van de Hulst, H. C., *Light Scattering by Small Particles* (New York: Wiley, 1957).
28. Mentzer, J. R., *Scattering and Diffraction of Radio Waves* (New York: Pergamon Press, 1955).
29. (a) de Ridder, C. M., and Peterson, L. G., "Scattering from a Homogeneous Plasma Cylinder of Infinite Length", MIT Lincoln Lab. Rep. 312G-4 (1962).
(b) de Ridder, C. M., and Edelberg, S., "Scattering from Plasma Cylinders with Radial Variations in Electron Density", *Proc. Symp. Plasma Sheath*, 1962 (to be published).
30. Montgomery, C. G., *Technique of Microwave Measurements* (New York: McGraw-Hill, 1947).
31. Biondi, M. A., and Brown, S. C., "Measurements of Electron Ion Recombination", *Phys. Rev.*, **76**, 1697 (1949).
32. Rose, D. J., and Brown, S. C., "Methods of Measuring Properties of Ionized Gases at High Frequencies, III", *J. Appl. Phys.*, **23**, 1028 (1952).
33. Buchsbaum, S. J., and Brown, S. C., "Microwave Measurements of High Electron Densities", *Phys. Rev.*, **106**, 196 (1957).
34. Dougal, A. A., and Goldstein, L., "Energy Exchange Between Electron and Ion Gases Through Coulomb Collisions in Plasmas", *Phys. Rev.*, **109**, 615 (1958).
35. (a) "Re-entry Physics Program", Semi-Annual Technical Summary Report to ARPA, Lincoln Lab., MIT (1962).
(b) Murphy, E. L., Edelberg, S., and Pippert, G. F., "Electromagnetic Studies of Ionized Wakes", MIT Lincoln Lab. Rep. No. 266 (April 1962).
36. Primich, R. I., and Hayami, R. A., "Millimeter Wavelength Focussed Probes and Focussed Resonant Probes for Use in Studying Ionized Wakes Behind Hypersonic Velocity Projectiles", IEEE, Millimeter and Submillimeter Conference, January, 1963.
37. Carswell, A. I., "Stimulation Studies of the Electromagnetic Properties of the Wake of a Re-entry Vehicle", RCA Victor DAMP Tech. Mono No. 61-10 (December 1961).
38. (a) King, R., Harrison, C. W., Jr., and Denton, D. H., Jr., "The Electrically Short Antenna as a Probe for Measuring Free Electron Densities and Collision Frequencies in an Ionized Region", *NBS Jour. Res.* D. **65**, 371 (1961).
(b) Haycook, O. C., and Baker, K. D., "Plasma Frequency Probe", *Electronics*, **354**, 31 (November 1962).
39. Bramley, E. N., "Impedance of a Short Cylindrical Dipole in the Ionosphere", *Planet Space Sci.*, **9**, 445 (1962).
40. (a) Takayama, K., Ikegami, H., and Miyazaki, S., "Plasma Resonance in a Radio Frequency Probe", *Phys. Rev. Letters*, **5**, 238 (1960).
(b) Ichikawa, Y. H., and Ikegami, H., "Theory of Resonance Probe", *Prog. Theor. Phys.*, **28**, 315 (1962).

41. (a) Levitskii, S. M., and Shashurin, I. P., "Measurement of the Charge Concentration in Plasma by Means of Super-High Frequency Probes", *Sov. Phys. Bull. Acad. Sci.*, **23**, 938 (1959).
(b) Kononov, B. P., Rukhadze, A. A., and Solodukhov, G. V., "Electric Field of a Radiation in a Plasma in an External Magnetic Field", *Sov. Phy. Tech. Phys.*, **6** [405 (Eng.), 565 (Rus.)] (1961).
42. Jahn, R. G., "Microwave Probing of Ionized-Gas Flows", *Phys. Fluids*, **5**, 678 (1962).
43. Merrifield, S. E., "Microwave Propagation Through Plasmas", *Second Symp. on Plasma Sheath* (April 1962).
44. Miller, J., and Coe, G., "Hypersonic Flow Field Instrumentation", *Second Symp. on Plasma Sheath* (April 1962).
45. Brundin, C. L., Talbot, L., and Sherman, F. S., "Flow Studies in an Arc-Heated Low-Density Supersonic Wind-Tunnel", University of California Inst. of Eng. Res. Rep. HE-150-181 (April 1960).
46. Talbot, L., Katz, J. E., and Brundin, C. L., "Comparison Between Langmuir Probe and Microwave Electron Density Measurements in an Arc-Heated Low-Density Wind Tunnel", *Phys. Fluids*, **6**, 559 (1963) and University of California Inst. of Eng. Rep. HE-150-186 (Jan. 1961).
47. Rothman, H. S., "Electromagnetic Scattering From an Extended Laminar Plasma Column", Stanford Res. Inst. Tech. Rep. No. 10 (February, 1963).
48. Rothman, H. S., Guthart, H. and Morita, T., "Electromagnetic Scattering from Extended Targets", Stanford Res. Inst. Tech. Rep. No. 6 (September, 1962).
49. Schultz, D. L., "Microwave Studies of the Properties of Ionized Air in a Shock Tube", *Proc. IV Conf. on Ionization Phenomena in Gases* (Amsterdam: North-Holland, 1960), 1118.
50. Oshima, L., "Microwave Measurements of Plasma Flow in a Supersonic Wind Tunnel", University of S. California Eng. Center Rep. 83-208 (AFOSR 1556) (September, 1961).
51. Pass, H. R., "K-Band Microwave Interferometer Description and Initial Experiments in Pilot Model of USC Low-Density Wind Tunnel", USCEC Rep. 56-217, AFOSR TN 60-1087 (1960).
52. Lin, S. C., "A Survey of Shock Tube Research Related to the Aerophysics Problem of Hypersonic Flight", AVCP Rep. AMP63 (AFCRL 700) (1961).
53. Carswell, A. I., "Microwave Scattering from Supersonic Plasma Flow-Fields" RCA Victor Res. Rep. No. 7-801-24 (January, 1963).
54. Huber, P. W., "Experimental Techniques for Exploring the Interaction of Microwave Energy with Ionized Flowfields" in *Electromagnetic Effects of Re-entry* (New York: Pergamon Press, 1961), 172.
55. (a) Goldstein, L., "Non-reciprocal Electromagnetic Wave Propagation in Ionized Gaseous Media", IRE Trans. MTT, **6**, 19 (1958).
(b) Bachynski, M. P., and Osborne, F. J. F., "Microwave Techniques for Measurement of Transient Plasma Properties", in *Gas Discharges and the Electricity Supply Industry* (London: Butterworths, 1962).
56. Brown, J., *Microwave Lenses* (London: Methuens, 1953).
57. Primich, R. I., "Microwave Techniques for Hypersonic Ballistic Ranges", in *Electromagnetic Effects of Re-entry* (New York: Pergamon Press, 1961).
58. Carswell, A. I., "Probe Studies of Supersonic Plasma Flow-Fields" (to be published).
59. Wharton, C. B., Howard, J. C., and Heinz, O., "Plasma Diagnostics Developments in the UCRL Pyrstron Program" Second U.N. International Conf. on Peaceful Uses of Atomic Energy, **32**, 388 (1958).

60. Osborne, F. J. F., "A Multiple-Probe Microwave System for Plasma Studies", *Can. J. Phys.*, **40**, 1620 (1962).
61. Lisitans, G., "Mikrowellen-Polar-Interferometer für Plasmadichte-Messungen" in *Proc. Vth International Symposium of Ionization Phenomena in Gases* (Amsterdam: North-Holland, 1962), 405.
62. Franzen, B., and Fuchs, W., "Use of the Corona Discharge for Measurements of Turbulence", in *Proc. IVth International Symposium of Ionization Phenomena in Gases* (Amsterdam: North-Holland, 1960), 549.
63. (a) Maiden, J., and St. Pierre, C., "Some Measurements of the Physical Properties of the Plasma Sheath Around Hypersonic Projectiles", in *Electromagnetic Effects of Re-entry* (New York: Pergamon Press, 1961), 196.
(b) Hey, J. S., "A Radio Method of Determining the Velocity of a Shock-Wave", *Nature*, **179**, 1184 (June, 1957).
(c) Cook, M. A., Doran, R. L., and Morris, G. L., "Measurement of Detonation Velocity by Doppler Effect at Three Centimetre Wavelength", *J. Appl. Phys.*, **26**, 426 (1955).
64. Dattner, A., "The Plasma Resonator", Ericson Technics No. 2, 310 (1957), Stockholm.
65. Herlofson, N., "Plasma Resonances in Ionospheric Irregularities", *Arkiv für Fysik*, **3**, 247 (1951).
66. Herschberger, W. D., "Absorption and Reflection Spectrum of a Plasma", *J. Appl. Phys.*, **31**, 417 (1960).
67. Messiaen, A. M., and Vandenplas, P. E., "Comparison of Experiments with the Theoretical Scattering Behavior of a Cold Plasma Cylinder", *Phys. Letters*, **2**, 193 (1962).
68. Battocletti, J. H., "The Dipolar Resonance of the Cylindrical Low-Pressure Arc Discharge", *IEEE Trans.* MTT-11, 193 (May, 1963).
69. Carswell, A. I., "Radio Frequency Excited Plasma Tunnel for Laboratory Studies of Supersonic Plasma Flow-Fields", *Rev. Sc. Instr.*, **34**, 1015 (1963).
70. Crawford, F. W., Kino, G. S., Self, S. A., and Spalter, J., "Some Measurements of Steady and Fluctuating Plasma Number Densities by a Microwave Method", Stanford Univ. M. L. Report No. 961 (October, 1962).
71. (a) Rytov, S. M., *Theory of Electrical Fluctuations and Thermal Radiation* (Moscow: Acad. Sci. Press, 1953).
(b) Levin, M. L., "The Electrodynamic Theory of Thermal Radiation", *Dokl. Akad. Nauk.*, **102**, 53 (1955); *See also JETP*, **4**, 225 (1957).
72. Bachynski, M. P., French, I. P., and Cloutier, G. G., "Antenna Noise Temperature in Plasma Environment", *Proc. IRE*, **49**, 1846 (1961).
73. Dicke, R. H., "The Measurement of Thermal Radiation at Microwave Frequencies", *Rev. Sci. Instr.*, **17**, 268 (1946).
74. Fields, H., Bekefi, G., and Brown, S. C., "Microwave Emission From Non-Maxwellian Plasmas", *Phys. Rev.*, **129**, 506 (1963).
75. George, N., "Radiation Patterns of the Noise Emission from a Gaseous Discharge", *Proc. IVth International Symposium of Ionization Phenomena in Gases* (Amsterdam: North-Holland, 1960), 743.
76. Keren, D., "Detection of Microwave Radiation from the Re-entry Plasma", IEEE, Millimeter and Submillimeter Conference, January, 1963.

19. Allen E. Fuhs: *Flight Instrumentation for Reentry Plasma Sheath*

A number of instruments for probing the plasma sheath during reentry are described. The instruments respond to the induced magnetic field formed by the interaction of the ionized gas flowing through an applied magnetic field. Flight models to measure the product of electrical conductivity and velocity, σu, and the σu profile are discussed. In addition, analysis and description of laboratory transducers for determining velocity, σu fluctuations, and average electron collision frequency are presented.

INTRODUCTION

Surrounding vehicles traveling at high speeds within the earth's atmosphere is a plasma sheath arising from the heating of air in the shock-wave, in the boundary layer, or in separated shear layers. The plasma sheath, which completely encases the vehicle and feeds the wake that extends downstream a distance of many body diameters, interferes with radio communication to and from the vehicle. These facts have been well known to the professional missileman and space scientist for many years; since the Mercury flights, the facts are equally familiar to the layman.

In addition to communication blackout, the plasma sheath causes other problems. Less dense plasmas, while not causing blackout, have adverse effects on electromagnetic wave propagation, including refraction of the waves, introduction of noise, distortion of antenna patterns, and mismatch of antennas. The radar cross section of a reentry vehicle may be enhanced by one, two, or three orders of magnitude depending on the radar frequency and the reentry vehicle. Refraction of the electromagnetic waves may make angular information from on-board radar of questionable value.

However, the plasma sheath is not entirely detrimental. Magnetoaerodynamic attitude control attempts to exploit this flow of conducting gases by developing forces on the vehicle. The advent of practical superconducting coils has caused renewed interest in this aspect of attitude control. The plasma sheath also makes possible magnetohydrodynamic (MHD) power generation. If one considers the enormous amount of kinetic and potential energy dissipated during reentry, it is apparent that only a small fraction of this energy need be extracted to have megawatts of power.

ED. NOTE: Dr. Fuhs is with the Plasma Research Laboratory, Aerospace Corporation, El Segundo, California. This work was sponsored under Air Force Contract No. AF 04(695)-169.

This paper reports on flight instrumentation being developed to gain information about the reentry plasma sheath. Discussion of the plasma sheath is continued in the next section. Topics to be discussed are the plasma sheath, flight instrumentation and laboratory meters developed to obtain information about the ionized air.

THE PLASMA SHEATH (1–7)

In order to circumvent or to find solutions for the problems (e.g., telemetry blackout and enhanced radar cross section) and exploit the opportunities (e.g., magnetoaerodynamic attitude control or MHD power generation during reentry), detailed knowledge of the ionized air forming the plasma sheath is essential. Information can be obtained from calculations, but in order to proceed with the calculations, idealizations and simplifications are often necessary. Experiments in hypersonic facilities yield useful information; however, it is difficult to duplicate all the similarity parameters. In-flight measurements can be used to provide valuable guides for additional theoretical and experimental work and as criteria to indicate where the calculations are sound and where important physical phenomena have been omitted.

In order to design instruments to measure a certain property of the plasma sheath it is necessary to know approximately the range of values that will be encountered during reentry. It is necessary to know the correct gain for the amplifiers. Although the information presented in this section was initially obtained to answer the obvious questions of amplifier gain and instrument design, it is of sufficient general interest to warrant inclusion here.

PARAMETERS INFLUENCING THE PLASMA SHEATH

The trajectory, or more specifically the altitude and Mach number of the vehicle has a pronounced influence on the plasma sheath. Table I, which is intended to demonstrate that increased velocity compounds the difficulties with electromagnetic wave propagation, lists typical values of the electron density, N_e, for equilibrium air behind a normal shock.

TABLE I. ELECTRON DENSITIES FOR DIFFERENT TRAJECTORIES

Trajectory	*Typical velocity* (ft/sec)	*Electron density*, cm^{-3}	
		200,000 ft alt	300,000 ft alt
Suborbital IRBM	15,100	7×10^{12}	6×10^{10}
Suborbital ICBM	23,200	8×10^{13}	8×10^{11}
Orbital	25,600	2×10^{14}	3×10^{12}
Superorbital (parabolic)	36,700	3×10^{16}	5×10^{14}

Body shape also influences the plasma sheath. Simple axisymmetric bodies are usually categorized as blunt- or sharp-nosed, depending on whether or not the bow shock wave is attached; however, for the purposes of plasma sheath analysis, these bodies are differentiated by the manner in which their sheath properties are determined. Thus, a blunt-nosed body is one whose sheath properties are determined by air that has passed through a normal or nearly normal shock wave. A sharp-nosed body is one whose sheath properties are determined by the viscous dissipation in the boundary layer, which on a sharp-nosed vehicle is supplied with air that has passed through a weak oblique shock.

There is also an intermediate category of vehicle that may be described as slightly blunted. The boundary layer on the forward part of a slightly-blunted vehicle is fed by high-entropy gases from the nose. At some point along the vehicle, the high-entropy flow is absorbed by the boundary layer; downstream from that point the boundary layer feeds on air that has been processed by an oblique shock.

The spatial distribution of temperature and electron density normal to the surface obviously depends on body bluntness. There are, of course, more complex body shapes, especially for manned reentry vehicles, aerospace planes, and other lifting bodies.

Another factor determining the properties of the plasma sheath is the ablation material. Vaporization and injection of the ablation material has a fluid mechanical effect on the boundary layer. Impurities in the ablator may seed the boundary layer and increase N_e. Ablation products influence the chemistry of the high-temperature air by altering compositions and electron densities. An additional degree of complexity is thus added to the plasma sheath.

PARAMETERS CHARACTERIZING THE PLASMA SHEATH

When a macroscopic approach is used to analyze wave propagation, (**8**) the plasma is characterized by its electrical permittivity, ε, and an electrical conductivity, σ. Attenuation and phase shift can be calculated if these are known.

In terms of microscopic plasma variables, ε and σ are functions of the plasma frequency, ω_p (or N_e), and the electron collision frequency, ν. In the presence of magnetic fields the ratio of electron-cyclotron frequency to collision frequency may be of importance.

Spatial distribution of ε and σ, which is defined both as the profiles normal and tangential to the vehicle surface, is required information for the analysis of wave propagation (**9, 10**). The model of a plasma filling a semi-infinite half space is inadequate for obtaining realistic predictions about the plasma sheath.

Table II contains information concerning the plasma sheath surrounding a sharp cone. The quantity $\omega_c/\nu B$ determines the strength of magnetic field required to make ω_c/ν equal to unity. This is the strength of the magnetic field required to make the plasma behave as an anisotropic medium. For example, in the flank

TABLE II. DATA FOR PLASMA SHEATH ON SHARP CONE

Altitude (ft)	$\omega_c/\nu B$ (per gauss)	ω_p (rad/sec)	ν (collision/sec)	σ (mho/m)	u (m/sec)	σu (mho/sec)	δ (cm)	N_e (cm^{-3})
Stagnation Region								
250	8.8×10^{-3}	1.77×10^{11}	2×10^{9}	140	—	—	—	10^{13}
200	1.25×10^{-3}	5.22×10^{11}	1.41×10^{10}	170	—	—	—	9×10^{13}
150	2.3×10^{-4}	1.51×10^{12}	7.6×10^{10}	270	—	—	—	7×10^{14}
100	3.2×10^{-5}	4.97×10^{12}	5.6×10^{11}	390	—	—	—	8×10^{15}
50	5.5×10^{-6}	4.46×10^{12}	3.2×10^{12}	55	—	—	—	8×10^{15}
Flank Region								
250	0.28	3×10^{9}	6.3×10^{7}	1.4	3500	4900	5	3×10^{9}
200	0.0354	10^{10}	5×10^{8}	1.8	3600	6500	1.5	3×10^{10}
150	6.4×10^{-3}	3×10^{10}	2.75×10^{9}	2.4	3600	8600	0.6	3×10^{11}
100	8.4×10^{-4}	7×10^{10}	2.1×10^{10}	2.3	3500	8100	0.2	1.6×10^{12}
50	1.3×10^{-4}	4.3×10^{10}	1.3×10^{11}	0.12	2800	340	0.08	6×10^{11}

region at 150,000 feet a magnetic field of 157 gauss gives $\omega_c/\nu = 1$. The d-c electrical conductivity, equal to $\omega_p^2 \varepsilon_0/\nu$, has been calculated. The plasma sheath thickness, δ, has been taken as being equal to the boundary-layer thickness. In Table II, δ is for a station 3 feet from the nose. The data are for a semivertex angle of 10 degrees, a wall temperature of 2000°K, and an ICBM trajectory with a velocity of 23,500 ft/sec at an altitude of 150,000 feet. The data were calculated using the information from Dix (**4**).

The instruments described in the following section measure σu. Hence σu has been calculated using as an estimate $u = u_\infty/2$. One advantage of an instrument that responds to σu is the relatively small change in this quantity with altitude. In the altitude range 250,000 to 100,000 feet, σu varies by less than a factor of 2, whereas N_e changes by a factor of 500. Instruments responding to N_e must have a wide dynamic range. The reason the σ does not change appreciably is that increases in N_e are compensated for by increases in ν.

In contrast to sharp-nosed vehicles, values of σu as high as 5×10^5 mho/sec may be observed in the flank region of blunt-nosed vehicles. This is 100 times larger than for a sharp-nosed vehicle. As a consequence, measurements of the plasma sheath on a sharp-nosed vehicle are significantly more difficult.

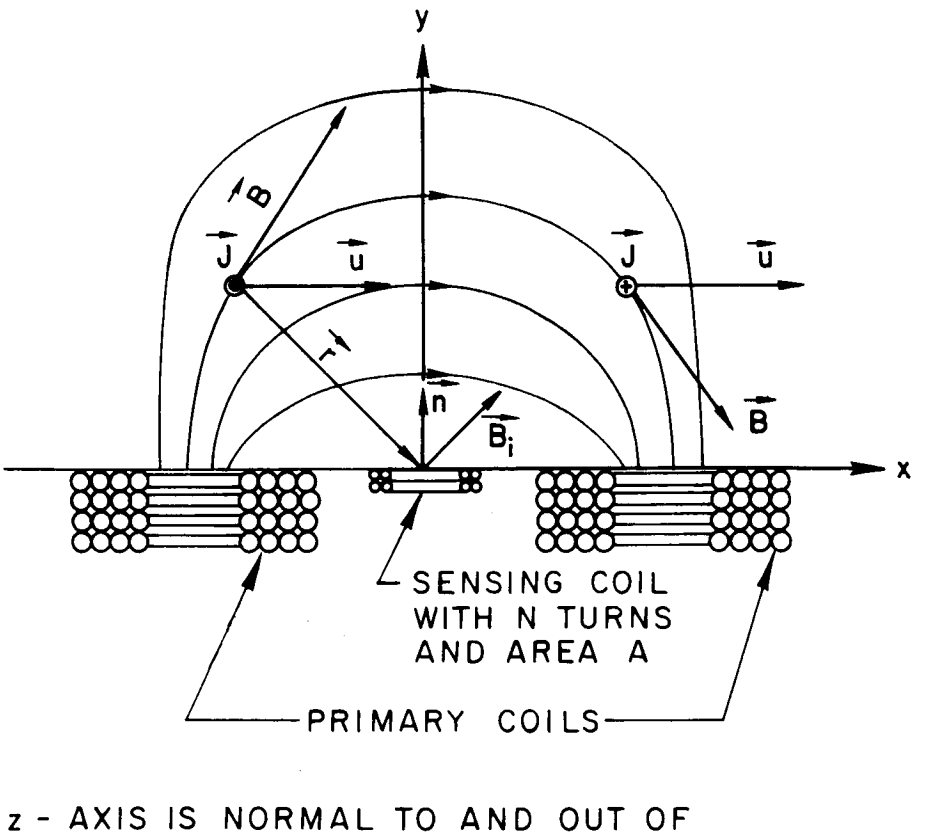

FIGURE 1. Transducer coil arrangement. An emf is induced in the sensing coil by the time rate of change of normal component of B_i.

FLIGHT INSTRUMENTATION DEVELOPED AT THE PLASMA RESEARCH LABORATORY

The several instruments described here for measuring plasma sheath properties are in various stages of development at the Plasma Research Laboratory. The first instruments described—three average σu meters and a σu profile instrument —have been flown or are soon to fly. The MHD flow angle indicator, the velocity meter, and the turbulence indicator have been tested in the laboratory. An instrument for the measurement of electron collision frequency has been theoretically analyzed but has not yet been tested in the laboratory. These instruments may be used to measure not only the reentry plasma sheath but also other high-speed, ionized-gas flows, including rocket exhausts, MHD generators, and arc plasma jets.

RELATION OF SIGNAL TO FLOW PROPERTIES

In previous publications (**1, 11**) the signal, which is the voltage induced in the sensing coil, was analyzed in detail. The analysis will be briefly reviewed here.

Consider a coil arrangement consisting of a sensing coil located between two primary coils as shown in Figure 1. The primary coils are driven at audio frequencies and provide a magnetic field $\vec{B}$ that penetrates into the plasma flowing at velocity $\vec{u}$. Currents, $\vec{J}$, are induced as a result of the motion of the conductor through the magnetic field. The induced magnetic field $\vec{B}_i$, which fluctuates at the frequency of $\vec{B}$, links with the sensing coil that has a voltage e. The currents $\vec{J}$ are equal to $\sigma(\vec{E}+\vec{u}\times\vec{B})$. The electrical conductivity σ is the d-c value and for ionized gases equals $\omega_p^2\varepsilon_0/\nu$. It can be shown (**2, 12**) that for the two-dimensional case $\vec{E}$ is zero, and for oblong primary coils (long dimension in the z-direction) $\vec{E}$ is negligible. The voltage in the sensing coil is

$$e = -\frac{NA\mu_0}{4\pi}\frac{\partial}{\partial t}\int_V \frac{\sigma(\vec{u}\times\vec{B})\times\vec{r}}{r^3}\cdot\vec{n}\,dV - N\frac{\partial}{\partial t}\int_A \vec{B}\cdot\vec{n}\,dA \tag{1}$$

The second integral represents the primary field that links the sensing coil; it is an unwanted voltage and is termed the null signal. By careful balance of the primary field this signal can either be eliminated or made negligibly small. Manipulation of the vectors as indicated in the first integral leads to

$$e = \frac{NA\mu_0\omega}{4\pi}\int_x\int_y\int_z \frac{\sigma(y)u(y)xB_y(x,y,z)}{r^3}\,dx\,dy\,dz \tag{2}$$

which can be rewritten as

$$e = \int_y \sigma u K\,dy \tag{3}$$

where

$$K(y) = \frac{NA\mu_0\omega}{4\pi}\int_x\int_z \frac{xB_y(x,y,z)}{r^3}\,dx\,dz \tag{4}$$

The function $K(y)$ is known as the influence function and can be readily measured in the laboratory (**11**). The influence function equals the signal that would result

from a unit layer of conducting material with unit conductivity moving at unit velocity and located at distance y.

AVERAGE σu TRANSDUCERS

A transducer with a single influence function and hence one signal yields a measurement of the average value of σu as given by

$$\overline{\sigma u} = \frac{e}{\int K\, dy} \tag{5}$$

An average σu transducer was flown successfully aboard a reentry vehicle.

Flight on RVX–2A

An instrument (**12**) using a transducer geometry similar to that shown in Figure 1 was flown on board the RVX–2A, a sphere-cone reentry vehicle. This reentry vehicle (R/V) followed a typical ICBM trajectory. Figure 2 shows the location of the transducer on the R/V and the geometrical relation of the flow field to the applied magnetic field. Figure 3 shows the results of the measurement.

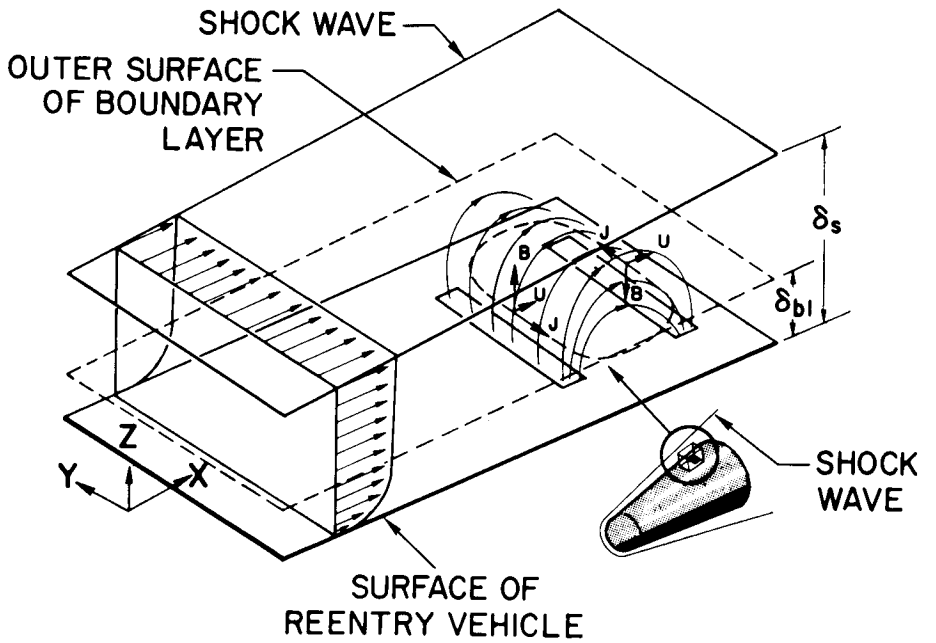

FIGURE 2. Flow field and location of transducer on reentry vehicle. The coils of the conductivity meter are located well aft on the reentry vehicle. The flow of conducting gas u interacts with the magnetic field B to provide a current density i.

The upper curve in Figure 3 is a plot of the angle of attack of the R/V as a function of time. Also indicated are the periods of fade and blackout of the telemetry. The lower solid curve shows $\overline{\sigma u}$ as a function of time; $\overline{\sigma u}$ was obtained

from the flight measurements of e, laboratory measurements of $\int K\,dy$, and equation (5). The electrical conductivity behind a normal shock was calculated for the RVX–2A trajectory. Results of the calculations for σ, based on the method outlined by Meyer (**13**), are shown on the right-hand side of the lower graph by the dashed curve, with values for mho/m.

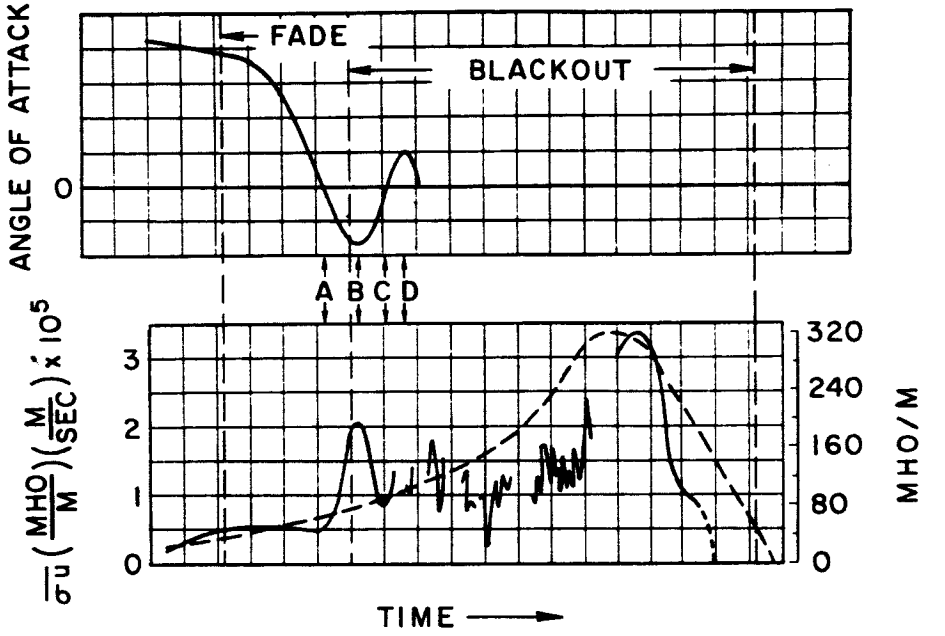

FIGURE 3. Observed value of $\overline{\sigma u}$ and the angle of attack of the reentry vehicle.

The meter signal follows the oscillation of the angle of attack, i.e., a local minimum of the signal corresponds to zero angle of attack. At time A (Figure 3) the angle of attack is zero, and $\overline{\sigma u}$ is at a minimum. At time B the angle of attack is at its peak value, and $\overline{\sigma u}$ has increased to a local maximum. This fact suggested the flow angle indicator, described in another section.

Axisymmetric Transducer Geometry (14–16)

Aerodynamic stability requires the center of gravity of the vehicle to be in front of the center of pressure. Conical reentry vehicles frequently require dense ballast placed far forward to achieve this condition. The ballast replaces a part of the payload. A transducer has been developed that serves two functions: it provides measurement of an average value of σu, and its weight serves as ballast. Figure 4 shows the coil arrangement, which has been tested in an arc jet. Analysis shows that most of the signal is due to the induced currents in a narrow region of the plasma flow concentric with the sensing coil. Two reasons account for this. First, the magnetic coupling between the sensing coil and the current rings in the gas falls off sharply as the separation between the two increases. Second, the applied magnetic field, which drives the currents, falls off rapidly with distance from the sensing coil. For the geometry shown in Figure 4, 95 per cent of the signal is due to the currents within a region in the gas twice the width of the sensing coil.

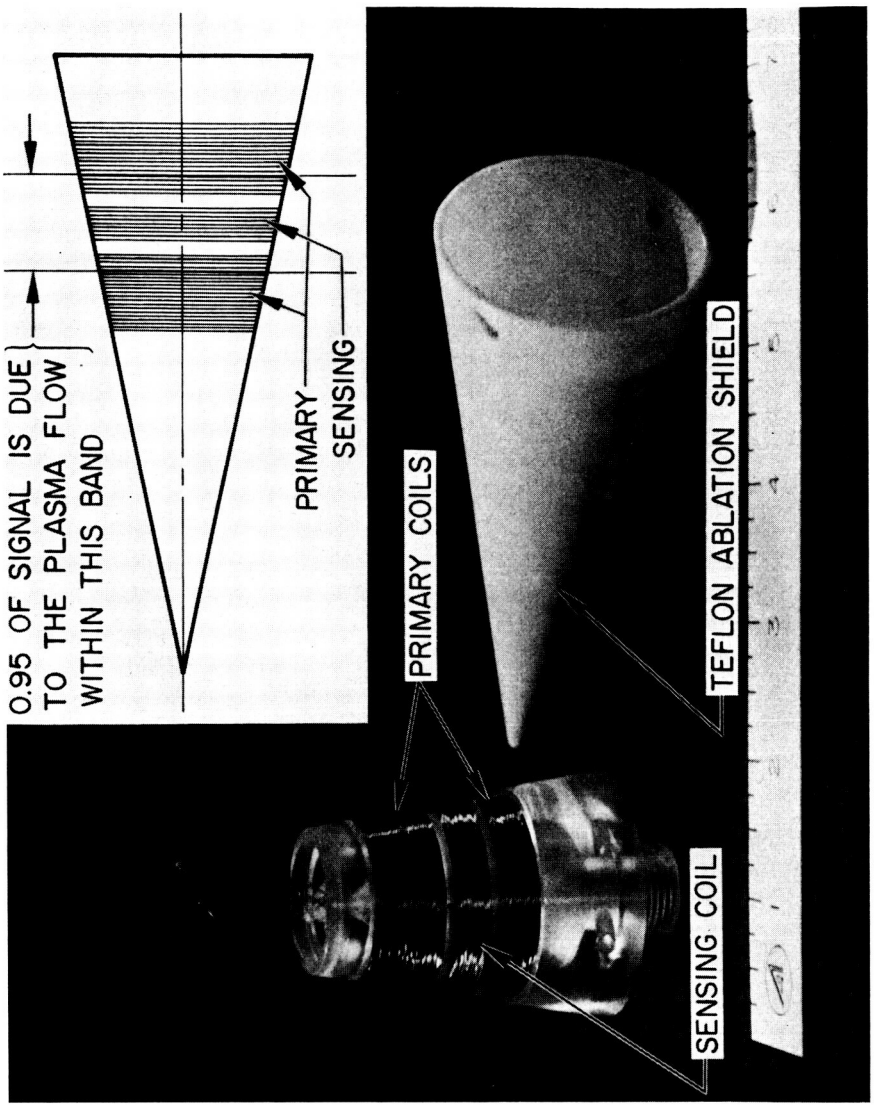

FIGURE 4. Average σu transducer geometry readily adaptable to cone designs.

(See the inset diagram in Figure 4.) This means that the plasma flow is sampled in the vicinity of the sensing coil, and interpretation of the signal is more meaningful since only a localized region contributes to the signal.

Transducer Using Permanent Magnets (17)

When the instrumentation program (**2**) was first initiated at the Plasma Research Laboratory it was necessary to decide whether to use a d-c or an a-c applied magnetic field. The first instruments developed used a-c. However, it is obvious that the induced field, B_i, exists with a d-c primary field. In order to measure σu with a thick metallic skin between the conducting flow and the transducer, a d-c meter is essential. If an a-c method is attempted, eddy currents in the skin attenuate both the applied magnetic field and the induced magnetic field.

The earth's magnetic field is approximately 500 milligauss. For one application aboard a reentry vehicle the calculated B_i varied between 1 and 10 milligauss. Hence cancellation of the earth's magnetic field is necessary. One method of cancellation is to use two magnetic detectors whose outputs are sensed differentially such that the signal due to earth's magnetic field cancels, whereas the signal due to plasma flow adds. Figure 5 schematically depicts one arrangement. Figure 6 is a photograph of the flight instrumentation package.

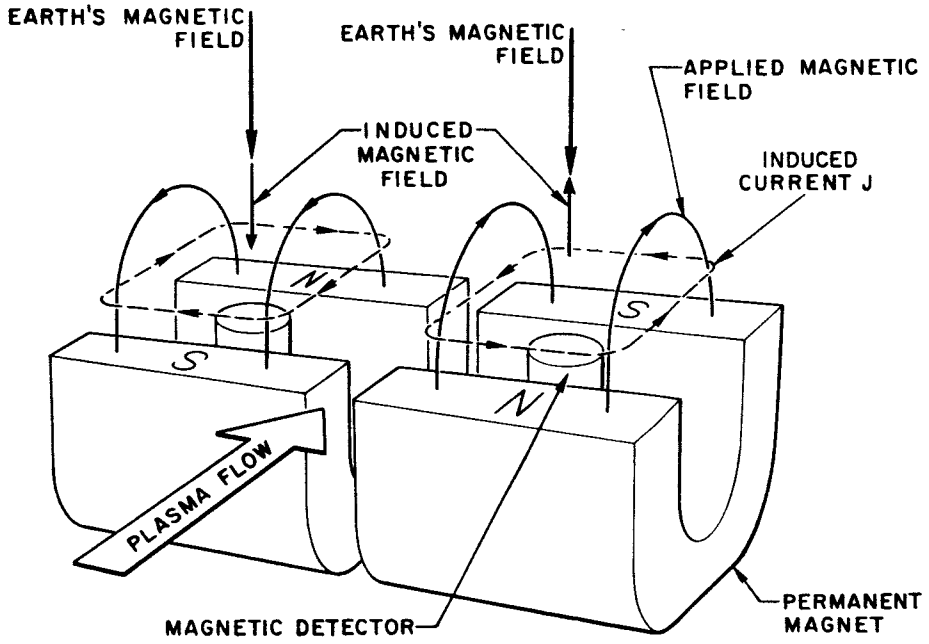

FIGURE 5. Cancellation of earth's magnetic field and addition of induced magnetic field due to plasma flow.

CONDUCTIVITY/VELOCITY PROFILE METER (1, 11)

If transducers with different magnetic field geometries are used, the flow of ionized gas can be sampled differently. Each geometry provides a different signal given by

$$e_i = \int_{\text{ablation surface}}^{\text{shock wave}} \sigma u K_i \, dy \tag{6}$$

where the subscript i identifies the different signals. The K_i are measured in the laboratory; the e_i are measured in flight. Distinctly different K_i can be obtained by changing the primary magnetic field geometry and by altering the geometrical relation between the induced magnetic field and the sensing coils.

From this information the σu profile can be calculated. One procedure is to divide the integration interval into discrete intervals Δy_j, which may be of unequal length. Having chosen the Δy_j, the corresponding $(\sigma u)_j$ values can be determined

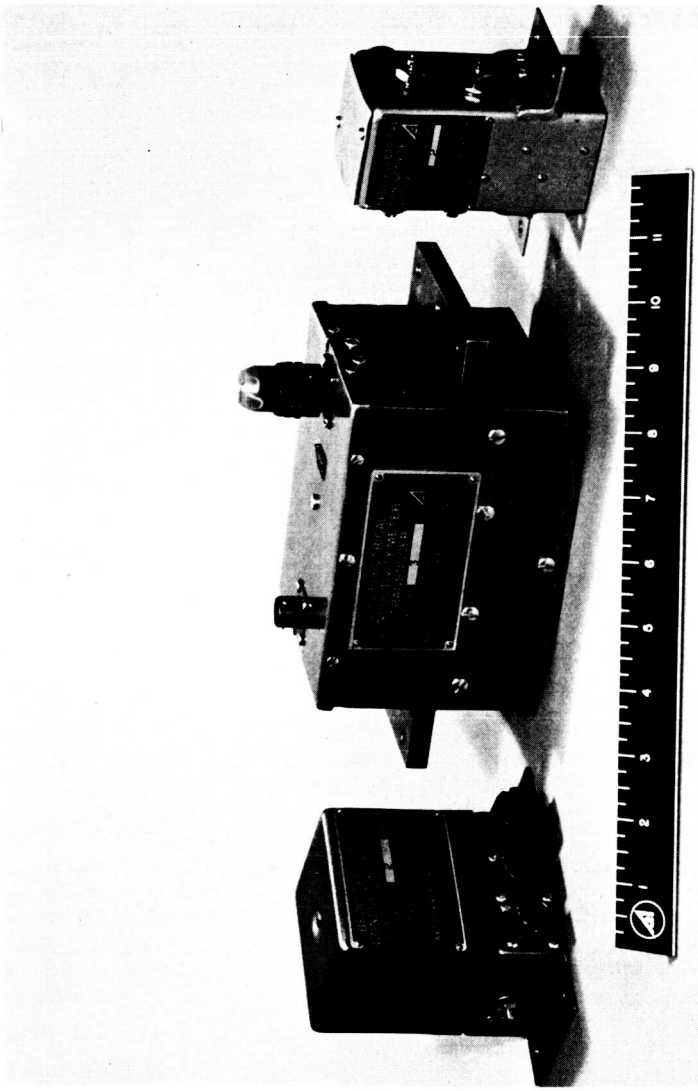

FIGURE 6. The flight instrument to measure σd has three components: transducer, 8 lb; electronics box, 2.5 lb; and compensation box, 1 lb.

as shown in Figure 7. For the case illustrated in Figure 7, a five-signal transducer is required. A three-signal transducer is shown in Figure 8. Other geometries, including a nine-signal transducer, have been considered and are discussed by others (**1, 11**).

The transducer illustrated in Figure 8 is designed to sample the plasma flow in different ways by having different scale primary fields. A plasma layer of Δy thickness appears to the small primary coil to be $\Delta y/R=1$ inch thickness and to be centered at $y/R=2$. The same plasma layer appears to the large primary coil to be $\Delta y/R=\frac{1}{3}$ inch thickness and to be centered at $y/R=\frac{2}{3}$. The plasma layer is measured by use of different portions of the influence function.

Using knowledge of e_1, e_2, and e_3, and the influence functions, K_1, K_2, and K_3, from the system shown in Figure 8, the profile of a spinning graphite disk was

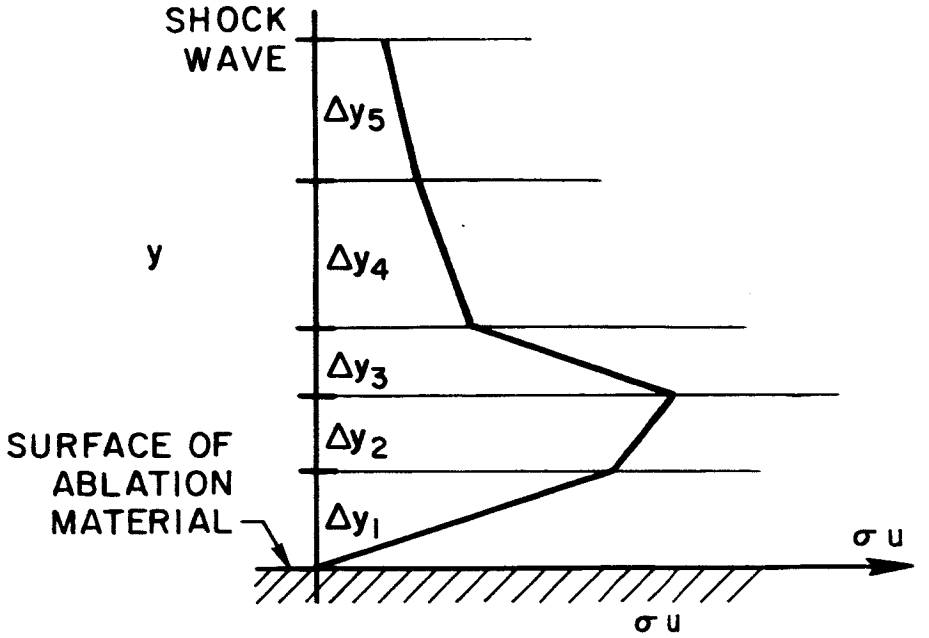

FIGURE 7. Illustration of the results of a calculation of a σu profile.

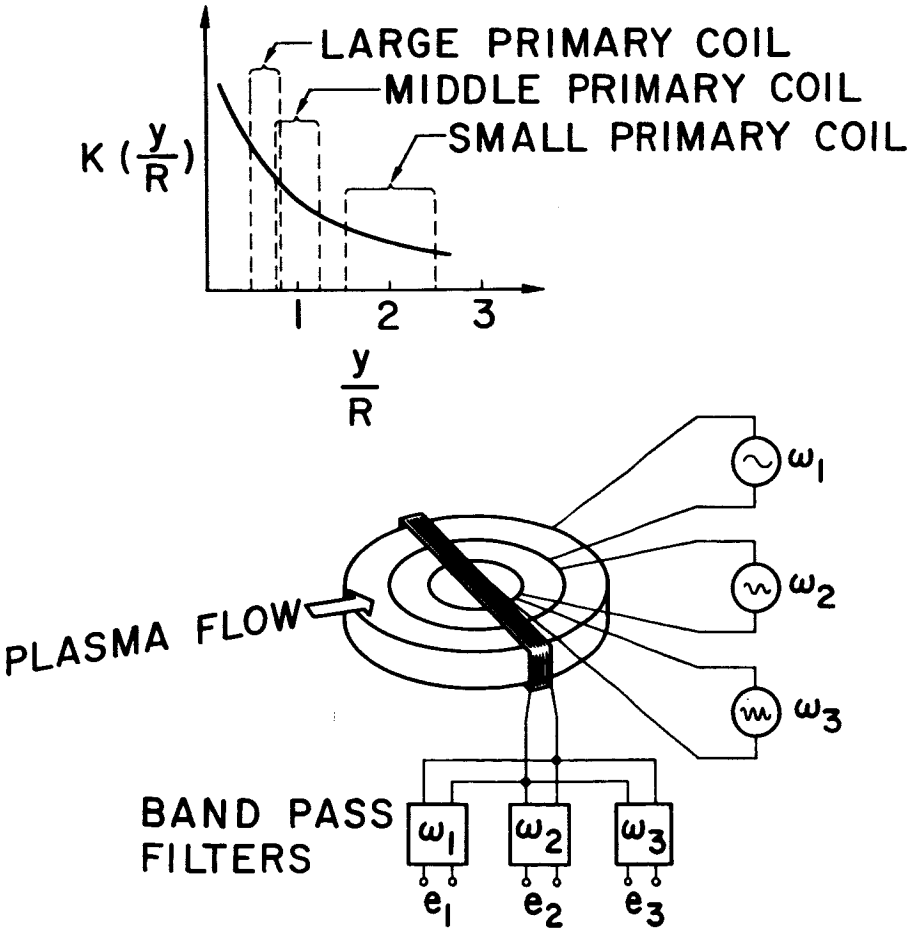

FIGURE 8. Coil geometry providing three different scale primary fields.

calculated. A comparison of the actual and measured profiles is shown in Figure 9. Three different experiments are plotted, with the disk located at 0.5, 1.0, and 2.0 inches from the transducer. The influence function for the smallest primary coil has been plotted in the bottom graph. The error in predicting the disk thickness, when the disk was 2 inches from the transducer, is due to the fact that the meter is not sensitive beyond about 3 inches.

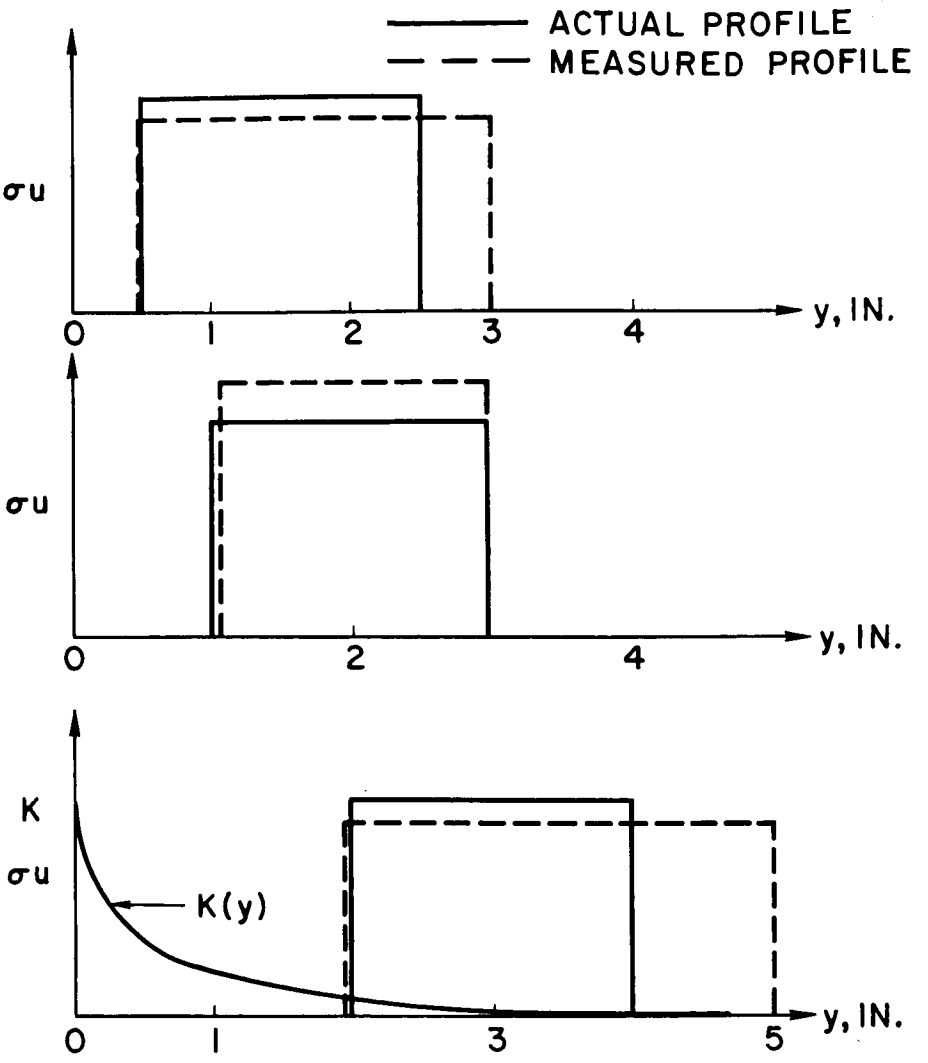

FIGURE 9. Comparison of actual and measured profiles.

A MHD profile meter (**18**) was built for flight aboard reentry vehicles. Figure 10 is a photograph of the instrument, which provides four continuous samples of the flow.

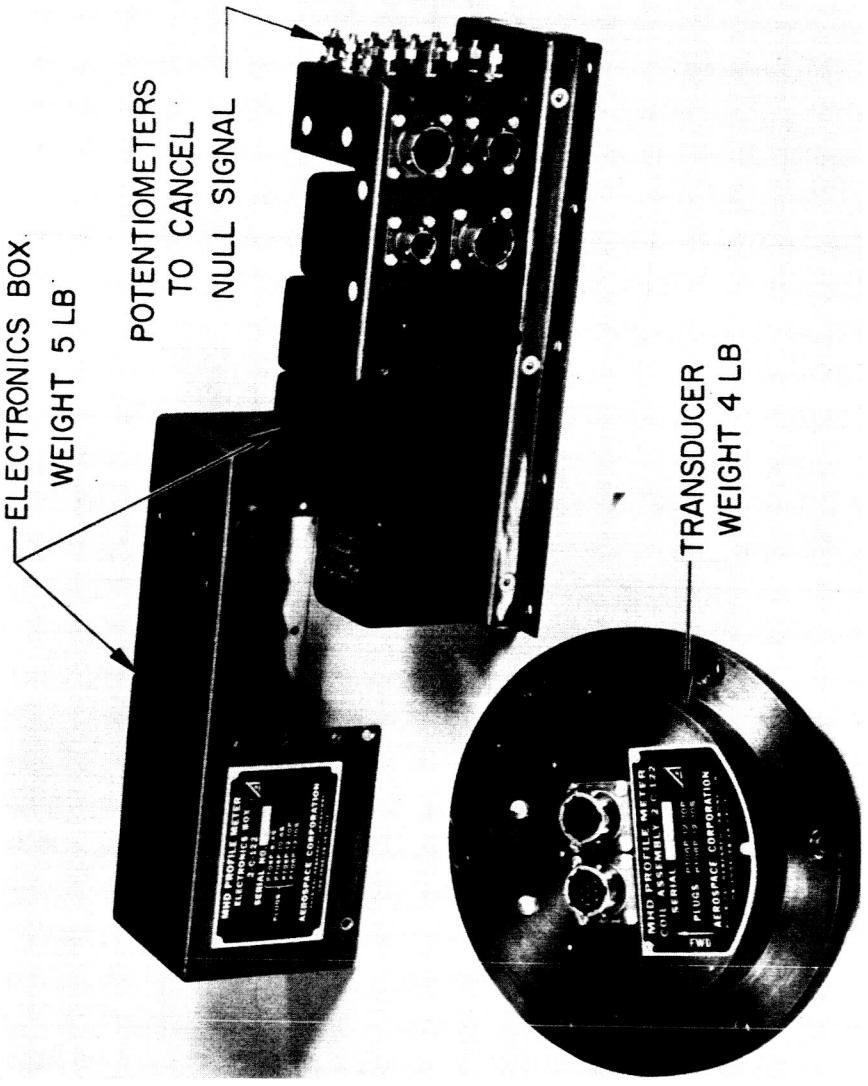

FIGURE 10. MHD electrical conductivity/velocity profile meter.

FLOW ANGLE INDICATOR (19)

The instruments described in this and the following two sections have been tested in the laboratory but have not been developed as flight instrumentation.

Using the MHD flow angle indicator is analogous to using two total head tubes displaced at a small angle to measure flow angles. When the pressure in each tube is equal, the bisector of the tube angle is parallel to the flow. The MHD flow angle indicator is shown in Figure 11. The transducer is not rotated to give equal signals, but the ratio of signal strength is used to calculate the flow angle. The equation relating signal ratio R to flow angle θ is

$$\theta = \arctan\left(\frac{1-R}{1+R}\,\frac{1}{\tan\alpha}\right) \tag{7}$$

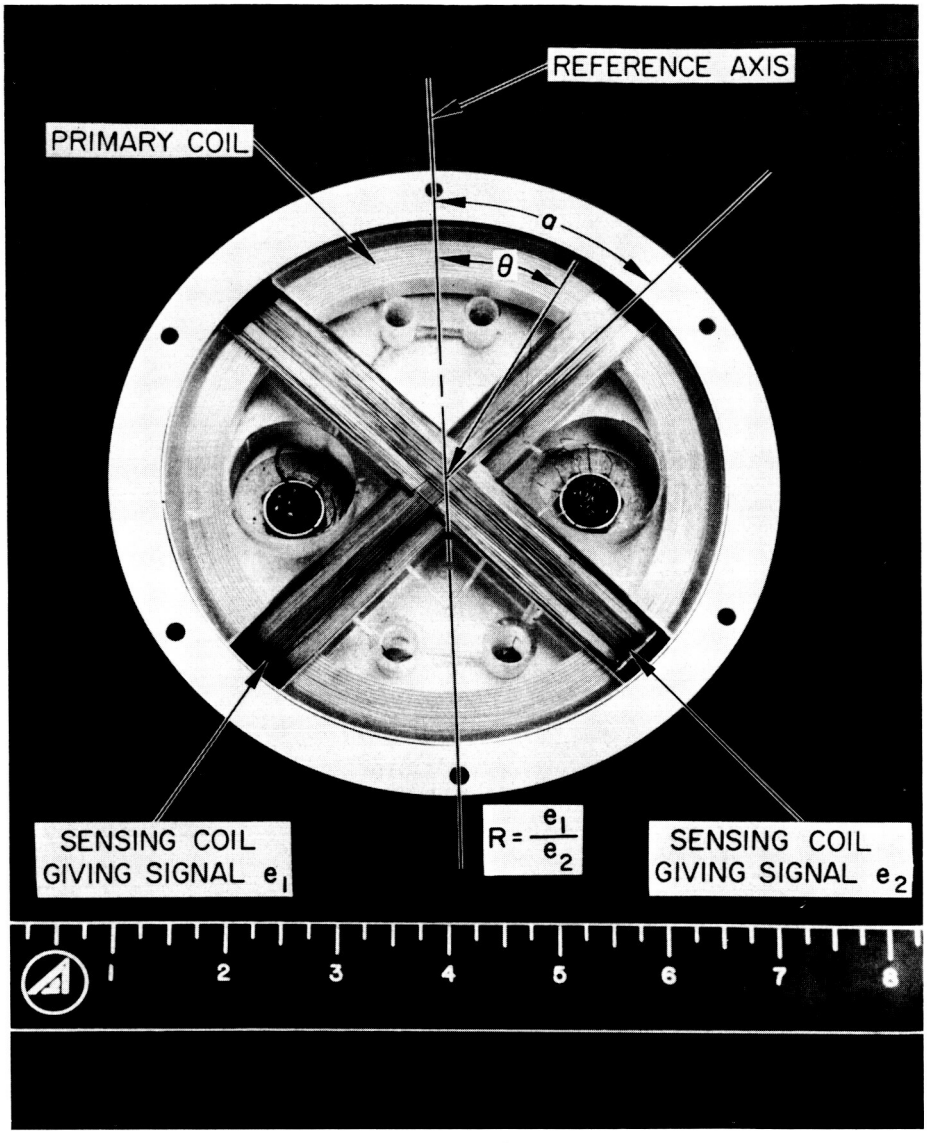

FIGURE 11. Crossed sensing coil geometry.

The symbols are defined in Figure 11. The angle α measures the location of the sensing coils in relation to the reference axis. When the plasma flow, which is above and parallel to the plane of the paper, deviates by an angle θ from the reference axis, sensing coil 2 has a larger signal than sensing coil 1. Equation (7) gives θ as a function of the signal ratio R and α. The transducer can yield the local flow angle θ without knowledge of σ or u of the ionized gas. However, if e_1 and e_2 are measured separately and the transducer is calibrated, *simultaneous* measurements of σu and θ are obtained.

Two different configurations have been built and tested: one is shown in Figure 11; the other is described in (**19**). The accuracy of the flow angle measurement is

1 degree ± 5 per cent for -45 degrees $< \theta < 45$ degrees. (For an angle of 40 degrees, the error may be ± 3 degrees.) For bounded θ, the α can be adjusted to give optimum performance.

AVERAGE ELECTRON COLLISION FREQUENCY (20)

A scalar electrical conductivity has been assumed in the previous sections. If a sufficiently large magnetic field is applied, the σ becomes a tensor. Table I gives the value of B required for a ratio of electron cyclotron frequency ω_c to collision frequency ν equal to unity. Equation (1) has been expanded, considering σ to be a tensor. For the coordinate system and coil arrangement shown in Figure 1, the result is

$$e = -\frac{NA\mu_0}{4\pi}\frac{\partial}{\partial t}\int_V \frac{u\sigma'}{1+\left(\frac{\omega_c}{\nu}\right)^2}\left[\left(\frac{\omega_z\omega_y}{\nu^2}+\frac{\omega_x}{\nu}\right)\left(-\frac{B_z x}{r^3}\right)+\left(1+\frac{\omega_z^2}{\nu^2}\right)\left(\frac{B_y x}{r^3}\right)\right. \tag{8}$$
$$\left.+\left(\frac{\omega_y\omega_x}{\nu^2}-\frac{\omega_z}{\nu}\right)\left(\frac{B_z z}{r^3}\right)-\left(\frac{\omega_x\omega_z}{\nu^2}+\frac{\omega_y}{\nu}\right)\left(\frac{B_y z}{r^3}\right)\right] dV$$

where ω_x, ω_y, and ω_z are the components of ω_c, and σ' equals $\omega_p^2\varepsilon_0/\nu$. Fortunately, most of the terms drop out in the integration as a result of symmetry. In final form the equation for the signal voltage is

$$e = -\frac{NA\mu_0}{4\pi}\frac{\partial}{\partial t}\int_V \frac{u\sigma'}{1+\frac{\omega_c^2}{\nu^2}}\frac{B_y x}{r^3}\,dV \tag{9}$$

Note that when $(\omega_c/\nu)^2 \ll 1$, equation (9) reduces to equation (2).

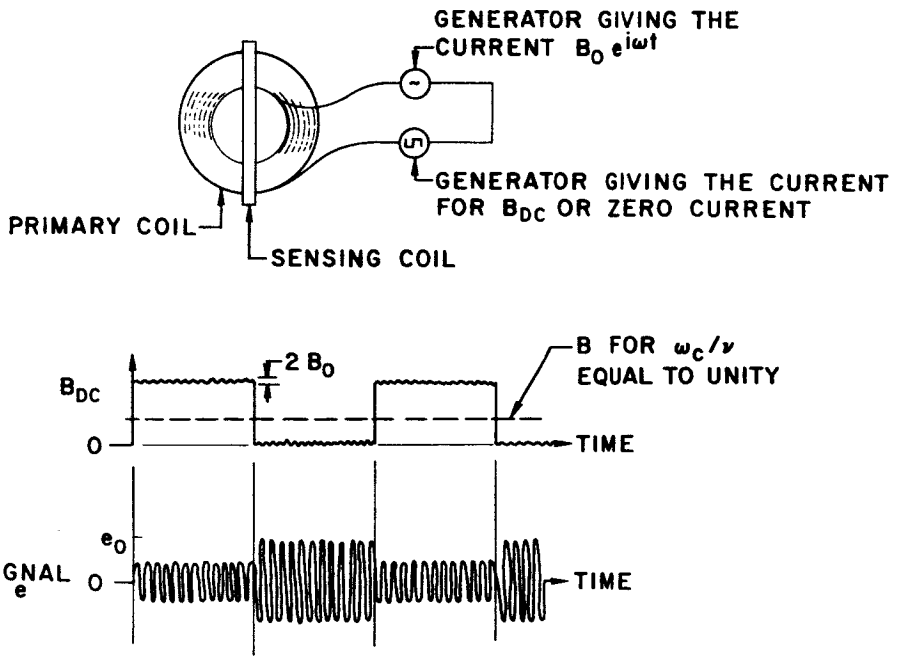

FIGURE 12. The excitation of the primary field and the anticipated signal.

An average value of the ratio ω_c/ν can be measured by using an applied magnetic field as illustrated in Figure 12. When an appropriately strong d-c field is applied, the denominator of the integrand in equation (9) exceeds unity, decreasing the signal. When the primary coil is excited only with weak a-c, the denominator is nearly unity and a signal e_0 is measured. An average value of the frequency ratio is given by

$$\left(\frac{\nu}{\omega_c'}\right)_{\text{average}} = \left(\frac{e}{e_0 - e}\right)^{1/2} \tag{10}$$

where $\omega_c' = eB_{dc}/m$.

VELOCITY MEASUREMENT

An experiment was performed using the coil arrangement shown in Figure 13 and an arc plasma jet. The primary coils were excited d-c and had alternating

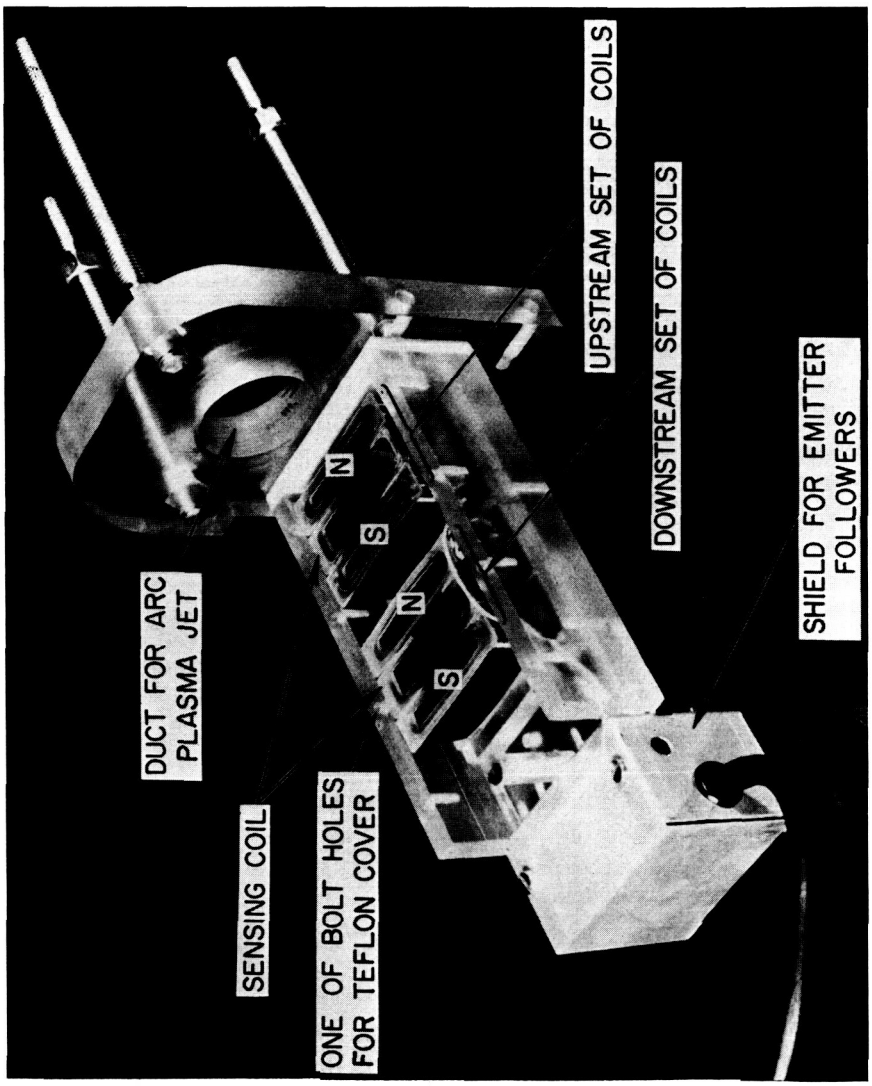

FIGURE 13. Velocity and turbulence transducer.

poles. Emitter followers were used to isolate the sensing coils from the distributed capacitance in the external leads. A flat frequency response from 10 to 100 kc was thus obtained.

Typical traces of the voltage induced in the sensing coils as a result of the plasma jet flowing through the steady applied magnetic field are shown in Figure 14. Voltages appearing at the upstream and downstream sensing coils are closely correlated. The cross correlation function

$$F(\tau) = \frac{\int e_1(t)e_2(t+\tau)\,dt}{\left(\int e_1^2\,dt\right)^{1/2}\left(\int e_2^2\,dt\right)^{1/2}} \tag{11}$$

was calculated as a function of τ for several oscillograms similar to Figure 14. Maximum values of F ranged from 0.85 to 0.92.

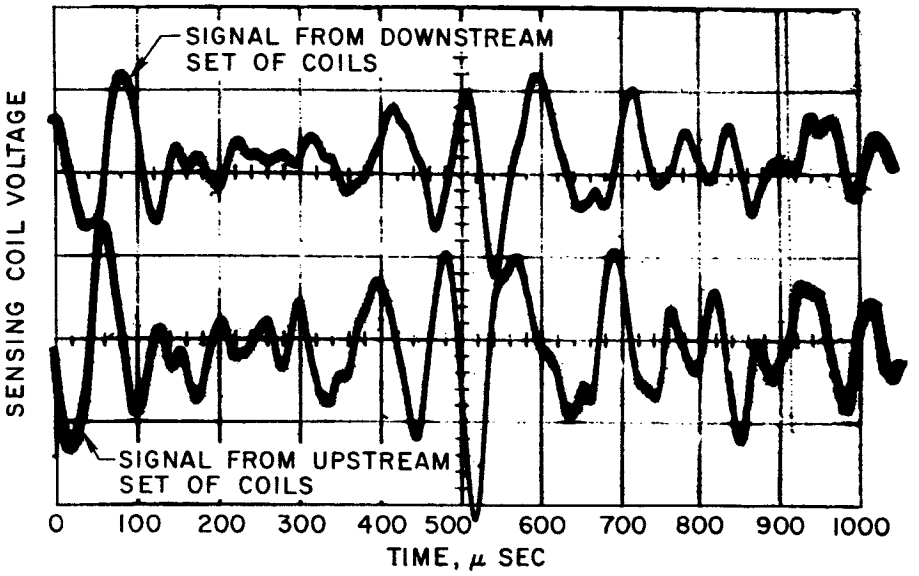

FIGURE 14. Typical signals from velocity transducer.

For the case shown in Figure 14 the peak value of F occurred at $\tau = 22$ μsec. The distance between the upstream and downstream coil sets was 7.9 cm giving a velocity of 3600 m/sec.

TURBULENCE INDICATOR

The preceding experiment is an example of serendipity. The aim was to measure velocity, and an average velocity measurement was obtained; however, it was discovered that additional information about the flow is contained in the noisy signal traces. The amplitude and spectrum of the signals illustrated in Figure 14 are related to σu fluctuations in the plasma stream.

Although the data obtained await thorough analysis, preliminary observations can be made. The time dependent terms in equation (1) are σ and u, and not B. The close correlation between the upstream and downstream signals indicates that

the σu fluctuations are convected, with only small changes due to the nonstationary terms. The spectrum is dictated by the response of the transducer to the different scale σu fluctuations. Experiments using wire loops that are moved through the applied magnetic field indicate that only loops in the range $0.5L$ to $2.0L$ cause significant signals (L being the length of one complete coil set in the streamwise direction).

The signals were obtained in an arc jet facility. It is not known whether similar fluctuations occur in the plasma sheath surrounding a reentry vehicle. One application of the turbulence indicator would be to detect on a reentry vehicle the transition from laminar to turbulent flow. Since the skin depth at 10 to 100 kc in most metals is very small, the turbulence transducer should be separated from the flow by dielectrics only.

SUMMARY

Several instruments have been developed which depend for their operation on the interaction of a high speed flow of ionized gas with an applied magnetic field. These meters are admirably suited for reentry experiments because the transducer can be located behind a protective wall and does not require probes that have to be inserted into the plasma.

The average σu meters in two geometrical arrangements have been developed for flight. One σu profile meter has been assembled (Figure 10) as a flight instrument; another model is under development. Instruments to measure local flow angle (Figure 11), average flow velocity, and fluctuations (Figure 13) have been tested in the laboratory. An average electron frequency meter (Figure 12) has been explored theoretically.

ACKNOWLEDGMENT

The first in the series of the electrical conductivity/velocity instruments was conceived by R. X. Meyer. His help and encouragement with the development of the other transducers is appreciated.

Frequent discussions with R. Betchov concerning various aspects of the instruments were extremely helpful. In addition, he suggested the velocity measurement experiment and helped with the development of the d-c version of the average σu transducer.

L. S. G. Kovasznay, consultant to Plasma Research Laboratory, provided new insight into the σu profile meter. He also reviewed the work done on the tensor conductivity (average ν measurement) and made helpful suggestions.

O. L. Gibb assembled, calibrated, and assisted with the design of the transducers. In addition, he is co-inventor of the MHD flow angle indicator. A. Y. Lu translated rough sketches into polished engineering designs. His assistance has been invaluable.

REFERENCES

1. Fuhs, A. E., "A Technique for Obtaining the Velocity-Electrical Conductivity Profile", TDR-594(1215-01)TN-2, Aerospace Corporation, El Segundo, California (30 June, 1961); see also *Proceedings of the Second Symposium on the Plasma Sheath* (Baltimore: Spartan Press, 1964).
2. Fuhs, A. E., "Development of a Device for Measuring Electrical Conductivity of Ionized Air During Reentry", STL/TR-60-0000-09256, Space Technology Labs., Los Angeles (September 20, 1960).

3. Rotman, W., and Meltz, G., eds., "Electromagnetic Effects of Reentry, Selected papers from Symposium on the Plasma Sheath: Its Effects on Communication and Detection", in *Planetary and Space Science*, **6** (June, 1961).
4. Dix, D. M., "Typical Values of Plasma Parameters Around a Conical Reentry Vehicle", TDR-169(3230-22)TN-1, Aerospace Corporation, El Segundo, California (November 7, 1962).
5. "Reentry Physics and Project Press Programs, Semiannual Technical Summary Reports to ARPA", Lincoln Lab., M.I.T. (June 30 and December 31, 1960; June 30 and December 31, 1961; June 30, 1962).
6. Huber, P. W., and Nelson, C. H., "Plasmas Frequency and Radio Attenuation", paper 61, *NASA University Conference on the Science and Technology of Space Exploration* (Chicago, 1962), **2**, 347-60 (NASA SP-11).
7. Pippert, G. F., and Edelberg, S., "The Electrical Properties of the Air Around a Reentering Body", IAS paper 61-40, AIAA(IAS), New York (1961).
8. Plugge, R. J., Chen, S., and Long, R. K., "Some Calculations of the Phase Shift and Attenuation Rates of the Hypersonic Plasma Sheath", Report 1021-3, Ohio State Univ. Research Foundation, Columbus (January 31, 1961).
9. Albini, F. A., and Jahn, R. G., "Reflection and Transmission of Electromagnetic Waves at Electron Density Gradients", *J. Appl. Phys.*, **32** (1), 75-82 (1961).
10. Daiber, J. W., and Glick, H. S., "Plasma Studies in a Shock Tube", AF-1441-A-4, Cornell Aeronautical Lab., Inc., Buffalo (July, 1961).
11. Fuhs, A. E., "Additional Comments on a Technique for Obtaining the Electrical Conductivity-Velocity Profile", TDR-930(2230-03)TN-5, Aerospace Corporation, El Segundo, California (March 22, 1962); see also *Proceedings of the Second Symposium on the Plasma Sheath* (Baltimore: Spartan Press, 1964).
12. Betchov, R., Fuhs, A. E., Meyer, R. X. and Schaffer, A. B., "Measurement of Electrical Conductivity of Ionized Air During Reentry", TDR-930(2230-03)TR-1, Aerospace Corporation, El Segundo, California (January 16, 1962); see also *Aerospace Eng.*, **21** (11), 54-55, 68-78 (1962).
13. Meyer, R. X., "The Electrical Conductivity of Air Up to 24000°K", GM-TR-0127-00420, Space Technology Labs., Inc., Los Angeles (June 26, 1958).
14. Fuhs, A. E., and Gibb, O. L., "A Velocity-Electrical Conductivity Transducer for Axisymmetric Reentry Vehicles", Technical Documentary Report, Aerospace Corporation, El Segundo, California (to be published).
15. Sheriff, J. A., *The Theory of Electromagnetic Flow Measurement* (New York: Cambridge University Press, 1962).
16. Lehde, H., and Lang, H. T., U.S. Patent 2,435,043 (1948).
17. Fuhs, A. E., Betchov, R., Gibb, O. L., and Abshear, J. R., "An Electrical Conductivity-Velocity Instrument Using DC Applied Magnetic Field", Technical Documentary Report, Aerospace Corporation, El Segundo, California (to be published).
18. Fuhs, A. E., and Gibb, O. L., "Magnetohydrodynamic Electrical Conductivity-Velocity Profile Instrument", Technical Documentary Report, Aerospace Corporation, El Segundo, California (to be published).
19. Fuhs, A. E., and Gibb, O. L., "A Magnetohydrodynamic Flow Angle Indicator", TDR-169(3153)TN-4, Aerospace Corporation, El Segundo, California (November, 1962); also, presented at Fourth Symposium on Engineering Aspects of Magnetohydrodynamics (April 10-11, 1963).
20. Fuhs, A. E., "Signal from the Electrical Conductivity/Velocity Meter for Tensor Conductivity", TDR-69(2119)TN-5, Aerospace Corporation, El Segundo, California (May 22, 1962).

20. Boris Ragent: *X-Ray Densitometer for Use in Plasma Streams*

An instrument has been constructed for the measurement of the mass density of a gas in a localized volume element. The density measurement is independent of the thermodynamic or hydrodynamic state of the gas and independent of the presence of equilibrium or transient flow conditions. The instrument is especially designed for application to density measurements in high-temperature gas streams.

The principle of operation involves the measurement of the scattering of a beam of moderately hard X-rays to establish the number of scattering centers present in a scattering volume. This volume is defined by the geometrical intersection of a well-defined pencil of X-rays and collimated viewing paths of detectors. The X-ray energy utilized is high enough so that the scattering is primarily incoherent from electrons, both bound and free, so that the number of X-rays scattered into a detector per unit time is proportional only to the total *electron density in the gas and not the chemical state of the gas. The gas mass density may be related to the total electron density since the number of electrons per gram is approximately constant for all common gases except hydrogen.*

Sample calibration data taken in helium and air are shown and typical applications are discussed.

INTRODUCTION

The utility of devices for producing high-enthalpy gas streams is often contingent upon the ability of the investigator to measure the internal properties of the gas or the interaction of these gas streams with matter. The measurement of the internal properties of the gas stream, which are necessary to define the state, may be distinguished by whether or not the measurement process itself depends upon the distribution of energy states within the gas or its motion. For example, measurements of temperature require that certain assumptions about energy partition in the gas be verified. On the other hand, it is desirable that independent measurements of such quantities as ambient pressure, velocity, or mass density should not require such considerations. It is further desirable that instruments to measure any of these latter quantities be designed to make localized measurements in the

ED. NOTE: Dr. Ragent is with the Vidya Division, Itek Corporation, Palo Alto, California.

gas stream since the quantity to be measured may vary strongly from point to point in the gas. The accuracy of a measurement made in a specified time must, of course, be consonant with the desired application.

This paper describes a technique for the measurement of the mass density of a gas in a localized volume element. The measurement is essentially independent of the state of the gas and only requires electrical neutrality in the volume element under consideration. The device described is especially designed for application to density measurements in high-temperature gas streams such as those generated in arc-heated wind tunnels, although the apparatus is equally well suited to measurements in lower-temperature gases.

PRINCIPLES OF THE METHOD

GENERAL

The scattering of X-rays in low-atomic-number gases, such as air and air constituents in the energy range from about 1 mev down to about 10 kev, is dominated by the Compton process, in which X-rays are scattered from electrons, both bound and free. The theoretical description of this process is given by the treatment of Klein and Nishina and predictions of the theory have been well verified experimentally. At energies below about 10 kev, the relative contribution to the total scattering due to coherent (Rayleigh) scattering becomes important.

The total mass density for a neutral gas can be related to the total electron density, including free and bound electrons if the elemental composition of the gas is known. Even if this composition is unknown, it is possible to relate the mass density to electron density to a high order of accuracy for the light gases unless hydrogen is present, in which case proper corrections must be applied. Thus, by selecting an energy region between 10 kev and 1 mev, the total scattering becomes

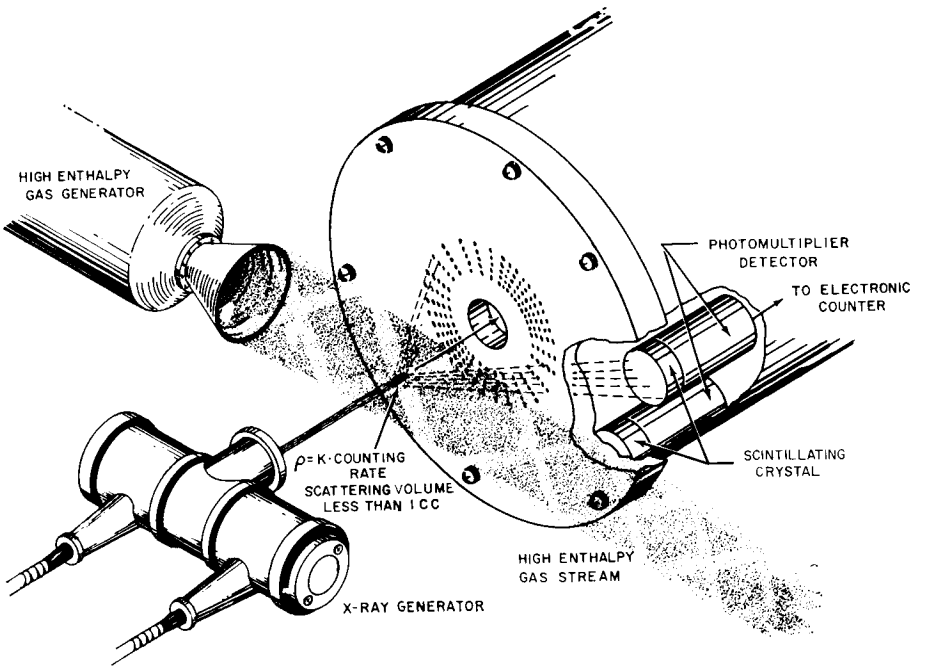

FIGURE 1. Schematic drawing of X-ray densitometer.

dependent only upon the total electron density or gaseous mass density rather than upon both the mass density and the chemical state of the gas or its state of motion. The X-ray energy range is easily established at the lower end by biasing detectors and associated discriminating circuitry to register only X-rays of energy greater than 10 kev, and at the upper end by the maximum energy available from the X-ray generator. The shape and size of a volume element under investigation is determined by the intersection of a geometrically well-defined beam of X-rays and similarly well-defined collimated scattering paths to detectors.

A sketch of the scattering geometry is shown in Figure 1. The counting rate in the detectors, I, is given by

$$I = n\xi\Phi \int \frac{d\sigma}{d\Omega}\, d\Omega \tag{1}$$

where n = density of scatterers, the total number of bound and free electrons per cm^3 ($\sim 3.8\times 10^{+16}$ at $\rho/\rho_0 = 10^{-4}$ for air)

$\frac{d\sigma}{d\Omega}$ = differential cross section for scattering into solid angle $d\Omega$ at angle θ with the original beam direction ($\int (d\sigma/d\Omega)\, d\Omega \simeq 2.4\times 10^{-27}$ for a typical geometry)

Φ = incident flux ($\sim 2\times 10^{12}$ photons/cm^2-sec for an X-ray tube operating at 100 ma at 100 kev)

ξ = detection efficiency, including window losses, geometric effects in the detector, etc. ($\sim \frac{1}{4}$)

Using the values cited $I \simeq 46$ counts per second at $\rho/\rho_0 \simeq 10^{-4}$ for air.

CORRELATION OF MASS DENSITY WITH ELECTRON DENSITY

As a typical example, the number of electrons per gram for various air-impurity mixtures as a function of impurity mass fraction x is shown in Table I and the fractional difference in the number of electrons per gram from pure air for the same air-impurity mixtures is given in Table II. It is evident that the number of electrons per gram in air mixtures remains constant to a very good approximation even for large admixtures of impurities. An exception to this statement occurs in the case of a mixture of hydrogen with other gases, since the number of electrons per gram of hydrogen is roughly twice as large as for all other low-atomic-number gases.

TABLE I. ELECTRONS PER GRAM, Q, FOR VARIOUS AIR-IMPURITY MIXTURES AS A FUNCTION OF MASS FRACTION OF IMPURITY ($\times 10^{-23}$).

Fractional mass of impurity	*Impurity element*		
	Copper	*Carbon*	*Wolfram (tungsten)*
0	3.00882	3.00882	3.00882
10^{-5}	3.00882	3.00882	3.00881
10^{-4}	3.00879	3.00882	3.00876
10^{-3}	3.00856	3.00882	3.00823
10^{-2}	3.00622	3.00883	3.00297
10^{-1}	2.98280	3.00894	2.95036

TABLE II. FRACTIONAL DIFFERENCE IN NUMBER OF ELECTRONS PER GRAM FOR AIR AND VARIOUS AIR-IMPURITY MIXTURES.

Fractional mass of impurity x	*Copper* $\frac{Q_{air}-Q_{Cu}}{Q_{air}}$	*Carbon* $\frac{Q_{air}-Q_{C}}{Q_{air}}$	*Wolfram (tungsten)* $\frac{Q_{air}-Q_{W}}{Q_{air}}$
10^{-5}	0	0	3.32×10^{-6}
10^{-4}	9.97×10^{-6}	0	1.99×10^{-5}
10^{-3}	8.64×10^{-5}	0	1.96×10^{-4}
10^{-2}	8.64×10^{-4}	-3.32×10^{-6}	1.94×10^{-3}
10^{-1}	8.65×10^{-3}	-3.99×10^{-5}	1.94×10^{-2}

THE DIFFERENCE IN X-RAY SCATTERING FOR HOT AIR AS COMPARED WITH COLD AIR

The utility of the densitometer depends upon the relative constancy of the response of the instrument when used with either hot gas or cold gas at the same mass density. Scattering differences that exist between hot gas and cold gas are due to the different component species present at different temperatures. For example, for air at $\rho=10^{-5}\rho_0$ the diatomic molecule O_2 begins to dissociate into two atoms of O at approximately 1500°K; at 4000°K, O_2 no longer exists (**1**) having been entirely converted to O. The scatter from a molecule of O_2 differs in detail from the scatter from an atom of O, since, due to interference among the electrons, the coherent scattering for photon energies of 0 to 40 kev is a function of the electronic structure of the particle and the scattering angle. At higher energies, the effect of the electronic binding and structure of the scattering particle becomes negligible.

The scatter intensity at angle θ per atom from a monatomic specie is (**2**)

$$I_\theta = zI_e\left[\frac{F^2}{z}+R\left(1-\frac{\sum f^2}{z}\right)\right] \tag{2}$$

where

$$R = \left[1+\frac{h}{mc\lambda}(1-\cos\theta)\right]^{-3}$$

The ratio of the scattered intensity per bound electron to the Thomson scattering for a free electron is (**2**)

$$S = \frac{I_\theta}{zI_e} = \frac{F^2}{z}+R\left(1-\frac{\sum f^2}{z}\right) \tag{3}$$

The scattered intensity at angle θ per diatomic molecule is

$$I_\theta = 2zI_e\left[\frac{F^2}{z}\left(1+\frac{\sin x}{x}\right)+R\left(1-\frac{\sum f^2}{z}\right)\right] \tag{4}$$

where

$$x = 4\pi\frac{s_{mn}}{\lambda}\sin\frac{\theta}{2}$$

and

$$s_{mn} = \text{internuclear distance}^2$$

We also have that the ratio of scattering of a bound electron in a molecule to the scattering from a free electron is

$$S = \frac{I_\theta}{2zI_e} = \frac{F^2}{z}\left(1+\frac{\sin x}{x}\right)+R\left(1-\frac{\sum f^2}{z}\right) \tag{5}$$

The values of F and $\sum f^2$ are given for a number of species in the literature (**3**).

Equations (2) and (3) are in excellent agreement with experimental data (**2**), but there is some difference between calculations made with equations (4) and (5) and the experimental data of Wollan (**4**). The values used here are the experimental values.

In order to compare the scatter from cold and from hot air, the ratio

$$\frac{S_{273^\circ K}}{S_{T^\circ K}}$$

was computed. This gives the ratio of the scatter at 273°K with that at T°K. In order to compute S_{air} the S for each particular component was obtained and the results weighted according to the specie population proportion at the temperature in question; the results were then summed. The air component population proportion at various temperatures was obtained from the tables of Moeckel and Weston (**1**) and the values of s_{mn} were taken from Compton and Allison (**2**).

In a wind tunnel air may be assumed to be heated in one chamber at a pressure of, say, 10 atmospheres and then expanded through a nozzle into another chamber at a pressure of approximately 100 microns. If the initial temperature is 8000°K, the air-stream temperature would be approximately 2400°K if the expansion is isentropic; if immediate freezing of the flow is assumed, the equilibrium composition corresponding to the temperature of 8000°K is maintained. Molecular dissociation is greatest for the frozen 8000°K case and, hence, the difference in X-ray scattering for the hot air as compared with the cold air will be larger for this case.

TABLE III. RESULTS OF CALCULATIONS OF DIFFERENCE IN SCATTERING FOR FROZEN AIR FLOW AS COMPARED WITH AIR AT 273°K ($\theta = 50^\circ$).

Photon energy (kev)	$\frac{S_{273^\circ K}}{S_{8000^\circ K}}$ (%)	$\frac{S_{273^\circ K}}{S_{10,000^\circ K}}$ (%)	$S_{273^\circ K}$ (%)
10	91.6 ± 5	89.7 ± 5	164 ± 5
20	96.5 ± 5	96.5 ± 5	107 ± 5
25	95.7 ± 5	92.3 ± 5	100 ± 5
30	95.4 ± 5	92.8 ± 5	96 ± 5
35.3	98.5 ± 5	97.3 ± 5	97 ± 5
45	~100 ± 5	~100 ± 5	~100 ± 5

The computational results are shown in Table III. In order to obtain the overall effect of the scattering difference, the results must be combined with the incident X-ray spectrum for the densitometer equipment. Operation of the X-ray tube at a peak energy of 100 kv was assumed. For this calculation the normalized spectrum of relative intensity per kv interval was assumed to be similar to that for 200 kv peak given in Hine *et al.* (**5**), on page 541.

The scattering per electron is then given by

$$N_{T^\circ} = \left(\frac{S_T}{S_{273}}\right)_{E_1} (S_{273})_{E_1} \left(\frac{d\sigma_c}{d\Omega}\right)_{E=0} \left(\frac{d\Phi}{dE}\right)_{E_1} dE_1\, d\Omega + \left(\frac{S_T}{S_{273}}\right)_{E_2} (S_{273})_{E_2} \left(\frac{d\sigma_c}{d\Omega}\right)_{E=0} \left(\frac{d\Phi}{dE}\right)_{E_2} dE_2\, d\Omega + \cdots \tag{6}$$

A comparison of N_{T° to N_{273° then gives the measure of the difference in scattering at T° as compared with 273°K. For the typical cases investigated for air at 8000° and 10,000°K the differences from air at 273°K amounted to less than 2%.

DESCRIPTION OF APPARATUS

Figure 1 is a schematic drawing of the apparatus and Figures 2a and 2b show the apparatus in place for a low-density wind-tunnel experiment.

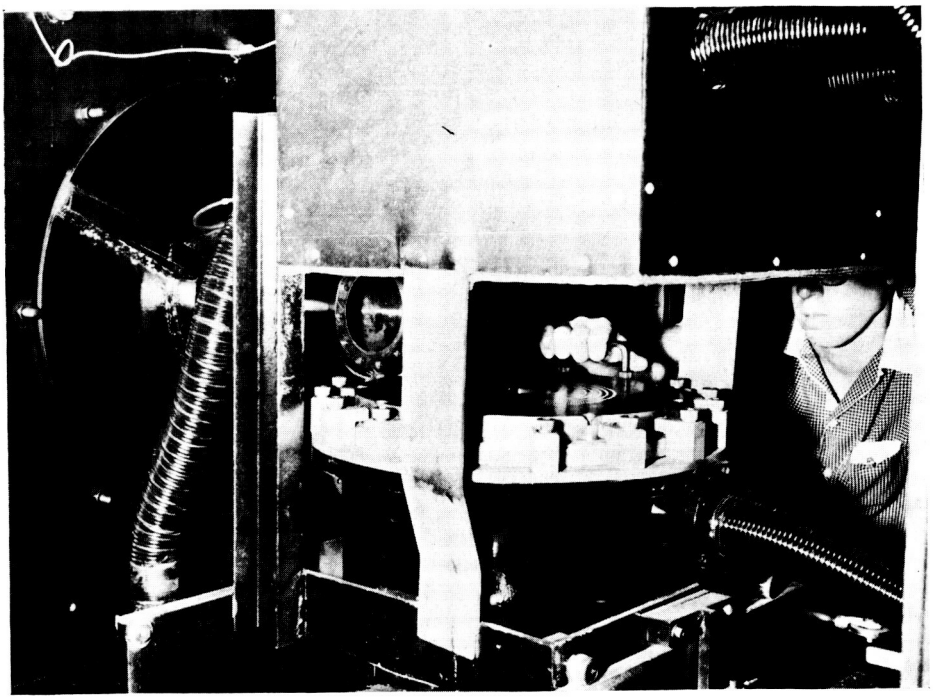

FIGURE 2a. Densitometer installed in low-density wind tunnel: south view.

X-RAY SOURCE AND COLLIMATOR

The X-ray source is a copper-backed, tungsten-insert, rotating-anode, high-voltage X-ray tube which is oil-cooled and is mounted in a specially-modified aluminum housing. The X-rays are emitted from a spot about 1.5 mm by 1.5 mm, and pass through a thin glass window, oil jacket, and plastic exit window. The total inherent filtration of the exit path is approximately 0.5 mm of equivalent aluminum absorber.

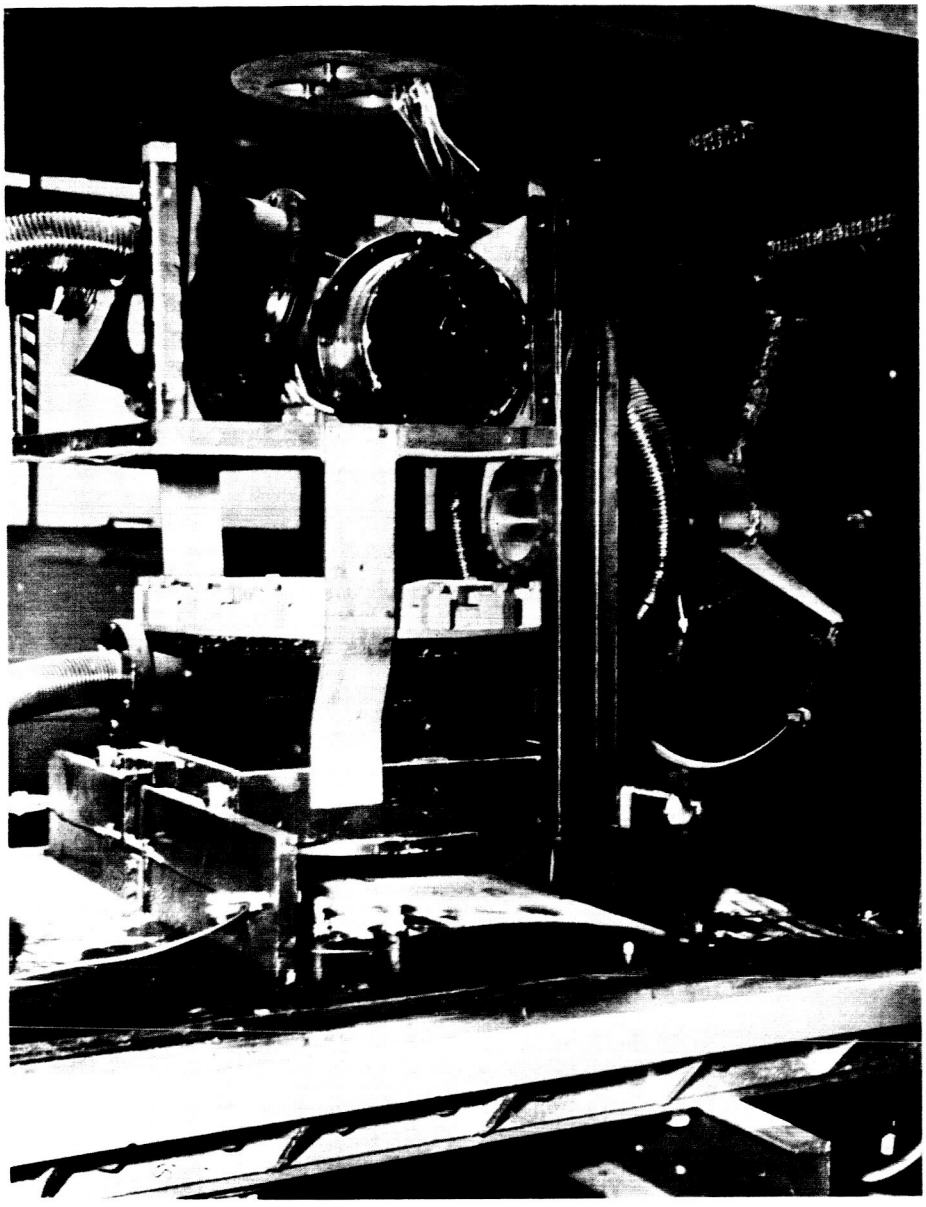

FIGURE 2b. Densitometer installed in low-density wind tunnel: north view.

A typical calculated energy spectrum for the X-ray photons emerging from the X-ray tube through 0.5 mm of inherent aluminum filtration at 100 kev peak voltage is given in Figure 3 and was calculated using the results of Kulenkampff as reported by Condon and Odishaw (**6**).

After passing out of the exit part of the X-ray tube housing, the X-rays pass through a collimator hole 0.062 inch in diameter by $\frac{3}{16}$ inch long in a block of lead. The external edges of this hole are shielded by a projecting block of lead so as to

prevent radiation scattered from these exit "lips" from reaching the detector collimating hole regions. The shape of the beam produced by this collimator is shown in Figure 8.

The alignment of the hole in the collimator with the focal spot of the X-ray tube is accomplished by using the alignment adjustments which allow motion of this collimator in the two transverse directions. The collimator is roughly located by taking "pin-hole" X-ray film exposures using a thin lead sheet with a small hole. Final adjustment of this collimator is accomplished by taking film exposures at different settings of the collimator screws. When the maximum intensity on the film has been obtained, the adjustments are locked in place. The final orientation of the X-ray beam with respect to the detector centerline is accomplished by moving the entire X-ray tube housing using the adjustment screws provided on the housing mounting brackets.

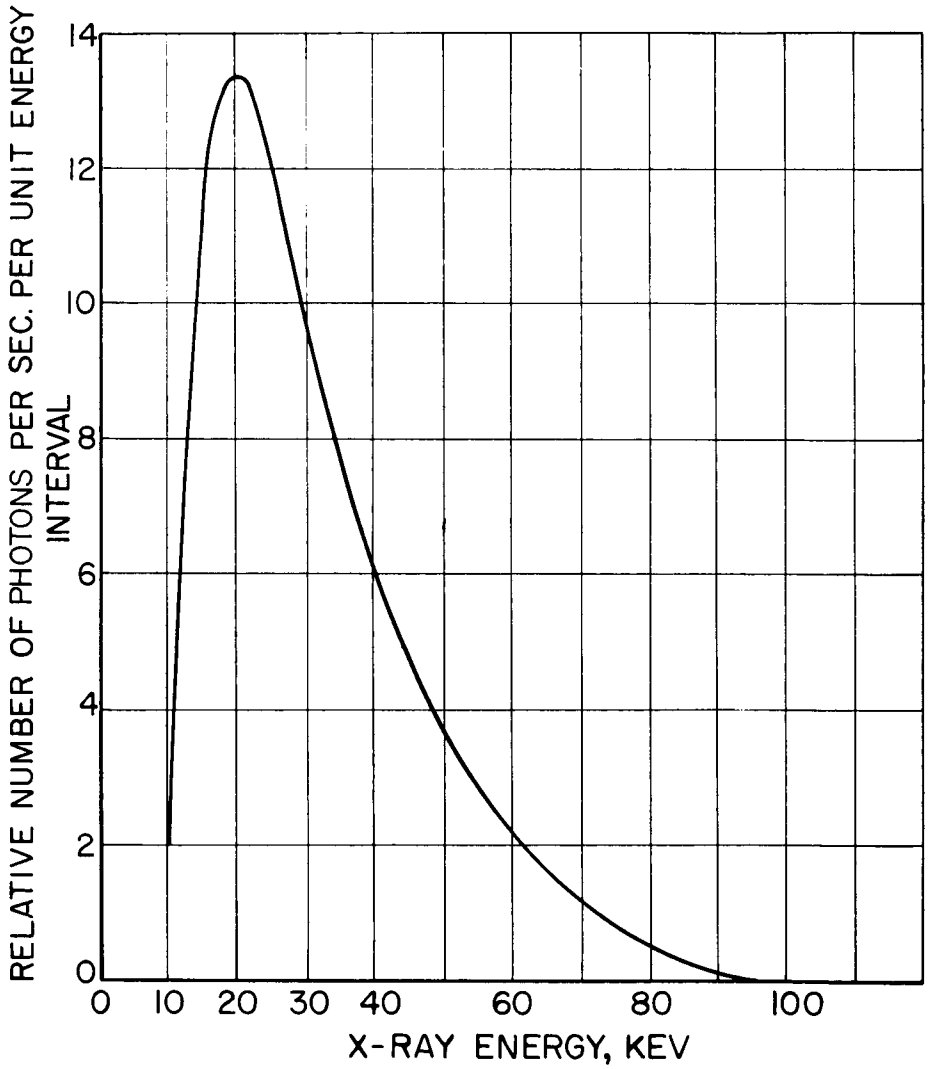

FIGURE 3. Typical thick-target X-ray spectrum for full-wave rectification at 100 KVP and 0.5 mm aluminum filtration.

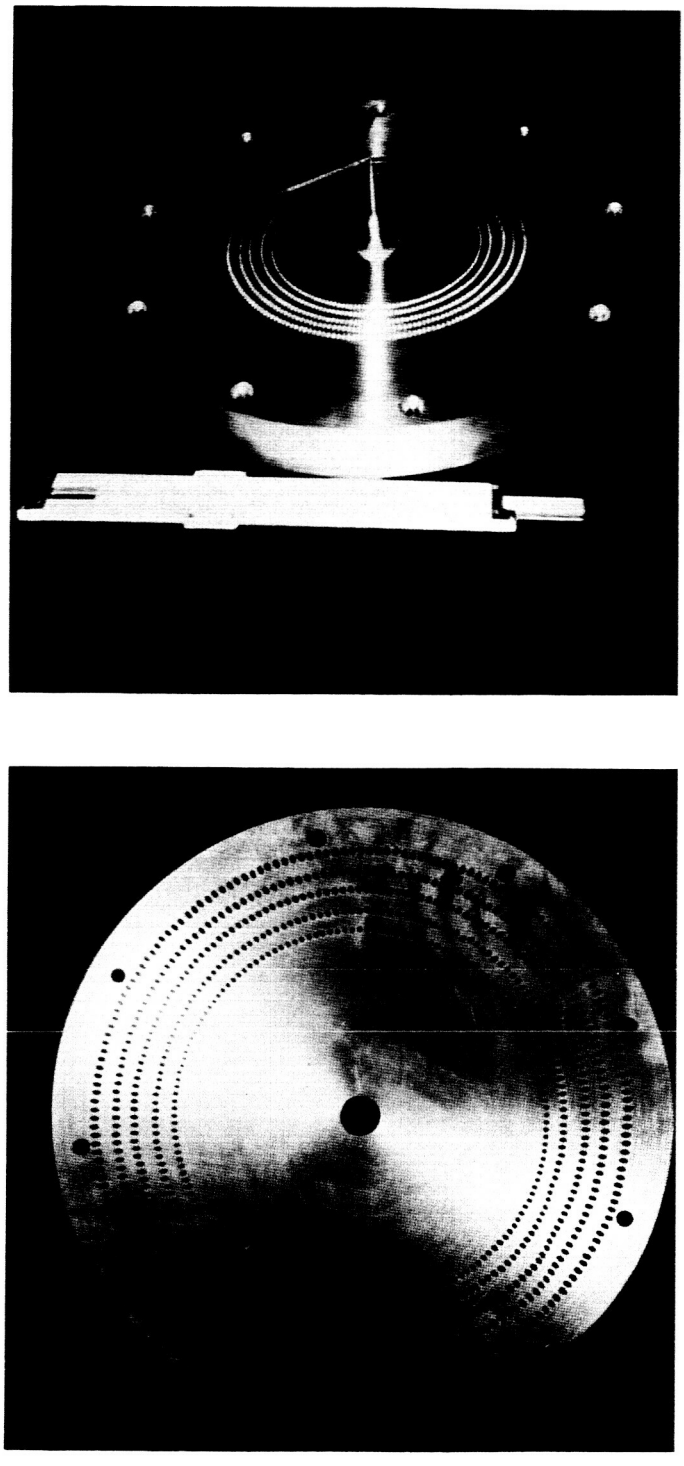

FIGURE 4. Collimator plate.

The entire housing is installed in a lead shielding box designed to contain all radiation scattered from the X-ray tube. All electrical connections to the X-ray tube are made through airtight flexible metal tubing connected to the atmosphere so that the X-ray tube operates at a pressure of 1 atmosphere.

DETECTOR UNIT

The detector unit consists of a collimating plate, scintillation detection units, monitor unit and X-ray catcher, amplifier chassis, and an airtight container.

The collimator unit consists of a forged brass plate $1\frac{3}{4}$-inches thick containing 846 holes averaging about 0.100 inch in diameter drilled in five concentric rings at an average angle of 50° to the collimator plate axis. These holes are drilled so that their axes intersect at a point on the plate axis 3 inches above the face of the plate. The average axial dimension of the volume intercepted by the intersection of rays drawn from the extreme edge of these holes and a narrow axial beam of X-rays is thus about 2 centimeters. Photographs of the collimator plate are shown in Figure 4.

The main detector unit contains eight photomultiplier scintillating crystal units installed inside the periphery of the detector unit housing so as to detect scattered X-rays which pass through the collimating holes. For the photomultiplier crystal units we used the Harshaw Integral Line Model No. 8–S–2. Electrical, magnetic, and radiation shielding have been provided by utilizing (in addition to the shielding furnished by Harshaw) three layers of magnetic shielding, $\frac{5}{16}$ inch of lead, and encasement of the entire assembly in a soft iron tube. The assembly is well grounded to the case. Electrical leads are brought out through the back end of the photomultiplier housings and are connected to the preamplifier chassis immediately below the detectors.

The major portion of the beam from the X-ray tube experiences no attenuation due to interaction with the gas in the wind tunnel in traversing the distance from the X-ray tube to the detector unit. The beam passes through a hole in the collimator plate into a hole in a lead block and is dissipated at the bottom of the lead block. A tube inserted into this lead block serves as an air-sealing mechanism. Some of the X-rays striking the bottom of this tube are scattered into the backward direction and impinge on the walls of the tube. A side hole in the lead block allows some of these scattered X-rays to be scattered again through the sealing-tube walls into the monitoring photomultiplier crystal detector. This unit is identical with the main counter assemblies. The output of the monitor tube is thus proportional to the X-ray beam and serves to act as a monitor for the beam. For very high air sample densities the response of the monitor detector will be caused, in part, by air scattering in the sealing tube. This contribution is negligible in most of the density ranges of interest. Figure 5 shows several views of the detector unit during assembly.

RECORDING AND CONTROL APPARATUS

Standard electronic power supplies, amplifiers, and counters are used to provide necessary power and to register the outputs of both the detector measuring the scattered events and the detector monitoring the intensity of the X-ray beam. The outputs of these counters as well as an electronic timer are registered on a digital recorder, which also registers the position of the apparatus in a traversing mechanism.

The lower energy detected by the detectors is established by a precision discriminator located in the non-overloading amplifiers and the peak energy of the

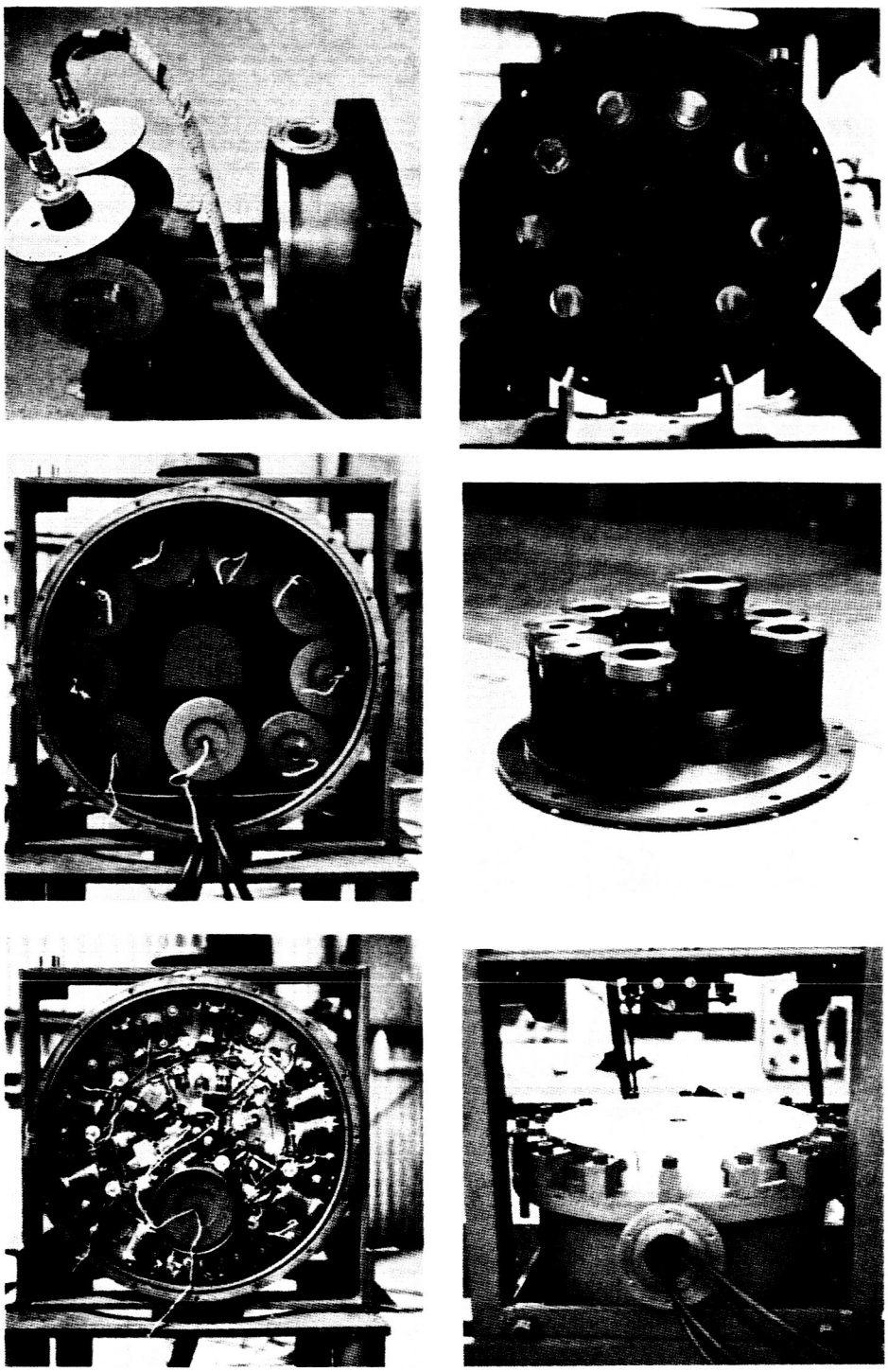

FIGURE 5. Photographs of detector unit in various stages of assembly.

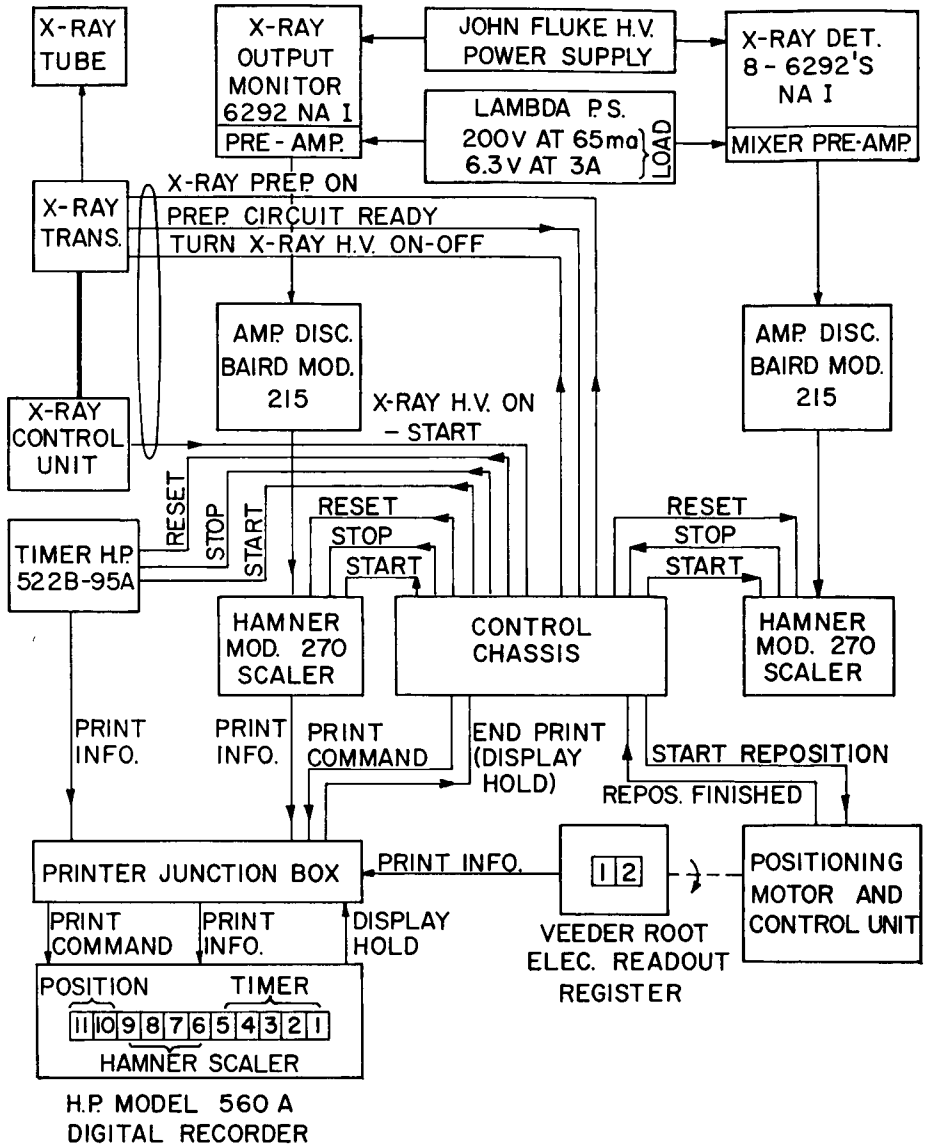

FIGURE 6. Block diagram.

X-ray source is controlled by the use of a well-established X-ray control unit and power supply. Figure 6 shows a block diagram of the apparatus and Figure 7 is a photograph of some of the electronic components.

TEST PROCEDURE AND CALIBRATION

SIZE OF SCATTERING VOLUME

The size of the scattering volume is determined by the intersection of the collimated paths to the detector and the pencil of X-rays emitted by the X-ray tube. From geometrical considerations the cross section of this volume was estimated to be as shown in Figure 8.

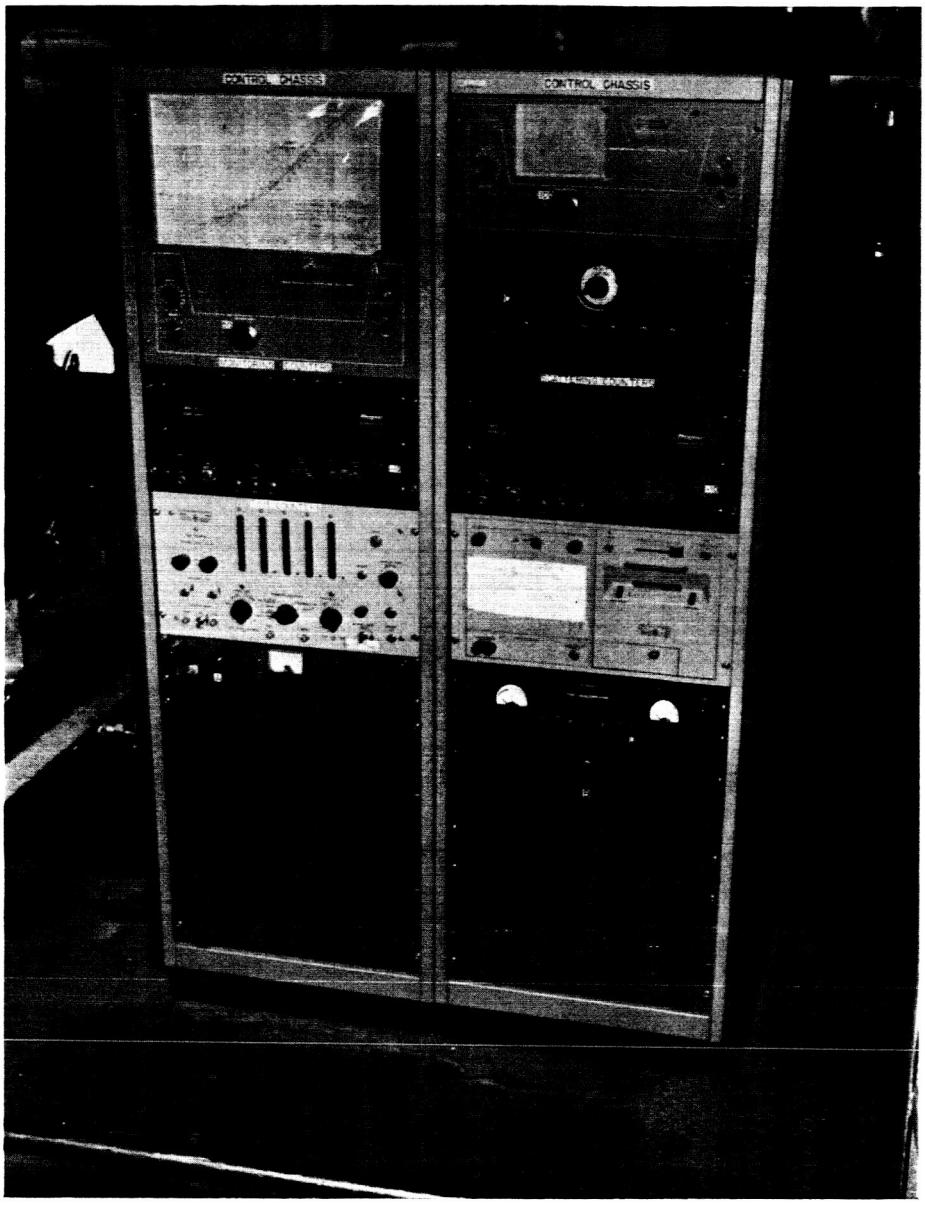

FIGURE 7. Counting rack.

The size of the scattering volume was measured by inserting a thin plate of glass in the beam and measuring the X-rays scattered from the plate into the detector as a function of the plate position. Figure 9 shows a typical response curve when the scattering plate was positioned in a plane perpendicular to the X-ray beam. The half-width of the response is about 2 centimeters. A direct exposure to the X-ray beam at 3 inches above the collimator plate shows that the beam is approximately a square in cross section with sides equal to about 0.3 inch in length.

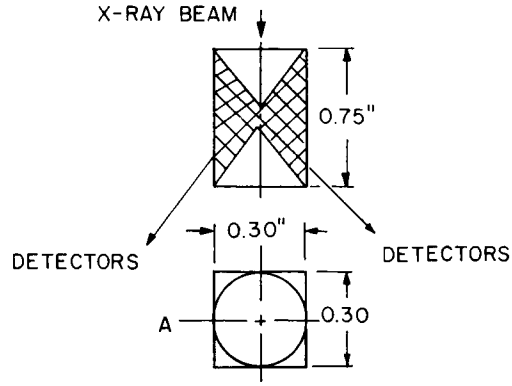

FIGURE 8. Sketch showing scattering volume dimension.

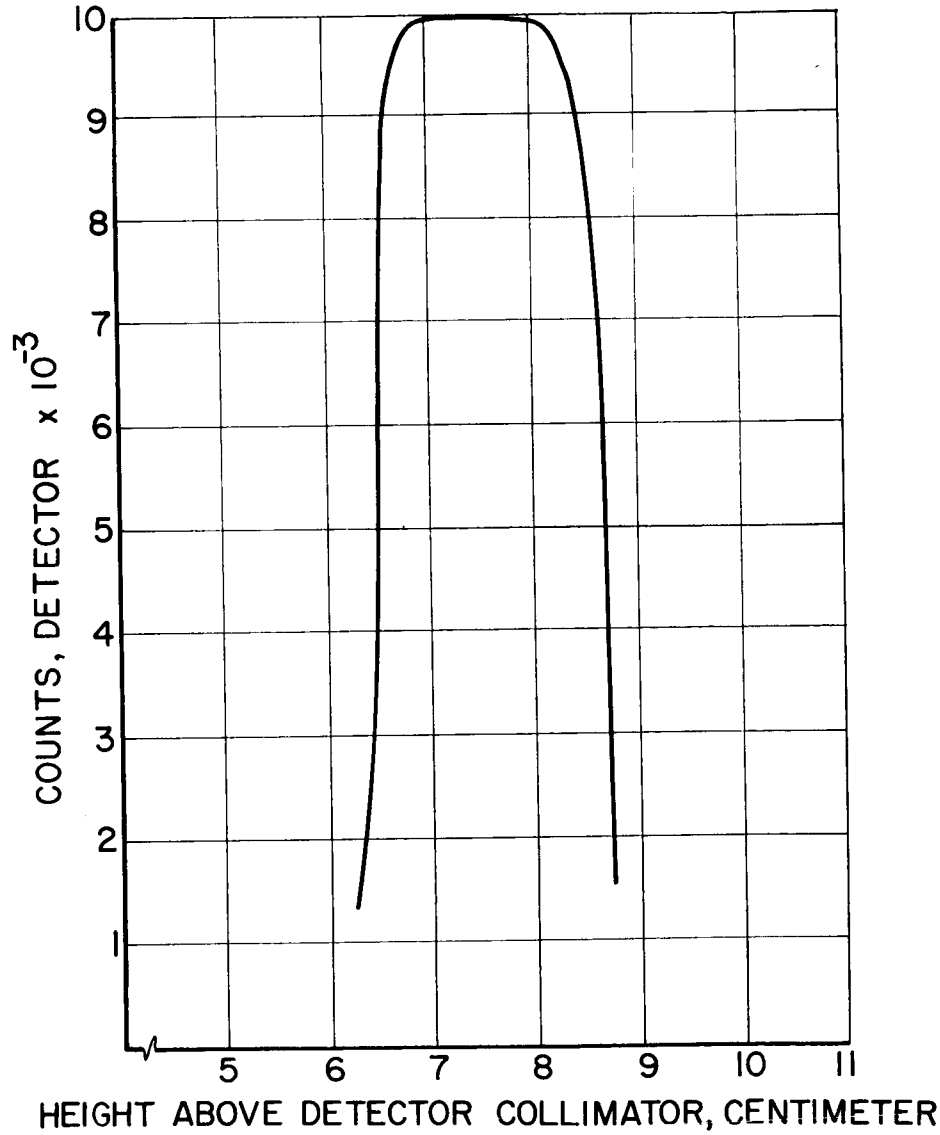

FIGURE 9. Response of detector to thin glass plate in plane perpendicular to X-ray beam versus height of plate.

CALIBRATION

The calibration of the densitometer is accomplished by measuring the amounts of scattered X-radiation relative to the incident X-ray intensity for a series of known gaseous densities. The readings in the scattered radiation counters and monitor counters must be corrected for counts due to background radiation or random spurious noise events.

For the lowest densities a correction must be made for the small contribution to the readings of the detectors caused by radiation scattered into the detectors by the apparatus itself even at $\rho=0$. Great care has been taken to minimize this latter quantity; however, this "leakage" radiation, in conjunction with statistical accuracy considerations, determines the lowest densities which can be measured. Using this correction, densities below $10^{-5}\rho_0$ may be measured.

The density measurements at high densities are limited by multiple scattering of X-rays in the test gas and by an increased contribution to the monitor detector readings due to scattering from the gas in the vicinity of the volume viewed by the monitor detector. Corrections for the latter effect may be made so that the multiple scattering in the gas and apparatus becomes the effective limitation on density. The upper density limitation for the present apparatus is estimated to occur at densities greater than $10\rho_0$.

The apparatus was installed and calibrated in a low-density wind tunnel evacuated by a pumping system utilizing a 5-stage stream ejector. Blank-off pressure levels of about 10 microns were available. It was found that the composition of the gas in the test volume contained appreciable proportions of water vapor due to backstreaming from the ejector system. It was therefore necessary that mass spectroscopic analyses of samples of gas taken from the region of the test volume be obtained in order to calculate the gas density from temperature and pressure measurements.

The calibrating test gases used were subsonic streams of air and helium, at approximately room temperature. Subsonic flow through a nozzle was established and the temperature and static pressure of the gas at the test volume were measured. Simultaneously, samples of the test gas were obtained for mass spectroscopic analysis. These data established the density of the gas at the test volume. Measurements of the scattered intensity detector reading and monitor reading at this density were then made.

If the readings in the scattered radiation detector, background readings in this detector, monitor readings, and monitor background readings are denoted as I, B_I, M_0, and B_M, respectively, it is evident that in the absence of secondary effects the density measured is proportional to the quantity $(I-B_I)/(M_0-B_M)$. B_M is generally negligible compared with M_0. Taking into account the amount of radiation scattered into the main detector by the apparatus itself, A, which is directly proportional to the beam intensity such that A/M_0 is a constant (important at low density), and the effect of the gas itself in contributing counts to the monitor detector (important at high density) the expression for density becomes

$$\frac{\rho}{\rho_0} = k_1 \frac{(I-B_I-A)}{(M_1-k_2\rho)} \simeq \frac{k_1}{M_1}(I-B_I-A)\left(1+\frac{k_2\rho}{M_1}\right) \tag{7}$$

where $M_1=M_0+k_2\rho$ is the monitor reading including its contribution due to air scattering.

The quantity k_1 is readily measured in the medium density ranges extending from $10^{-3}\ \rho_0$ to $10^{-1}\ \rho_0$, A is determined by measuring the value of I as ρ goes to

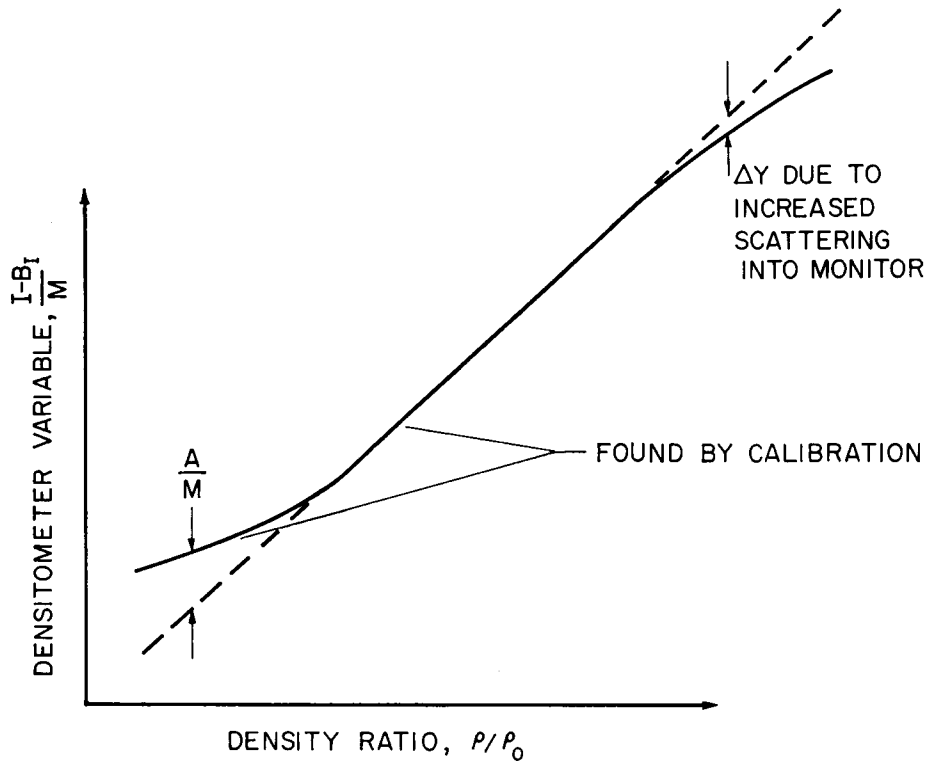

FIGURE 10. Schematic representation of typical calibration curve.

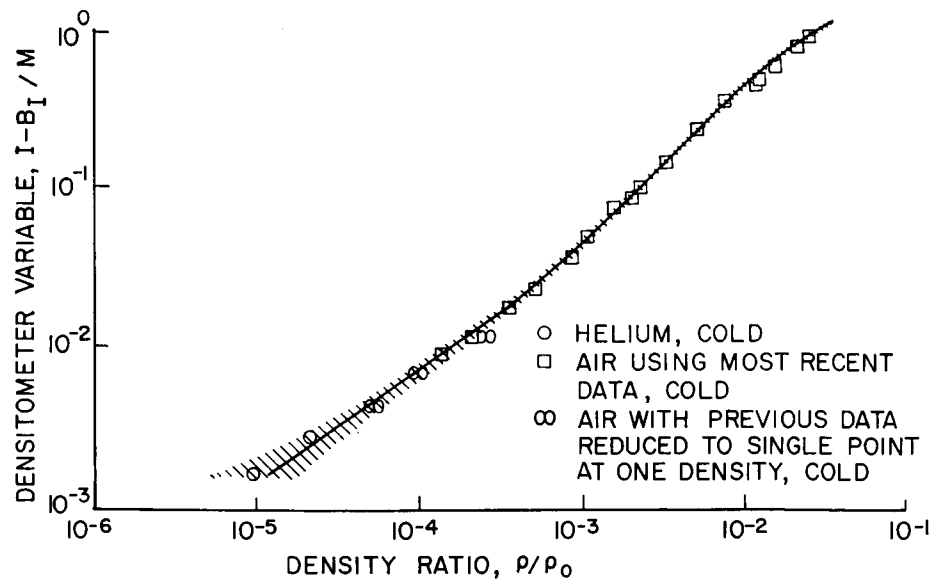

FIGURE 11. Calibration curve.

zero, and k_2 may be determined from measurements made in the higher density regions.

The accuracy of any measurement is limited by statistical considerations imposed by the limited number of random scattering events which occur during any measuring period and the random nature of the background. The maximum integrated X-ray beam flux is limited by heating considerations of the X-ray tube anode, and the period for a measurement is usually fixed by the experimental conditions so that at a given density level the maximum statistical accuracy which may be achieved in a given measurement is fixed. If the background rate without the X-ray beam on has been well established it is easily shown that the fractional standard deviation in a measurement is given to a good degree of approximation by

$$\frac{\Delta\left(\frac{\rho}{\rho_0}\right)}{\frac{\rho}{\rho_0}} \simeq \frac{I^{1/2}}{I-B_1} \tag{8}$$

Figures 10, 11, and 12 summarize these considerations. Figure 10 is a schematic representation of the typical calibration curve showing the deviation from linearity at low density due to the internal scattering and at high densities due to enhanced monitor readings. Figure 11 is an actual calibration curve showing that the useful range of the instrument extends from high densities down to densities well below 10^{-4} ρ/ρ_0. The points on this diagram indicate actual data points and the shaded band indicates the standard deviations in a measurement at the indicated density for a 10-second sampling time for the actual apparatus. Figure 12 shows the percent standard deviation in the density ratio ρ/ρ_0 as a function of density ratio for two sampling times for the apparatus as finally constructed.

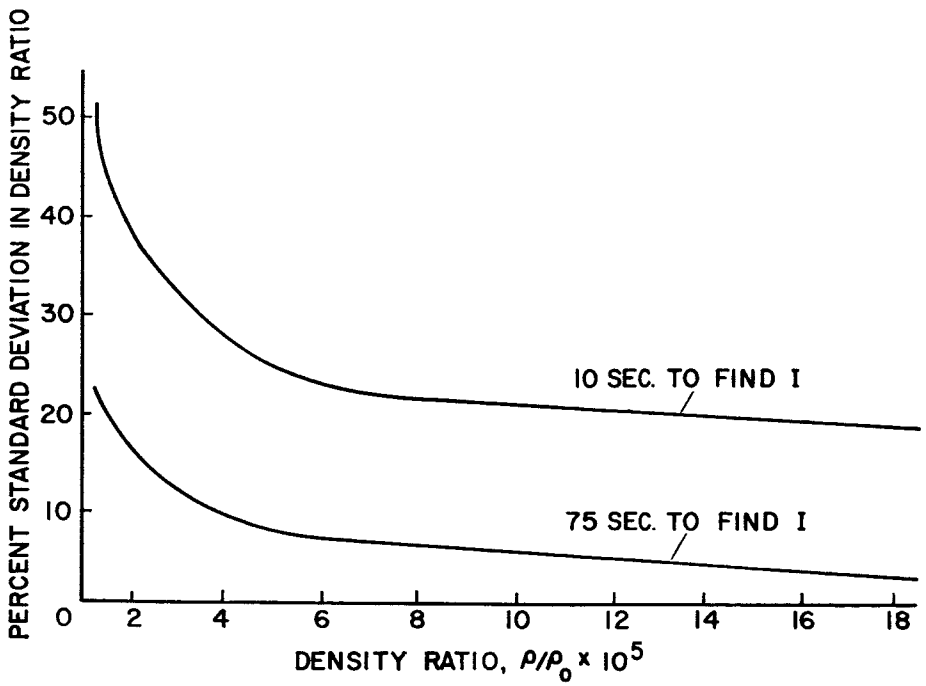

FIGURE 12. Percent standard deviation as a function of density ratio.

PRELIMINARY APPLICATIONS USING THE APPARATUS

The first application of this apparatus in discovering the extent of backstreaming from the steam ejector pumps has already been mentioned. The utility of the device in calibrating other static and dynamic density measuring techniques has also been established.

Measurements of the density and density profiles of an arc-heated gas after expansion in a hypersonic nozzle are in progress, aimed at comparing the state of the gas with predictions based upon various criteria for freezing of the flow. Another application of this apparatus involves its use in conjunction with an impact probe to measure the localized velocity of a hypersonic gas stream. The results of these experiments will be reported in the future.

NOMENCLATURE

A	Contribution to reading in scattered radiation detector due to radiation scattered into detector at $\rho=0$
B_I	Background reading in scattered radiation detector
B_M	Background reading in monitor detector
c	Light velocity
$\frac{d\sigma}{d\Omega}$	Differential cross section for scattering into solid angle $d\Omega$ at angle θ with the original X-ray beam, cm^2/steradian
$\frac{d\sigma_c}{d\Omega}$	Differential cross section defined above for Compton scattering
F	Atomic scattering factor
h	Planck's constant
I	Counting rate in scattered radiation detector
I_e	Thomson scattering per electron
I_θ	Intensity of radiation scattered at angle θ
k_1	Calibration constant
k_2	Constant of proportionality relating additional contribution to monitor detector to air density ρ
m	Electron mass
M_1	Reading in monitor detector
M_0	Reading in monitor detector corrected for air scattering effect
n	Density of scatterers, total number of bound and free electrons per cm^3
N_T	Net scattering per electron in gas at temperature $T°$
Q	Electrons per gram
R	Defined in equation (2)
S	Ratio of scattered intensity per bound electron to the Thomson scattering from a free electron at a given X-ray energy
s_{mn}	Internuclear distance between mth and nth atoms in a molecule
T	Temperature
x	Impurity mass fraction
z_j	Number of electrons per neutral j particle
θ	Scattering angle
λ	Wave length
ξ	Detection efficiency
ρ	Density, gms/cm^3
ρ_0	Air density at 70°F and 1 atmos, 7.52×10^{-2} lb/ft^3, 1.205×10^{-3}gm/cm^3
Φ	Incident X-ray flux, photons/cm^2-sec
$\sum f^2$	Incoherent scattering function

ACKNOWLEDGMENTS

The author wishes to acknowledge the contributions of Messrs. C. E. Noble and J. Crumal of Vidya who actively participated in the design and construction of the densitometer. Thanks are also due to the entire Heat Transfer Branch, Ames Research Center, NASA, and especially to Professor George Leppert and Mr. Charles Landrum who calibrated the instrument.

This work was supported by the National Aeronautics and Space Administration under Contract NAS2-261.

REFERENCES

1. Moeckel, W. E., and Weston, K. C., "Composition and Thermodynamic Properties of Air in Chemical Equilibrium", *NACA TN 4265* (1957).
2. Compton, A. H., and Allison, S. K., *X-Rays in Theory and Experiment* (New York: Van Nostrand, 1957).
3. James, R. W., and Brindley, G. W., "Some Numerical Calculations of Atomic Scattering Factors", *Phil. Mag.*, Series 7, **12**, 81 (1931).
4. Wollan, E. O., "Scattering of X-rays from Gases", *Phys. Rev.*, **37**, 862 (1931); *Proc. Nat. Acad.*, **17**, 475 (1931).
5. Hines, G. J., and Brownell, G. L., *Radiation Dosimetry* (New York: Academic Press, 1956).
6. Condon, E. U., and Odishaw, H., *Handbook of Physics* (New York: McGraw-Hill, 1958), 7-119.

21. T. Herbert Dimmock and William R. Kineyko: *Ionization Profiles in Low-Pressure Exhausts*

The ionization profile along the axis of a seeded, Mach 3, high-altitude rocket exhaust has been mapped by microwave and probe techniques. The ionization density in the jet was as high as 10^{13} *electrons/cm*^{3} *and was found to vary half an order of magnitude between expansion and shock regions.*

The relaxation in the jet was evaluated from the measured data. Since the ionization was found to follow the gas density profile, it was concluded that the relaxation time was at least as long as the transit time between the shock waves, and that the residence time in the shock zone was sufficient to sustain this ionization. Cases in which the residence time is less than the thermalizing time are also illustrated.

The thermodynamic properties in the jet were measured by pressure and temperature probes and by line reversal spectroscopy. Unfortunately, it was necessary for the probe dimensions to be comparable to the jet dimensions, thus reducing the excursions in pressure and temperature along the profile and resulting in average values only.

The microwave method was found to be suitable for analysis of low pressure seeded jets as long as the collision frequency is of the order of 10^9 *sec*$^{-1}$ *and the electron density lies between* 5×10^{11} *and* 2×10^{13} *electrons/cm*^{3}*. Such a plasma would then have a d-c conductivity of the order of* 100 *mhos/m.*

INTRODUCTION

At the high combustion temperatures required for efficient rocket propulsion some of the combustion species are ionized even when conventional rocket fuels are used. If easily-ionized additives are introduced along with the propellants, simple calculations show that one might expect 10^{14} ions/cm^3 or a mole fraction of 10^{-5} ions/neutral particle. One would thus predict that a suitable electric, magnetic, or Lorentz force field could be used to accelerate the charged particles which would

ED. NOTE: Mr. Dimmock and Mr. Kineyko are with the Thiokol Chemical Corporation, Reaction Motors Division, Denville, New Jersey. This work was supported by the Air Force Office of Scientific Research under Contract No. AF 49(638)–305.

exchange momentum with the neutral particles to produce a measurable alteration of the rocket thrust vector. This research program was therefore undertaken to determine whether such ionization could be produced, and to determine the interaction of the ionized plasma with external electric, magnetic, and electromagnetic fields. Specifically, the objective was to study ionization relaxation processes in seeded, high-temperature, supersonic exhausts, to consider the effects of ambient pressure and chemical composition on this relaxation, and to investigate some of the parameters which control the electromagnetic interaction process in the high-altitude exhaust.

The significance of the ionized species in rocket exhausts cannot be emphasized too strongly. It is well known that the ionized jet and plume in the wake of a rocket booster or sustainer attenuate and deflect electromagnetic control signals making the problem of sustained ground guidance difficult, if not impossible. Although much has been done to suppress ionization in the wake of high-performance rockets by the use of electron-scavenging additives, this approach invariably occurs at the expense of the high performance which dictated the *a priori* selection of propellants. The aim of this program is to investigate some of the

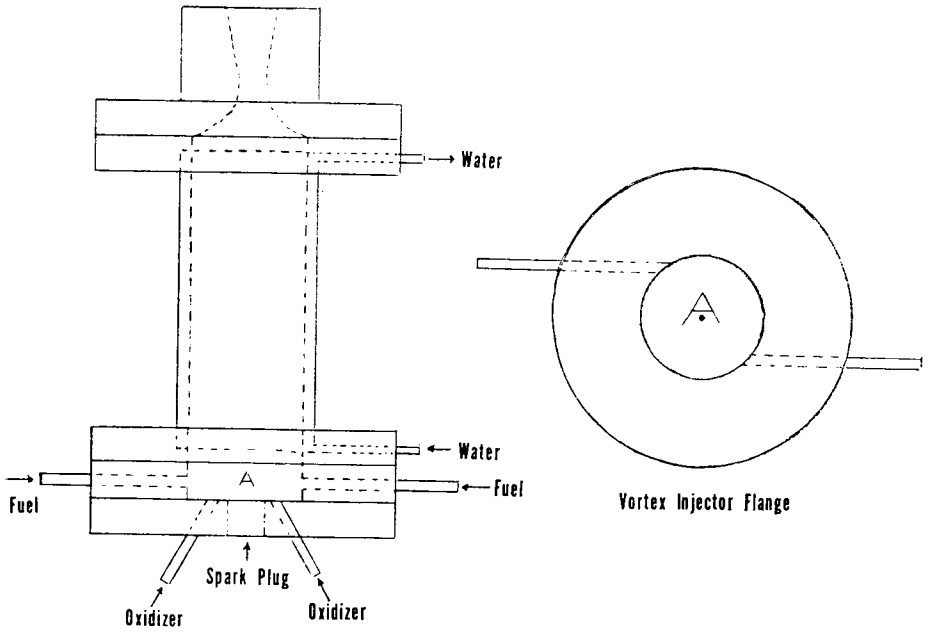

FIGURE 1. Rocket test engine.

sources of ionization, and the time scale for relaxation in a seeded, high-altitude, low-Mach-number exhaust. Some of the thermodynamic and transport properties in the jet have been determined; information on rate processes was inferred from these properties. In addition, a variety of plasma measurement techniques were employed, and the range, accuracy, and limitations of each method for jet diagnostics was found and will be indicated.

APPARATUS

The test engine sketched in Figure 1 consisted of a water-cooled cylindrical chamber 3.5 inches long with 1.25-inches I.D. The chamber was fitted with an uncooled copper nozzle having a $\frac{5}{16}$-inch throat diameter and a 3.08 exit/throat

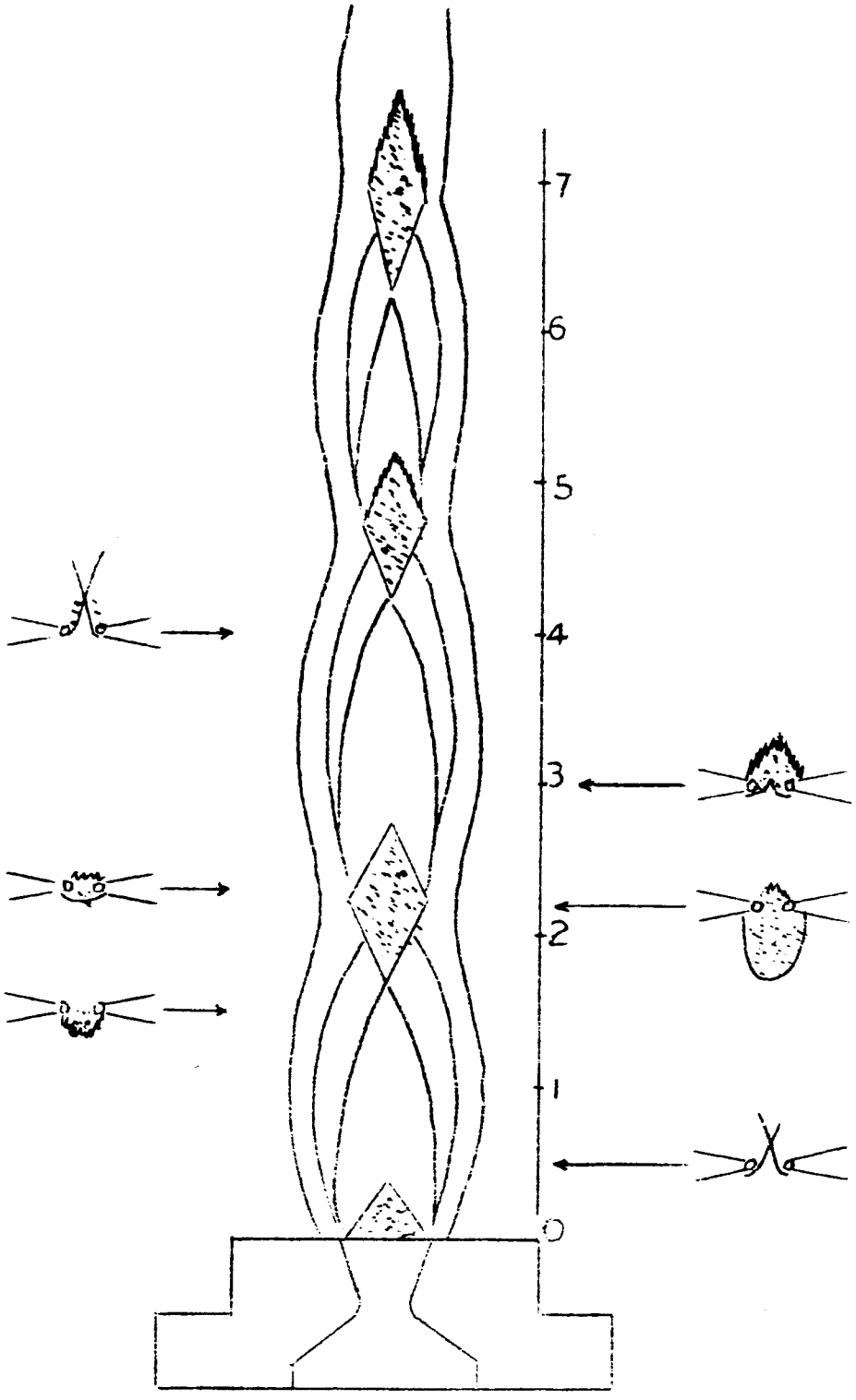

FIGURE 2. Shock structure in the rocket jet and on the conductivity probes.

area ratio.† The injector which completed the chamber closure consisted of a copper block with two $\frac{1}{4}$-inch gas ports and a surface-gap spark plug igniter. Two types of injectors were used: premixed and vortex. In the premixed injection, stoichiometric mixtures of ethylene (C_2H_4) and oxygen (O_2) were introduced into the chamber by the impinging jet injector attached to the chamber. In the vortex injection, oxygen was fed through both ports of the impinging injector, and ethylene was introduced through another tangential injector block located between the impinging injector and the chamber. The entire engine assembly was mounted on a platform which could be raised or lowered by a motor-driven worm gear. This was done in order to explore the axial properties of the jet without having to move the probing equipment.

The rocket engine was fired into a 20-cubic-foot tank fitted with a pumping system having a capacity of 600 ft^3/minute at 1–20 torr. Figure 2 is a sketch of the typical shock structure which occurs in the jet under running conditions. The propellant flow rate was 40 standard liters/minute (SLM) and the tank (ambient) pressure was 5 torr.

The rocket engine was seeded with aqueous solutions of alkali metal salts which were metered into the chamber through a hypodermic needle in the injector plate. Alkali seeding could be controlled by changing either injection flow rate or salinity. For most of the tests, a cesium injection of 1% of propellant mass injection was maintained while using a 1-molar cesium nitrate solution.

The propellant flow rates, which were 28 and 40 SLM, and the throat diameter were chosen to provide a subatmospheric chamber pressure (125 and 180 torr, respectively) and thus a low Mach number, high-temperature jet. The area ratio between the exit and the throat was selected for optimum expansion to an ambient pressure of 10 torr. A conical nozzle was used with an 18 degree half-angle.

Since it was desired to conduct a heat balance on the engine, the chamber coolant flow rate and temperature rise were monitored. The chamber temperature could readily be found from a measurement of the heat loss per mole of propellants, the total propellant injection, and the chamber pressure.

The density and temperature profile of the jet were measured in order to compare the ionization which was to be measured with the equilibrium value. The density was determined from either (1) measured values of free-stream pressure and temperature, or (2) isentropic calculations based on measurements of stagnation pressure and temperature and free-stream pressure.

Two methods of temperature measurement were used; shielded thermocouples and spectroscopic sodium-line reversal. The plasma probes used for pressure and temperature measurement are sketched in Figure 3. Referring to Figure 3a, it can be seen that the tungsten/iridium thermocouple junction was located in a semi-stagnant gas zone and was double-shielded by boron nitride tubes. Successful use of this probe was limited, mainly by erosion, to pressures below 10 torr and to mass flow rates of 28 SLM or lower. To supplement this restricted range of temperature measurements, the jet was seeded with sodium and the temperature was measured by line reversal using a 15,000-lines/inch, 1.5 meter grating spectrograph. This method was only useful at 10 torr and above, and at flow rates of 40 SLM or greater.‡

Figures 3b and 3c show the boron nitride probes which were used for total and

† The L^* for this engine (chamber volume/throat area) was 56 inches.

‡ This was mainly due to the weak line intensity which necessitated the use of a larger entrance slit so that the reversal line could not be accurately detected. At 5 torr there was enough luminosity in the first two shock diamonds to measure the temperature with a 50-degree uncertainty, however.

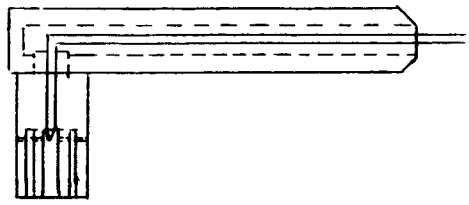

FIGURE 3a. Stagnation thermocouple.

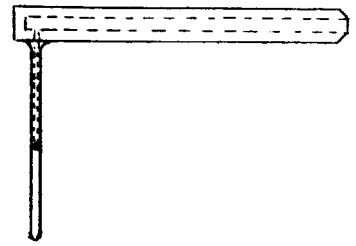

FIGURE 3b. Total pressure probe.

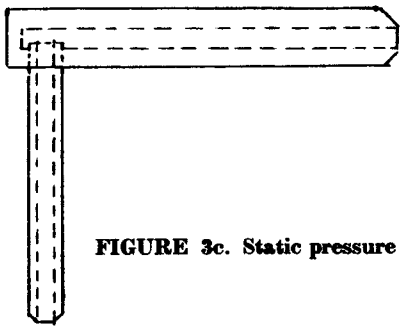

FIGURE 3c. Static pressure probe.

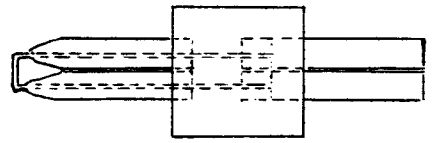

FIGURE 3d. Conductivity probe.

static pressure measurements. Although these probes were made as small as possible, their dimensions were still comparable with the spacing between shocks in the jet (as determined from lines of maximum luminosity). For measurements in regions of rapid pressure change (shock diamond), it was decided, therefore, that the reading most nearly represented the pressure at the port-holes rather than at the nose, and this convention was used throughout.†

The ionization in the jet was measured by probes and microwave absorption methods. Figure 3d shows the probe used for conductivity measurements. This probe, which is supported by an insulated mount and is water-cooled, has a conducting surface $\frac{1}{2}$ inch long and 0.020 inch in diameter. Two of these probes were inserted into the flame so that their axes were parallel and separated by $\frac{1}{4}$ inch. The plane of the probes was made normal to the direction of gas flow. The probes were used in a series circuit which included a variable potential source (monitored by a precision voltmeter) and an X-Y recorder. The X-Y recorder, which measured the voltage drop across a precision resistor in the series circuit, had a maximum sensitivity equivalent to 1 microampere per inch on the Y-axis. Axial profile measurements were made by changing the position of the test engine as described above and applying a known d-c voltage to the probes. An a-c sweep voltage was applied to the X-axis of the recorder whose frequency was adjusted until the horizontal travel of the pen matched the traverse of the probes down the jet axis. In this way a fully resolved profile of probe current versus axial position was obtained for any desired d-c probe voltage.

The microwave measurements were made using the two standard circuit arrangements shown in Figure 4. The Raytheon QK 290 reflex klystron was modulated by a square wave. The transmitted, received, and reflected signals

† The magnitude of this error was indicated by a separate experiment in which the probe diameter was halved but the L/D was maintained at 10. It was found that the effect of a larger probe was to moderate the variation in the pressure profile.

were monitored on a multi-channel recorder. The transition from wave guide to the horn/lens system was through a transition piece at the entrance to the horn. The radiant, circularly polarized energy from the horns was focused into a $\frac{3}{4}$-inch-diameter (for 90% of the transmitted energy) beam at the flame. This was done by using teflon lenses ($f/1 = 8.75$ inches, $f/1.5$) whose dielectric constant was fixed over a wide frequency range.

DISCUSSION OF IONIZATION MEASUREMENT METHODS

Conventional Langmuir probe theory as applied to static gases is unsuitable for supersonic flow applications. The principle problem which arises in employing a

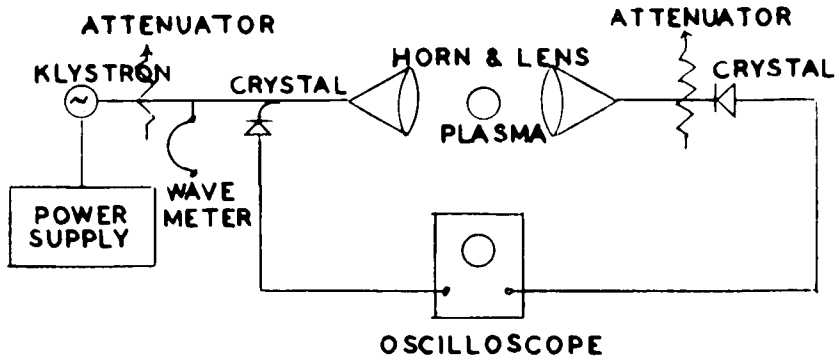

ATTENUATION CIRCUIT

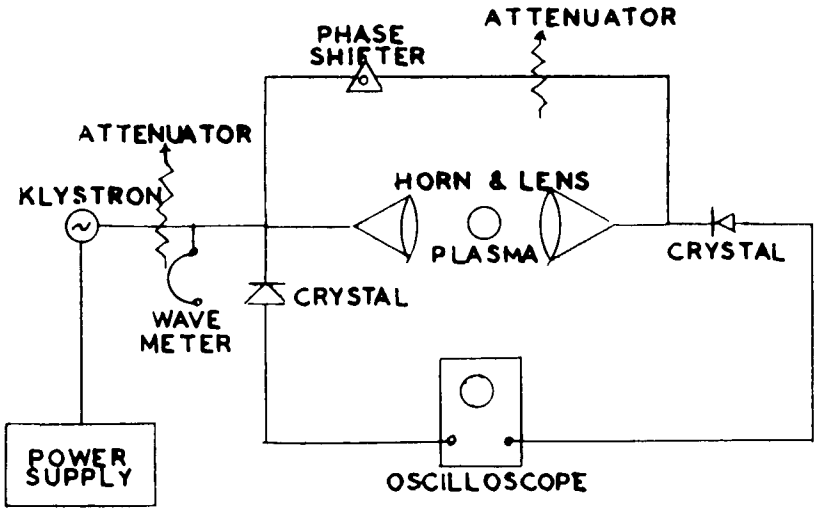

INTERFEROMETER CIRCUIT

FIGURE 4. Block diagram of microwave circuits.

Langmuir probe in a plasma jet is that if a conventional electrode is used, the space charge sheath formed around the probe is so distorted by the flow as to make interpretation of the measurements impossible. In a laboratory experiment on unseeded exhausts at Reaction Motors Division, however, Dr. Fleischer demonstrated experimentally that in an unseeded supersonic stream the voltage-current relationship between two probes follows Ohm's law rather than the Langmuir–Childs theory, exhibiting a linear volt-ampere relationship instead of the usual sigmoid curve characteristic of space-charge limited currents. The slope of this volt-ampere curve, i.e., the probe resistance, was found to be linear and to increase with increasing probe separation.† If an infinite parallel cylinder approximation is used, the relationship between probe resistance and jet conductivity is a geometric one given by the equation

$$\sigma = \frac{\cosh^{-1}(c/d)}{RL} \simeq \frac{\log(2c/d)}{RL} \tag{1}$$

where c, d, and L are electrode separation, diameter, and length, respectively, and $R = V/I$ is the probe resistance. Further tests in seeded jets revealed, however, that the method was only valid for regions with homogeneous plasma between the probes, and that in highly seeded jets, a deposit forms on the probe which inhibits current flow in the plasma circuit. For this reason the ionization densities reported herein were obtained from microwave measurements exclusively.

A complete analysis of microwave measurements of plasma properties is given by Warder *et al.* (**1, 2**), and Kannelaud (**3**). It will be briefly summarized here using the notation of Warder.

The propagation through a plasma by a plane wave of incident amplitude E_0 is

$$E = E_0[1 - \exp(-\gamma x + j\omega t)] \tag{2}$$

where $j = \sqrt{-1}$, ω is the microwave angular frequency, x is the plasma thickness and γ is the complex propagation constant given by

$$\gamma = \alpha + j\beta \tag{3}$$

In equation (3), α is the attenuation constant and β is the phase constant. By combining with Maxwell's equations the Lorentz macroscopic equation for charged particle motion in an oscillating electric field, one can relate α and β to ω, and to the properties of the plasma of thickness x as follows:

$$\alpha = \frac{\beta_0}{2}\left[\frac{\omega_p^2/\omega^2}{(1-\omega_p^2/\omega^2)^{1/2}}\left(\frac{\nu_c}{\omega}\right)\right] \tag{4}$$

$$\beta = \beta_0(1-\omega_p^2/\omega^2)^{1/2} \tag{5}$$

$$\Delta\beta = x(\beta_0 - \beta) \tag{6}$$

where ν_c is the electron–atom collision frequency, ω_p is the plasma frequency ($\omega_p^2 = ne^2/\varepsilon_0 m$), ε_0, and β_0 are the permittivity and phase constant ($\beta_0 = \omega/c$) of free space, respectively, and n, e, and m are the concentration, charge, and mass of the electrons, respectively.

Finally, the electrical conductivity of the plasma may be written

$$\sigma = Re\left(\frac{J}{E}\right) = \frac{ne^2}{m}\frac{\nu_c}{\nu_c^2 + \omega^2} \tag{7}$$

† Such linearity, of course, occurs only in a uniform plasma. The uniformity of the plasma was first demonstrated by stepwise measurement across the plasma made with a fixed probe separation.

and the d-c conductivity derived from equation (7) is:

$$\sigma_{dc} = ne^2/\nu_c m \tag{8}$$

In the highly-seeded, low-pressure jet, however, the plasma frequency is often very close to the microwave angular frequency. Under these conditions $\sigma/\omega\varepsilon > 1$ and the reflections at the interface likewise reduce the received signal. Warder has shown that the reflection can be calculated from the phase and attenuation:

$$\Gamma^2 = \frac{\alpha^2+\beta_0^2(\beta/\beta_0-1)^2}{\alpha^2+\beta_0^2(\beta/\beta_0+1)^2} \tag{9}$$

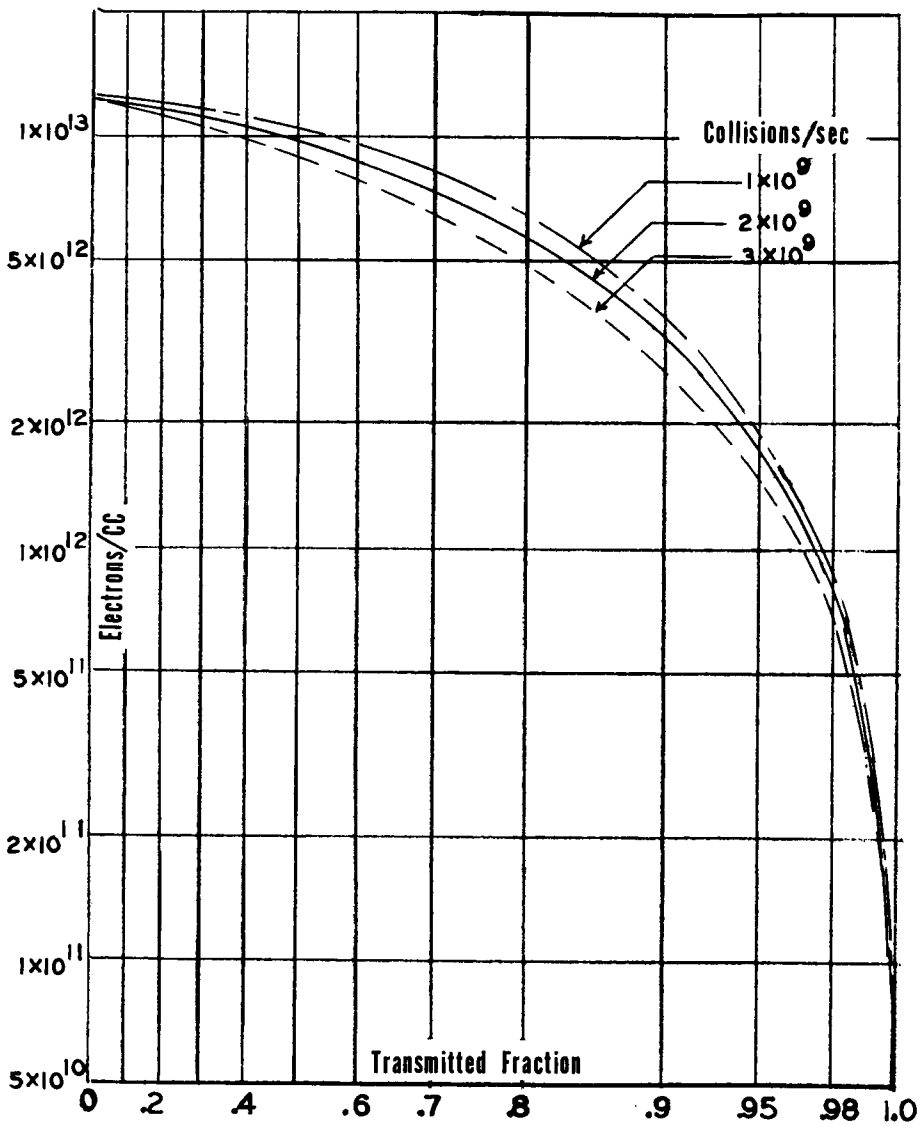

FIGURE 5. Microwave transmission through plasmas.

Then, from elementary optical considerations, the transmitted fraction, Δ, of the received signal is

$$\Delta = 1 - \Gamma - T \tag{10}$$

where $T = e^{-\alpha z}$ is the attenuation through the flame. Figure 5 is a plot of the transmitted fraction, Δ, versus the electron concentration for a KA-band frequency of 31.8 Kmc in reduced pressure plasmas.

TABLE I. OPTIMUM PROPELLANT PERFORMANCE—SEEDED

A. *Ingredients*

Name	*Symbol*	*Feed temp.*	*Density*	*Mol. wt.*
Ethylene	C_2H_4	298.15°K	0.001 gm/cc	28.05
Oxygen	O_2	298.15°K	0.001 gm/cc	32.00
Cesium Nitrate	$CsNO_3$	298.15°K	3.685 gm/cc	194.92
Water	H_2O	298.15°K	1.00 gm/cc	18.016

Composition Weights		
	7% *Seeding*	14% *Seeding*
C_2H_4	22.614	22.614
O_2	77.386	77.386
$CsNO_3$	1.206	2.282
H_2O	6.194	11.718

B. *Thermal Data*

	7% *Seeding*	14% *Seeding*
Gamma bar	1.069	1.074

C. *Rocket Parameters*

	7% *Seeding*		14% *Seeding*	
	Shifting	*Frozen*	*Shifting*	*Frozen*
A/A^*	7.628	6.13	7.55	5.806
C^*	4729.5	4402.8	4678.8	4632.7
I_{sp} (ideal)	234.08	209.23	231.09	218.22
I_{sp} (space)	261.09	232.67	257.58	238.44
Exhaust Conditions:				
Pressure, psia	0.10	0.10	0.10	0.10
Temp., °K	2083.7	1492.7	2002.5	1341.8
Mol. wt.	28.508	26.33	28.294	26.304
Chamber Conditions:				
Pressure, psia	3.87		3.87	
Temp., °K	2646.8		2583.7	
Mol. wt.	26.33		26.304	

D. *Products of Combustion*

	7% *Seeding*			14% *Seeding*		
	Chamber	*Shifting*	*Frozen*	*Chamber*	*Shifting*	*Frozen*
CO	0.14023	0.06122	0.14023	0.11307	0.03714	0.11307
CO_2	0.25501	0.36671	0.25501	0.25892	0.36299	0.25893
Cs	0.00152	0.00164	0.00152	0.00270	0.00291	0.00270
H	0.01733	0.00465	0.01733	0.01267	0.00227	0.01268
OH	0.04908	0.01549	0.04908	0.04174	0.01009	0.04174
H_2	0.03500	0.01692	0.03500	0.03196	0.01218	0.03196
NO	0.00046	0.00013	0.00046	0.00056	0.00012	0.00056
O_2	0.07393	0.03725	0.07393	0.06367	0.02633	0.06367
N_2	0.00053	0.00076	0.00053	0.00107	0.00139	0.00107
O	0.01560	0.00394	0.01560	0.01073	0.00137	0.01073
H_2O	0.41132	0.49219	0.41132	0.46290	0.54321	0.46290

RESULTS

Table I lists propellant performance data which were obtained theoretically for the stoichiometric CH_4/O_2 propellants seeded (7% and 14%) with $CsNO_3$ solutions. The propellant flow rate was 40 SLM.† For the 7% seeding case, these values were used to determine the equilibrium ionization in the chamber, which was 9.9×10^{13} electrons/cm^3.

The exit plane conditions for frozen and shifting chemical equilibrium in the nozzle are also given. Depending upon pressure and velocity conditions in the nozzle, the chemical process may be in frozen equilibrium to the exit plane, shifting equilibrium to the exit plane, or shifting part way and frozen the remainder of the way. If the reaction is in frozen equilibrium, the heat loss by expansion in the nozzle will depress the gas temperature to a low value T_1 at the exit plane. If chemical equilibrium prevails, the continuing exothermic reaction in the nozzle will result in an exit temperature T_2. If the reaction freezes part way down the nozzle, an intermediate exit temperature T_3 will result. The ionization density may also be considered in the same way. If it follows the density changes in the nozzle, the kinetic process may be considered to be frozen; if it is described by the Saha equation, it may be considered to be in shifting equilibrium. The frozen and shifting data of Table I were used to obtain equilibrium ionization densities at the exit plane, namely 4.1×10^9 and 2.2×10^{12} electrons/cm^3 respectively. The values of ionization in the chamber (n_{ch}) and at the exit plane for frozen (n_{fc}) and shifting (n_{sc}) chemical equilibrium in the nozzle are shown in Figure 6.

In order to properly analyze the relaxation of ionization in the jet, it is necessary to measure the changes in ionization apart from the gross density changes. For this purpose a density profile down the jet axis is required. Such a profile was calculated from the theoretical exit-plane conditions and the measured pressure and temperature profile of the jet. Figure 7 shows the pressure and temperature profiles in the 40 SLM jet. The temperature was determined by sodium line reversal; the pressure was measured with a mercury manometer using the probes shown in Figure 3b and 3c. The location and approximate shape of the shock diamonds are also shown for reference. The stagnation pressure, p_{0y}, is the pressure behind the normal shock on the probe. When the tip of the probe passes through a pressure discontinuity in the jet stream (e.g., the leading edge of a shock diamond), the

† The measured heat loss was included for these calculations.

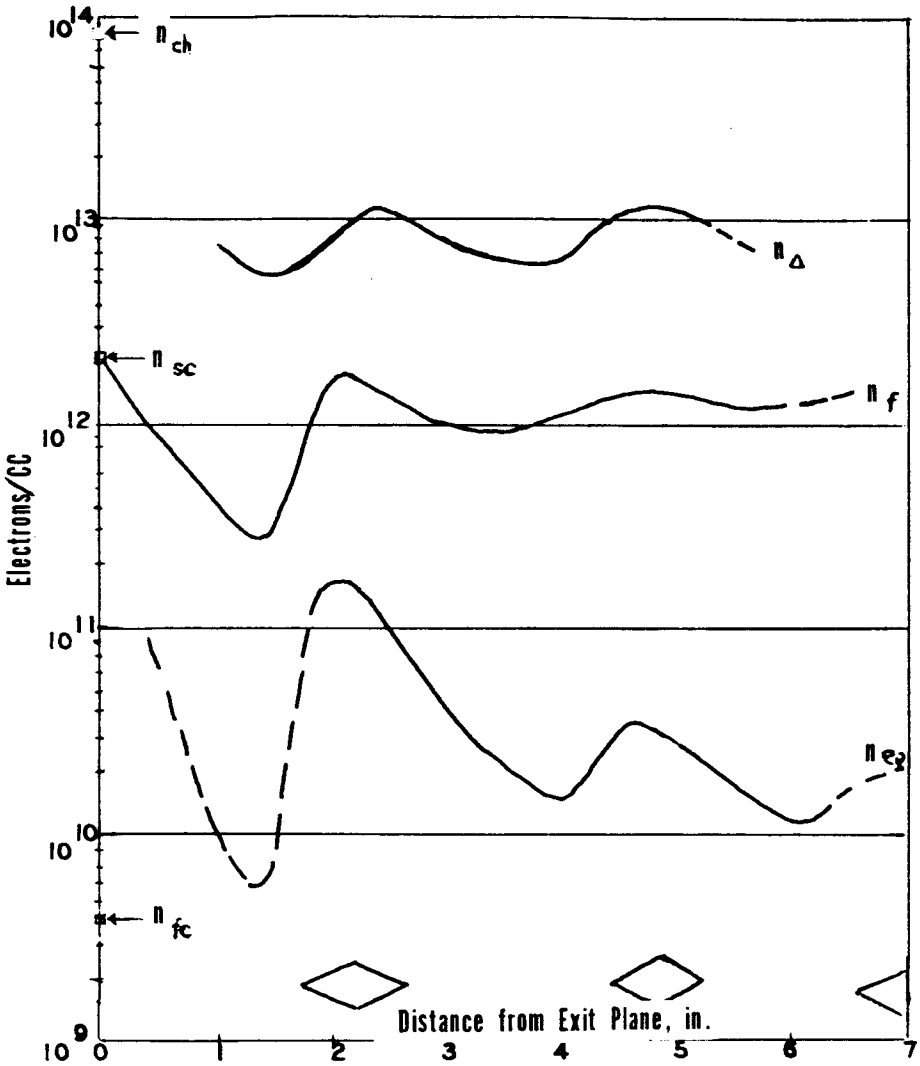

FIGURE 6. Electron concentration in the jet.

shock on the probe ceases to be a normal shock due to interaction with the jet shock. For this reason the p_{0y} curve shows the unexpected rising inflection at the shock diamonds. Likewise, in measuring stream pressures, if the jet shock lies between the probe tip and the probe port, the indicated stream pressure will be affected by the interaction of the two shock fronts. Thus the indicated pressure is incorrect for the region immediately upstream of the leading edge of the shock diamonds.

It is of interest to calculate the electron–atom collision frequency in the plasma from the measured temperature, pressure, and composition of the plasma. The collision frequency in a weakly ionized plasma may be defined as

$$\nu_c = \bar{c} \sum_i n_i Q_i = cm \sum_i x_i Q_i \tag{11}$$

where $\bar{c} = \sqrt{8kT/\pi m}$ is the random thermal speed of the electrons and n_i x_i and Q_i are the number density mole fraction and collision cross-section of the ith specie.

TABLE II. FACTORS AFFECTING ELECTRON COLLISIONS IN THE JET

Element	$Q \times 10^{15}$ (cm^2)	*Mole fraction* x_i			$\bar{x}_i Q_i \times 10^{15}$ (cm^2)
		Shifting	*Frozen*	*Average*	
Cs	3.6	0.0029	0.0027	0.003	0.0108
H_2O	3.6	0.543	0.4629	0.503	1.8100
O_2	0.31	0.026	0.0637	0.045	0.0140
CO	0.81	0.037	0.113	0.075	0.0607
CO_2	1.2	0.363	0.259	0.311	0.3910
OH	—	0.010	0.042	0.026	—
H_2	0.85	0.012	0.032	0.022	0.0187
Other	0.8	—	—	0.015	0.0120
Σ				1.000	2.3172

Table II shows the pertinent species in the combustion exhaust and their collision cross sections (**4**). Thus equation (11) may be written

$$\nu_c = 7.24 \times 10^{11} p/T^{1/2} \text{ sec}^{-1} \qquad (12$$

where pressure and temperature are in psia and °K, respectively. This expression was plotted for our pressure and temperature profiles (Figure 7) and is shown in Figure 8.

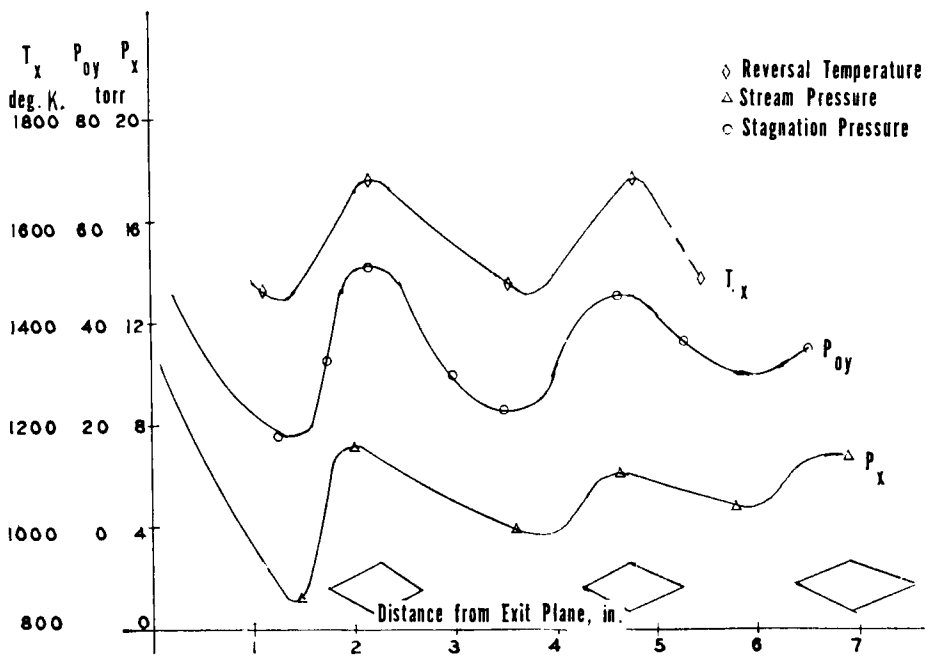

FIGURE 7. Pressure and temperature profiles in the jet.

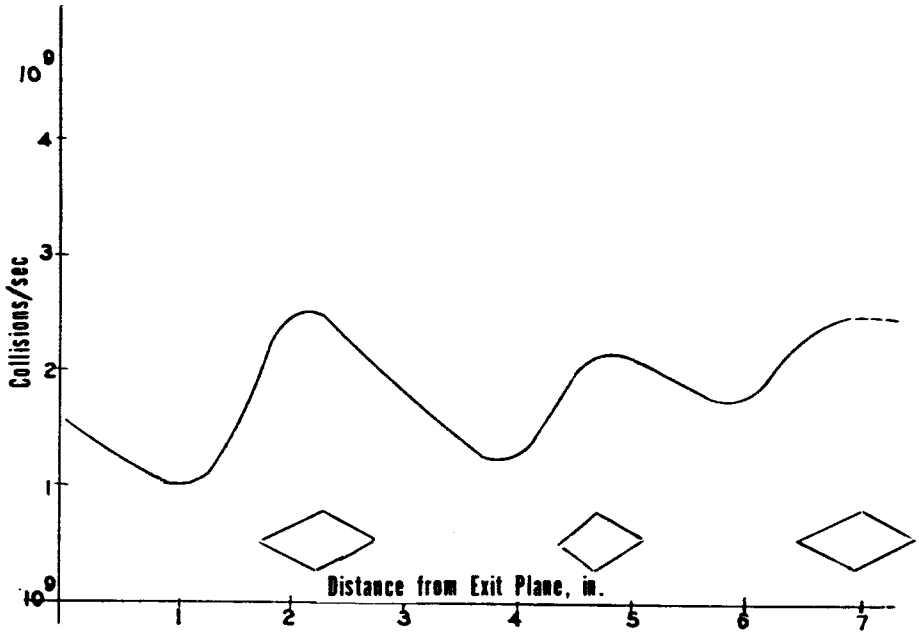

FIGURE 8. Collision frequency profile in the jet.

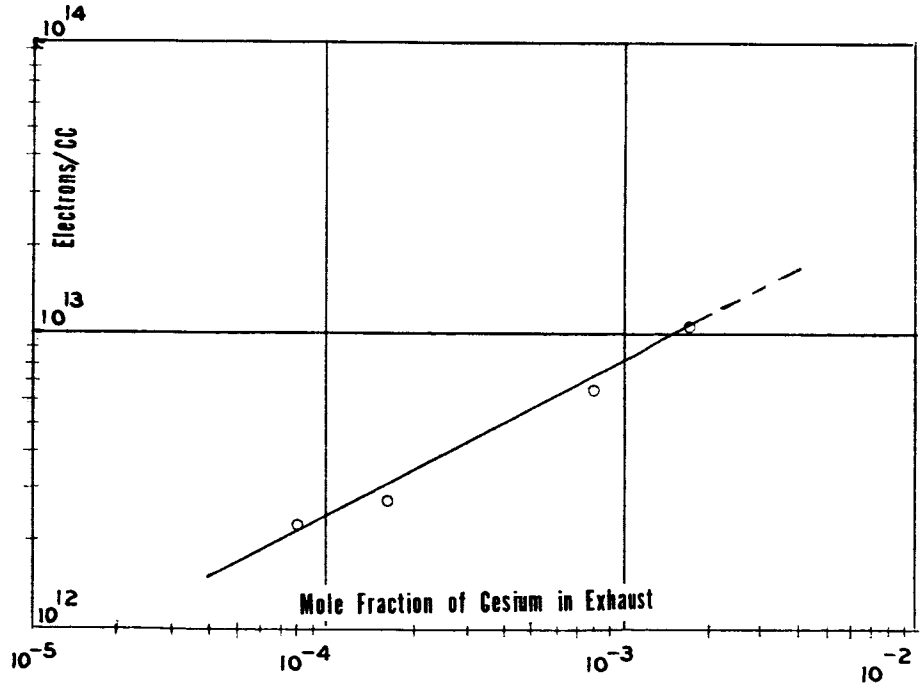

FIGURE 9. Influence of seeding on jet ionization.

Before attempting to measure the jet ionization profile, the linearity of the detection equipment was established. Cesium nitrate solutions with molarities from 0.01 to 1.0 were prepared and injected into the 40-SLM 5-torr jet. Attenuation and phase shift measurements were then made using the circuit shown in Figure 4. The resulting electron concentration in the first shock diamond is plotted in Figure 9. The concentration obtained from the microwave measurements, n_Δ, was obtained from Figure 5. The linearity of the n_Δ curve implies that the microwave measurements are at least self-consistent over the range of additive concentrations which were used. Furthermore, the slope of one-half agrees with the value obtained by Padley and Sugden for large additive concentrations (**5**). Static tests indicated that reflections from the nozzle plate of the engine could be detected as long as the beam axis was less than 2 inches from the metal plate. For this reason a traverse down the axis was limited to that portion of the jet in excess of 2 inches downstream from the exit plane. To obtain a correct reading in the first expansion, therefore, a stationary measurement was first made so that the effect of reflection could be eliminated by subtraction.

The ionization in the 7% seeded jet was measured by microwave attenuation at the center of the first two shock diamonds and the first two expansion regions. The curve labeled n_Δ in Figure 6 is a typical ionization profile through these measured points. (The shape of this curve was made similar to the conductivity probe curves as discussed below.)

If the cesium concentration in the jet remains at 0.15 mole % (i.e., if frozen chemical equilibrium is assumed), the equilibrium ionization at each point in the jet can also be computed when the jet pressure and temperature are known. This was done by using the temperature pressure profiles of Figure 7 and is shown in Figure 6 by the curve labeled n_{eq}. Finally, if the exit-plane ionization density, n_{sc}, is multiplied by the normalized density in the jet,† ρ/ρ_0, a completely frozen ionization profile in the jet will be obtained, and this is indicated by the curve labeled n_f.

From Figure 2 it can be seen that the thickness of the shock diamonds for the first two shocks was 1.25 and 1.0 centimeters, respectively. Since this value is less than the beam width of the microwave probe, the measured electron density of the diamonds is less than the true axial density. The relative size of the shock diamonds, expansion regions, and the microwave beam are given in Table III along with the attenuation data shown in Figure 6. The indicated electron densities are calculated by assuming a homogeneous core with thickness given by the average value in Table III.

TABLE III. JET MICROWAVE MEASUREMENTS

Location	*Distance to exit* (inches)	*Trans. frac.*	*Jet diameter*			$\bar{n}_\alpha$ ($\times 10^{12}$)	$\bar{\sigma}$ $(\Omega m)^{-1}$
			Uniform core (cm)	*Total* (cm)	*Avg.* (cm)		
First expansion	1.00	0.724	3.00	3.00	3.00	7.4	105.00
First shock	2.25	0.276	1.25	2.25	1.75	11.3	159.00
Second expansion	3.50	0.704	3.00	3.00	3.00	7.6	107.00
Second shock	4.75	0.363	1.00	2.00	1.50	11.2	158.00

The d-c conductivity as shown in equation (8) was determined from the microwave attenuation measurements in the jet; it is also given in Table III. The

† Assuming shifting chemical equilibrium in the nozzle, ρ_0 is the density at the exit plane.

averaged value $\bar{\sigma}$ lies between 100 and 160 mhos/m, and was evaluated from the average thickness using 2×10^9 coll/sec for ν_c.

In searching for a mechanism which would explain why n_Δ always exceeded n_{eq} in Figure 6, it was decided to make measurements of the characteristics of the spectral emission from the jet. If equilibrium conditions prevail in the jet, the spectrum of the jet should be similar to the spectrum of the mantle of a propane/air atmospheric flame; absence of such equilibrium could easily explain the anomalous high ionization.

Two types of injection were used in these tests: premixed and vortex. In both cases the C_2H_4 was bubbled through liquid iron pentacarbonyl, $Fe(CO)_5$, to insure the presence of iron in the exhaust. Table IV lists the tests and the results. Spectra were made to determine the effect of jet mixing, stoichiometry, and injector type.

TABLE IV. SPECTRAL LINES IN SEEDED EXHAUSTS AT 10 TORR (FUEL, C_2H_4/O_2; FLOW RATE, 28 SLM; ADDITIVE, Fe $(CO)_5$)

		Mixture				*Shroud*				
No.	*Type*	*Stoich*	*Rich*	*Iron*	*Exposure*	*Air*	*None*	*Color*	*Lines*	*Intensity*
1	Premixed	X			10 min		X	light blue	OH band	—
2	Premixed	X		X	10 min		X	orange and green	3922.51 3895.66 3856.37 3820.43 3760.05 3749.49	55 35 85 500 6 400
3	Premixed		X		10 min		X	invisible		
4	Premixed		X	X	10 min		X	light green	3840.44 3760.05 3743.56 3581.20	80 6 60 600
5	Premixed		X		10 min	X		light violet	none	
6	Premixed		X	X	10 min	X		white plume with orange exit cone	3824.44 3749.49 3733.32 3649.51 3631.46 3621.46 3605.46 3581.2 3570.1 3100.67 3055.26 2999.51 2813.3 2788.1 2733.6	80 400 70 16 200 24 24 600 400 26 6 36 42 70 70
7	Vortex	X		X	20 sec	X			see Fig. 10	

For the jet mixing tests, a laminar air flow shrouded the jet and the pumping capacity was increased to maintain the ambient pressure at 5 torr. Figure 10a shows a spectrum which was obtained with the vortex injector and the air shroud, using a Hilger spectrograph (50 micron slit) and Type 1-0 film. Figure 10b shows a 60-second exposure of the propane/air flame mantle made for comparison.† The

† This was a flame burning on an open burner.

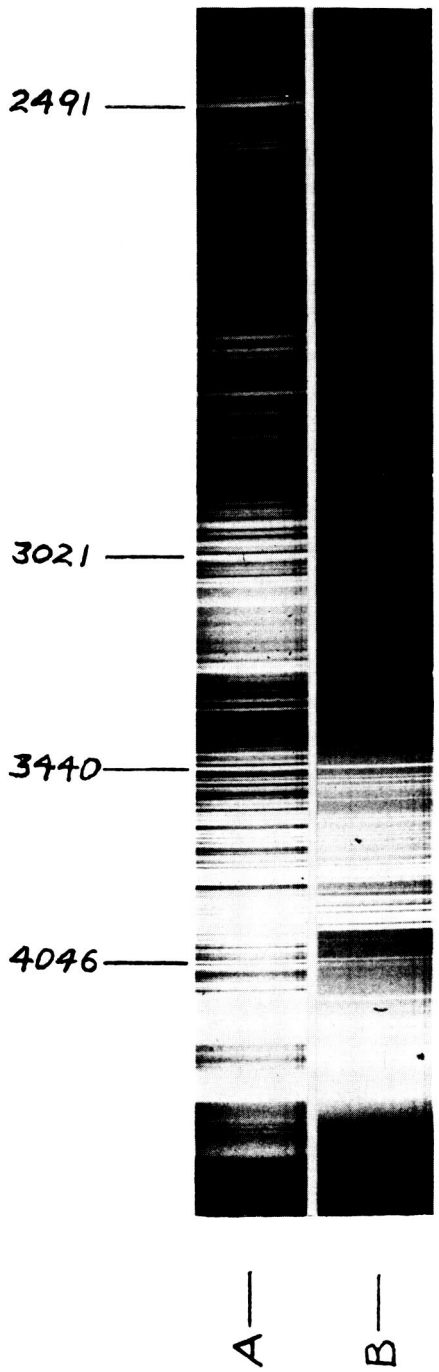

FIGURE 10. Spectra of rocket exhaust and open flame, Hilger F/4 quartz spectrograph, slit width 0.05 mm.

jet spectrum shows strong iron lines down to 2200 Å indicating a very high excitation temperature. In the propane flame, although the flame temperature is approximately equal to the jet temperature, the iron lines in the far ultraviolet are missing and the intensity distribution is dissimilar. The 4050 Å group of iron lines is a

good indication of non-equilibrium conditions. Iron appears strong in the jet spectrum but weak in the propane spectrum. Thus there seems to be strong indication that non-equilibrium conditions prevail in this case.

DISCUSSION

By comparing the n_f, n_Δ, and n_{eq} curves in Figure 6, the evidence indicates that:

(1) the ionization, which is in kinetic equilibrium in the chamber, maintains this equilibrium only part way down the supersonic nozzle;
(2) when the collision frequency is sufficiently reduced in the nozzle, the ionization relaxation becomes kinetically frozen, i.e., it varies with gas density only; and
(3) the ionization which occurs in the jet exhibits variations in intensity which follow the density profile in the jet and not the Saha equilibrium profile, and thus the jet ionization may be considered kinetically frozen.

Frozen kinetic equilibrium is not hard to visualize if the transit time between the shock diamonds is much smaller than the relaxation time. To find the transit time, the jet velocity is required. The jet velocity was determined to be 1.75 km/sec by measuring the Mach angle and using the equation

$$M = v/a = (\sin \theta)^{-1} \tag{13}$$

where $a = \sqrt{\gamma_g RT}$ is the speed of sound and θ is the Mach angle. Thus the transit time is seen to be

$$\tau = \frac{\Delta x}{v} \simeq 25 \ \mu\text{sec}$$

If this time is assumed to be the minimum electron half-life, then the maximum relaxation rate is just

$$\frac{dn}{dt} = \frac{n}{\tau} = 7.4 \times 10^{16} \frac{\text{electrons}}{\text{cm}^3 \text{ sec}}$$

It is known from shock tube experiments (**6**) that the ionization process is not instantaneous for gases passing through a shock front but requires approximately 20 μsec to thermalize. If the residence time of the jet gases in the leading half of the shock diamond exceeds this time, ample time for the gas to come to ionization equilibrium should be available. Then one would expect that the exit plane electron concentration would be suddenly raised by the first shock to a value proportional to the shock strength. It would then decrease at an exponential rate governed by the relaxation process and the cycle would be repeated at each successive shock. When, however, the residence time in the shock is less than the thermalizing time, the gas does not reach the ionization level which theoretically exists behind the shock. Furthermore, if the time interval between the shock diamonds is small, the reduction in ionization will also be small so that the average value of ionization may even increase down the jet axis. Figure 11 shows this effect demonstrated by probe curves made in the 28-SLM unseeded jet. The underexpanded 2-torr jet had an axial velocity of approximately 900 m/sec and a residence time in the first shock of approximately 30 μsec. The 10-torr jet had axial velocity of 1700 m/sec and residence time of approximately 13 μsec. The rise in the average intensity level down the axis of the 10-torr jet is apparent.

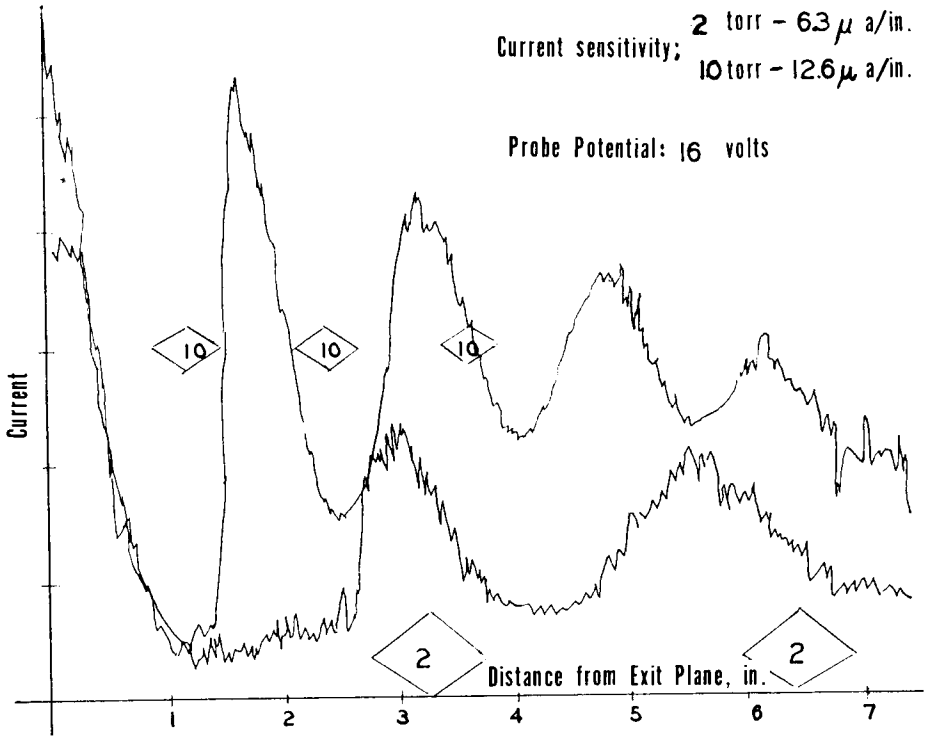

FIGURE 11. Typical conductivity probe curves in unseeded jets.

CONCLUSIONS

A study of the electrical and thermodynamic properties of a seeded, Mach-3 rocket exhaust at an equivalent altitude of 20–25 miles has been undertaken. This operating range was decided upon since the jet can be uniformly seeded, and the temperature and ionization can be measured by radiation methods.

The variations in the ionization density and dielectric properties of the jet were mapped, and the relaxation and attenuation properties of the seeded, high-altitude rocket exhaust were investigated. It was found that the profile of ionization down the jet depends upon the conditions at the exit plane and upon two other major factors: (1) the gas residence time in the shock diamond; and (2) the gas transit time between shocks.

Moreover, the data allows two possible relaxation mechanisms: (1) shock-induced ionization, which decays slowly according to the jet time-scale; and (2) frozen ionization, which is controlled only by chamber and nozzle conditions and follows the density profile identically.

The ionization in the jet is seen to exceed the Saha value (Figure 6) at all points in the jet of the premixed stoichiometric rocket. This is evidence of an electron density greater than the equilibrium value. The spectrographic analysis of the jet showed that the energy distribution in the excited states was also modified; excited lines were obtained which were not evident in the mantle of an atmospheric propane/air flame. Such non-equilibrium was attributed largely to an after-reaction of fuel-rich jets with the surrounding environment, since it was most prominent with shrouded, vortex jets.

It was fortuitous that our seeded jet (at 5 torr) produced a microwave operating point in the center of the narrow band lying between transparency ($n=5\times10^{11}$ cm^{-3}) and opacity ($n=1.2\times10^{13}$ cm^{-3}). Thus the 1-cm, KA-band microwave system is well suited to the study of seeded flames only at low pressures (where the collision frequency is of the order of 10^9 sec^{-1}).

ACKNOWLEDGMENTS

The authors wish to thank Mr. V. J. Siminski for his assistance in performing the experimental work, and Mr. W. Marsh, Dr. David Fleischer, and Mr. Ernest Hinck for their assistance in data evaluation. The funds granted to this project by the Air Force Office of Scientific Research are gratefully acknowledged.

REFERENCES

1. Warder, R. C., Brodwin, M., Cambel, Ali Bulent, "Microwave Measurements of Magneto-Gas-Dynamic Plasmas", *ASTIA AD-266-593* (August, 1961).
2. Warder, R., Nighan, W. L., Brodwin, M., and Cambel, Ali Bulent, "Microwave Diagnostics of Arc Heated Plasmas", in *Dynamics of Manned Lifting Planetary Entry* (New York: Wiley and Sons, 1963).
3. Kannelaud, J., and Whitmer, R. F., "Improved Microwave Techniques for Measuring Plasma Parameters", *ASTIA AD-225-405* (July, 1959).
4. Sutton, G. W., "The Theory of Magnetohydrodynamic Power Generators", G. E. Space Sciences Laboratory R62 SD990. Contract AF49(638)-914 (December, 1962).
5. Padley, P. J., and Sugden, T. M., "Some Observations on the Production and Recombination of Ions and Electrons from Metallic Additives in Hydrogen and Hydrocarbon Flames", *Proc. 8th Int. Symp. Comb.* (Baltimore: Williams and Wilkens Co., 1962), 164.
6. Wiese, W. C., Berg, H. F., and Griem, H. R., "Measurement of the Structure of Strong Shocks in Helium-Filled T-Tubes", *Phys. Fluids*, **4**, 2, 250 (1961).